3rd International Symposium on High-Temperature Metallurgical Processing

3rd International Symposium on High-Temperature Metallurgical Processing

Proceedings of a symposium sponsored by
the Pyrometallurgy Committee and
the Energy Committee of
the Extraction and Processing Division of
TMS (The Minerals, Metals & Materials Society)

Held during the
TMS 2012 Annual Meeting & Exhibition
Orlando, Florida, USA
March 11-15, 2012

Edited by

Tao Jiang
Jiann-Yang Hwang
Patrick Masset
Onuralp Yucel
Rafael Padilla
Guifeng Zhou

WILEY
A John Wiley & Sons, Inc., Publication

TMS

Published by John Wiley & Sons, Inc., Hoboken, New Jersey.
Published simultaneously in Canada.

Library of Congress Cataloging-in-Publication Data is available.

ISBN 978-1-11829-141-2

Printed in the United States of America.

10 9 8 7 6 5 4 3 2 1

WILEY

A John Wiley & Sons, Inc., Publication

TMS

TABLE OF CONTENTS
3rd International Symposium on High Temperature Metallurgical Processing

3rd International Symposium on High Temperature Metallurgical Processing

High Efficiency New Metallurgical Technology

Reduction and Titanium Production

Basic Research of Metallurgical Process

Alloy and Materials Preparation

Sintering and Synthesis

Energy and Environment

Treatment and Recycling of Solid Slag/Wastes

Pelletizing and Raw Materials Processing

Preface

This book collects selected papers presented at the 3rd International Symposium on High-Temperature Metallurgical Processing organized in conjunction with the 2012 TMS Annual Meeting in Orlando, Florida, USA.

As the title of symposium suggests it is on thermal processing of minerals, metals and materials and intends to promote physical and chemical transformations in the materials to enable recovery of valuable metals or produce products such as pure metals, intermediate compounds, alloys, or ceramics through various treatments. The symposium was open to participants from both industry and academia and focused on innovative high-temperature technologies including those based on non-traditional heating methods as well as their environmental aspects such as handling and treatment of emission gas and by-products. Since high-temperature processes require high energy input to sustain the temperature at which the processes take place, the symposium intends to address the needs for sustainable technologies with reduced energy consumption and reduced emission of pollutants. The symposium also welcomed contributions on thermodynamics and kinetics of chemical reactions and phase transformations that take place at elevated temperature.

Given the spread among numerous journals - not always easily accessible to many researchers – we decided to compile information on research activities in the area of metallurgy at elevated temperature in an easily accessible source and this book is the result. The availability of focused scientific information into a few accessible resources should be attractive and gratifying to many researchers.

Over 300 authors have contributed to the symposium with a total of 94 presentations. After reviewing the submitted manuscripts, 62 papers were accepted for publication on this book. The book is divided into eight sections and each section has different focus. It includes: High Efficiency New Metallurgical Technology, Reduction and Titanium Production, Basic Research of Metallurgical Process, Alloy and Materials Preparation, Sintering and Synthesis, Energy and Environment, Treatment and Recycling of Solid Slag/Wastes, and Pelletizing and Raw Materials Processing.

This is the second book exclusively dedicated to this important and burgeoning topic published in the 21 century. We hope this book will serve as a reference for both new and current metallurgists, particularly those who are actively engaged in exploring innovative technologies and routes that lead to more energy efficient and environmentally sustainable solutions.

This book could not materialize without contributions from the authors of included papers, time and effort that reviewers dedicated to the manuscripts, and help from the publisher. We thank them all! We are also grateful to Ms. Yanfang Huang and Mr. Guihong Han for their assistance in collating the submitted abstracts and manuscripts.

Tao Jiang, Jiann-Yang Hwang, Patrick Masset, Onuralp Yucel, Rafael Padilla, and Guifeng Zhou

December 2011

Editors

Tao Jiang was born in 1963 in Anhui, China, Tao Jiang received his MS degree in 1986 in metallurgy and Ph.D. degree in mineral processing in 1990, both from Central South University of Technology, China. Then he worked at the university for ten years as an assistant professor and full professor (from 1992). From 2000 to 2003, he was a Visiting Scientist in the University of Utah.

Since 2003, Dr. Jiang has been a Professor in the School of Minerals Processing & Bioengineering at Central South University. He was elected as Specially-appointed Professor of Chang Jiang Scholar Program of China in 2008 and was appointed as dean of the school in 2010. Some of his current research activities include beneficiation, agglomeration, reduction and utilization of complex iron ores, and extraction of refractory gold ores. He has accomplished more than 30 projects from the government and industry, including National Science Fund for Distinguished Young Scholars program. Dr. Jiang has published 248 technical papers, 5 books, holds 25 patents and has more than 30 conference presentations.

Currently, Dr. Jiang serves as vice-Chair of the TMS Prometallurgy Committee, member of Ironmaking Committee, Chinese Society for Metals.

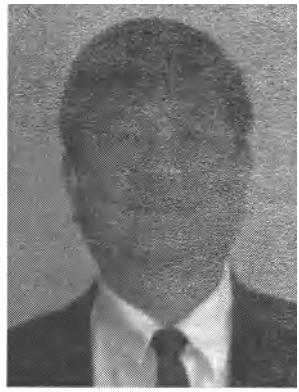

Jiann-Yang (Jim) Hwang is a Professor in the Department of Materials Science and Engineering at Michigan Technological University. He is also the Chief Energy and Environment Advisor of the Wuhan Iron and Steel Group Company. He has been the Editor-in-Chief of the Journal of Minerals and Materials Characterization and Engineering since 2002. Several universities have honored him as a Guest Professor, including the Central South University, University of Science and Technology Beijing, Chongqing University, Kunming University of Science and Technology, etc.

Dr. Hwang received his B.S. degree from National Cheng Kung University (Taiwan) in 1974, M.S. in 1980 and PhD in 1982, both from Purdue University. He joined Michigan Technological University in 1984 and has served as its Director of the Institute of Materials Processing from 1992 to 2011. He has been a TMS member since 1985. His

research interests include the characterization and processing of materials and their applications. He has been actively involved in the areas of separation technologies, pyrometallurgy, microwaves, hydrogen storages, ceramics, recycling, water treatment, environmental protection, biomaterials, and energy and fuels. He has more than 20 patents, published more than 200 papers, and founded several companies. He has chaired the Materials Characterization committee and the Pyrometallurgy committee in TMS and has organized several symposiums.

Patrick Masset was born in 1974 in Saint Pierre d'Albigny (France), Patrick obtained his Ph.D thesis at the National Polytechnic Institute of Grenoble in 2002. From 2003 to 2005, he was a post-doc at the Institute for Transuranium (European Commission) in Karlsruhe (Germany) before joining Dechema in Frankfurt/Main (Germany) as a Research Associate. In 2009, he was appointed as Research Group Leader at the Technical University of Freiberg (Germany). In 2010, he obtained his habilitation in the field of High Temperature Materials at the University of Pierre and Marie Curie in Paris, France and is a lecturer at the University of Freiberg and the University of Savoy (France). Since January 2012, he is the Head of the Department "New Materials" at the Research Centre ATZ in Sulzbach-Rosenberg in Germany. His research activities are focused on the development of new materials for energy and power engineering.

Onuralp Yucel was born in 1961 in Diyarbakir, Turkey; Onuralp completed his technical education with a PhD in Metallurgical Engineering from Istanbul Technical University (ITU) where he is currently holding the post of Professor since 2002. He was a Visiting Scientist in Berlin Technical University between 1987 and1988. He carried out Post Doctoral Studies at New Mexico Institute of Mining and Technology, Socorro, USA between 1993 and 1994. Prof. Yücel has as many as 147 publications/ presentations to his credit, which include topics like, technological developments in the production of wide range of metals, ferroalloys, advanced ceramic powders and application of carbothermic and metalothermic processes among others. He is currently the director of ITU, Applied Research Center of Material Science & Production Technologies since 2006.

Dr. Rafael Padilla received his Ph. D. and M.Sc. degrees in Metallurgy from the University of Utah in 1984and 1977, respectively, and Professional Engineering Title as Metallurgical Engineer from the Technical University of Oruro, Bolivia in 1975. Dr. Padilla joined the Department of Metallurgical Engineering, University of Concepcion, Chile in 1986, and currently holds the rank of Professor in that Department. He has conducted research involving thermodynamics and kinetics of metallurgical reactions in both pyrometallurgy and hydrometallurgy, volatilization of toxic minor elements in copper metallurgy, mathematical modeling of solvent extraction processes, atmospheric leaching and pressure leaching of refractory copper and arsenic sulfides. His present research interests continue on the development of new processing methods for primary sulfides including chalcopyrite, enargite, and molybdenite.

Guifeng Zhou received his BS degree in Materials Science and Engineering from the Northwest Industry University (China) in 1984, his MS degree in Materials and Heat Treatment from the HuaZhong University of Science and Technology in 1990, and earned his Ph.D. degree in Materials Physics and Chemistry from the University of Science and Technology Beijing in 2000. He did some research regarding microalloying technology at University of Pittsburgh for a year and a half as a senior visiting scholar.

Dr. Zhou is the vice director of the R&D Center of Wuhan Iron & Steel (Group) Corp., also is a professor and Ph.D. advisor of Wuhan University of Science and Technology. His work is concentrated on new steel product development, microstructure and mechanical property of materials. Dr. Zhou has published over 20 technical papers, holds 4 patents, and won national progress prize in science and technology for three times. He is an expert with the State Department on special allowance, a member of the editorial board of RESEARCH ON IRON AND STEEL, and has been the member of the Chinese Metals Society, the Quality Control Society of China and the Science and Technology Association

3rd International Symposium on High-Temperature Metallurgical Processing
Edited by: Tao Jiang, Jiann-Yang Hwang, Patrick Masset, Onuralp Yucel, Rafael Padilla, and Guifeng Zhou
TMS (The Minerals, Metals & Materials Society), 2012

3rd International Symposium on High-Temperature Metallurgical Processing

High Efficiency New Metallurgical Technology

Session Chairs:
Tao Jiang
Merete Tangstad

3rd International Symposium on High-Temperature Metallurgical Processing
Edited by: Tao Jiang, Jiann-Yang Hwang, Patrick Masset, Onuralp Yucel, Rafael Padilla, and Guifeng Zhou
TMS (The Minerals, Metals & Materials Society), 2012

A LABORATORY INVESTIGATION OF THE REDUCTION OF THE SIDERITE IRON ORE TO IRON NUGGET

Panishev N.V. , Redin E.V.
Magnitogorsk Iron & Steel Works (MMK)
Open Joint Stock Company
93 Kirova St, Magnitogorsk 455002, Russia

Pilshchikov V.I.
Hares Engineering GmbH
Post Box 86, Kiev 170, 031170 Ukraine

Siderite, Rotary Hearth Furnace, ITmk3, Iron Nugget

Abstract

The Bakal (South Ural, Russia) deposit of iron ore bearing iron carbonate (siderite) with the capacity of more than 1 billion tones belongs to the MMK. This ore cannot be fully processed via blast furnace technology because of high content of MgO. According to the investigations carried out in the USA and Japan in 1999-2004 the ITmk3 (Ironmaking Technology mark three) RHF technology is a breakthrough in Ironmaking. Four iron ore types (hematite, magnetite, high and low Al_2O_3/SiO_2) were tested. Reduction, melting and slag removal can be achieved in just 10 min. The main objective of the investigation is to establish optimum operation conditions for the production of iron nuggets from iron carbonate bearing ore via the ITmk3 by means of the lab scale testing. Green pellets were processed via a lab tube (chamber) furnace to simulate RHF conditions. This preliminary test work provides valuable information which may be used for large-scale testing in a commercially sized RHF.

Introduction

The ITmk3 process upon which this paper focuses was developed by Kobe Steel in its research facilities in 1996 [1]. After pilot testing at Kobe Steel's Kakogava Works in 1999-2004 the pilot demonstration plant was built and operations were successfully carried out by Mesabi Nugget joint venture in 2002-2004. Steel Dynamics has committed to building the commercial plant at the Mesabi Nugget site in Hoyt Lakes (Minnesota). Only 4 iron ore types (hematite, magnetite, high Al_2O_3/SiO_2 and low Al_2O_3/SiO_2), as well as 4 coal types with range of volatility, ash and fixed carbon were tested. Results were consistent with nugget characteristics confirming ITmk3's flexibility with respect to raw material inputs. At the same time, no research in the field of nugget from iron carbonate bearing ore with high content of MgO has been done. Such kind of iron ore is restricted for charging into the blast furnace due to contamination of MgO. The reason for restriction is the limitation of load of MgO in the blast furnace. If a lot of MgO enters the blast furnace, slag becomes viscous. The viscous slag is obstacle for stable operation of the blast furnace.

Objectives of Investigation

The main objective is to find optimum operation conditions for the production of iron nuggets from the iron carbonate (siderite) bearing ores via the rotary hearth furnace by means of the laboratory testing.

Methodology

The first step in the investigation involved performing lab scale testing on the iron nugget components. Samples of iron ore, fluxes, binder (clay), coal fines and coke breeze (as reductant) were chemically and physically analyzed.

Typical ore testing included particle size analysis, % S, % CO_2, % metal components, % gangue components. Typical reductant testing included particle size analysis, % carbon, % sulfur, % volatiles, % ash and ash analysis for % metal and gangue components.

A pellet blend developed from this testing, defining carbon reductant addition, binder, particle size. A blend was mixed followed by rolling green pellets.

Green pellets were processed via a lab tube furnace or a chamber furnace. Using such kind of furnaces to simulate RHF conditions, was it possible to vary several parameters such as furnace retention time (10-15 min), temperature (1350-1450°C).

After the allotted time in the hot furnace, the nuggets and slag were quenched, then analyzed for % C, % S, % Fe in iron nuggets, and % gangue components in slag.

Results and Discussion

Each raw material is different in distribution of the particle size and chemical compositions (See Table 1).

Table 1.Dry Chemical Composition of Raw Materials, wt. %

Material	Fe	CaO	SiO_2	MgO	Al_2O_3	CO_2	C	CaF_2
Bakal Iron Ore	34.0	2.2	3.2	9.8	1.2	29.0	-	-
Coke Breeze	0.9	0.7	8.0	0.3	3.1	-	87.0	-
Quartzite	0.5	0.4	95.6	-	0.6	-	-	-
Clay	1.8	0.4	51.0	0.8	35.3	-	-	-
Fluor-spar	-	1.0	36.8	0.5	0.6	-	-	52.5

Mainly considered are raw material preparation (weighing, blending, grinding), pelletizing, heating, reacting and melting control. In particular, material preparation is very important, since influence of the properties of raw materials on operational results (especially

the temperature of melting of gangue) is large. Thus a precise preparation work for raw materials is needed for desirable and stable operation.

Raw materials were blended in a disc grinder at a predetermined mixing ratio to reach desirable temperature (1300-1400°C) of melting of gangue [2]. Gangue composition is shown below (See Table 2).

Table 2. Chemical Composition of Gangue, wt.%

CaO	MgO	Al_2O_3	SiO_2
20.0-41.5	5.0-16.5	5.0-15.0	40.0-60.0

Particle size of -200 meshes for raw materials usually results in higher iron metallization. More intimate contact between carbon and iron oxide speeds reaction. Ability to pelletize determines maximum particle size. The mixing ratio was determined to give good conditions of palletizing and the reactions in the furnace. The ratio of fix carbon to iron oxides and other properties of raw materials were analyzed. Then the mixing ratio was determined (binder - 1-2%, coke breeze -18-20%, fluxes -12-18%, iron ore -60-69%) with this information. The mixture was fed on the palletizing disc, and made into green pellets. Diameter of green pellet is less than 20 millimeters. If the pellet is too large, heat transfer rate is too slow inside the pellet. Green pellets were dried in the chamber furnace (150-300°C). The dried pellets were fed in the roasting furnace. To reach conditions for better reactions and heat exchange entire pellet bed must be heated to 1350-1450°C. Nuggets contained 96-97% of iron and 2-3% of carbon.

Carbonates (siderite, magnesite, dolomite, etc.) in the pellets dissociate when temperature of the pellets is above 600°C.

$$FeCO_3 = FeO + CO_2 \quad (1)$$

$$MgCO_3 = MgO + CO_2 \quad (2)$$

$$CaCO_3 = CaO + CO_2 \quad (3)$$

Carbon and iron oxide react when temperature of the pellets is above 1100°C.

$$C + CO_2 = 2CO \quad (4)$$

$$FeO + CO = Fe + CO_2 \quad (5)$$

$$FeO + C = Fe + CO \quad (6)$$

Formation of pig iron and melting of nuggets and slag from gangue take place when temperature of the pellets is above 1300°C.

$$3Fe + C = Fe_3C \quad (7)$$

$$3Fe + 2CO = Fe_3C + CO \quad (8)$$

Thus, the RFH should have heating, reduction and melting zones. Temperature in each zone should be controlled to get a good performance that is required in each zone. In heating zone, heat transfer for heating up the pellets and dissociation of carbonates should be taken into account. Oxidation of the gas is high here, because no reduction reaction takes place. In reduction zone, temperature and atmosphere of the gas should be controlled to get a high reaction rate. The reduction reactions in this zone are very fast. At last, in melting zone, the conditions should be controlled to promote the reduction reactions, formation of pig iron (iron nugget) and melting of pig iron and slag.

Conclusions

The possibility of production of iron nugget from iron carbonate bearing ore with high content of MgO via ITmk3 process has been established. The initial promise shown by the ITmk3 process in laboratory tests may be used for large-scale testing in a commercially sized RHF.

ITmk3 technology is a simple process with a single-step furnace operation. Reduction, melting and slag separation completes within 10-15 minutes. Process temperature is 1350-1450°C.

ITmk3 technology makes no harmful impact on environment since the process does not require coking and sintering plants.

References

1. J.A. Hansen, "Mesabi Nugget-The New Age of Iron", AISTTech 2004 Proceedings. 2004, vol.1, 545-550.

2. N.L. Zhilo, *Formation and Characteristics of Blast Furnace Slag* (Moscow: Metallurgy, 1974), 120.

3rd International Symposium on High-Temperature Metallurgical Processing
Edited by: Tao Jiang, Jiann-Yang Hwang, Patrick Masset, Onuralp Yucel, Rafael Padilla, and Guifeng Zhou
TMS (The Minerals, Metals & Materials Society), 2012

COMPOSITE AGGLOMERATION PROCESS OF IRON FINES

Tao Jiang[1], Youming Hu, Guanghui Li, Yufeng Guo,
Zhengwei Yu, Xiaohui Fan, Yuanbo Zhang, Yongbin Yang

School of Minerals Processing and Bioengineering, Central South University, Changsha, Hunan 410083, P.R. China

Keywords: Sintering, Pelletizing, Composite Agglomeration, Blast Furnace Burden

Abstract

Composite agglomeration process (CAP), as an innovative method for preparing blast furnace burden, was developed and has been put into operation in China. CAP is different from traditional agglomeration processes of iron-bearing materials involving sintering and pelletizing. Compared to the traditional agglomeration processes, CAP is characterized by several strengths such as permission of diverse iron-bearing materials in production, obvious improvement of permeability in the feed bed, decreasing the fuel consumption and remarkably increasing the productivity of sintering machine. Furthermore, the use of the composite agglomerates prepared with CAP is capable of obviating the negative effects caused by the differences in quality of sinter and pellets on the operation of blast furnaces. This paper mainly presents an overview of the principle and applications of CAP.

Development Background and Principle of CAP

The traditional agglomeration processes including sintering and pelletizing have been the two predominant methods for preparing ironmaking burden from iron-bearing materials. Sintering is a way for agglomeration by heating the coarser fine ores (general granularity 0~10mm). The mechanical strength of irregular porous sinter is obtained by the solidification of molten phase at high temperature process. It has been shown that the production of high basicity sinter (R=1.8~2.2) is characterized by low energy consumption and high efficiency compared to low basicity sintering. Meantime, the finished high basicity sinter is characterized by good mechanical strength and metallurgical performance. Pelletizing is another way for agglomeration by firing wet green pellets, which are balled from the fine grained iron ores or concentrates. Based on the differences of chemical compositions, the finished pellets can be divided into acidic oxidized pellets, fluxed pellets, magnesium-bearing pellets, and so on. The acidic oxidized pellets are the dominant products of modern pelletizing.

At present, the combination of self- or super-fluxed sinter and acidic oxidized pellets is the common application of their products in blast furnace in China and most of other countries. However, there are several shortcomings with the use of acidic oxidized pellets along with high basicity sinter. First, the higher bulk density leads to the tendency for pellets to "sink" into the coke layer during burden descent, resulting into the segregation of burdens although

[1] Corresponding author: Tao Jiang, Professor, E-mail: jiangtao@csu.edu.cn.

some approaches has been undertaken to offset the differences among the varied iron bearing burdens, effects of varied iron bearing burdens on the operation of blast furnace are still inevitable. Second, this kind of burden structure is not readily achieved considering that commercial pellets are only produced in a few countries and pelletizing plants must be built to meet the increasing demand of pellets in most of countries, particularly in China. The last but important is that, the increasing inferior or non-traditional iron-bearing materials such as fine grained concentrates obtained from refractory ores through grinding and concentrating mill, and iron-bearing wastes (dust and slug) from various plants can't be efficiently employed by single sintering process or single pelletizing process, and call for new agglomeration process.

Composite agglomeration process (CAP) was developed in order to overcome the weakness of oxidized pellets associated with their ball shape and make the best of the increasing non-traditional iron-bearing materials [1-10]. An innovative technological thought in CAP is proposed based on the differences in the properties of pelletizing, sintering and firing of varied iron-bearing materials. In the CAP, all of raw materials are classified into pelletizing feeds and matrix feeds. Subsequently, those two classified feeds are pretreated respectively, and fired together in sintering machine. The pelletizing feeds include fine grained ores, concentrates obtained from the grinding process of refractory and complex iron ores, iron-bearing secondary resources, binders and fuels sometimes. A small amount of ground fuel addition (less than 1.0 mass %) in the pelletizing feeds contributes to the quality of finished pellets when hematite or specularite concentrates are pelletized, while fuel addition in pelletizing feeds can be neglected for magnetite pellets feed. The matrix feeds consist of coarser ore fines, fluxes, fuels and return fines. Sometimes, iron concentrates are also included in matrix feeds when the proportion of iron concentrates to the whole iron-bearing materials is above 60%.

The principle of CAP can be seen from Fig.1. As displayed in Fig.1, pelletizing feeds are mixed and agglomerated into green pellets with 8~16 mm diameter; matrix feeds are blended, granulated and made into a primary mixture with 3~8 mm diameter. Afterwards a secondary mixture is prepared by mixing those green pellets with the primary mixture, and the secondary mixture is subsequently distributed onto the sintering machine. Finally, the mixture is produced into the composite agglomerates consisting of basic sinter and acidic pellets by ignition and down draft firing. In the composite agglomerates, acidic pellets are well embedded in basic sinters. According to the study of the mineralization mechanism, the mechanical strength of acidic pellets in mixture is obtained by solid phase consolidation; and the mechanical strength of matrix is due to fusion phase bonding.

Compared to traditional agglomeration processes, CAP is characterized by several strengths such as permission of diverse iron-bearing materials in production, obvious improvement of permeability in the feed bed, decreasing the energy consumption and absolutely increasing the productivity of sintering machine. For example, overall basicity of composite agglomerates can be adjusted from 1.2 to 2.2 by changing the proportion of acidic pellets. The use of the composite agglomerates is capable of eliminating the negative effects of burden segregation which are caused by the different property of sinter and pellets in blast furnaces. Meantime, the problems accompanying with the use of the increasing complex ores or non-traditional iron-bearing materials can also be solved by CAP.

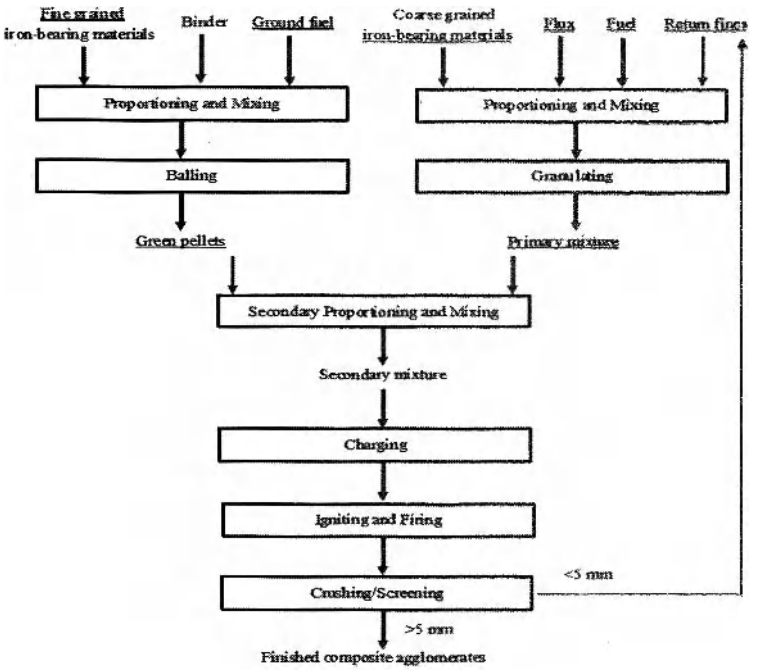

Fig.1 Principle of CAP

Function and Applications of CAP

Preparation of Ironmaking Burden Characterized by Low Basicity

The iron-bearing materials were obtained from Lianyuan Iron and Steel Plant, China. Under the condition of feed bed height 600 mm, the preparation of ironmaking burden characterized by low basicity using CAP and traditional sintering process (TSP) were respectively conducted in lab. The results are shown in Table I.

As displayed in Table I, the tumbler index of finished products obtained from TSP is decreased from 63.0% to 52.7% with decreasing the overall basicity from 2.0 to 1.5, accompanying with the productivity decreasing from 1.65 $t \cdot m^{-2} \cdot h^{-1}$ to 1.47 $t \cdot m^{-2} \cdot h^{-1}$. When the overall basicity is 1.2, the tumbler index of finished products and the productivity are separately 45.9% and 1.37 $t \cdot m^{-2} \cdot h^{-1}$.

It can also be seen from Table I, although the tumbler index of finished products obtained from CAP is decreased with the decrease of overall basicity, the tumbler index of finished products, the sintering speed and the productivity of CAP are obviously high. The tumbler index of finished products is 58.7% under the condition of the overall basicity 1.2. And the coke dosage and the suction negative pressure in the CAP can be obviously lowered.

Table I. Comparison of CAP and TSP in the Field of Preparing Ironmaking Burden with Different Basicity

Process	Experimental conditions			Experimental indexes		
	Overall basicity	Suction negative pressure (kPa)	Coke dosage (mass %)	Vertical sintering speed ($mm \cdot min^{-1}$)	Productivity ($t \cdot m^{-2} \cdot h^{-1}$)	Tumbler index (+6.3mm, mass %)
TSP	2.0	10	4.5	19.85	1.65	63.0
CAP	2.0	8	4.0	23.41	2.16	67.3
TSP	1.6	10	4.5	19.75	1.46	54.2
CAP	1.6	8	4.0	21.69	1.95	63.1
TSP	1.5	10	4.5	19.70	1.47	52.7
CAP	1.5	8	4.0	23.13	2.01	62.3
TSP	1.4	10	4.5	20.75	1.42	50.0
CAP	1.4	8	4.0	23.30	1.85	61.8
TSP	1.2	10	4.5	20.87	1.37	45.9
CAP	1.2	8	4.0	23.04	1.80	58.7

Preparation of Ironmaking Burden from High Iron and Low Silica Materials

The high iron low silica materials were firstly balled into pellets. The overall basicity of the final mixture is fixed at 1.9. The results for preparation of ironmaking burden using CAP are listed in Table II.

Table II. Preparation of Ironmaking Burden from High Iron and Low Silica Materials using CAP

Process	Experimental conditions			Experimental indexes		
	Proportion of Pellets (mass %)	SiO_2 (mass %)	TFe (mass %)	Vertical sintering speed ($mm \cdot min^{-1}$)	Productivity ($t \cdot m^{-2} \cdot h^{-1}$)	Tumbler index (+6.3mm, mass %)
TSP	0	4.51	57.66	21.10	1.39	64.17
CAP	10	4.37	58.01	21.54	1.42	65.24
CAP	20	4.26	58.28	23.73	1.57	66.47
CAP	40	4.06	58.77	24.98	1.71	71.12

As seen from Table II, the tumbler index of finished products obtained from CAP, the vertical sintering speed and the productivity of CAP are increased with the increase of the proportion of pellets. The tumbler index of finished products, the vertical sintering speed and the productivity of CAP are respectively 71.12 mass%, 24.98 $mm \cdot min^{-1}$ and 1.71 $t \cdot m^{-2} \cdot h^{-1}$ under

the condition of the ratio of pellets 40 mass%.
Compared with TSP, the tumbler index of finished products, the vertical sintering speed and the productivity of CAP are obviously high. Meantime, it can be seen that the content of SiO_2 is decreased, while total iron (TFe) grade is increased.

Achievement of Ultra-high Feed Bed in Preparation of Ironmaking Burden

The iron-bearing materials were also obtained from Baosteel Company, China. Experimental conditions are fixed as follows: the proportion of balling concentrates 40 mass%, overall basicity 1.9 and suction negative pressure 8 kPa. The effects of feed bed height on the experimental indexes of CAP are shown in Table III.

Table III. Effects of Feed Bed Height on Experimental Indexes of CAP

Process	Feed bed height (mm)	Vertical sintering speed ($mm \cdot min^{-1}$)	Productivity ($t \cdot m^{-2} \cdot h^{-1}$)	Tumbler index (+6.3mm, mass %)
TSP	600	19.85	1.65	63.0
CAP	600	24.56	2.23	60.9
CAP	700	23.33	1.97	63.0
CAP	800	21.45	1.80	65.2
CAP	900	20.98	1.73	65.9

As seen from Table III, the feed bed height has an obvious improvement on the tumbler index of finished products obtained from CAP. Although the productivity and the vertical sintering speed are both decreased with increasing the feed bed height, the productivity of CAP with the bed height of 900 mm is still higher than that of TSP at 600 mm.

Preparation of Ironmaking Burden from Refractory Iron-bearing Materials

Specularite. Specularite concentrates are characterized by bad high-temperature reactivity, which restrict the large-scale application of them in either pelletizing or sintering production. The effects of the proportion of specularite concentrates are shown in Table IV.

Table IV. Effects of the Proportion of Specularite Concentrates on Experimental Indexes of CAP

Process	Proportion of Specularite (mass %)	Vertical sintering speed ($mm \cdot min^{-1}$)	Yield (%)	Productivity ($t \cdot m^{-2} \cdot h^{-1}$)	Tumbler index (+6.3mm, mass %)
TSP	0	21.10	78.45	1.390	64.17
TSP	20	15.85	69.92	0.929	63.45
CAP	20	23.73	79.32	1.572	66.47
CAP	25	23.90	79.81	1.604	67.08
CAP	40	24.98	81.33	1.710	71.12

It can be seen from Table IV, the experimental indexes are decreased significantly with the increase of the proportion of specularite in TSP. Especially, the productivity of TSP is reduced by 30% or more when the proportion of specularite is increased from 0% to 20%. Compared to TSP, however, the experimental indexes of CPA are improved significantly with the increase of the proportion of specularite.

Fluorine-bearing Iron Concentrates. Former studies showed that addition of fluorine-bearing iron concentrates into sintering feeds decreases the mechanical strength of sinter by promoting the formation of low strength cuspidine. The addition of fluorine-bearing iron concentrates into pelletizing feeds can also deteriorate the quality of finished pellets. The fluorine-bearing iron concentrates in this section were obtained from Baotou Iron and Steel Company, China. The content of fluorine is 0.34%. The proportion of fluorine-bearing iron concentrates to iron-bearing concentrates is set at 40% (mass). And fluorine-bearing iron concentrates were firstly balled into pellets in CAP. The results are listed in Table V.

Table V. Comparison of CAP and TSP in the Field of Preparing Ironmaking Burden from Fluorine-bearing Iron Concentrates

Process	Overall basicity	Vertical sintering speed ($mm \cdot min^{-1}$)	Productivity ($t \cdot m^{-2} \cdot h^{-1}$)	Tumbler index (+6.3mm, mass %)
TSP	2.2	21.52	1.395	57.71
TSP	1.6	18.32	1.420	51.45
CAP	1.6	20.08	1.504	64.05

As demonstrated in Table V, the tumbler index and the productivity in CAP are both higher than those in TSP. Compared to TSP, the tumbler index of finished products obtained from CAP is 64.05% when overall basicity is 1.6, with productivity is 1.504 $t \cdot m^{-2} \cdot h^{-1}$.

Iron-Bearing Dusts & Sludges. With the rapid development of iron and steel industry, lots of metallurgical dusts and sludges are generated. When used in sintering or pelletizing production, they deteriorate the performances of production due to their poor hydrophilicity and bad ballability. Comparison of CAP and TSP in the field of preparing ironmaking burden from iron-containing dusts & sludges is displayed in Table VI.

Table VI. Comparison of CAP and TSP in the Field of Preparing Ironmaking Burden from Iron-containing Dusts & Sludges

Process	Treatment of dusts & sludges	Vertical sintering speed ($mm \cdot min^{-1}$)	Productivity ($t \cdot m^{-2} \cdot h^{-1}$)	Tumbler index (+6.3mm, mass %)
TSP	Without dusts & sludges	23.87	1.475	65.20
TSP	Blended into sintering mixture	21.65	1.355	63.41
CAP	Prepared into pellets	23.73	1.580	65.93

As shown in Table VI, the addition of dusts and sludges has an obvious negative effect on the tumbler index and the productivity in TSP. Compared to TSP, the productivity and the tumbler index of finished products in CAP are improved obviously by preparing dusts &

sludges into pellets.

Vanadium/titanium-bearing Magnetite. Because of small specific surface area and poor ballability, vanadium/titanium-bearing magnetite is difficult for the production of oxidized pellet. Meantime, the mechanical strength of sinter is decreased with increasing proportion of vanadium/titanium-bearing magnetite in the sintering production.
The vanadium/titanium-bearing magnetite concentrates in this section were obtained from Panzhihua Iron and Steel Company, China. The proportion of vanadium/titanium-bearing magnetite concentrates to iron-bearing materials is 55%. The test result is listed in Table VII. Compared to TSP, various indexes in CAP are improved obviously.

Table VII. Comparison of CAP and TSP in the Field of Preparing Ironmaking Burden from Vanadium/titanium-bearing Magnetite

Process	Coke dosage (kg/t)	Vertical sintering speed ($mm \cdot min^{-1}$)	Yield (%)	Productivity ($t \cdot m^{-2} \cdot h^{-1}$)	Tumbler index (+6.3mm, mass %)	Permeability index (JPU)
TSP	63.01	21.00	73.89	1.258	55.20	0.174
CAP	57.37	22.71	81.30	1.570	62.13	0.211

Industrial Application of CAP

The CAP had been put into industrial production in Baotou iron and steel company since April, 2008. The iron-bearing materials were mainly composed of fluorine-bearing iron concentrates during testing. Under the condition of overall basicity 1.53, the operation rate of sintering machine was improved 2.81% by using CAP. Meantime, the average daily yield was increased by 210 t/d. The fuel consumption was reduced by 7.87 kg/t.
Ironmaking operation showed that the TFe grade of blast furnace burden was increased by 0.19% when the finished composite agglomerates were used. The dosage of silica stone was decreased from 25.87 kg/t to 13.6 kg/t. The slag rate was reduced by 41.0 kg/t. The productivity of blast furnace was increased by 0.209 $t/m^3 \cdot d$, with the dosage of coal powder injection increased by 6.77kg/t. From three years of production operation, the overall economic efficiency of CAP is very significant. All of TSP in Baotou iron and steel plant will be replaced by CAP in the future.

Comprehensive Comparison of CAP with Other Agglomeration Processes

The technological characteristics of several agglomeration processes involving CAP, sintering, pelletizing and hybrid pelletized sintering (HPS) are summed up and listed in Table VIII.
From Table VIII, it can be found that CAP is different from those agglomeration processes of iron-bearing materials involving sintering, pelletizing and HPS. Based on the technological characteristics, CAP can be considered as alternative to traditional agglomeration processes for ironmaking burden.

Table VIII. Comprehensive Comparison of CAP with Other Agglomeration Processes

Agglomeration Process	Sintering	Pelletizing	HPS [11-14]	CAP
Size range of raw materials	0-10 mm	-0.045mm accounting for 80%~90%	0~5 mm	Pelletizing Materials: -0.075 mm 60%~90% Matrix materials: -10 mm
Type of raw materials	Fine ores or concentrates	Concentrates	Concentrates or fine ores	Fine ores, Concentrates or iron-containing dusts & sludges
Granulation or pelletizing preparation	All of materials are granulated into 3~10 mm in diameter	All of materials are pelletized into12~16 mm in diameter	All of materials are pelletized into 5~10 mm in diameter	Matrix materials are granulated into 3~10 mm, Pelletizing materials are pelletized into 8~16 mm in diameter
Adding manner of fuels	All is added into feeds	Heating by external system	A part is added into feeds and the rest is used to pack the pellets	All is added into feeds
Requirement for drying process	Not needed	Needed	Needed	Not needed
Consolidation mechanism	Consolidation via molten phase	Consolidation via solid phase	Consolidation via solid phase	Consolidation via molten liquid phase and solid phase
Appearance of finished products	Irregular lumps	Ball shape	botryoidal micropellet aggregates	Irregular lumps of acidic pellets embedded in high basicity sinter
Overall basicity of product	1.8~2.2	<0.2	<1.2 or >2.0	1.2~2.2

Conclusions

Composite agglomeration process (CAP) is an innovative method for preparing blast furnace burden. Compared to sintering and pelletizing processes, CAP is characterized by many advantages such as suitability for varied iron-bearing materials in production, obviously improving the permeability of the feed bed, reducing the energy consumption and increasing the productivity of sintering machine. The overall economic efficiency of CAP is very significant when the finished agglomerates are used in ironmaking operation. Therefore, CAP is a promising agglomeration processes for ironmaking burden.

Acknowledgements

The authors want to express their thanks to the supports from Iron and Steel Plants including

Lianyuan, Baoshan, Baotou, Taiyuan, Kunming, the supports of professor Lingtan Kong, Tianjun Yang, and Weixing Wang, and the financial supports from National Science Fund for Distinguished Young Scholars (Grant No. 50725416) and National Science Foundation of China (Grant No. 50604015) for this study.

References

1. T. Jiang et al., "Composite Agglomeration Process of Iron Ore Fines" (Patent 200510032095.6 in China).
2. T. Jiang et al., "A Distribution Method of Feeds for Composite Agglomeration Process of Iron Ore Fines" (Patent 200910303235.7 in China).
3. G.H. Li et al., "A Method for Preparation of Low Basicity Sinter" (Patent 200710034842.9 in China).
4. G.H. Li et al., "A Sintering Method for High Proportion of Specularite Concentrates" (Patent 2009103032342.2 in China).
5. T. Jiang et al., "A Method for Preparation of Acidic Pellets" (Patent 99115416.9 in China).
6. T. Jiang et al., "Composite Agglomeration Process (CAP) for Preparing Blast Furnace burden", *Ironmaking & Steelmaking*, 37(1) (2010), 1-7.
7. G.H. Li et al., "Study and Application of Composite Agglomeration Process of Fluoric iron concentrate" (Paper presented at the Proceeding of 5th International Congress on the Science and Technology of Ironmaking, Shanghai, Oct, 2009), 149-153.
8. T. Jiang et al., "Concept and Research of Composite Agglomeration Process of Iron Ore Fines" (Paper presented at the Proceeding of 2006 National Annual Conference on Technical Exchange of Sintering & Pelletizing, Hohhot, Jun, 2006), 1-6.
9. T. Jiang et al., "Composite Agglomeration Process of Iron Ore Fines" (Paper presented at the Proceeding of 2006 National Annual Conference on Technical Exchange of Pelletizing, Zhangjiajie, Sep, 2006), 52-56.
10. T. Jiang, K.C. Zhang and Y.M. Hu, "Study on Mineralization Mechanism of Composite Agglomeration Process of Iron Ore Fines" (Paper presented at the 06'International Conference on Agglomeration of Iron ores, Changsha, Nov, 2006), 36-41.
11. N. Sakamoto et al., "Development of New Iron Ore Agglomeration Process" (Paper presented at the 5th International Symposium on Agglomeration, 1989), 69-278.
12. Y.S. Wen, Y.Q. Li and J.S. Zheng, "Development and Application of HPS/MPS Process", *Anhui Metallurgy*, 3(2004), 40-44.
13. Q.S. Wu, "HPS Practice on A New Sinter Machine in Anyang Steel Plant", *Sintering and Pelletizing*, 22(4) (1997), 17-21.
14. Z.Z. Zhang and G.X Shi, "Differences between HPS/MPS Process and Other Agglomeration Process", *Sintering and Pelletizing*, 23(5) (1998), 9-12.

3rd International Symposium on High-Temperature Metallurgical Processing
Edited by: Tao Jiang, Jiann-Yang Hwang, Patrick Masset, Onuralp Yucel, Rafael Padilla, and Guifeng Zhou
TMS (The Minerals, Metals & Materials Society), 2012

INVESTIGATION OF PYROMETALLURGICAL NICKEL PIG IRON (NPI) PRODUCTION PROCESS FROM LATERITIC NICKEL ORES

Onuralp Yucel[1], Ahmet Turan[1,2], Halil Yildirim[1]

[1]Istanbul Technical University; Chemical Metallurgical Faculty, Department of Metallurgical and Materials Engineering; Maslak, Istanbul, 34469, Turkey
[2]Yalova University, Yalova Community College, 77100, Yalova, Turkey

Keywords: Lateritic Nickel Ore, Nickel Pig Iron

Abstract

Nickel is mainly used in stainless steel production as ferronickel. In recent years, low grade ferronickel or nickel pig iron (NPI) is used in stainless steel production to reduce expenditure of nickel price. In this study, Turkey East Anatolian region lateritic nickel ores were directly introduced carbothermal reduction to produce NPI. Firstly the raw lateritic ore that contains 0.9% Ni, 0.054% Co and 2.3% Cr was mixed with metallurgical grade coal at different stiochometric ratios. The samples were smelted at 1600-1650 °C temperature range in an induction furnace for 25 min. In the second experimental set, different processes times were carried out from 15 to 35 min. The raw material, obtained alloys and slags were analyzed by using XRD (X-Ray Diffractometer), XRF (X-Ray Fluorescence Spectrometer), AAS (Atomic Absorption Spectrometer) and EPMA (Electron Probe Micro Analyzer) techniques.

Introduction

Nickel is an important element that has many application areas in the industry and there are a lot of kinds of nickel products such as refined metal, powder, sponge etc. 65% of metallic nickel is used in stainless steel, 12% is consumed as superalloy and non ferrous alloy because of its superior corrosion and high temperature properties [1].

Nickel is a transition metal that is mined from mainly two types of ore deposits as sulphide ores and lateritic ores. Although 73% of nickel ores are laterites, 55% of primary production is from sulphide ores [1, 2]. The importance of lateritic ores is increasing due to the increase in nickel prices and decrease in reserves of sulphide ores.

There are pyrometallurgical, hydrometallurgical and combined (pyro-hydrometallurgical) methods which are used for the extraction of nickel from lateritic ores. HPAL (High temperature pressure acid leaching) is generally used to recover nickel and cobalt from laterite nickel ores. It is suitable for the plants processing ores with low magnesium oxide and aluminum oxide content. Lateritic ores are exposed to hot acidic leaching around ~250 °C to dissolve cobalt and nickel under high pressure. The main disadvantage for HPAL is the high cost of titanium autoclaves. Process is complex and difficult to control due to the high pressure and heating of the process [2, 3 and 4].

AL (Atmospheric leaching) is being replaced with HPAL due to low costs and more suitable for the smaller scale plants. AL includes direct leaching of laterite ores in the organic or inorganic acids and obtaining Ni, Co hydroxides in the solution. Solution can be enriched by using SX and

metallic nickel and cobalt are recovered by EW or precipitating. In the heap leaching process, milled ore is fed by dilute acid from the top, and nickel and cobalt are digested. Collected solution is treated for metal recovery. In the agitation leach, crushed and ground ore is leached in a heated tank. Temperature has a beneficial effect on the metal recovery with decrease of the process duration [3, 4].

Caron Process (Combined-pyro-hydrometallurgy) was first developed by Caron in the 1920s and first used in the Second World War in Nicaro, Cuba. It can be used for high iron limonitic ores and tolerates more Mg than other acid leaching processes. In this process, ore is blended and dried, then reduced in a roaster by using fuel and air around 700 °C. The product is generally iron-nickel alloy. Hot and reduced ore is cooled in a roaster under reducing atmosphere and quench in ammoniacal ammonium carbonate solution in the tanks. Nickel and Co are precipitated as carbonate form from solution. The recovery is lower compared to pyrometallurgical and hydrometallurgical processes. The first step of this process also consumes high energy [4, 5].

Ferronickel smelting of laterite ores is generally performed by using fossil fuels (coal, oil, natural gas, etc.) as reductant in a rotary kiln. Nickel and cobalt are firstly reduced because iron has greater affinity for oxygen. The product is charged to converter for refining after discarding slag containing unreduced iron oxide, magnesium and silica. The end-product is ferronickel alloy which contains 25% nickel. This unrefined ferronickel is refined using soda ash, lime or calcium carbide to remove sulphur content. Air is blown through molten and desulphurized ferronickel to oxidize carbon, phosphorus and other impurity elements. This process is energy intensive but new furnace technologies reduce the energy costs [2, 4 and 5].

Nickel Pig Iron (NPI) production is a new trend which was first developed about 50 years ago but not used commercially until some Chinese pig iron producers changed their production methods into nickel pig iron without new investments. NPI production first began in blast furnaces using laterite ores imported from Indonesia, Philippines and New Guinea. The process is almost same as pig iron production. The difference is that the ore contains more nickel. The blast furnace products contain 2-10% of nickel. The technology also performed using electric arc furnaces and rotary kilns [4, 6 and 7].

In this study, experiments were performed in an induction furnace with graphite crucibles. Lateritic ores were employed as raw material to produce nickel pig iron from East Anatolian Region. The effect of optimum reductant ratio and process time was examined.

Experimental Studies

East Anatolian Region raw lateritic nickel ore samples were crushed and ground by using a jaw crusher, cone crusher, roller crusher and a vibratory cup mill. Average particle size of 275 μm was calculated by using screen analysis for the ground ore. Ore was homogenized at the end of the mill treatment process.

Homogenized ore was characterized by using different analyzing techniques including XRD, XRF and AAS. Also amount of fixed carbon, volatile materials and ash in metallurgical coke were analyzed. According to X-ray diffraction results (XRD, PANalytical PW3040/60) shown in Figure 1, these ores contain mainly quartz, magnetite, hematite and magnesium chromium oxide phases and slightly nickel iron oxide.

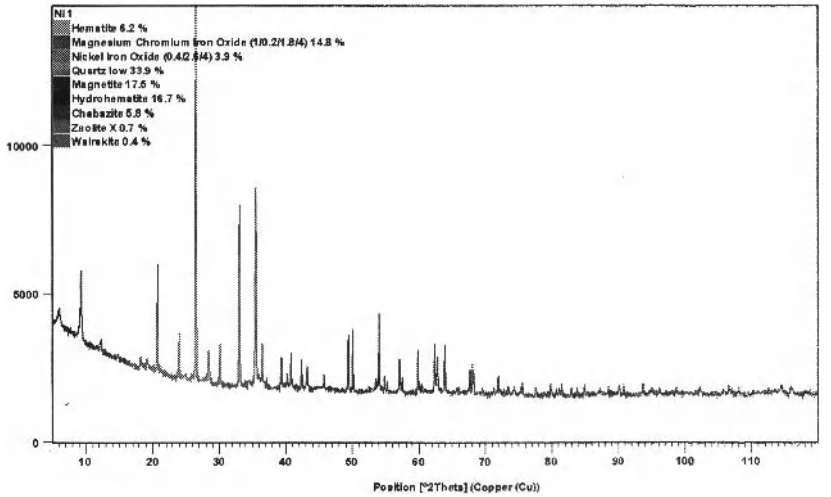

Figure 1. XRD Pattern of Raw Lateritic Nickel Ore

The quantitative analysis of raw lateritic ore was performed using AAS (Perkin Elmer Analyst 800) and XRF (Thermo SCIENTIFIC, NITON XL3t). Results are shown in Table I.

Table I. Quantitative Analysis of Raw Lateritic Nickel Ore

%Ni	%Fe	%Cr	%Co	%Mn	%Mg	%Al
0.90	30.11	2.30	0.054	0.31	4.99	1.80
%Sr	**%Ca**	**%Zn**	**%S**	**%Ti**	**%SiO_2**	**%LOI**
0.003	0.096	0.036	0.044	0.024	40.61	2.50

In the first experimental set, effect of reductant amount was carried out. Lateritic ores and coke were dried in a dryer at 105 °C for 2 hours. 100 g ore and metallurgical coke (from 5g to 35g) were mixed and charged into an induction furnace which is commercially designed for F9 and F10 graphite based crucibles. These mixtures were held for 25 minutes in the furnace at temperature range of 1600-1650 °C. It was observed that charged mixtures began to melt around 10^{th} minute (1350-1400 °C) and reached the maximum temperature about 15^{th} minute. Metallic and slag phases were obtained after smelting. Slags were discarded and grinded. Magnetic-metallic and non-magnetic parts of the slags were separated by using magnetic separation process. Magnetic parts were added to the metallic phase to re-melt. General flowchart of the process is shown in Figure 2. The homogenized metal buttons were characterized using XRF, AAS, EPMA techniques. The most efficient experiment in recovery of Ni and Co was P4 mixture with 30 g reductant and 100 g ore.

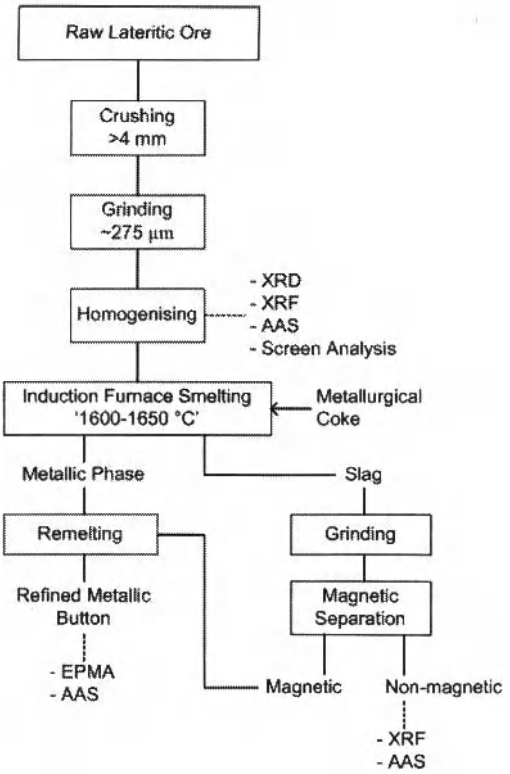

Figure 2. General Flowchart of the Process

In the second experimental set, effect of process duration was carried out. P4 mixture was smelted in different process durations from 15 min. to 35 minutes. The same experimental and characterization procedures as in the first experimental set were employed for the second experimental set with different process times.

Results and Discussion

In the first experimental set up, the most efficient result was the experiment coded P4 with 100 g ore and 30 g coke mixture as 88.13% efficiency in nickel recovery. The experiment P1, 100g ore and 5 g coke mixture, has the highest nickel concentration in the metal buttons. However, nickel recovery increases with increase in the amount of reductant, nickel concentration in the alloy decreases. Ni, Co and Cr contents are shown in Table II and metal recovery efficiency is shown in Figure 3 with increasing reductant/charged ore percentage. Oxygen affinity of Ni and Co is less than other metals in the ore so that their reduction capacities are more than others at low reductant/charged ore ratios. With increasing reductant/charged ore ratios their concentration

decrease because there is enough reductant for the reduction of other metals as can be seen in Table II and Figure 3

Table II. Ni, Co and Cr Content of Metallic Buttons with Different Amounts of Metallurgical Coke

Sample	Reductant/ Charged Ore, %	Duration, Min.	%Ni	%Co	%Cr	Ni Recovery, %	Co Recovery, %	Cr, Recovery, %
P1-25	5	25	6.94	0.43	0.81	51.74	53.43	2.33
P2-25	10	25	4.07	0.23	2.01	67.65	63.71	13.48
P3-25	20	25	3.17	0.17	2,90	65.72	58.74	23.22
P4-25	30	25	3.00	0.17	4.05	88.13	83.23	45.95
P5-25	35	25	2.87	0.15	4.32	77.01	67.08	44.77

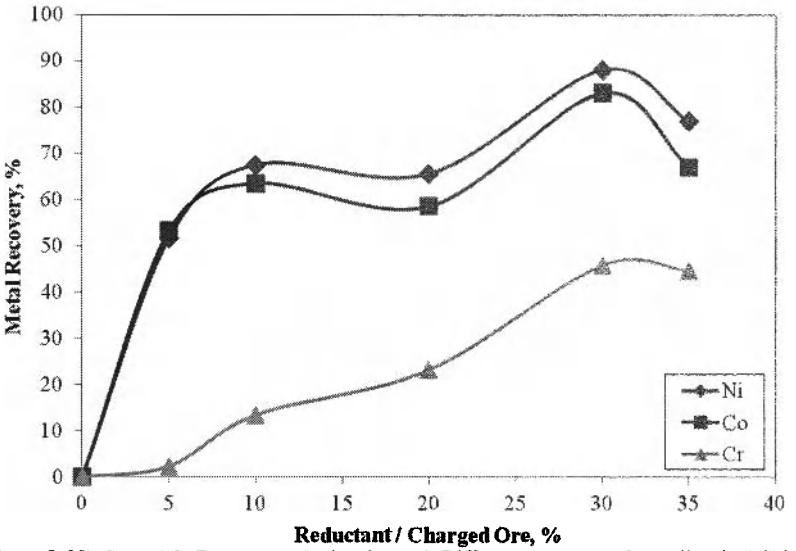

Figure 3. Ni, Co and Cr Recovery Efficiencies with Different Amounts of Metallurgical Coke

Process duration is also another parameter that affects metal recoveries. As seen in Table III and Figure 4, efficiency in metal recovery increases with the increase of process duration. At constant reductant/charged ore ratio (30%) Ni and Co concentrations slightly change with the increase of process duration. Ni, Co and Cr recoveries increase rapidly till 30th minute. After 30th minute, metal recoveries are close to each other.

Table III. Ni, Co and Cr Content of Metallic Buttons with Increasing Process Duration and 30% Constant Metallurgical Coke Addition

Sample	Reductant/ Charged Ore, %	Duration, Min.	%Ni	%Co	%Cr	Ni Recovery, %	Co Recovery, %	Cr, Recovery, %
P4-15	30	15	3.40	0.13	4.81	16.21	10.33	8.86
P4-20	30	20	3.09	0.22	4.99	45.8	54.35	28.57
P4-25	30	25	3.00	0.17	4.05	88.13	83.24	45.96
P4-30	30	30	3.15	0.19	5.54	97.55	98.06	66.27
P4-35	30	35	2.94	0.17	5.07	97.93	94.38	65.24

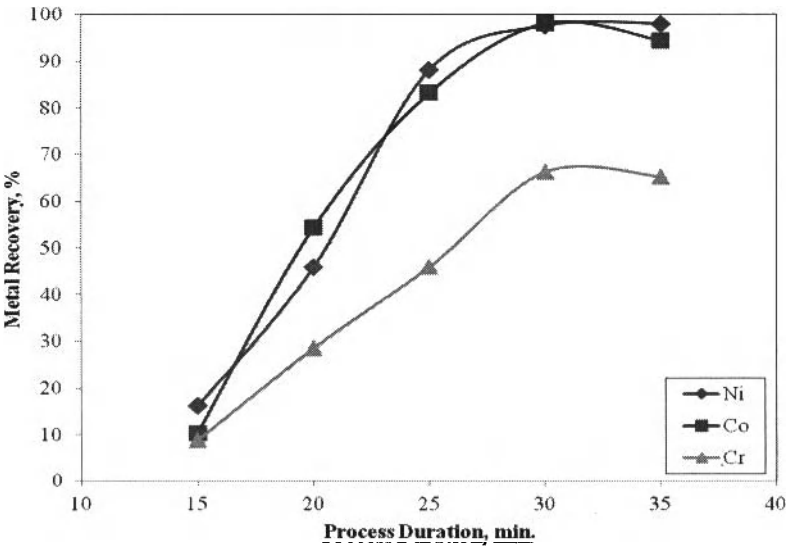

Figure 4. Ni, Co and Cr Recovery Efficiencies with Increasing Process Duration and 30% Constant Metallurgical Coke Addition

Conclusion

The effects of reductant/charged ore ratio and process duration on metal recovery efficiency were examined. East Anatolian Region lateritic nickel ores were successfully smelted using an induction furnace with graphite based crucibles.

In the first experimental set, P4 has the highest Ni-Co recovery efficiency as 88.13% and 83.23% respectively. P4 has also satisfactory Cr concentration as 4.05%. P1 has the highest Ni and Co concentration as 6.94% and 0.43% and has only 0.81% Cr concentration.

In the second experimental set, Ni and Co concentrations in the alloy slightly change with the increase of process duration but their recovery efficiencies change rapidly with increasing in the time. The highest recoveries were achieved as 97.55% Ni and 98.06% Co with the addition of 30% of metallurgical coke and for the process time of 30 minute and 97.93% Ni and 94.38% Co for 35 minutes.

REFERENCES

1. Jungah Kim, Gjergj Dodbiba, Hideaki Tanno, Katsunori Okayaa, Seiji Matsuo, Toyohisa Fujita, "Calcination of Low-grade Laterite for Concentration of Ni by Magnetic Separation," *Minerals Engineering*, 23 (2010), 282–288.
2. R.R. Moskalyk, A.M. Alfantaz, "Nickel Laterite Processing and Electrowinning Practice," *Minerals Engineering*, 15 (2002), 593–605.
3. J.A. Johnson, B.C. Cashmore, R.J. Hockridge, "Optimization of Nickel Extraction from Laterite Ores by High Pressure Acid Leaching with Addition of Sodium Sulphate," *Minerals Engineering*, 18 (2005), 1297.
4. E. Buyukakıncı, "Extraction of Nickel from Lateritic Ores" (M.Sc. thesis, Middle East Technical University, 2008).
5. A.R. Burkin, *Extractive Metallurgy of Nickel* (New York, NY: John Wiley & Sons, 1982).
6. Michael Widmer, "Nickel Pig Iron in China" (Report, Bank of America-Merrill Lynch, 2009).
7. R.P. Das, "Global Scenario for the Extraction of Nickel from Lateritic Nickel Ore and Sukinda Deposit" (Paper presented at the International Seminar on Development of Nickel and PGM Resources, Bhubaneswar, India, 27-28 November 2010).

3rd International Symposium on High-Temperature Metallurgical Processing
Edited by: Tao Jiang, Jiann-Yang Hwang, Patrick Masset, Onuralp Yucel, Rafael Padilla, and Guifeng Zhou
TMS (The Minerals, Metals & Materials Society), 2012

NOVEL PROCESS FOR UTILIZING LOW-GRADE MANGANESE OXIDE ORES BY SULFUR-BASED REDUCTION ROASTING-ACID LEACHING

Tao Jiang, Zhixiong You, Yuanbo Zhang*, Daoxian Duan, Guanghui Li

(School of Minerals Processing & Bioengineering, Central South University, Changsha, Hunan 410083, China)

Key Words: Low-grade Manganese Ores, Manganese Dioxide, Reduction Roasting, Sulfur

Abstract

Manganese is mainly consumed by steel and battery industries. In recent years, it is essential to utilize the low-grade manganese oxide ores with total manganese grade below 25%, as the high quality manganese ore resources are becoming scarce with the rapid development of the steel industry. Conventional pyro-metallurgical processes for utilizing manganese oxide ores are characterized by high production cost and energy consumption, low productivity, serious environmental pollution, etc. In this study, reduction thermodynamic of MnO_2 reduced by sulfur was firstly carried out. Then, a novel process of reduction roasting with sulfur followed by acid leaching was developed to recover manganese from the very low-grade manganese oxide ores. Effects of main factors, including temperature, reduction time and S/Mn mole ratio, were investigated, and a high leaching efficiency of Mn above 95% was obtained under optimal conditions.

Introduction

High/middle-grade manganese oxide ores are generally used in the metallurgical industries, particularly in steel plants and ferro-alloy units. The consumption of metal manganese in the ferro-alloy industry accounts for 85- 90% of the total Mn demanded [1]. Therefore, high quality manganese ore resources are becoming scarce with the rapid development of steel industry. It is essential to make good use of large quantity of low-grade manganese ores (TMn < 25%) presently available.

Low-grade manganese ores are conventionally processed by pyro/hydro-metallurgical or direct reductive leaching methods. Process of reduction roasting followed by acid leaching plays an important role in the treatment of low-grade manganese ores [2]. The pyro-metallurgical methods include processes of coal-based reduction roasting [3-5], pyrite reduction roasting [6] and sulphation roasting [7-8]. The obvious disadvantages of the above methods are higher roasting temperature and more energy consumption.

* Corresponding author: Yuanbo Zhang, email: zybcsu@126.com

A great deal of direct reductive leaching processes have been studied including leaching with sulfur dioxide [9], pyrite in acidic media [10], hydrogendioxide [11], bioleaching with different microorganisms [12], ferrous iron [13] and organic reducing agents [14-15]. Among these processes, leaching approaches using various organic matters as reductants have been focused on to process low-grade manganese ores. The problems of these methods are the purification of Mn from leaching solution and recovery of precious metals.

The utilization of waste or secondary materials for the reduction of manganese oxide ores has been recently arousing the public concern. In the present work, a novel process for utilizing the low-grade manganese ores by reduction roasting followed by acid leaching was put forward, using sulfur residues as reductants. Thermodynamic analysis of different reactions in the Mn-S-O system was firstly carried out. Then, effects of roasting temperature and time, S/Mn mole ratio on the leaching efficiency of Mn were investigated.

Experimental

Materials

The low-grade manganese ores used in this study are obtained from Hunan province, China, and the sample is crushed and ground to 80% passing 74um in advance. The chemical composition of the ore is given in Table 1. From Table 1 it can be seen that total manganese grade of the sample is only 21.10%. XRD pattern of the sample, presented in Figure 1, indicates that manganese mainly exists in the form of lithiophorite ($(Al, Li)MnO_2(OH)_2$), and the main gangue minerals are hematite (Fe_2O_3) and quartz (SiO_2). Grade of sublimed sulfur used as reductant is above 99%. The chemical phase analysis of manganese reveals that the sample ore is mainly composed of manganese dioxide (MnO_2, 95.74%), with small amounts of manganese carbonate ($MnCO_3$, 2.51%) and manganous silicate ($MnSiO_3$, 1.75%).

Table I. Main Chemical Composition of the Manganese Ore (mass fraction, %)

Mn	TFe	Al_2O_3	SiO_2	CaO	MgO	S	P	Li	LOI*
21.10	10.69	6.90	31.62	2.25	0.12	0.15	0.089	0.0056	12.15

*LOI: Loss on ignition.

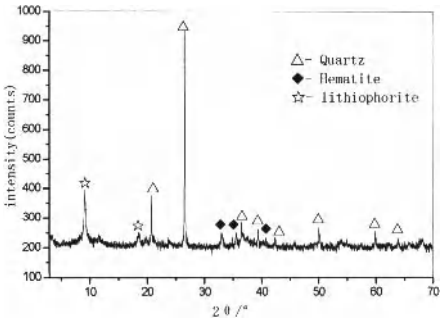

Figure 1. XRD Pattern of the Manganese Ore

Methods

The ground manganese ore and chemically pure sublimed sulfur were put into a closed stainless steel reactor after mixed thoroughly together, and then roasted at given temperature for certain period in an electrically heated muffle furnace. The reduced samples were cooled in inert atmosphere. In each test, 10 grams reduced samples were weighed and leached in a 400ml beaker using a stirrer with rotating speed of 400 $r \cdot min^{-1}$. The samples were filtered subsequently, and the leached residues were washed for three times with distilled water then dried for chemical analysis. All the leaching experiments were conducted at room temperature for 30min in a solution of 50ml H_2O and 1M H_2SO_4. The experimental flowsheet was presented in Figure 2. The leaching in the solution of H_2O was attributed to appraise the formation amount of $MnSO_4$. The leaching efficiency of Mn can be calculated as follows:

$$\gamma = (1 - \frac{m_1 \times \beta}{m_0 \times \alpha}) \times 100\% \quad (1)$$

Where: γ is the leaching efficiency of Mn, %;

m_0 is the weight of reduced product, g; α is Mn grade of reduced product, %;

m_1 is the weight of leached residue, g; β is Mn grade of leached residue, %.

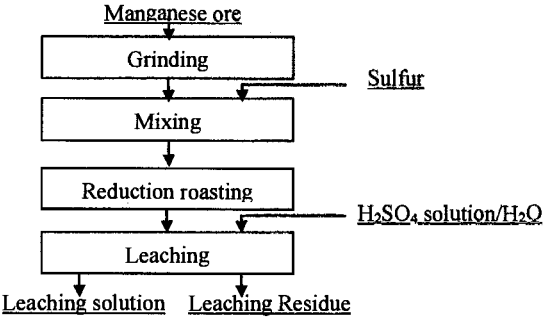

Figure 2. Experimental flowsheet

Thermodynamic Analysis of MnO_2 Reduced by Sulfur

The reaction procedure of MnO_2 reduced by sulfur was very complicated because sulfur exists in the form of liquid state at the temperature between 119 °C and 445 °C, and then begins to sublimate above 445 °C. However, manganese can exist in the form of Mn_2O_3, Mn_3O_4, MnO, MnS, MnS_2 and $MnSO_4$. In this study, the transformation procedure of MnO_2 was analyzed at the temperature range of 392~718 K and 718~1100 K, respectively.

Figure 3 shows ΔG_T^θ-T result of major reactions of MnO_2 reduced by sulfur in the closed system. At the temperature range 392~718 K, sulfur existed in the form of liquid state. Almost all ΔG_T^θ values of the reactions were much less than zero, which indicated the

reactions were easy to proceed. As observed, MnO_2 was easily reduced to Mn_2O_3 (bixbyite) and subsequently to Mn_3O_4 (hausmannite) theoretically. It can be also seen from Figure 3, that Mn_3O_4 is reduced to MnS_2 (manganese disulfide) or MnS (manganese sulfide) depending on the temperature. MnS_2 was easier formed under 539 K and MnS prevailed above 539 K. But, MnS_2 was unstable above 543 K, and it can release element sulfur and MnS. It was noteworthy to refer to the reaction between MnS and Mn_3O_4 was impossible as ΔG_T^θ of this reaction was above zero at the temperature range of 392 K~718 K. As a result, the main reduced products of MnO_2 by sulfur were $MnSO_4$ and MnS.

The form of MnS was unwanted, the main reason for which is that the release of H_2S was unavoidable while subsequently leached in a H_2SO_4 solution. The roasting temperature was enhanced in order to reduce the generation of MnS. Figure 4 presents the ΔG_T^θ - T results of reactions in the Mn-S-O system at 718 K ~1100 K. It is necessary to emphasize that sulfur existed in the form of gaseous phase, namely S_2 vapour. Compared with Figure 3, there are two obvious differences existing in Figure 4. Firstly, the formation of MnO was easier than that of MnS, while Mn_3O_4 was likely reduced by S_2 vapour. Secondly, the reaction between Mn_3O_4 and MnS was possible because ΔG_T^θ of this reaction decreases sharply below zero at 718 K~1100 K. Therefore, intermediate product MnS disappeared and the final products were $MnSO_4$ and MnO. It is obviously observed that SO_2 is easily reacted with MnO_2. However, higher temperature was unfavorable for the formation of $MnSO_4$.

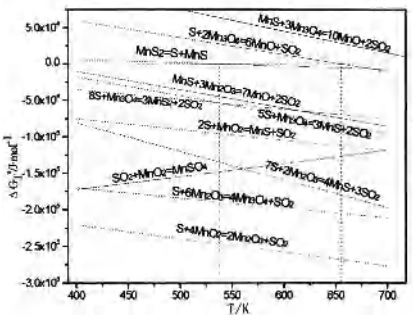

Figure 3. ΔG_T^θ-T Results of Reactions in the Mn-S-O System at 392~718 K

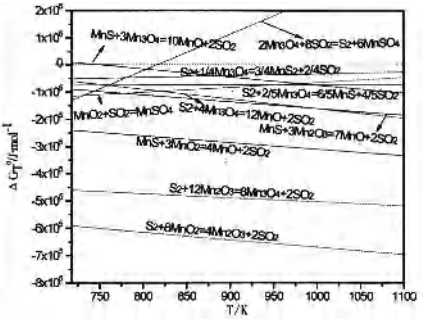

Figure 4. ΔG_T^θ-T Results of Reactions in the Mn-S-O System at 718~1100 K

Results and Discussion

Many factors have obvious effects on the recovery of Mn from low-grade manganese ore by reduction roasting- acid leaching process. Sulfur is used as reducing agent. In this paper, the leaching efficiency of Mn affected by roasting temperature, S/Mn mole ratio and roasting time is investigated, respectively.

Effects of Roasting Temperature

Effects of roasting temperature on the leaching efficiency of Mn were shown in Figure 5. All tests were performed under conditions of reduction time 30 min and S/Mn mole ratio 0.50.
It can be seen that acid leaching efficiency of Mn increased from 79.55% to 95.12% with the roasting temperature increasing from 350 °C to 500 °C, and then it remains a constant approximately, which was attributed to the reaction between Mn_3O_4 and MnS was impossible. At this temperature range, the main reduced products were $MnSO_4$ and MnS, which resulted in the release of H_2S while acid leaching. As far as the water leaching efficiency of Mn is concerned, it decreased obviously when the temperature is above 550 °C due to the inhibition of reaction between SO_2 and MnO_2 at higher temperature. Therefore, the suitable roasting temperature of 550 °C was recommended.

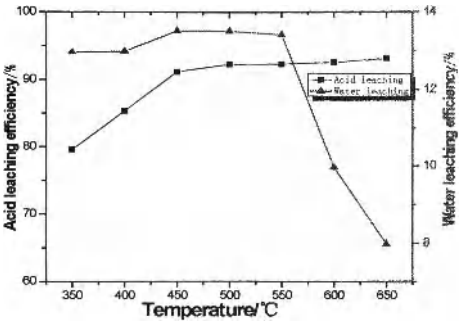

Figure 5. Effects of roasting temperature on the leaching efficiency of Mn

Effects of S/Mn Mole Ratio

The leaching efficiency of Mn as a function of S/Mn mole ratio was given in Figure 6 under the condition of reduction time 30min and roasting temperature 550° C.
From Figure 6, it can be seen that both the acid and water leaching efficiency of Mn increased with S/Mn mole ratio increasing. When the S/Mn mole ratio is between 0.50 and 0.57, the maximum of 95.12% acid leaching efficiency and 17.00% water leaching efficiency were obtained, respectively. The final reduced products are composed of MnO and $MnSO_4$. The leaching efficiency remained a constant when MnO_2 and Mn_3O_4 are converted completely to MnO or $MnSO_4$.

Effects of Roasting Time

The effect of roasting time on the leaching efficiency of Mn was plotted in Figure 7. All the experiments were carried out under conditions of reduction temperature 550°C and S/Mn mole ratio 0.50.
It can be concluded from Figure 7 that the reduction rate of manganese dioxide was rapid. The acid leaching efficiency of 81% is achieved after the sample ores are reduced with sulfur for only 2min. The leaching efficiency of Mn increased obviously as the roasting time increases from 2min to 10min. This can be explained thermodynamically that ΔG_T^{θ} values of

the reactions of MnO_2 reduced by sulfur are much less than zero, presented in Figure 4. The suitable reduction time of 10min should be chosen at 550 °C.

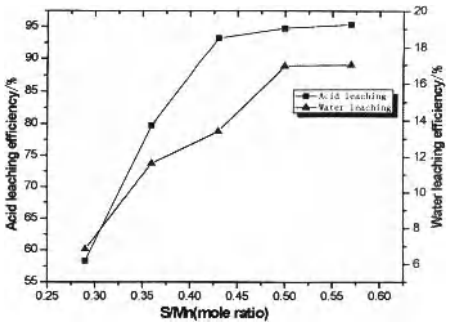

Figure 6. Effects of S/Mn Mole Ratio on the Leaching Efficiency of Mn

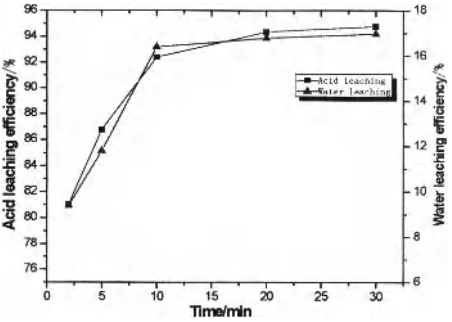

Figure 7. Effects of Roasting Time on the Leaching Efficiency of Mn

XRD Analysis of the Reduzates

Figure 8 shows the XRD patterns of reduced residues after the sample manganese ores are reduced under conditions of roasting time 30min, S/Mn mole ratio 0.50 and roasting temperature between 350 °C - 650 °C.

It can be observed that lithiophorite ((Al, Li)$MnO_2(OH)_2$) in the sample manganese ores disappeared whereas new manganese phases, including $MnSO_4$, MnS and MnO, appeared after the samples are roasted with sulfur. Compared all the XRD patterns, it was found that $MnSO_4$ existed at all roasting temperatures, however, the diffraction peak of $MnSO_4$ in reduced residues at lower temperature (< 500 °C) is stronger than that at higher temperatures (> 550 °C), which was in accordance with the water leaching efficiency presenting a decline tendency above 550 °C. It is noteworthy to mention that MnS, always existing at 350 °C-500 °C, disappeared at the temperatures above 550 °C, and MnO immediately appeared after that. When the temperature reaches 550 °C, the intermediate product MnS easily reacted with Mn_3O_4, so MnS was not observed in the reduced residues.

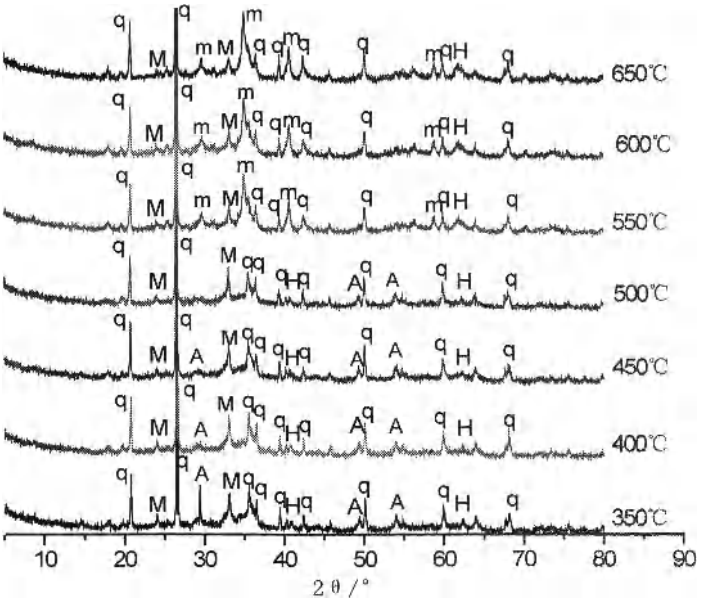

Figure 8. XRD Pattern of Manganese Ore Reduced by Sulfur at Different Temperature (A-MnS,m-MnO,M-$MnSO_4$,q-SiO_2,H-Fe_2O_3)

Conclusions

(1) The reduction procedure of MnO_2 by sulfur was different and the final reduzates differ depending on the roasting temperature. MnS and $MnSO_4$ were the main reduced products at 350 °C- 500 °C while MnO and $MnSO_4$ were the final products above 550°C.

(2) A novel process to recover manganese from low-grade manganese ore (TMn 21.1%) by reduction roasting acid leaching was developed, using sulfur as reducing agents. The optimal parameters were recommended as roasting temperature 500 °C, roasting time 10min and S/Mn mole ratio 0.50, and a high leaching efficiency above 95% was obtained the optimal conditions.

(3) The reduction reactions of MnO_2 by sulfur happened at a relatively low temperature and the speed was very fast. It was a promising process for utilizing the low-grade manganese ores compared with the traditional coal-based reduction roasting method.

Acknowledgements

The authors want to express their thanks to National science fund for distinguished young scholars (No. 50725416) and Key Programs of Science and Technology from Hunan Province (No. 2010FJ1011) for financial support of this research.

References

1. Corathers, L.A., "Geological Survey(USGS) Minerals Yearbook: Manganese", (2005), Date accessed: 21/6/2007, U.S.
2. W. Zhang, C.Y. Cheng, "Manganese metallurgy, recovery and control - a literature review. Part I: Manganese Metallurgy, " *CSIRO Minerals*, Australia, 89(2006), 137-159.
3. Ring Kononov, Oleg Ostrovskl, and Samir Ganguly, "Carbothermal Solid State Reduction of Manganese Ores," Phase Development, *ISIJ International*, 49 (8)(2009), 1115-1122.
4. N.J. Welham, "Activation of the carbothermic reduction of manganese ore," *Int. J. Miner. Process*, 67(2002), 187-198.
5. Bjørn Sorensen et al., "Phase compositions of manganese ores and their change in the process of calcination," *International Journal of Mineral Processing*, 94(2010), 101-110.
6. C.X. Yang et al., "Trace element transformations and partitioning during the roasting of pyrite ores in the sulfuric acid industry," *Journal of Hazardous Materials*, 167(2009), 835-845.
7. Freitas et al., "Sulfation of carajas manganese ore with gaseous SO_2," Transactions of the Institution of Mining and Metallurgy Section C - *Mineral Processing and Extractive Metallurgy*, 102, C130-C131.
8. Kh.S. Abou-El-Sherbini, "Simultaneous extraction of manganese from low grademanganese dioxide ore and beneficiation of sulfur slag," *Separation and Purification Technology*, 27(2002), 67-75.
9. C. Abbruzzese, "Percolation leaching of manganese ore by aqueous sulfur dioxide," *Hydrometallurgy*, 25(1990), 85-97.
10. A.G. Kholmogorov et al., "The production of manganese dioxide from manganese ores of some deposits of the Siberianregion of Russia," *Hydrometallurgy*, 56(2000), 1-11.
11. Tao Jiang et al., "Simultaneous leaching of manganese and silver from manganese-silver ores at room temperature," *Hydrometallurgy*, 69(2003), 177-186.
12. C. Abbruzzese et al., "Biogical and chemical processing of low-grade manganese ores," *Minerals Engineering*, 3(4) (1990), 307-318.
13. Mohammad Sh. Bafghi et al., "Reductive dissolution of manganese ore in sulfuric acid in thepresence of iron metal," *Hydrometallurgy*, 90(2008), 207-212.
14. Haifeng Su et al., "Reductive leaching of manganese from low-grade manganese ore in H_2SO_4 using cane molasses as reductant," *Hydrometallurgy*, 93(2008), 136-139.
15. D. Hariprasad et al., "Leaching of manganese ores using sawdust as a reductant," *Minerals Engineering*, 20(2007), 1293-1295.

3rd International Symposium on High-Temperature Metallurgical Processing
Edited by: Tao Jiang, Jiann-Yang Hwang, Patrick Masset, Onuralp Yucel, Rafael Padilla, and Guifeng Zhou
TMS (The Minerals, Metals & Materials Society), 2012

EQUIPMENT FOR PILOT SCALE EXPERIMENTS OF NO_X-EMISSIONS FROM THE SILICON PROCESS

Ingeborg Solheim[1], Roar Jensen[1] and Nils Eivind Kamfjord[2]
[1]SINTEF Materials and Chemistry, Alfred Getz vei 2, N-7465 Trondheim;
ingeborg.solheim@sintef.no
[2]Elkem Silicon, Alfred Getz vei 2, N-7465 Trondheim; nils-eivind.kamfjord@elkem.no
Key word: Silicon Process, pilot scale furnace, NO_X emissions

Abstract

SINTEF has carried out several pilot scale silicon process experiments in the past, but always with an open off gas system. In order to test the possibilities in running a semi closed furnace operation, a new off gas hood has been designed and tested. The off gas hood is designed to collect all off gases to gain insight into the phase compositions in the off gas and at the same time have the opportunity to monitor and maintain the charging/stoking of the furnace. The furnace hood has regulation and control of the air inlet into the combustion zone in two different heights. The off gas temperature and composition was continuously monitored and analyzed during the experiment. In order to expand the knowledge on NO_X-formation in silicon metal production, such information is vital.

Introduction

Because of the negative environmental impact, the attention towards all kinds of NO_X emissions increases in Norway. The authorities' demand towards better surveillance and control of emissions increases as well.

Earlier and new industrial measurements in FeSi- and Si-metal furnaces reveal quite high NO_X-emission. The measurements also show that the NO_X formation (mainly as thermal NO_X) is distinct connected to the formation of dust ($SiO \rightarrow SiO_2$) in the combustion chamber above the furnace surface, when the temperature is high and the access to N_2/O_2 is good. This means that stoking, charging and temperature straight above the furnace surface is important factors for the NO_X formation.

Silicon is produced in submerged arc furnaces, where quartz reacts via several sub reactions, with wood, charcoal, and coal. The required energy is supplied by carbon electrodes. The production route for ferrosilicon is similar, with addition of iron oxides. CO and SiO-gas escapes out on top of the furnace where it burn with air and form CO_2 and SiO_2.

Basically there are three main mechanisms producing NO_X; thermal NO_X, fuel NO_X and prompt NO_X. In ferroalloy industry, thermal NO_X is the most relevant, but fuel NO_X, from the oxidation of nitrogen components in the reduction material, can also be a significant source. Thermal NO_X is a result of direct oxidation of N_2 from the air at high temperature. NO_X-formation increases with combustion temperature, time spent at high temperature and the O_2 and N_2-contents present in the combustion chamber. The oxygen and nitrogen produce various oxides of nitrogen, mainly NO, but also a lesser degree of NO_2 and N_2O.

NO form nitric acid when that reacts with moisture in the atmosphere to a component of acid rain. In addition NO_X lead to formation of tropospheric ozone and thereby contribute to several forms of respiratory disorders. This is the main environmental impact of the NO_x emission.

In order to expand the knowledge on NO_X-formation in silicon metal production, a pilot scale experiment in a 400 kVA silicon furnace has been carried out. A new off gas hood was designed with a view to be able to copy and manipulate the formation mechanisms for NO_X by controlling the flow of false air into the off-gas system.

The resulting NO_X-values corresponding to the different air inlet to the furnace top, showed significantly differences between the different air inlet geometries.

Furnace

The experiment was carried out in a 400 kVA furnace operated at 160 kW. It is single phase furnace with adjustable current and voltage supply. The power supply can be operated with both AC and DC. Maximum DC current is 8000 A and maximum DC voltage is 300 V. Maximum AC current is 5700A and maximum AC voltage is 215 V. In this case AC was chosen. The furnace is connected to an off gas system, monitoring composition and temperature of the gas, and with filter collecting coarse and fine particles in the end.

Based on the observation from industrial measurements, the off gas hood was designed with the opportunity to control the false air inlet in to the combustion chamber, and at the same time be able to maintain the stoking and charging operations. A sketch and a picture of the furnace are shown in figure 1.

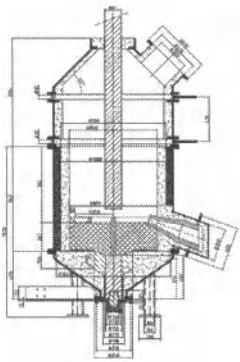

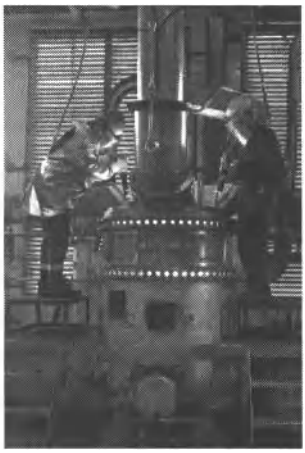

Figure 1: The figure shows a sketch of the furnace and a picture of the furnace in action.

After the experiment it is possible to take out a cast plate of cross section through the center of furnace and investigate more closely the material in different zones of the furnace. This is made possible by a special construction of the furnace body. It is constructed with an outer steel mantle which is dividable horizontally just below the tap hole. The top is also dividable vertically in order to be able to apart the furnace pot into two halves. This particularly design reveal an option to fill the furnace with epoxy after ended experiment. The molded mass can then be removed in one piece. It is a very useful technic in post experimental studies, to cut the entire furnace in slices, and subsequently drill out samples from decided positions for analysis. Figure 2 shows a typical cross section of the furnace after ended experiment and a schematic overview of the different reaction zones.

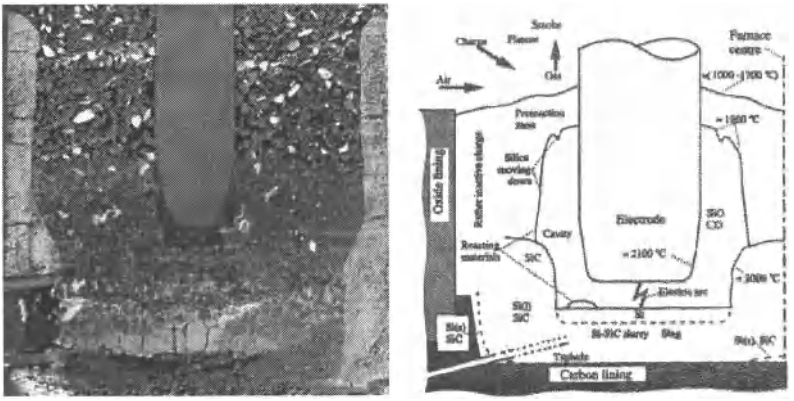

Figure 2: Typical cross section of pilot furnace after ended experiment and a schematic overview of the different reaction zones (not from the current experiment) /4/.

The bottom lining was stamped with conductive SiC. In the bottom a graphite electrode was used with the power connected via copper bars and a copper bolt below the furnace. In the side lining an Al_2O_3-based paste was used. The gap between the steel mantle and side-lining was filled with a 5 cm thick layer of silver sand (SiO_2).

The top electrode is a 15 cm (6 inches) graphite electrode that can be adjusted up and down.

Off Gas System

The hood was constructed with two sets of perforated rings. The holes perforating the ring had a diameter of 35 mm, giving a total opening area of each ring of 0,096 m^2. Each set of ring consist of one inner fixed ring one outer adjustable ring. The distance between the two set of rings were 500 mm.

The hood was also provided with two stoking gates and two gates for charging raw materials into the furnace.

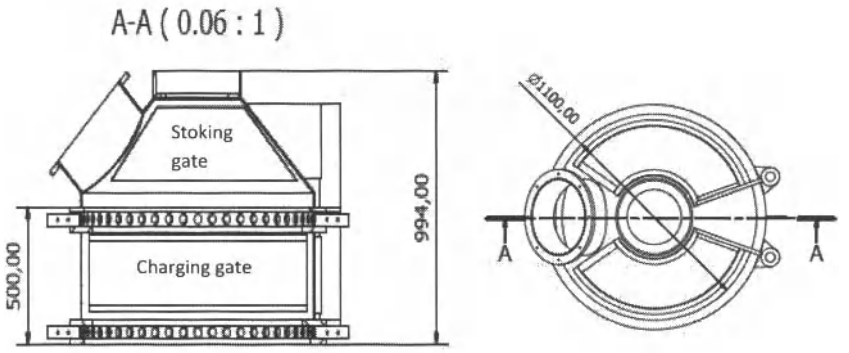

Figure 3: Details of the off gas hood.

Furnace Operation

A critical factor to succeed the furnace operation in this scale, is a proper bottom lining. The conductive SiC lining was primary preheated for 500°C during 1 day and further baking with coke bed for 1 more day. The furnace is ready for raw material feeding after a total preheating equivalent to accumulated 1120 kWh. Raw material was charged into the furnace for 15 hours before the operation was stable and the furnace ready for the first tapping.

The furnace was run using AC power. The current was fixed at 4000 A, and the voltage fluctuate around 40 V. The resulting effect was stable around 160 kW. The furnace was tapped every 250 kWh. During tapping the electrode was gradually adjusted down, to end up in the bottom when the furnace was "empty". After ended tapping the power supply was switched off in order to stoke down the furnace top with pneumatic tools. The electrode was then raised 5 cm and the furnace switched on. The furnace was then ready to rapidly be reloaded up to ¾ level, and then gradually refilled up to normal level (20 cm from pot edge).

Raw material used for this experiment was quartz (3-25 mm) and coke (3-15 mm). In addition wood chips (20-50 mm), was added to increase charge permeability, to "ventilate" the charge. The raw material mix started with a carbon cover of 80 %, gradually increase up to 97 %.

The silicon pilot furnace was operating for 44 hours, producing with a silicon yield of 62 %. It was tapped 13 times, giving a total of 87 kg's of silicon.

The main purpose with the experiment was off gas analysis connected to NO_X-formation, so the furnace parameters were focused to optimise the NO_X-production, and not the Si-production.

Critical electrical parameters were continuous logged during the experiment. The effect/time-plot is showed in figure 4.

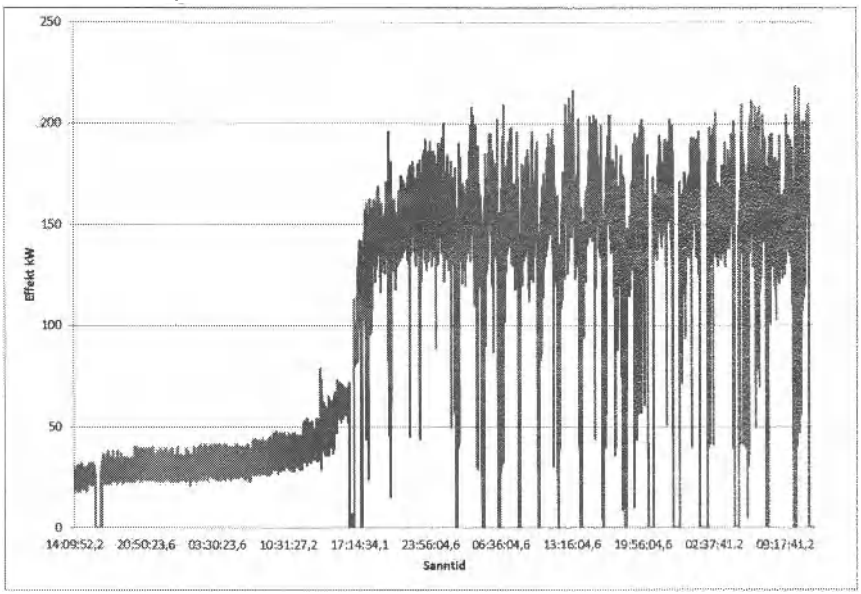

Figure 4: Variation in power with experimental time.

Measurements

A schematic overview of the furnace, off gas system and test points is shown in Figure 5.

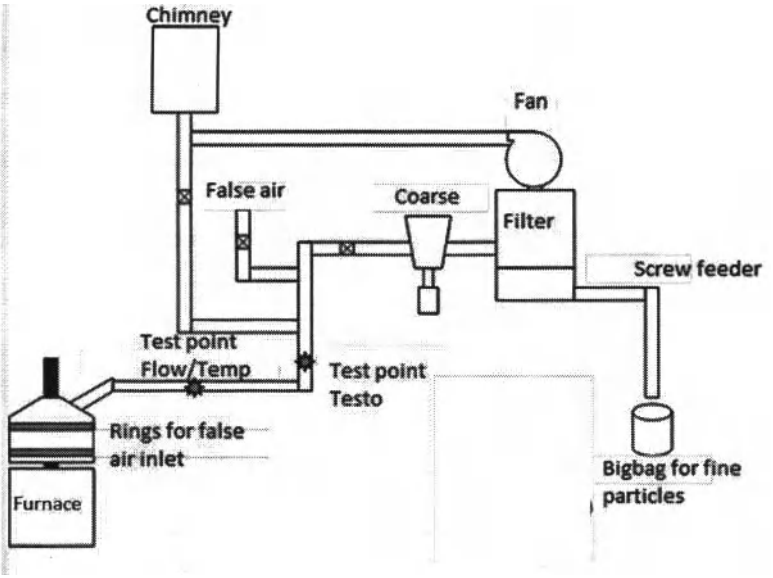

Figure 5: Sketch of the pilot furnace, off gas system and test points.

Results

Some of the results from furnace operation are summarized in Table I

Table I: A summary of metal produced, dust produced, and effect spent.

Tap nr	Real time	Time hours	Metal produced kg	Dust produced kg	kWh pr production period	Furnace effect kW	kWh/kg Si
1	15:00	12	4,65	1,59	1742	145	374,62
2	16:30	1,5	4,5	0,02	214	170	47,55
3	18:17	1,75	3,6	0,09	253	170	70,28
4	20:11	2	3,52	0,01	254	147	72,16
5	22:02	2	3,97	0,01	261	160	65,74
6	24:09	2	2,37	5,44*	308	172	129,95
7	26:15	2	8,4	15,43	306	168	36,43
8	28:00	1,75	3,35	0,85	280	140	83,58
9	30:34	2,5	7,32	4,0	311	150	42,49
10	33:00	2,5	18,2	0,70	305	164	16,76
11	35:28	2,5	15,22	1,2	302	164	19,84
12	38:45	3,25	12,39	27,3	398	164	32,12
13	41:41	3	4,5	1,0	379	162	84,22
14	44:27	3	0	14,36	381	164	-

The temperature and off gas analysis was measured close to the furnace surface. To analyze the off gas a Testo 350XL [5] was used and the measurements where done continuously throughout the experiment. The measurements are done with a measuring cell with an accuracy of 2 ppm from zero to 40 ppm and 5% of measured value for measurements above 40 ppm. The Testo instrument measures CO, CO_2, O_2, NO, NO_2 and SO_2. The results are shown in Figure 8

The working hypothesis in advance was expressed in three statements:

A. The NO_X-formation is controlled of the SiO combustion occurring when the crater gas meet air straight above the surface of the furnace (raw material charge.)
B. The inflow of air, and the flow conditions, straight above the charge surface controls the amount of NO_X formed.
C. The amount of NO_X formed can be manipulated by the *amount* false air, and *where* the false air is let in to the combustion chamber.

The main objective of the experiment was then to:

1. Measure the NO_X as a function of the *height of the* air inlets above the charge surface.
    a. The upper level was 700 mm above the surface.
    b. The lower level was 200 mm above the surface.
2. Measure the NO_X formation as a function of the *amount* of air let in, by adjusting the rings in 6 different configurations.
    a. Both rings open
    b. Both rings closed
    c. Upper ring open
    d. Lower ring open
    e. Upper ring half open
    f. Lower ring half open

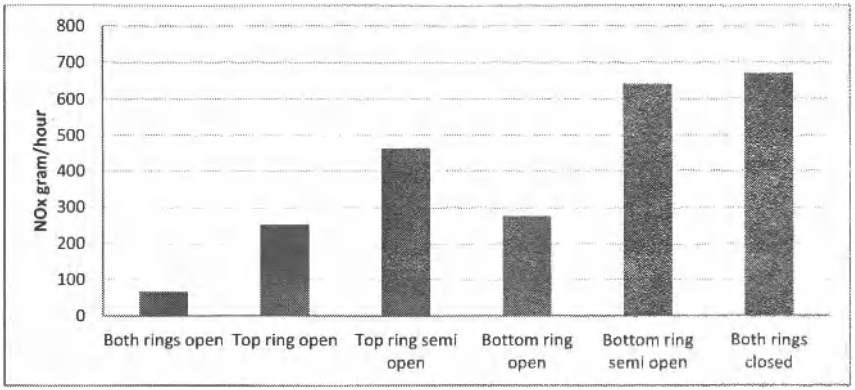

Figure 8: Measured NO_X emissions for the different ring configurations. NO_X-emissions are given in grams/hour. /1/

Discussion

Both the level and the difference of the different ring constellations are surprisingly high. Particularly interesting are the results showing that the NO_x level rise with a decreasing amount of air let into the furnace. This shows the ability to form NO_x even at a low supply of N_2 and O_2. One explanation might be that at a low inflow of air the overall velocity field through the hood is reduced, forming "hot spots" of air heated by the SiO combustion and still containing enough N_2 and O_2 to form NO_x. In that respect the velocity fields inside the hood will have a substantial effect on the NO_x formation /1/.

Conclusions

This first experiment to establish the method showed that the pilot furnace was a good and efective tool for investigating the mechanisms for NO_x formation. The specially designed hood and the set up of off gas measurements were important to achieve this. Further experiments with varying conditions can give insight about mechanisms behind emissions of NO_x in Si and FeSi furnaces and how the industry can reduce these.

The resulting NO_X-values corresponding to the different air inlet to the furnace top, showed significantly differences between the different air inlet geometries. The experimental set up and the hood design was suitable in order to make a controlled off gas study within a fixed geometry.

Based on the data acquired from our experiment we can conclude the following for the pilot scale silicon furnace:

- Having the inlet of cold air close to the charge surface produces more NO_x than moving it higher towards the off gas channel.
- Decreasing the inlet of air to the combustion chamber increases the amount of NO_x produced substantially.
- Based on the NO_x results there is reason to believe that the velocity fields inside the hood influences the NO_x formation significantly.

Understanding the mechanisms in NO_x formation connected to the silicon process is of vital importance for working towards reduced emissions.

References

1. Nils Eivind Kamfjord, Halvard Tveit, Ingeborg Solheim: Pilot Scale measurements of NOx emissions from the Silicon Process. TMS, March 11-15, 2012, Orlando, FL.
2. De Nevers, N. (2000). *Air pollution control engineering.* Boston, McGraw-Hill.
3. Zeldovich, J. B. (1946). "Oxydation of Nitrogen in Combustion and Explotion", *Comptes Rendus (Doklady) de L'Acadèmie des Sciences de l'URSS* **LI**(3): 217-220
4. Schei, A., J. K. Tuset, Tveit, H. (1998). *Production of High Silicon Alloys*, Tapir forlag, Trondheim
5. TESTO. "Testo 350XL Portable Combustion Analyzer Specifications."

3rd International Symposium on High-Temperature Metallurgical Processing
Edited by: Tao Jiang, Jiann-Yang Hwang, Patrick Masset, Onuralp Yucel, Rafael Padilla, and Guifeng Zhou
TMS (The Minerals, Metals & Materials Society), 2012

SLIDE GATE SYSTEMS FOR COPPER TAPPING

Klaus Gamweger[1]

[1]RHI AG, Magnesitstrasse 2, 8700 Leoben, Austria

Keywords: Copper Tapping, Slide Gate, Anode Furnace, Rotary Holding Furnace

Abstract

This paper introduces an innovative solution to open and close the tap hole of different furnace types in the copper industry with a slide gate system. Two plates with defined drilled holes are slid against each other, which enables effective starting and stopping of the copper flow as well as throttling. Typically, the copper is poured via a tap hole into a launder system by rotating the furnace into an appropriate position. Control of the casting rate is also performed in this manner. Or, in case of stationary furnaces the tap hole is opened by oxygen lancing and closed manually with a clay- or copper-cone. These procedures show a lot of disadvantages including splashing, oxygen pick-up, and energy losses as well as a severe danger for the working staff. All these problems can be overcome with an appropriate slide gate system.

Introduction

The control of the casting rate of a copper anode furnace usually is performed by rotating the furnace into an appropriate position. This implies that the taping starts with the tap hole at a very high position. Copper splashing and an uncontrolled oxygen pick up are - with several more disadvantages - the consequences. RHI AG has developed an innovative solution for copper applications to open and close the tap hole with a slide gate system which allows also an accurate control of the flow rate. By using this system it is possible to start the casting procedure with the tap hole at the deepest position, directly above the launder.
This paper presents this new slide gate system in detail and shows the advantages in production and safety issues.

Mechanical Parts

The COP FLOW slide gate is a compact system, engineered with only a few components and containing heavy-duty refractory parts. It is a high performance tool with an enormous yield potential and which allows a quick and simple exchange of the refractory parts. The slider can be swung-out laterally for the plate exchange. For the change of the well block, the whole slide gate unit can be laterally swung away. Short down times of the furnace and consequential savings on energy are a result of all the above.

Description of the Mechanical Unit

The COP FLOW slide gate is a two plate, linear, hydraulically driven system. There are three different sizes available, CF60, CF80 and CF100. The number indicates the maximum tap hole diameter in mm.
The bottom and slider refractory plate are identical in shape and size and can be exchanged in a very short time. This is done by swiveling-out the movable slider over a hinge on the housing

(Figure 1). After the plate exchange the slider is swiveled-back into normal working position. If also the well block has to be changeable the whole ladle gate unit can be swiveled over a double hinge.

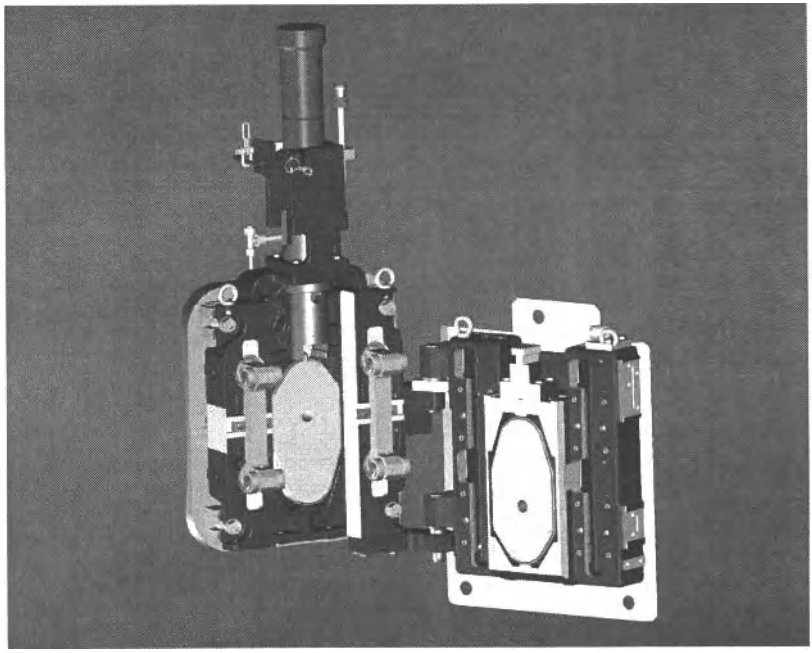

Figure 1. Opened Slide Gate COP FLOW 60

The interlocked positioning of the plates is achieved by a double wedge design. Two permanent magnets are holding the plates in place.
The defined tension force of the system is generated trough four pre-set tension elements, which are equipped with high temperature resistant spiral disc springs and integrated into the housing. Moving hydraulically the slider over the ramps into the working position activates the tensioning of the system.
The steel encased refractory plates and exchangeable nozzle are delivered ready to use. No tools are needed and there is no additional work in a workshop. The standard nozzle for copper has a shoulder and is set to a mechanical stop. Therefore the position of the nozzle and the mortar joint thickness are exactly defined.
The short build-in height of the COP FLOW slide gate does not require expensive structural modifications on the existing installations.

Advantages of the Mechanical Unit

- The system consists of only 2 main parts: a laterally swiveling slider for easy handling of the plates and a fixed or laterally swiveling housing which includes the four tension elements and two roller supports.
- Self-tensioning system through the extra mounting stroke, no further hydraulic mounting tool is needed.
- The system can be operated in vertical and horizontal position and is so suitable for any furnace type.
- The long working stroke guarantees a higher life of the refractory plates.
- An increased safety is achieved by massive refractory components.
- The refractory parts can be exchanged quickly and easily without any additional mechanical fixing.
- There are only a few spare parts needed, what minimizes the costs for maintenance and operation.

Refractory Components

The tap hole area is exposed to a severe erosion attack additional to the thermo-chemical load which is affecting the refractories in the vessel in general. RHI AG offers especially for the copper industry developed high resistant alumina-chromium oxide refractories to withstand the high requirements.

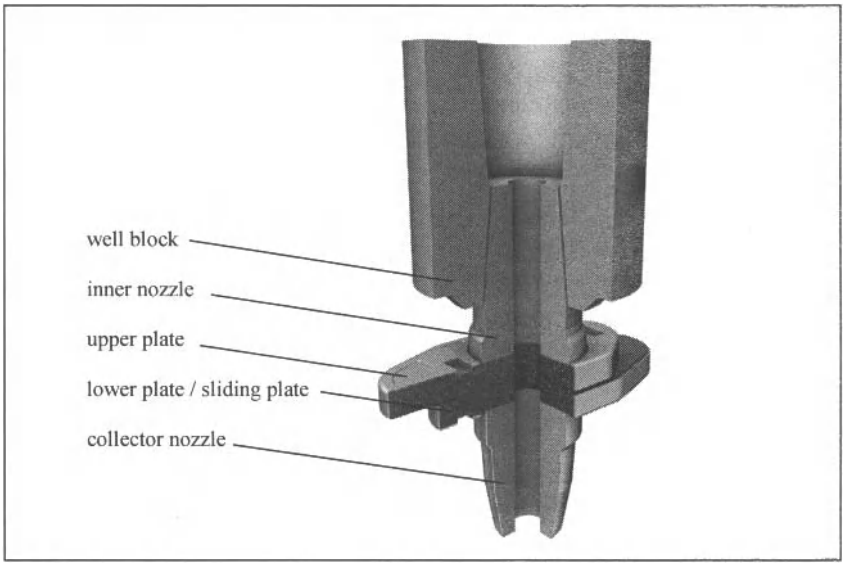

Figure 2. Refractory Tap Hole Components of the Slide Gate System.

The brick lining surrounding the tap hole is installed in two flat arches above and underneath it. This gives the best stability in case of a partial repair of the tap hole arrangement. The interface from lining to well block is done by a low cement alumina/chromium-oxide castable.
The tap hole itself – shown in Figure 2 - consists of a well block, an upper nozzle, the two plates (where the lower one is sliding) and a collector nozzle. The well block usually has the same life time than the rest of the lining and stays in the furnace whereas the plates and nozzles have to be exchanged on a regular basis. The base steel plate has a screwed special opening to give the possibility also for a well block change if necessary.
The upper nozzle and the plates are made of a high fired alumina/chromium-oxide refractory, which was developed especially for the requirements in the copper industry. Additionally they are tar impregnated for an enhanced infiltration resistance. The abrasion wear is most severe during casting in throttling mode, when the tapping channel is not fully opened.
The lower nozzle, also called collector nozzle gives a concentrated copper stream and minimizes the oxygen pick-up and splashing. For this nozzle a SiC material is used. It prevents a freezing of droplets at the end of the nozzle.
The selection of the mortars for installation has an important influence on the lifetime of the system. All parts have to be densely connected to prevent a copper infiltration in between. Two different mortars are used. A phosphor bonded alumina/chromium-oxide mortar with very high strength and adherence for connecting the plates and nozzles to each other. For putting the inner nozzle into the well block a SiC mortar is in use. With this mortar the cleaning of the well block surface after removing the worn out inner nozzle is easier and can be done without damaging the well block.

Industrial Application

The slide gate system is installed onto anode furnaces or rotary holding furnaces (Figure 3 and 4) to upgrade a standard tap hole. The main reasons to install the slide gate were to reduce the splashing of the copper which cases a lot of cleaning between each heat as well as the safe and easy flow regulation during tapping.

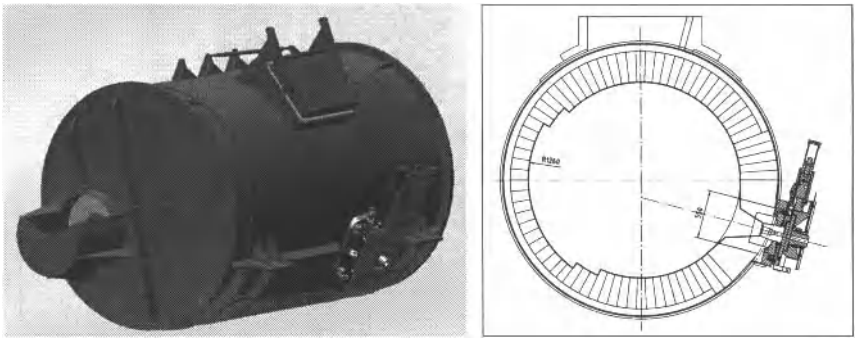

Figure 3 and 4. Installation of the Slide Gate System.

Installation

The installation is carried out during a new installation of the brick lining. Usually it is possible to place the slide gate system at the original tap hole position, so no significant adjustments in the steel structure are necessary. Only the base plate of the slide gate has to be welded to the steel shell. The refractory lining is completed with two flat arches above and underneath the tap hole opening. The well block is put on place with its centerline exactly positioned. The interface between the well block and the surrounding lining is cast. Subsequently the slide gate is mounted on the base plate and nozzles and plates are installed.
For safety reasons it has to be sure that it is possible to move the slide gate above the copper bath if an emergency occurs. In case of power failure, a back-up power generator is available at the anode furnace. Additionally the hydraulics are installed in such a way that the slide gate closes automatically in case of emergency.
If the furnace layout shows the slide gate located on the same side than the tuyeres, the slide gate is immerged for a long time period also during oxidation and reduction. To prevent freezing of copper in the tapping channel during this time the lower plate is equipped with nitrogen purging (Figure 5). For this reason this moving plate has a small drilling and is connected to a nitrogen pipe. When the slide gate is closed the outlet of the drilling lies exactly in the tapping channel. So a constant flow of nitrogen keeps the channel open.

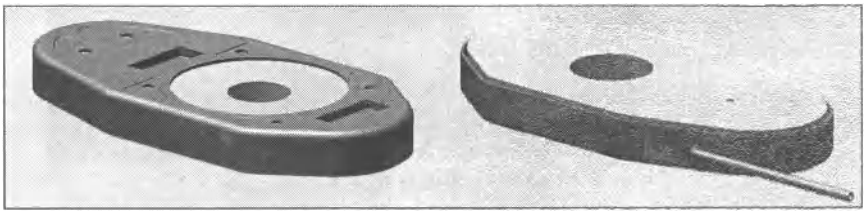

Figure 5. Upper Plate and Lower Plate with Nitrogen Piping.

Due to the low distance between slide gate and casting launder an adequate heat protection is installed. It prevents an overheating of slide gate, hydraulic system and nitrogen pipes.

Results

The following reported results were obtained at Metallo-Chimique N.V. (Belgium) [1]. Because of its special position – tap hole and poling tuyeres are on the same side of the furnace - the tap hole is submerged all the time during poling and casting. The total immersion time is 7 to 7,5 hours per heat and approximately 80 heats are processed per month.
In the original setup the casting was started with the casting hole at height and as the anode furnace is emptied during the cast it is turned downwards. However, a large accretion is build in the launder. Because the batch wise work, this accretion causes a lot of copper return and damage to the launder when removing it. Because the slide gate allows to start casting with the casting hole at its lowest point, this build-up in the launder are avoided. The slide gate also eliminates almost completely the splashing and the cleaning is minimal. Before, more than 120 MT of copper had to be removed from the surroundings and re-melted.
Because always casting from the lowest point in the anode furnace, no slag is entrained in the anodes. Thus, an improvement of the surface quality of the anodes can been seen.

The slide gate allows to regulate the copper flow from the anode furnace to the intermediate ladle (so no turning up and down of the anode furnace anymore). If the intermediate ladle would have been on load cells, it is thinkable to even automate this. It is also possible to stop for a short while the copper flow and restart casting without any problems.

Figure 6. Slide Gate with Heat Protection Shield in O

Operation.

The limiting factor for the lifetime of the installed refractories is the oxygen lancing in cases where the copper freezes in the tap hole. With the help of the above described nitrogen purging via the lower plate the tap hole can be kept open or during sporadic heats leaves only a thin layer to be lanced. Thus the wear of the inner nozzle is significantly reduced and a life time of more than six weeks was obtained.
The plates show a lifetime of up to 16 heats and the well block hasn't to be changed during the two years life time of the anode furnace. Only small gunning repairs were necessary.

Summary of Benefits

- Improved safety for operators due to remote controlled opening and closing procedure.
- Accurate controlled and steady flow and reduced maintenance for furnace drive. Only one small part has to be moved, not the entire furnace.
- Slag free casting due to tapping from the bottom of the furnace.
- Reduced splashing and therefore reduced cleaning effort due to the low tapping position.
- Reduced oxygen pick-up due to the small distance between tap hole and launder.
- Higher anode quality due to low oxygen content and slag free casting.
- Immediate emergency stop is possible by simple push-button operation.

Summary

It could be shown that the especially for the copper industry adapted slide gate system meets all operational and safety requirements. Increased productivity as well as decreased fuel consumption and CO_2 emissions due to reduced rejects could be obtained. The slide gate eliminates almost completely the splashing and the cleaning is minimal.
For the future a big potential for slide gate applications on different vessels in the copper industry can be predicted.

References

1. Steven Smets (Metallo-Chimique N.V.), "Experiences with Slide Gate System Installation at an Anode Furnace" (Internal presentation at Metallo-Chimique N.V., Beerse, Belgium), 4 February 2010)

3rd International Symposium on High-Temperature Metallurgical Processing
Edited by: Tao Jiang, Jiann-Yang Hwang, Patrick Masset, Onuralp Yucel, Rafael Padilla, and Guifeng Zhou
TMS (The Minerals, Metals & Materials Society), 2012

RECOVERY OF HUANGMEI LIMONITE BY FLASH MAGNETIC ROASTING TECHNIQUE

Wen Chen[1], Xinghua Liu[1], Zeyou Peng[1], Qiulin Wang[1]

[1]Changsha Research Institute of Mining and Metallurgy Co.,Ltd.; 966 Lushan South Road; Changsha, Hunan, 410012, China

Keywords: Limonite, Flash Magnetic Roasting, Recovery

Abstract

Limonite is a collective for iron hydroxide argillaceous materials. It is very difficult to be treated due to the wide variation in specific gravity and magnetism and the high argillization rate in the course of grinding and beneficiation. The iron ore in Huangmei, Hubei, China is the typical representative of limonite. If the limonite is processed using conventional physical beneficiation methods (e.g. magnetic separation, gravity separation, flocculation-desliming-flotation, or a combined process of the three), it can only be obtained an iron concentrate grade of 51.98% and an iron metal recovery of 86.64%. However, the technique of flash magnetic roasting-magnetic separation can improve the concentrate grade to 61.03%, iron recovery to 91.17%. This paper describes the tests of recovering limonite by flash magnetic roasting in detail.

Introduction

Limonite (mFe_2O_3, nH_2O)[1] is a general designation for hydrous iron hydroxides and argillaceous matters. Limonite is hard to be separated because of its complicated geneses, comparatively weak magnetism, nonuniform grain size and being easily slimed during grinding. So most small and medium enterprises sell deslimed limonite product which was dealt with just by simple methods of washing, magnetic separation or gravity separation and so on. In recent years with the iron ore prices soaring, significant progress was made in mineral processing research of limonite. Laboratory research and industrial test results showed that flocculation-desliming-flotation process and roasting-magnetic separation process are the two best methods to recover limonite till now. To compare these two methods, roasting-magnetic separation process is superior to flocculation-desliming-flotation process in aspects of beneficiation indexes and industrial stability.

The large amount of basic research results showed that the key favorable technological parameters affecting flash roasting are narrow particle size, improving the rate of heat exchange between thermal current and ore particles, increasing the contact area between reducing atmosphere and ore particle surface, and so on.

According to above research results, Changsha Research Institute of Mining and Metallurgy (abbreviated to CRIMM) developed flash magnetic roasting technology and designed a set of corresponding test equipment, and the differences between this test equipment and shaft furnace, rotary kiln are as follows: ore roasting state changed from accumulation state roasting into suspended photocatalyst roasting, the contact area between thermal current and ore particle surface is 3000～4000 times larger than that in rotary kiln and the rate of heat exchange improved greatly due to the ore particle diameter of feed reduced to 0.2 mm or so. This paper describes the roasting-magnetic separation tests of Huangmei limonite in detail, and the roasting tests were carried out in flash magnetic roasting test equipment.

Test Equipments and Methods

Test Sample

The limonite ore sample is from Huangmei, Hubei, China. The results of main chemical composition of limonite ore and the chemical phase of iron are listed in Tables I and II, respectively.

Table I. Main Chemical Composition Analysis of Sample /%

Component	Content	Component	Content	Component	Content	Component	Content
TFe	38.14	Al_2O_3	4.50	BaO	2.33	S	0.72
FeO	1.62	CaO	1.57	Na_2O	0.035	LOI	9.71
Fe_2O_3	52.73	MgO	0.26	K_2O	0.42	TFe/FeO	23.54
SiO_2	23.63	MnO	1.90	P	0.0027	Alkaline coefficient	0.065

Table II. Chemical Phase Analysis of Iron /%

Iron phase	Fe in magnetite	Fe in limonite (or hematite)	Fe in carbonate	Fe in sulfide	Fe in silicate	Total
Content	0.02	36.17	0.4	0.24	1.31	38.14
Distribution rate	0.05	94.83	1.05	0.63	3.44	100.00

According to the comprehensive research results of microscopic identification, X-ray diffraction analysis and scanning electron microscopy analysis, the metallic minerals are mainly limonite, the second one are romanechite; hematite and pyrite are distributed sporadically. The main gangue minerals are quartz and barite.

Test Equipments

The main equipment used in tests is flash magnetic roasting equipment which contains preheater, reacting furnace, airheater, dust pelletizing system and control system, and so on. The equipment structure and internal material flow states are given in Fig. 1. In addition, the other equipments include XMB-67 type ball mill (Φ200 mm×240mm), drum type low intensity magnetic separator and SHP high intensity magnetic separator, and so on.

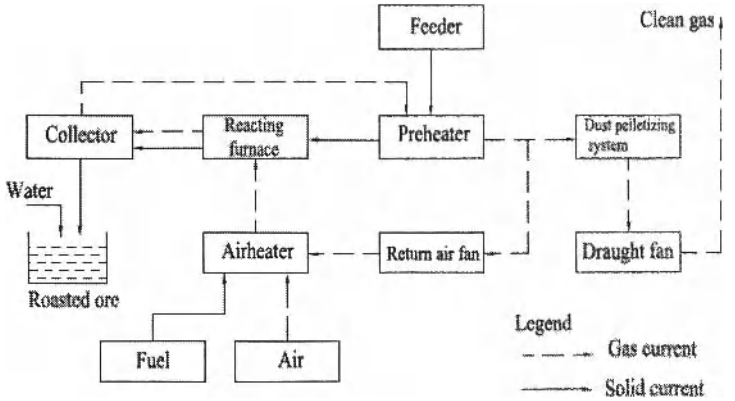

Fig. 1. Structure of flash magnetic roasting equipment and internal material flow states

Test methods

Based on mechanism analysis of thermodynamics and dynamics, the chemical reactions occurred in the process of magnetic roasting are as below[2]:

$$3Fe_2O_3 + CO - 2Fe_3O_4 + CO_2 \qquad -53.2KJ/mol \qquad (1)$$

$$3FeCO_3 - Fe_3O_4 + 2CO_2 + CO \qquad +205.86KJ/mol \qquad (2)$$

The key technological parameters influencing conversion degree of magnetite are roasting temperature, CO concentration and solid/gas ratio. Firstly, the conditioning tests of different parameters were carried out on crude ore in flash magnetic roasting equipment, and then to check roasting effect, low intensity magnetic separation (LIMS) tests were carried out on roasted ore under the condition of grinding fineness of 91.05%-0.045mm and magnetic field intensity of 1500 Oe. Secondly, preconcentration tests were conducted on roasted ore obtained from the condition of optimal roasting technological parameters, and then grinding fineness tests and magnetic field intensity tests were implemented on rough concentrate from

preconcentration tests. Finally, process flow tests were conducted on the basis of above conditioning tests.

As comparison, detailed conditioning tests of high intensity magnetic separation (HIMS) were carried out on crude ore. But this paper just describes the process flow test results of HIMS for comparative analysis.

Results and Discussion

Conditioning Tests of Flash Magnetic Roasting on Crude Ore

The conditioning tests of temperature, CO concentration and solid/gas ratio were carried out on crude ore in flash magnetic roasting equipment, the test results are described as follows.

Roasting Temperature Tests. Roasting temperature tests were conducted under the condition of CO concentration of 3.5% and solid/gas ratio of 0.5 kg/Nm^3, and LIMS test results of the obtained roasted ores are shown in Fig. 2.

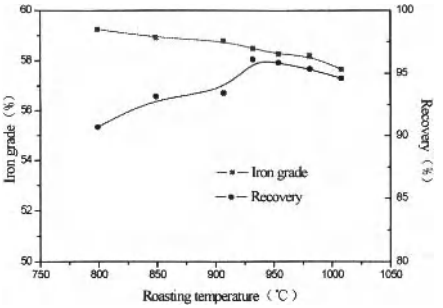

Fig. 2. LIMS test results of roasted ores obtained from roasting temperature tests

The test results showed that the quality of roasted ore was very good, under the condition of a wide temperature range of 799～1008 ℃, the concentrate with iron grade of 57～59% and recovery of 93～96% was obtained. The comprehensive consideration of iron grade and recovery of magnetic concentrate, a wide temperature range of 850～950 ℃ was selected to conduct subsequent tests, and meanwhile this roasting temperature was not high and easy to be controlled.

CO Concentration Tests. CO concentration tests were conducted under the condition of roasting temperature between 850 ℃ to 950 ℃ and solid/gas ratio of 0.5 kg/Nm3, the LIMS test results of the obtained roasted ores are shown in Fig. 3.

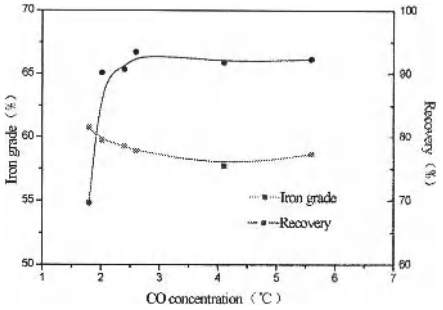

Fig. 3. LIMS test results of roasted ores obtained from CO concentration tests

It is known from Fig. 3 that with CO concentration increasing from 1.80% to 2.02%, the iron grade of magnetic concentrate was decreased from 60.75% to 59.73% and recovery was increased from 69.63% to 90.14%; when CO concentration was increased to 5.6%, the iron grade of magnetic concentrate was decreased to 58.65%, but recovery increased to 92.25%. In order to obtain good magnetic separation indexes, therefore, the CO concentration should be controlled above 2.0% during the process of roasting.

Solid/gas Ratio Tests. Solid/gas ratio tests were conducted under the condition of roasting temperature between 850 ℃ to 950℃ and CO concentration of about 2.6% , the LIMS test results of the obtained roasted ores are shown in Fig. 4.

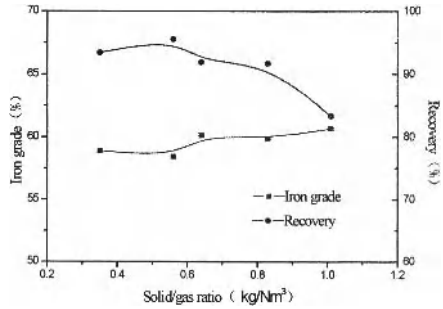

Fig. 4. LIMS test results of roasted ores obtained from solid/gas ratio tests

The above test results showed that with solid/gas ratio increasing from 0.35 kg/Nm^3 to 1.01 kg/Nm^3, the iron grade of magnetic concentrate was almost not changed, but recovery was gradually decreased. When the solid/gas ratio was 0.83 kg/Nm^3, the recovery was 91.68%; When the solid/gas ratio increased to 1.01 kg/Nm^3, the recovery was 83.32%.

The optimal roasting technological parameters were obtained through above conditioning test results, the roasting temperature should be controlled in a range of 850~950 ℃, the CO concentration was above 2.0% and solid/gas ratio was below 0.8 kg/m^3. The roasted ore as the feed to the following LIMS tests was obtained under this optimal roasting condition.

Conditioning Tests of LIMS on Roasted Ore

Preconcentration Tests of Roasted Ore. At first, preconcentration tests were carried out on roasted ore under the condition of different low magnetic field intensities, the test results shown in Fig. 5.

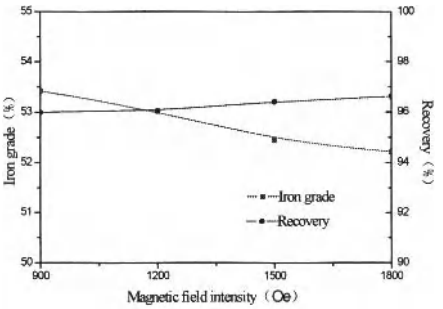

Fig. 5. Preconcentration test results of the roasted ore

It is known from Fig.5 that with the magnetic field intensity decreasing from 1800 Oe to 900 Oe, the iron grade of magnetic concentrate increased from 52.22% to 53.42%, and 1.2 percentage points rose; but the recovery decreased from 96.62% to 96.00%, and 0.62 percentage points were reduced. It can be seen that reducing magnetic field intensity appropriately can improve the grade of iron concentrate to a certain extent, and the loss of recovery is small. The magnetic field intensity of 1500 Oe was selected to conduct preconcentration test and produce rough concentrate for the subsequent tests.

Grinding Fineness Tests of Rough Concentrate. Under the condition of magnetic field intensity of 1500 Oe, grinding fineness tests were carried out on rough concentrate obtained from preconcentration tests, the results shown in Fig. 6.

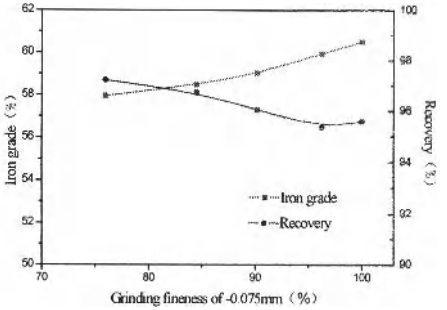

Fig. 6. Grinding fineness test results of rough concentrate

The above test results showed that with grinding fineness increasing from 75.94% -0.075 mm to 96.24% -0.075 mm, the iron grade of magnetic concentrate was increased from 57.94% to 59.92%; when the grinding fineness increased to 91.05% -0.045 mm, the iron grade was just 60.49%. The comprehensive consideration of iron grade and recovery of magnetic concentrate, the grinding fineness of 96.24% -0.075 mm was selected to conduct following tests.

Magnetic Field Intensity Tests of Rough Concentrate. Under the condition of grinding fineness of 96.24% -0.075 mm, magnetic field intensity tests were carried out on rough concentrate, the results shown in Fig. 7.

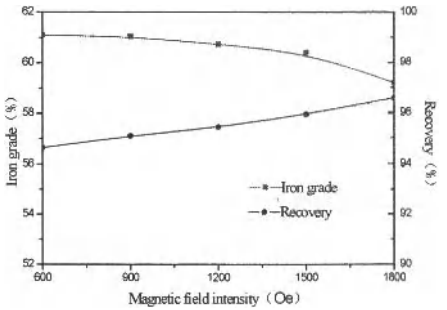

Fig. 7. Magnetic field intensity test results of rough concentrate

It is known from Fig.7 that with the magnetic field intensity increasing from 600 Oe to 1800 Oe, the iron grade of magnetic concentrate was decreased from 61.09% to 59.20%, but the recovery was increased from 94.64% to 96.58%. When the magnetic field intensity was 900 Oe, the iron grade of concentrate was 61.03% and the recovery was 95.10%. The magnetic field intensity of 900 Oe was selected to conduct process flow tests.

Process Flow Tests

Process Flow Tests of Flash Magnetic Roasting-LIMS on Crude Ore. On the basis of above conditioning tests, the process flow tests of flash magnetic roasting- LIMS were carried out on crude ore, the results are listed in Table Ⅲ and the flowsheet is shown in Fig. 8.

Table Ⅲ Results of Flash Magnetic Roasting-LIMS Process Test /%

Product	Yield	Iron grade	Recovery
Concentrate	56.87	61.03	91.17
Tailings	33.42	10.06	8.83
LOI	9.71	0.00	0.00
Crude ore	100.00	37.45	100.00

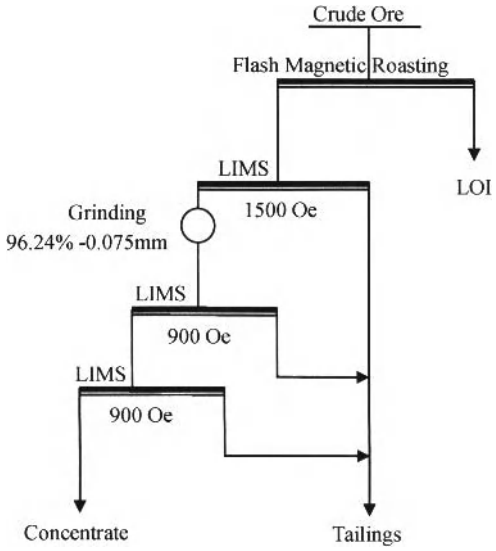

Fig. 8. Flowsheet of flash magnetic roasting-LIMS process

Process Flow Tests of HIMS on Crude Ore. As the comparison of flash magnetic roasting-LIMS process flow, the HIMS process flow tests were conducted on the basis of detailed conditioning tests, the results are listed in Table Ⅳ and the flowsheet is shown in Fig. 9.

Table Ⅳ. Results of HIMS Process Test /%

Product	Yield	Iron grade	Recovery
Concentrate	62.42	51.98	86.64
Tailings	37.58	13.31	13.36
Crude ore	100.00	37.45	100.00

The iron concentrate with yield of 56.87%, iron grade of 61.03% and recovery of 91.17% was obtained through flash magnetic roasting-LIMS process. While using HIMS process, the iron concentrate with iron grade of 51.98% and recovery of 86.64% could be obtained. It can be seen that the iron grade was 9.05 percentage points higher and the recovery was 4.53 percentage points higher than that of HIMS process.

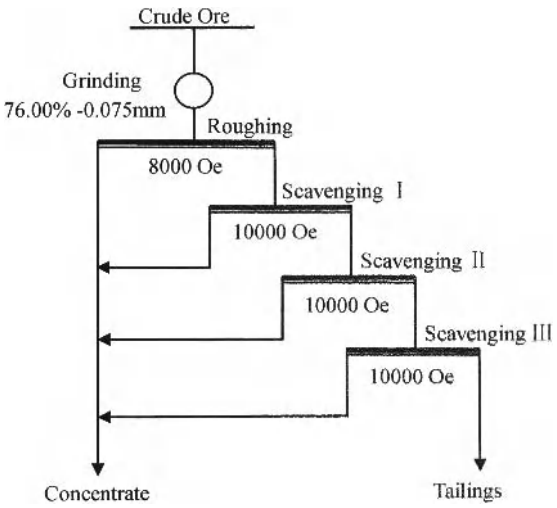

Fig. 9. Flowsheet of HIMS process

Conclusion

(1) When using the flash magnetic roasting equipment to process Huangmei limonite ore, the optimal technological parameters were obtained by the following: the roasting temperature was from 850 ℃ to 950 ℃, the CO concentration was above 2.0% and solid/gas ratio was below 0.8 kg/m^3. The roasting tests show that the flash magnetic roasting technology has good adaptability and operability.

(2) The flash magnetic roasting-LIMS is a satisfactory process of dealing with

Huangmei limonite ore. Using flash magnetic roasting-LIMS process, the iron concentrate with iron grade of 61.03% and recovery of 91.17% could be obtained. The iron grade was 9.05 percentage points higher and the recovery was 4.53 percentage points higher than that of HIMS process.

(3) The flash magnetic roasting- LIMS technology provides a new way for exploiting and utilizing the complex refractory limonite, hematite and siderite ores.

References

[1] Zhou Leguang. Ore Foundation(3nd.ed)(.Beijing: Metallurgical Industry Press, 2007) 154-195. (in Chinese)

[2] Zhang Maojun et al.. Handbook of Mineral Processing (Volume 3: Part3). (Beijing: Metallurgical Industry Press, 1991) 353-359. (in Chinese)

3rd International Symposium on High-Temperature Metallurgical Processing
Edited by: Tao Jiang, Jiann-Yang Hwang, Patrick Masset, Onuralp Yucel, Rafael Padilla, and Guifeng Zhou
TMS (The Minerals, Metals & Materials Society), 2012

STUDIES ON ALTERNATIVE BLAST FURNACE BURDEN STRUCTURE WITH HIGH PROPORTION SINTER

Jianjun Fan[1,2], Guanzhou Qiu[1], Tao Jiang[1], Yufeng Guo[1], Yongbin Yang[1], Meixia Cai[2]

1. School of Minerals Processing and Bioengineering, Central South University, Changsha, 410083, Hunan, China;
2. Taiyuan Iron and Steel (Group) Co. Ltd., Taiyuan, 03003, Shanxi, China.

Keywords: Acidic sinter, Sintering property, Metallurgical property, Disintegration

Abstract

A series of sintering and metallurgical experiments were carried out to optimize the blast furnace burden structure in this study. The results indicated that the sinter disintegrated seriously with basicity around 1.4, and after this "turning point", the sintering properties were improved gradually with the increase of basicity of sinter. Based on the results, an idea was put forward which focused on producing two different kinds of sinter with different basicity. Different with the original burden structure of 85% sinter with basicity 1.4-1.5 + 15% pellets, an alternative new BF burden structure was proposed by the following structure: 44% sinter with basicity 1.05 + 44% sinter with basicity 1.87 + 12% pellets. This new alternative BF burden structure has been adopted by some steel plants.

Introduction

In recent years, conventional blast furnace (BF) process was put into operation to produce hot metal in "A" steel plant. "A" steel plant owns two sets of sinter strands at present. Because the sinter production capacity exceeds the actual requirements of BF, a burden structure with 85-90% self-made sinter + 10-15% purchased pellets is adopted to take advantage of the low-cost sinter. But the serious problems encountered with the BF operators are that the sinter disintegrated easily during transportation and storage process. Therefore, the rate of return fines is very high after sinter being screened.

In order to regulate blast furnace slag composition, as well known, the basicity of the sinter must be between 1.4-1.5. According to production practices and researches [1-3], the sinter with basicity around 1.4-1.5 is classified as low-quality sinter. The reason lies in that it transforms from acidic sinter to high basicity sinter and the complex mineralogical composition result in the low quality. Especially restricted by raw material condition, the SiO_2 content of the sinter in "A" steel plant ranges from 7%-8%, which promotes the formation of dicalcium silicate (C_2S), and the consequent phase transformation(from β -C_2S to γ-C_2S) results in the disintegration of sinter[4].

But for acidic and higher basicity sinter, the results are quite different. The researches indicate that for acidic sinter, magnetite and Ca-fayalite dominate the main bonding phase[5-6]. The physical strength is high enough to guarantee the strength of the sinter. For higher basicity sinter, magnetite, hematite and calcium ferrite are the main mineralogical composition[7-8]. Therefore, the sinter with higher basicity possesses good physical strength.

In order to improve the sinter quality of "A" steel plant, a series of experiments were conducted on to replace the current low quality sinter by producing other two kinds of sinter with different basicity. Finally, a new kind of BF burden structure was proposed according to metallurgical experiments and metallurgical properties of different burden structure.

Sintering Properties

Raw Materials

The chemical compositions of raw materials are shown at Table Ⅰ.

Table Ⅰ The Chemical Compositions of Raw Material (wt %)

Name	TFe	FeO	SiO_2	Al_2O_3	CaO	MgO	LOI
Iron Ore 1	65.12	28.04	7.95	0.34	0.36	0.24	0.89
Iron Ore 2	62.83	3.28	3.46	2.53	0.32	0.08	2.97
Iron Ore 3	64.82	27.36	6.87	0.47	0.46	0.53	1.87
Miscellaneous Ore	53.8	9.8	7.65	1.72	10.65	2.16	2.87
Limestone	/	/	1.36	0.38	50.52	2.38	49.8
Dolomite	/	/	2.1	0.45	29.35	18.36	48.6
Lime	/	/	2.3	0.35	85.3	3.23	3.62

LOI: Loss on ignition.

Methods

The sintering apparatus consisting of a 300 mm diameter×700 mm high sinter pot, which was used to simulate the industrial sintering. The proportioned raw materials including iron ore, flux, coke and sinter return fines were mixed uniformly and then added water into the mix. The moisture in the mix was controlled at a suitable level by calculating moisture of raw materials in advance. Before being loaded into the sinter pot, the mix was granulated for 3 min in a 1200 mm long×800 mm diameter drum, with a rotation speed of 18 rpm.

The granulated mix was then charged into sinter pot, the mix was ignited with 1050℃ for 2 min under 6 kPa suction pressure. After ignition, the suction pressure increased to 12 kPa and the exhausted gas temperature was monitored continuously. The sintering time was taken from the ignition to exhausted gas reaching the highest temperature. The finished sinter cake was dropped from 2m height three times to simulate the actual condition in a commercial sinter plant. Subsequently, the sinter was screened with 50, 40, 25, 16, 10 and 5 mm square aperture screen.

The sinter above 5 mm was the finished sinter of pot test and that minus 5 mm was the return fines. Finally the finished sinter was tested to determine the relative technical indices.

Results of Sinter

The experiments were performed according to the actual raw material condition of "A" steel plant by implementing the sinter pot tests with following designed sinter basicity (CaO/SiO_2): 0.6, 0.8, 1.0, 1.4, 1.8, 2.0, 23.

In this program, tests were carried out to determine the effect of sinter basicity on the following technical indices: vertical sintering speed($V_\perp$) , productivity, mean size of sinter mix, tumble index of finished sinter, +40 mm percentage of finished sinter, 25-40 mm percentage of finished sinter and -5 mm percentage of finished sinter after being cooled in ambient air for two hours.

A series of sinter pot tests were carried out by regulating mix moisture and coke rate so as to get best results. The results are shown at Table II.

Table II Summaries of the Sintering Results

Sinter No.	1	2	3	4	5	6	7
Designed Basicity (CaO/SiO_2)	0.6	0.8	1.0	1.4	1.8	2.0	2.3
$V_\perp$, mm/min	13.83	16.33	22.53	22.02	24.59	26.03	29.95
Productivity, $t/(m^2.h)$	1.36	1.44	1.75	1.80	1.84	1.95	2.09
Mean Size of Sinter Mix, mm	3.27	3.63	4.21	4.17	4.35	4.57	4.48
Tumble Index (+6.3 mm), %	60.07	60.67	60.70	64.4	66.8	68.5	71.4
Product Size Distribution, %							
+40mm	25.43	28.81	18.81	15.37	10.49	9.94	6.89
25-40 mm	23.71	20.08	30.41	33.04	33.72	34.84	34.30
- 5 mm*	1.49	3.15	3.87	6.13	4.87	3.14	2.32

***The finished sinter was cooled in ambient air for two hours.**

Discussions on Sintering Properties

(1) For vertical sintering speed($V_\perp$), it is increased gradually with the increase of sinter basicity. But the $V_\perp$ keeps at extremely low level when sinter basicity is less 1.0, the productivity also demonstrates the similar trend. Such results are mainly attributed to the smaller mean size of sinter mix, for sinter mix with basicity 0.6 (No.1) and 0.8 (No.2), there is lower proportion of lime added in the mix, so the mean size of blend materials is 3.27 mm and 3.63 mm respectively, which has a detrimental effect on granulated bed permeability during subsequent sintering process. When it comes to sinter mix with basicity 1.0 (No.3), the mean size of mix reaches 4.21 mm since much more lime is added in the mix, which would guarantee reasonable permeability during subsequent sintering process. The results also show that there is marked increase for $V_\perp$ and productivity when the basicity increase from 1.0 to 1.4.

(2) For physical strength, which represents by tumble index (TI), it is nearly at the same level when the sinter basicity varies from 0.6 (No.1) to 1.0 (No.3), but a rapid increase occurs when the basicity over 1.4 (No.4).
(3) For size distribution, the results indicate that for +40 mm percentage of finished sinter, it is in reverse proportion to sinter basicity, while for 25-40 mm percentage of finished sinter, it is in direct proportion to sinter basicity. For blast furnace operators, they prefer sinter with the size of 25-40 mm to that of larger size over 40 mm ,because intermediate-sized sinter is conducive to quicker reduction during it's descent from BF stock-line to bosh. So from this perspective, it is suggested to produce higher basicity sinter so as to optimize size distribution of sinter.
(4) In order to assess the sinter disintegration during its storage or transportation process, the experiments were performed by cooling the sinter naturally at ambient air for two hours and then evaluate the fracture toughness of sinter by screening the sinter with 5 mm square aperture screen.
The results indicate that the sinter disintegrates seriously and -5mm percentage climbs to maximum level of 6.13% when sinter basicity around 1.4 (No.4), while for acidic sinter and higher basicity sinter, -5 mm percentage shows decreasing trends. It was observed on site that the new cracks formed along the surface of the finished sinter and very fine gray powder formed erratically, the sinter become brittle slowly. This is the so called "self disintegration" for sinter with higher level of SiO_2 and FeO content, this phenomena are also reported in other researches[9].
So it is suggested to avoid the production of sinter with basicity around 1.4 based on the consideration of sintering property comprehensively.

Chemical and Mineral Composition of Sinter

Methods

The determination of mineralogy and microstructure of the sinter were finished by using optical microscope, and the mineral composition of the sinter was quantified by manual point counting technique. The chemical and mineral analyses of the sinter are shown at Table Ⅲ and Table Ⅳ.

Results and Discussions

(1) For acidic sinter (No.1, No.2 and No.3), it is found that Ca-fayalite and gangue dominate the bonding phase, very little of dicalcium silicate is observed. These bonding phase only shrink in volume and there is no remarkable fracture occurring among the phase, such simple mineral phase could guarantee the sinter physical strength.
(2) For No.4 sinter, the proportion of Ca-fayalite decreases while that of dicalcium silicate (C_2S) increases to 5%-8%. During the subsequent cooling sage, the C_2S always goes through phase transformation (from β -C_2S to γ-C_2S) and the volume of sinter increases by nearly 10%, which results in the disintegration of sinter, so the sinter became brittle during subsequent storage or

transportation process.

(3) For No.5 sinter and other high basicity sinter, calcium ferrite dominates the bonding phase and Ca-fayalite disappears gradually. Since calcium ferrite could stabilize the transformation of β -C_2S and it also could increase bonding phase strength, so the physical strength of sinter improves gradually with the increase of sinter basicity.

So it is suggested to avoid the production of sinter with basicity around 1.4 because of phase transformation (from β -C_2S to γ-C_2S).

Table III The Chemical Analysis of Sinter

Sinter No.	1	2	3	4	5	6	7
TFe, %	62.23	6134	60.15	57.76	56.46	55.94	54.62
FeO, %	14.96	12.32	10.66	9.21	8.85	8.43	8.23
SiO_2, %	7.74	7.68	7.57	7.28	7.61	7.48	7.40
Al_2O_3, %	1.29	1.28	1.26	1.21	1.21	1.19	1.16
CaO, %	4.69	6.06	7.55	10.50	14.27	14.74	16.49
MgO, %	1.30	1.30	1.50	2.51	2.19	2.51	2.64
Actual Basicity	0.60	0.78	0.99	1.44	1.87	1.97	2.22

Table IV The Mineral Analysis of Sinter

Sinter No.	1	2	3	4	5	6	7
Magnetite, %	72-75	68-72	65-70	58-65	51-58	47-51	40-47
Hematite, %	5-7	5-9	7-9	7-10	7-10	8-11	8-12
Dicalcium Silicate, %	/	/	3-6	5-10	10-15	10-12	8-10
Calcium Ferrite, %	/	/	1-2	8-13	13-20	20-27	27-32
Ca-Fayalite, %	5-8	3-5	5	3-5	1-2	/	/
Gangue, %	8-12	11-13	8-12	8-9	7-8	7-8	7-8
Others, %	2-3	2-3	2-3	2-3	1-2	1-2	1-2

Study of Metallurgical Properties

Based on the previous researches, a bold idea was put forward, which characterized with producing acidic sinter (basicity less 1.2) plus higher basicity sinter (basicity over 1.6) to replace the sinter with basicity around 1.4-1.5. So metallurgical property experiments such as 900℃ reduction index and 550℃ low temperature reduction degradation index were performed, but much more researches were concentrated on melting - dripping properties of integrated burden, so as to determine the reasonable burden structure when using two different kinds of sinter.

Test Standard and Methods

The tests on reduction index and low temperature reduction degradation index were finished in

compliance with ISO 7215 and ISO 4696 respectively. The results are presented by RI and RDI respectively.

The experiments for melting-dripping properties were carried out in softening-melting experimental set-up. It consists of a furnace with graphite resistance heating element capable of raising temperature of the furnace to 1600℃, alumina reaction tube, graphite sample vessel, load applying device, melt-down product collecting chambers. The sample vessel containing sinter/pellet was placed at the centre of the furnace with the help of supporting stand. The sample was heated through a programmed heating pattern in an attempt to simulate the blast furnace conditions existing between the stock-line and the bosh. During heating process, the sample was reduced by reducing gases. The test conditions are as follows:

- Maximum temperature: 1600℃; • Sample vessel diameter: 48mm.
- Sample bed height: 100mm; • Particle size range: 8-10mm; • Gas flow: 15 L. min^{-1} at NTP;
- Gas composition: 0–200℃ : N_2 only, 200-1600℃: 30% CO and 70% (N_2+H_2) ;
- Heating rate: 0-200℃: manual, 200-900℃: 10℃. min^{-1}, 900-1600℃: 3℃. min^{-1} ;
- Applied load: 98 kPa at 900℃ until end of the test.

The results are represented by T_{10}, T_{40}, T_s, T_m, ΔP_m, ΔP_s and (S). The (S)[10] is calculated by formula (1).

$$(S) = \int_{T_m}^{T_f} (\Delta P_m - \Delta P_s) \cdot dT \ (\text{KPa} \cdot ℃) \qquad (1)$$

Where, T_{10} and T_{40} refer to start-softening and end-softening temperature (℃) respectively, T_s and T_m refer to start-melting and start-dripping temperature (℃) respectively, ΔP_s refers to start-melting pressure (50×9.8 Pa), ΔP_m refers to maximum pressure (×9.8 Pa). The (S) represents comprehensive indices of integrated burden, the lower the (S), the better indices for integrated burden structure.

Results and Discussions

The results on RI and RDI are shown at Table V, while the results of melting-dripping properties of integrated burden are shown at Table VI.

Discussions on RI and RDI. (1)For reduction degree (RI), it is increased gradually with the increase of sinter basicity. As above-mentioned discussions, for acidic sinter, fayalite and gangue dominate the bonding phase, very little calcium ferrite is observed, since fayalite is difficult to be reduced, so the reduction index of acidic sinter is very low compared with high basicity sinter. With the increase of the sinter basicity, more calcium ferrite are formed, the proportion of magnetite decreases while that of hematite increases, since calcium ferrite and hematite are easy to be reduced easily compared with magnetite, so reduction index increases gradually with the increase of sinter basicity. (2) For low temperature reduction degradation index (RDI), it is decreased gradually with the increase of sinter basicity, but it is all at low level, which mainly results from the high SiO_2 continent of the sinter and the increasing MgO content in the sinter.

Discussions on Melting-Dripping Properties of Integrated Burden Structure. (1) For test A, B and C, compared with base test I, ΔP_m shows higher level with the No.1 sinter proportion increases from 30% to 42% , which indicates that the cohesive zone permeability of BF deteriorate, so the properties of integrated burden structure deteriorate if adopting A, B, or C burden structure. (2) For test D, E and F, compared with test I, ΔP_m also shows higher level with the No.2 sinter proportion increases from 35% to 48%, the (S) also shows higher level, which indicates that the properties of integrated burden also deteriorate if adopting D, E, or F burden structure. (3) For test G and H, compared with test A, B, C, D, E and F , ΔP_m decreases to 360 × 9.8 Pa and 500× 9.8 Pa respectively, the (S) also decreases to 334 kPa.℃ and 705 kPa.℃ respectively, which indicates that the properties of integrated burden structure improve. It is confirmed that higher basicity (CaO/SiO_2=2.0) sinter plus acidic sinter (CaO/SiO_2=1.0) could replace the low quality sinter with basicity around 1.4. (4) The comprehensive indices of Test G are better than that of test H and test I, so the integrated burden structure of 44% No.3 S+44% No.6 S+12% P could replace the original integrated burden structure of 85% No.3 S+15% P.

Table V Metallurgical Properties of Different Basicity Sinter

Sinter No.	1	2	3	4	5	6	7
Basicity (CaO/SiO_2)	0.60	0.78	0.99	1.44	1.87	1.97	2.22
RI, %	41.45	45.36	68.51	70.02	73.89	73.45	74.36
RDI (-3.15 mm, %)	16.8	14.0	13.4	12.2	11.8	10.0	11.7

Table VI Melting-Dripping Properties of Integrated Burden Structure

Test No.	Burden Structure	T_{10}, ℃	T_{40}, ℃	Ts, ℃	T_m, ℃	ΔT, ℃	ΔP_m, ×9.8 Pa	S, kPa.℃
A	30%No.1S*+58% No.5S+12%P*	1185	1270	1310	1450	140	800	1029
B	33%No.1S+55% No.6S+12%P	1180	1255	1315	1440	125	1000	1163
C	42% No.1S+46% No.7S+12%P	1160	1250	1300	1445	145	1220	1662
D	35% No.2S+53% No.6S+12%P	1150	1260	1290	1420	130	860	1031
E	38% No.2S+50% No.6S+12%P	1165	1270	1335	1440	105	1060	1039
F	48% No.2S+40% No.7S+12%P	1160	1280	1290	1460	170	800	1249
G	44% No.3S+44% No.6S+12%P	1180	1250	1350	1460	110	360	334
H	47% No.3S+41% No.6S+12%P	1180	1260	1280	1440	160	500	705
I*	85% No.3S+15%P	1165	1275	1320	1445	125	570	637

***S and P refer to sinter and pellet respectively. Test I refers to base test.**

Conclusions

(1) For acidic sinter, the sintering properties of the sinter with basicity 1.0 are better than that of the sinter with basicity ranging from 0.6 to 0.8.

(2) The so called "self disintegration" occurs and sinter disintegrates seriously with sinter

basicity around 1.4.

(3) For higher basicity sinter, the sintering properties improve gradually with the increase of sinter basicity.

(4) For RI of sinter, it is increased gradually with the increase of sinter basicity, while the RDI decreases with the increase of sinter basicity.

(5) For melting - dripping properties of integrated burden structure, the maximum pressure level (ΔP_m) increases sharply when higher basicity sinter plus sinter with basicity 0.6 or 0.8 respectively, the (S) also shows higher level, which indicates that the properties of integrated burden deteriorate if adopting such burden structure.

(6) The maximum pressure (ΔP_m) decreases to lower level when higher basicity sinter plus sinter with basicity around 1.0, the (S) also demonstrates similar trends, which indicates that the properties of integrated burden improve.

(7) It is confirmed that the integrated burden structure of 44% No.3 S+44% No.6 S+12% P could replace the original integrated burden structure of 85% No.3 S+15% P.

(8) An alterative BF integrated burden structure is proposed, which characterizes with acidic sinters (basicity less 1.2) plus higher basicity sinter (basicity over 1.6) to replace the sinter with basicity around 1.4-1.5.

References

1. Qinchen Zhang. *The theory and process of sintering practice* (Changsha: Central South University of Technology Press, 1992), 203-204. (In Chinese)
2. Zhiwu Liu, Qinghua Tang, and Ansheng Hu, "Production of acidic pellet-sinter and sinter with high basicity and their smelting effect," *Iron-Making*, 19 (5) (2000), 15-17. (In Chinese)
3. Shinong Yang, "The study of reasonable blast burden structure at AnShan steel," *Sintering and Pelletizing*, 9 (5) (1984), 1-11. (In Chinese)
4. Jinzhi Zhang, "The study of metallurgical properties of sinter with different silica content," *Sintering and Pelletizing*, 9 (6) (1984), 1-9. (In Chinese)
5. Yongjun Liu, Xilin Li, and Zhi-jun Song, "The practice of acidic sinter production in Aanyang steel," *Iron and Steel*, 38 (9) (2003), 1-3. (In Chinese)
6. Baocai Dai, Bingyan Gao, "Experiment and production of low silica acid sinter," *Sintering and Pelletizing*, 28 (2) (2003), 48-50. (In Chinese)
7. Chengjia Li, Ju Ding, and Jianqi Zhang, "The industrial trials and production of high basicity sinter," *Sintering and Pelletizing*, 6 (4) (1981), 25-34. (In Chinese)
8. Fangchen Lu, "Mineral composition of high basicity sinter in Xintai steels and its influence," *Sintering and Pelletizing*, 25 (1) (2000), 17-19. (In Chinese)
9. Jinglan Fu, "The study on mineral composition and metallurgical property of different basicity sinter" (Paper presented at the 1979 CSM annual meeting of iron-making. Beijing, 1979), 98-104. (In Chinese)
10. Manxin Xu, Gensheng Feng," Test and study of burden design for the blast furnace in Shijiazhuang steels," *Sintering and Pelletizing* ,23(6)(1998), 1-3. (In Chinese)

3rd International Symposium on High-Temperature Metallurgical Processing
Edited by: Tao Jiang, Jiann-Yang Hwang, Patrick Masset, Onuralp Yucel, Rafael Padilla, and Guifeng Zhou
TMS (The Minerals, Metals & Materials Society), 2012

HYDROTHERMAL SULFIDATION OF CARBONATE-HOSTED ZINC-LEAD ORE WITH ELEMENTAL SULFUR

Cunxiong Li, Chang Wei, Jiqiang Liao, Zhigan Deng, Hongsheng Xu, Yan Song, Xingbin Li, Minting Li

Kunming University of Science and Technology, Faculty of Metallurgical and Energy Engineering, Kunming, 650093, P R. China

Keywords: Carbonate Hosted Zinc-lead Ore, Hydrothermal Sulfidation, Sulfidation Edtent, Flotation

Abstract: Direct flotation of oxidized zinc-lead ore is characterized by recovery of zinc and lead only around 55% and 50%, respectively. Mineralogical analysis shows that the sample used in the present study is a carbonate hosted zinc-lead ore, with a zinc and lead carbonate content that accounts for 80.14% and 75.63% of the total minerals, respectively. The carbonate hosted zinc-lead ore was hydrothermally sulfidized with elemental sufur and the experimental data indicated that under the conditions employed up to 75% zinc and 82% lead sulfidation extent were achieved. As a result of pre-sulfidation followed by flotation, the recoveries of zinc and lead into flotation concentrate were over 90%. A flotation concentrate was obtained with 52% Zn and 37% Pb from the materials which was treated by sulfidation.

Introduction

Sulfide ores are the primary source of zinc and lead, and they are becoming depleted; thus, metallurgical investigators are interested in using abundant oxidized zinc-lead ore reserves. The high-grade zinc-lead oxidized ore, which normally has a zinc content higher than 15%, can be disposed of by acid leaching and electrolysis. However, the low-grade ore, which has a zinc content lower than 10%, is difficult to smelt with pyrometallurgy and hydrometallurgy, and the processes are very complicated and expensive in terms of production flow and energy consumption. Therefore, making the low-grade oxidized zinc-lead ore more beneficial has become more important in recent years. Flotation is the most common process, and the primary method of recovering zinc and lead from sulfide or oxide minerals. It is well known that there is a difference between sulfurized and oxidized minerals regarding their separation by flotation. Flotation of zinc and lead oxidized minerals is extremely complex because of the similarities in the physicochemical and surface chemistry of the constituent minerals. There are no known direct-acting collectors capable of producing single metal concentrates [1-3].

Therefore, it is common practice to sulfurize oxide lead-zinc minerals prior to flotation to

prepare their surfaces to receive the collectors generally adopted for concentrating sulfide. There have been extensive investigations into the sulfidation of oxidized zinc-lead ore and zinc-lead ores containing oxidized constituents. The ore is subjected to a sulfidizing operation, such as a treatment with hydrogen sulfide gas or its equivalents [4-5] or sodium sulfide [6-12] or sulfidation roasting with the element sulfur [13].

The objective of this study was to investigate the sulfidation of a carbonate-hosted zinc-lead ore with sulfur under hydrothermal conditions, which were applied prior to flotation and could contribute to improving the flotation recovery of zinc and lead. In such a sufidizing operation, the oxidized ore constituents may be merely filmed with the stable metal sulfide compounds, or they may be converted to a greater or lesser extent into stable metal sulfide compounds. In the first part of the present study, we studied the sulfidation of carbonate-hosted zinc-lead ore with elemental sulfur under hydrothermal conditions and characterized the solid phases as a function of the sulfidation level by chemical analysis. The solid phases were then concentrated by a conventional flotation flow sheet.

Experiment

Materials

The chemical composition of carbonate-hosted zinc-lead ore used in the present study is shown in Table I. Mineralogical compositions of zinc and lead in the sample were identified by chemical analysis, and the results are shown in Table II.

Table I Chemical Composition of Carbonate-hosted Zinc-lead Ore

Element	Zn	Fe	SiO_2	Pb	S	As	CaO	MgO	Al_2O_3	Ag
Concentrate(%,ω)	11.27	2.17	2.73	3.45	3.15	0.003	15.21	13.38	1.39	58g/t

This ore includes calamine, hemimorphite, zincite, sphalerite and hydrozincite as zinc minerals, cerussite, galena, and lead oxide as lead minerals, hematite, limonite, dolomite, calcite, and quartz as other minerals. We can observe in table 2 that among zinc minerals, zinc carbonate is account for 80%. Mineralogy analysis also shows that most of zinc oxide and carbonate minerals were in very fine particles. Some of them are closely associated with limonite, and most of them are disseminated in the gangue minerals independently. Table 3 shows the chemical analysis of the carbonate-hosted zinc-lead ore in different size fraction.

Table II Phase Composition of Zinc and Lead in the Sample

Constituent/%	Zn		Pb	
	content	Percentage	content	Percentage
carbonate	9.04	80.14	2.61	75.63
silicate	1.64	14.59	0	0
sulfide	0.35	3.12	0.23	6.55
others	0.24	2.15	0.61	17.82
Tatal	11.27	100	3.45	100

Table III Chemical Analyses of the Sample

Particle size, μm	Zn, %	Pb, %
147–106	10.35	3.49
106–74	11.23	3.03
74–58	10.78	3.24
58–48	12.01	3.67
48–42	11.38	3.24
42–37	10.98	3.42

In the laboratory scale tests, elemental sulfur (>99% pure, powder) was used as the sulfidizing agent, and the effects of the dosage of sulfur, temperature, time and particle size were investigated in relation to the sulfidation of carbonate-hosted zinc-lead ore. The solid phases were concentrated by a conventional flotation flow sheet. The ratio of solid mass to liquid volume (S/L) was 1:10 g/mL, which was maintained for all sulfidation experiments. The slurry was stirred at a speed of 600 rpm.

Equipment and procedure

The experimental apparatus used for sulfidation of the carbonate-hosted zinc-lead ore consisted mainly of a 2 L autoclave, which was equipped with a heating mantle, a PID temperature controller, a variable speed stirrer and an internally mounted cooling coil a horizontal tube furnace and ancillary equipment. The flotation tests were conducted in a 2 L flotation cell (type XFD). The process flow sheet is shown in Fig.1.

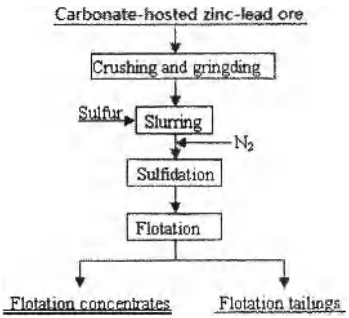

Fig. 1 The Process Flowsheet of Sulfidation and Flotation

One hundred grams of ground carbonate-hosted zinc-lead ore was added at one time to the autoclave. The procedure consisted of slurring the ore with sulfur and water at the set liquid solid ratio in the autoclave. Nitrogen was admitted for about three minutes, and heating the solution to the temperature of the experiment for some time. At the end of the experiment, the autoclave was rapidly cooled with water, and the solution was filtered for collecting the solid phases. The solid

phases were characterized by X-ray diffraction (XRD) and chemical analysis and then concentrated by flotation. The sulfidation rate of zinc or lead can be calculated by the formula.

$$\varphi = 100\% \times \frac{\alpha - \beta_1}{\beta_2 - \beta_1} \quad (1)$$

Where φ is sulfidation rate of Zn or Pb; α is the content of Zn or Pb in the form of sulfide in sulfidation product; β_1 is the content of Zn or Pb in the form of sulfide in raw ore; and β_2 is the content of Zn or Pb in raw ore.

Results and discussion

Sulfidization of carbonate-hosted zinc-lead ore

Effect of reagent dosage of sulfur The sulfidation rates of zinc and lead were also affected by the dosage of sulfidizing agent. In this study, a reagent mole ratio of sulfur to the sum quantity of zinc and lead in the raw ore from 0.8 to 2 was selected, and its effect on sulfidation of carbonate-hosted zinc-lead ore was studied. The results were shown in Fig. 2. As we can see from Fig. 2, the sulfidation rate of zinc depends significantly on the dosage of sulfur in the 0.8 to 2.0 range. Increasing the sulfur dosage from 0.8 to 1.4 resulted in a pronounced increase in the sulfidation rate of lead. However, a further increase in the sulfur dosage from 1.4 to 2.0 did not substantially increase the sulfidation rate.

Effect of temperature Sulfidation of oxidized zinc-lead ore was conducted at temperatures varying from 120 °C to 220 °C, and the results are presented in Fig. 3. It can be seen from Fig. 3 that the temperature has a significant effect on the sulfidation rates of zinc and lead. The sulfidation rate of lead increased from 23% to 83% when the temperature increased from 120°C to 180 °C; Meanwhile, the sulfidation extent of zinc increased from 14% to 75%. The sulfidation rates of zinc and lead increased slowly with further increasing in temperature.

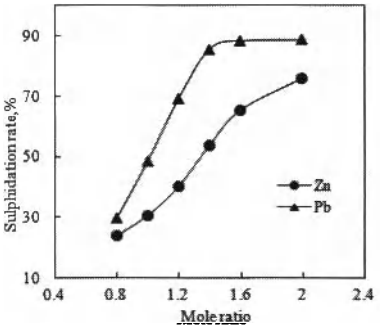

Fig.2 Effect of dosage of sulphur on the sulfidation of carbonate-hosted zinc-lead ore. Conditions: particle size 74–58 μm, 180°C, 240 min.

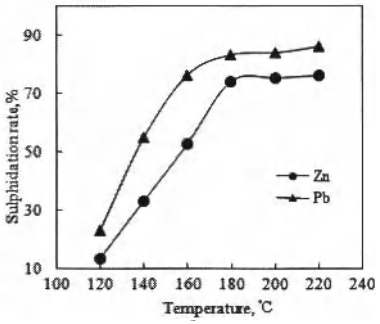

Fig.3 Effect of temperature on sulfidation of carbonate-hosted zinc-lead ore. Conditions: particle size 74–58 μm, 240 min, sulfur dosage 2.0.

Effect of reaction time The effect of holding time on the sulfidation of carbonate-hosted zinc-lead ore was studied in the range of 60 to 360 min. Fig. 4 shows the variation in the sulfidation of zinc and lead as a function of the holding time. It can be observed in this figure that there was a transparent increase in the sulfidation rate of zinc when the holding time was prolonged from 60 min to 180 min. The sulfidation rate of lead increased greatly from 62% to 83% when the holding time increased from 60 to 180 min. Beyond 180 min, there was no significant increase in the sulfidation rate of lead.

The Effect of Particle Size The effect of particle size on the sulfidation of carbonate-hosted zinc-lead ore was studied using different size fractions (147–106 μm, 106–74 μm, 74–58 μm, 58–48 μm, 48–42 μm, 42–37 μm), and the results are shown in Fig. 5.

These results in Fig. 5 indicate that the sulfidation rate of zinc and lead increased slowly with decreasing particle size. Considering that the fine particle size may cause poor flotation separation, a size fraction of 74–58 μm was chosen in the following experiments.

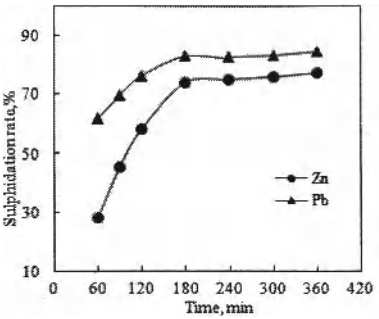

Fig.4 Effect of time on the sulfidation of carbonate-hosted zinc-lead ore. Conditions: particle size 74–58 μm, 180°C, sulfur dosage 2.0.

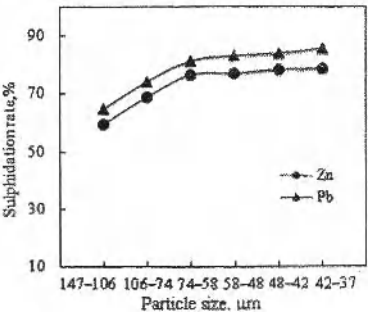

Fig.5 Effect of particle size on sulfidation of carbonate-hosted zinc-lead ore. Conditions: 180°C, 240 min, sulfur dosage 2.0

Characterization of the sulfidized materials Experiments were performed with a particle size of 74-58 μm and a sulfur dosage of 2.0 at 180 °C for 240 min. The sulfidized materials were chemically analyzed and the phase composition of zinc and lead in the sulfidized materials is listed in table 4. From table 4, it can be concluded that phase composition of zinc and lead change substantially when compared to the raw material. Zinc sulfide accounts for 76.93% of the total zinc minerals and lead sulfide accounts for 90.14% of its total minerals. Using formula (1), the sulfidation extent of zinc and lead can be calculated as over 75% and 82% under the conditions employed, respectively. By comparing table 2 to table 4, it can also be concluded that both zinc and lead carbonate minerals are more easily sulfidized than their silicate minerals.

In the hydrothermal sulfidation process the majority of zinc, lead and iron, which existed as oxide forms in the raw ore, are transformed into their sulfides by. Gangue minerals, such as quartz and calcite are still in their original forms.

Table 4 Mineralogical Compositions of Zinc and Lead in the Sulfidized Material

Constituent/%	Zn		Pb	
	content	Percentage	content	Percentage
carbonate	1.23	10.91	0.03	0.9
silicate	1.17	10.38	0	0
sulfide	8.67	76.93	3.11	90.14
others	0.20	1.78	0.31	8.99
Tatal	11.27	100	3.45	100

The influence of sulfidation pretreatment on flotation

The carbonate-hosted zinc-lead ore was pretreated under hydrothermal conditions with a particle size of 74-58 μm and a sulfur dosage of 2.0, at 180 °C for 240 min. The zinc and lead in this product was concentrated by a conventional mixed flotation process without desliming. The untreated raw material was also concentrated using the same process, and the results are shown in Fig. 6.

The flotation reagent regime incorporated the following components: float reagent–butyl xanthate (670 g/t), frother–pine camphor oil (40g/t), dispersant–sodium hexametaphosphate (280g/t), and activator-copper sulfate (1500g/t).

Fig. 6a shows extremely poor recoveries of zinc and lead in the flotation concentrate from the unsulfided sample. The recovery of lead and zinc into the flotation concentrate was only around 55% and 50%, respectively. The mass balance was within ±2%. The discrepancies in the mass balance are possibly attributable to a loss of fine sulfide particles during washing. Flotation for this sample after sulfidation (Fig. 6b) gave much higher recoveries of over 91% zinc and 90% lead in the concentrate. A flotation concentrate treated by sulfidation was obtained with 52% Zn and 37% Pb from the materials.

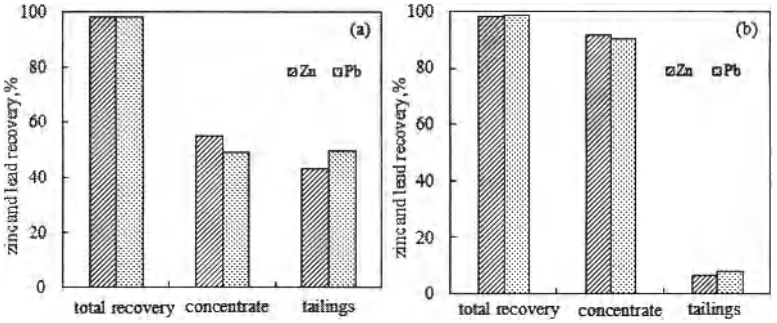

Fig.6 Recoveries of zinc and lead during flotation of unsulfided (a) and sulfided (b) carbonate-hosted zinc-lead ore.

Conclusions

1) The zinc-lead ore used in the present study includes smithsonite as main zinc minerals and cerussite as lead mineral; and calcite, dolomite, quartz, and kaoling as gangue minerals. Zinc and lead carbonate minerals account for 80.14% and 75.63% of all minerals, respectively. Therefore, the sample is a carbonate-hosted zinc-lead oxide ore.

2) The o carbonate-hosted zinc-lead ore was sulfidized under the following conditions: particle size 74-58 μm and a sulfur dosage of 2.0 at 180 °C for 240 min. The phase composition of zinc and lead change substantially when compared to the raw material. The sulfidation extent of zinc and lead was over 75% and 82%, respectively.

3) Both zinc and lead carbonate minerals were more easily sulfidized than their silicate minerals in the present study.

4) Flotation of the unsulfided sample was ineffective, with less than 55% recovery of zinc and lead, after sulfidation. The recoveries of zinc and lead into flotation concentrate were over 90%. A flotation concentrate was obtained with 52% Zn and 37% Pb from the materials, which were treated by sulfidation.

5) The sulfidation of the carbonate-hosted zinc-lead ore with sulfur under hydrothermal conditions, which were applied prior to flotation and can improve the flotation recovery of lead and zinc. Therefore, application of metallurgical processes is proposed for zinc and lead recovery from the carbonate-hosted zinc-lead ore.

Acknowledgement

The authors gratefully acknowledge the Major State Basic Research Development Program of China (project no. 2007CB613605), NSFC (Natural Science Fund Council, China, 50904030) and Yunnnan Province Applied Basic Research Item (project no. 2009ZC010M) for the financial support of this work.

Reference

1. M.Rey, "The flotation of oxidized ores of lead copper and zinc". (Paper presented at the IMM. Recent Developments in Mineral Dressing Symposium, London, 1953), 41–548.

2. Barbaro, M., *Lead and zinc ores-flotation* (Rome, Academic Press, 2000), 15-34.

3. M.Irannajad, M.Ejtemaei, and M.Gharabaghi, "The effect of reagents on selective flotation of smithsonite-calcite-quartz," *Minerals Engineering*, 22(9-10)(2009),766–771.

4. Thompson, J.W., 1960. Sulfidation and flotation of ores: United States, 1334721.

5. Y.V.Laptev, V.S.Shevchenko and F.K.Urakaev, "Sulphidation of valleriite in SO_2 solutions," *Hydrometallurgy*, 98(3-4)(2009), 201–205.

6. S.Castro, J.Goldfarb and J.Laskowski, "Sulphidizing reactions in the flotation of oxidized

copper minerals," *International Journal of Mineral Processing*, 1(2)(1974), 141–161.

7. M.Yamada, T.Shoji, T.Onada and J.Shimoiizaka, "Flotation of zinc carbonate," *Chemical Abstracts*, 84(1976),182-894.

8. G.Caproni, R.Ciccu, M.Ghiani and I.Trudu, "The processing of oxidized lead and zinc ores in the Campo Pisano and San Giovanni Plants," *Minerals Engineering*, 3(13)(1979), 71–91.

9. G.Önal, G.Bulut, A.Gül, K.T.Perek and F.Arslan, "Flotation of Aladag oxide lead–zinc ores," *Minerals Engineering*, 18(2)(2005), 279–282.

10. C.A.Pereira, A.E.C.Peres, "Reagents in calamine zinc ores flotation,". *Minerals Engineering*, 18(2)(2005), 275–277.

11. S.H.Hosseini, Forssberg and Eric, "Adsorption studies of smithsonite flotation using dodecylamine and oleic acid," *Minerals and Metallurgical Processing*, 23(2)(2006), 87-95.

12. F. A.Keqing, J.D.Miller and Li Guang-hui, "Sulphidization flotation for recovery of lead and zinc from oxide–sulfide ores," *Transactions of Nonferrous Metals Society of China*, 15(5)(2005), 1138–1147.

13. Li Yong, Wang Ji-kun, Wei Chang, Liu Chun-Xia, Jiang Ji-Bo and Wang Fan, "Sulfidation roasting of low grade lead–zinc oxide ore with elemental sulfur," *Minerals Engineering*, 23(7)(2010), 563–566.

3rd International Symposium on High-Temperature Metallurgical Processing
Edited by: Tao Jiang, Jiann-Yang Hwang, Patrick Masset, Onuralp Yucel, Rafael Padilla, and Guifeng Zhou
TMS (The Minerals, Metals & Materials Society), 2012

3rd International Symposium on High-Temperature Metallurgical Processing

Reduction and Titanium Production

Session Chairs:
Patrick Masset
Ting'an Zhang

3rd International Symposium on High-Temperature Metallurgical Processing
Edited by: Tao Jiang, Jiann-Yang Hwang, Patrick Masset, Onuralp Yucel, Rafael Padilla, and Guifeng Zhou
TMS (The Minerals, Metals & Materials Society), 2012

PREPARATION OF TITANIUM ALLOY FROM TITANIA-BEARING BLAST FURNACE SLAG

Run Huang[1], Chenguang Bai[1], Xuewei Lv[1], Songli Liu[2]

[1]College of Materials Science & Engineering, Chongqing University, Chongqing 400044, China
[2]College of Materials Science & Engineering, Pan Zhihua University, Pan Zhihua 617000, China
E-mails: huangrun_2008@126.com. bguang@cqu.edu.cn

Keywords: Titania-bearing Blast Furnace Slag, Aluminothermic Process, Titanium Alloy

Abstract

Titanium alloy was prepared from titania-bearing blast furnace slag (Ti-BF slag) by aluminothermic process in an induction furnace. The effects of aluminum amount on the titanium silicon yield and titanium recovery ratio were studied. The phase transformation and chemical composition of the prepared alloy were investigated by X-ray diffractometry (XRD) and X-ray fluorescence (XRF) respectively. It was found that the mass fraction of silicon and aluminum increased with increasing the aluminum amount, however, the mass fraction of titanium increased first and then decreased with increasing the aluminum amount. Furthermore, both the titanium alloy yield and titanium recovery ratio increased with the increase of aluminum amount. The main phases of the alloy were Ti_xSi_y and $AlTi_3$. The titanium alloy samples prepared in various conditions had a composition (wt.%): 38–50% Ti, 29-34% Si, 4-11 Al%, 1.6-2.2 Mn%.

Introduction

Panzhihua and Xichang regions in the southwest of China are rich in vanadium-titanium magnetite containing iron, vanadium, titanium and gangue. According to the characteristics of the resource, iron and vanadium are successfully recovered with a blast furnace process and a converter process. However, most content of titanium are entered in the blast furnace slag with TiO_2 22% -26% and metallic Fe 2%–6% called Ti-BF slag. Due to the dispersed distribution of Ti in various fine grained mineral phases with a complex combination between Ca, Al and Si, it is difficult to recover the Ti components[1]. This slag is generated at a current rate of 3.6 million tons per year, which adds to the existing 70 million tons of slag produced so far[2]. The slag has had to be piled as large as the mountains, which not only waste of resources but also cause a pollution of the environment. Therefore, the study of integrated utilizing Ti-BF slag has become very significant.

In the past years, several mineral and metallurgy processes for treating the slag have been studied, such as flotation separation combined with magnetic separation, hydrometallurgy and melting reduction [3-6]. And the main processes included selective precipitation separation of Ti-BF slag with metallurgical modification[7], preparation of $TiCl_4$ by high-temperature carbonization and low-temperature selective chlorination[8], preparation of Ti-Si alloy by Plasma smelting

reduction[9], recovery of TiO_2 by direct mineral processing enrichment[10] and preparation of new mineral wool[11]. However, the recovery efficiency for Ti components of those processes were poor, so far the slag has not been efficiently utilized. The slag results in a waste of the resource and the pollution of environment. This study examined the effect of aluminum amount on the titanium alloy yield, titanium recovery ratio, the phase transformation and the chemical composition of the prepared alloy.

Experimental

The chemical compositions of Ti-BF slag and Aluminum ingot, which are supplied by Panzhihua Iron & Steel (Group) Co., China and Xuzhou Dongfeng Aluminum Co., China respectively, are shown in Table I. Combining the chemical analysis with the XRD patterns of the Ti-BF slag, the main phases are shown in Fig.1. The schematic of the smelting experimental apparatus is shown in Fig.2. It was designed by the Shanghai experimental electric furnace company, with power from a 150 kVA medium frequency induction furnace generator (1.0 kHz single phase). The graphite heating crucible, in which the Ti-BF slag was melt and reacted with aluminum, was 180 mm high with a 80 mm diameter. The upper graphite lid could keep a strong reducing atmosphere at high temperature.

Table I. Chemical Composition of the Raw Materials (wt.%)

	Aluminum ingot			Ti-BF slag						
Components	Al	Si	Fe	TiO_2	SiO_2	FeO	CaO	MgO	MnO	Al_2O_3
(wt.%)	95.00	3.68	0.73	20.78	26.48	1.61	26.17	8.57	0.73	14.61

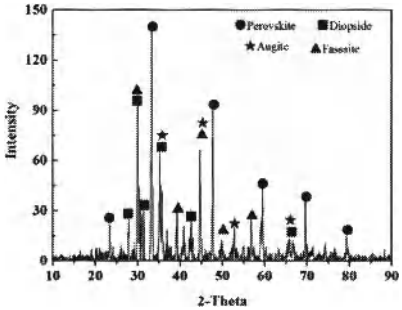

Fig. 1 XRD Patterns of Ti-BF Slag

Fassaite: $(Ca_{0.968}Mg_{0.578}Fe_{0.220}Al_{0.161}Ti_{0.059})(Si_{1.728}Al_{0.272})O_6$

Augite: (Mg, Fe, Al, Ti)(Ca, Mg, Fe, Na)(Si, Al)$_2O_6$

Diopside: Ca(Mg, Al)(Si, Al)$_2O_6$ Perovskite: $CaTiO_3$

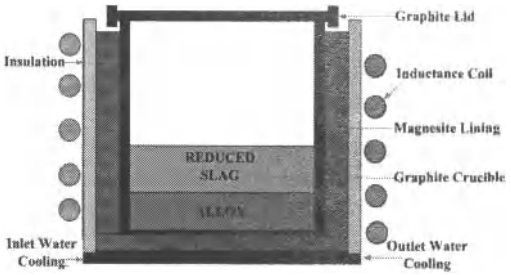

Fig. 2 Setup of the Experimental

On the basis of the chemical analysis of the Ti-BF slag and the reactions of aluminum with TiO_2, SiO_2, FeO and MnO, the stoichiometric amount of aluminum necessary to reduce these oxides to elementary substance are 9.35%, 15.89%, 0.40% and 0.17% of the Ti-BF slag respectively. In other words, 25.81g aluminum was required for reduction of 100g Ti-BF slag. If add more than the stoichiometric amount of aluminum, the aluminum would increase fast in the alloy [12]. So the levels of aluminum addition were 12%, 14%, 16%, 18%, 20%, 22% and 24% in this study. Since the reaction product of the reduction, alumina is solid at high melting temperature, the separation of the slag and metal is a very significant process. Consequently, we used a slag of CaF_2-CaO because of its better fluidity and ability to absorb alumina. On the other hand, due to the high content of CaO in the Ti-BF slag, only 5% CaF_2 was added into the Ti-BF slag[13]. In each experiment, 1.0 kg Ti-BF slag and 50g CaF_2 were completely mixed and then melted in the graphite crucible. The total amount of aluminum ingot was divided into three parts, which was added in the graphite crucible respectively while the mixed samples fully melted. After feeding the aluminum, the graphite lid must be covered immediately. The power and holding time of the heating process were shown in table 2. After solidification, the reduced slag and alloy block were easily separated from the smelted samples. The prepared alloys were analyzed for various elements and phases by X-ray fluorescence and X-ray diffraction.

Table II. Heating Process of the Experiment

	Melting slag		Feeding Al		
P (kW)	25	35	25	25	25
t (min)	15	8	5	5	5

Results and Discussion

Titanium Recovery and Titanium Silicon Yield

The titanium recovery and titanium silicon yield were calculated by Equations 1 and 2, respectively.

$$\text{Titanium recovery} = \frac{\omega}{W} \times 100 \quad (1)$$

$$\text{Titanium silicon yield} = \frac{a}{A} \times 100 \quad (2)$$

where, ω and W stand for the titanium weight in the produced alloy and in the Ti-BF slag, a and A are the weight of Fe + Ti+ Si + Mn in the produced alloy and in the Ti-BF slag. The relationship of titanium recovery and titanium silicon yield and aluminum amount was shown in Fig.3. It is shown that both the titanium alloy yield and titanium recovery ratio increased with the increase of aluminum amount. The titanium recovery is from 48% to 85% with increasing the aluminum amount from 12% to 24%. When the aluminum amount is low or approaching the stoichiometric amount, the increasing ratio of the titanium recovery has the same phenomenon, which is becoming slow. Because the lower content of aluminum is not enough to reduce the titania. When the content of aluminum is approaching the stoichiometric amount, the titanium was reduced about 85% and the residual titanium was little. So the reaction of titania with aluminum is gradually becoming equilibrium. If add more aluminum, the reaction rate is still slow. On the other hand, the amount of titanium silicon yield has the same tendency with titanium recovery. When the amount of aluminum is higher than 22% the titanium recovery had already reached the maximum, however, the amount of alloy yield still increased. According to the chemical composition of the alloy described later, only the content of silicon increased. That's indicated that the reduction of titania with aluminum preceded the reduction of silica.

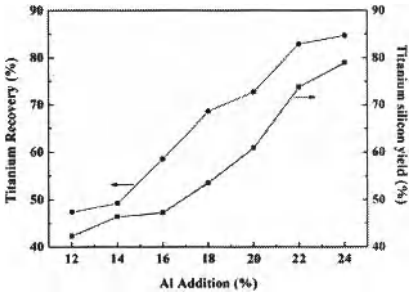

Fig. 3 Titanium Recovery and Titanium Silicon Yield as a Function of Al Addition

Phases of the Alloy

The phases of the alloy were detected after aluminathermic reduction with different aluminun addition, as shown in Fig.4. It's abviously shown that the phase of C only could be found when the alumiun amount was from 12% to 16%. We want to understand whether it reacted with the alloy or penetrated into the alloy. According to the mass fraction of C in the alloy and mass of the alloy, the mass of C in the alloy was calculated that was shown in table 3. It is indicated that the mass fraction of C in the alloy decreased with the increase of aluminun amount while the mass of

C in the alloy nearly keep constent. It could be got a conclusion that C was penetrated into the alloy and formed a saturated solution with the alloy. On the other hand, due to the mass of alloy increased with the increase of aluminun amount, the relative content of C in the alloy decreased while the phase of C couldn't be detected. The main phases are $TiSi_2$, Ti_5Si_3, $AlTi_3$ and $Ti_7Al_5Si_{12}$. When the content of aluminum increased, the phase of the alloy was conversed to $TiSi_2$, $AlTi_3$ and $Ti_7Al_5Si_{12}$, which were corresponding with the chemical composition of the alloy described in the next paragraph.

Table III. Mass Fraction and Mass of C in the Alloy at Different Al Addition

Al addition (wt.%)	12	14	16	18	20	22	24
C in alloy (wt.%)	8.01	9.49	3.62	3.41	2.43	2.19	2.52
C in alloy (g)	5.21	6.62	5.10	6.25	4.83	5.15	6.63

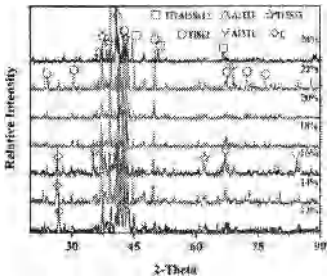

Fig. 4 XRD Patterns of the Alloy at Different Al Addition

Mass Fraction of Elements in the Alloy

According to the compositions of the Ti-BF slag and the aluminum ingot, the mass fractions of the elements in the alloy were calculated by the FACTSage software, as shown in Fig. 5(a). It's implied that the mass fraction of titanium increased first and then decreased with increasing the aluminum amount. And the mass fraction of silicon increased with increasing the aluminum amount until the amount of aluminum is 26%. It's also indicated the titanium was previously reduced by aluminum. However, the increase rate of silicon was faster than titanium. That's why the mass fraction of titanium increased first and decreased. On the other hand, the aluminum was directly melted in the alloy when the content of aluminum addition was higher than 22%. That's why the amount of silicon decreased later. The experimental data was shown in Fig.5 (b). It's shown that the calculated data had a good agreement with the experimental data. The experimental data of the aluminum amount in the alloy was higher than the calculated data. It's owing to the thermodynamic calculation is unable to considerate the influence of the dynamics. The low melting point (660°C) of aluminum ingot would be melted rapidity. Similarly, FeO was hardly reduced to metal iron when the content of FeO was very low in the slag. So the calculated mass fraction of iron was decreased obviously and the experimental data not.

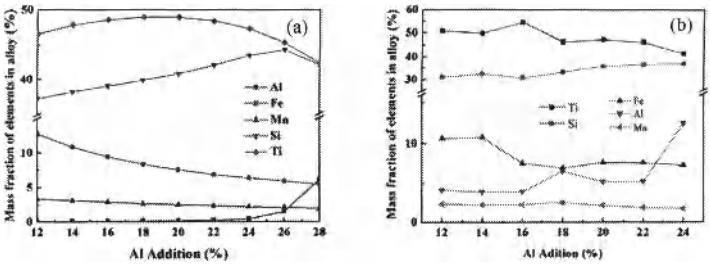

Fig. 5 Effect of Al Addition on the Mass Fraction of Elements in the Alloy
((a) Calculated Data, (b) Experimental Data)

Conclusions

This work studied the preparing of titanium alloy in an induction furnace and the mass fractions of the elements in the alloy were calculated with the software of FACTSage. The conclusions are summarized as follows:

(1) The titanium alloy could be prepared by this method and the main phases of the alloy were Ti_xSi_y and $AlTi_3$.
(2) Titanium recovery and titanium silicon yield increased with increasing the aluminum addition.
(3) The mass fraction of silicon and aluminum increased with increasing the aluminum amount, however, the mass fraction of titanium increased first and then decreased with increasing the aluminum amount.
(4) The content of aluminum in the alloy increased fast when the aluminum amount of charge reached to the stoichiometric aluminum.

Acknowledgments

The authors are especially grateful to the Fund of Integrated Utilization on Panzhihua High Titanium-bearing BF Slag (Grant No.2010CY-G-1-1), Institutions of Higher Learning Fund (Grant No.CDJZR11130002) and Chongqing University Postgraduates' Science and Innovation Fund (Grant No. CDJZR11130028).

References

1. Hegui, D., *Theory of Smelting V and Ti-Magnetite by Blast Furnace.*(Beijing, China: Science Press, 1996), 144-182.
2. Li, X. and J. Pu, "The Latest Developments of Integrated Utilization on Panzhihua High Titanium-bearing BF Slag," *Iron Steel Vanadium Titanium*, 32(2).(2011), 10-14.

3. Wu, F.X., et al., "Hydrogen peroxide leaching of hydrolyzed titania residue prepared from mechanically activated Panzhihua ilmenite leached by hydrochloric acid," *International Journal of Mineral Processing*, 98(1-2).(2011), 106-112.
4. Huang, Z.Q., M.H. Wang, and X.H. Du, "Kinetics of sulphuric acid leaching of perovskite concentrate," *Transactions of the Institution of Mining and Metallurgy Section C-Mineral Processing and Extractive Metallurgy*, 111.(2002), C166-C167.
5. Liu, X.H. and Z.T. Sui, "Kinetics of leaching Ti-bearing slag by dilute sulphuric acid," *Acta Metallurgica Sinica*, 39(3).(2003), 293-296.
6. Shixi, H., et al., "Preparation alloy and residue from titanium-bearing blast furnace slag of metalothermic reduction," *Ferro-Alloys*, 5.(2007), 20-23.
7. Mingyu, W., et al., "Selective enrichment of TiO_2 and precipitation behavior of perovskite phase in titania bearing slag," *Transactions of Nonferrous Metals Society of China*, 16(2).(2006), 421-425.
8. Pangang Group Research Institute Co., L. "Resaerch on the carbonization technology of Pangang BF slag".(in Papers of the 2010's Conference on Integrated Utilization on Panzhihua High Titanium-bearing BF Slag. Panzhihua, China. 2010.), 1-10.
9. Chushao, X. and L. Tianfu, "The Smelting Process of Ferroallys Using Titanium-Bearing Slags from Blast Furnace," *Mining and Metallurgical Engineering*, 8(2).(1988), 41-46.
10. Zhiyong, Y., Z. Wenbin, and C. Haifang, "Recovering valuable element from smelting waste slag through combining of mineral processing and metallurgy," *Express Information of Mining Industry*, 1.(2007), 29-31.
11. Yun, Y., A. Jinqing, and Y. Zhiyuan. "Preparation of new mineral wool from high titanium-bearing BF slag".(in Papers of the 2010's Conference on Integrated Utilization on Panzhihua High Titanium-bearing BF Slag. Panzhihua, Chian. 2010.), 54-58.
12. Pourabdoli, M., et al., "A New Process for the Production of Ferrotitanium from Titania Slag," *Canadian Metallurgical Quarterly*, 46(1).(2007), 17-23.
13. Maeda, M., et al., "Aluminothermic Reduction of Titanium-Oxide," *Materials Transactions Jim*, 34(7).(1993), 599-603.

3rd International Symposium on High-Temperature Metallurgical Processing
Edited by: Tao Jiang, Jiann-Yang Hwang, Patrick Masset, Onuralp Yucel, Rafael Padilla, and Guifeng Zhou
TMS (The Minerals, Metals & Materials Society), 2012

BASIC RESEARCH OF DIRECT PYROLYSIS PERFORMANCE OF $MgCl_2$ IN MOLTEN STATE

ZHANG Ting'an, LV Guozhi, DOU Zhihe, LIU Yan, NIU Liping, ZHAO Qiuyue, HE Jicheng

Key Laboratory of Ecological Utilization of Multi-metal Intergrown Ores of Ministry of Education, School of Materials and Metallurgy, Northeastern University, Shenyang, Liaoning 110004 , China

Keywords: Molten state $MgCl_2$, Pyrolysis, Crystallite Structural transformation, Dynamic analysis

Abstract

This paper proposed a new method of Mg and Cl_2 circulating for titanium sponge production by direct pyrolysis and thermal reduction process. Effects of pyrolysis temperature, pyrolysis time and partial pressure of oxygen on pyrolysis efficiency were researched, and the crystallite structural transformation of MgO productions at different pyrolysis temperature and time were analyzed by XRD. The experimental results indicates that the pyrolysis temperature and time effects the pyrolysis efficiency obviously, and the reasonable pyrolysis conditions by using $MgCl_2$ in molten state are as follows: the pyrolysis temperature is 1100℃, pyrolysis time is 60min and the partial pressure of oxygen is 100%, the pyrolysis efficiency get above 95% at this conditions. The dynamic analysis of molten magnesium chloride pyrolysis reaction shows that, as a chemical reaction process control, the response of the apparent activation energy Ea=70.4 kJ/mol.

Introduction

Titanium is a young metal, it is applied in industrial until the Second World War. It is 160 years from the discovery of titanium to the industrial production of ductility titanium by magnesium reduction method in the United States in 1948. As a new kind of metal, titanium and titanium material are better than the traditional metal materials in mechanical properties, heat resistance and thermal conductivity. Titanium is a kind of landmark structure and function material, which is called "space metal", "Marine metal", "Intelligent metal" [1-3]. Although the study of new methods of titanium smelting get more at present, Kroll method and Hunter method are really applied to industrial production methods for titanium smelting, and Hunter method is already discontinued because of costs at present. The core technology in Kroll method of sponge titanium production process can be come down to two circulation, namely the cycle of magnesium and chlorine in preparation-process of titanium sponge. In the traditional Kroll method, the cycle is realized through magnesium chloride which is produced by the electrolytic magnesium reduction process in hot molten state. But because investment of equipment for electrolysis method is too high, this method has not been used by most titanium sponge production enterprise in China. At present most titanium sponge production enterprise in China produce titanium sponge by the outsourcing of titanium tetrachloride, but the

main disadvantage of this method is that the by-product of magnesium chloride is difficult to deal with.

Based on the reasons above, northeastern university proposes a method dealing with by-products magnesium chloride from titanium sponge smelting by the way of direct pyrolysis and achieving the circle of chlorine in titanium smelting, achieving circulation of magnesium through preparation of metal magnesium by aluminum heat or silicon heat reduction .This paper focuses on the influence on pyrolysis process of anhydrous magnesium chloride by technology conditions, the circumstance of magnesium chloride crystal structure transformation in the process of pyrolysis of magnesium chloride is determined by phase analysis, and analysis of dynamics process of pyrolysis[4-8] .

Experimental

Anhydrous magnesium chloride in experiments is from a titanium industry company in China, getting from titanium metallurgical process by distillation process, purity>99%.

Effects of temperature, pyrolysis time, partial pressure of oxygen and gas flow rate on pyrolysis efficiency of molten state magnesium chloride through pyrolysis experiments by homemade SK2-4-12 type of tubular pyrolysis furnace. The experimental process will first rise tubular pyrolysis furnace temperature to setting point, and then put high aluminum crucible with magnesium chloride to sieve plate of furnace body, then blow oxygen and nitrogen gas mixture of different oxygen concentrations, start to time 1 min after stability of temperature, stop blow gas after the response time and toke the material in tube out.

Determine concentration of chlorine ion in the pyrolysis products by titration method, calculate pyrolysis efficiency through formula (2-1):

$$\eta=[1-1.338\times m(Cl)]\times 100\% \quad (1)$$

In formula: η- *decomposition rate of magnesium chloride;*
m(Cl) –concentration of chlorine ion in the product.

Results And Discussion

Thermodynamic Analysis of Pyrogenation Process

The overall reaction of pyrolysis process for magnesium chloride is:

$$2MgCl_2+O_2(g)=2MgO(s)+2Cl_2(g) \quad (2)$$

The change of gibbs free energy of the reaction from 298 K to 1673 K and the relation curve between reaction equilibrium constant and temperature as shown in figure 1 shows:

From the results of gibbs free energy in figure 1 we can conclude: when the reaction temperature is less than 810K , gibbs free energy of direct pyrogenation process of molten state magnesium chloride is positive. When the reaction temperature is more than

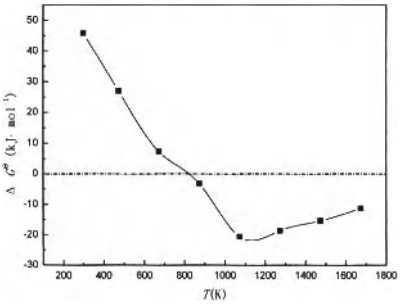

Fig.1 Curve of standard Gibbs free energy and temperature from 298K to 1600K

810K, the gibbs free energy of direct pyrogenation process of molten state magnesium chloride presents the state of rising first and descending then, the minimum appeared near 1100 K, the reaction equilibrium constant achieves maximum near 1100 K, lnK is 2.3.

The relationship between oxygen partial pressure and chlorine partial pressure of initial reaction, is further studied when temperature is 873K~1473K, the results are shown as figure 3.The figure indicates that when temperature is 873K~1473K, there is little influence of gas partial pressure on the process of $MgCl_2$ direct pyrolysis, when p_{O2} is 0.02mpa, the minimum chlorine partial pressure meets the direct pyrolysis condition is about 0.5 atm, in the thermodynamic investigation range, initial reaction partial pressure of chlorine up to 3 atm above. [9,10]

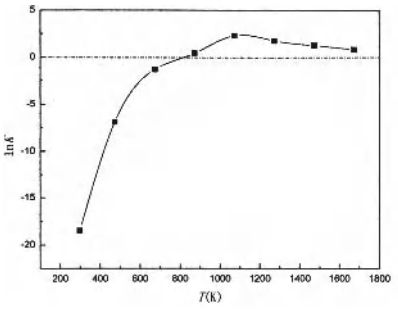

Fig.2 Curve of equilibrium constant and temperature from 298K to 1600K

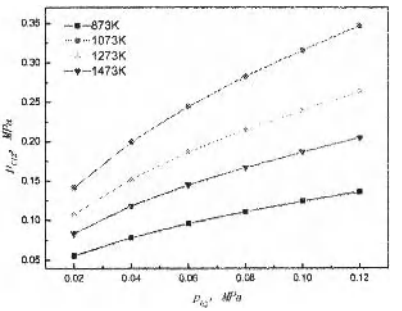

Fig.3 Relationship between reaction gibbs free energy and vapor partial pressure

Research On The Process of $MgCl_2$ Direct Pyrolysis

Investigate the influence of pyrolysis temperature and pyrolysis time on the content of chlorine and pyrolysis efficiency in products in the condition that partial pressure of p_{O2} is1.0 atm.the results are shown as figure 4 and figure 5.

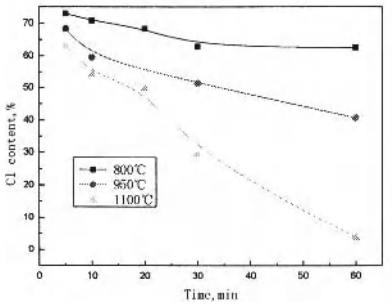

Fig.4 Effect of temperature on Cl content of melting $MgCl_2$ through roasting

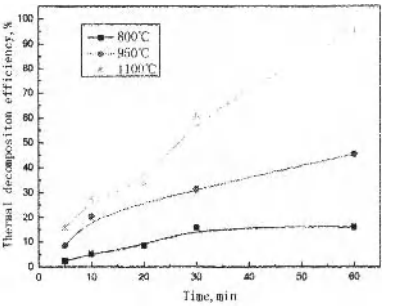

Fig.5 Effect of temperature on decomposition efficiency of melting $MgCl_2$

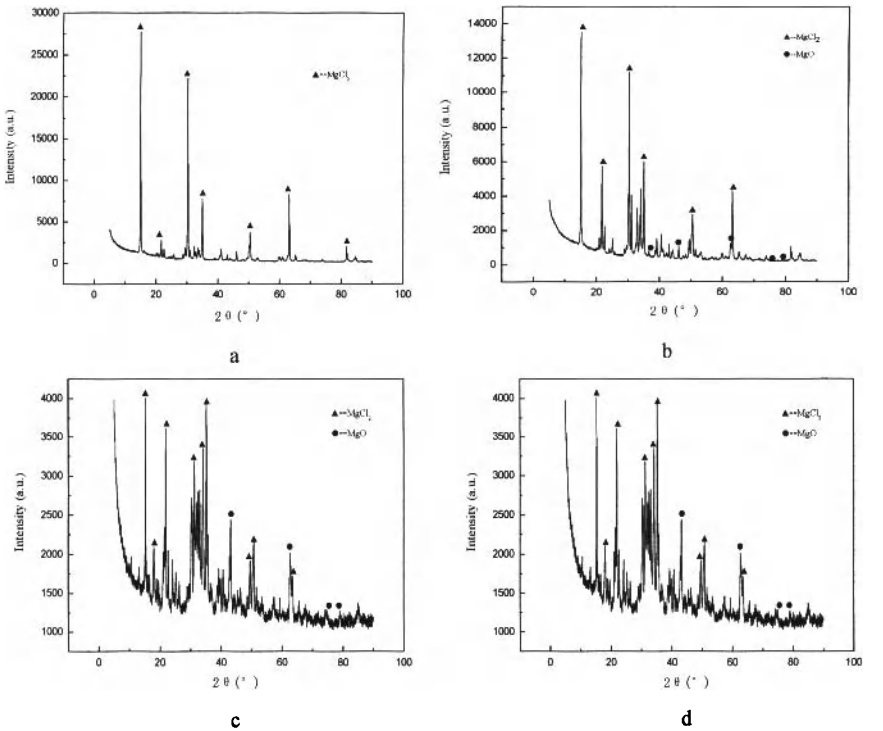

Fig.6 Effect of decomposition temperature on phase of production

a-raw $MgCl_2$; b-800℃, c-1000℃, d-1100℃

From experimental result we can see, pyrolysis temperature and pyrolysis time have a great influence on content of Chlorine in magnesium oxide product and pyrolysis efficiency of magnesium chloride. Pyrolysis rate of molten state magnesium chloride increase significantly when the temperature reaches 1100℃. The pyrolysis efficiency of molten state magnesium chloride reaches 95.12% when pyrolysis temperature at 1100℃, pyrolysis time at 60min and partial pressure of oxygen at 1.0atm. XRD patterns of pyrolysis products of molten state magnesium chloride at different pyrolysis temperature were shown by figure 6, through analysis of XRD figures, we can get table 1 and table 2:

Analysis results in table 1 and table 2 indicate: when the pyrolysis temperature is 800℃, in the XRD diffraction figure of pyrolysis product MgO, the height of diffraction peak is 707.28, the half width is 0.1948 when the 2θ is 43°. As the temperature grows, the height of diffraction peak of MgO gradually raises, the half width decreases. When the temperature is 1100℃, the height of diffraction peak is 35678.82, the half width is 0.1624. When the 2θ is 62°,the height of diffraction peak is 676.48 and the half width is 0.3168 for MgO at 800℃,the height of diffraction peak is 20098.75 and the half width is 0.0792 for MgO at 1100℃. This shows that the stability of the product of

magnesium chloride pyrolysis is increasing with the rise of temperature,it is against the process of magnesium chloride pyrolysis when the temperature is greater than 900 °C from thermodynamics angle, but the reaction rate increases with the rise of temperature from dynamics angle. Overall look, the half width of magnesium oxide product is getting smaller, the crystallization of magnesium oxide phase also gradually completes with the rise of temperature. From the experiment results, we can see that conversion rate of magnesium chloride is improved with the rise of temperature. Further investigation of oxygen partial pressure without water in the process of pyrolysis magnesium chloride was affected and the results as shown in Table 2.

Table 1 XRD analysis results of pyrolysis products at different temperature

Temperature/°C	Content	parameters					
		2θ(°)	Height	d-spacing	FWHM	abc	Aβγ (°)
800	MgO	43.0036	707.28	2.10334	0.2922	4.1980	90
		62.4218	676.48	1.48652	0.3168		
		78.9723	82.61	1.21137	0.1188		
1000	MgO	37.2353	148.38	2.41483	0.0974	4.2090	90
		43.1641	1101.84	2.09589	0.1948		
		62.6129	798.93	1.48244	0.2772		
		75.0302	112.67	1.26492	0.2376		
		78.9298	148.21	1.21191	0.1188		
1100	MgO	37.0616	4448.48	2.42575	0.0974	4.2030	90
		43.0233	35678.82	2.10242	0.1624		
		62.4118	20098.75	1.48673	0.0792		
		74.7943	2479.47	1.26832	0.1188		
		78.7331	6302.68	1.21445	0.1188		

Take a further investigation about effects of partial pressure of oxygen on pyrolysis of molten state magnesium chloride, the results are shown in Table 2.

Table 2 Transform rate of $MgCl_2$ at different oxygen pressure

	Oxygen pressure		
	0.4atm	0.7atm	1atm
Decomposition rate (%)	85.95	89.52	95.12
Chlorine content of MgO (%)	10.5	7.83	3.65

From the results in table 2 we know that pyrolysis efficiency of molten state magnesium chloride increase gradually with the increase of oxygen partial pressure, resolution ratio of molten state magnesium chloride is 95.12% when oxygen partial pressure is 1 atm, this result agrees with the thermodynamic calculation results well.

Dynamics Research of Pyrolysis Process of Molten State Magnesium Chloride

Pyrolysis reaction of molten state magnesium chloride as follows:

$$2MgCl_2+O_2(g)=2MgO(s)+2Cl_2(g) \quad (3)$$

From the reaction above, it is easy to see that pyrolysis process of molten state magnesium chloride is a process involving multiphase reaction of gas -liquid、liquid-solid, steps of pyrolysis reaction may include:

(1) Oxygen diffusion from the main reaction atmosphere to reaction interface;

(2) Diffusion of magnesium chloride in molten state to the reaction interface

(3) Reaction between oxygen and magnesium chloride in the reaction interface;

(4) The chlorine generated to the main reaction atmosphere.

In the analysis of pyrolysis process dynamics of molten state magnesium chloride, assuming the reaction process as chemical reaction control in level 1, kinetic equation of reaction :

$$-\frac{d\alpha}{dt} = k_a m_{MgCl_2} \qquad \cdot(4)$$

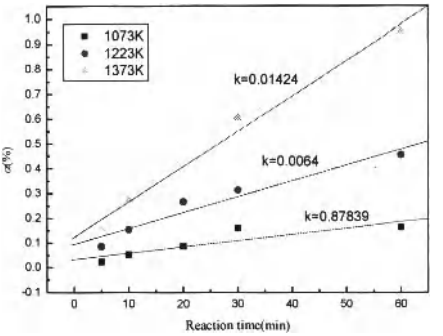

Fig.7 Molten state magnesium chloride pyrolysis reaction rate constant figure

In the formula:

α—The decomposition efficiency of the magnesium chloride ; m_{MgCl_2}—Efficiency of magnesium chloride in reaction; t-reaction time; k_a—Reaction constant rate.

According to the experimental results of pyrolysis experiment of molten state magnesium chloride, rendering the relation between pyrolysis rate and time, the result is shown as Fig.7, because this process is controlled by chemical reaction, magnesium chloride in the interface in the chemical reaction is a constant quality , the reaction rate and reaction time is linear relationship, so the slope of the fitting line are respectively for 1073 K, 1223 K and 1373 K reaction rate constant of molten state magnesium chloride.

According to arrhenius formula:

$$k = A\exp(-\frac{Ea}{RT}) \qquad (5)$$

In the formula

Ea—the apparent activation energy of response ;

A- the former factor of index number;

R-gas constant, for 8.314 kJ/mol;

T-reaction temperature.

Take logarithmic on both sides of the formula, we get the formula below:

$$\ln k = \ln A - \frac{Ea}{RT} \qquad (6)$$

Plot according to the different temperature reaction rate constant and corresponding $\frac{1}{T}$,The results are shown in figure 8 .

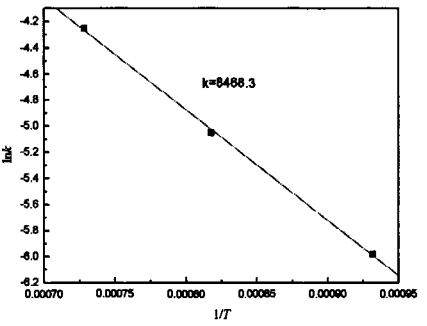

Fig.8 Relations diagram between ln*k* and 1/*T*

Through the linear calculation, the linear slope is -8468.3, namely:

$$\frac{Ea}{R} = 8468.3 \quad (7)$$

So the apparent activation energy of the reaction is Ea = 70.4 kJ/mol.

Acknowledgement

This research was supported by the National Natural Science Foundation of China (NO. 51004033, 51074044, 51002025),

Conclusion

1. The thermodynamic analysis for the pyrogenation process of molten state magnesium chloride shows that: gibbs free energy in the process of pyrolysis magnesium chloride raises first and then descends with the temperature rise. Along with the increase of the pressure of O_2 and the decrease of the pressure of Cl_2, the gibbs free energy of no water magnesium chloride pyrolysis reaction can be reduced in the temperature range of 873 K ~ 1473 K. When the pressure of p_{O2} is 0.02Mpa, the minimum chlorine partial pressure for pyrolysis process is up to 0.5 atm.
2. The optimal condition of pyrolysis for molten state magnesium chloride: pyrolysis time is 60min ,pyrolysis temperature is 1100℃and the partial pressure of oxygen is 1 atm, the pyrolysis efficiency is 95.12% , eventually lattice constant of pyrolysis products MgO is 4.2030.
3. Kinetics analysis of pyrolysis process for molten magnesium chloride shows that, the reaction process as a chemical reaction control at level 1, the apparent activation energy of the reaction Ea = 70.4 kJ/mol

Reference

1. Du Ji-hong. Progress of Titanium Extraction Technology [J], Rare Metal Materials and Engineering,2008,10.
2. Hu Qing-xiong. Application and Prospect of Titanium [J], Chinalco, 2003, (20) : 11-15.
3. Chen Fu-liang,Li Song-chun,Chen Li-sheng,Gao Jin-jin. Discuss the Application of Titanium [J], Yunnan Metallurgy, 2010, (224) : 58-60.
4. Zhang Jing-hong,Zhou Qi-li,Zhang Xiang-yi. Extraction Technology of Magnesium Oxide Progress from Brine[J],Inorganic Salt Industry, 2010, 1 (8) : 7-9.
5. Gao Jie,Di Xiao-liang,Li Yu-yun. Trend of the Development of Magnesium Oxide and its Production Methods [J], Chemical Production and Technology, 2005 (5) : 36-39.
6. Ge Hai-wen,Deng Tian-long,Guo Ya-fei. Research Progress of Active Magnesium Oxide Production Process in Our Country [J], Guangdong Trace Elements Science 2010, (5) : 29-34.
7. Xie Ying-hui, He Yu-ji. Study of High Purity Magnesium Oxide [J], Eea HuYan and Chemical Engineering, 2001, (6) : 16 -18.
8. Fang Yu-xun,He Ren-bin,Liu Yan-hong. Brine-Dolomite prepare Hydroxide and Magnesium Oxide Through Microwave Catalytic Magnesium [J], Inorganic Salt Industry, 2005 (S1) : 35-37.
9. O.Kubaschewski, C.B.Alcock. Metallurgical Thermochemistry[M], Beijing: Metallurgical Industry Press, 1985, 22-26.
10. Liang Ying-jiao,Che Yin-chang. Inorganic Thermodynamic Data Manual [M], Shenyang: Metallurgical Industry Press, 1993,1,46,49,172,173.

3rd International Symposium on High-Temperature Metallurgical Processing
Edited by: Tao Jiang, Jiann-Yang Hwang, Patrick Masset, Onuralp Yucel, Rafael Padilla, and Guifeng Zhou
TMS (The Minerals, Metals & Materials Society), 2012

CHLORINATION OF TITANIA FEEDSTOCKS

Samantha Moodley[1], Rauf Hurman Eric[2], Cevat Kucukkaragoz[2], Aditya Kale[3]

[1]Exxaro Resources, Pretoria West, 0001, South Africa
[2]University of the Witwatersrand, Johannesburg, 2000, South Africa
[3]Mintek, Johannesburg, 2125, South Africa

Key words: Chlorination, Titania Feedstocks, Fluidization, Blowover

Abstract

Two titania slags, rutile and synthetic rutile were chlorinated with petroleum coke and CO in a small bubbling fluidized bed reactor. The study aims to identify differences in chlorination mechanism, compare conversion rates, blowover and the chlorination of impurities for the various titania feedstocks at different temperatures.

Chlorination rates were highest at 1000°C; rutile chlorination significantly increases as temperature increases from 800°C to 1000°C. At 1000°C, synthetic rutile had the highest chlorination conversion rate; this was followed by Slag B which in turn was more reactive than Slag A and rutile. The mechanism for slag, synthetic rutile (SR) and rutile chlorination differs. Synthetic rutile feed is porous, providing a larger surface area for the chlorination reaction, hence the highest conversion rates was attained. Titania slag becomes porous with the initial chlorination of FeO and MnO whilst rutile remains solid. As the porosity of slag particles increases so does its tendency to be elutriated. Ti_2O_3 is oxidized within the early stages of chlorination during the chlorination of FeO and MnO. Ti_2O_3 not oxidized is then rapidly chlorinated.

Introduction

Titanium dioxide (TiO_2) is the most common compound of titanium, about 95 - 98% of extracted titanium minerals is processed into TiO_2 white pigment [1]. Two processing routes exist for the production of TiO_2 pigments, i.e., sulphate and chloride based processes. In the chloride process, titania feedstock is fed to a fluidized bed reactor together with reductant and chlorine gas. A temperature of 1000 - 1300°C is maintained in the reaction zone and apart from silica, zirconia, uranium and thorium, virtually all the metal oxides in the feed are converted to their respective chlorides [2]. Chlorine is recovered and recycled back to the reactor.

The feed to the chlorinator includes a number of titania feedstocks namely, synthetic rutile (SR), natural rutile, upgraded titania slag (UGS) and titania slag produced from ilmenite smelting. Natural rutile is the preferred feedstock for chlorination but due to dwindling reserves other titania feedstocks are substituted as feed for pigment production.

Fluidized bed technology is employed for the chlorination process, so feedstock physical characteristics such as density, size and shape factor is of importance. The feedstock has to have sufficient grain size and bulk density in order for the material to fluidize and to minimize

blowover carryovers from the chlorinator. A high elutriation rate translates to a shorter residence for particles in the fluidized bed which in turn negatively affects conversion efficiencies.

Since feedstock origin and production techniques differ, the physical properties and phase chemistry differ of the feedstocks will also differ, this will in turn impact the way in which each feedstock reacts in the chlorinator, although the TiO_2 content might be similar.

A number of studies have been completed on the chlorination kinetics of different feedstocks [3, 4, 5, 6, 7, 8]. Few studies have addressed the microstructural changes of titanium-bearing materials during the chlorination reaction [9, 10, 6]. Zhou et al., [9] studied the changes in ilmenite, SR, rutile, beneficiated slag and found that the rapid chlorination of easily chlorinated iron oxide in titania slag creates porosity that extends deeply into the interior of the particles. Nell and den Hoed [10] found that chlorination is associated with significant increases in particle porosity (even for rutile), which is brought about by the rapid initial chlorination of FeO and MnO (in ilmenite and slag) and (it is argued) by the chlorination of Ti_2O_3 which forms at high-energy surface sites.

This paper considers the chlorination of two slags, rutile and SR, the impact of elutriation on chlorination efficiencies and effects of Ti_2O_3 on chlorination.

Experimental Details

Samples - The test samples (i.e., Slag A, Slag B, rutile and SR) were subjected to carbochlorination experiments at temperatures ranging from 800°C to 1000°C in a fluidized bed reactor. Petroleum coke (i.e., 1.5 - 5mm, 97% Carbon) and CO gas was added as reductant. Slag A and rutile was acquired from South African producers whilst Slag B and SR were from international producers. In order to minimize the effect of size on chlorination rate, a common size range was selected for the experiments (i.e., 106 - 300μm). Den Hoed and Nell [10] found that at carbon levels lower than 15wt%, availability of carbon was the rate limiting step but once the stoichiometric requirement is exceeded the reaction proceeds unhindered. In this experimental procedure, 17wt% coke was added to the feedstock.

Apparatus - The chlorination experiments were conducted in an externally heated quartz reactor (80mm in diameter and 1100 mm in length). A porous distributor plate supported the charge and allowed for the even distribution of fluidizing and chlorination gases. Bed temperature was measured with a K type thermocouple. The crossover duct allows for the passage of the product gases and elutriated particles from the quartz reactor into the gas system. The crossover duct is connected to a condenser. High boiling point metal chlorides are condensed in the condenser and uncondensed gases are vented off to the caustic scrubber. Gas velocity is reduced in the round bottom flask and blowover settles out here. Figure 1 is an illustration of the experimental set up.

Procedure - The charge (i.e., 200g feedstock and 40g petroleum coke) was fluidized with argon during the heat up. Approximately 2% of the feed was elutriated during the heat up; this amount was considered insignificant in comparison to the feed mass. When the bed temperature reached the desired experiment temperature, the argon gas was switched off and a CO and Cl_2 mixture was fed to reactor. Gas flow (i.e., Cl_2, CO) was controlled by rotameters to give a superficial gas velocity of 39.8cm/s. The flow rates of Cl_2 and CO gas were maintained at 8Nl/min and 4Nl/min respectively. The total gas pressure inside the fluid bed reactor was approximately 85kPa, the

partial pressure of Cl_2 gas in the fluid bed reactor was approximately 57kPa. Upon completion of the test, the blowover and bed residue was collected. The large carbon particles were screened out of the bed sample. The blowover and bed sample was washed with water and dried at 105°C for 2 hours. Thereafter the material was roasted at 900°C for 2 hours to burn off fine coke particles.

Analytical Techniques - The chemical analysis of feed material and chlorinated bed samples were determined by Inductively Coupled Plasma Optical Emission Spectrometry (ICP – OES) techniques, particle size by screening and density by helium pycnometry. X-Ray diffraction (XRD) and Scanning Electron Microscope (SEM) were used for mineralogical characterization of the feed and the chlorinated bed samples, equipment and software details are described elsewhere [11].

Using the masses of the feed, bed residue and blowover, the conversion to gaseous chlorides was calculated as follows:

$$Conversion(\%) = \frac{M_i - (M_E + M_B)}{M_i} \quad (1)$$

M_i is the initial mass of sample charged to reactor, M_e is the mass elutriated from the reactor and M_b is the mass of sample remaining in the reactor at the end of the experiment. The degree of conversion is affected by kinetics of the reaction as well physical properties of feedstock since blowover is considered.

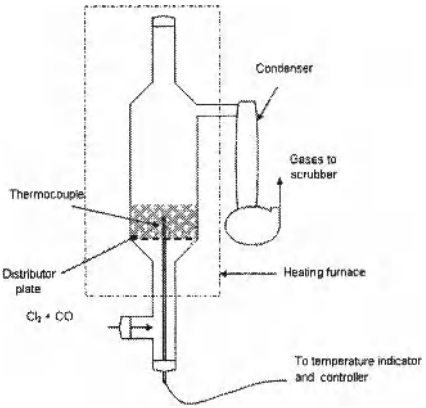

Figure 1: Schematic of Experimental Set up for Chlorination Experiments

Results and Discussion

Sample Characterization

Feedstock chemical composition is reported in Table I.

Table I: Feedstock Chemical Composition, Average Particle Size and Density

	Slag A	Slag B	Rutile	SR
SiO_2 (wt%)	1.64	1.49	1.44	0.80
Al_2O_3 (wt%)	1.02	1.64	0.31	1.80
FeO (wt%)	8.60	1.96	0.49	3.43
Fe (metallic) (wt%)	0.00	1.03	0.00	0.10
TiO_2 (equivalent)*(wt%)	87.46	95.02	95.69	92.77
Ti_2O_3 (wt%)	23.42	38.80	0.00	10.30
TiO_2 (wt%)	61.92	51.90	95.69	81.40
CaO (wt%)	0.22	0.26	0.08	0.10
MgO (wt%)	0.73	0.25	0.01	0.31
MnO (wt%)	1.90	2.80	0.01	1.00
Impurities† (wt%)	1.11	0.73	1.52	0.76
d_{50} (μm) of feed	294	218	110	151
Average density(kg/m^3)	4025	4033	4172	4254

* Ti^{3+} and Ti^{4+} expressed as TiO_2, † sum of Na_2O, Nb_2O_5, K_2O, Cr_2O_3, V_2O_5, P_2O_5, ZrO_2

The slags are products of ilmenite smelting and as a result of the milling process is more brittle, angular and irregularly shaped than rutile and SR. Slag A and B has a wider particle size distribution than rutile and SR. The difference in the shape and size is evident from the scanning electron microscope (SEM) back scattered electron (BSE) images, Figure 2.

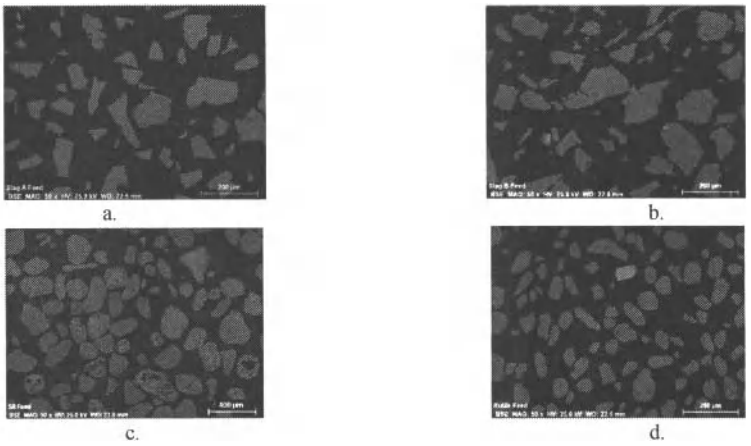

Figure 2: BSE Images of a Section through a. Slag A, b. Slag B, c. SR, d. Rutile

There are four phases (i.e., solid solution, rutile, metallic iron and glassy) present in high titania slags [12]. The major phase is a solid solution referred to as the M_3O_5 phase. This phase is a solid solution of the end members $FeTi_2O_5$, Ti_3O_5, $MnTi_2O_5$, $MgTi_2O_5$, Cr_2TiO_5, Al_2TiO_5 and V_2TiO_5 [13]. The glassy phase was present in various shapes and sizes throughout most of the Slag A and Slag B particles. The glassy phase consists of mainly of SiO_2, with smaller amounts of Al_2O_3 and TiO_2. Tabular lath like rutile crystals with fine grained metallic iron precipitates was found in Slag A. Bessinger [14] and Toromanoff and Habashi [15] also found metallic iron to be present in the rutile phase in the slag.

The iron present in Slag A is between 1 and 2 μm whereas in Slag B it is approximately 20μm and associated with carbon. The chemistry and size of the iron droplets suggest that the iron was trapped in a viscous slag and did not precipitate during cooling as with Slag A. A magnified Slag A particle showing the various phases is presented in Figure 3a. In the magnified particle, the dark grey phase is the silicate/glassy phase, the light grey is the M_3O_5 phase, the bright spots are the Fe and the intermediate grey bands are the rutile.

The SR sample is a product of the acid leaching process. The leaching of the iron fraction leaves behind a porous particle with TiO_2 content above 90%. The sample contained a few particles that appear to have escaped the leaching process with iron fraction still present. A porous particle and iron containing particle is shown alongside each other in Figure 3b. The rutile sample primarily consists of unaltered rutile particles with a few zircon grains.

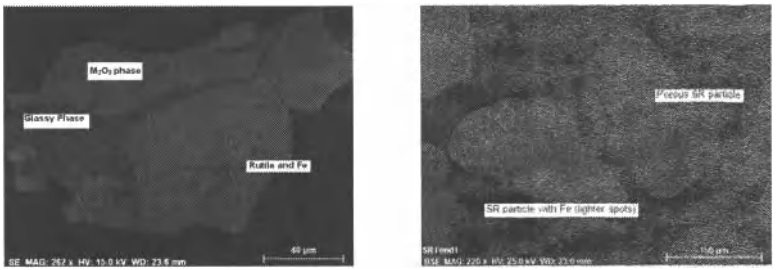

a. b.

Figure 3: BSE Image of a Section through a. Slag A Feed and b. SR Feed

Chlorination Results

Effect of Temperature - Slag A, Slag B and rutile were chlorinated at 800, 900 and 1000°C with coke and CO. Results are presented in Figure 4 and 5, the conversion (%) is calculated using Equation 1. Temperature had a significant effect on the overall conversion rate with the chlorination of rutile especially hindered at lower temperatures. Slag B shows the highest degree of conversion, with Slag A following closely behind. At 800°C, only 15% of rutile is chlorinated compared to 60% at 1000°C. It is clear to see why the commercial chlorination process is carried out at temperatures of 1000°C and higher. Iron chlorination in Slag A and Slag B is complete at 800°C. MnO chlorination in rutile is complete at 800°C, MnO chlorination in the slags improves slightly with increasing temperature. The chlorination of Al_2O_3 to $AlCl_3$ significantly improves

with increasing temperature; there is a 40% improvement in Al_2O_3 chlorination when the temperature is increased from 800°C to 1000°C. MgO chlorination in the Slag A and Slag B improves with increasing temperature. Complete MgO chlorination is achieved in the rutile sample at 800°C. The mass balance indicates that there is more SiO_2 in the bed sample than at the start of the reaction; this difference is approximately 1g to 2g and is considered insignificant compared to the total sample mass. This is likely due to analytical error. However, this indicates that SiO_2 does not chlorinate significantly during the experiment.

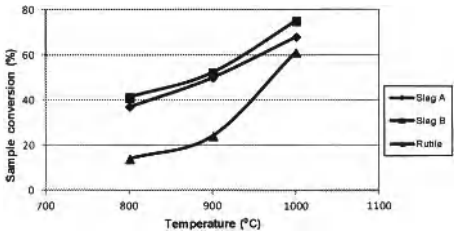

Figure 4: Chlorination of Three Feedstocks for 3 hours

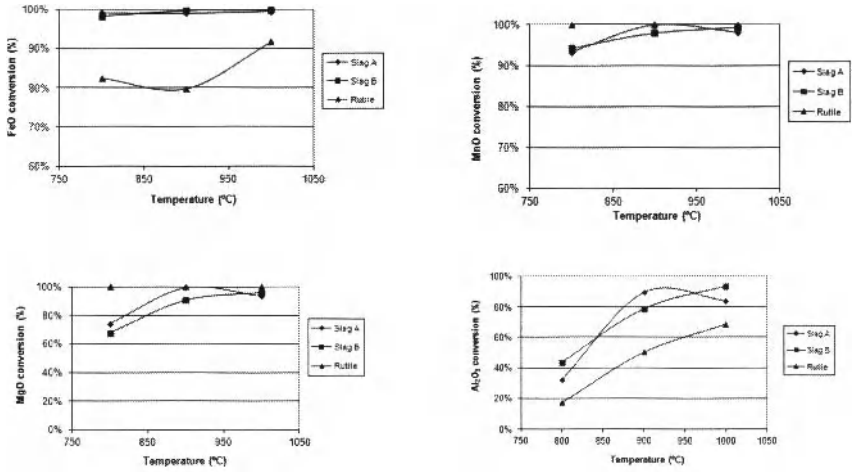

Figure 5: Chlorination of FeO, MnO, Al_2O_3 and MgO for 3 hours

Effect of Time - The conversion results from the chlorination experiments conducted at 1000°C is shown in Figure 6, the blowover and bed residue is given in Table II. After 3 hours of chlorination, the highest degree of conversion was achieved with the SR sample; this was followed by Slag B, Slag A and rutile. Slag A and rutile blowover increased with increasing

reaction time. Although the conversion of Slag A and SR differ by 23% after 3 hours of chlorination, the remaining bed sample after the experiment was similar. The difference in conversion results was due to the blowover, a significant amount of partially reacted Slag A particles was elutriated after 3 hours whereas blowover from the SR experiment was low. Blowover decreases chlorinator efficiency and this effect is illustrated with Slag A where degree of conversion of Slag A was lowered because 53g of partially reacted feedstock was blown out of the reactor during the 180 minute experiment.

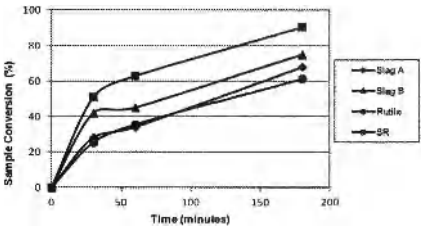

Figure 6: Conversion of Slag A, Slag B, SR and Rutile at 1000°C

Table II: Blowover and Remaining Bed Mass of Slag A, Slag B, SR and Rutile after Chlorination at 1000°C for Different Times

Feedstock	Blowover (g)			Remaining Bed Sample (g)		
	30 (minutes)	60 (minutes)	180 (minutes)	30 (minutes)	60 (minutes)	180 (minutes)
Slag A	2	7	53	142	125	11
Slag B	4	2	3	112	108	48
Rutile	0	1	30	149	128	47
SR	0	1	1	98	71	18

Chlorination Mechanism - The remaining bed samples after the 30, 60 and 180 minute experiments at 1000°C were collected and prepared for SEM analysis. BSE images of the 1000°C, 30 minute experiments are presented in Figure 7. The BSE images together with chemical analysis and EDS analysis provided vital information towards identifying and understanding the difference in the chlorination mechanism between the feedstocks. With the exception of samples that were chlorinated for 1 minute, rutile was identified as the major titania phase in all the bed samples. A study of the surface of the bed samples after 30 minutes of chlorination shows different levels of porosity between Slag A, Slag B and SR samples.

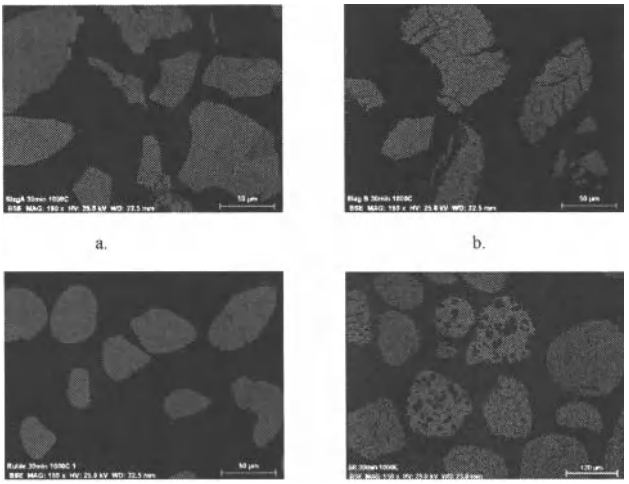

a. b.

c. d.

Figure 7: BSE Images of a Section through a. Slag A, b. Slag B, c. Rutile, d. SR after 30 minutes of Chlorination at 1000°C

Slag A and Slag B - BSE images of Slag A after 1 minute of chlorination at 1000°C is shown in Figure 8. The chemical analysis of the bed samples indicates that 80% of FeO and 63% MnO was chlorinated during the first minute of the experiment. The chlorination of Fe and Mn leaves behind porous particles with a large surface area for subsequent reaction. Small amounts of Cl_2 were identified on the boundary of the pores. The presence of chlorine around the pores indicates that the reactive gases diffused into the slag particle and chlorination was not restricted to the outer surface. Pore size increases with increasing chlorination duration and the particles become lighter and can be elutriated from the reactor. This is evident with Slag A as blowover increased from 7g to 50g after 60 and 180 minutes of chlorination. Silica removal was many times slower than TiO_2 chlorination; unreacted free-lying silicate pieces collected in the bed after the chlorination of the rest of the particle that it was initially apart of.

Slag B (i.e., the higher TiO_2 content slag) feed was brittle and contained more cracks than Slag A. Due to the lower iron content; the porosity was not as widespread as in Slag A after 30 minutes of chlorination. However the larger Fe droplets in Slag B feed left behind larger pores upon chlorination. Chlorine attack widens the cracks causing particle breakage; the smaller pieces of slag are then converted to gaseous metal chloride before the particle is elutriated.

Figure 8: BSE Image of a Section through Slag A after 1 minute of chlorination at 1000°C

Rutile - After 30 minutes of chlorination, the rutile particles are dense and smooth show no signs of porosity. Rutile particles grow smaller as chlorination proceeds according to a shrinking core mechanism.

Synthetic rutile - SR feed particles are porous so the surface area available for chlorination was large from the start. After 30 minutes of chlorination, the initial pores left behind by the leaching of the iron have grown into larger pits. The SR particles are rapidly chlorinated before they are elutriated.

Effect of Ti_2O_3 - During ilmenite smelting, some TiO_2 is reduced to Ti_2O_3 according to reaction 3.

$$2\,TiO_2 + C = Ti_2O_3 + CO \qquad (3)$$

Ti_2O_3 is not desired as it does not increase the equivalent TiO_2 content of slag but consumes more electrical energy and carbon [16]. Le Roux [6] chlorinated slag in the absence of reductant (i.e., no coke and/or CO) and found that chlorination reactions still took place albeit to a lesser extent. It was demonstrated by mass balance methods that there was sufficient Ti_2O_3 to act as reductant for the chlorination of FeO and MnO. The remaining Ti_2O_3 was rapidly chlorinated.

In this study, experiments were conducted with CO and coke; so thermodynamic calculations were done to determine whether chlorination with coke, CO, or Ti_2O_3 would be more thermodynamically feasible. Using Factsage Version 6.1, a thermodynamic software tool, the change in Gibbs free energy at 1000°C for Reactions 4 to 9 was determined. The change in Gibbs free energy is negative for all six reactions; however reaction with Ti_2O_3 for both FeO and MnO chlorination is more negative indicating that these reactions are more thermodynamically favorable.

$$MnO + Ti_2O_3 + Cl_2 \rightarrow MnCl_2 + 2TiO_2 \qquad (\Delta G = -277\ kJ/mol\ MnO) \qquad (4)$$

$$MnO + CO + Cl_2 \rightarrow MnCl_2 + CO_2 \qquad (\Delta G = -191\ kJ/mol\ MnO) \qquad (5)$$

$$MnO + C + Cl_2 \rightarrow MnCl_2 + CO \qquad (\Delta G = -243\ kJ/mol\ MnO) \qquad (6)$$

$$FeO + Ti_2O_3 + Cl_2 \rightarrow FeCl_2 + 2TiO_2 \qquad (\Delta G = -273\ kJ/mol\ FeO) \qquad (7)$$

$$FeO + CO + Cl_2 \rightarrow FeCl_2 + CO_2 \qquad (\Delta G = -187\ kJ/mol\ FeO) \qquad (8)$$

$$FeO + C + Cl_2 \rightarrow FeCl_2 + CO \qquad (\Delta G = -239\ kJ/mol\ FeO) \qquad (9)$$

Slag A was chlorinated for 1 minute at 1000°C with petroleum coke (17wt% of charge) to determine the effect of Ti_2O_3 on chlorination. The mass balance is presented in Table III. After 1 minute of chlorination, 5g of Ti^{3+} was chlorinated and 74% of Ti^{3+} oxidized to Ti^{4+}. According to stoichiometry there was sufficient Ti_2O_3 to act as reductant for the chlorination of MnO and FeO.

Table III: Slag A Mass Balance After 1 minute of Chlorination at 1000 °C

Elements	Feed Material		Bed Sample		Mass chlorinated (g)	Conversion (%)
	Analysis (%)	Mass (g)	Analysis (%)	Mass (g)		
Ti (tot)	52.42	104.83	55.90	99.89	4.94	5%
Ti^{3+}	15.51	31.02	1.89	3.38	27.64	
Ti^{4+}	36.91	73.81	53.98	96.46		
FeO	8.60	17.20	1.89	3.38	13.82	80%
MnO	1.90	3.80	0.78	1.39	2.41	63%

The result of the 1 minute experiment has shed some light on the difference between the TiO_2 chlorination rate of Slag A and Slag B (Figure 9). TiO_2 chlorination in Slag A after 30 minutes of chlorination at is only 20% after 30 minutes, whereas chlorination in Slag B is 41%, the difference is likely due to the Ti_2O_3 content of the slag's, Slag B has 39 % whereas Slag A has 23%. The results of the 1 minute chlorination experiment show that Ti_2O_3 not oxidised in the chlorination of FeO and MnO is then rapidly chlorinated, since Slag A has a higher FeO content compared to Slag B (i.e., 9 % vs 2 %) there is less Ti_2O_3 available for chlorination, in addition Slag B had a higher Ti_2O_3 content to start with. This provides an explanation as to why chlorination in Slag B was higher than Slag A.

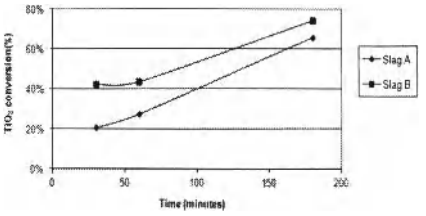

Figure 9: TiO_2 Conversion of Slag A and Slag B at 1000°C

Although rutile and Slag B feed have approximately the same $TiO_{2\ (equivalent)}$ content (i.e., 95%), overall conversion of rutile after 180 minutes is 14% lower than Slag B. This is likely due to combination of the effects of rapid chlorination of the Ti_2O_3 fraction in Slag B and the Fe content in Slag B which leaves behind a porous matrix and larger surface area for subsequent chlorination.

Conclusion

Chlorination rate increases with increasing temperature and the chlorination of rutile is most affected by lower temperatures. At 1000°C, SR had the highest chlorination conversion rate; this was followed by Slag B which in turn was more reactive than Slag A and rutile.

SR feed is porous; this allows for easy diffusion of reactive gases and chlorination proceeds quickly. The rapid chlorination of iron from slag leaves behind a porous high titania matrix with a large surface area for subsequent reaction. In this process, the density of the slag is lowered and it can be elutriated from the reactor. Rutile chlorination proceeds along the surface of the particle; so particle size decreases with increasing chlorination time.

Ti_2O_3 acts as reductant for the chlorination of FeO and MnO, Ti_2O_3 not oxidized is rapidly chlorinated.

Acknowledgements

Exxaro is acknowledged for permission to publish this paper. Appreciation is also expressed to Annabe Walliser and Jill Richards for SEM and XRD work.

References

1. H. Kotze, D. Bessinger, and J. Beukes, "Ilmenite Smelting at Ticor SA", South African Pyrometallurgy Conference, Cradle of Human Kind, South African Institute of Mining and Metallurgy, (2006), 203 – 214
2. T.P. Battle, D. Nguyen, and J.W. Reeves, "The Processing of Titanium-containing ores", The Paul E. Queneau International Conference, Extractive Metallurgy of Copper, Nickel and Cobalt, The Minerals, Metals and Materials Society, (1993), 925- 943
3. Y.K. Rao, and B.K Chadwick, "Chlorination of Rutile (TiO_2) with CO – Cl_2 – He gas mixtures", Trans. Instn Min. Metall, 97, (1988), 167 – 179
4. A. J. Morris, and F. Jensen, "Fluidized Bed Chlorination Rates of Australian Rutile", Metallurgical Transactions B, (1976), 89 – 93
5. W.E. Dunn, "High temperature chlorination of TiO_2 Bearing Minerals", Trans AIME, 218, (1960), 6 – 12
6. J.T. Le Roux, "Fluidized bed chlorination of Titania slag" (MSc, University of Pretoria, 2001)
7. H.Y. Sohn and L. Zhou, "The Kinetics of Carbochlorination of Titania slag", Canadian Journal of Chemical Engineering, 76, (1998), 1078 – 1082
8. H.Y. Sohn, L. Zhou, and K. Cho, "Intrinsic Kinetics and Mechanism of Rutile Chlorination by CO and Cl_2 Mixtures", Ind. Eng. Chem. Research, 37, (1998), 3800 – 3805
9. L. Sohn, Y.H. Sohn, G.K. Whiting, and K. Leary, "Microstructural Changes in Several Titaniferous materials", I & EC Research, 35, (1996), 954 – 962
10. J. Nell and P. Den Hoed, "The Carbochlorination of Rutile, Titania Slag and Ilmenite in a Bubbling Fluidized-bed Reactor", XXII International Mineral Processing Congress, Cape Town, (2003), 133 – 143

11. S. Moodley, "A Study of the Chlorination Behaviour of Various Titania Feedstocks" (MSc thesis, University of the Witwatersrand, 2011)
12. D. Bessinger, H. Du Plooy, P.C. Pistorius, and C. Visser, "Characteristics of Some High Titania Slag", Heavy Minerals Conference, Johannesburg, South Institute of Mining and Metallurgy, (1997), 151 – 156
13. H. Kotze, "Investigation into the Effect of Cooling Conditions on the Particle Size Distribution of Titania Slag" (PhD thesis, University of Pretoria, 2007)
14. D. Bessinger, "Cooling Characteristics of High Titania Slag" (MSc thesis, University of Pretoria, 2007)
15. I. Toromanoff, and F. Habashi, "The Composition of a Titanium Slag from Sorel", Journal of the Less common metals, 97, (1984), 317 – 329
16. P.C. Pistorius, "The Relationship Between FeO and Ti_2O_3 in Ilmenite Smelter Slags" Scandinavian Journal of Metallurgy, (2001), 120 – 125

3rd International Symposium on High-Temperature Metallurgical Processing
Edited by: Tao Jiang, Jiann-Yang Hwang, Patrick Masset, Onuralp Yucel, Rafael Padilla, and Guifeng Zhou
TMS (The Minerals, Metals & Materials Society), 2012

Experimental Study on the Pulverization and Reduction Behavior of sinter in Oxygen Blast Furnace

Yihua Han, Jingsong Wang, Rongzong Lan, Lintao Wang, Xiaojian Zuo, Qingguo Xue

State Key Laboratory of Advanced Metallurgy, University of Science and Technology Beijing
30 Xueyuan Road, Haidian District, Beijing, 100083 P. R.China

Keywords: Blast Furnace, Oxygen, Sinter, Low Temperature Reduction Pulverization, Reduction Behavior.

Abstract

Using the facility of reduction experiment, the low temperature reduction pulverization and reduction behavior of sinter in oxygen blast furnace (OBF) were studied. Through analyzing the results, the difference of pulverization and reduction behavior of sinter in OBF and conventional blast furnace (BF) were discussed. Furthermore, the effect laws of reduction temperature and the content of CO and H_2 on reduction behavior of sinter were studied. Also the controlling step of iron oxide reduction was discussed. Compared with BF, the low temperature reduction pulverization of sinter became serious at 773 K; reduction rate became faster at 1173 K; reduction time became less and final reduction degree was increased in OBF. With increasing of H_2 and CO contents, the reduction of sinter was promoted. The reduction process was controlled by interface chemical reaction at the earlier stage and by interface chemical reaction and internal diffusion at the final stage.

Introduction

The new ironmaking technology of Oxygen Blast Furnace (OBF) is most likely to be used in large-scale application process. The concept relies on the removal of the CO_2 contained in the top gas of the blast furnace. Therefore the useful components, i.e. $CO+H_2$, can be recycled back into the furnace and reused as reducing agents. In addition, injecting oxygen (O_2) into the furnace instead of preheated air, removes unwanted nitrogen (N_2) from the gas. Under the pressure of CO_2 emissions in iron and steel making, the growing international shortage of coking coal resources and the rising price of coke, OBF has attracted attentions of both domestic and foreign researchers, because it has so many advantages such as high productivity, high PCI rate, low coke rate, high gas reducing capability and high top gas calorific value, etc [1-7]. As a result of recycling most of the top gas after CO_2 removal and injecting oxygen into the furnace, the reduction capacity of blast furnace gas will be increased, so the metallurgical behavior of OBF's iron burden is different from traditional blast furnace. Therefore, it is one of the keys to develop this technology, which studies the metallurgical behavior of sinter in OBF. The purpose of this paper is to study the low temperature reduction pulverization and reduction behavior of sinter at the atmosphere of OBF, which includes the difference of low temperature reduction pulverization and reduction behavior of sinter in oxygen blast furnace and conventional Blast Furnace (BF). It will provide theoretical basis for the development of OBF.

Experimental

Table I shows the chemical analysis of sinter used in the experiments. All of the experiments were carried out in a gas-solid reaction apparatus, which can measure the iron weight

continuously and this is shown schematically in Figure I. The granular size of the sinter was in the range of 10mm to 12.5 mm and the sample weighted 500 g. The diameter of reaction tube is 75 mm. The sinter sample was set on packed alumina balls. The reducing gas mixture was injected from the top of the tube, down along the outer fringe of the reaction tube and then up into the reaction tube. The reducing gas was preheated by the alumina balls before reducing the sample. The weight of the sample was measured continuously by an electric balance on top of the furnace during the whole experiment.

Table I. Composition of Sinter (wt.%)

T_{Fe}	SiO_2	CaO	MgO	Al_2O_3	S	TiO_2	FeO
52.40	6.56	13.18	2.40	2.05	0.024	0.192	9.10

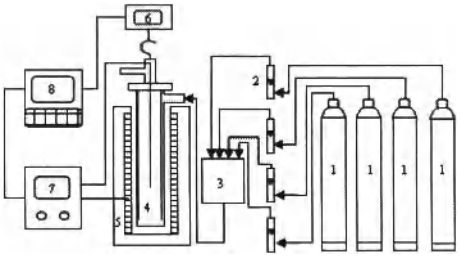

1- Gas cylinder; 2- Flowmeter; 3- Gas mixer; 4- Reaction tube; 5- Reduction furnace; 6-Electric balance; 7-Temperature controller; 8- Data processing system

Figure1. Schematic Layout of Experimental Apparatus

Experimental Procedure

Reduction behavior experiment:

The sample was heated up to the predetermined experimental temperature and during the heating process it was protected by N_2. Then the gas mixture was introduced into the reaction tube with a flow of 15 L/min. The flow of the gas mixture was not stopped until the weight of the sample remained stable for some time, which meant that the sinter was reduced completely. The gas mixture was then switched back to N_2 and the sample was cooled down to 298 K in the N_2 atmosphere. The experiment temperatures were set at 1173 K, 1273 K and 1373 K. Table 2 shows some parameters of reduction experiment.

Table II. Parameters of Reduction Experiment

Case	Volume Flow, $L \cdot min^{-1}$	Temperature, K	Gas concentration, %			
			CO	H_2	N_2	CO_2
1	15	1173	71	15	12	2
2	15	1173	30	0	70	0
3	15	1173	71	0	29	0
4	15	1173	30	15	55	0
5	15	1273	71	15	12	2
6	15	1373	71	15	12	2

Low temperature reduction pulverization experiment:

The sample was heated up to the predetermined experimental temperature and during the heating process it was protected by N_2. Then the gas mixture was introduced into the reaction tube with a flow of 15 L/min. The experiment temperature was set at 773 K. The total reduction process lasted for 60 min. The gas mixture was then switched back to N_2 and the sample was cooled down to 298K in the N_2 atmosphere. At last, put the sample in a drum, and the drum was running 10 min with the speed of 30 r/min. The weights of the sample which remained in 6.30 mm, 3.15 mm and 0.5 mm sieve were measured by a balance. Then low temperature reduction pulverization behaviour was measured by its percentage.

Results and Discussion

Low Temperature Reduction Pulverization of Sinter

The experiment results of low temperature reduction pulverization of sinter at the atmosphere of OBF (Case 1) and BF (Case 2) are shown in Table III, respectively. The results of Table III show that low temperature reduction pulverization of sinter in Case 1 is serious compare with Case 2, which $RDI_{+3.15}$ is on the low side, 82.7% while $RDI_{-0.5}$ is on the high side, 3.7%. In Case 2, $RDI_{+3.15}$ of sinter is on the high side, 92.6% while $RDI_{-0.5}$ is on the low side, 1.9%. The reason may be that the concentrate of CO and H_2 in the reducing gas of Case 1 is high and the reduction potential of the gas is high, which promote the reduction process ($Fe_2O_3 \rightarrow Fe_3O_4 \rightarrow FeO$) of sinter. The transformation of crystalline shape is observed during the reduction process, the transformation from hexagonal structure of Fe_2O_3 to the cubic structure of Fe_3O_4 lead to volume swelling and serious pulverization of sinter.

Table III. Results of Low Temperature Reduction Pulverization Experiment

Case	Volume Flow, $L \cdot min^{-1}$	Temperature, K	Gas concentration, %				Experiment result, %		
			CO	CO_2	H_2	N_2	$RDI_{+6.3}$	$RDI_{+3.15}$	$RDI_{-0.5}$
1	15	773	40	32	10	18	61.4	82.7	3.7
2	15	773	20	20	0	60	81.6	92.6	1.9

Reduction Behavior of Sinter

In this paper, reduction degree RI is the mass percentage of the oxygen that is reduced from Fe_2O_3 to Fe:

$$RI = \left[\frac{0.11W_1}{0.43W_2} + \frac{M_1 - M_t}{M_0 \times 0.43W_2} \times 100 \right] \times 100 \quad (1)$$

Where, M_0 is the initial mass of the sample, M_1 is the mass of the sample before reduced, M_t is the mass of the sample reduced t min later, W_1 is the mass percentage of FeO in the initial sample, W_2 is the mass percentage of total Fe in the initial sample.

Comparative Analysis of Sinter Reduction in Different Blast Furnace Atmosphere

Figure 2(a) shows the relationships between reduction degree RI with time for reduction of sinter in OBF (Case1) and BF atmospheres (Case2) at 1173 K. It can be found that the sinter reduced faster in OBF atmosphere than that in BF atmosphere. The measured RI of the sinter is up to

98.2% when the sinter reduced in OBF atmosphere at 1173 K for 117 min, while only 88.3% in BF atmosphere at 1173 K for 180 min. Therefore, it can be seen that because the improvement of gas reduction potential in OBF, sinter reduction has been promoted greatly.

Figure 2(b) shows the relationships between reduction rate RI′ with time for reduction of sinter in OBF (Case1) and BF atmospheres (Case2) at 1173 K. Also, it can be found that RI′ ($3.73\%\cdot min^{-1}$) of sinter reduction in OBF atmosphere is much higher than that in BF atmosphere ($1.10\%\cdot min^{-1}$) at the initial stage, and its advantage kept for about 70 min.

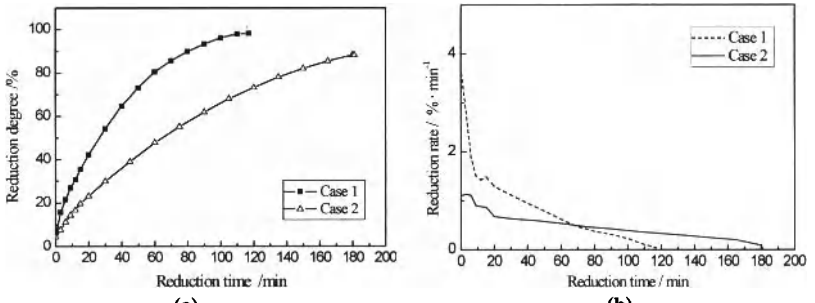

(a) (b)

Figure 2. Reduction Degree and Reduction Rate of Sinter with Time at OBF and BF Atmosphere

Effect of Reduction Temperature on Reduction Behavior of Sinter

Figure 3(a) and Figure 3(b) show the variation of the degree and rate of sinter reduction with time at the three experimental temperatures of 1173 K, 1273 K and 1373 K. This figures show that with increasing temperature, the reduction rate increased and the reduction time decreased, which lead to an increase of the final degree of reduction. At the early stage of reduction the reaction rate is fast, but the reduction curve becomes relatively flat at the final stage in OBF. The final degree of reduction of the sinter reaches as high as 99.24% and the reduction time is only 63 min at 1373 K. Under the same atmosphere, the final reduction degree reaches 99.15% and 98.20%, the reduction time is 78 min and 117 min at 1273 K and 1173 K, respectively.

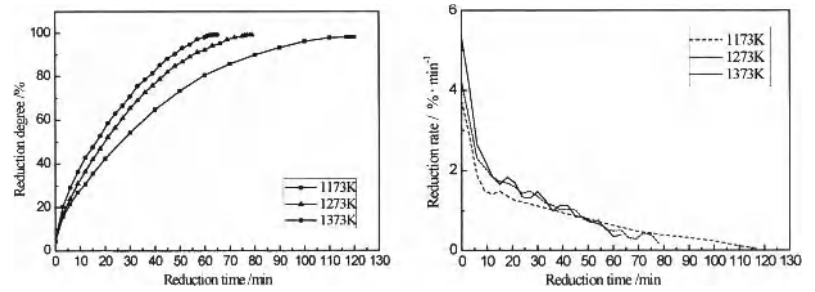

(a) (b)

Figure 3. Reduction Degree and Reduction Rate of Sinter with Time at Different Temperatures

Effect of CO and H_2 Contents on Reduction Behavior of Sinter

Figure 4(a) and Figure 4(b) show the relationships between RI and RI′ with time for reduction of sinter at 1173 K with different reducing atmospheres, where Case 2, Case 3 and Case 4, respectively. By comparing Case 3 with Case 2 in Figure 4, it can be seen that the reduction of sinter improved with the increase of CO concentration, the reduction degree RI increased from 88.3% to 92.3%. And the reduction rate is also increased greatly, the time-duration of sinter reduction decreased from 180 min to 140 min. According to Figure 6, the reduction of sinter improved after 15% H_2 was added into the reductive gas, and the final reduction degree RI increased from 88.3% (Case 2) to 97.8% (Case 4). Besides, the reduction rate increased significantly as well, the reduction rate in the early stage increased from 1.10%·min^{-1} (Case 2) to 2.80%·min^{-1} (Case 4). While comparing Case 4 with Case 3 in Figure 6, it can also be found that although the reductive gas (CO+H_2) accounts for 71% of Case 3, which is much higher than that of Case 4, the sinter reduction degree RI in the two atmospheres have almost no difference in the initial 90 min. But 90 min later, reduction degree RI of sinter in Case 4 atmosphere is higher than that in Case 3 atmosphere, its final reductive degree RI (97.8%) is 5.5% higher than that (92.3%) in Case 3. It can be seen that the reductive ability of H_2 is better than CO in the final stage.

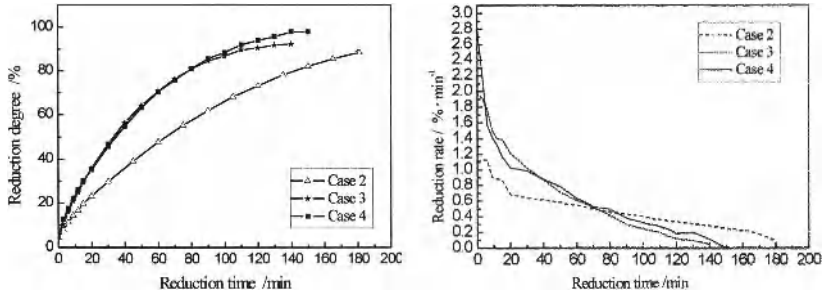

(a) (b)

Figure 4. Reduction Degree and Reduction Rate of Sinter with Time at Different Atmospheres

Controlling Step of Iron Oxide Reduction in OBF

The kinetic behaviour of the iron oxide reduction under such a high reducing atmosphere can be described by using an approximate 'unreacted core model' [8]. According to the unreacted core model, the derived integral expression [9] of the kinetics of the iron oxide reduction:

$$\frac{\rho_O r_0}{C_A^0 - C_A^e}\frac{f}{k_g} + \frac{\rho_O r_0^2}{6D_e\left(C_A^0 - C_A^e\right)}[1-3(1-f)^{2/3}+2(1-f)] + \frac{K}{k_+(1+K)}\frac{\rho_O r_0}{C_A^0 - C_A^e}[1-(1-f)^{1/3}] = t \quad (2)$$

Where, f is the degree of reduction, r_0 is the radius of original ore ball, t is the chemical reaction time, ρ_O is the density of oxygen of solid-phase content, C_A^0 is the initial volume concentration

of reduction gas, C_A^e is the balance volume concentration of reacting gas, k_g is the mass transfer coefficient of gas phase in phase boundary layer, D_e is the effective diffusion coefficient of reducing gas A in product layer, k_+ is the positive interface reaction rate constant, and K is the reaction equilibrium constant.

The first part in the left of equation: $\frac{\rho_O r_0}{C_A^0 - C_A^e}\frac{f}{k_g}$ shows the contribution of the external diffusion, the second part: $\frac{\rho_O r_0^2}{6D_e(C_A^0 - C_A^e)}[1-3(1-f)^{2/3}+2(1-f)]$ shows the contribution of the internal diffusion, the third part: $\frac{K}{k_+(1+K)}\frac{\rho_O r_0}{C_A^0 - C_A^e}[1-(1-f)^{1/3}]$ shows the contribution of the interface chemical reaction. Under the normal condition, when the flow of reducing gas is 15L/min, the flow rate is 56.6 mm/s. When the flow rate of gas is close to, or above, 50mm/s, the resistance of gas external diffusion can be neglected in the study of kinetics of iron oxide reduction, therefore, Equation 2 can be simplified as:

$$\frac{\rho_O r_0^2}{6D_e(C_A^0 - C_A^e)}[1-3(1-f)^{2/3}+2(1-f)]+\frac{K}{k_+(1+K)}\frac{\rho_O r_0}{C_A^0 - C_A^e}[1-(1-f)^{1/3}]=t \qquad (3)$$

Dividing both sides of Equation 3 by $1-(1-f)^{1/3}$, the equation becomes:

$$\frac{t}{1-(1-f)^{1/3}}=\frac{\rho_O r_0^2}{6D_e(C_A^0 - C_A^e)}[1+(1-f)^{1/3}-2(1-f)^{2/3}]+\frac{\rho_O r_0 K}{k_+(1+K)(C_A^0 - C_A^e)} \qquad (4)$$

When the gas-solid reaction is hybrid controlled by internal diffusion and interface chemical reaction, this kinetics equation can be used. From the first part in the left of Equation 3 the reaction time of solid phase reactant t is proportional to $[1-3(1-f)^{2/3}+2(1-f)]$ when reduction process is controlled by internal diffusion process. From the second part in the left of Equation 3 the reaction time of solid phase reactant t is proportional to $[1-(1-f)^{1/3}]$ when reduction process is controlled by interface chemical reaction process. From Equation 4, the term $t/1-(1-f)^{1/3}$ is proportional to $[1+(1-f)^{1/3}-2(1-f)^{2/3}]$ when reduction process is hybrid controlled by both internal diffusion and interface chemical reaction processes.

Therefore, it is possible to plot $[1-3(1-f)^{2/3}+2(1-f)]$ versus t, $[1-(1-f)^{1/3}]$ versus t and $t/1-(1-f)^{1/3}$ versus $[1+(1-f)^{1/3}-2(1-f)^{2/3}]$. From these plots the controlling unit of the sinter reducing reaction can be identified.

$[1-3(1-f)^{2/3}+2(1-f)]$ and $[1-(1-f)^{1/3}]$ are plotted in Figure 5 as a function of time t, to show the experimental reduction results of sinter in TGR-OBF at the high temperature stage. According to the figure, through the reduction process, $[1-(1-f)^{1/3}]$ is linear with t, but $[1-3(1-f)^{2/3}+2(1-f)]$ is linear with t only at the final stage of reduction, which shows that the reduction process at the early stage of sinter is controlled only by interface chemical reaction

at 1173 K, 1273 K and 1373 K, but is hybrid controlled by internal diffusion and interface chemical reaction after a period. For the reduction process at 1173 K, 1273 K and 1373 K, the start time of the reducing reaction, which is hybrid controlled by internal diffusion and interface chemical reaction, are 30 min, 21 min and 18 min, respectively.

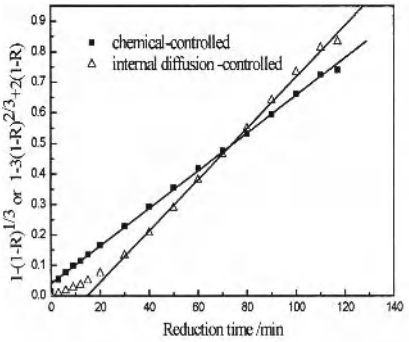

(a) 1173K

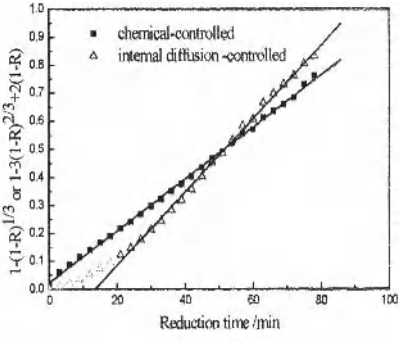

(b) 1273K

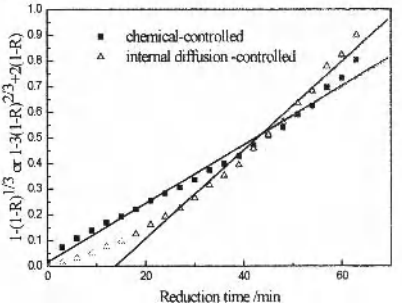

(c) 1373K

Figure 5. Comparison Curve of Chemical-controlled with Internal Diffusion -controlled Reaction at Different Temperatures

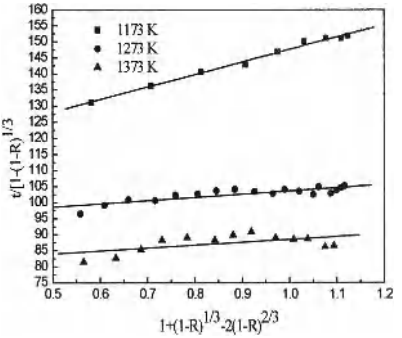

Figure 6. Mixed Control Plot at Different Temperatures

To verify whether it is hybrid controlled by both interface chemical reaction and internal diffusion at the final stage, $t/1-(1-f)^{1/3}$ as a function of $[1+(1-f)^{1/3}-2(1-f)^{2/3}]$ was plotted as shown in Figure 6. It can be seen that there is a good linear relationship between $t/1-(1-f)^{1/3}$ and $[1+(1-f)^{1/3}-2(1-f)^{2/3}]$ at the final stage of the reduction at 1173K, 1273K and 1373K. It confirms that the reduction reactions are hybrid controlled by both interface chemical reaction and internal diffusion.

Conclusions

(1) Low temperature reduction pulverization of sinter in OBF was serious compared with BF, which $RDI_{+3.15}$ was on the low side, 82.7% while $RDI_{-0.5}$ was on the high side, 3.7%.
(2) It could be found that the sinter reduced faster in OBF atmosphere than that in BF atmosphere at 1173K.
(3) In OBF, with the increase of the temperature, the reduction rate of sinter increased, the reduction time decreased, and the final reduction degree increased.
(4) With increasing of H_2 and CO contents in the reducing atmosphere, the reduction of sinter was promoted, but H_2 affected more significant than CO to the reduction of sinter.
(5) The reduction process was controlled by interface chemical reaction at the earlier stage and by interface chemical reaction and internal diffusion at the final stage.

Acknowledgments

The authors gratefully acknowledge the support of the National Basic Research Program of China (973 Program) (No.2012CB720401) and the National Key Technology R&D Program (No.2011BAC01B02).

References

[1] G.Q. Zuo, A. Hirsch, "The Trial of the Top Gas Recycling Blast Furnace at LKAB's EBF and Scale-up" (Paper presented at Proceedings of the 4th Ulcos seminar, Essen, Germany, 1-2 October 2008), 1-4.
[2] G. Danloy, et al., "ULCOS-Pilot testing of the Low-CO_2 Blast Furnace process at the experimental BF in Lulea", *Revue de Metallurgie*, 1(2009), 1-8.
[3] H. Hannu et.al., "Optimization of top gas recycling conditions under high oxygen enrichment in the blast furnace", *ISIJ Int.*, 50(7)(2010), 931-938.
[4] H. Hannu et al. "Multi-objective optimization of ironmaking in the blast furnace with top gas recycling", *ISIJ Int.*, 50(10)(2010), 1380-1387.
[5] M.S. Qin et al., "Blast furnace operation with full oxygen blast", *Ironmaking and Steelmaking*, 15(6)(1988), 287-292.
[6] M.S. Qin, Z.K. Gao and G.L Wang, "Study on blast furnace operation with all oxygen blast", *IRON & STEEL*, 22(12)(1987), 1-4.
[7] M.S. Qin, J.L. Zhang, "Oxy-coal technique of blast furnace", *IRON & STEEL*, 28(9)(1993), 9-13.
[8] X. K. Huang, *Principle of Ferrous Metallurgy* (Beijing, PRC: Metallurgical Industry Press, 1990), 291-295.
[9] X. L. Wang, *Ferrous Metallurgy (Ironmaking)* (Beijing, PRC: Metallurgical Industry Press, 2006), 90-93.

3rd International Symposium on High-Temperature Metallurgical Processing
Edited by: Tao Jiang, Jiann-Yang Hwang, Patrick Masset, Onuralp Yucel, Rafael Padilla, and Guifeng Zhou
TMS (The Minerals, Metals & Materials Society), 2012

FORMATION OF Ti(C,N) IN BLAST FURNACE SLAG BEARING HIGH TiO_2

Shiwei Ma, Guibao Qiu, Qingyu Deng, Wang Hua

College of Materials Science & Engineering, Chongqing University, Chongqing 400044, China
E-mails: mashiwei146484@163.com

Keywords: Blast Furnace Slag Bearing Titania, Thermodynamics, Ti(C,N), FactSage

Abstract

The flow properties of the blast furnace slag bearing high TiO_2 at high temperature like the viscocity may change a lot due to the formation of the carbonitride inside, causing serious problems on the separation between the metal and the slag. Therefore, the critical condition of the formation of Ti(C,N) in blast furnace is vital importance for the ironmaking process with iron ore bearing titania. In this study, the formation of Ti(C,N) in blast furnace and the influences of various factors on the Ti(C,N) formation are investigated by FactSage. It is found that the mass of Ti(C,N) would reach the maximum at 1480 °C, and the product is mainly TiN below 1620 °C, while it is mainly TiC above 1620 °C. The order of the factors by the importance from strong to weak was: temperature, the content of TiO_2 in slag, basicity of slag, the content of MgO and Al_2O_3.

Introduction

The titanium dioxide (TiO_2) in iron ore bearing titania will be partly reduced by carbon to titanium carbonitride (Ti(C,N)) in blast furnace, causing serious problems on the separation between the metal and the slag because of the change of flow property. Therefore, the critical condition of the formation of Ti(C,N) in blast furnace is vital importance for the ironmaking process, especially for the smelting of iron ore bearing titania. Extensive experimental data in regard to the formation of Ti(C,N) has been reported in numerous papers[1-6]. However, only some discrete data can be obtained by experiment, and it is difficult to detect the mass of Ti(C,N) in slag. In addition, the experiment is difficult to be proceeded when the temperature is above 1600 °C. Therefore, it is very difficult to make clear the critical condition of the formation of Ti(C,N) by experiment.

In the present study, the thermodynamics software FactSage was used to study the critical condition for the formation of Ti(C,N) in slag. In addition, the influences of various factors on the formation of Ti(C,N) were investigated, including temperature and slag

composition (TiO_2,MgO,Al_2O_3 and basicity). FactSage has developed many years and been widely used in metallurgy and other fields [7-11]. It is one of the largest fully integrated database computing systems in chemical thermodynamics in the world. Especially it has slag-iron database which is suitable for calculating the reaction and thermodynamics equilibrium between slag and iron at high temperature. Therefore, it is feasible and reasonable to investigate the formation of Ti(C,N) in slag by FACTSage. Finally, the ultimate purpose of this study is to find out some measures to prevent or reduce the formation of Ti(C,N), keeping blast furnace operation more smoothly when the iron ore bearing high titania is smelted in blast furnace.

FactSage Modeling

The **Equilib** module was mainly used when the formation of Ti(C,N) was predicted by FactSage. A 1:2 mass ratio of slag to pig iron (100g slag, 200g pig iron) was inputted into this module. The calculations were performed using slag composition and iron presented in **Table I** and **Table II**, respectively, mixed with excess carbon, and heated in the temperature range to 1100 °C to 1800 °C in a nitrogen atmosphere. As slag **T3**, **A3**, **M3** and **B4** have the same composition, therefore, slag **T3** is regard as the basic slag to predict the formation of Ti(C,N) in slag at different temperatures. The influence of slag composition on the formation of Ti(C,N) was predicted at 1425 °C,1450 °C and 1475 °C. All parameters are list in **Table III**.

Table IV. The Composition of Slag (wt%)

Slag	TiO_2	Al_2O_3	MgO	CaO	SiO_2	V_2O_5	Basicity
T1	22.0	14	8.0	29.67	26.03	0.3	1.14
T2	23.0	14	8.0	29.14	25.56	0.3	1.14
T3	23.5	14	8.0	28.87	25.33	0.3	1.14
T4	24.0	14	8.0	28.61	25.09	0.3	1.14
T5	25.0	14	8.0	28.07	24.63	0.3	1.14
A1	23.5	12	8.0	29.94	26.26	0.3	1.14
A2	23.5	13	8.0	29.41	25.79	0.3	1.14
A3	23.5	14	8.0	28.87	25.33	0.3	1.14
A4	23.5	15	8.0	28.34	24.86	0.3	1.14
A5	23.5	16	8.0	27.81	24.39	0.3	1.14
M1	23.5	14	7.0	29.41	25.79	0.3	1.14
M2	23.5	14	7.5	29.14	25.56	0.3	1.14
M3	23.5	14	8.0	28.87	25.33	0.3	1.14
M4	23.5	14	8.5	28.61	25.09	0.3	1.14
M5	23.5	14	9.0	28.34	24.86	0.3	1.14
B1	23.5	14	8.0	28.14	26.06	0.3	1.08
B2	23.5	14	8.0	28.39	25.81	0.3	1.10

Table V. Continued

Slag	TiO_2	Al_2O_3	MgO	CaO	SiO_2	V_2O_5	Basicity
B3	23.5	14	8.0	28.63	25.57	0.3	1.12
B4	23.5	14	8.0	28.87	25.33	0.3	1.14
B5	23.5	14	8.0	29.11	25.09	0.3	1.16

Table VI. The Composition of Pig Iron (wt%)

Pig iron	Fe	C	Ti	V	Si	P	S
Mass fraction	94.64	4.50	0.23	0.30	0.19	0.06	0.08

Table VII. Model Parameters

Temperature(°C)	Pressure(atm)	Slag(g)	Pig iron(g)	Solution
1100—1800	2	100	200	FToxid-slag FSstel-LIQUID

Results and discussions

Influence of Temperature on the Formation of Ti(C,N)

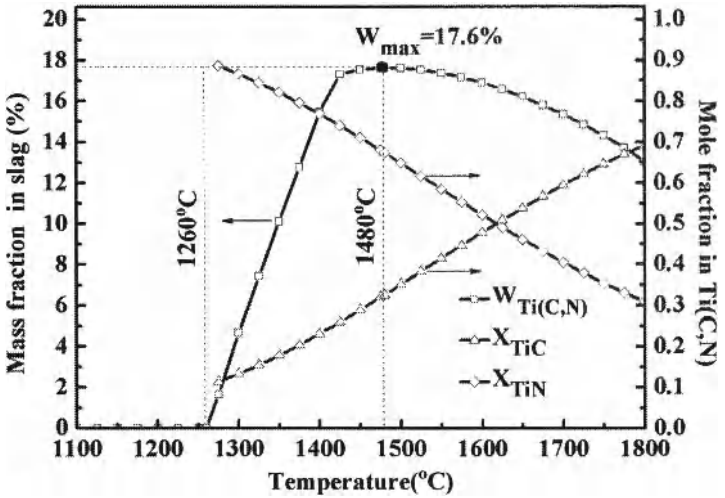

Fig. 1. The relationship between temperature and mass fraction of Ti(C,N) in slag as well as mole fraction of X_{TiC}, X_{TiN} in Ti(C,N)

The results of calculation on the slag-iron system in nitrogen at temperatures between 1100 °C and 1800 °C carried out in the present study are shown in **Fig. 1**. It can be seen

from **Fig. 1** that, at temperatures below 1260 °C, the solid solution Ti(C,N) was not formed. At a temperature of 1260 °C, the solid solution Ti(C,N) began to form, and its mass fraction in slag increased with increasing temperature at temperatures between 1260 °C and 1480 °C. This change can be analyzed thermodynamically based on the following reactions to form TiN, TiC or Ti(C,N):

$TiO_2+2C+1/2N_2 = TiN+2CO$ $\Delta G_r^0=375900-255.86T$ (J/mol) (1)

$TiO_2+3C = TiC+2CO$ $\Delta G_r^0=527400-336.56T$ (J/mol) (2)

The initial reaction temperatures for reactions (1) and (2) are 1196 °C and 1294 °C, respectively. Therefore, it is reasonable for the formation of Ti(C,N) at a temperature of 1260 °C.

At a temperature of 1480 °C, the mass of Ti(C,N) in slag reached the maximum, which would imply that TiO_2 in slag can't be reduced by carbon any more with increasing temperature. This can be demonstrated by **Fig. 2**. The mass fraction of TiO_2 in slag decreased with increasing temperature, and only 1.45 wt pct of TiO_2 can be observed in slag at 1480 °C. At temperatures above 1480 °C, the mass fraction of TiO_2 in slag increased hardly with increasing temperature. Thererfore, the temperature in the lower blast furnace should be controlled below 1480 °C as possible as in order to avoid the formation of large amount of Ti(C,N).

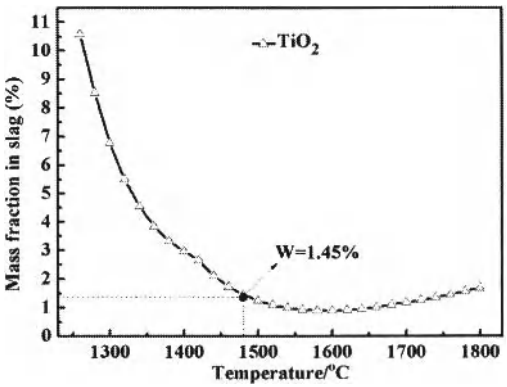

Fig. 2. The relationship between temperature and mass fraction of TiO_2 in slag

It also can be seen from **Fig. 2** that the mass fraction of Ti(C,N) decreased with increasing temperature at temperature above 1480 °C. This is mainly caused by the transformation of titanium from TiN and TiC to [Ti] in liquid iron. Therefore, the

solubilities of titanium ([Ti]) in liquid iron increased with increasing temperature. This can be demonstrated by **Fig. 3**. It can be seen from **Fig. 3** that, at a temperature of 1480 °C, only 0.25 wt pct of Ti dissolved in liquid iron. However, the solubilities of titanium increased to 1.92 wt pct at 1800 °C. The overall reactions of this process are summarized in reactions (3) and (4):

$$TiC - [Ti]+[C] \quad (3)$$

$$TiN - [Ti]+1/2N2 \quad (4)$$

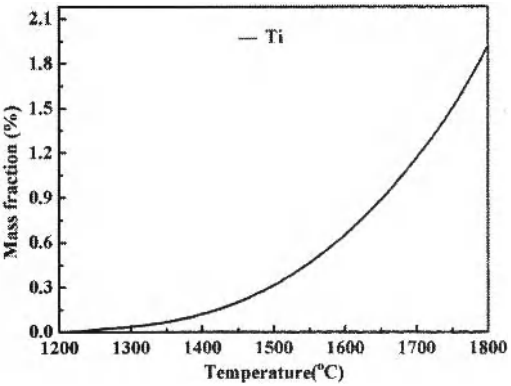

Fig. 3. The relationship between temperature and mass fraction of Ti in liquid iron

The change of mole fraction of TiC and TiN in Ti(C,N) are also shown in **Fig. 1.** From **Fig. 1**, it can be seen that it is mainly TiN at lower temperature (1260°C<T<1620 °C), $X_{TiC}<X_{TiN}$. However, X_{TiC} increased with increasing temperature, while X_{TiC} decreased. At a temperature of 1620 °C, $X_{TiC}=X_{TiN}$; then X_{TiC} would be greater than X_{TiN} with increasing temperature. That is to say, it is mainly TiC at high temperature (T>1620 °C). This change can be analyzed thermodynamically based on the following reaction:

$$TiN+ C - TiC+1/2N_2 \quad (5)$$

The initial reaction temperature (T_0) for reaction (5) ($\Delta G=0$) would change with changing activities of TiN and TiC. The relationship between T_0 and a_{TiN}, a_{TiC} are list in **Table VIII**, which was calculated by **Reaction** module. As Ti(C,N) is regard as an ideal solid solution, therefore, $X_{TiN}=a_{TiN}$ and $X_{TiC}=a_{TiC}$. The result is in a good agreement with the result in **Fig. 1**, which was calculated by **Equilib** module. And it is also in agreement with previous results of Che.YC[12].

Table IX. The Initial Reaction Temperature for Reaction (5) at Different a_{TiN} and a_{TiC}

P_{N2} (atm)	a_{TiC} (X_{TiC})	a_{TiN} (X_{TiN})	T_0 (°C)
1	0.103	0.897	1260
1	0.178	0.822	1350
1	0.231	0.769	1400
1	0.289	0.711	1450
1	0.352	0.648	1500
1	0.415	0.585	1550
1	0.478	0.522	1600
1	0.539	0.461	1650
1	0.595	0.405	1700
1	0.646	0.354	1750
1	0.691	0.309	1800

Influences of Slag Composition on the Formation of Ti(C,N)

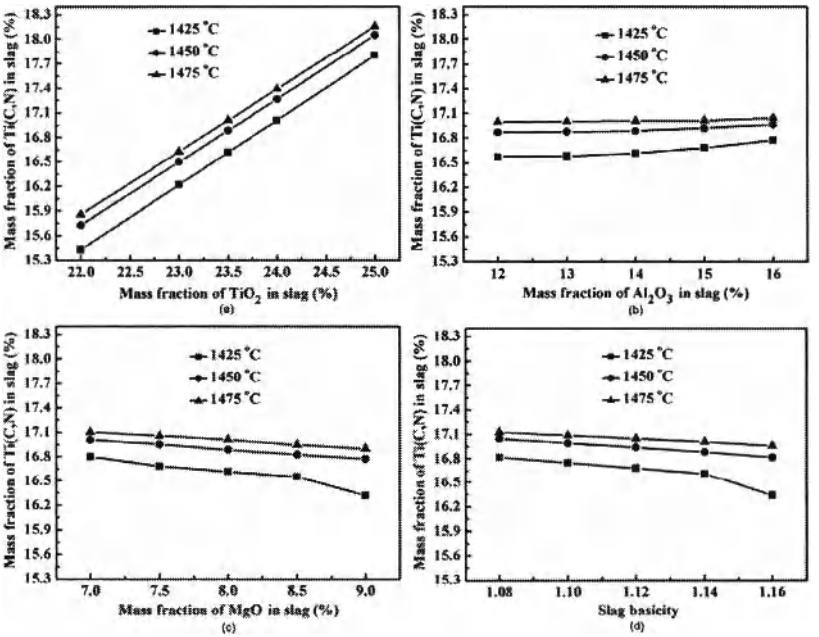

Fig. 4. The relationship between mass fraction of Ti(C,N) and slag composition at 1425 °C,1450 °C,1475 °C: (a)-different content of TiO_2, (b)-different content of Al_2O_3,

(c)-different content of MgO, (d)-different slag basicity.

The results of influences of slag composition on the formation of Ti(C,N), which were predicted by FactSage, are shown in **Fig. 4**. **Fig. 4 (a), (b), (c)** and **(d)** show the influence of TiO_2,Al_2O_3, MgO and basicity in slag on the formation of Ti(C,N), respectivily. It can be seen from **Fig. 4 (a)** that the mass of Ti(C,N) increased with increasing TiO_2 in slag. This is mainly caused by the activity of TiO_2 (a_{TiO2}).The a_{TiO2} increased with increasing mass fraction of TiO_2 in slag, therefore, the mass of TiO_2 reduced by carbon increased, which would lead to the increase of mass of Ti(C,N). From **Fig.4 (b), (c)** and **(d),** it can be seen that the infulence of Al_2O_3, MgO and basicity in slag is small compared with TiO_2. To some extent, the increase of MgO, slag basicity and decrease of Al_2O_3 can restrain the formation of Ti(C,N). Therefore, the ideal slag composition should satisfy the following demands: low TiO_2,Al_2O_3 and high MgO,slag basicity. The results are in a good agreement with previously experimental results of Du.HG [4].

Conclusions

At 1-atm N_2 pressure, the critical condition for the formation of Ti(C,N) is that the temperature should reach approximately 1260 °C (1533K). The mass of Ti(C,N) reach the maximum at a temperature of 1480 °C. And it is mainly TiN in solid solution Ti(C,N) at temperatures below 1620 °C , however, TiN will be replaced by TiC at temperatures above 1620 °C. Therefore, it is mainly TiC at high temperature. The order of the factors by the importance from strong to weak was: temperature, the content of TiO_2 in slag, slag basicity, the content of MgO and Al_2O_3.

However, additional optimization of the parameters in the thermodynamic FactSage database can improve the accuracy of calculations. So the method that using FACTSage to predict the formation of Ti(C,N) in blast furnace can save a large amount of human and material resources.

Acknowledgements

This study was financially supported by Key Project of Chinese National Programmes for Fundamental Research and Development (Grant No.51090383).

Reference

1. N.J Welham, P.E. Willis, "Formation of TiN/TiC-Fe composites from ilmenite ($FeTiO_3$) concentrate,"*Metallurgical and Materials Transactions B-Process Metallurgy and Materials Processing Science*, 29 (5) (1998), 1077-1083.

2. C.G. Bai, "Study on Some Physical Chemistry Problems of Blast Furnace Slag-Bearing Titania," (D. thesis, Chongqing University, 2003), 20-35.

3. Z.Y. Cai, S.H. Cao, Z. Xie, "Influence of temperature on synthetic Ti(C, N) whisker by carbon thermal reduction method," *Materials Science and Engineering of Powder Metallurgy*, 03(2007), 151-155.
4. H.G. Du, G. Du, "Study on the formation of Ti(C,N) in blast furnace," *ACTA METALLURGICA SINICA*, 03(1991), 89-94.
5. Y.M. Gao, et al., "Experimental Study on Carbothemlal Reduction of Blast Furnace Slag Bearing Titania," *J.of Anhui UniVersity of Technolog (Natural Science)*, 25 (01) (2008), 1-4.
6. C.D. Xu, R. Lin, "Important Physical-Chemistry Problems for theReduction of Vanadium-Titanium Magnetite in Pan Zhihua at High Temperature," *IRON STEEL VANADIUM TITANIUM*, Z1(1980), 1-10.
7. S.Q. Zhou, W. Zhao, W.H. Xiong, "Thermodynamics of the Formation of Contiguity between Ceramic Grains and Interface Stuctures of Ti(C,N)-based Cermets," Int. *Journal of Refractory Metals & Hard Marerials*, 27(2009), 740-746.
8. A.D. Pelton, "Thermodynamic database development—modeling and phase diagram calculations in oxide systems," *Rare Metals*, 25 (05) (2006), 473-480.
9. E. Jak, et al., "Thermodynamic optimisation of the FeO-Fe2O3-SiO 2 (Fe-O-Si) system with FactSage," *International Journal of Materials Research*, 98(2007), 847-854.
10. A. Kostov, B. Friedrich, "Zivkovic.Predicting thermodynamic properties in Ti-Al binary system by FactSage," *Computational Materials Science*, 37(2006), 355-360.
11. V. Dyk, J. C, "An improved thermodynamic factsage simulation to simulate mineral matter transformation during a fixed bed counter-current gasification process, validated with ht-xrd," *Annual International Pittsburgh Coal Conference*, 29(2008), 25-35.
12. Y.C. Che, "Thermodynamics discussion for the precipitation of Ti(C,N) in blast furnace," *IRON STEEL VANADIUM TITANIUM*, 03(1982), 22-29.

3rd International Symposium on High-Temperature Metallurgical Processing
Edited by: Tao Jiang, Jiann-Yang Hwang, Patrick Masset, Onuralp Yucel, Rafael Padilla, and Guifeng Zhou
TMS (The Minerals, Metals & Materials Society), 2012

RESEARCH ON CARBONTHERMAL REDUCTION BEHAVIOR OF ILMENITE

Yufeng Guo, Lirong Chen, Tao Jiang, Wenjie Weng, Feng Chen

(Central South University, Changsha, Hunan Province 410083)

Key words: Ilmenite, Reduction, Carbon-burdened, Titanium Nitride

Abstract

In this paper, the carbonthermal reduction behavior and the influencing factors of Panzhihua ilmenite under the condition of carbon-burdened were systematically investigated. The results show that the ilmenite forms into titanium nitride during the reduction process at 1200 oC under the condition of carbon-burdened. Carbon-burdened is beneficial to the reduction of iron oxide, but less favorable for the growth of iron grain.

Introduction

The titanium ferrous resources are very rich in Panzhihua-xichang area, accounting for about 38.85% of the world's proved reserves [1]. However, TiO_2 grade of this kind of ilmenite is low and calcium magnesium content is high, it generally requires preconcentration to titanium-rich material—titanium slag or synthetic rutile.

Chlorination process is an advanced method for production of titanium dioxide, which should takes high quality titanium-rich material with low content of calcium and magnesium as raw materials (the content of MgO and CaO are less than 1.0%). Ilmenite in Panxi area, however, contains high calcium and magnesium; it is not suitable as a raw material for chloride process. Methods of producing titanium-rich materials which have been applied in industry are electric smelting, various acid leaching and reduction rust [2-5]. There still exist some problems such as CaO and MgO removed not thoroughly, low resource utilization, high energy consumption and environmental pollution.

Based on the previous methods of preparing titanium-rich materials and the research results, a new process of preparation of titanium-rich materials is presented in this paper. This process is based on the chlorination speed of TiCN is far higher than that of other impurities, thus carbon nitriding titanium chlorinated selectively and other impurities left in slag. TiN can be used in chlorination process and the production of ceramic material.

The solid and liquid reduction behaviors of carbon-burdened titanium are investigated in this study by using X-ray diffraction, optical microscopy and scanning electron microscopy for laying the foundation to fulfill the carbon nitriding process of ilmenite.

Material and Methods

Material Properties

The fine-grained flotation concentrate of titanium ore used in this study was provided by the PanZhiHua Iron and Steel Company. The main chemical composition of the sample is shown in Table 1. 95.60% of the titanium ore had a particle size of 0.076mm. Reducing coal was bituminous coal received from Shanxi in China, Proximate analysis and ash melting points for coal are shown in Table 2. The pelletizing binder was a multi-functional composite binder F, which is a patented product developed by Central South University [6].

Table I. Chemical Compositions of Ilmenite Concentrations /wt%

Composition	TiO_2	TFe	FeO	V_2O_5	K_2O	Na_2O	MnO
Content	46.63	30.17	30.29	0.060	0.0057	0.029	0.48
Composition	CaO	Al_2O_3	MgO	SiO_2	S	P	Ig
Content	0.86	0.50	5.34	4.00	0.11	0.004	0.16

Table II. Industry Analysis and Ash Analysis of Coal

Coal	Industry Analysis /%				Volatile matter(1 ~8)	Ash Fusion /°C			
	M_{ad}	A_d	V_{daf}	F_{cad}		DT	ST	HT	FT
Bitumino-us coal	20.36	4.48	27.38	47.78	2	1260	1280	1290	1290

Research Methods

Ilmenite, certain molar ratio of C and 1% F binder were thoroughly mixed and pelletized to Ø10×10 mm pellets with certain pressure on a high-energy hydraulic pellet machine, drying. Reduction was carried out in high temperature furnace with N_2, using additives to strengthen the reduction process [7]. Firstly, put the pellets (about 25 g) with excessive bituminous coal in a graphite crucible. Secondly, put the graphite crucible in the resistance furnace (Ø120 mm) when the temperature rises to the setting one, time and stay warm for the fixed time. Thirdly, turn off the N_2 valve, take out and cover the graphite crucible with waste coal, cooling. Sampling and analysis: use the metallization rate to measure the reduction degree of titanium iron; the X-ray diffraction (Cu anode target, Kal wave length for 1.54056 A) to analyze the phase composition change of ilmenite during reduction process; the SX-40 type optical

microscope to analyze the microscopic structure, the particle shape and distribution state of each reduction products

Results and Analysis

Effects of Dosage of Carbon

Effects of internal carbon on metallization rate, phase composition and micro structure of reduction products are shown in Figure 1, Figure 2 and Figure 3. When experimenting, keep the reduction temperature at 1300 °C for 2 h and the amount of internal carbon was measured by C: Ti.

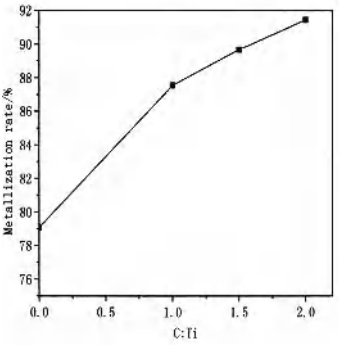

Figure 1. Effect of Carbon-burdened on metallization rate of reduction

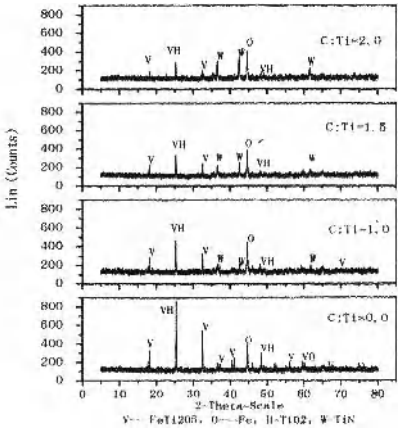

Figure 2. The X-diffraction Figure of the Reduction Products of different amount of internal carbon

As is shown in Figure 1, the metallization rate of the product increased from 79.08% to 91.43% as the C: Ti value increased from 0 to 2.0. The results suggested that increasing internal carbon was favorable to the metallization rate of the products.

From Figure 2, with no carbon-burdened, the phases were $FeTi_2O_5$, TiO_2, and Fe. When C: Ti= 1.0, the $FeTi_2O_5$ diffraction peak decreased, TiN diffraction peak appeared, and the quantity of TiN gradually increased with carbon increasing.

These results indicated that with none-internal carbon, the reactions were almost the reduction of $FeTiO_3$, which generated $FeTi_2O_5$, iron and TiO_2. Chemicals reactions are as follows:

$$FeTiO_3+C=Fe+TiO_2+CO_2, \quad (1)$$

$$FeTiO_3+C=FeTi_2O_5+Fe+CO. \quad (2)$$

When the carbon increases to 1.0, under the environment of nitrogen-containing below 1743K which is the melting point of $FeO \cdot TiO_2$, the possible reactions in the

reduction process are as follows [8]:

$$FeTiO_3 + 4\ C = Fe + TiC + 3\ CO \quad (3)$$

$$FeTiO_3 + 3\ C + 1/2\ N_2 = Fe + TiN + 3\ CO. \quad (4)$$

At high temperature, as TiN is more stable than TiC, TiC will transform to TiN easily, so TiN is the main reduction products [9]. The possible reaction in the system also contains:

$$TiO_2 + 2C + 1/2N_2 = TiN + 2CO \quad (5)$$

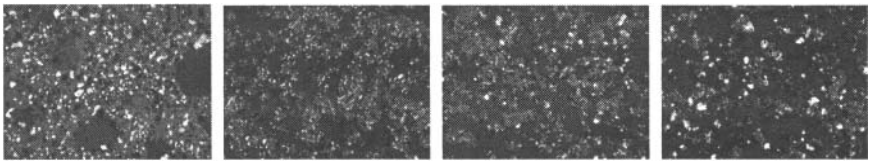

C:Ti=0.0 C:Ti=1.0 C:Ti=1.5 C:Ti=2.0

Figure 3. Microstructure of the Reduction Rroducts of Different Amount of Internal Carbon in scale (x200 times) (white-iron, gray- anosovite, gold-TiN)

As is shown in Figure 3, with no-carbon-containing, the iron grain size of the reduction products was biggest, distributing in the anosovite. With the amount of carbon increased, the iron grain size became smaller. The results suggested that internal carbon was conducive to the reduction of iron, but unfavorable to the migration of iron particles, going against the increasing of iron grain size. When the C: Ti value increased from 1.0 to 2.0, the color of the surface of reduction products changed from lavender to cyan, purple Ti (C, N) generated inside[10]. Under the conditions of C: Ti value between 1.5 to 2.0, as the iron particles migrate, connect with each other, the grain size increased obviously. Due to the lattice constants of TiC (0.4 329nm) and TiN (0.4 235nm) were much closed to each other, it was easy to form the solid solution of Ti(C, N). Along with the different percentages of TiN and TiC, the color of Ti (C, N) presented a series of changes. When the percentage of TiN (%) is close to 85% and TiC(%) nearly 15%, the color is purple as shown in the picture. When C: Ti = 2.0, the metal particles edges were becoming irregular, with angular and the size of iron particles was equal to that of none-internal carbon.

Effects of Reaction Temperature

The effects of temperature on metallization rate, phase composition and micro structure of reduction products are shown in Figure 4, Figure5 and Figure6. Other parameters kept constant : C/Ti=2.0, reduction time is 2 h.

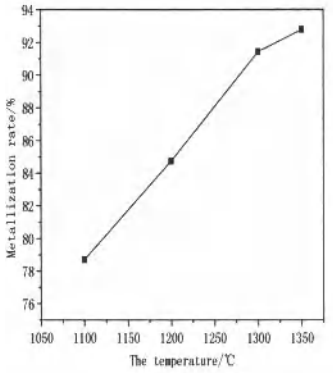

Figure4. Relationship of Different Temperature and metallization rate

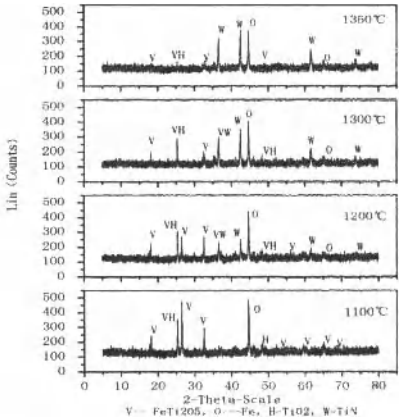

Figure5. X-diffraction Pattern of the Reduction Products at different temperature

As is shown in Figure4, at 1350 °C, the metallization rate increased to 92.79%, which indicated that temperature was favorable to the metallization rate of products.

From Figure 5, under the temperature of 1200 °C, the phases of the reduction products were $FeTi_2O_5$, Fe and TiO_2. When the temperature was higher than 1200 °C, the phase of $FeTi_2O_5$ disappeared gradually and a little TiN generated. Above 1300 °C, the phases changed unconspicuously.

The results suggested that when the reduction temperature was below 1200 °C, the changes were only the transformation of $FeTiO_3$ to $FeTi_2O_5$. At 1300 °C, the reduction of TiO_2 and Fe were almost completed and the only change was TiO_2 transforming to TiN. The temperature that TiO_2 changing to TiN was 1201 °C as thermodynamic calculation shows. The main reaction was:

$$FeTiO_3 + 3\,C + 1/2\,N_2 = Fe + TiN + 3\,CO \qquad (6)$$

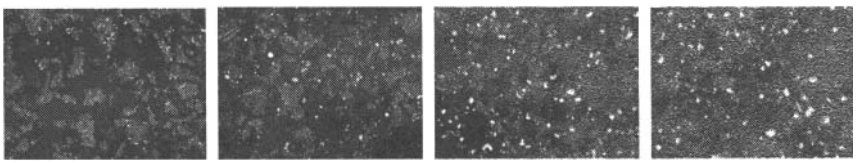

1100°C 1200°C 1300°C 1350°C

Figure 6. Micro-structureof the reduction products at different temperature (x200 times) (white-iron, gray- anosovite, gold-TiN)

As shown in Figure6, at 1100 °C, the iron particles were very small, distributing in $FeTi_2O_5$, little amaranthine TiN generated. As the temperature increased to 1200°C, the diameter of iron particles increased. Large particles of iron can be seen accidentally, mingling with TiN. At 1300 °C, the size of iron grain increased obviously.

The color of TiN gradually became deeper, from wheat to light purple, which was related to the rising percentage of TiN. The iron became to melt and the iron particles and TiN were mingled more and more when the temperature continues to rise. The results showed that temperature was beneficial to iron grain growth and the formation of TiN.

Effects of Reaction Time

The effects of time on metallization rate, phase composition and micro structure of reduction products are shown in Figure 7, Figure 8 and Figure 9. Other parameters kept constant : C/Ti=2.0, the reduction temperature was 1300 °C.

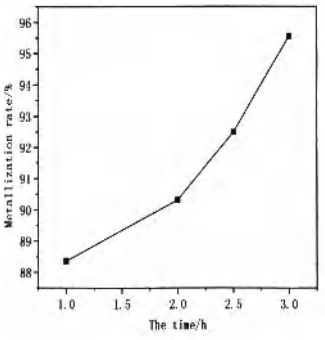

Figure 7. The relationship of different time-metallization rate

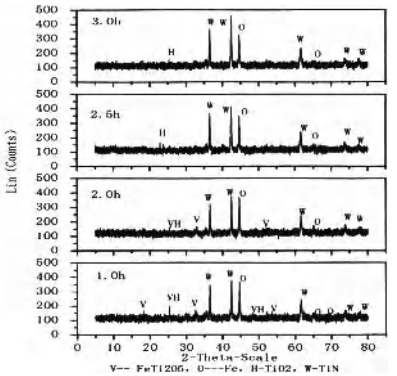

Figure 8. The X-diffraction figure of the reduction products in different time

As shown in Figure 7, when the reduction time was 1.0 h, the metallization rate was only 88.65%, when the time was prolonged to 3.0h, the metallization rate increased to 95.55%. The results indicated that prolonging the reduction time was conducive to the increasing of metallization rate.

From Figure 8, when the reduction time was less than 2.0 h, the phases were TiN, Fe and $FeTi_2O_5$. When the time was prolonged to 2.5h, the $FeTi_2O_5$ phase disappeared and TiN generated a lot. The results showed that the reduction of TiO_2 and Fe almost completed, the only reaction was the changing of TiO_2 to TiN. Continue prolonging the time to 3.0h, the phase composition barely changed. The results suggested that prolonging reduction time was favorable to the reduction of iron and the generation of TiN.

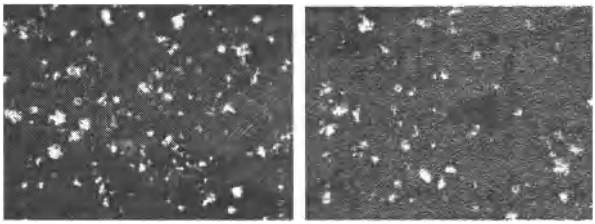

1.0 h 3.0 h

Figure 9. Microstructure of the reduction products in different time (x200 times) (white-iron, gray- anosovite, gold-TiN)

As shown in Figure 9, prolonging the reduction time, the size of iron particles changed little, but the amount of TiN increased obviously. As the reduction time increased from 1 h to 3 h, the color of the reduction products was changed from lavender to purple. The molten iron particles became bigger and the quantity of TiN increased gradually.

Conclusions

(1) Increasing the amount of internal carbon was favorable to the reduction of iron and the generation of TiN; Little internal carbon hampered the migration of iron particles, going against iron grain size to grow up, but when the amount of internal carbon increased to a certain amount, this kind of resistance would be weakened

(2) Rising the reduction temperature or prolonging the reduction time were conducive to increasing metallization rate, the generation of TiN and the grain size of iron. But the effect of temperature was more obvious.

Acknowledgements

The authors want to express their appreciation to The National Basic Research Program of China (973 Program) (No.2007CB613606) for financial support of this research.

References

[1] Jiahua Yu, Honggui Liu, "The present production situation of titanium and rich titanium material at home and abroad," *The world of non-ferrous metal*, 6(2003).
[2] Guozhu Deng, "Production situation of rich-titanium materials and the development in the future," *Titanium industry development*, 5(2000),1~5.
[3] Henn J.H. and Barclay J.A, "A review of proposed processes for making rutile substitutes," Inf Circ.U.S.Bur.mines, 4(1970),27.
[4] Jingdong Liang, "Flotation theory and the practice," Beijing: metallurgical mineral

smelting of industry press, 10(1995), 330~394.
[5] Guozhu Deng and Xuefei Wang, "The ways of making rich- titanium materials with using panzhihua titanium concentrates ," *Steel-Vanadium and Titanium*, 23 (2002), 14~17.
[6] Jiang Tao, etc., "A kind of complex polymer-based pellet and its use method," China CN 101693950A[P].
[7] Jindong Liang, "Carbonitriding of blast furnace slag---mineral separation of preliminary research and imagine, "*The briefing of Science and Technology* ",2(1988), 10~15.
[8] Suresh K,Gupta etc., "Reduction dynamics of ilmenite with graphite", *Steel -Vanadium and Titanium*,3(1989),51~55.
[9] Fusheng Pan, Aitao Tang andLi Kui, Reaction and Synthesis of Titanium Boride and Composite Materials (Chongqing university press.2005),21~23.
[10] MoWei, Guozhu Deng and Fangcheng Luo, "*Titanium Metallurgy Bearing* "(Beijing: science press. 1998), 118~198.

3rd International Symposium on High-Temperature Metallurgical Processing
Edited by: Tao Jiang, Jiann-Yang Hwang, Patrick Masset, Onuralp Yucel, Rafael Padilla, and Guifeng Zhou
TMS (The Minerals, Metals & Materials Society), 2012

REDUCTION KINETICS OF LOW GRADE HEMATITE ORE

Yongzhong Xiao, Zhen He, Tiejun Chun*, Deqing Zhu, Jian Pan,

School of Minerals Processing and Bioengineering, Central South University, Changsha 410083, Hunan, PR China

Keywords: Low Grade Hematite; Direct Reduction; Reduction Kinetics; Apparent Activation Energy

*Corresponding author: E-mail: springcsu@126.com

Abstract

In this paper, the reduction kinetics of low grade hematite ore was calculated. Mineralogy shows that the ROM (run of mine) ore is of low grade hematite ore type, assaying 27.2 wt% Fe_{total} and with main valuable minerals of hematite. The reduction kinetics shows that the reduction reaction rates of pellets with additive and without additive are all controlled by diffusion through the product layer. The calculated apparent activation energy of pellets with 12 wt% complex additive is 8.55 KJ/mol, dropping 62.23% compared to that of pellets without additive.

Introduction

With the rapid development of iron and steel industry in China, there has been a soaring demand for iron ores in the past decade. The imports of iron ores have increased from 148 million ton in 2003 to 620 million ton in 2010[1]. Therefore, large quantities of low grade iron resources are necessary to utilize in China at the moment. During the past years, extensive research has been carried out on the low grade hematite ores [2-6], such as reverse floatation, gravity separation, high-gradient magnetic separation and direct reduction-magnetic separation. Direct reduction-magnetic separation is an innovation way to treat the low grade hematite [7]. However, the research of reduction kinetics of low grade hematite is few. Some research about the reduction kinetics of reducing iron oxides by CO was studied [8]. The results indicated that the apparent activation energy is 8.0-28 KJ/mol when the reducing reaction is controlled by internal diffusion. The apparent activation energy is 50-75_KJ/mol when the reducing reaction is controlled by chemical reaction. In this paper, the reduction kinetics of pellets was also been studied.

Experimental Procedure

Raw Materials

The ROM superfine low grade iron ore samples were provided by Lianyuan steel company, Hunan Province, China. Chemical compositions analysis (Table I) indicates that the iron content of ROM ore is only 27.2wt%_Fe.

The complex additive is the off-white power containing some calcium, and is produced according to the invention patent held by Central South University [9].

Table I. Chemical Composition of ROM Iron Ore Sample (mass %)

Element	TFe	FeO	SiO_2	Al_2O_3	CaO	MgO	Na_2O	P	S	LOI
Content	27.23	2.91	49.51	3.72	1.45	1.34	0.13	0.063	0.025	3.97

Experimental Procedure

The experimental procedure includes pelletizing and direct reduction of pellets by standard gas.

Pellets were made from the mix of low grade hematite and bentonite, or mix of low grade hematite and 12% complex additive in a disc Pelletier of 0.8 m in diameter and 0.2 m rim depth, using rotational speed at 38 rpm and inclined at 47° to the horizontal. The green pellets were transferred into the oven to dry at 105°C for 2 h.

The direct reduction was done in the shaft furnace, controlled automatically. The reduction gas containing 30%_CO and 70%_N_2 was used in this study, and the flow rate is 1.5_L/min. When reduction was over, N_2 was used cooling to the room temperature.
Study included examination of reduction kinetics of pellets without additive and with 12% complex additive. In this study, the un-reaction core model of for reduction reaction was chosen to calculate the related parameters. If the reduction reaction is controlled by chemical reaction on surface of un-reacted core, $1-(1-f)^{1/3}$ is linear with t (min). If the reduction reaction is controlled by diffusion through the product layer, the relation between $1+2(1-f)-3(1-f)^{2/3}$ and t (min) is linear.

The *RI* (reduction index) equation is as follows:

$$RI = \left[\frac{0.11W_1}{0.43W_2} + \frac{m_0 - m_t}{m_0 \times 0.43W_2} \times 100 \right] \times 100\% \quad (1)$$

$$f = RI/100 \quad (2)$$

Where, RI is reduction index, wt%; m_0 is the weight of pellets before reduction (g); m_t is the weight of reduced pellets reduction for some time (g); W_1 is the FeO content of pellets before reduction (wt %); W_2 is the Fe_{total} content of pellets before reduction (wt %); f is reacted fraction of reduction.

Results and Discussions

From Fig.1 and 2, the reduction index increases markedly when exceed reduction time from 0 to 40 min, and then keeps augment when continue to prolong reduction time. On the other hand, reduction temperature also can improve the reduction index. The higher temperature is elevated, the higher reduction index is obtained. The reduction index of pellets with complex additive is superior to this of pellets without additive under the same conditions.

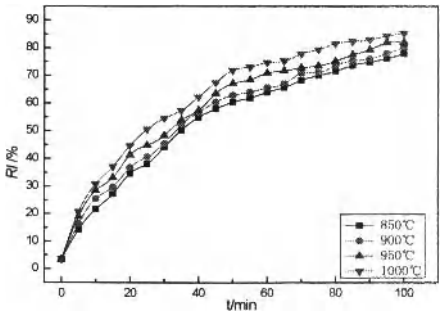

Figure1. Isothermal Reduction Curves of RI vs. t When Reducing Pellets without Additive

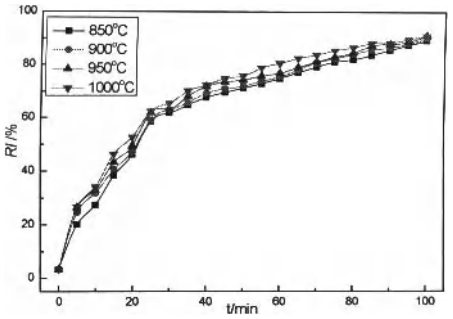

Figure2. Isothermal Reduction Curves of *RI* vs. t When Reducing Pellets with Additive

According to the experimental data from Fig.1 and Fig.2, plots of $1-(1-f)^{1/3}$ vs. t and $1+2(1-f)-3(1-f)^{2/3}$ vs. t are depicted, and $1+2(1-f)-3(1-f)^{2/3}$ vs. t possesses the excellent linear relation (Fig.3 and Fig.4). Therefore, the reduction reactions of pellets without additive and with complex additive are controlled by diffusion through the product layer.

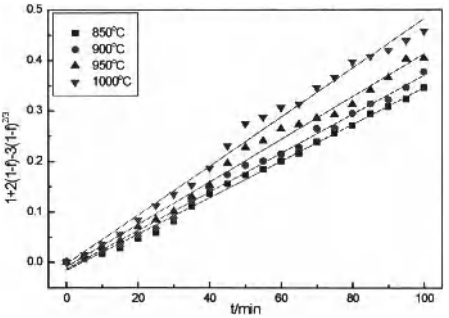

Figure3. Line of $1+2(1-f)-3(1-f)^{2/3}$ vs. t When Reducing Pellets without Additive at 850°C to 1000°C

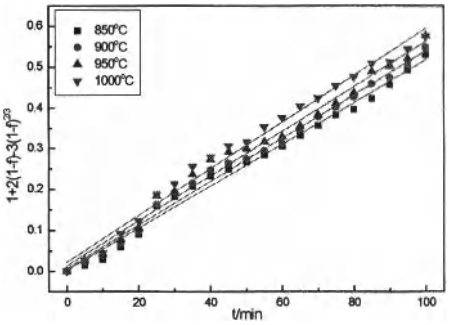

Figure4. Line of $1+2(1-f)-3(1-f)^{2/3}$ vs. t When Reducing Pellets with Additive at 850 ℃ to 1000℃

Using the results in Figure 3 and Figure 4, the reduction rate constant k (slop of line) at different temperatures were achieved and are shown in Tables 2 and 3. In order to calculate the apparent activation energy, the plot of $\ln k$ vs. 1/T should be as straight line with a slop of $-E/R$ and the intercept of $\ln k_0$, according to Arrhenius equation:

$$\ln k = \ln k_0 - \frac{E}{RT} \tag{3}$$

Where, k is reduction rate constants; E is the activation reduction energy (J/mol); R is the constant of 8.314 J/ (mol·K); T is the temperature (K);

Table II. The Reduction Rate Constant k (slop of line) at Different Temperatures (without additive)

Temperature/℃	850	900	950	1000
k / ($\times 10^{-3}$)	3.62	3.84	4.22	4.86
$\ln k$	-5.62	-5.56	-5.47	-5.33
R^2	0.995	0.994	0.990	0.990

*Footnote: R^2 is linear coefficient

Table III. The Reduction Rate Constant k (slop of line) at Different Temperatures (with additive)

Temperature/℃	850	900	950	1000
k / ($\times 10^{-3}$)	5.13	5.33	5.49	5.72
$\ln k$	-5.27	-5.23	-5.20	-5.16
R^2	0.989	0.991	0.986	0.986

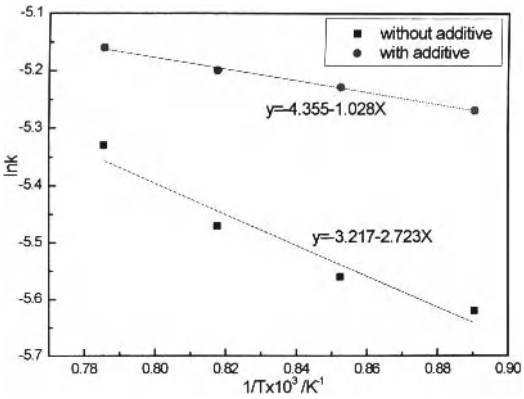

Figure5. Line of Arrhenius on $\ln k$ against 1/T for the Reduction of Pellets without Additive and with Additive

Using equation (3) and results from Tables II and III, the linear fittings between $\ln k$ and 1/T were calculated and are shown in Figure 5. The slops of the lines are –E/R and the apparent activation energy of pellets without additive and with complex additive are calculated as 22.64KJ/mol and 8.55 KJ/mol, respectively. The apparent activation energy of pellets with additive drops 62.23% compared to those of pellets without additive. Therefore, the reduction reaction of two types pellets are controlled by internal diffusion, which are consistent with the excellent linear relation between $1+2(1-f)-3(1-f)^{2/3}$ and t.

Conclusions

Reducing reaction kinetics analysis of pellets indicates that the reaction rates of pellets without additive and with 12wt% complex additive are controlled by diffusion through the product layer. The activation energy of two types pellets are22.64 KJ/mol and 8.55KJ/mol, respectively.

References

1. China iron & steel association, *http://www.chinaisa.org.cn/*, 2011.
2. Zhu, D Q and Zhai, Y, "Beneficiation of super micro-fine low-grade hematite ore by coal-based direct reduction-magnetic concentration process," *Journal of Central South University (Science and Technology)*, 3(12) (2008), 1132-1133.
3. Xu, B, Zhuang, J M and Bai, G H, "Study on coal-based direct reduction process in utilizing the low-grade and hard-to-separate iron ores," *Multipurpose Utilization and Mineral Resources*, 7(6) (2001), 20-23.
4. Sun, B Q, "Progress in China's beneficiation technology for complex refractory iron

ores," *Metal Mine*, 2(3) (2006), 11-13.
5. Yuan, Z T, Han, Y X and Li, Y J, "Advancement and developing trend of iron ore concentrating," *Non-ferrous Mining and Metallurgy*, 22(5) (2006), 10-13.
6. Paclovic, S and Brandao, P R G, "Adsorption of starch, amylase, amylopectin and glucose monomer and their effect on the flotation of hematite and quartz," *Minerals Engineering*, 16(2003), 1117-1122.
7. Zhu, D Q, Xiao, Y Z, Chun, T J and Pan, J, "An innovative process on beneficiation of superfine low grade hematite ore" 2nd International Symposium on High-Temperature Metallurgical Processing, TMS ,2(2011),309-318.
8. Liu, J H and Zhang, J Y, "Assessment of apparent activation energies for reducing iron oxides by CO and CO-H2" *Journal of Iron and Steel Research*, 12(2000), 5-9.
9. Zhu, D Q, Jian, P, Li, Q H, Chun, T J, et al, *China Patent*, Patent number: 200910311021. 4.

3rd International Symposium on High-Temperature Metallurgical Processing
Edited by: Tao Jiang, Jiann-Yang Hwang, Patrick Masset, Onuralp Yucel, Rafael Padilla, and Guifeng Zhou
TMS (The Minerals, Metals & Materials Society), 2012

VISCOSITY EVOLUTION OF BLAST FURNACE SLAG BEARING TITANIUM

Hua Wang, Guibao Qiu, Qingyu Deng, Shiwei Ma

College of Materials Science & Engineering, Chongqing University, Chongqing 400044, China
E-mails: whsmiling@cqu.edu.cn. qiuguibao@cqu.edu.cn

Keywords: BF slag, Titanium, Viscosity

Abstract

The flow behavior of the blast furnace slag bearing titanium, like viscosity, play an importance role during the iron-making process with the vanadium-titanium magnetite, which is a very special minerals in Panzhihua, China. The dependency of the viscosity on the chemical composition like TiO_2, Al_2O_3, MgO, binary basicity (CaO/SiO_2), temperature, reaction time were studied. The experiments showed that the viscosity decreased with the increase of TiO_2, MgO content and binary basicity, and it increased with the increase of Al_2O_3 content and temperature. The viscosity showed a slight decrease within 60mins' reaction with graphite crucible, however, it increased rapidly afterwards with the formation of Ti(C, N).

Introduction

The ordinary iron ore has been an essential part of raw materials for vanadium-titanium magnetite smelting in Panzhihua to avoid a series of problems, such as slag thickening, adhesive bond of slag and hot metal, etc. The ratio of vanadium-titanium magnetite has been decreased gradually since 1970s, and has down to about 65% now. However, with the substantial appreciation of price of imported ordinary iron ore, Panzhihua Iron and Steel Group aims to increase the ratio of vanadium-titanium magnetite and decrease the dependence on ordinary iron ore in order to lower the cost of smelting process.

Thus, the flow behavior of the blast furnace slag bearing titanium would change and influence the iron-making process. So simulation research on the flow behavior of the blast furnace slag has great importance for improving the ratio of vanadium-titanium magnetite. In general, the viscosity of the blast furnace slag depends on chemical ingredients such as TiO_2, Al_2O_3, MgO, basicity, temperature, reaction time and atmosphere.

Experimental Methods

Materials and Apparatus

The chemical composition of the slag is shown in Table I . Slag 1# (6#, 11#, and 16#) represented the chemical compositions of the slag taken from Panzhihua iron works, including the main compositions (27.33%CaO, 24.54%SiO_2, 14.55%Al_2O_3, 8.43%MgO, and 22.65% TiO_2) and the minor compositions (0.36%V_2O_5, 1.12%FeO, 0.51%MnO, and 0.51% CaF_2). Single factor method was used in the experiment and the chemical composition was altered on the base of slag 1#. Other slags were obtained by adding pure chemical reagents to the basic slag.

Table II . Chemical Composition of Slag (wt %)

Slag#	CaO	SiO_2	MgO	Al_2O_3	TiO_2	R(CaO/SiO_2)
1	27.33	24.54	8.43	14.55	**22.65**	1.11
2	26.80	24.06	8.43	14.55	**23.65**	1.11
3	26.27	23.59	8.43	14.55	**24.65**	1.11
4	25.75	23.12	8.43	14.55	**25.65**	1.11
5	25.22	22.65	8.43	14.55	**26.65**	1.11
6	27.33	24.54	**8.43**	14.55	22.65	1.11
7	26.80	24.06	**9.43**	14.55	22.65	1.11
8	26.27	23.59	**10.43**	14.55	22.65	1.11
9	25.75	23.12	**11.43**	14.55	22.65	1.11
10	25.22	22.65	**12.43**	14.55	22.65	1.11
11	27.33	24.54	8.43	**14.55**	22.65	1.11
12	26.80	24.06	8.43	**15.55**	22.65	1.11
13	26.27	23.59	8.43	**16.55**	22.65	1.11
14	25.75	23.12	8.43	**17.55**	22.65	1.11
15	25.22	22.65	8.43	**18.55**	22.65	1.11
16	27.33	24.54	8.43	14.55	22.65	**1.11**
17	27.56	24.31	8.43	14.55	22.65	**1.13**
18	27.79	24.09	8.43	14.55	22.65	**1.15**
19	28.01	23.87	8.43	14.55	22.65	**1.17**
20	28.23	23.65	8.43	14.55	22.65	**1.19**

Slag viscosity was measured by rotating cylinder method using a rotatory viscosimeter operating under N_2 atmosphere. The schematic diagram of rotatory viscosimeter is shown in Figure 1. The viscosimeter was regularly calibrated before the experiment using a series of standard silicon oils of known viscosities. About 300g of single sample was used in the viscosity measurement to ensure at least 45mm deep of the slag bath so that the molybdenum spindle was thoroughly submerged.

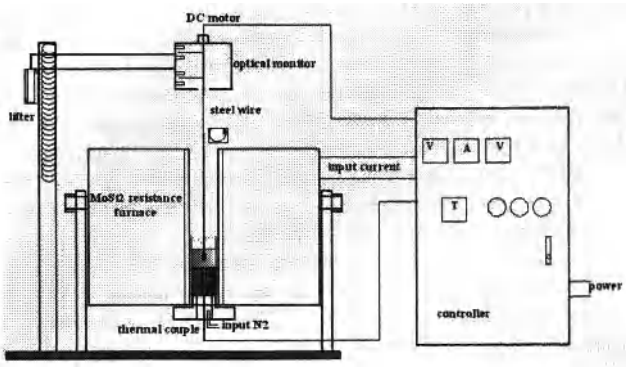

Figure 1. Schematic Diagram of Rotatory Viscosimeter

Procedure

The viscosity of slag 1-20# was detected in the corundum crucible to invest the effects of chemical composition on viscosity evolution. For example, Slag1-5# aims to invest the effect of TiO_2 content while keeping the proportion of other components constant. Slag11-15#, Slag6-10#, Slag16-20# focused on the effect of Al_2O_3 content, MgO content, basicity (CaO/ SiO_2), respectively while the TiO_2 content was kept as the same as the basic slag. The viscosity measurement was executed at 1450℃ when the slag was completely molten and thoroughly mixed. In consideration of the possibility of gradual reduction of titania to titanium protoxide and the concomitant influence on slag viscosity, hot preservation of the basic slag for about 240mins was carried out and the viscosity was measured every 30mins in the graphite crucible, which acted as reductant.

Results and Discussion

The experimental results are presented and discussed below in terms of the effects of chemical composition and reaction time on viscosity evolution of blast furnace slag bearing titanium.

Effect of TiO_2 Content on Slag Viscosity

The effect of TiO_2 content on slag viscosity was investigated through Slag1-5#, with TiO_2 content varying from 22.65% to 26.65% while the proportions of all other components remained constant. The results are shown in Figure 2.

Slag viscosity decreased with the increase of TiO_2 content. As TiO_2 belongs to a weakly acidic oxide, the electrostatic potential of Ti^{4+} is intermediate between that of Si^{4+} and Ca^{2+}, thus TiO_2 in the slag neither exists in the form of metallic cation as CaO, nor has a strong tendency to constitute complex anion as SiO_2. According to earlier research[1], in SiO_2-TiO_2 binary slag system, TiO_2 inclines to form $[TiO_6]^{8-}$ octahedral structure when the content of TiO_2 is more than 15wt% and increases, and eventrually totally $[TiO_6]^{8-}$ octahedral structure in the range of more than 49wt% TiO_2. In this paper, the TiO_2/ ($TiO2+SiO_2$) ratio is about 48wt%, accordingly TiO_2 mainly forms $[TiO_6]^{8-}$, which dispersedly embeds in and breaks up the network of silica composite anion $Si_xO_y^{z-}$. As a result, the size of viscous flow unit in the slag becomes smaller and thus improving the rheological properties of the slag.

Correlate Figure 2 with Figure 6, it could be seen that when TiO_2 content was raised from 22.65% to 26.65% by 4%, the slag viscosity decreased slightly before reduction, and significantly the viscosity of slag containing 26.65% TiO_2 after 4hours' reduction only increased by 0.2Pa.S to about 0.45Pa.S, which remain normal and would not deteriorate the blast furnace process.

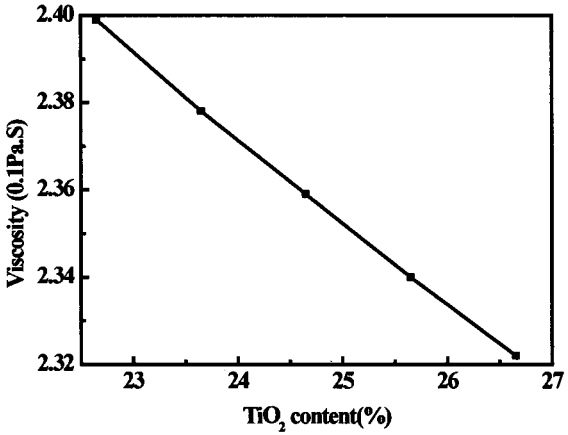

Figure 2. Slag Viscosity as a Function of TiO_2 Content(1450℃)

Effect of Basicity on Slag Viscosity

The effect of binary basicity (CaO/SiO_2) on slag viscosity was investigated through Slag16-20#.

The results are shown in Figure 3.

Slag viscosity decreased with the increase of binary basicity in the range of 1.11 to 1.19. Among all components acting as network modifiers, the effect of CaO is most significant, because of its strong ionization tendency. In the range of basicity in this paper, the increase of basicity benefits slag thinning. It is worth noting that the excessive increase of basicity will get the opposite effect owning to the precipitation and dispersion of calcium silicate in the slag.

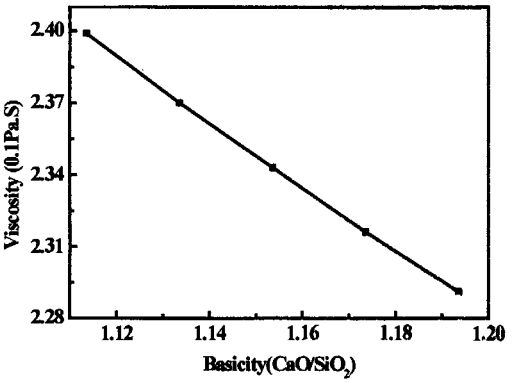

Figure 3. Effect of Binary Basicity (CaO/SiO_2) on Slag Viscosity(1450℃)

Effect of MgO Content on Slag Viscosity

The effect of MgO content on slag viscosity was investigated through Slag6-10#. The results are shown in Figure 4.

Slag viscosity decreased with the increase of MgO content from 8.43% to 12.43%. MgO can play the role of network modifier and destructuralizes $Si_xO_y^{z-}$. Moreover, MgO can react with other components (SiO_2, Al_2O_3, $2CaO.SiO_2$,etc.) to form a series of complex chemical compounds such as melilite $[(Ca,Mg)_3.(Si,Al)_2O_7]$, manganolite $[Ca_3MgSi_2O_8]$, monticellite $[CaMgSiO_4]$, in which the components are in eutectic state and thereby lower the melting point of the slag as well as the viscosity. From Figure 4, it is convinced that the MgO content in this paper is reasonable. The optimal MgO content might be greater, however, it must be controlled strictly to avoid the formation of spinel and periclase, which has a high melting point and precipitates in the slag, hence thickening the slag.

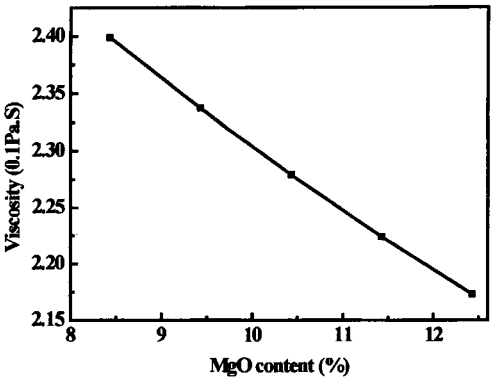

Figure 4. Effect of MgO Content on Slag Viscosity(1450℃)

Effect of Al_2O_3 Content on Slag Viscosity

The effect of Al_2O_3 content on slag viscosity was investigated through Slag11-15#. The results are shown in Figure 5.

Slag viscosity showed a linear increase when Al_2O_3 content increased from 14.55% to 18.55%. The fusion temperature of Al_2O_3 is as high as 2050℃, consequently with the increase of Al_2O_3 content in the slag, the free-running temperature of the slag raises and so does the viscosity of the slag at the same temperature. The experimental result in this paper is in line with iso-viscosities diagram of $CaO-SiO_2-Al_2O_3$ ternary system[2].

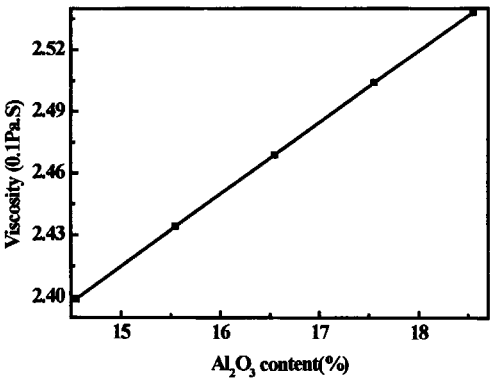

Figure 5. Effect of Al_2O_3 Content on Slag Viscosity(1450℃)

Effect of Reaction Time on Slag Viscosity

A series of experiments were conducted for slag 5# to investigate the rheological properties of the slag as a function of reaction time (continue for 4 hours and every other 30mins). The results are shown in Figure 6. It could be obtained from the oxygen potential figure[3] that TiO_2 in the slag is most likely to be reduced to Ti_2O_3 and TiO initially. According to the $\triangle G$-T formulas as follows:

$$TiO_2 + C\text{-}TiO + CO \quad \Delta G^{\ominus} = 312000 - 189.24T(J/mol) \quad (1)$$
$$\Delta G^{\ominus} = 0, \quad T = 1649K = 1376$$

$$2Ti_3O_5 + C\text{-}3Ti_2O_3 + CO \quad \Delta G^{\ominus} = 258509 - 170.03T(J/mol) \quad (2)$$
$$\Delta G^{\ominus} = 0, \quad T = 1520K = 1247$$

The generation of Ti_2O_3 and TiO start at the temperature of about 1247℃ and 1376℃, respectively. They are much lower than the experimental one, therefore it is rational to infer the formation of certain amount of Ti_2O_3 and TiO initially (<60mins), which play a part in thinning the slag[4]. Afterwards, titanium protoxides were further reduced to Ti(C,N), which highly dispersed in the slag, acted as a heterogeneous phase and caused fast thickening of the slag[5].

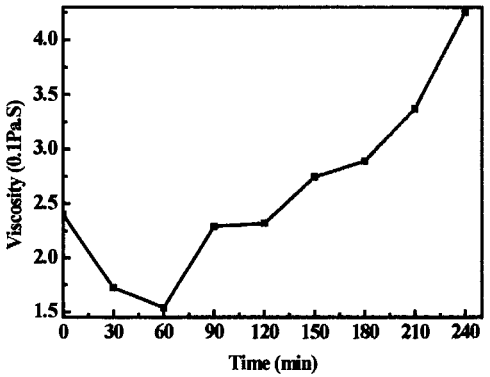

Figure 6. Viscosity Evolution of Slag5# as a Function of Reaction Time(1450℃)

Conclusions

The viscosity evolution of blast furnace slag bearing titanium with the change of chemical composition like TiO_2, Al_2O_3, MgO, binary basicity (CaO/SiO_2), temperature, reaction time were

studied. The results can be summarized as follows:

(1) The slag viscosity decreased slightly with the increase of TiO_2 content from 22.65% to 26.65% before reduction; and significantly the viscosity of slag containing 26.65% TiO_2 only increased by 0.2Pa.S to about 0.45Pa.S after 4hours' reduction, which remain normal and would not deteriorate the blast furnace process, so that it is promising to improve the ratio of vanadium-titanium magnetite in Panzhihua iron works.

(2) The increase of binary basicity and MgO content benefited slag thinning in the chemical composition range in this paper, however, the increment should be limited to avoid the production of compounds with high melting point thus getting opposite effect.

(3) The viscosity increased with the increase of Al_2O_3 content and temperature.

(4) The viscosity showed a slight decrease within 60mins' reaction with graphite crucible, however, it increased rapidly afterwards.

Acknowledgements

The study was financially supported by Key Project of Chinese National Programmes for Fundamental Research and Development (Grant No.51090383).

References

1. Shaoli Yang, Jifu Sheng, *Technology of Ilmenite Smelting for Production of Titanium-bearing Slag and Pig Iron* (Beijing, BJ: Metallurgical Industry Press, 2006), 221-222.

2. Xi H. Huang, *Ferrous Metallurgy Principle* (Beijing, BJ: Metallurgical Industry Press, 2008), 211-215.

3. Gui H. Du, *The Principle of Vanadium-titanium Magnetite Smelting in Blast Furnace Process* (Beijing, BJ: Science Press, 1996), 41-43.

4. Handfiel, et al., "Titanium Bearing Ore and Blast-Furnace Slag Viscosity," *Journal of Metals*, 24(9)1972, 37-42.

5. G.C. Bai, "Study on Some Physical Chemistry Problems of Blast Furnace Slag-Bearing Titania" (Ph.D. thesis, Chongqing University, 2003), 19-26.

3rd International Symposium on High-Temperature Metallurgical Processing

Basic Research of Metallurgical Process

Session Chairs:
Onuralp Yucel
Bing Xie

3rd International Symposium on High-Temperature Metallurgical Processing
Edited by: Tao Jiang, Jiann-Yang Hwang, Patrick Masset, Onuralp Yucel, Rafael Padilla, and Guifeng Zhou
TMS (The Minerals, Metals & Materials Society), 2012

THERMAL DECOMPOSITION AND REGENERATION OF WÜSTITE

Zhiwei Peng[1], Jiann-Yang Hwang[1], Zheng Zhang[1], Matthew Andriese[1], Xiaodi Huang[1],

[1]Department of Materials Science and Engineering, Michigan Technological University, Houghton, MI 49931, USA

Keywords: Kinetics, Thermal Decomposition, Non-isothermal Heating, X-ray Diffraction

Abstract

The thermal decomposition and regeneration behaviors of wüstite were investigated by *in situ* high temperature X-ray diffraction (HT-XRD) under non-isothermal condition at heating rate of 4 K min^{-1} in vacuum ranging from 294 K to 973 K. Wüstite on heating decomposes to magnetite and iron up to 823 K, above which it exhibits marked tendency to regenerate. Investigation of thermal stability of the reaction system shows that the decomposition proceeds under kinetic reaction control while the regeneration is under thermodynamic control. Kinetics study based on the Coats-Redfern integral approximation method indicates that the decomposition reaction follows a Komatsu-Uemura model-based diffusion-controlled kinetics with activation energy of 32.860 kJ mol^{-1}. The thermodynamics analysis of regeneration reaction demonstrates that wüstite regenerates at lower temperature than stoichiometric ferrous oxide.

Introduction

Owing to its importance in preparing various magnetic ceramic/metal nanocompostites or nanocrystals with high values of coercivity for the application as recording media, wüstite (non-stoichiometric ferrous oxide) has been attracting the attention of scientists over a long period [1-6]. The thermal behavior of wüstite was investigated by several researchers and phase transformations due to thermal decomposition and regeneration of wüstite during the heating in a specific temperature range was observed [7-9]. In spite of wüstite being found to dissociate to magnetite and iron at temperatures lower than 848 K and then regenerates at higher temperature, a clear understanding of the reaction mechanisms is clearly lacking [9].

The decomposition kinetics has not been studied yet mainly due to the characteristics of the product. It is well known that most of investigations for the decomposition kinetics of materials such as carbonates [10-12], selenites [13], permanganates [14], metal oxalates [15,16], etc. are based on the corresponding thermogravimetric measurements. In these studies, one product of the decomposition reactions is generally gas or vapor, resulting in the weight loss during the measurements where the decomposition degree (reaction fraction) of reactant can be determined. Since the products formed in the decomposition of wüstite are both solids, the conventional kinetic analysis relying on the weight change via thermogravimetry (TG) during the heating is not useful.

In order to understand the thermal decomposition process and the effect of solid products on the decomposition mechanism of wüstite, it is necessary to adopt an untraditional characterization technique. In this work, we propose to use *in situ* high temperature X-ray diffraction (HTXRD)

to determine the decomposition degree of wüstite, from which a suitable kinetic function for describing the decomposition reaction mechanism of wüstite was found using the Coats-Redfern method. Meanwhile, thermodynamics of the regeneration reaction of wüstite at high temperatures was analyzed based on the calculated kinetics data.

Experimental

Wüstite powder samples (99% purity) with particle size of 0.5-1.0 μm were supplied by Sigma Aldrich (USA). Due to non-stoichiometry characteristic of the sample, room temperature X-ray diffraction (RT-XRD) using a conventional Scintag XDS2000 powder X-ray diffractometer with a graphite monochromator and Cu Kα radiation was first employed to determine the lattice parameter. The specific molecular formula of the sample was then identified by comparing the datum obtained with that on the corresponding JCPDS card.

The phase transformations of the sample during the heating were characterized by high temperature X-ray diffraction (HT-XRD). The measurements were conducted in vacuum at given temperatures ranging from 294 K to 973 K using PANalytical X'Pert PRO X-ray diffractometer with Cu Kα radiation at constant heating rate of 4 K min^{-1}. The XRD pattern at each specified temperature was rapidly produced (<5 minutes). The phases presented in the patterns were identified and the decomposition degrees of wüstite at various temperatures were calculated through area integrations of the phase peaks using Origin 8.1 program.

Results and Discussion

The RT-XRD pattern of wüstite sample is shown in Figure 1. The main peaks were indexed with corresponding crystallographic planes and the lattice parameter was found to be 4.036 Å through the calculation using DMSNT software. The sample was identified as $Fe_{0.925}O$ (JCPDS card: 89-0686).

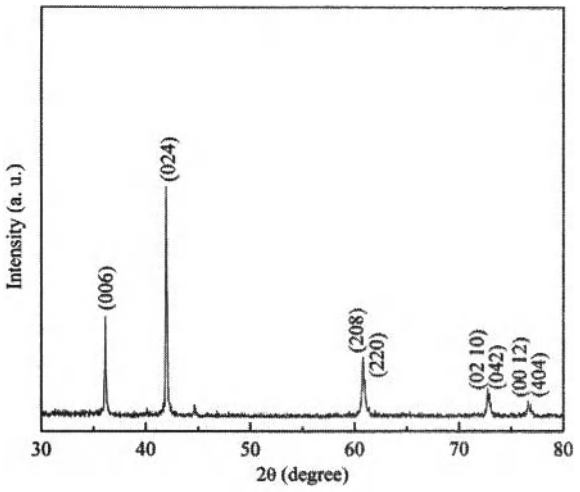

Figure 1. RT-XRD pattern of $Fe_{0.925}O$.

As mentioned before, HT-XRD was used to identify the phase transformations of wüstite in the temperature range of 294 K to 973 K. The XRD patterns are depicted in Figure 2. As shown by the patterns, $Fe_{0.925}O$ is found to be stable without apparent phase change below 573 K. At higher temperatures until 823 K, it is noticed that there is obvious thermal decomposition reaction. Wüstite decomposes to magnetite (Fe_3O_4) and iron (Fe) and the decomposition degree increases with temperature in this temperature range. The decomposition reaction can be described as follows:

$$4Fe_{0.925}O = 0.7Fe + Fe_3O_4 \quad (1)$$

At 873 K and above, it is shown that the peaks of the magnetite and iron disappear due to regeneration of wüstite, as indicated by the following reaction:

$$0.7Fe + Fe_3O_4 = 4Fe_{0.925}O \quad (2)$$

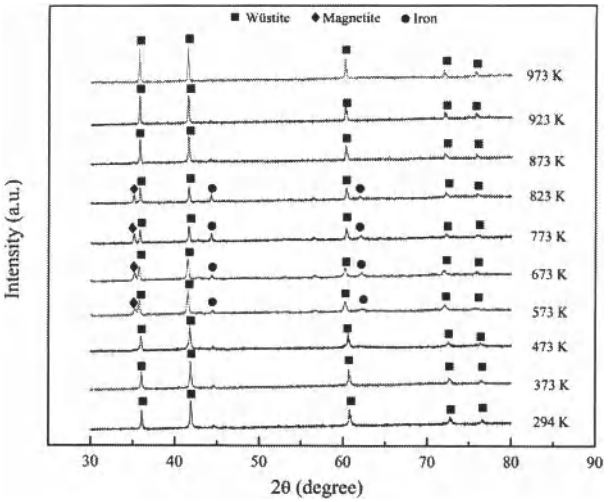

Figure 2. HT-XRD patterns of the sample at various temperatures.

The HT-XRD patterns clearly demonstrate that decomposition and regeneration of wüstite occur in the investigated temperature range. For understanding the basic mechanism of these transformations, it is of importance to study the reaction thermodynamics. Sufficient literature reviews indicate that the thermodynamic properties of $Fe_{0.925}O$ are unavailable. Owing to the similarity between the stoichiometric FeO and wüstite, the study of stoichiometric FeO based on the corresponding data may shed light on the mechanism of phase transformation of wüstite. This is started with the determination of standard Gibbs free energy changes (ΔG^0) for decomposition and regeneration of FeO.

The standard Gibbs free energy changes with temperature (T) for the reactions of formations of stoichiometric ferrous oxide (FeO) and magnetite (Fe_3O_4) are expressed as follows:

$$Fe + \frac{1}{2}O_2 = FeO \tag{3}$$

$$\Delta G^0 \backsimeq -263700 + 64.35T \qquad (298\,K \leq T \leq 1644\,K) \tag{4}$$

$$3Fe + 2O_2 = Fe_3O_4 \tag{5}$$

$$\Delta G^0 = -1102200 + 307.4T \qquad (298\,K \leq T \leq 1808\,K) \tag{6}$$

After several mathematical operations for Eq. (4) and Eq. (6), the relationship between temperature and the standard Gibbs free energy change for decomposition of FeO can be written as

$$4FeO = Fe_3O_4 + Fe \tag{7}$$

$$\Delta G^0 = -47400 + 50T \qquad (298\,K \leq T \leq 1644\,K) \tag{8}$$

The standard Gibbs free energy change for the regeneration of FeO is then given by

$$Fe_3O_4 + Fe = 4FeO \tag{9}$$

$$\Delta G^0 = 47400 - 50T \qquad (298\,K \leq T \leq 1644\,K) \tag{10}$$

The temperature dependences of standard Gibbs free energy change (ΔG^0) for the decomposition and regeneration of FeO are plotted in Figure 3.

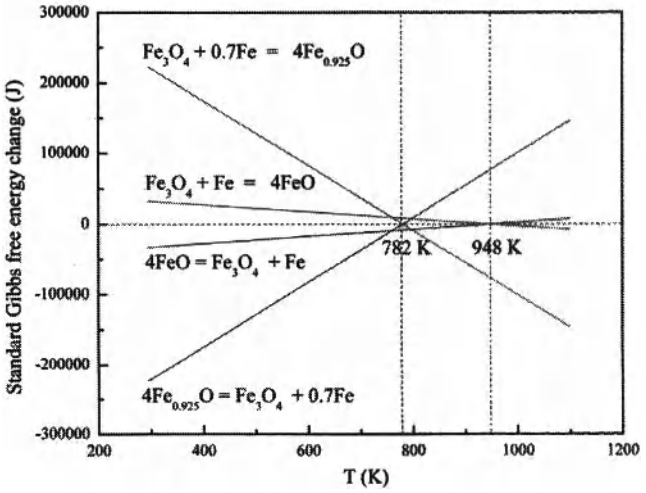

Figure 3. ΔG^0 for the decomposition and regeneration of FeO and $Fe_{0.925}O$.

As illustrated in Figure 3, at temperature lower than 948 K, the decomposition of FeO is possible although the tendency is not strong. However, it should be noted that the decomposition should decrease with increasing temperature. This is contradictory with the phenomenon observed in the HT-XRD patterns of wüstite. Thus, it may be sufficient to conclude that the decomposition of

wüstite proceeds under kinetic control instead of thermodynamic control. On the contrary, at temperature above 948 K, it is found that the tendency of regeneration of FeO increases with temperature. This can be used to account for the similar regeneration reaction of wüstite.

Kinetics of decomposition of wüstite

Since the decomposition of wüstite is assumed under kinetic control, the analysis of kinetic characteristics can be performed. Without weight loss in the reaction, the data of decomposition degree derived from traditional TG curve cannot be obtained. Instead, it is found that area integrations of peaks for the phases observed in the HT-XRD patterns may provide good approximation for the decomposition degree at each temperature. The decomposition degree is calculated by following equation:

$$\alpha = \frac{S_T}{S_{T_0}} \tag{11}$$

where S_T is the area of wüstite peak at given temperature and S_{T0} is the area of wüstite peak at room temperature (294 K). Figure 4 shows an example for the integration of the peak for wüstite corresponding to (024) plane at 294 K.

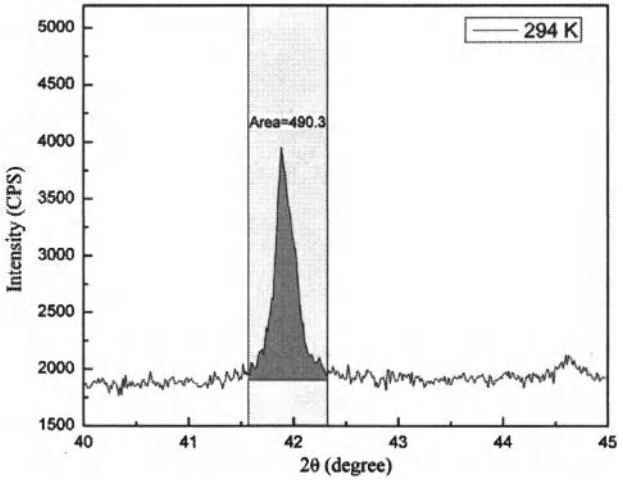

Figure 4. Integration of the peak corresponding to (024) plane.

The areas of other peaks at other temperatures could be determined through the same operation. The variation of decomposition degree for the whole temperature range covered is shown in Figure 5. The quite small values of decomposition degree lower than 573 K agree well with the observation from XRD patterns. The decomposition degree subsequently increases rapidly until 773 K and then the reaction rate slows down between 773 K and 823 K, as demonstrated by apparent weaker intensity of wüstite peaks with increasing temperature. In the last stage, it is shown that the decomposition degree drops down dramatically corresponding to the absence of the peaks of the magnetite and iron in the HT-XRD patterns.

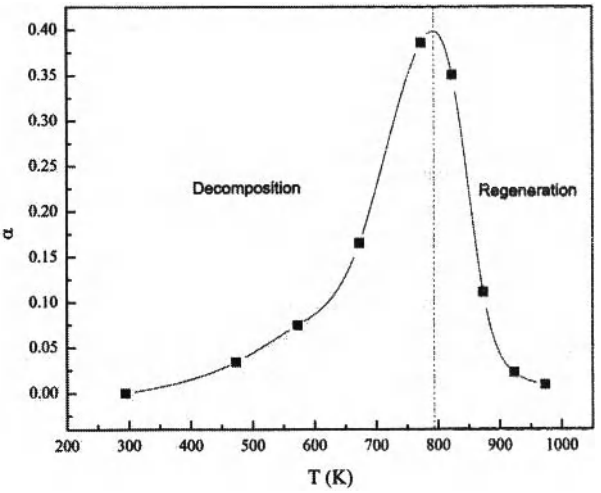

Figure 5. Variation of decomposition degree of $Fe_{0.925}O$ with temperature.

The decomposition kinetics can be determined by the Coats-Redfern relation:

$$\ln\frac{g(\alpha)}{T^2} = \ln\left(\frac{AR}{\beta E}\right) - \frac{E}{RT} \tag{12}$$

where $g(\alpha)$ is the kinetic function of decomposition degree α, A is the frequency factor (min^{-1}), E is the activation energy ($J\,mol^{-1}$), R is the gas constant (R=8.314 J mol^{-1} K^{-1}) and β is the ramp rate in the heating (K min^{-1}).

The kinetic function of $g(\alpha)$ is related to the algebraic expression of function $f(\alpha)$, depending on different reaction mechanisms. The general formula for $f(\alpha)$ is given as

$$f(\alpha) = \alpha^m(1-\alpha)^n[-ln(1-\alpha)]^p \quad (13)$$

where m, n and p are the empirical exponent factors and one of them is always zero.

As indicated by Eq. (12), a plot of $ln[g(\alpha)/T^2]$ against $1/T$ gives the best linear fit representing the most probable decomposition mechanism of the material. The activation energy (E) and frequency factor (A) can be derived from the slope and intercept of the straight line, respectively.

Analysis of the decomposition process of wüstite below 823 K shows the experimental data best delineate a straight line by using Komatsu-Uemura (anti-Jander) equation based on diffusion-controlled mechanism (Correlation coefficient R^2=0.984). Corresponding kinetic function of $g(\alpha)$ can be formulated as:

$$g(\alpha) = \frac{3}{2}\left[(1+\alpha)^{\frac{1}{3}} - 1\right]^2 \quad (14)$$

The activation energy (E) and frequency factor (A) are found to be 32.860 kJ mol^{-1} and 0.0594 min^{-1}, respectively.

Thermodynamics of regeneration of wüstite

As shown in Figure 5, the decomposition degree decreases rapidly with increasing temperature, indicating a rapid achievement of reaction equilibrium. Under this assumption, at temperature above 823 K, the temperature dependence of ΔG^0 for the reaction was calculated using the equilibrium constant k dependent on the decomposition degree α:

$$k = \frac{(1-\alpha)^4}{\left(\frac{0.7\alpha}{4}\right)^{0.7}\left(\frac{\alpha}{4}\right)} \quad (15)$$

The standard Gibbs free energy change can thus be calculated by:

$$\Delta G^0 = -RT\ln k \quad (16)$$

The linear fit (correlation coefficient R^2=0.9924) shows the temperature dependence of the standard Gibbs free energy change for the regeneration reaction of $Fe_{0.925}O$:

$$\Delta G^0 = 358598 - 459.35T \quad (17)$$

The above equation indicates that the wüstite starts to regenerate at around 782 K, as shown in Figure 3. This temperature is much lower than that for regeneration reaction of stoichiometric ferrous oxide (FeO).

With known ΔG^0 for the regeneration reaction, the standard Gibbs free energy change of $Fe_{0.925}O$ ($\Delta G^0_{Fe0.925O}$) can be obtained using the following equations:

$$\Delta G^0 = 4\,\Delta G^0_{Fe_{0.925}O} - \Delta G^0_{Fe_3O_4} - 0.7\Delta G^0_{Fe} \tag{18}$$

$$\Delta G^0_{Fe_3O_4} = \Delta H^0_{Fe_3O_4} - T\Delta S^0_{Fe_3O_4} = \int_{298}^{T} C_{p,Fe_3O_4}dT - T\int_{298}^{T}\frac{C_{p,Fe_3O_4}}{T}dT \tag{19}$$

$$\Delta G^0_{Fe} = \Delta H^0_{Fe} - T\Delta S^0_{Fe} = \int_{298}^{T} C_{p,Fe}dT - T\int_{298}^{T}\frac{C_{p,Fe}}{T}dT \tag{20}$$

$$C_{p,Fe_3O_4} = 104.2096 + 178.5108\times10^{-3}T + 10.6151\times10^{-6}T^2 + 1.132534 \times 10^{-9}T^3 \tag{21}$$

$$C_{p,Fe} = 37.12 + 6.17\times10^{-3}T \tag{22}$$

Therefore, the temperature dependence of standard free energy change of $Fe_{0.925}O$ in the regeneration reaction can be written as

$$\Delta G^0_{Fe_{0.925}O} = 144702.3 - 381.288T \tag{23}$$

Finally, it should be mentioned that above thermodynamics analysis is based on the measured kinetic data under the assumption of quick reaction equilibrium achievement. Verification of such assumption requires further work on accurate thermodynamics properties measurements.

Conclusions

The decomposition and regeneration reactions of wüstite in the temperature range of 294 K to 973 K were studied using *in situ* HT-XRD. It is shown that the decomposition proceeds under kinetic control with activation energy of 32.860 kJ mol^{-1}, following a Komatsu-Uemura model-based diffusion mechanism. The regeneration of wüstite succeeds then at much lower temperature than that for the same reaction of stoichiometric ferrous oxide.

Acknowledgements

This work was supported by the Michigan Public Service Commission, U.P. Steel, and the United States Department of Energy under Award No. DE-FC36-01ID14209.

References

[1] M. Yin, Z. Chen, B. Deegan, and S. O'Brien, "Wüstite Nanocrystals: Synthesis, Structure and Superlattice Formation," *J. Mater. Res.*, 22 (2007), 1987-1995.

[2] M. Gheisari, M. Mozaffari, M. Acet, and J. Amighian, "Preparation and Investigation of Magnetic Properties of Wüstite Nanoparticles," *J. Magn. Magn. Mater.*, 320 (2008), 2618-2621.

[3] M. Mozaffari, M. Gheisari, M. Niyaifar, and J. Amighian, "Magnetic Properties of Mechanochemically Prepared Iron–wüstite (Fe–Fe_yO) Nanocomposites," *J. Magn. Magn. Mater.*, 321 (2009), 2981-2984.

[4] L. Takacs, "Metal-metal Oxide Systems for Nanocomposite Formation by Reaction Milling," *Nanostruct. Mater.*, 2 (1993) 241-249.

[5] J. Ding, W. F. Miao, E. Pirault, R. Street, and P. G. McCormick, "Mechanical Alloying of Iron–hematite Powders," *J. Alloy. Compd.*, 267 (1998), 199-204.

[6] K. Tokumitsu and T. Nasu, "Preparation of Lamellar Structured α-Fe/Fe3O4 Complex Particle by Thermal Decomposition of Wüstite," *Scripta. Mater.*, 44 (2001), 1421-1424.

[7] B. Andersson and J. O. Sletnes, "Decomposition and Ordering in Fe1-xO," *Acta. Cryst.* A33 (1977), 268-276.

[8] L. Broussard, "The Disproportionation of Wustite," *J. Phys. Chem.*, 73 (1969), 1848-1954.

[9] Z. Peng, J. Y. Hwang, J. Mouris, R. Hutcheon, and X. Sun, "Microwave Absorption Characteristics of Conventionally Heated Nonstoichiometric Ferrous Oxide," *Metall. Mater. Trans. A*, 42 (2011), 2259-2263.

[10] L. Yue, M. Shui, and Z. Xu, "The Decomposition Kinetics of Nano-crystalline Calcite," *Thermochim. Acta*, 335 (1999), 121-126.

[11] D. Dollimore, P. Tong, and K. S. Alexander, "The Kinetic Interpretation of the Decomposition of Calcium Carbonate by Use of Relationships Other than the Arrhenius Equation," *Thermochim. Acta*, 282/283 (1996), 13-27.

[12] K. N. Ninan, K. Krishnan, and V. N. Krishnamurthy, "Kinetics and Mechanism of Thermal Decomposition of Insitu Generated Calcium Carbonate," *J. Therm. Anal.*, 37 (1991), 1533-1543.

[13] L. T. Vlaev, V. G. Georgieva, and G. G. Gospodinov, "Kinetics of Isothermal Decomposition of $ZnSeO_3$ and $CdSeO_3$," *J. Therm. Anal. Calorim.*, 79 (2005), 163-168.

[14] M. E. Brown, "The Prout-Tompkins Rate Equation in Solid-state Kinetics," *Thermochim. Acta*, 300 (1997) 93-106.

[15] T. Palanisamy, J. Gopalakrishnan, B. Viswanathan, V. Srinivasan, and M. V. C. Sastri, "Kinetics of Thermal Decomposition of Some Metal Oxalates," *Thermochim. Acta*, 2 (1971), 265-273.

[16] W. W. Wendlandt, T.D. George, and G. R. Horton, "The Thermal Decomposition of Thorium(IV), Uranium(IV), and the Rare-earth Metal(III) Oxalate Hydrates. Differential Thermal Analysis and Weight-loss Studies," *J. Inorg. Nucl. Chem.*, 17 (1961), 273-280.

3rd International Symposium on High-Temperature Metallurgical Processing
Edited by: Tao Jiang, Jiann-Yang Hwang, Patrick Masset, Onuralp Yucel, Rafael Padilla, and Guifeng Zhou
TMS (The Minerals, Metals & Materials Society), 2012

COMPETITIVE PRECIPITATION AND GROWTH OF SPINEL CRYSTALS IN VANADIUM SLAG

Xie Zhang, Bing Xie, Jiang Diao, Xiaojun Li

College of Materials Science and Engineering, Chongqing University, Chongqing 400044, China

Keywords: competitive precipitation and growth, kinetics, spinel crystals, vanadium slag

Abstract

Vanadium is widely utilized as an important element to improve the quality of alloyed steels in iron and steel industry. Moreover, the crystallization process of V-containing spinels plays a significant role due to the aim of achieving a fairly larger size of spinel crystals in vanadium extraction. Thus, a comprehensive exploration and discussion on the competitive precipitation and growth of vanadium, chromium and titanium spinel crystals in vanadium slag during a cooling process were carried out in the present study on the basis of a crystallization kinetic model. To be more specific, the abilities of forming crystal, precipitation order and suitable temperature range for crystallization of the three kinds of spinels were discussed with both theoretical and experimental methods.

Introduction

Vanadium is an important element which is used almost exclusively in ferrous and non-ferrous alloys due to its excellent physical properties such as high tensile strength, hardness, and fatigue resistance [1]. Various kinds of processes of vanadium extraction from V-containing hot metal are available at present. However, only four processes which are the Highveld process (South Africa), the Pan-steel process (China), the NTMK duplex process (Russia) and the New Zealand steel process (New Zealand) take the dominant positions [2, 3]. Although the type of reactor and the initial vanadium content in hot metal are different in these techniques, they share the same principle that vanadium is oxidized by oxygen into vanadium slag.

The vanadium extraction process of Pan-steel in China is schematically illustrated in Figure 1. It is characterized by concentrating the vanadium to spinel phases in vanadium slag, then extracting vanadium oxide via salt roasting and leaching of slag. As an intermediate product, the quality of vanadium slag has a significant effect on the follow-up vanadium extraction process. Furthermore, the quality of vanadium slag is determined by the proportion and grain size of V-containing spinels to a large extent. To be specific, Chen and Yang [4] found that large spinel crystal size could promote vanadium oxidation rate as silicate phases would impede the oxidation of V-containing spinels by decreasing the exposing probability. Therefore, research on the competitive precipitation and growth of spinel crystals will beneficial for improving the quality of vanadium slag. Diao *et al.* [5, 6] reported the mineralogical characterization and growth of spinel crystals under different kinds of conditions by experiments. However, systematic and theoretical analyses on the competitive precipitation and growth of spinel crystals in vanadium slag are seldom reported. Thus, this work attempts to carry out a comprehensive exploration and discussion on the crystallization ability, the precipitation sequence and the optimum temperature range for crystallization of spinels in vanadium slag from the point view of kinetics, and give experimental verification to the calculated results in the meantime.

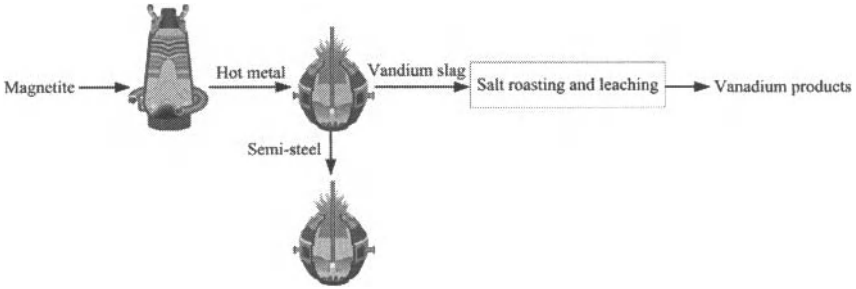

Figure 1. Vanadium extraction process of Pan-steel in China

Mathematical Model

It is widely accepted that the crystallization of spinels in vanadium slag can be mainly divided into two stages, i.e. nucleation and growth. According to the classic crystallization kinetic model reported by Turnbull [7-9], the nucleation rate can be expressed as:

$$I = DN_0 a^{-2} \exp[-\Delta G^* (kT)^{-1}] \quad (1)$$

where I is the nucleation rate per unit volume; D is the diffusion coefficient; T is the absolute temperature; k is the Boltzmann's constant; a is the lattice parameter of the crystal; N_0 is the number of molecules (or atoms) in per unit volume, i.e. $N_0 = 1/a^3$.

ΔG^* is the critical free energy change of nucleus formation and it can be expressed as

$$\Delta G^* = b \cdot \sigma^3 / \Delta G_V^2 \quad (2)$$

where b is a constant determined by the nucleus shape and for spherical nuclei, $b = 16\pi/3$; σ is the crystal-liquid interfacial tension and ΔG_V is the free energy change per unit volume associated with the crystallization.

The nucleation rate I can be expressed by equation (3) when combining equation (1) and equation (2)

$$I = DN_0 a^{-2} \exp[-b\sigma^3 (\Delta G_V^2 kT)^{-1}] \quad (3)$$

Where $\Delta G_V = \Delta H_m \Delta T / (V \cdot T_m)$, ΔH_m is the molar heat of fusion and V is the molar volume of the crystal; $\Delta T = T_m - T$, T_m is the melting point of the crystal and expressed in kevins.

Suppose T_r is the reduced temperature defined by $T_r = T/T_m$ and ΔT_r is defined by $\Delta T_r = \Delta T / T_m$, i.e. $\Delta T_r = 1 - T_r$; α is the reduced crystal-liquid interfacial tension defined by $\alpha = \sigma (V^2 N_A)^{1/3} / \Delta H_m$, where N_A is the Avogadro's constant; β is the reduced molar heat of fusion defined by $\beta = \Delta H_m / (R \cdot T_m)$ and R is the gas constant. Thus, a new expression form of I is obtained as equation (4) shows

$$I = DN_0 a^{-2} \exp[-b\alpha^3 \beta (\Delta T_r^2 T_r)^{-1}] \quad (4)$$

Take the Stokes-Einstein equation $D = kT/(3\pi a\eta)$, where η is the viscosity, into consideration, then the nucleation rate I can be given by

$$I = N_0 kT (3\pi a^3 \eta)^{-1} \exp[-b\alpha^3 \beta (\Delta T_r^2 T_r)^{-1}] \quad (5)$$

The growth rate U can be expressed as [10]

$$U = Dfa^{-1}[1 - \exp(-\Delta H_m \Delta T_r (RT)^{-1})] \quad (6)$$

where f is the fraction of acceptor sites in the crystal surface and $f = \begin{cases} 1 & \Delta H_m < 2RT_m \\ 0.2\Delta T_r & \Delta H_m > 4RT_m \end{cases}$.

Thus, U is obtained as

$$U = fkT(3\pi a^2\eta)^{-1}[1-\exp(-\beta\Delta T_r / T_r)] \quad (7)$$

Determination of Parameters

Typical industrial vanadium slag sample was obtained from Pan-steel in China and chemical composition of the slag sample which was analyzed by X-ray fluorescence spectroscopy (XRF) is given in Table I.

Table I. Chemical composition of the experimental slag sample, wt-%

FeO	V_2O_3	SiO_2	TiO_2	MnO	MgO	CaO	Cr_2O_3	Al_2O_3
34.7	12.3	18.4	12.5	8.2	4.1	2.8	3.4	2.6

The main phases of vanadium slag in Pan-steel which have been reported [11] are spinels and silicates. Diao *et al.* [5] confirmed this by X-ray diffraction (XRD) and Energy Dispersive X-ray Spectroscopy (EDS or EDX) analyses of vanadium slag samples from Pan-steel. The results showed that V, Ti and Cr are concentrated in the spinel phases and Ca, Si are concentrated in the silicate phases. Fe, Mn, Mg, Al and O are coexisted in both phases. That is to say, the spinel phases in vanadium slag includes $Fe_xV_{3-x}O_4$, Fe_2TiO_4, $FeCr_2O_4$ and $(Mg, Mn)_x(V, Cr, Ti, Al)_{3-x}O_4$. Nevertheless, since the concentration of Mg and Mn is fairly low to be compared with Fe, and the similarity of Fe-spinels and (Mg, Mn)-spinels is relatively high, only Fe-spinels are taken into consideration in the present study. Thus, the spinel crystals concerned about in this study are FeV_2O_4, $FeCr_2O_4$ and Fe_2TiO_4. Parameters of structure and melting point of these spinel crystals are given in Table II.

Table II. Parameters of structure and melting point of three kinds of spinel crystals

Spinel type	Structure type	Lattice parameter a, Å	Melting point, K
FeV_2O_4	face-centered cubic (FCC)	8.543 [12]	2023 [13]
$FeCr_2O_4$	face-centered cubic (FCC)	8.378 [14]	2273 [15]
Fe_2TiO_4	face-centered cubic (FCC)	8.509 [16]	1668 [17]

In the preceding model, a key parameter is viscosity of the vanadium slag which is studied. However, due to the high oxidability and high melting point of vanadium slag, viscosity of vanadium slag is hard to be measured. In the report of Turnbull [8], the viscosity is regarded as constant or illustrated by empirical equation for a specific system. Recently, some more empirical equations of slag viscosity are applied to model computation, yet the accuracy of viscosity value is still limited and some components of the slag are neglected. In this study, viscosity of vanadium slag is calculated by the National Physical Laboratory (NPL) model [18] in order to get a relatively precise result. The optical basicities of components of vanadium slag which are used for calculation in this work are from literatures [18, 19] and given in Table III.

Table III. Values of the optical basicities of components of vanadium slag

FeO	V_2O_3	SiO_2	TiO_2	MnO	MgO	CaO	Cr_2O_3	Al_2O_3
1.0	0.55	0.48	0.61	1.0	0.78	1.0	0.55	0.60

Experience indicates that the reduced molar heat of fusion β lies between 1 and 10 for most substances [8]. The reduced crystal-liquid interfacial tension α has been measured directly only in a few instances and there is no rigorous theory for predicting it. What's more, fundamental thermodynamic data of vanadium is so deficient and hard to be calculated or measured. Therefore, values of α and β are referenced from other reports [20, 21] which are already in

accordance with the experimental one, i.e., $\alpha = 1/3$ and $\beta = 1$. It is worth noting that although the three kinds of spinels which are taken into consideration are different materials and their properties related to the values of α and β are different, yet wide applications of the above-mentioned kinetic model have shown that for the crystallisation phases of similar type from metallurgical melts or slags, the values of α and β are nearly the same. Thus, it is reasonable to regard the values of α and β of the three kinds of spinels as the same when we have no rigorous theory for predicting them or effective method to measure them.

Experimental Verification

The sample from Pan-steel in China was applied to an experiment which was designed to give verification to the calculated results.

A 12 kW box type electric resistance furnace was employed as the experimental apparatus with a proportional integral differential (PID) controller. The industrial vanadium slag samples were milled to particles less than 0.1mm. A slag mixture of 50 g which was charged into an MgO crucible (inner diameter: 50 mm, height: 75 mm) was heated and melted in the furnace at 1673 K. After 30 minutes, the MgO crucible was quickly taken out from the furnace and cooled naturally in the air or cooled down to a predetermined temperature at a rate of 5 K min^{-1}, and then held it up for 30 min before taken out from the furnace. After being cooled down to room temperature, slag samples were polished by silicon carbide. Morphology of the vanadium slag was studied by scanning electron microscopy (SEM). Mean diameter of spinel crystals was measured in 10 different fields of view by image analysis software. Herein, mean diameter is the average length of diameters measured at 2 degree intervals and passing through object's centroid.

Results and Discussion

V-containing spinel phases are wrapped up by silicate phases [2] just as Figure 2 shows and a relatively thicker silicate phase shell would slow down the oxidation reaction rate during the roasting process remarkably. In other words, large grain size of spinels could increase the exposure probability of spinels from being wrapped by silicate phases under the same level of grinding. Meanwhile, the mean diffusion path from O_2 and sodium salt to spinel crystals will be shorter. Therefore, it is worthwhile to determine the crystallization ability, the precipitation order and the optimum temperature range which benefits the nucleation and growth of spinels in order to get a fairly larger size of spinel crystals.

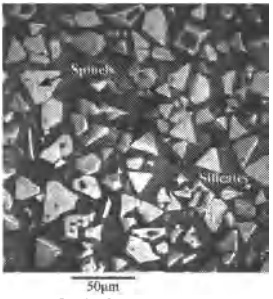

Figure 2. SEM image of spinel and silicate phases in vanadium slag

Based on the kinetic model illustrated above, nucleation rate and growth rate of these three kinds of spinels are calculated and shown in Figures 3-5. It can be seen that a peak comes into being in both the nucleation rate and the growth rate. Actually, this is reasonable because both

the nucleation rate and the growth rate are greatly influenced by two contradictory factors, i.e. the degree of supercooling and the diffusive mass transfer in vanadium slag. Moreover, the three kinds of spinel crystals show differences in both values of nucleation rate and growth rate and suitable temperature range. Particularly, both the nucleation rate and growth rate of $FeCr_2O_4$ spinels peak at a larger value and a higher temperature. FeV_2O_4 spinels take the intermediate place and Fe_2TiO_4 spinels show the least in values of both nucleation rate and growth rate, and the lowest in peak temperature.

Furthermore, crystallization ability of the three kinds of spinels can be deduced from Figures 3-5 as well. In detail, Wu and Chen [22] found that the ability of forming amorphous solid of a substance can be expressed by $(T_U - T_I)/T_I$ on the basis of the crystallization theory reported by Turnbull [8] and Uhlmann [10]. Where T_I and T_U are the peak temperature of nucleation rate I and growth rate U, respectively. In the work of Wu and Chen [22], a larger value of $(T_U - T_I)/T_I$ of a substance would indicate its better ability of forming amorphous solid. In other words, the spinel in vanadium slag with a smaller value of $(T_U - T_I)/T_I$ would precipitate more easily. Therefore, based on the calculated results which are shown in Figures 3-5, the crystallization abilities of the spinels in vanadium slag are achieved and given in Table IV.

Table IV. Crystallization abilities of the three kinds of spinels in vanadium slag

Spinel type	T_U, K	T_I, K	$(T_U - T_I)/T_I$
FeV_2O_4	1657	1209	0.3706
$FeCr_2O_4$	1830	1336	0.3698
Fe_2TiO_4	1403	1023	0.3715

It can be clearly seen from Table IV that differences among the values of $(T_U - T_I)/T_I$ of three kinds of spinels exist and the crystallization abilities of spinels in vanadium slag keep to the following order: $FeCr_2O_4$ > FeV_2O_4 > Fe_2TiO_4. Moreover, to be compared with the calculated results of Wu and Chen [22], the values of $(T_U - T_I)/T_I$ of three kinds of spinels are at a low level. That's to say, the crystallization abilities of the spinel phases are all relatively good and the spinel phases are easily to precipitate.

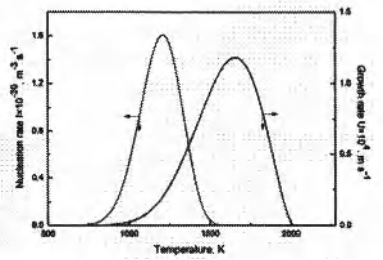

Figure 3. Nucleation rate and growth rate of FeV_2O_4 spinel crystals

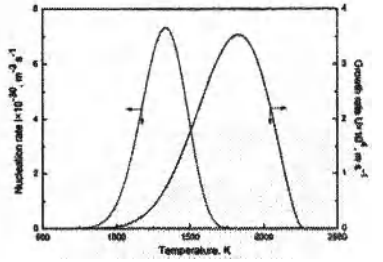

Figure 4. Nucleation rate and growth rate of $FeCr_2O_4$ spinel crystals

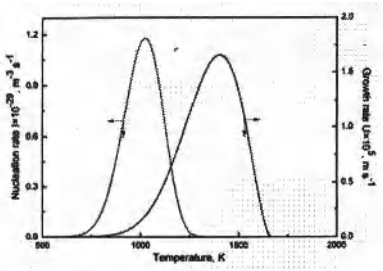

Figure 5. Nucleation rate and growth rate of Fe_2TiO_4 spinel crystals

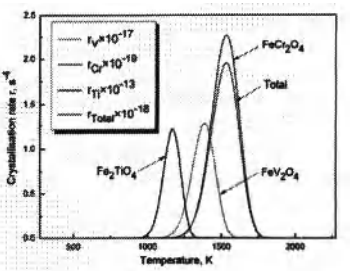

Figure 6. Crystallization rates of the three kinds of spinel crystals and the total

However, it is still difficult to give an accurate optimum temperature range for the spinel crystals by now. Therefore, it is quite necessary to make a combination of the nucleation rate and growth rate. Johnson and Mehl [23] derived the volume fraction φ of new phase as a function of nucleation rate I, growth rate U and time t. Specifically, φ is given by

$$\varphi = 1 - \exp(-\frac{\pi}{3} I U^3 t^4) \tag{8}$$

Herein, the crystallization rate r is defined as $r = 1/3\pi IU^3$ and the curves of crystallization rate r versus temperature are given in Figure 6. The total crystallization rate r_{Total} is defined by a function of the crystallization rates of the three kinds of spinel crystals. It is noteworthy that there is an assumption of V, Cr and Ti only existing in the three kinds of spinel crystals which have been discussed. Thus, the total crystallization rate r_{Total} is given by

$$r_{Total} = \sum_{i=1}^{3} w_i r_i \tag{9}$$

where w_i and r_i are the mass fraction and crystallization rate of the three kinds of spinel crystals respectively. The mass fraction of FeV_2O_4 spinel is 0.313 while those of $FeCr_2O_4$ and Fe_2TiO_4 are 0.086 and 0.601 respectively.

It can be seen from Figure 6 that the total crystallization rate is dominated by $FeCr_2O_4$ spinel crystals. In other words, the suitable temperature range for the crystallization of spinel crystals in vanadium slag is enhanced by the chromium spinels and thus, a lower content of chromium is preferred in order to contribute to the vanadium extraction.

More importantly, the precipitation sequence of the three kinds of spinels in vanadium slag can be deduced from Figure 6. Specifically, the precipitation of spinels in vanadium slag during cooling acts up to the sequence of $FeCr_2O_4 \rightarrow FeV_2O_4 \rightarrow Fe_2TiO_4$. It is noteworthy that both the crystallization abilities and precipitation order of spinels which are from model calculation are sufficiently supported by a fact that the central part of spinels is mainly consisted of Cr_2O_3, V_2O_3 and MgO while the outer part of spinels is mostly made of Ti_2O_3, Al_2O_3 and Fe_2O_3 [24].

A suitable heat treatment condition on vanadium slag can be proposed in order to get a better phase formation and a larger size of V-containing spinels since the precipitation order of spinels has obtained. Figure 7 shows the suitable heat treatment conditions on vanadium slag. θ represents the cooling rate and 1533 K, 1385 K and 1171 K are the temperature where the crystallization rates of the three kinds of spinels peak at, respectively. In this figure, θ_1 to θ_6 are the controlling parameters of a cooling process. As a larger size of V-containing spinels is preferred, θ_3 should be set at a relatively small value in order to provide the V-containing spinels

with enough time of nucleation and growth. In contrast, the precipitation of other phases is in favor of being restricted, i.e. $\theta_1 \sim \theta_6$ except θ_3 should be set at a large value, especially for θ_5 and θ_6. To be applied more simply in vanadium extraction industry, vanadium slag should be tapped from converter for several heats to give the spinels enough time to precipitate and grow. Furthermore, the vanadium slag can be water quenched at the temperature around 1100 ℃ (< 1385 K appropriately) in order to restrict the growth of silicate phases after being tapped from converter.

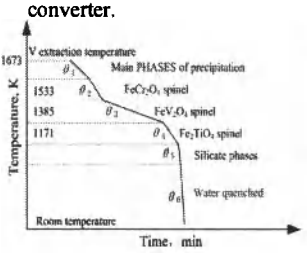

Figure 7. Suitable heat treatment condition on vanadium slag

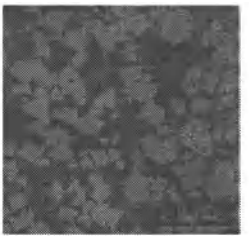

Figure 8. Representative SEM photomicrograph of vanadium slag sample

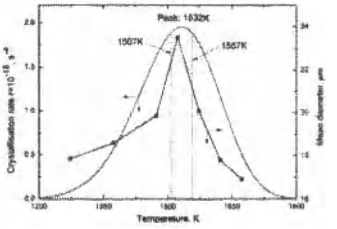

Figure 9. Crystallization rate and mean diameter of spinel crystals

Representative SEM photograph of vanadium slag which is used for the measurement of mean diameter of spinel crystals are shown in Figure 8. Furthermore, a comparison between the calculated results and experimental one is given in Figure 9. Specifically, a larger value in crystallization rate would be beneficial for achieving a larger mean diameter of spinel crystals. Based on this point, the optimum temperature range for a larger value in calculated crystallization rate and that for a larger mean diameter of spinel crystals in experiment should be accordant. Obviously, Figure 9 just demonstrates this point.

The peak temperature T_{peak} of total crystallization rate r_{Total} is shown in Figure 9 as 1532 K and the optimum temperature range for the crystallization of spinels is defined as $T_{peak} \pm 25K$, i.e. 1507-1557 K. It is notable that this temperature range is beneficial for the crystallization of the total spinels instead of V-containing spinels only. Actually, the optimum temperature for the V-containing spinels is slightly lower from the view of the calculated results.

Conclusions

The following conclusions can be drawn from the present work:

(1) Though the concentration of chromium in vanadium slag is relatively low, yet crystallization rate of the total spinels is greatly affected by the chromium spinels present.

(2) The crystallization abilities of spinels in vanadium slag are quantified with the index of $(T_U - T_l)/T_l$ and keep to the following order: $FeCr_2O_4 > FeV_2O_4 > Fe_2TiO_4$.

(3) The precipitation of spinels in vanadium slag during a cooling process acts up to the sequence of $FeCr_2O_4 \rightarrow FeV_2O_4 \rightarrow Fe_2TiO_4$ and a suitable heat treatment condition on vanadium slag is proposed.

(4) The optimum temperature range which benefits the nucleation and growth of spinel crystals is obtained as 1507-1557 K by both theoretical calculation and experiment.

Acknowledgements

The authors would like to express their thanks to the financial supports from National Natural Science Foundation of China (Grant No. 51090382).

References

[1] R. R. Moskalyk and A. M. Alfantazi, "Processing of vanadium: a review," *Minerals Engineering*, 16 (2003), 793-805.

[2] D. X. Huang, *Vanadium extraction and steelmaking*, (Beijing: Metallurgical Industry Press, 2000), 26.

[3] M. Lindvall: "Selective oxidation of vanadium prior to iron and phosphorus" (MSc thesis, Luleå University of Technology, 2006), 10-12.s

[4] D. H. Chen and S. D. Yang, "Systematic evaluation of the quality of vanadium slag," *Hebei Metallurgy*, 73 (1993), 19-23.

[5] J. Diao, et al., "Growth of spinel crystals in vanadium slag and their characterisation," *Crystal Research and Technology*, 44 (2009), 707-712.

[6] J. Diao, et al., "Mineralogical characterisation of vanadium slag under different treatment conditions," *Ironmaking and Steelmaking*, 36 (2009), 476-480.

[7] D. Turnbull, "Formation of crystal nuclei in liquid metals," *Journal of Applied Physics*, 21 (1950), 1022-1028.

[8] D. Turnbull, "Under what conditions can a glass be formed?," *Contemporary Physics*, 10 (1969), 473-488.

[9] J. C. Fisher, et al., "Rate of Nucleation of Solid Particles in a Subcooled Liquid," *Science*, 109 (1949), 168-169.

[10] D. R. Uhlmann, "A kinetic treatment of glass formation," *Journal of Non-Crystalline Solids*, 7 (1972), 337-348.

[11] J. Z. Zhou and X. P. Chen, *Vanadium resource exploitation 40 years in Panzhihua*, (Panzhihua: Panzhihua Iron and Steel Corporation, 2005).

[12] R. B., et al., "Zur Kristallchemie der Vanadin(III)-Spinelle," *Zeitschrift fuer Anorganische und Allgemeine Chemie*, 369 (1969), 306-312.

[13] S. M. Liao and T. L. Bo, *Vanadium Metallurgical Abroad*, (Beijing: Metallurgical Industry Press, 1985), 102.

[14] S. G. and C. D. E., "Magnetic structures in $FeCr_2S_4$ and $FeCr_2O_4$," *Journal of Applied Physics*, 35 (1964), 954-955.

[15] I.Barin, *Thermochemical Data of Pure Substances*, (Weinheim: VCH, 1989).

[16] M. B., et al., "The influence of crystal structure on the photoresponse of iron-titanium oxide electrodes," *Journal of Applied Crystallography*, 11 (1978), 121-124.

[17] G. Eriksson and A. Pelton, "Critical evaluation and optimization of the thermodynamic properties and phase diagrams of the $MnO-TiO_2$, $MgO-TiO_2$, $FeO-TiO_2$, $Ti_2O_3-TiO_2$, Na_2O-TiO_2, and K_2O-TiO_2 systems," *Metallurgical and Materials Transactions B*, 24 (1993), 795-805.

[18] K. C. Mills and S. Sridhar, "Viscosity of ironmaking and steelmaking slags," *Ironmaking and Steelmaking*, 26 (1999), 262-268.

[19] E. Bordes-Richard, "Multicomponent oxides in selective oxidation of alkanes theoretical acidity versus selectivity," *Top Catal*, 50 (2008), 82-89.

[20] B. Li and Z. T. Sui, "Glass crystallization kinetics of $CaO-MgO-Fe_2O_3-Al_2O_3-SiO_2$ slags," *Chinese Journal of Materials Research*, 13 (1999), 412-415.

[21] P. X. Zhang, et al., "Study on crystallization kinetics of component containing boron in $MgO-B_2O_3-SiO_2-Al_2O_3-CaO$ slag," *Chinese Journal of Materials Research*, 9 (1995), 66-70.

[22] W. Jinhua, et al., "A new method to estimate the ability of forming amorphous solids," *physica status solidi (a)*, 101 (1987), K1-K3.

[23] W. A. Johnson and P. A. Mehl, "Reaction kinetics in processes of nucleation and growth," *Transaction of American Institute of Mining, Metallurgical, and Petroleum Engineers*, 135 (1939), 416-441.

[24] H. A. ВаroЛИН, *Bainite in steels*, (Beijing: Metallurgical Industry Press, 1982), 2.

3rd International Symposium on High-Temperature Metallurgical Processing
Edited by: Tao Jiang, Jiann-Yang Hwang, Patrick Masset, Onuralp Yucel, Rafael Padilla, and Guifeng Zhou
TMS (The Minerals, Metals & Materials Society), 2012

EXPERT SYSTEM FOR GRATE-KILN PELLET PRODUCTION BASED ON MATHEMATICAL MODELS OF TEMPERATURE FIELD

Xiaohui Fan, Yi Wang, Xuling Chen

Central South University; No.932 South Yuelu Road; Changsha, Hunan, 410083, P.R. China

Keywords: Pellet, Grate-kiln, Expert system, Mathematical model, Temperature field.

Abstract

The current control method of grate-kiln iron ore oxide pellet production is lack of accuracy and normalization due to the limited detection conditions. Therefore, mathematical models of grate-kiln temperature field are presented. With calculation of gas-particle heat transfer as well as enthalpy changes of moisture evaporation and magnetite oxidation, the thermal history of pellets throughout grate-kiln process can be acquired and used for production status estimation. Taking the calculated results as well as detected data in production as inputs, process parameters such as running speed, fan opening and coal injection rate as adjusting objects, expert system for grate-kiln pellet production is outlined. And the preheating section dominated control strategy is explained. Results of production application show that the stability rate of gas temperature in gas hood of preheating section is increased from 91.0% to 94.2%, compressive strength and first grade rate of pellet are increased by 3.62% and 2.36%, respectively, while FeO content is 18.18% lower. Control guidance of this expert system can solve production anomalies effectively, stabilize grate-kiln iron ore oxide pellet production and improve pellet quality.

Introduction

Steel industry in China has developed rapidly in recent years. China's crude steel production in 2010 is nearly 627 million, which is 44.2% of the world total production. Burden with higher quality is demanded by enlargement and modernization of blast furnaces. And oxide pellet production has become a growing concern. In 2010, the total production of pellet in China is 110 million, and about 60% is produced by grate-kiln process.

However, after decades of practice, grate-kiln pellet production control in China is still semi-empirical & semi-instrumental, which is lack of accuracy and normalization. One of the reasons affecting the improvement of grate-kiln pellet production control is the dependence on empirical knowledge, while expert system is an effective solution for the problems caused by difference in experience level and operational habit, as well as device complexity. Another reason is the difficulty in detecting some crucial parameters, such as grate-kiln temperature field, due to the limited detection conditions. Mathematical model can make up the deficiencies of existing detection techniques and provide expert system for grate-kiln pellet production with easy access to a wealth of real time production information.

Mathematical models of grate-kiln pellet induration process have been put forward since 1960s. Models for grate process are based on the basic principles of heat transfer, and distinguished by the physical-chemical reactions taken into account [1, 2]. For kiln, plenty of models have been established based on different assumptions and analytical methods, including one-dimensional axial model [3], corss-section model [4], quasi-three-dimensional model [5], flame zone model [6], etc. However, applications of these models are basically limited to parameter adjustment during pellet plant design and system evaluation after putting into use, due to hard captured input data, difficulties in early computer programming and unsatisfied solutions.

This study is focused on control of grate-kiln pellet production. Mathematical models of grate-kiln temperature field are presented which lay the data foundation for the subsequently discussed expert system. Control strategy and search strategy of expert system for grate-kiln pellet production is outlined in succession. Control accuracy and normalization of grate-kiln pellet production are improved.

Mathematical Models of Grate-Kiln Temperature Field

Mathematical Model of Grate Temperature Field

Gas is blown vertically through the pellet bed on grate. Various of physical-chemical reactions take place during grate process, including water evaporation, condensation, oxidation of magnetite, as well as carbonates decomposition, carbon combustion, etc. according to the specific process. Considering a heat transfer unit of pellet bed, under steady state, the energy balance equations of solid phase and gas phase are as follow:

$$\rho_s(1-\varepsilon)C_p\frac{\partial T_p}{\partial t}(x,t)=hA[T_g(x,t)-T_p(x,t)]+Q_1(x,t)+Q_2(x,t)+q_2(x,t)-q_1(x,t) \quad (1)$$

$$M_gC_g\frac{\partial T_g}{\partial x}(x,t)=hA[T_p(x,t)-T_g(x,t)](1-a)+q_2(x,t) \quad (2)$$

Mathematical model of kiln temperature field

Inside of the rotary kiln, heat is released by fuel combustion and chemical reactions of pellets, transferred among pellets, gas flow and kiln wall by conduction, convection and radiation. Considering a radial slice of length dz at any position along the kiln axis, energy balance equations for pellets, gas flow and kiln wall are as follow:

$$M_{kp}C_p\frac{dT_p}{dz}=h_{g-ep}A_{g-ep}(T_g-T_p)+h_{cw-cp}A_{cw-cp}(T_w-T_p)+h_{ew-ep}A_{ew-ep}(T_w-T_p)+Q_{reaction-pellet} \quad (3)$$

$$M_{kg}C_g\frac{dT_g}{dz} = h_{g-ew}A_{g-ew}(T_w - T_g) + h_{g-ep}A_{g-ep}(T_p - T_g) + Q_{reaction-gas} \quad (4)$$

$$\dot{h}_{g-ew}A_{g-ew}(T_g - T_w) - h_{cp-cw}A_{cp-cw}(T_w - T_p) - h_{ep-ew}A_{ep-ew}(T_w - T_p) = h_{sh-a}A_{sh-a}(T_{sh} - T_a) \quad (5)$$

Nomenclature

A	pellet area for heat transfer, cm^2/cm^3
A_{cw-cp}	heat transfer area between kiln wall covered by pellets and pellets that covers the kiln wall, m^2
A_{ew-ep}	heat transfer area between exposed kiln wall and top surface of pellet bed, m^2
A_{g-ep}	heat transfer area between gas and top surface of pellet bed, m^2
A_{g-ew}	heat transfer area between gas and exposed kiln wall, m^2
A_{sh-a}	heat transfer area between kiln outer shell and ambient environment, m^2
C_g	specific heat of air, J/g.K
C_p	specific heat of pellets, J/g.K
h	heat transfer coefficient between gas and pellets, J/K.s
h_{cw-cp}	heat transfer coefficient between kiln wall covered by pellets and pellets that covers the kiln wall, $J/(m^2.K)$
h_{ew-ep}	heat transfer coefficient between exposed kiln wall and top surface of pellet bed, $J/(m^2.K)$
h_{g-ep}	heat transfer coefficient between gas and top surface of pellet bed, $J/(m^2.K)$
h_{g-ew}	heat transfer coefficient between gas and exposed kiln wall, $J/(m^2.K)$
h_{sh-a}	heat transfer coefficient between kiln outer shell and ambient environment, $J/(m^2.K)$
M_{kg}	mass flow rate of gas in kiln, g/s
M_g	mass flow rate of gas through pellet bed on grate, $g/cm^2.s$
M_{kp}	mass flow rate of pellets in kiln, g/s

Q_1	heat release rates of oxidation of magnetite, J/s.cm
q_1	heat release rates of water evaporation, J/s.cm
Q_2	heat release/absorb rates of possible reactions such as carbonates decomposition, sulfides decomposition and oxidation, according to the specific production process, J/s.cm
q_2	heat absorb rates of water condensation, J/s.cm
$Q_{reaction-gas}$	reaction heat in gas, J/m
$Q_{reaction-pellet}$	reaction heat in pellet bed, J/m
t	time, s
T_a	temperature of ambient environment, °C
T_g	temperature of gas, °C
T_p	temperature of pellets, °C
T_{sh}	temperature of kiln outer shell, °C
T_w	temperature of kiln wall, °C
x	bed depth, cm
z	length of rotary kiln, m
a	fraction of heat transfer which goes to evaporation
ε	porosity in pellet bed
ρ_s	density of ore, g/cm^3

Expert System

Grate-kiln pellet induration process has multiple links, and comprehensive analysis of dozens of variables is required for production control. Therefore, timely production adjustment with consideration of all the variables is hard to achieve.

Production status of grate process can be considered essentially normal when temperatures of preheating section are controlled in suitable ranges, due to the existence of air circulation.

Therefore, a preheating section dominated control strategy was established, as shown in Figure 1. Where node A~H represent gas temperature in gas hood of preheating section, height of pellet bed, running speed of grate, inlet gas temperature of main exhaust fan, roasting temperature of pellet in kiln, gas temperature in wind box of preheating section, pellet bed temperature of preheating section and pellet bed temperature of tempered preheating section, respectively.

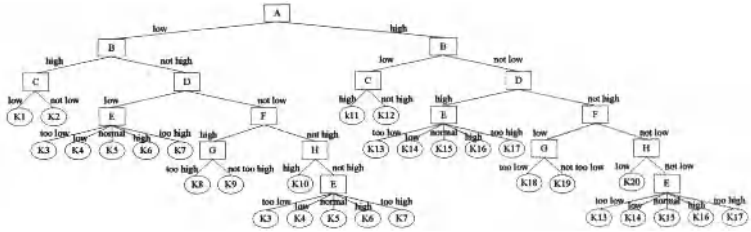

Figure 1. Preheating section dominated control strategy

Control guidance is taken out following the "production status estimation - cause analysis - adjustment measure selection" proceeding. And the cause analysis is based on status estimation of parameter A~H:

(1) fluctuation of pellet amount involved in heat transfer:

(A is abnormal) + (B is abnormal and opposite to the abnormality of A) + (C is abnormal and opposite to the abnormality of B) -> running speed of grate is abnormal

(A is abnormal) + (B is abnormal and opposite to the abnormality of B) + (C is normal or in line with the abnormality of B) -> pellet amount is abnormal

(2) unreasonable level of heat in the whole grate-kiln-cooler system:

(A is abnormal) + (B is normal or in line with the abnormality of A) + (E is normal or in line with the abnormality of A) -> coal injection rate is abnormal

(3) unreasonable distribution of heat between grate and kiln:

(A is abnormal) + (B is normal or in line with the abnormality of A) + (E is abnormal and opposite to the abnormality of A) -> opening of main exhaust fan is abnormal

(4) unreasonable distribution of heat among sections of grate:

(A is abnormal) + (B is normal or in line with the abnormality of A) + (D is normal or opposite to the abnormality of A) + (F is abnormal and opposite to the abnormality of A) + (abnormal level of G) -> opening of regenerative fan is abnormal

(A is abnormal) + (B is normal or in line with the abnormality of A) + (D is normal or opposite to the abnormality of A) + (F is normal or in line with the abnormality of A) + (H is abnormal and opposite to the abnormality of A) -> opening of regenerative fan is abnormal

Based on the results of cause analysis, measures on adjusting objects, i.e. pellet amount, running speed of grate, kiln speed, coal injection rate, opening of main exhaust fan and opening of regenerative fan, were established as K1~K20 shown in Figure 1.

System Application

Software of grate-kiln pellet production expert system was developed by Visual C++ programming. Functions such as data reading, model calculation and expert system control guidance were realized.

This system was put into field practice in a certain pellet plant in China. Production data at time 2010-07-01 11:08:02 were collected as shown in Table I.

Table I. Production data

Parameter	Data
Green pellet moisture	10.1%
Green pellet magnetite content	0.002618 mol/g-pellet
Height of pellet bed	197 mm
Running speed of grate	2.72 m/min
Air flowrate of updraught drying section	0.1353 g cm^{-2} s^{-1}
Inlet gas temperature of updraught drying section	113 °C
Air flowrate of downdraught drying section	0.1087 g cm^{-2} s^{-1}
Inlet gas temperature of downdraught drying section	307 °C
Air flowrate of tempered preheating section	0.1345 g cm^{-2} s^{-1}
Inlet gas temperature of tempered preheating section	763 °C
Air flowrate of preheating section	0.1076 g cm^{-2} s^{-1}
Inlet gas temperature of preheating section	1079 °C
Rotate speed of kiln	0.58 r/min
Coal injection rate	1.04 kg/s
Flow rate of secondary air	76.42 kg/s

Grate-kiln temperature field was calculated. The results are shown in Figure 2 and Figure 3.

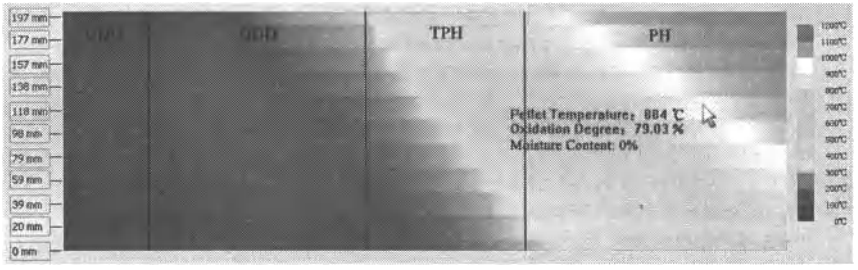

Figure 2. Two-dimensional visualization of pellet bed temperature field on grate

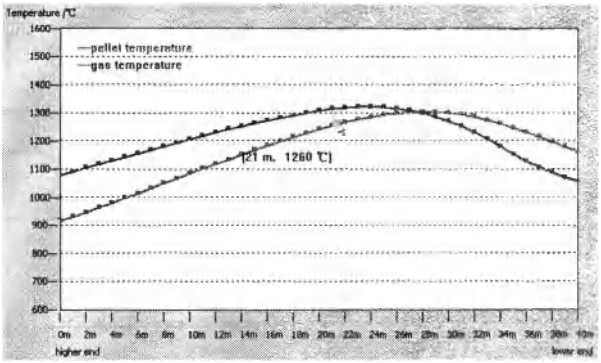

Figure 3. One-dimensional visualization of temperature field in kiln

The results show that pellet bed temperature of tempered preheating section and preheating section are 489 °C and 915 °C respectively, and roasting temperature of pellet in kiln is 1302 °C.

For this production status, "increase opening of regenerative fan" was displayed on the software interface as suggestion of adjustment measures, which was consistent with the conclusion drawn from personal expertise of operators in production site. According to the production records, the opening of regenerative fan was increased by operator, and 9 minutes later, production status was back to normal and stabilized.

During months of production application, good results have been received. The comparison of gas temperature fluctuations in gas hood of preheating section and pellet quality indexes before and after system application are shown in Figure 4 and Table II.

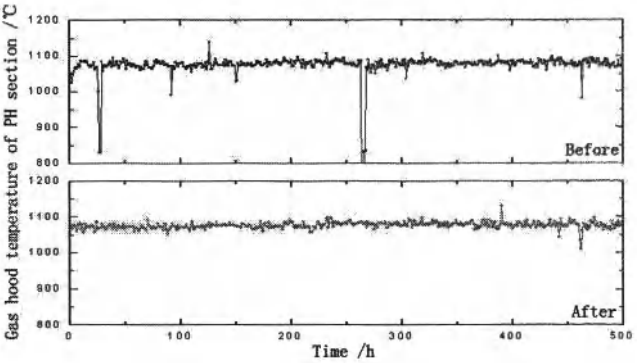

Figure 4. Gas temperature fluctuations in gas hood of preheating section before and after system application

Table II. Pellet quality indexes before and after system application

Time	FeO /%	Compressive strength /N·pellet^{-1}	Abrasion resistance index /%	Sieve index /%	First grade rate /%
2010	0.33	2649	5.74	2.73	92.64
2011 (Jan~Aug)	0.27	2745	5.66	1.68	94.83

Figure 4 and Table II indicate that expert system for grate-kiln pellet production can stabilize the thermal status of grate-kiln system, and increase pellet quality effectively. The stability rate of gas temperature in gas hood of preheating section was increased from 91.0% to 94.2%; the compressive strength and first grade rate of pellet were increased by 3.62% and 2.36%, respectively, while FeO content was 18.18% lower.

Conclusions

1) Mathematical models of grate-kiln temperature field were developed by analysis of heat transfer and physical-chemical reactions during pellet induration process. Critical production data such as pellet bed temperature of tempered preheating section, pellet bed temperature of preheating section and roasting temperature of pellet in kiln can be obtained.

2) Expert system was built base on the combination of calculated results of temperature field models and detected data in production. And a preheating section dominated control strategy has been established.

3) Software was programmed and applied in a pellet plant. The application effect was demonstrated through a case study and months of production results. It proves that this system can solve production anomalies effectively, stabilize grate-kiln pellet production and improve pellet quality.

References

1. R.W. Young, M. Cross, and R.D. Gibson, "Mathematical Model of Grate-Kiln-Cooler Process Used for Induration of Iron Ore Pellets", *Ironmaking and Steelmaking*, 6 (1) (1979), 1-13.

2. J.A. Thurlby, "A Dynamic Mathematical Model of the Complete Grate/Kiln Iron-Ore Pellet Induration Process", *Metallurgical Transactions B*, 19B (1) (1988), 103-112.

3. Aichun Ma et al., "A One-Dimensional Thermal Model for the Alumina Clinker Kiln", *Energy for Metallurgical Industry*, 23 (1) (2004), 23-26.

4. P.V. Barr, J.K. Brimacombe, and A.P. Watkinson, "A Heat-Transfer Model for the Rotary Kiln: Part II. Development of the Cross-Section Model", *Metallurgical transactions B*, 20 (3) (1989), 403-419.

5. A.A. Boateng, *Rotary Kilns* (Oxford, UK: Elsevier Inc., 2008), 216-224.

6. J.P. Gorog, T.N. Adams, and J.K. Brimacombe, "Heat Transfer from Flames in a Rotary Kiln", *Metallurgical transactions B*, 14 (3) (1983), 411-424.

3rd International Symposium on High-Temperature Metallurgical Processing
Edited by: Tao Jiang, Jiann-Yang Hwang, Patrick Masset, Onuralp Yucel, Rafael Padilla, and Guifeng Zhou
TMS (The Minerals, Metals & Materials Society), 201

THE INFLUENCE OF SODIUM OXIDE ON THE DISTRIBUTION BEHAVIOR OF SOME ELEMENTS AT THE S-FURNACE OF THE MITSUBISHI PROCESS

Yusuke Kimura[1], Ken-ichi Yamaguchi[1]

[1]Mitsubishi Materials Corp. Central Research Institute;
15-2 Onahama-fukimatsu, Iwaki, Fukushima Pref., 971-8101, Japan

Keywords: Mitsubishi Process, Copper Smelting, Recycling, Slag, Sodium Oxide

Abstract

Secondary materials have long been processed at the S-furnace of the Mitsubishi continuous copper smelting and converting process at Naoshima Smelter and Refinery. Intensive recycling in the recent years has formed concerns that impurities in the secondary materials may cause drastic changes in the chemical properties of the CL-slag, which is separated from matte in the smelting stage. Among various impurities included in secondary materials, the authors have studied the influences of sodium oxides in the CL-slag because the behavior of sodium oxide has scarcely been studied with respect to the copper smelting slag. The examinations have been applied experimentally on the distribution between slag and matte of arsenic whose acidic characteristics suggest strong affinity to sodium-oxide of basic characteristics in silicate melts. The results have been discussed by thermodynamic evaluations and the results of pyro-tests at the commercial furnace.

Introduction

At Naoshima Smelter and Refinery, the existing line of the Mitsubishi continuous copper smelting and converting process has been operated since 1991. The Mitsubishi Process consists of three furnaces namely the S-, CL- and C-furnace as shown in Figure 1. In the S-furnace, copper concentrate and powdery secondary materials (scraps, sludges, etc) are charged through the top lances with oxygen enriched air. The other secondary materials of lumpy shapes are charged through the chute installed on the furnace roof. Charged materials are smelted by the reaction heat in accordance with the oxidization of copper concentrate. The mixed melt of matte and slag overflows through the launder into the CL-furnace, where the melt is separated into slag and matte by the difference of their specific gravity. Matte is siphoned out and sent to the C-furnace and converted to blister copper continuously. The CL-slag overflows continuously through the slag outlet to be water-granulated. Granulated slag is sold as a raw material used for the cement production and so on. Various secondary materials have been processed at the S-furnace of Naoshima Smelter and Refinery. Intensive recycling in the recent years has formed concerns that the chemical properties of the CL-slag may change drastically due to impurities originating from secondary materials. Among various impurities included in secondary materials, the authors have studied the influence of sodium oxide in the CL-slag because the impact of sodium oxide has scarcely been studied with respect to the copper smelting slag. The examinations have been applied experimentally on the distribution between slag and matte of arsenic whose acidic characteristics suggest strong affinity to sodium-oxide of basic characteristics in silicate melts.

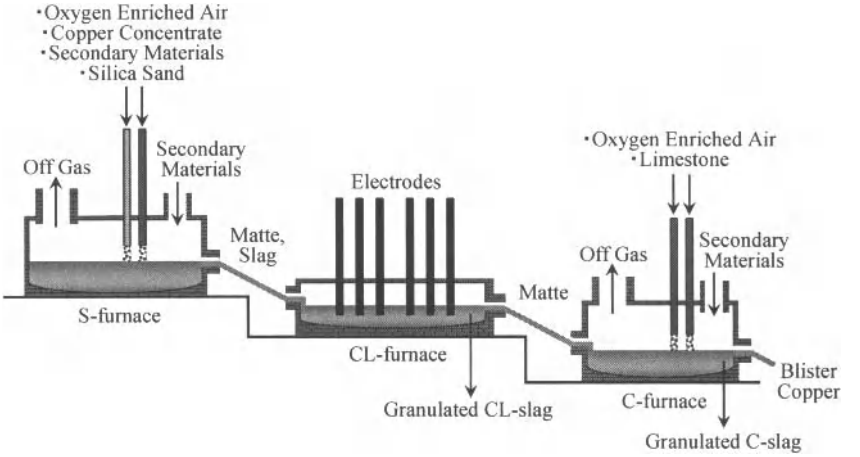

Figure 1. Schematic diagram of Mitsubishi Process at Naoshima Smelter and Refinery.

Influence of Sodium Oxide on Copper Loss in Slag

Relation between the Magnetite Content and Copper Loss in the CL-slag

It is known that the formation of magnetite in the CL-furnace gives rise to an increase in slag viscosity and the formation of 'false bottom' (muddy layer) between slag and matte, resulting in the increase in copper loss to the slag. The primary cause of copper loss at the CL-furnace has actually been ascribed not to the chemical dissolution but to the suspension of copper matte droplets caused by the magnetite precipitation [1]. Therefore the influence of sodium oxide on copper loss can indirectly be evaluated by the influence of sodium oxide on the magnetite activity in slag. The relation between the concentration of sodium oxide and magnetite activity in the CL-slag was calculated using the regular solution model [2-4].

Influence of Sodium Oxide on Magnetite Activity in CL-slag

The effect of sodium oxide concentrations on the iso-activity line of the magnetite in the CL-slag is shown in Figure 2. The hatched areas illustrate the composition at which solid substances indicated in the areas precipitate from the slag. The area inside circle indicates the range of the composition of the CL-slag during the ordinary operation. It is notable that the magnetite activity increases slightly with the Na_2O concentration changing from 0.2mass% to 0.4mass%. However, such order of activity change is located within the area of slag composition change at the usual operation. Consequently, even if secondary materials with high sodium content are processed at the expected feeding rate (i.e. Na_2O content in slag will double that of the present level), the change of copper loss is considered not to exceed the range of usual operation.

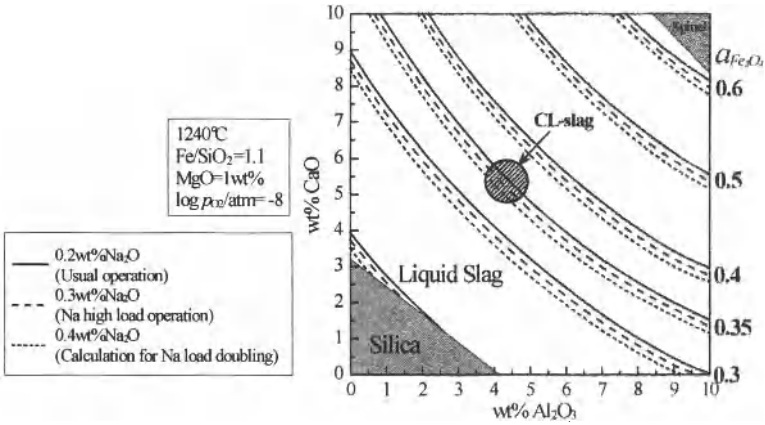

Figure 2. Influence of sodium oxide on the magnetite activity in the CL-slag.

Laboratory Experiments

Figure 3 is the oxygen-sulfur potential diagram which was calculated using published data [5, 6]. This figure shows the stability fields of condensed phases for the Cu-Fe-S-O-SiO_2 system at 1250°C. Oxygen and sulfur potentials (corresponding to $\log p_{O2}$ and $\log p_{S2}$) are taken as the vertical and horizontal axes, respectively. Within the gray-colored area slag and matte coexist, so the thermodynamic state at the S-furnace approximately corresponds to the black dot area where the iso-matte grade line of 68%Cu meet the previous measurement in the S-furnace of $\log p_{O2}$=-8. This laboratory experiments were conducted within the region framed by the ellipse including the equilibrium state of the S-furnace. Small amount of calcium arsenate was added to the system of Cu-Fe-S-Mg-Al-Ca-Si-O-S, which forms slag and matte under the controlled atmosphere.

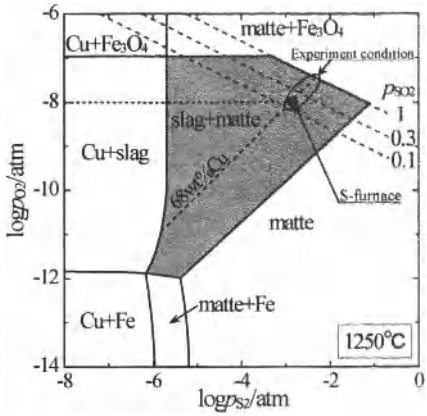

Figure 3. Phase stability diagram for the Cu-Fe-S-O-SiO_2 system at 1250°C.

Influence of Oxygen on the Behavior of Arsenic

In this study the preliminary test below was conducted on the system in which sodium oxide is not included. Using Figure 3, along the iso-matte grade line (68%Cu), the SO_2 partial pressure was changed at 0, 0.13, 0.5, and 1 atm. The oxygen potential was thereby changed in accordance with the SO_2 partial pressure along the 68%Cu line. After the experiment, the arsenic concentration in slag and matte was chemically analyzed. The distribution ratio of arsenic between slag and matte was expressed as $L_{As}^{S/M}$.

Figure 4 shows the relation between arsenic concentration in matte and $L_{As}^{S/M}$ at 1250°C. Note that $L_{As}^{S/M}$ in this study is constant regardless of the arsenic concentration in matte and strongly depends on the p_{SO2}. These tendencies of $L_{As}^{S/M}$ correspond well to those reported previous investigations [7, 8].

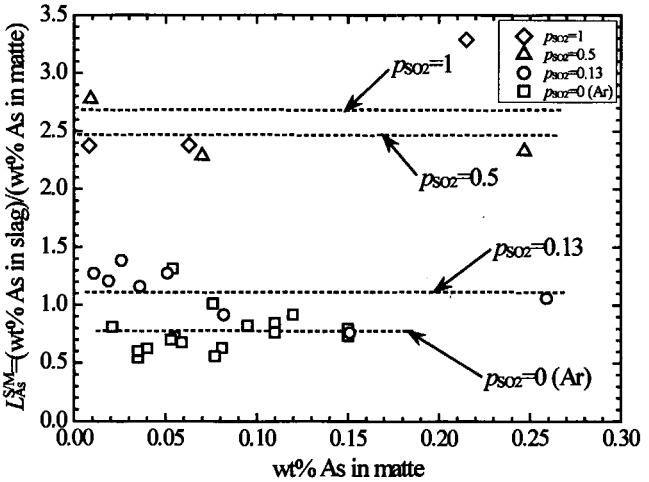

Figure 4. Relation between the arsenic concentration in matte and the distribution ratio of arsenic between slag and matte at 1250°C.

Figure 5 shows the relation between the oxygen potential and $L_{As}^{S/M}$ in the logarithmic scale. From this figure it is clear that the distribution ratio of arsenic increases with increasing the oxygen potential. The regression line from the data has the slope of about 3/4 that well corresponds with the theoretical slope from the following redox reaction.

$$As(l) + 3/4O_2(g) = AsO_{1.5}(l) \quad (1)$$

The increment of $L_{As}^{S/M}$ against the oxygen potential agrees well with the values reported in previous literatures [9-11].

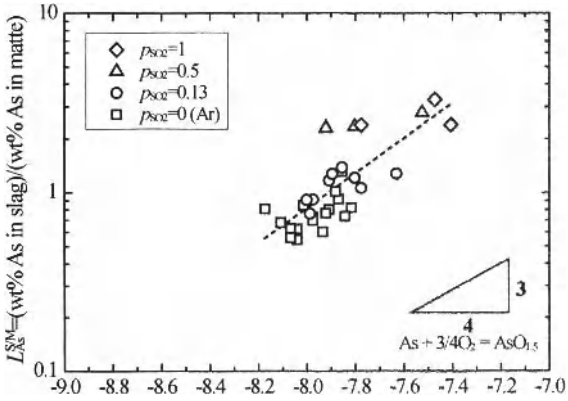

Figure 5. Relation between oxygen potential and the distribution ratio between slag and matte.

Influence of Sodium Oxide on the Behavior of Arsenic

The experiment was conducted to investigate the influence of Na_2O concentration in slag on the distribution ratio of As between slag and matte. Reagent grade Na_2CO_3 was added to slag to control the Na_2O concentration in the wide range from 0.5 to 5mass% in slag. The specimen were melted under pure argon (p_{SO2}=0) or the argon-SO_2 mixture (p_{SO2}=0.13atm).

Figure 6 shows the relation between the Na_2O concentration in slag and $L_{As}^{S/M}$. The value of $L_{As}^{S/M}$ was normalized to $\log p_{O2}$=-8 to exclude the influences of any factors except Na_2O. The regression lines that obtained from each p_{SO2} show no clear relation between the Na_2O concentration in slag and the distribution ratio of As, $L_{As}^{S/M}$.

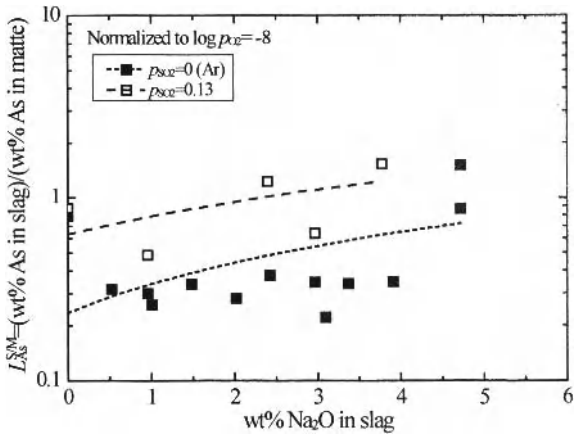

Figure 6. Relation between the Na_2O concentration in slag and $L_{As}^{S/M}$

Influence of Sodium Oxide on Oxygen Potential

The experiments were conducted to investigate the influence of sodium oxide on the oxygen potential in slag. In these experiments, arsenic was not added to the specimen and temperature was controlled to 1300°C in addition to 1250°C under the stream of argon. Figure 7 shows the relation between the Na_2O concentration and the oxygen potential in slag. It is noted that the oxygen potential tends to decrease slightly as the Na_2O concentration in slag increases. The change in the oxygen potential is only about 0.1atm even if Na_2O dissolves into slag by about 4mass% at 1250°C. Such change in the oxygen potential may affect the distribution ratio of arsenic ($L_{As}^{S/M}$) in accordance with Figure 5.

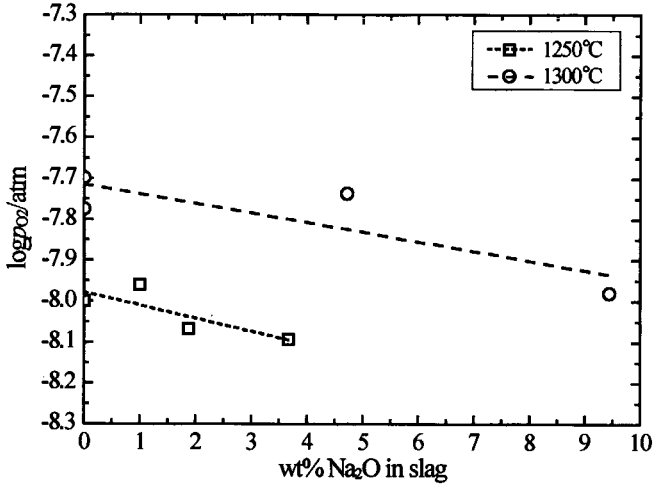

Figure 7. Relation between the Na_2O concentration and oxygen potential in slag.

Examination at the S-Furnace

It was deduced from the laboratory experiments that the distribution of arsenic less affected by Na_2O in slag and, in contrast, much affected by the oxygen potential over the range encountered in the S-furnace. The authors have examined how the oxygen potential changes when following two events happens individually:

1. With or without processing of secondary materials containing high sodium in the same bed of concentrates.
2. Before and after changing the bed of concentrates at no processing of the secondary materials containing high sodium.

Figure 8 shows the operating conditions and the measured oxygen potential during the examinations. Oxygen potential ($\log p_{O2}$) normalized to 1250°C was changed between -8.4 and -7.6 during the examinations. When secondary materials with high sodium content were processed, the oxygen potential was stable at about -8.1 in the period of measurement. Without the processing of secondary materials containing high sodium, $\log p_{O2}$ fluctuated widely. After

the change of the bed while stopping the charge of secondary materials containing rich sodium, the oxygen potential stayed between -7.7 and -7.8. Supposing that all measured values of oxygen potential in the S-furnace follow the normal distribution, the two-tailed test was applied on the results. The statistics indicates that the measured values have no significant difference (more than 1%) regardless operating conditions. It is therefore deduced that the variation in the oxygen potential caused by the processing of secondary materials with high sodium content lies within the range of ordinary fluctuation happening in the normal operation.

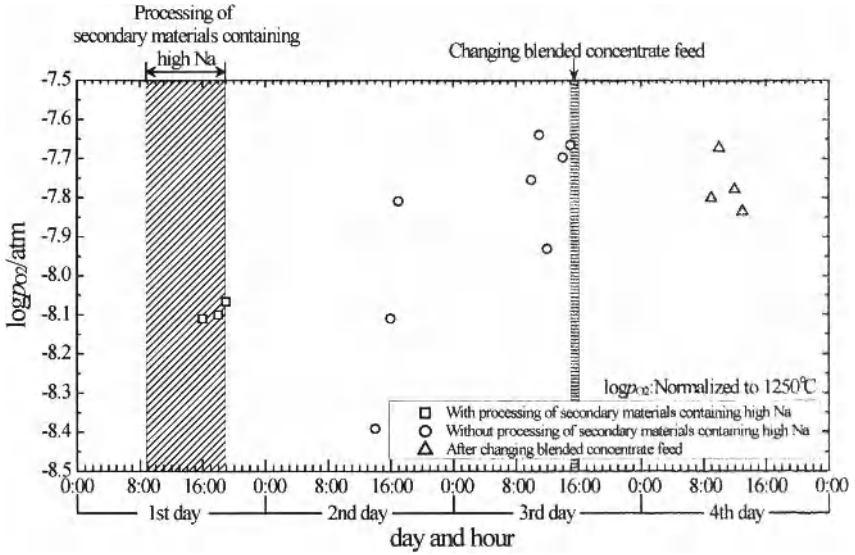

Figure 8. Operating conditions and measured oxygen potential during the examinations at the S-furnace. (Oxygen potential is normalized to 1250°C.)

Concluding Remarks

The authors have demonstrated that sodium oxide has negligible influence on the copper loss and the distribution behavior of arsenic into the CL-slag. Accordingly, it is suggested that sodium included in secondary materials does not disturb the operations of the S-furnace of the Mitsubishi process even if the input of sodium is intensively increased.

Recycling in copper smelter requires conscious mind because copper losses to slag may cancel out the recovery of valuable metals in secondary materials if the furnace operation becomes rough. Its importance has been demonstrated in the long operations at Naoshima smelter where the treatment of secondary materials has increased greatly while maintaining copper loss to slag at 0.7mass% or less. The successful results in the operations have been supported by consistent knowledge of metallurgical slags such as the present paper has provided concisely.

References

1. F. Tanaka, "Reducing Copper Losses in the Mitsubishi Process: A Pyrometallurgical Approach," *Cu2007, Vol. VII, Process Control, Optimization, and Six Sigma*, ed. R.L. Stephens and G.A. Eltringham, (Montreal, Canada: The Canadian Institute of Mining, Metallurgy and Petroleum, 2007), 145-157.

2. S. Ban-ya, "Mathematical Expression of Slag-Metal Reactions in Steelmaking Process by Quadratic Formalism Based on the Regular Solution Model," *ISIJ International*, 33 (1993), 2-11.

3. S. Ban-ya, "Recent Perspectives on the Structural Models and Thermodynamic Properties of Molten Iron and Slag," *The 42nd Nishiyama Technical Lectures*, (Tokyo, Japan: The Iron and Steel Institute of Japan, 1976), 67-109. (in Japanese)

4. S. Ban-ya, M. Hino, and T. Nagasaka, "Estimation of Water Vapor Solubility in Molten Silicates by Quadratic Formalism Based on the Regular Solution Model," *ISIJ International*, 33 (1993), 12-19.

5. A. Yazawa, "Thermodynamic Considerations of Copper Smelting," *Canadian Metallurgical Quarterly*, 13 (1974), 443-453.

6. Y. Takeda, "Thermodynamic Evaluation of Copper Loss in Slag Equilibrated with Matte," *Metallurgical and Materials Processing: Principles and Technologies*, vol. I, ed. F.Kongoli *et al.*, (Warrendale, PA: TMS, 2003), 341-357.

7. K. Itagaki, "Thermodynamic Study of Oxygen-Smelting of Copper or Nickel Mette," *Second International Conference on Processing Materials for Properties*, ed. B. Mishra and C. Yamaguchi, (Warrendale, PA: TMS, 2000), 815-820.

8. A. Yazawa, M.Oida, and Y. Nishikawa, "Distribution Equilibria for Ni, Co, As, Sb and Cu between Matte and Slag," *Journal of the Mining and Metallurgical Institute of Japan*, 98 (1982), 963-968. (in Japanese)

9. G.Roghani, Y. Takeda, and K.Itagaki, "Phase Equilibrium and Minor Element Distribution between FeO_X-SiO_2-MgO-Based Slag and Cu_2S-FeS Matte at 1573K under High Partial Pressures of SO_2," *Metallurgical and Materials Transactions B*, 31B (2000), 705-712.

10. A.Yazawa, S. Nakazawa, and Y. Takeda, "Distribution Behavior of Various Elements in Copper Smelting Systems," *Proc. Advances in Sulfide Smelting*, ed. H.Y. Sohn, D.B. George, and A.D. Zunkel, (New York, NY: AIME, 1983), 99-117.

11. M. Kashima et al., "Distribution of Minor Elements among Liquid Copper, White Metal and Silica-Saturated Slag," *Journal of the Mining and Metallurgical Institute of Japan*, 96 (1980), 907-911. (in Japanese)

3rd International Symposium on High-Temperature Metallurgical Processing
Edited by: Tao Jiang, Jiann-Yang Hwang, Patrick Masset, Onuralp Yucel, Rafael Padilla, and Guifeng Zhou
TMS (The Minerals, Metals & Materials Society), 2012

Effect of Temperature on Equilibrium Phase Relation and Liquidus of $CaO-SiO_2-Al_2O_3-FeO_x$ System

Nan Wang[1], Zongshu Zou[1], Z. Zhang[2], Y. Xiao[2], Y. Yang[2]

[1] School of Materials and Metallurgy, Northeastern University, Shenyang, China
[2] Delft University of Technology, Delft, the Netherlands

Keywords: Vitrified bottom ash, $CaO-SiO_2-FeO_x-Al_2O_3$ system, Liquidus, Equilibrium phase

Abstract

Thermodynamic calculation is applied to make an investigation on the equilibrium phase relations and liquids of $CaO-SiO_2-Al_2O_3-FeO_x$ system for different temperatures. The calculated results with FactSage6.1 show that the effect of temperature on the the equilibrium phase relations and liquidus of $CaO-SiO_2-Al_2O_3-FeO_x$ system and its sub-systems is appreciable. The liquid phase regions enlarge with increasing temperature from 1573K to 1873K, while the primary phase fields reduce distinctly.

Introduction

The main oxide components of vitrified bottom ash slag are CaO, Al_2O_3, SiO_2, Fe_2O_3, MgO, and Na_2O, accounting for more than 90% of the bottom ash by weight[1]. During slag processing, the knowledge of thermodynamic properties and liquidus temperature in the related slag systems is highly required [2, 3], which is not yet available. Through literature survey [4-6], it is clear that the systematic information on the concerned complex slag system is scarce. So far the engineers in the field have to make assumptions of the thermodynamic properties of the simplified oxide system, without taking into consideration the interactions of the different oxide components, which hinders the development of the slag valorization and utilization. In order to provide thermodynamic properties for the application of the vitrified bottom ash, the six-component oxide system ($CaO-MgO-Al_2O_3-SiO_2-FeO_x-Na_2O$) is highly required. A preliminary phase diagram of the $CaO-MgO-Al_2O_3-SiO_2-FeO_x-Na_2O$ system can be obtained from extrapolation of the thermodynamic functions of constituent subsystems such as $CaO-SiO_2-FeO_x-MgO$, $CaO-SiO_2-FeO_x-Al_2O_3$, $CaO-SiO_2-Na_2O-MgO$ and $CaO-SiO_2-Na_2O-Al_2O_3$. In this work, the equilibrium phase relation and liquidus of $CaO-SiO_2-FeO_x-Al_2O_3$ system, one subsystem of the concerned complex slag system, are calculated and the effect of temperature is also discussed.

Equilibrium Phase Relation and Liquidus of $CaO-SiO_2-Al_2O_3-FeO_x$ System

$CaO-Al_2O_3-FeO_x$ System

The equilibrium phase relations of $CaO-Al_2O_3-FeO_x$ system for different temperatures are calculated by using FactSage program, as shown in Fig. 1. It can be noted, for the $CaO-Al_2O_3-FeO_x$ system at 1673K, that there exists a relatively large liquid phase area adjacent to the region with less than 50 mass% Al_2O_3. Five two-phase coexisting regions, including liquid and CaO, liquid and $3CaO{\cdot}Al_2O_3$, liquid and $CaO{\cdot}Al_2O_3$, liquid and $CaO{\cdot}2Al_2O_3$ as well as liquid and spinel solid solution are found in the $CaO-Al_2O_3-FeO_x$ system. Otherwise, three primary phase regions of $3CaO{\cdot}Al_2O_3$, $CaO{\cdot}Al_2O_3$ and $CaO{\cdot}2Al_2O_3$ appear along the boundary of $CaO-Al_2O_3$ system respectively. Figure 2 shows the effect of temperature on the liquidus of $CaO-Al_2O_3-$

FeO_x system. With the increase of temperature from 1673K to 1773K, the liquid phase area of CaO-Al_2O_3-FeO_x system enlarges and extends to the high Al_2O_3 region, which resulting in the sharp reduction of the primary phase fields of $CaO{\cdot}Al_2O_3$ and $CaO{\cdot}2Al_2O_3$ respectively. With further temperature increasing to 1873K, the primary phase fields of $CaO{\cdot}2Al_2O_3$ and spinal solid solution reduce, and those ones of $CaO{\cdot}Al_2O_3$ and $3CaO{\cdot}Al_2O_3$ dispear.

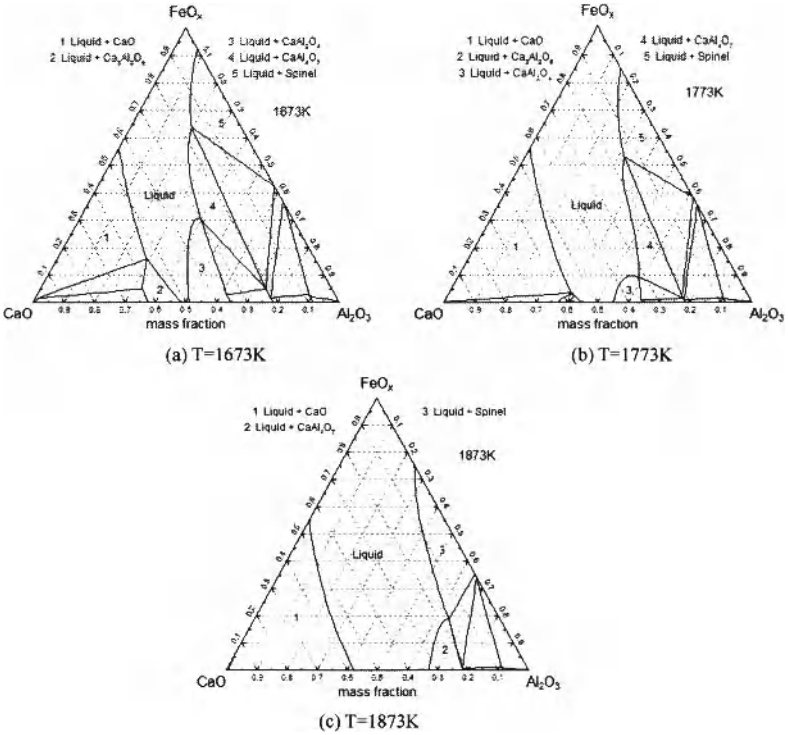

(a) T=1673K

(b) T=1773K

(c) T=1873K

Fig. 1 Isothermal sections of the CaO-Al_2O_3-FeO_x system at different temperatures

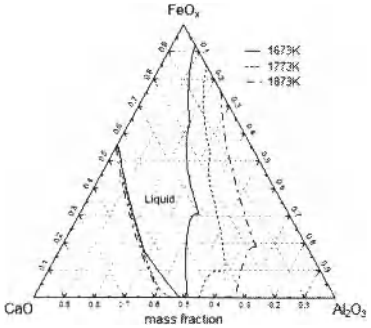

Fig. 2 Effect of temperature on the liquidus of CaO-Al_2O_3-FeO_x system

SiO_2-Al_2O_3-FeO_x System

The equilibrium phase relations of SiO_2-Al_2O_3-FeO_x system for different temperatures are shown in Fig. 4. There exists a relatively small liquid phase region for SiO_2-Al_2O_3-FeO_x system at 1573K and the equilibrium phase relation is simple. Three primary phase fields, including SiO_2, mullite and spinel solid solution, can be found. With the temperature increasing to 1673K, the liquid phase region enlarges. The primary phase field of spinel solid solution appears along the boundary of FeO_x-Al_2O_3 system, and the mullite solid solution exists in the SiO_2-Al_2O_3 binary system. At 1773K, the liquid phase area increases furtherly, and the primary phase field of Al_2O_3 begins to appear around the high Al_2O_3 zone. The primary phase field of spinel solid solution reduces slightly and that one of mullite enlarges.

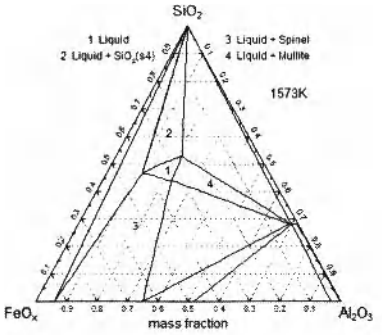

(a) T=1573K

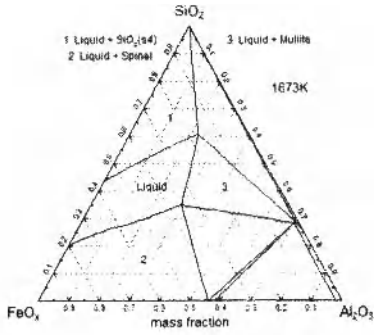

(b) T=1673K

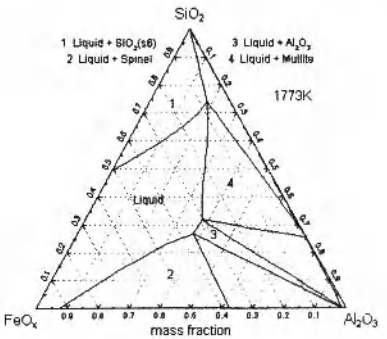

(c) T=1773K

Fig. 3 Isothermal sections of the SiO_2-Al_2O_3-FeO_x system at different temperatures

Effects of temperature on the liquidus of SiO_2-Al_2O_3-FeO_x system are shown in Fig. 4. With the increase of temperature from 1573K to 1773K, the liquid phase area of SiO_2-Al_2O_3-FeO_x system expand, while the two-phase and three-phase coexisting regions reduce. In addition, crystal transformation from tridymite to cristobalite occurs, and the equilibrium phase relations in high Al_2O_3 region change with the emergence of two-phase region of liquid and Al_2O_3.

CaO-SiO_2-Al_2O_3-FeO_x System

Figure 5 shows the equilibrium phase relations of CaO-SiO_2-Al_2O_3(8.3mass%)-FeO_x system for different temperatures. The liquid phase region exists in the low FeO_x area, and five primary phase fields such as SiO_2, $CaSiO_3$, a'-Ca_2SiO_4 solid solution, $Ca_2Fe_2O_5$ and spinel solid solution can be noted. At 1773K, the liquid phase zone extends to the high FeO_x area. The primary phase field of $CaSiO_3$ disappears with the emergency of CaO. At 1873K, the liquid phase area enlarges furtherly, and the primary phase field of spinel solid solution disappears.

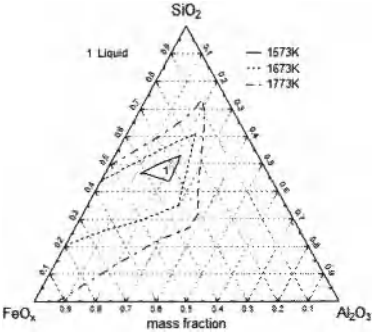

Fig. 4 Effect of temperature on the liquidus of SiO_2-Al_2O_3-FeO_x system

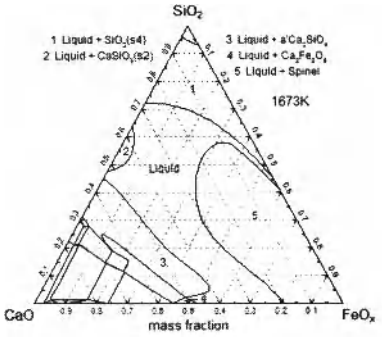

(a) T=1673K

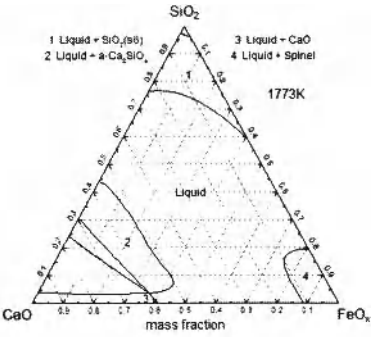

(b) T=1773K

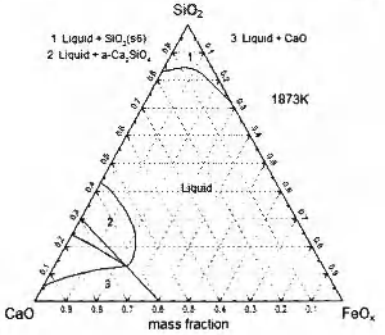

(c) T=1873K

Fig. 5 Isothermal sections for the CaO-SiO_2-Al_2O_3(8.3%)-FeO_x system

Figure 6 shows the effect of temperature on the liquidus of $CaO\text{-}SiO_2\text{-}Al_2O_3$ (8.3%)-FeO_x system. With the temperature increasing from 1673K to 1873K, the liquid phase area enlarges.

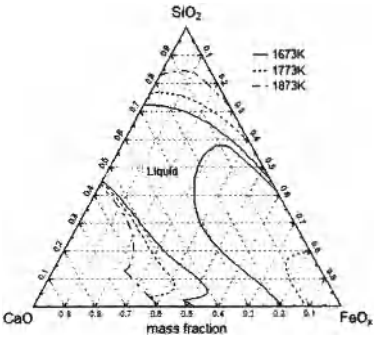

Fig. 6 Effect of temperature on liquidus of $CaO\text{-}SiO_2\text{-}Al_2O_3$ (8.3%)-FeO_x system

Conclusions

(1) For $CaO\text{-}Al_2O_3\text{-}FeO_x$ system, a large liquid phase region exists adjacent to the zone with less than 50mass% Al_2O_3 at 1673K. The liquid phase region of $CaO\text{-}Al_2O_3\text{-}FeO_x$ system reduces and extends to the high FeOx region with the decreasing temperature.
(2) A relatively small liquid phase region of $SiO_2\text{-}Al_2O_3\text{-}FeO_x$ system exists at 1573K and the equilibrium phase relation is simple. The liquid phase region of $SiO_2\text{-}Al_2O_3\text{-}FeO_x$ system enlarges with the temperature increasing to 1773K.
(3) The liquid phase region of $CaO\text{-}SiO_2\text{-}Al_2O_3\text{-}FeO_x$ system exists in the low FeO_x area, and five primary phase fields can be noted. At 1773K, the liquid phase zone extends to the high FeO_x area. The primary phase field of $CaSiO_3$ disappears with the emergency of CaO. At 1873K, the liquid phase area enlarges furtherly, and the primary phase field of spinel solid solution disappears.

Acknowledgements

This research work was supported by the National Natural Science Foundation of China (Grant No. 50974034) and the Royal Netherlands Academy of Arts and Science (KNAW) (Project 08CDP026).

References

[1] Y. Xiao et al., "Vitrification of Bottom Ash from a Municipal Solid Waste Incinerator," *Waste Management*, 28 (6)(2008), 1020-1026.
[2] S. Y. Kim, T. Matsuto, and N. Tanaka, "Evaluation of Pre-treatment Methods for Landfill Disposal of Residues from Municipal Solid Waste Incineration," *Waste Manage Res*, 21 (2003), 416-423.
[3] K. L. Lin, C. T. Chang, "Leaching Characteristics of Slag from the Melting Treatment of Municipal Solid Waste Incinerator Ash," *Journal Hazardous Materials*, B135(2006), 292-302.
[4] G. Eriksson et al., "Critical Evaluation and Optimization of the Thermodynamic Properties and Phase Diagrams of the $CaO\text{-}Al_2O_3$, $Al_2O_3\text{-}SiO_2$ and $CaO\text{-}Al_2O_3\text{-}SiO_2$ Systems," *Metall. Trans. B*, 24 (50)(1993), 807-816.

[5] Z. Zhang, "Literature Review of the $CaO-Al_2O_3-SiO_2-FeO_x-MgO-Na_2O$ System of Vitrified Bottom Ash Slag from Municipal Solid Waste Incinerators" (Internal Report, TU Delft, 2007).
[6] A. D. Pelton, "Thermodynamic Database Development Modelling and Phase Diagram Calculations in Oxide Systems," *Rare Metals*, 25(5)(2006), 473-480.

3rd International Symposium on High-Temperature Metallurgical Processing
Edited by: Tao Jiang, Jiann-Yang Hwang, Patrick Masset, Onuralp Yucel, Rafael Padilla, and Guifeng Zhou
TMS (The Minerals, Metals & Materials Society), 2012

VISCOSITY DETERMINATION OF THE FREEZE SLAG IN REACTION SHAFT OF FLASH SMELTING FURNACE

Jinliang Wang[1], Yanxin Wu[1], Liwei Liang[1], Chuanfu Zhang[2]

[1]School of Metallurgical and Chemistry Engineering, Jiangxi University of Science and Technology; Ganzhou, Jiangxi, 341000, China
[2]School of Metallurgical Science and Engineering, Central South University; Changsha, Hunan, 410083, China
Keywords: Flash Smelting Furnace; Reaction Shaft; Freeze Slag; Viscosity

Abstract

According to the reaction shaft operation characteristics during the flash smelting process, 15 groups of slag samples containing high Fe_3O_4 were prepared by some chemical reagents, and then the slag viscosities were measured using a RTW-10 type synthetic test instrument for melt physical property by the rotating cylinder method. The effects of Fe/SiO_2 ratio (m_{Fe}/m_{SiO_2}), Fe_3O_4 content ($w_{Fe_3O_4}$), Cu_2O content (w_{Cu_2O}), MgO content (w_{MgO}) and CaO content (w_{CaO}) on the slag viscosity were also studied. Results show that slag viscosity is decreased with the increase of temperature, m_{Fe}/m_{SiO_2}, w_{Cu_2O}, w_{MgO} and w_{CaO}, and with the decrease of $w_{Fe_3O_4}$, under the range of slag contents: m_{Fe}/m_{SiO_2} 1.36~1.78, $w_{Fe_3O_4}$ 17.83%~21.18%, w_{Cu_2O} 3.51%~8.34%, w_{MgO} 2.21%~6.57%, w_{CaO} 6.22%~9.87% and temperature range of 1250 °C~1450 °C. Only $w_{Fe_3O_4}$ and w_{CaO} have great influence on the slag viscosity when temperatures as high as 1400 °C or so. To form a freeze slag with higher viscosity inside the reaction shaft, $w_{Fe_3O_4}$ should be more than 20% and w_{CaO} should be less than 6%.

Introduction

Since its appearance in 1949, Outokumpu flash smelting technology has making continuous innovation and has become the most competitive intensified smelting technology [1], widely considered to be the standard clean smelting process [2]. At present, flash smelting technology is adopted to newly build or reconstruct most of the world's copper or nickel smelting enterprise [3]. Reaction shaft is the most important part of the flash smelting furnace. During the flash smelting process, reaction shaft must be able to withstand the following harsh conditions at the same time: 1) high temperature varying from 1400 °C to 1500 °C. 2) strong oxidative atmosphere containing 50% - 80% oxygen. 3) solid particles and melt with speed up to 100 m/s. 4) high acidic or basic slag with strong chemical corrosiveness. 5) smelting gas containing 50% - 80% SO_2. 6) matte with strong dissolution.

Especially now, as the Four High (High feed, High matte grade, High oxygen concentration, High volumetric heat capacity) technology [4] has being used to improve the single production ability of the flash smelting furnace, the furnace heat load has being increased correspondingly, and thus, the flash smelting furnace, especially the inner wall of reaction shaft, will be damaged more rapid [5]. Therefore, how to protect the reaction shaft is the main problem to be solved for intensified flash smelting process.

Viscosity is one of the important physical properties of slag. The research of influence factors on the slag viscosity is significant to form a freeze slag inside reaction shaft, with compact structure,

good heat insulation, certain intensity, appropriate thickness and reasonable distribution, to extend furnace life, to reduce energy consumption, and to promote production safety.

In recent years, several investigations have been conducted on slag viscosity. Sichen et al. studied experimentally of the viscosities in the $CaO-Fe_nO-SiO_2$ slags [6], Shahbazian studied experimentally of the viscosities in $CaO-FeO-SiO_2-CaF_2$ slags [7], Chengjun et al. studied viscosity and crystallization temperature of $CaO-SiO_2-Na_2O-CaF_2-Al_2O_3-MgO$ system [8], Chuanfu et al. measured the viscosity of high magnesium content slag of $FeO-SiO_2-CaO-MgO$ system [9], Zhenan et al. studied the effects of Al_2O_3 on viscosity of Ni electro-furnace slag [10], and Wright et al. studied the viscosity of a $CaO-MgO-Al_2O_3-SiO_2$ melt containing spinal particles [11].

However, compared with general smelting slag, the freeze slag contains higher Fe_3O_4 due to the slag fractional dissolution and oxidization inner the reaction shaft during flash smelting process [12], and the research on the viscosity of this kind of freeze slag has not been reported.

In this work, the viscosities of the freeze slag in reaction shaft of flash smelting furnace were measured experimentally by rotating cylinder method, and the relationship between the viscosity and the slag composition was also studied. The purpose of this research is to provide basic data for the mechanism research and industry application of the reaction shaft protection technology by freezing slag.

Experiment

Materials And Preparation Of Slag Samples

The materials used in the present work include reagent grade MgO, Al_2O_3, SiO_2, CaO, Cu_2O, Fe_3O_4, Fe_2O_3 and iron. While the Fe, Fe_3O_4 and Fe_2O_3 powder were dried at 393 K overnight, the CaO, MgO and SiO_2 powder was calcined at 1273 K for 12 hours in a muffle furnace to decompose any carbonate or hydroxide before use.

In order to prepare the slag, FeO was prepared by mixing stoichiometric Fe_2O_3 and pure iron powder and sintering in an iron crucible under Ar gas protection at 1573 K for about 8 hours. The preprocessed mixture was then mixed with other reagents and was packed in a corundum crucible. After the corundum crucible was placed in a resistance furnace, the reaction chamber was flushed by Ar gas for a couple of hours. Thereafter, a constant low flow of Ar (0.05 L/min) was maintained during the slag preparation. The slag sample was heated up to a temperature of 1550 °C and held at that temperature for more than 12 hours. After furnace cooling, the slag was taken out and accurately examined to ascertain that the sample had completely been melted. The slag was then broken into small pieces and was stored in bottle before being used in the viscosity measurement.

According to the actual freeze slag composition characteristics during the flash smelting process [12], 15 groups of slag samples containing high Fe_3O_4 were prepared. The measured composition of the slag samples is listed in Table I.

It can be seen from Table I that the test purpose of A groups from A1 to A3, B groups from B1 to B3, C groups from C1 to C3, D groups from D1 to D3 and E groups from E1 to E3 is to investigate the influence on slag viscosity (η) of the Fe/SiO_2 ratio (m_{Fe}/m_{SiO_2}), Fe_3O_4 content ($w_{Fe_3O_4}$), Cu_2O content (w_{Cu_2O}), MgO content (w_{MgO}) and CaO content (w_{CaO}), respectively.

It should be noted that the effect of the Al_2O_3 content on the freeze slag viscosity was not considered, since the Al_2O_3 content in freeze slag is very low and changes very little during the copper flash smelting practice.

Apparatus And Procedure

The rotating cylinder method was employed for viscosity measurements. Figure 1 shows the experimental equipment.

Table I. The measured composition of the slag samples

Group No.	MgO (wt %)	Al_2O_3 (wt %)	CaO (wt %)	Fe_3O_4 (wt %)	Cu_2O (wt %)	FeO (wt %)	SiO_2 (wt %)	m_{Fe}/m_{SiO_2}
A1	1.56	1.11	10.52	16.98	2.19	37.29	30.35	1.36
A2	1.55	1.22	11.17	17.71	2.32	38.58	27.45	1.56
A3	1.61	1.15	11.41	18.53	2.23	40.01	25.06	1.78
B1	1.63	1.35	12.61	17.53	2.57	40.01	24.3	1.80
B2	1.54	1.18	12.43	19.94	2.36	37.87	24.68	1.78
B3	1.48	1.24	11.94	21.18	2.65	36.82	24.69	1.78
C1	1.56	1.25	10.12	17.59	3.51	40.84	25.13	1.77
C2	1.63	1.31	12.31	16.35	5.63	39.16	23.61	1.79
C3	1.54	1.39	11.42	17.78	8.34	36.49	23.04	1.79
D1	2.21	1.58	12.01	16.39	2.64	40.53	24.64	1.76
D2	3.78	1.03	11.52	16.56	2.58	40.14	24.39	1.77
D3	6.57	1.29	11.08	18.26	2.43	36.85	23.52	1.78
E1	1.49	1.15	9.87	17.24	2.71	42.23	25.31	1.79
E2	1.46	1.21	7.98	16.78	2.65	43.71	26.21	1.76
E3	1.64	1.23	6.22	17.85	2.49	44.06	26.51	1.78

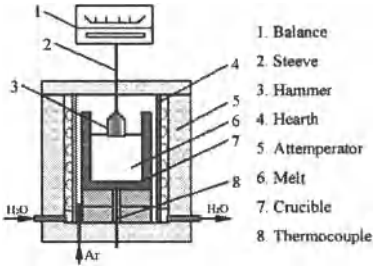

Figure 1. RTW-10 type synthetic test instrument for physical property of the melt

A $MoSi_2$ heated furnace with the highest temperatures up to 1600 °C was used for the measurements, and the variation of the temperature in the uniform temperature zone of the furnace was less than 0.5 °C in the entire experimental temperature range. A Pt-10 pct Rh/Pt thermocouple in an alumina attemperator was placed in contact with the bottom of the crucible so that the slag temperature could be measured accurately during the experiment. A stream of argon gas was introduced through the gas inlet near the bottom of the furnace. The gas was led out through the gas outlet on the top of the furnace. After flushing the reaction chamber for 1 hour, the flow rate of argon gas was reduced. Thereafter, a constant flow of Ar (about 0.2 L/min) was maintained during the entire course of the experiment.

The slag sample weighed by the balance about 180 g for each set of measurement, which corresponds to a slag depth of about 4 cm for a crucible diameter of 4.5 cm. The molybdenum

crucible with the slag sample was then positioned in the even temperature zone of the furnace. The slag was heated to a desired temperature at a heating rate of 5 K/min and held at that temperature for 20 minutes to reach thermal equilibration. When the thermal equilibrium was obtained, viscosity measurements were carried out. The viscosity measurements were carried out during the cooling cycle at a rate of 1 K/min.

Results and Discussion

Effect Of The Fe/SiO_2 Ratio On Viscosity

The effect of m_{Fe}/m_{SiO_2} on the slag viscosity (η) was investigated by changing the m_{Fe}/m_{SiO_2} but keeping the percentage of other components constant. The result is presented in Figure 2.

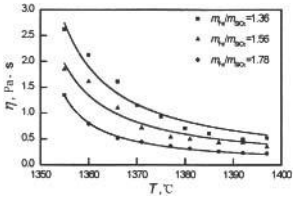

Figure 2. Effect of m_{Fe}/m_{SiO_2} on the freeze slag viscosity

It can be seen from Figure 2 that η is decreased with the increasing m_{Fe}/m_{SiO_2}. That is because the SiO_2 content in the freeze slag is reduced when m_{Fe}/m_{SiO_2} increases, and then the complex anion $Si_xO_y^{z-}$ is decreased accordingly, resulting in the decrease of the freeze slag viscosity.
It also can be seen from Figure 2 that the effect degree of m_{Fe}/m_{SiO_2} on the freeze slag viscosity declines slowly as the temperature (T) increases, and the effect becomes not quite apparent when T is close or up to 1400 °C. The reason may be that, according to the ionic theory, the complex anion $Si_xO_y^{z-}$ will be gradually dissociated as the temperature increases, and thus, there are mainly simpler anions with smaller ion radius at that high temperature.

Effect Of The Fe_3O_4 content On Viscosity

The effect of $w_{Fe_3O_4}$ on the slag viscosity (η) was investigated by changing the $w_{Fe_3O_4}$ but keeping the m_{Fe}/m_{SiO_2} and the percentage of other components constant. The result is presented in Figure 3.

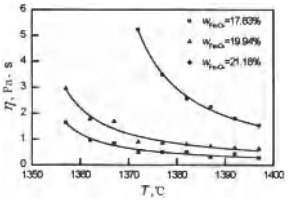

Figure 3. Effect of $w_{Fe_3O_4}$ on the freeze slag viscosity

It can be seen from Figure 3 that η is increased with the increasing $w_{Fe_3O_4}$, especially when $w_{Fe_3O_4}$>20%, η is increased rapidly. That is because Fe_3O_4 is a oxide with high melting point and big proportion. This feature is also an important reason for the freeze slag in reaction shaft of flash smelting furnace to resist the scour of high-speed melt flow and to protect the furnace wall.
The curve in Figure 3 also indicate that the effect degree of $w_{Fe_3O_4}$ on the freeze slag viscosity declines slowly as the temperature (T) increases.
Therefore, only when $w_{Fe_3O_4}$ is be more than 20 %, the viscosity of molten slag is so high (η>2.0 Pa.s) to form a freeze slag inside the reaction shaft, due to the inner chamber temperature of reaction shaft is up to 1400 °C~1500 °C.

Effect Of The Cu_2O content On Viscosity

The effect of w_{Cu_2O} on the slag viscosity (η) was investigated by changing the w_{Cu_2O} but keeping the m_{Fe}/m_{SiO_2} and the percentage of other components constant. The result is presented in Figure 4.

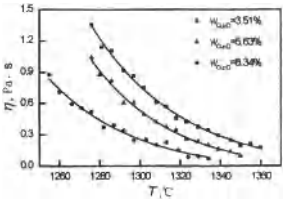

Figure 4. Effect of w_{Cu_2O} on the freeze slag viscosity

It can be seen from Figure 4 that η is decreased with the increasing w_{Cu_2O}. That is because the O^{2-} dissociated from Cu_2O can make the complex anion $Si_xO_y^{z-}$ split into some ions with simpler structure, resulting in the decrease of the freeze slag viscosity.
It also can be seen from Figure 4 that the effect degree of w_{Cu_2O} on the freeze slag viscosity declines slowly as the temperature (T) increases.

Effect Of The MgO content On Viscosity

The effect of w_{MgO} on the slag viscosity (η) was investigated by changing the w_{MgO} but keeping the m_{Fe}/m_{SiO_2} and the percentage of other components constant. The result is presented in Figure 5.

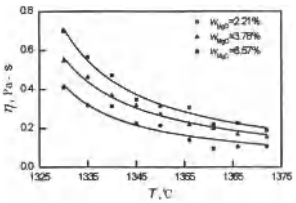

Figure 5. Effect of w_{MgO} on the freeze slag viscosity

It can be seen from Figure 5 that η is decreased with the increasing w_{MgO}. That is because, similar to w_{Cu_2O}, the O^{2-} dissociated from MgO can make the complex anion $Si_xO_y^{z-}$ split into some ions with simpler structure, resulting in the decrease of the freeze slag viscosity.
It should be noted that Cu_2O or MgO will dissolve out from liquid slag and form high melting point solids when w_{Cu_2O} or w_{MgO} is out of the content range in slag: w_{Cu_2O} 3.51%~8.34%, w_{MgO} 2.21%~6.57%, discussed in this work. And then, the freeze slag viscosity will be increased.

Effect Of The CaO content On Viscosity

The effect of w_{CaO} on the slag viscosity (η) was investigated by changing the w_{CaO} but keeping the m_{Fe}/m_{SiO_2} and the percentage of other components constant. The result is presented in Figure 6.

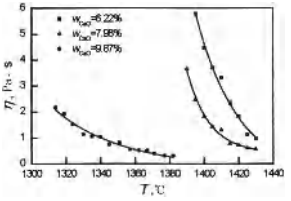

Figure 6. Effect of w_{CaO} on the freeze slag viscosity

It can be seen from Figure 6 that η is decreased rapidly with the increasing w_{CaO}. That is because the alkaline oxide CaO can easy supply O^{2-} to make the complex anion $Si_xO_y^{z-}$ split into some ions with simpler structure. But the effect trend will weaken as the temperature (T) increases. Therefore, in order to form a freeze slag with higher viscosity inside the reaction shaft, CaO flux should be reduce to decrease the amount of CaO content in freeze slag in flash smelting process.

Conclusion

In this work, the viscosities of the freeze slag in reaction shaft of flash smelting furnace were measured experimentally by rotating cylinder method, and the relationship between the viscosity and the slag composition was also studied. Results show that the slag viscosity is decreased with the increase of temperature and only $w_{Fe_3O_4}$ and w_{CaO} have great influence on the slag viscosity when temperatures is close or up to 1400 °C. The slag viscosity is decreased with the increase of m_{Fe}/m_{SiO_2}, w_{Cu_2O}, w_{MgO} and w_{CaO}, but with the decrease of $w_{Fe_3O_4}$.
In order to form a freeze slag with higher viscosity inside the reaction shaft, $w_{Fe_3O_4}$ should be more than 20% and w_{CaO} should be less than 6%, due to the inner chamber temperature of reaction shaft is up to 1400 °C~1500 °C.

Acknowledgement

This study was supported in part by the National Natural Science Foundation of China (50904027) and the Scientific Research Fund of Jiangxi Provincial Education Department, China (GJJ09241).

References

1. J.L. Wang et al., "Control Optimization of Copper Flash Smelting Process Based on Genetic Algorithms," *The Chinese Journal of Nonferrous Metals*, 17(1) (2007), 156-160.
2. R.R. Moskalyk and A.M. Alfantazi, "Review of Copper Pyro-metallurgical Practice: Today and Tomorrow," *Minerals Engineering*, 16(10) (2003), 893-919.
3. S. Fiscor, "Outokumpu Technology Makes Process Improvements Possible," *Engineering and Mining Journal*, 205(9) (2004), 43-45.
4. P. Hanniala, L. Helle and I.V. Kojo, "A Look into the Future of the Copper Smelting Business" (Paper presented at ICHNM' 2002 a New Century International Conference on Metallurgical High Technology and New Materials of Heavy Nonferrous Metals, Kunming, China, April, 2002), 19.
5. H.R. Chen et al., "Operation Optimization of Concentrate Burner in Copper Flash Smelting Furnace," *Transactions of Nonferrous Metals Society of China*, 14(3) (2004), 631-636.
6. F.Z. Ji and S. Seetharaman, "Experimental Studies of the Viscosities in the $CaO\text{-}Fe_nO\text{-}SiO_2$ Slags," *Metallurgical and Materials Transactions B*, 28(5)(1997), 827-834.
7. F. Shahbazian, "Experimental Studies of the Viscosities in the $CaO\text{-}FeO\text{-}SiO_2\text{-}CaF_2$ Slags," *Scandinavian Journal of Metallurgy*, 30(5)(2001), 302-308.
8. C.J. Liu and M.F. Jiang, "Viscosity and Crystallization Temperature of $CaO\text{-}SiO_2\text{-}Na_2O\text{-}CaF_2\text{-}Al_2O_3\text{-}MgO$ System," *Journal of Northeastern University*, 23 (7) (2002), 656-659.
9. D.W. Zeng et al., "Viscosity Determination of High Magnesium Content Slag of $FeO\text{-}SiO_2\text{-}CaO\text{-}MgO$ System," *Journal of Central South University of Technology*, 28 (4) (1997), 342-346.
10. Z.N. Jin et al., "The Effects of Al_2O_3 on Viscosity of Ni Electro-Furnace Slag," *Journal of Northeastern University*, 23 (9) (2002), 848-850.
11. S. Wright, "Viscosity of a $CaO\text{-}MgO\text{-}Al_2O_3\text{-}SiO_2$ Melt Containing Spinal Particles at 1646 K," *Metallurgical and Materials Transactions B*, 31 (1) (2000), 97-104.
12. Z. Chen, "A Research on Mathematical Models of Flash Smelting System and On-line Simulative Monitoring of Frozen Profile of Reaction Shaft in Copper Flash Furnace" (Ph.D. thesis, Central South University, 2002), 54-57.

3rd International Symposium on High-Temperature Metallurgical Processing
Edited by: Tao Jiang, Jiann-Yang Hwang, Patrick Masset, Onuralp Yucel, Rafael Padilla, and Guifeng Zhou
TMS (The Minerals, Metals & Materials Society), 2012

Effect of MgO Content on Melting Features and Viscosity of SiO2-CaO-MgO-Al2O3-FeO Slag in Nickel Laterite Metallurgy

Xuewei Lv[1], Cheng Pan[1], Chenguang Bai[1] , Guibao Qiu[1], Meilong Hu[1]

[1]College of Materials Science and Engineering ,
Chongqing University , China

Keywords: MgO content, Melting features, Viscosity

Abstract

Physic-chemical properties of slag at high temperature play an important role in the pyrometallurgical process of production of ferronickel alloy. It determines the operation efficiency, metal recovery ratio, energy consumption and the distribution of elements like S and P between the slag and metals. In the present work, the effect of MgO content in the slag on melting features and viscosity of the slag was investigated. The MgO content in the SiO_2-CaO-MgO-Al_2O_3-FeO in the quinary slag system varied from 14.5% to 22.5%. The results shown that all slag samples begin to softening at the same temperature, the softening temperature, melting temperature, flowing temperature decrease with the increase of MgO content when the MgO content is in range of 14.5 and 20.5 pct mass, and when MgO content up to 22.5 percent, the temperatures increase sharply. Besides the inflection point temperature of viscosity-temperature curve increase with the increase of MgO when the MgO content is in range 16 and 22.5 pct mass.

Introduction

Nickel is very important to modern society, without it, we would not be able to share many things in our daily life, such as airplanes, computers and many stainless steel appliances in our homes and workplaces1.. It is the essential element of the stainless steel making, and about 65% of the nickel consumed in the world is used to make stainless steel2., so with the increase of stainless steel, the nickel production and demand has continued to increase3..

Nickel is produced from two distinct ore types: nickel sulfide deposits and oxide nickel laterite deposits. The great majority of world's known nickel resources are contained in laterite deposits3.. The laterite ores are normal classified into two groups: the high-iron laterite ore and high-magnesia laterite ore1.. Typical composition of high-magnesia laterite ore is in the range 1-3%, and these ores are suitable for pyrometallurgical process to produce ferronickel4..

Normally, laterite ores contain high silica and magnesium, especially for the high-magnesium laterite ore. So in the most widely used process: Rotary kiln – EAF route, there would form a great number of slag. The physic-chemical properties of the slag play an important role to affect the operation efficiency since the slag properties have a significant influence on nickel and iron recovery ration, energy consumption, sulfur and phosphorus distribution ratio between slag and metal etc5, 6.. So it is necessary to investigate the properties of the slag to increase the metal recovery ratio, save energy, increase sulfur and phosphorus capability of slag. The physic-chemical of slag includes melting feature, viscosity, density etc. These properties are dependent on composition and structure of the slag. So, it is important to investigate the effect of composition on physical properties. Meanwhile, due to the content of MgO in high-magnesium laterite is in the range 15-25%, for this reason, the influences of MgO content in the slag on melting temperature and viscosity were mainly investigated in this study.

Experimental

Materials and Preparation of the Slag

The material used in the present work is shown in Table 1. The slag was come from a ferroalloy company. Reagent-grade SiO2, CaO, MgO, Al2O3 were used to adjust the content of MgO in the slag being in the range of 15% and 23%, at the same time, the ratio of SiO2, Al2O3 and CaO was constant, and no FeO was added. In order to make the composition be uniform, the mixture (raw slag and reagent) was re-melted at 1450℃ in a MgO crucible at Ar atmosphere for 1 hour before the measurements of melting feature and viscosity. After homogenization, the slag melt was quenched and was then crushed for later experiments. The chemical composition of the re-melted slag is shown in Table 2. The slag which was used to measure the melting feature was milled to make the particle size was less than 0.074mm, then the fines was pressed in a cylindrical sample mode to obtain the test samples with a size of 2×3mm.

Table 1 Chemical Compositions of the Raw Slag

Composition	SiO_2	CaO	Al_2O_3	MgO	FeO	Ni	Cr_2O_3
Content/%	42.16	18.84	5.99	20.8	7.72	0.04	1.5

Table 2 Chemical Compositions of the Slag Studied in the Present Work

Sample	SiO_2	CaO	Al_2O_3	MgO	FeO	$(CaO+MgO+Al_2O_3+FeO)/SiO_2$
1#	49.65	20.7	6.21	14.59	5.42	0.945015
2#	47.89	20.26	6.06	16.05	5.96	1.009188
3#	46.13	19.83	5.92	17.51	6.5	1.078691
4#	44.37	19.39	5.77	18.97	7.04	1.153257
5#	42.61	18.95	5.63	20.43	7.58	1.234217
6#	41.28	18.45	5.47	22.45	7.56	1.306444

Experimental Apparatus and Procedure

(1) Melting Features

Melting features measurement system includes three parts: sample hold, heating system, image system. Measuring mechanism of this system is that the sample height change with the material melting as raising temperature. Sample was placed in the center of the heating furnace, and temperature raise at the speed at 15℃ Per minute. According to the references7., the soften temperature, melting temperature, flow temperature are defined as the temperature at which the sample height decrease to 75%, 50%, 25% of the original height respectively. And the start soften temperature is considered as the temperature at which the sample height start to decrease.

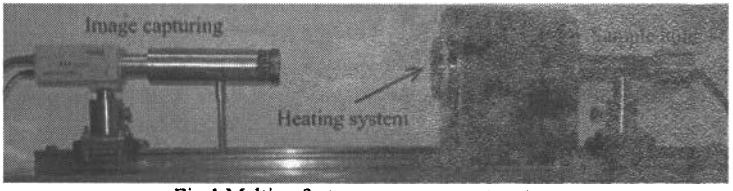

Fig.1 Melting features measurement system

(2) Viscosity

The rotating cylinder method was employed for viscosity measurements. The experimental apparatus, measurement principle and the calibration method had been explained in detail in earlier literatures 5, 6, 8, 9.. In each run, 120 grams slag powder was hold in a MgO crucible(φ45 ×60mm), and it was placed in a graphite crucible. The graphite crucible was locked into the reaction chamber of MoSi2 furnace in an Ar atmosphere in the heating process. The temperature was controlled by a Pt-30mass%Rh/Pt-6mass%Rh thermocouple and a proportional integral differential (PID) controller. The temperature fluctuations was about ±2℃. In order to make the slag melt completely, the slag was molten for 2 hours when the temperature reached to 1470℃ which was based on the melting temperature. Then, the molybdenum spindle was immersed into the slag and was held in the middle of the melt. When the temperature was kept stable for about 20 minutes, then the viscosity was continuously measured while the temperature fallen at the speed of 5℃ per minute. When the viscosity up to 2 Pa·s, the measurement was stopped, then the temperature was reheated to 1450℃. After keeping the temperature unchanged for about 1 hour, the isothermal viscosity was measured. Finally, the spindle was taken out from the melt slag.

Results and Discussion

Melting Features

Fig.2 shows the effect of MgO content on the melting features of SiO_2-CaO- MgO- Al_2O_3-FeO slag. From Fig.2, it can be obtained that all the slag have the same begin to softening temperature which is about 1230℃, that means there exists same low melting temperature materials in different slag. The softening temperature, melting temperature and flowing temperature decrease with the increase of MgO content when the MgO content is in the range of 14.5 and 20.5 pct mass, and as MgO content is up to 22.5 pct mass the temperatures increase sharply. The lowest melting temperature is lower than the highest melting temperature about 40℃, that is important for energy saving in pyrometallurgical process of production of ferronickel alloy. The temperature interval between begin to softening temperature and softening temperature is bigger than 40 ℃, but the temperature difference between softening temperature and melting temperature or between melting temperature and flowing temperature is smaller than 10℃. From the above, it can obtain that the main material phases of the samples have the similar tendency of the melting temperature with the content of MgO.

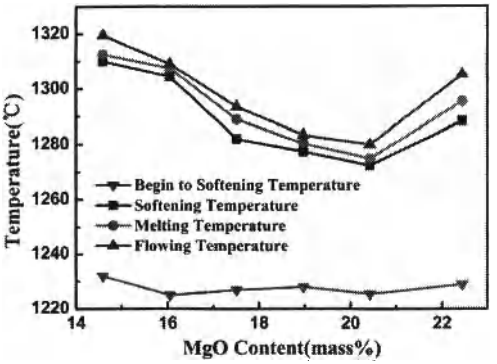

Fig.2 The effect of MgO content on the Melting Feature of slag

Viscosity

Fig.3 shows the viscosity of the slag by varying MgO content as a function of temperature. In Fig.3, it can be observed that the viscosity curve doesn't have obvious inflection point temperature when MgO content is 14.5 pct mass, it means that in other slag which have more MgO(>15%), there is some solid phase formed during the cooling process. The inflection point temperature increases with the increase of MgO content when the MgO content is in the range of 17.5 and 22.5 pct mass. The slag with 17.5 pct mass MgO content has the lowest inflection temperature and the widest solid-liquid coexisting region, however the slag with 16 pct mass MgO has the smallest viscosity when the temperature is in the range of 1370℃ and 1470℃.

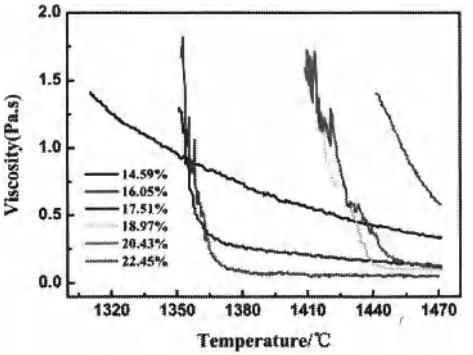

Fig.3 Viscosity of different slag by varying MgO content as a function of temperature

Conclusions

The effect of MgO content in the slag on melting features and viscosity of the slag was investigated in present study. The results shown that:

(1) The softening temperature, melting temperature, flowing temperature decrease with the increase of MgO content when the MgO content varies from 14.5% to 20.5%, and when MgO content up to 22.5%, the temperatures increase sharply.

(2) the inflection point temperature of viscosity-temperature curve increase with the increase of MgO when the MgO content is in range 16 and 22.5 pct mass.

Reference

1. Bergman, R.A., *Nickel production from low-iron laterite ores: Process descriptions (vol 96, pg 137, 2003).* Cim Bulletin. **96**(1073)(2003): 67-67.
2. Kim, J., et al., *Calcination of low-grade laterite for concentration of Ni by magnetic separation.* Minerals Engineering. **23**(4)(2010): 282-288.
3. Pan, C., et al., *Gaseous Reduction of Pellets of Laterite Ore Containing Carbon.* Metalurgia International. **16**(1)(2011): 5-9.
4. *<the past and the future of nickel laterites.pdf>.*
5. Lee, Y.S., et al., *Influence of basicity and FeO content on viscosity of blast furnace type slags containing FeO.* Isij International. **44**(8)(2004): 1283-1290.
6. Kim, J.R., et al., *Influence of MgO and Al2O3 contents on viscosity of blast furnace type slags containing FeO.* Isij International. **44**(8)(2004): 1291-1297.
7. Lv, X., et al., *Behavior of liquid phase formation during iron ore sintering.* ISIJ International. **51**(5)(2011): 722-727.
8. Shahbazian, F., et al., *Experimental studies of viscosities of some CaO-CaF2-SiO2 slags.* Ironmaking & Steelmaking. **26**(3)(1999): 193-199.
9. Ji, F.Z., S.C. Du, and S. Seetharaman, *Experimental studies of the viscosities in the CaO-FenO-SiO2 slags.* Metallurgical and Materials Transactions B-Process Metallurgy and Materials Processing Science. **28**(5)(1997): 827-834.

3rd International Symposium on High-Temperature Metallurgical Processing
Edited by: Tao Jiang, Jiann-Yang Hwang, Patrick Masset, Onuralp Yucel, Rafael Padilla, and Guifeng Zhou
TMS (The Minerals, Metals & Materials Society), 2012

INFLUENCE OF SILICON CONTENT IN HOT METAL ON MINERALOGICAL CHARACTERIZATION AND PHYSICO-CHEMICAL PROPERTIES OF VANADIUM SLAG

Chongyang Zhao, Bing Xie, Qingyun Huang, Xiaopeng Zhen, Xie Zhang

College of Materials Science and Engineering, Chongqing University,
Chongqing 400044, P. R. China

Keywords: Vanadium slag, Mineralogical characterization, Melting point, Viscosity

Abstract

Extracting vanadium from vanadium containing hot metal into vanadium slag by BOF is the main vanadium production process in China. In this paper, the influence of Si content in hot metal on the quality of vanadium slag is analyzed. Synthetic vanadium slag with different SiO_2 content were melted at 1673 K and then cooled to 303K at the cooling rate of 3℃/min. Optical microscopy, SEM, EDS and XRD were used to analyze the mineralogical phases and crystallization behavior of vanadium slag. The results show that vanadium slag mainly contains spinel phase and silicate phase; V is enriched in the spinel phases while Si is concentrated in Fe_2SiO_4 $CaFeSi_2O_6$ and $(Fe,Mn)_2SiO_4$ as silicate phase. The melting point of slag increases gradually with the addition of SiO_2; whereas viscosity decreases with an addition of 15~19% SiO_2 and increases with an addition of 19~27% SiO_2.

Introduction

Vanadium is an important element which is used almost exclusively in ferrous and non-ferrous alloys. The major vanadium products include FeV, V_2O_5, V_2O_3, VN and Al-V-Ti alloy. Furthermore, vanadium slags are mostly produced by oxidizing the elements in V-containing hot metal during a duplex refining process. Therefore, the process of removing vanadium from hot metal has its significance on the subsequent process[1].

The extraction of vanadium is greatly affected by the mineralogical composition of vanadium slag[2], the distribution of the elements between the spinel and silicate phases and its physic-chemical properties. These characteristics of vanadium slag have been studied in some details. It has been reported that Si mainly exists mainly in the form of silicate which wraps the spinel crystals while small amount of Si stands as phosphorus quartz or diopside[2] Chen *et al.*[3, 4] points out, when SiO_2 content in vanadium slag increased every 1%, V_2O_5 decreased 1.48%. Moreover, silicate phases would embarrass the oxidation of V-containing spinels through decreasing the exposing probability[5]. Meanwhile, melting point and viscosity of vanadium slag has been greatly influenced by the SiO_2 content. Therefore, this work attempts to analyze the above-mentioned questions systematically.

Experimental

Experimental setup and sample

It has been reported that SiO_2 plays a significant role in the formation and growth of spinel and affects the quality of slag directly. Representative vanadium slag sample is obtained from Pan-steel in China; its composition is analyzed and listed as S2 in Table I. The content of SiO_2 in vanadium slag is set around 15~27% according to the field data in Pan-steel.

So the compositions of slag samples are listed in Table I. A mixture slag of 100g charged in an MgO crucible were heated and melted in furnace at 1673 K and then cooled to 303K at the cooling rate of 3℃/min. The quantitative phase composition of the slag is determined by optical microscope, scanning electron microscopy (SEM), energy disperse X-ray spectrum (EDS) and X-ray diffraction (XRD) analyses. The temperature when vanadium slag melted to the shape of hemisphere is defined as its melting point. The viscosity of slag was measured by flowing length method and it will be illustrated specifically later.

Table I. Chemical compositions of experimental slags, wt-%

Sample	SiO_2	CaO	TiO_2	V_2O_3	P	MgO	MnO	FeO
S1	15.00	4.0	10	8.00	0.3	3.0	10	37.00
S2	19.00	4.0	10	8.00	0.3	3.0	10	37.00
S3	23.00	4.0	10	8.00	0.3	3.0	10	37.00
S4	27.00	4.0	10	8.00	0.3	3.0	10	37.00

Measurement of the viscosity of vanadium slag

The viscosity of vanadium slag cannot be measured by the conventional method of cylinder rotation since its high content of FeO and high melting point. However, the flowing length method cannot be affected by these conditions. It thus is suitable for measuring the viscosity of vanadium slag.

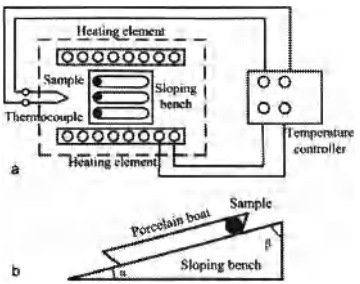

Figure.1. Schematic diagram of measuring viscosity

Measurement apparatus is schematically shown in Figure 1[6]. This method assumes that there is enough liquidity, so that the flow length of the molten slag has a relationship with the flow performance (viscosity, interfacial tension, wetting Angle), flow time etc. The relations can be expressed as equation (1):

$$L = \frac{1}{\rho}\sqrt{r/2}\cdot\sqrt{\sigma\cdot\cos\theta/\eta}\cdot\sqrt{t} \qquad (1)$$

Where, L- flow length, mm

σ- interfacial tension of slag, N/m

θ- wetting angle (°)

η- viscosity of slag, Pa • s

t- time, s

The apparatus was calibrated by the samples listed in Table II. These samples were made to the same shape and weight (0.5g). The temperature was set at 1100℃, and kept for two minutes. At the same time, the porcelain boat filled with slag sample was placed on the inclined plane (15°) of a firebrick. The firebrick was then put into the furnace. The sample was melted at 1400℃ for 10 min. After that, the samples were taken out to measure the length of the slag with vernier caliper when they have been cooled down in the air. At last, use the same method to measure the flow length of vanadium slags.

Table II. Composition of reference slag, wt%

Sample	CaO	SiO_2	Al_2O_3	Na_2CO_3	CaF_2	$\sum$
1	39.47	31.13	6	15.39	14.4	106.39
2	36.88	33.72	6	15.39	14.4	106.39
3	35.41	35.19	6	15.39	14.4	106.39
4	33.81	36.79	6	15.39	14.4	106.39
5	32.06	38.54	6	15.39	14.4	106.39
6	30.13	40.47	6	15.39	14.4	106.39
7	28.00	42.60	6	15.39	14.4	106.39
8	22.99	47.61	6	15.39	14.4	106.39
9	20.01	50.59	6	15.39	14.4	106.39
10	18.71	52.29	6	15.39	14.4	106.79
11	16.64	53.96	6	15.39	14.4	106.39

Table III. Flowing length of reference slag, mm

NO.	1	2	3	4	5	6	7	8	9	10	11
1	38.16	30.32	29.63	29.14	29.18	26.79	26.38	26.58	24.33	24.97	19.45
2	48.96	30.01	29.63	28.99	26.35	28.07	26.22	24.49	24.17	22.92	18.79
3	47.09	30	26.58	27.39	27.35	29.54	—	24.43	24.2	23.38	—

The equation of viscosity can be deduced from these data by SPSS software:

$$Y = 51374.269/x^3 \tag{3.2}$$

The correlation coefficient is 0.994, is high enough to be used for the follow-up measurement of slag viscosity.

Results and discussion

Mineralogical chacterization of vanadium slag

It is widely known that vanadium is multivalent element which has multiple oxidation states of VO, V_2O_3, V_2O_4 and V_2O_5 [7]. However, during the process of vanadium oxidation in converter, V is dominantly 3+ and forms stable spinel phases via react with iron oxides [8].

As shown in Figure 2(a), vanadium slag mainly contains the spinel and silicate phase. The white one is V-containing spinel phase while Si mainly appears in silcate phase. Figure 2(b) (c) showed the tridimensional spinel. The spinel is wrapped by the silicate phase.

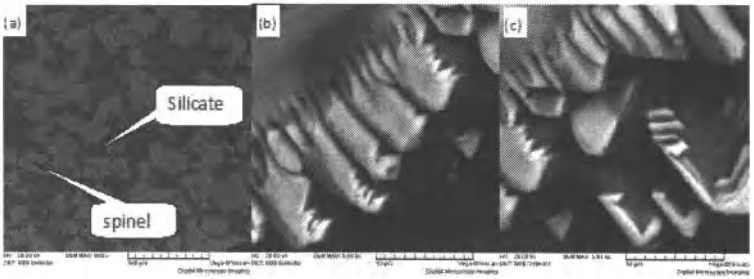

Figure.2. Image (SEM) of vanadium slag

Figure 3 gives the results of map scan, and Table IV illustrates the phase composition of sample 1 analyzed by EDS. From these photographs, it can be clearly seen that the distribution of the main elements. Almost the entire V is concentrated in the spinel phase, while Si and Ca are existed in the silicate phase. Fe, O, Ti are existed in both of the two phases. But different from the distribution of the O, most of the Fe and Ti appears in the spinel phase. The distribution ratio of Fe, O and Ti between the spinel and silicate phase is 31/4, 1/2, and 48/9. Still there is a little Mg in the middle part of the silicate phase.

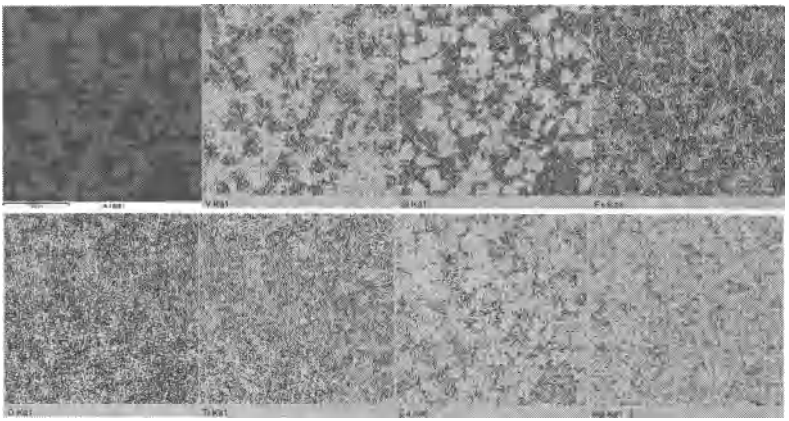

Figure.3. Map results of vanadium slag

Table IV. EDS results of sample S1, wt%

phase	O	Si	Mg	Ca	Ti	V	Fe	total
Spinel	19.93		1.51		12.51	11.55	47.17	100
Silicate	40.26	21.52		14.04	2.56		14.55	100

In order to study the phase composition of the vanadium slag, sample S1 was analyzed by XRD and the result is given in Figure 4. The analyses of XRD pattern and EDS demonstrate

that Fe_2VO_4, Fe_2TiO_4 and Fe_2SiO_4 are the main phase in vanadium slag. Still, little $CaFeSi_2O_6$, $(Fe,Mn)_2SiO_4$, MnV_2O_4, $MgTi_2O_4$, MgV_2O_4 and $FeMn_2O_4$ are also found in the slag.

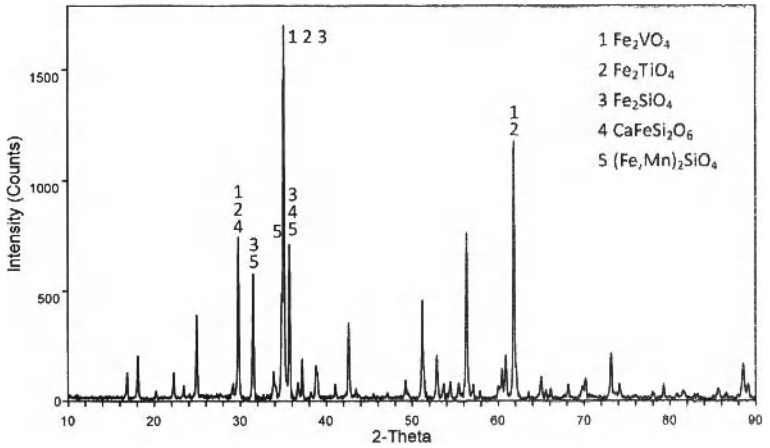

Figure.4. X-ray diffraction pattern of slag S1

Influence of Si content on the melting point of vanadium slag

The results of the melting point of samples have been shown in Table V and Figure 5.

Table V. The melting point of samples,℃

Sample	1	2	3	average
S1	1255	1269	1271	1265
S2	1312	1302	1311	1308.3
S3	1322	1322	1311	1321.7
S4	1337	1358	1347	1347.3

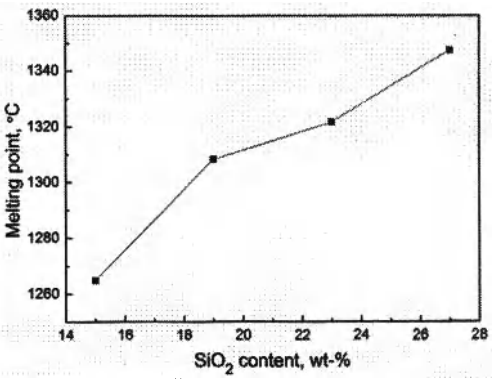

Figure.5. The relation between melting point and SiO_2 content

As can be seen from Figure 5, the melting point of vanadium slag would be higher when increasing the SiO_2 content in the slag. This is because the pyroxene (melting point: 1390℃[9]) and fayalite (melting point: 1205℃) in vanadium slag are tend to saturated while the amount of quartz (melting point: 1670℃) increases with the increasing with the increasing of SiO_2 and this would result in a rise in the melting point of vanadium slag.

Influence of the Si content on the viscosity of vanadium slag

With the method illustrated in previous section, the viscosity of vanadium slag were achieved and given in Table VI and Figure 6.

Table VI. Viscosity of samples

sample	first/mm	second/mm	third/mm	average/mm	viscosity/Pa•s
S1	34.94	29.87	58.01	40.94	0.749
S2	67.23	51.39	38.94	52.52	0.355
S3	29.86	67.37	50.07	49.10	0.434
S4	31.26	36.41	42.39	36.69	1.040

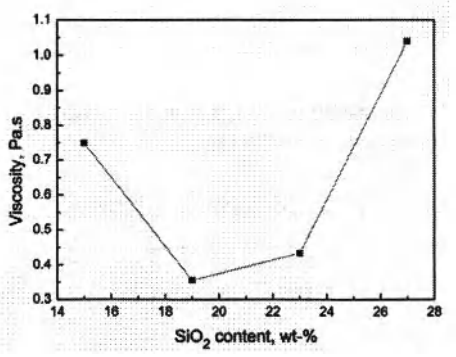

Figure.6. The relation between viscosity and SiO_2 content

The basicity (CaO/SiO_2) of vanadium slag in Pan-steel is between 0.15 and 0.27, and this is referred as acid slag. The melt viscosity depends mainly on the size of Si-O composite anion in slag[10]. A decline of O^{2-} can be seen in the molten slag when the content of SiO_2 increased, and which would result in the formation complicated ion such as $Si_2O_7^{6-}$, $Si_3O_9^{6-}$ and $Si_4O_{12}^{6-}$ with SiO_4^{4-}. The steps are as follows[11]:

$$SiO_2+2O^{2-}=SiO_4^{4-}$$
$$SiO_4^{4-}+SiO_4^{4-}=Si_2O_7^{6-}+O^{2-}$$
$$Si_2O_7^{6-}+SiO_4^{4-}=Si_3O_9^{6-}+2O^{2-}$$
$$Si_3O_9^{6-}+SiO_4^{4-}=Si_4O_{12}^{6-}+O^{2-}$$
$$\cdots\cdots$$

The more complicated, the larger radius of the Si-O complex compound ion will be and hence causes an increasing of the viscosity of the slag. Vanadium slag is an extremely complex slag system. It can be seen in Figure 6 that the viscosity of vanadium slag shows a tendency that reducing first and then increased with the increase of the content of SiO_2 at 1400℃. The viscosity ranges from 0.1 to 1.0 Pa•s and a transition can be seen at the SiO_2

content of 19%. This can be interpreted that when the SiO_2 content is low, it would be easier for SiO_2 to react with FeO and MnO and engender low melting point silicate phase such as fayalite, and which would lead to a smaller viscosity [12], lower melting point, and better liquidity of the slag. When content of SiO_2 exceeds 19%, the amount of quartz would increase with the increase of the content of SiO_2, and which would result in a rise in viscosity of the slag. Furthermore, SiO_2 can form a series of complex anions, which can also cause an increase in the viscosity. The industry production of Pan-steel shows that SiO_2 can be used in a certain range to dilute the slag, and improve the liquidity of vanadium slag. This is accord with the results of experiment.

Conclusions

According to the current situation of Pan-steel on extracting vanadium from hot metal, a series of experiments were designed to research on the influence of Si content in hot metal on the mineralogical characterization and physico-chemical properties of vanadium slag. The following conclusions can be drawn from the present work:

(1) The main phases of vanadium slag are spinel and silicate phase. For the spinel phase, Fe_2VO_4 is dominated and a small amount of other spinels such as Fe_2VO_4, Fe_2TiO_4, MnV_2O_4, $MgTi_2O_4$, MgV_2O_4 and $FeMn_2O_4$ are also existed. The silicate phase exists mainly in the form of fayalite. Besides, a small quantity of $CaFeSi_2O_6$ and $(Fe, Mn)_2SiO_4$ also exists in silicate phase.

(2) The melting point of vanadium slag increases gradually with an addition of SiO_2 in the range of 15-27%.

(3) The viscosity of vanadium slag shows a trend to be lower with addition of 15~19% SiO_2 and higher with addition of 19~27% SiO_2.

References

[1] G. P. Zhang, "Effect of phase structure and chemical composition of vanadium slag on degree of conversion in the roasting," *Ferroalloy Plant of Maanshan*, 5 (1991), 17-19.

[2] L. A. Smirnova, et al., "Vanadium slags obtained on removing vanadium from low silicon hot metal in the oxygen converter," *Steel in Translation*, 5 (2010), 472 - 478.

[3] D. Chen and S. Yang, "Systematic evaluation of the quality of vanadium slag," *Hebei Metallurgy*, 73 (1993), 19-23.

[4] D. H. Chen and S. D. Yang, "Research on the formation of vanadium slag," *Hebei Metallurgy*, 1 (1993), 19-23.

[5] J. Diao, et al., "Growth of spinel crystals in vanadium slag and their characterisation," *Crystal Research and Technology*, 44 (2009), 707-712.

[6] J. Zeng, "Research on composition and properties of continuous casting mold fluxes," Iron Steel Vanadium Titanium, 23 (2002), 47-53.

[7] K. Righter, S. R. Sutton, M. Newville, L. Le, C. S Schwandt, H. Uchida, B. Lavina, and R. T. Downs, Am. Mineral.91, 1643 (2006).

[8] Y. Qu, Steelmaking Theory, 2nd edition. (Metallurgical Industry Press, Beijing, 1994), p. 175.

[9] G. Liang and X. Fang, " Research on the characteristics of diopside and use in ceramics," *Guangdong Construction News*, B03 (2007), 1-4.

[10] X. Huang, *The principle of the ferrous metallurgy*, (Metallurgical Industry Press, Beijing,

2008).
[11] R. Tan, "Application of vanadium and vanadium alloy," *Iron Steel Vanadium Titanium*, 1 (1987), 16-22.

[12] A.L.Li. Study on deoxidize the slag with high vanadium, *Degree thesis of Kunming University of Science and Technology*,2006.

3rd International Symposium on High-Temperature Metallurgical Processing
Edited by: Tao Jiang, Jiann-Yang Hwang, Patrick Masset, Onuralp Yucel, Rafael Padilla, and Guifeng Zhou
TMS (The Minerals, Metals & Materials Society), 2012

ANALYSIS OF INFLUENCE FACTORS ON THE MELTING POINT OF THE FREEZE SLAG INSIDE FLASH SMELTING FURNACE BRICKLESS REACTION SHAFT

Jinliang Wang[1], Chuanfu Zhang[2]

[1]School of Metallurgical and Chemistry Engineering, Jiangxi University of Science and Technology; Ganzhou, Jiangxi, 341000, China
[2]School of Metallurgical Science and Engineering, Central South University; Changsha, Hunan, 410083, China
Keywords: Brickless Reaction Shaft, Freeze Slag, Melting Point

Abstract

Brickless reaction shaft is the latest progress for flash smelting furnace. However, there are many factors influence the melting point of the freeze slag inside brickless reaction shaft, and their variational regularities are not obvious, thus, it is difficult for conventional methods to analyze accurately the complex data. In this research, the experiment data of slag melting point were processed based on optimal discrimination plane. For this method, two orthogonal vectors were firstly built up based on the Fisher's criterion, and then the experiment data were projected onto the two vectors, thus, two-dimensional feature vectors were extracted as criteria to determine the factors effect degree on the slag melting point. Results show that the CaO content is the greatest factor to the melting point of the freeze slag inside brickless reaction shaft, the content of Fe_3O_4, SiO_2, Cu_2O and MgO is the second, and the FeO content is the last.

Introduction

Brickless reaction shaft is the latest progress of flash smelting furnace reaction shaft. To research the influence factors on the slag melting point inside the brickless reaction shaft is significant to form freeze slag with compact structure, good heat insulation, certain intensity, appropriate thickness and reasonable distribution, to extend furnace life, to reduce energy consumption, and to promote safe production.

However, due to the complex components, there are many factors influence the melting points of the freeze slag inside brickless reaction shaft, and their variational regularities are not obvious. Therefore, it is difficult for conventional methods, such as variance analysis, data fitting, etc., to analyze accurately the complex experiment data.

Pattern recognition can easily classify information, even if there are many influencing factors. For pattern recognition, there are some sub-disciplines such as discriminant analysis, feature extraction, error estimation, cluster analysis (together sometimes called statistical pattern recognition), grammatical inference, parsing and matching (sometimes called syntactical and structural pattern recognition) [1, 2].

The theory of statistical pattern recognition has been largely developed since 1960s. And some major developments have been made, including the formulation of pattern recognition as a Bayes decision theory problem [3], nearest neighbor decision rules (NNDRs) and density estimation[4], use of Parzen density estimate in nonparametric pattern recognition [5], leave-one-out method of error estimate [6], use of statistical distance measures and error bounds in feature evaluation[7], Fisher linear discriminant and multicategory generalizations[8,9], supervised parameter

estimation and unsupervised learning by decomposition of mixture densities [10], K-mean algorithm [11,12,13], and similarity-based methods [14], etc.
Optimal Discrimination Plane (ODP) approach was developed by Fisher's criterion method, which is a clustering method developed during 1930s, but till 1970s the second orthogonal vector with greatest deviation from the one-dimensional Fisher vector was proposed by Sammon. Thus when the train samples are projected onto the two orthogonal vectors, two-dimensional view come into being, named ODP [15,16].
In this paper, ODP was applied to analyze the influence factors on the melting point of the freeze slag inside brickless reaction shaft, to seek an effective way to process complex experiment data.

ODP Data Analysis Principle

ODP is a special case of multiple discriminant analysis, so its principle can be discussed from the multiple discriminant analysis process.
It is assumed that there are C classes, and $X_i (i = 1,2,\cdots,C)$ represents the C groups of samples, one of which can be expressed by $X = [x_1, x_2, \cdots, x_p]^T \ (X \in X_i)$, where p is the number of factors.
The analysis aim is to find the transform T to make Y has the biggest distinguish, which is given by formula (1).

$$Y = T^T X = \begin{bmatrix} T_1^T \\ \vdots \\ T_d^T \end{bmatrix} X = \begin{bmatrix} Y_1 \\ \vdots \\ Y_d \end{bmatrix} \tag{1}$$

where T is $d \times d$ matrix, Y is a d-dimensional column vector.
In order to deduce the transformation, the discrimination criteria R is defined as follow:

$$R = \frac{P^T B P}{P^T W P} \tag{2}$$

where $P = [p_1, p_2, \cdots p_p]^T$ is the discrimination vector need to ascertain, R is among-class matrix, W is the summation of within-class matrixes. They are given by following formulae.

$$B = \sum_{i=1}^{C} N_i [m_i - m][m_i - m]^T \tag{3}$$

$$W_i = \sum_{X \in X_i} [X - m_i][X - m_i]^T \tag{4}$$

$$W = \sum_{i=1}^{C} W_i \tag{5}$$

$$m_i = [m_{i1}, m_{i2}, \cdots m_{ip}]^T \tag{6}$$

$$m = [m_1, m_2, \cdots m_p]^T \tag{7}$$

where N_i and m_i are the number and the average vector of the class i samples, respectively, and m is the average vector of all samples.

In order to get the best values of P, the formula (8) is constructed as follow.

$$\frac{\partial R}{\partial P}=\frac{\partial}{\partial P}\left(\frac{P^{\mathrm{T}}BP}{P^{\mathrm{T}}WP}\right)=\frac{2}{(P^{\mathrm{T}}WP)^2}[(P^{\mathrm{T}}WP)BP-(P^{\mathrm{T}}BP)WP]=0 \tag{8}$$

then the equation (10) can be deduced from formula (8) on the assumption of formula (9).

$$\lambda=\frac{P^{\mathrm{T}}BP}{P^{\mathrm{T}}WP} \tag{9}$$

$$(B-\lambda W)P=0 \tag{10}$$

To solve the formula (10) is equal to solve the follow characteristic equation:

$$|B-\lambda W|=0 \tag{11}$$

Following are the deduce process of solving the equation (11).

$$B-\lambda W=WW^{-1}(B-\lambda W)=W(W^{-1}B-\lambda I) \tag{12}$$

$$|W(W^{-1}B-\lambda I)|=|W||(W^{-1}B-\lambda I)| \tag{13}$$

$$|(W^{-1}B-\lambda I)|=0 \quad (if \quad |W|\neq 0) \tag{14}$$

where W^{-1} and B can be computed based on the samples. Thus, the root λ of equation (14) can be calculated, which are the B eigenvalues relative to W.
For each non-zero λ_i, there is a P_i making the equation (15) valid.

$$[B-\lambda_i W]P_i=0 \tag{15}$$

Because B is the summation of C matrixes, the rank of each of which is not larger than 1, there are only C-1 ranks for B and C-1 non-zero eigenvalues for equation (11). Those eigenvalues are known as the discrimination values, and their corresponding eigenvectors are the discrimination vectors needed. Generally, two vectors of them are selected to form discrimination plane, which have the biggest discrimination values. Then the optimal mapping is expressed as follow.

$$Y=TX=\begin{bmatrix}P_1^{\mathrm{T}}\\P_2^{\mathrm{T}}\end{bmatrix}X=\begin{bmatrix}y_1\\y_2\end{bmatrix} \tag{16}$$

However, if there are only two classifications for the whole pattern samples, only one discrimination vector P_1 can be acquired by the above-mentioned method. Here P_1 maximizes the among-class distinguish and minimizes the within-class distinguish, named Fisher criterion, and can be expressed as

$$P_1=\alpha W^{-1}[m_1-m_2]=\alpha W^{-1}\Delta \tag{17}$$

where α is the normalized constant of P_1, $\Delta=m_1-m_2$.

Sammon proposed the method to construct the second vector P_2 shown as the formula (18).

$$R = \frac{P_2^{\mathrm{T}} B P_2}{P_2^{\mathrm{T}} W P_2} \tag{18}$$

If P_2 orthogonalizes with the P_1 and maximizes the R, P_2 is named Sammon criterion and can be gotten by formula (19), where β is the normalized constant of P_2.

$$P_2 = \beta[W^{-1} - \frac{\Delta^{\mathrm{T}}(W^{-1})^2\Delta}{\Delta^{\mathrm{T}}(W^{-1})^3\Delta}(W^{-1})^2]\Delta \tag{19}$$

Because Fisher criterion and Sammon criterion both maximize the among-class distinguish and minimize the within-class distinguish, the projection values of $|m_1 - m_2|$ or $|m_1 - m_3|$ onto the two orthogonal vectors can reflect the distinguish degree of two types of samples, and $|(m_{1j} - m_{2j})d_j|$ (where d_j is the component of discrimination vector) can reflect the contribution ratio of each factor to the classification.

Therefore, if the classification of two types of samples is clear in the projection plane, the effect of each factor on classification can be identified by $m_1 - m_2$ in combination with P_1 and P_2.

Freeze Slag Melting Points Analysis

Experiment Data

According to the actual freeze slag composition characteristics during the flash smelting process, 15 groups of slag samples containing high Fe_3O_4 were prepared by some chemical reagents, and then the slag melting points were measured using a ZDHR-200 type intelligent ash melting point test instrument. The experiment results are listed in Table I.

Table I. Slag Melting Point Experiment Data

No.	A	B	C	D	E	F	G	Y	Class
1	1.56	10.52	16.98	2.19	37.29	30.35	1.11	1390	1
2	1.55	11.17	17.71	2.32	38.58	27.45	1.22	1370	2
3	1.61	11.41	18.53	2.23	40.01	25.06	1.15	1355	2
4	1.63	12.61	17.53	2.57	40.01	24.3	1.35	1360	2
5	1.54	12.43	19.94	2.36	37.87	24.68	1.18	1375	1
6	1.48	11.94	21.18	2.65	36.82	24.69	1.24	1425	1
7	1.56	10.12	17.59	3.51	40.84	25.13	1.25	1337	2
8	1.63	12.31	16.35	5.63	39.16	23.61	1.31	1326	2
9	1.54	11.42	17.78	8.34	36.49	23.04	1.39	1297	2
10	2.21	12.01	16.39	2.64	40.53	24.64	1.58	1355	2
11	3.78	11.52	16.56	2.58	40.14	24.39	1.03	1350	2
12	6.57	11.08	18.26	2.43	36.85	23.52	1.29	1345	2
13	1.64	6.22	17.85	2.49	44.06	26.51	1.23	1430	1
14	1.46	7.98	16.78	2.65	43.71	26.21	1.21	1410	1
15	1.49	9.87	17.24	2.71	42.23	25.31	1.15	1361	2

It can be seen from Table I that there are seven factors influence the freeze slag melting point (Y, °C), including MgO content (A, wt %), CaO content (B, wt %), Fe_3O_4 content (C, wt %), Cu_2O content (D, wt %), FeO content (E, wt %), SiO_2 content (F, wt %) and Al_2O_3 content (G, wt %) in the freeze slag inside brickless reaction shaft.
It should be noted that the effect of the Al_2O_3 content (G) on the freeze slag melting point was not considered, since the Al_2O_3 content changes very little, and only 0.05 difference between its maximum and minimum value.

Influence Factors ODP Analysis

Classification. There are 15 groups of experiment data, each of which includes six factors and one index. The data can be classified into two classes, and the first class includes 5 data whose Y is no less than 1375 °C.
Normalization And Vectors Calculation. To eliminate the dimension effect of the factors, the original data should be normalized to symmetrical distribution, and thus, the average of each factor values is 0 and the variance is 1.
The average vector m_1 of class 1 samples and m_2 of class 2 can be computed based on the normalized data as follow.

$$m_1 = (-0.3987, -0.5851, 0.5803, -0.4113, 0.1290, 0.6732)^T \tag{20}$$

$$m_2 = (0.1994, 0.2925, -0.2901, 0.2057, -0.0645, -0.3366)^T \tag{21}$$

Then, the difference vector between class 1 and class 2 can be calculated.

$$m_1 - m_2 = (-0.5981, -0.8776, 0.8704, -0.6170, 0.1935, 1.0098)^T \tag{22}$$

Projecting Onto The ODP. P_1 and P_2 can be calculated according to the formula (17) and formula (19), respectively.

$$P_1 = (-3.3679, -6.2270, 1.5121, -3.1618, -4.8153, -0.5091)^T \tag{23}$$

$$P_2 = (0.1690, -0.6993, 2.5159, 0.7161, 0.8771, 2.1653)^T \tag{24}$$

Then, the two-dimensional feature vectors y_1 and y_2 were attained by projecting the normalized data onto the two orthogonal axes P_1 and P_2, and the ODP is shown in Figure 1.

$$\begin{aligned} y_1 = (&9.7033, 8.2006, 3.1324, 6.6188, 3.3453, 3.1454, -0.0528, -4.8406, \\ &1.0590, -6.6957, -7.6444, -3.8754, 0.5955, -9.0351, -3.6563)^T \end{aligned} \tag{25}$$

$$\begin{aligned} y_2 = (&4.7391, 4.0346, 1.5643, 3.3172, 1.7346, 1.5285, 0.1054, -2.4890, \\ &0.6451, -3.7218, -3.4737, -2.0172, 0.3035, -4.4251, -1.8456)^T \end{aligned} \tag{26}$$

As can be seen from Figure 1 that the two class samples occupy different regions respectively, that means the classification is so good that it can be used to identify the effect of each factor.

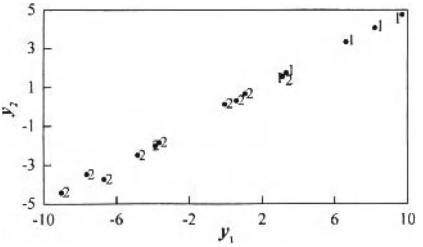

Figure 1. Sample projection onto the optimal discrimination plane

Factor Analysis. The absolute values of the product of the $m_1 - m_2$ components and P_1 components are (2.0142, 5.4647, 1.3162, 1.9508, 0.9315, 0.5141).

The absolute values of the product of the $m_1 - m_2$ components and P_2 components are (0.1011, 0.6137, 2.1899, 0.4418, 0.1697, 2.1866).

Then, the average absolute values of above two products are (1.0576, 3.0392, 1.7530, 1.1963, 0.5506, 1.3504).

It can be seen from those results that the effect sort of the factors on freeze slag melting points is BCFDAE, in other words, the CaO content is the greatest factor to the melting points of the freeze slag inside brickless reaction shaft, the content of Fe_3O_4, SiO_2, Cu_2O and MgO is the second, and the FeO content is the last.

The analysis results are in good agreement with the theory analysis data reported by Ref. [17].

Conclusion

Although there are many factors influence the melting point of the freeze slag inside brickless reaction shaft, but the experiment data of the freeze slag melting point were processed effectively by ODP data analysis method. Results show that the CaO content is the greatest factor to the melting point of the freeze slag inside brickless reaction shaft, the content of Fe_3O_4, SiO_2, Cu_2O and MgO is the second, and the FeO content is the last.

The ODP data analysis method is based on the "Birds of a feather flock together" characteristic of pattern recognition and depends on the inherent law and classified information of experiment data. This method is effective to analyze complex data with multiple factors whose variational regularities are not obvious, and can be applied widely to many fields.

Acknowledgement

This study was supported in part by the National Natural Science Foundation of China (50904027) and the Scientific Research Fund of Jiangxi Provincial Education Department, China (GJJ09241).

References

1. P. Stepanic, I.V. Latinovic and Z. Djurovic, "A New Approach to Detection of Defects in Rolling Element Bearings Based on Statistical Pattern Recognition," *The International Journal of Advanced Manufacturing Technology*, 45 (1/2) (2009), 91-100.

2. D.S. Aml et al., "Well-being Analysis for Composite Generation and Transmission Systems Based on Pattern Recognition Techniques," *generation, transmission & distribution, IET*, 2(2) (2008), 202-208.
3. C.K. Chow, "An Optimum Character Recognition System Using Decision Functions," *IEEE Trans. Electron. Comput.*, (6) (1957), 247-254.
4. T.M. Cover and P.E. Hart, "Nearest Neighbor Pattern Classification," *IEEE Trans. Inf. Theory*, 13(1) (1967), 21-27.
5. E. Paarzen, "On Estimation of a Probability Density Function and Mode," *The Annals of Mathematical Statistics*, 33(3) (1962), 1065-1076.
6. P.S. Lachenbruch, and R.M. Mickey, "Estimation of error rates in discriminant analysis," *Technometrics*, (10) (1968), 1-11.
7. T. Kailath, "The divergence and Bhattacharyya distance measures in signal selection," *IEEE Trans. Commun. Technol.*, (15) (1967), 52-60.
8. C. Liu and H.Wechsler, "A shape and texture based enhanced fisher classifier for face recognition," *IEEE Trans. on Image Processing*, 10(4)(2001), 598–608.
9. C. Liu and H.Wechsler, "Gabor Feature Based Classification Using the Enhanced Fisher Linear Discriminant Model for Face Recognition," *IEEE Trans. on Image Processing*, 11(4)(2002), 467–476.
10. A.K. Jain, R.P.W. Duin and J. Mao, "Statistical pattern recognition: a review," *IEEE Transactions on Pattern Analysis and Machine Intelligence*, 22 (1) (2000), 4-37.
11. A. Ahmad and L. Dey, "A *k*-mean clustering algorithm for mixed numeric and categorical data," *Data & Knowledge Engineering*, 63 (2) (2007), 503-527.
12. M.C. Su and C.H. Chou, "A Modified Version of the K-means Algorithm With a Distance Based on Cluster Symmetry," *IEEE Transactions on Pattern Analysis and Machine Intelligence*, 23 (5) (2001), 674-680.
13. S.S. Khan and A. Ahmad, "Cluster center initialization algorithm for *K*-means clustering," *Pattern Recognition Letters*, 25 (11) (2004), 1293-1302.
14. E. Pekalska and R.P.W. Duin, "Automatic pattern recognition by similarity representations," *Electron. Lett.*, 37 (3) (2001), 159–160.
15. J.W. Sammon, "An Optimal Discriminant Plane," *IEEE Transactions on Computers*, 19 (9) (1970), 826-829.
16. D.F. Ge, and X. Qu, "Feature extraction based on optimal discrimination plane in ECG signal classification," *Advanced Data Mining and Applications*, 4093(2006), 143-149.
17. L.W. Liang, "A Research on Phychemical Properties of the Freeze Slag Inside Flash Smelting Furnace Brickless Reaction Shaft" (M.S. thesis, Jiangxi University of Science and Technology, 2011), 37-38.

3rd International Symposium on High-Temperature Metallurgical Processing
Edited by: Tao Jiang, Jiann-Yang Hwang, Patrick Masset, Onuralp Yucel, Rafael Padilla, and Guifeng Zhou
TMS (The Minerals, Metals & Materials Society), 2012

3rd International Symposium on High-Temperature Metallurgical Processing

Alloy and Materials Preparation

Session Chairs:
Rafael Padilla
Jianliang Zhang

3rd International Symposium on High-Temperature Metallurgical Processing
Edited by: Tao Jiang, Jiann-Yang Hwang, Patrick Masset, Onuralp Yucel, Rafael Padilla, and Guifeng Zhou
TMS (The Minerals, Metals & Materials Society), 2012

IMPROVING HOT WORKABILITY OF LEDEBURITIC TOOL STEELS

M. Fazarinc[1], G. Kugler[1], I. Perus[1] and M. Terčelj[1],

[1]Faculty of Natural Science and Engineering, University of Ljubljana, Askerceva cesta 12, 1000 Ljubljana, Slovenia

Keywords: Ledeburitic tool steels, process parameters, hot workability.

Abstract

Ledeburitic tool steels are highly alloyed steels used for specific highly loaded applications but are characterized by low and variable hot workability. In this contribution the importance of selecting the right choice of some essential process parameters, i.e. casting temperature, solidification rate and soaking temperature, needed for improving the intrinsic hot deformability of ledeburitic tool steels, is studied. An inappropriate selection of casting temperature and cooling rate results in precipitation of unusual eutectic carbides that decreases the hot workability, whereas with the selection of appropriate soaking temperature the temperature range of safe hot working can be broadened. For each initial as-cast microstructure individually determined soaking temperature should be selected.

Introduction

The surface cracking during hot deformation of ledeburitic tool steels reduces mechanical properties and their industrial yield. These tool steels have high hardness, wear resistance and high tempering resistance on one hand, and high flow stresses and low hot deformability on the other. Decreased hot deformability of the tool steels is attributed to the type, size, shape, distribution, fraction of eutectic carbides and/or other phases, grain growth, etc. at upper limit while precipitation of secondary carbides and decreased recrystallization rate at lower limit of the safe hot deformation temperature range, [1-6].

The occurrence of cracks on most exposed areas of workpiece are related to the areas where similar conditions related to upper and/or lower limit of temperature working range prevail, i.e. areas with accelerated cooling, areas with higher value of accumulated strains where also decreased recrystallization rate with simultaneously presence of higher tensile stresses takes place, furthermore areas of workpiece which are due to combustion conditions in furnace heated to higher temperatures, etc. Thus the areas, where combination of previously mentioned conditions prevails, are more exposed to cracking. This additionally requires that hot deformability of ledeburitic tool steel should be considered as a complex problem. Publications in the literature with regards to hot deformability of tool steels are predominately of a partial nature thus all reasons for unexpected occurrence of cracks are not sufficiently explained in available literature so far. Furthermore modern practice proves that previous processing parameters significantly influence the hot deformability and thus this cannot be considered as a constant value. During heating, soaking and hot deformation various processes take place: decay (decomposition) of carbides, formation of new carbides, dissolution of carbides and of alloying elements, etc. Thus depending on variation of process parameters and chemical composition, that consequently influences the processes related to carbides, shifting of decreased deformability at both limits of temperature working range to higher and/or to lower temperatures can occur, [1-14].

In this contribution the importance of proper selection of casting temperature, cooling rate and soaking temperature on hot workability of ledeburitic tool steels of AISI M42 - type is presented.

Applied Materials and Experiments

Applied Tool Steels

The proposed approach will be illustrated with particular results obtained in thermo-mechanical processing of ledeburitic tool steels, i.e. AISI M42 (super HSS) and W.Nr. 1.2690. All these steels contain C and carbide-forming elements, i.e. Cr, W, Mo and V with the chemical compositions are given in **Table 1**. The microstructure of these steels consists of a martensitic matrix in which the ledeburitic and secondary carbides are present. In **Fig. 1a** typical microstructures of ledeburitic tool steels for as-cast initial state are presented.
An optical microscope (OM, Carl Zeiss AXIO Imager.A1m) and a field-emission gun scanning electron microscope (FE SEM) in combination with an attached EDS (INCA x-SIGHT LN_2 with INCA ENERGY 450 software) and EBSD (INCA CRYSTAL 300) analytical tools were used to observe the microstructures and to determine the type of carbides.

Table 1: Chemical composition of applied tool steels in (wt%): M42, D2 and W.Nr.1.2690.

	C	Si	Mn	Cr	Mo	V	W	Co
AISI M42	1.09	0.26	0.25	3.81	9.32	1.09	1.40	8.20
W.Nr. 1.2690	1.17	0.24	0.26	11.3	1.35	1.48	2.24	-

Industrial and Laboratory Tests for Selection of Appropriate Process Parameters

The influences of the selected casting temperature on hot workability, the influence of cooling rate on obtained microstructure and selecting of appropriate soaking temperature for selected microstructure were studied, combining laboratory and industrial experiments. The industrial investigation of the hot workability involved studies of the influence of the casting temperature, cooling rate and soaking temperature on the initial microstructure and occurrence of cracking during the hot forging and hot rolling of ingots and billets. Laboratory hot compression tests for selection of appropriate soaking temperatures were carried out on Gleeble 1500D thermo-mechanical simulator. Appropriate soaking temperature was determined individually for each of three different as-cast initial states (obtained at three different cooling rates) applying special procedure; the criterion for the assessment was the appearance of cracks on the compressed specimen's surface at appointed strain, strain rate and soaking time and the corresponding microstructure of the deformed cylindrical specimen with initial dimensions Φ =10 mm x 15 mm. The procedure was repeated from initial 1200 °C and with decreasing temperatures in 20 °C steps until the compressed sample exhibited a crack-free surface. A detailed description of this procedure for determining the appropriate soaking temperature is given elsewhere, [1]. The hot workability of selected tool steels was verified in industrial conditions using previously laboratory-determined soaking temperature and then compared with a too-high temperature.

Casting at Various Temperatures and Testing of Hot Workability

Results of the influence of casting temperature on hot workability will be given at forging of W.Nr. 1.2690 tool steel. Hot forging of ingots with Φ = 143 mm, that were cast with a too-high and at appropriate temperature, respectively, were carried out and appearance of internal cracks in the central region of the forged and rolled billets were investigated.

Laboratory Determination of Appropriate Soaking Temperature for Various Initial As-cast Microstructures and Hot Workability

Importance of selection of appropriate soaking temperature for initial as-cast microstructures obtained at various cooling rates; i.e. at cooling rate of 0.25K/s and 0.16 K/s, on hot workability will be presented for M42 tool steel. Namely cooling rate strongly influences the obtained microstructure, selection of appropriate soaking temperature and consequently also on hot workability. Applying of previously described procedure (section 2 and in [1]) for hot compression test on Gleeble 1500D appropriate soaking temperatures for each initial as-cast microstructure individually were assessed. After this hot rolling of ingots as well as continuously casted billets were carried out and hot workability was assessed.

Results

Influence of Casting Temperature on Obtained Microstructures and on hot Workability

During the ultrasonic investigation of the soft-annealed billets Φ = 143 mm from the W.Nr. 1.2690 tool steel, hot-forged from ingots that were cast at a too-high temperature, for some billets or parts of billets internal defects were detected in their central region. The temperature of heat at the end of the vacuum treatment was 1512 °C, which was recognized as being a too-high temperature. **Figure 1a** shows microstructure of carbide stringer perpendicular to the forging direction in the central region of a hot-forged and soft-annealed billet, which consist of spheroidised carbides, a larger quantity of ledeburitic carbides than is usual for this type of steel, microporosity and ferrite. Detail of carbide stringer is shown in **Figures 1b** where beside carbides M_7C_3 and $M_{23}C_6$ which are usually present in these types of tool steels also MC and M_6C carbides were found. All these carbides were confirmed by combined EBSD and EDS analyses. Inspection of microstructure also shows larger eutectic colonies with larger eutectic carbides, especially in the center part of the ingot, and consequently in stringers carbide regions in the microstructure after plastic deformation. This kind of morphology is a consequence of too-high casting temperature and results in more intensive segregations of vanadium and tungsten and the precipitation of their carbides. Despite enormous carbide segregations in the ingot core the deformed ingot did not crack during the radial hot forging. But during the subsequent hot rolling of the billets to a round profile of Φ 61 mm, where tensile stress states were present, the yield was approximately 15% lower in comparison to the charges that were cast at the optimum temperature. Here is worth mentioning that the microstructure which was taken from the center of the forged and rolled billet (ingot previously casted at optimum temperature), consists of ferrite, spheroidised M23C6-type carbides and smaller ledeburitic M_7C_3-type carbides while no MC and M_6C-type carbides were found.
A detailed investigation of the internal cracks from the central region of the billets with the optical microscope, FE SEM and the combined EDS and EBSD analyses of microstructure showed that cracks do not follow the stringers consisting of the usual M_7C_3 and $M_{23}C_6$ types of carbides but rather along the stringers that contain previously mentioned carbides, that are unusual for this type of tool steels and are not present if the casting temperature is optimum; i.e. small vanadium eutectic carbides and small complex eutectic carbides (see **Figures 1c-d**).

The complex carbides are composed of small vanadium carbides of type VC surrounded by M_7C_3 in the central part and of precipitated $M_{23}C_6$ in the outer part. Thus in the regions where the carbide segregations of these vanadium and complex carbides are present, the tool steel cracks during hot deformation.

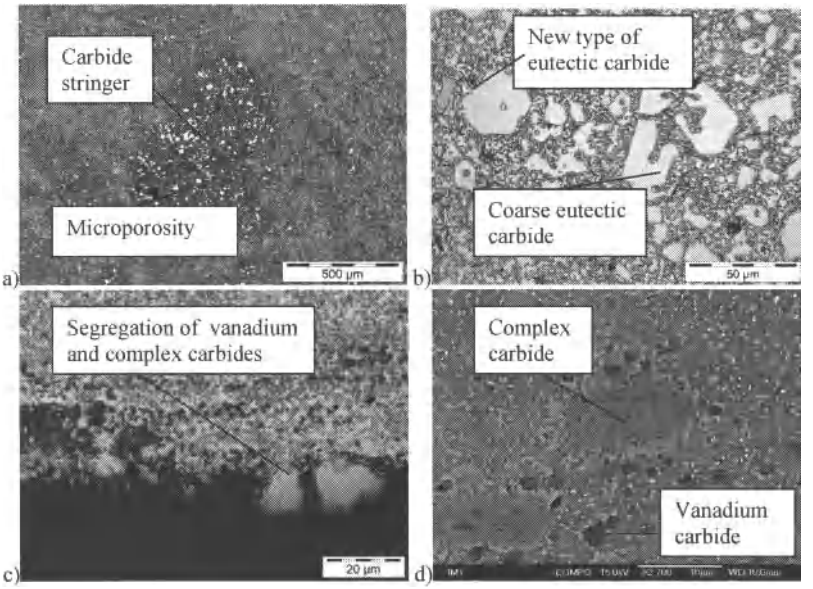

Figure 1: The microstructure of a soft-annealed forged billet of Φ=143 mm from W.Nr. 1.2690 tool steel (perpendicular to the deformation direction): enormous carbide stringer in the center of the billet, OM (a); larger eutectic carbides and a new type of carbide in the base microstructure from spheroidised carbides and ferrite in the carbide stringer, OM (b), appearance of cracking in the central part of the soft-annealed rolled billet steel along unusual segregations of "yellow-colored" vanadium carbides, OM (c); segregation of vanadium and complex carbides near crack (d).

Appropriate Soaking Temperature and Hot Workability for Various Initial As-cast Microstructures

Influence of Soaking Temperature on Hot Workability for Microstructures in Casted Ingot

In the casted ingot varieties of microstructure is usually obtained since each selected spot on ingot cross-section towards ingot centre underwent different cooling rate. Thus for M42 tool steel and cooling rate of 0.25 K/s a microstructure shown on **Figure 2a** was obtained; the fine lamellar as-cast microstructure with precipitated M_2C type of carbides. On other hand at cooling rate of 0.16 K/s beside M_2C type of carbides also for this tool steel unusual, i.e. M_6C type of carbide precipitated (see **Figure 2b**). For cooling rate of 0.25 K/s and applying of inappropriate, i.e. too high soaking temperature (1180 °C), a microstructure with coarse grains and coarse eutectic carbides (**Figure 2c**) in final rolled piece was obtained. Further, it was found out that in the case of too high soaking temperature at upper limit of temperature working range, due to coarsening of carbides, the hot workability is decreased. Namely the

number of small carbides decreases and the size of big carbides increases although their fraction changes according to phase equilibrium (diagram). On the contrary in the case of an appropriate soaking temperature (1150 °C) the initial as-cast microstructure can be transformed into a fine grained microstructure with fine and equally (regularly) distributed eutectic carbides (**Figure 2d**); the number of big carbides is reduced and results in increased hot workability at upper and lower limits of temperature working range. Thus, the coarser carbides and/or carbide clusters, that have been formed during soaking, represent the spots for initiation of micro-cracks so during initial stage of hot deformation as well as during final stage of hot deformation; thus by applying of appropriate soaking temperature the process of coarsening of carbides should be (will be) avoided that lead to extending of temperature range of safe hot working.

Furthermore these results show that the process of dissolution of fine carbides and coagulation as well as growth of coarser carbides during soaking before hot deformation is irreversible. In the case of applying of too high soaking temperature with subsequent hot rolling the coarser carbides that form during soaking cannot be broken down and consequently coarser eutectic carbides are present in the final microstructure which also influence on mechanical properties of final-product. Thus applying of soaking at too high temperature leads to decreased deformability so at upper as well as lower limits of temperature working range. This recognition play important role especially at hot deformation in several heats (cycles) in industrial conditions.

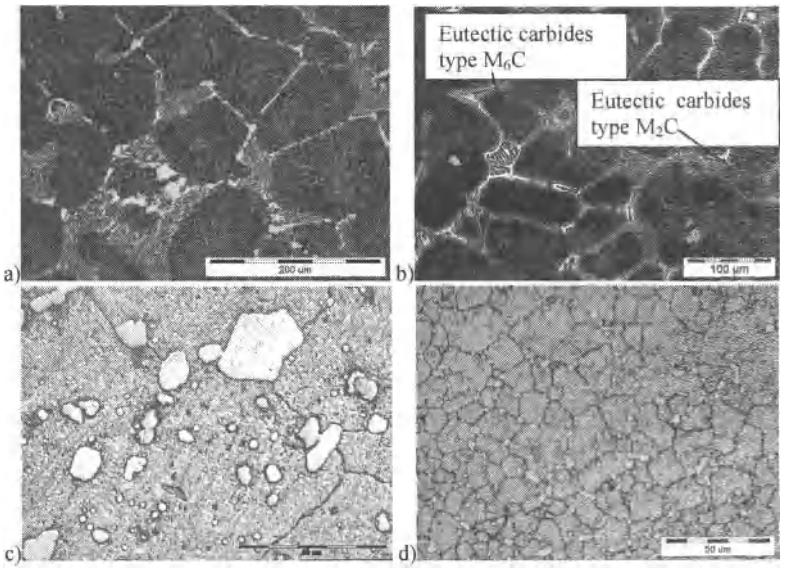

Figure 2: Microstructure for AISI M42 tool steel obtained at solidification rate of 0.25 K/s (a) and at solidification rate of 0.16 K/s (b), obtained microstructure at hot rolling applying of inappropriate (too high) soaking temperature of 1180 °C for (c) and microstructure obtained in rolled piece at appropriate soaking temperature 1150 °C (d) for obtained microstructure at cooling rate of 0.25 K/s.

Too slow cooling rates (microstructure on **Figure 2b**), as in the case of casting at too-high temperature (for W.Nr. 1.2690 tool steel (**Figure 1**)), result in occurrence of a new type of carbides that leads to decreased hot deformability as it has been already presented in the case of casting at too high temperature. Thus too high casting temperature and too slow cooling rates at ledeburitic tool steels cannot be considered as mutual independent but as mutual dependent influential parameters.

Influence of Soaking Temperature on Hot Workability for Microstructure in Continuously Cast Billet

Influence of initial microstructure on selection of appropriate soaking temperature (M42 tool steel) will be illustrated on continuously cast billet square of 130 mm. **Figure 3a** shows as-cast microstructure 25 mm under the surface of the billet. Regarding to described procedure in section 2 or in [1] temperature of 1140 °C was determined as appropriate soaking temperature. **Figures 3b-c** show the results of the influence of soaking on coarsening of carbides so at appropriate (1140 °C) as well as at to high (1170 °C) temperature and their influence on hot deformability. During soaking at 1170 °C coarse carbides were formed that lowers hot deformability; this results in cracking along previous dendrite grain boundaries, where they are concentrated **(Figure 3b)**. At soaking temperature of 1140 °C the coagulation and coarsening of carbides was not remarkable and the deformed sample did not crack **(Figures 3c)**. It means that also in the case of soaking at too high temperature and subsequent hot deformation on lower temperature (a.m. 1140 °C) the material would exhibit lower hot deformability due to presence of oversized carbides in matrix. Applying of soaking temperature of 1150 °C, which was appropriate soaking temperature for microstructure obtained at cooling rate of 0.25 K/s, at the microstructure shown on **Figure 3a** resulted in decreased hot deformability. Thus for each initial as-cast microstructure appropriate soaking temperature should be selected.

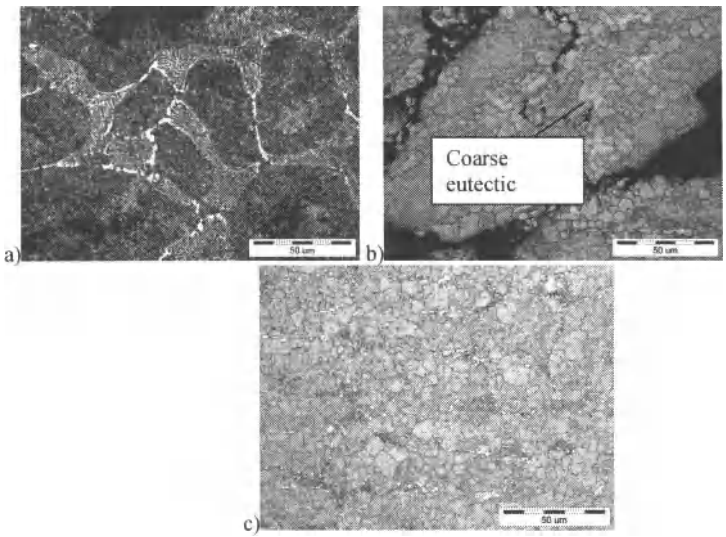

Figure 3: Influence of soaking temperature on coarsening of carbides and on hot deformability for continuously cast M42 tool steel on upper limit of temperature range: initial

as-cast microstructure (a), soaking and deformation temperature 1170 °C (b); soaking and deformation at temperature of 1140 °C (c).

Conclusions

The results of the study of the influences of casting temperature, cooling rate and soaking temperature on the hot workability of ledeburitic tool steels can be summarized as follows:

- Selecting the correct values for casting and soaking temperatures as well as for cooling rate improves the intrinsic hot workability of the investigated ledeburitic tool steels.
- At a too-high casting temperature small unusual and/or small complex carbides additionally precipitate in the matrix during solidification. Cracking during hot deformation then predominately occurs along these carbides.
- A too-low cooling rate results in the formation of a new type of carbides, which are usually not formed during solidification at higher cooling rate. Due to their different properties they deteriorate hot workability and influence the properties of the final products.
- The soaking temperature influences the dissolution, the spheroidisation, the coagulation and the growth of carbides, the growth of austenitic grains. Selecting the appropriate soaking temperature extends the temperature range of safe hot working, so at the lower as well as at upper limits. A too-high soaking temperature for a particular soaking time results in coarser carbides that leads to decrease of the hot workability at both limits of the temperature working range.

References

1. T. Večko Pirtovšek, G. Kugler, M. Godec, M. Terčelj, "Microstructural characterization during the hot deformation of 1.17C-11.3Cr-1.48V-2.24W-1.35Mo ledeburitic tool steel", *Materials Characterization*, 62/2 (2011), 189-197.
2. H. J. McQueen and C. A. C. Imbert, *Influence of carbides on the hot working of steel. Deformation, Processing and Properties of Structural Materials*, ed. E.M. Tallef, C. K. Syn, and D. R. Lesuer, (The Minerals, Metals & Materials Society, 2000), 79-92.
3. J. Liu, H. Chang, R. Wu, T.Y. Hsu, X. Ruan, "Investigation on hot deformation behaviour of AISI T1 high-speed steel", *Materials Characterization* 45 (2000), 175-186.
4. C.A.C. Imbert, H.J. McQueen, Hot ductility of tool steels, Canadian Metallurgical Quarterly 40 (2001) 235-244.
5. M. R. Ghomashchi, C. M. Sellars, "Microstructural Changes in As-cast M2 Grade High Speed Steel during Hot Forging", *Metallurgical Transactions A*, 24A (1993), 2171-2180.
6. C. Rodenburg, M. Kryzanowski, J.H. Beynon, W.M. Rainforth, "Hot workability of spray-formed AISI M3:2 high speed steel", *Materials Science and Engineering A*, 386 (2004), 420-427.
7. H. Brandis, E. Haberling, H. H. Weigard, *Metallurgical Aspects of Carbides in High Speed steels, Processing and Properties of High Speed Tool Steels*, ed. M.G.H. Wells and L.W. Lherbier, (TMS_AIME, 1980), 1-18.
8. Dennis W. Hetzner, William Van Geertruyden, "Crystallography and metallography of carbides in high alloy steels", *Materials Characterization*, 59 (2008), 825-841.
9. D. Peidao, S. Gongqi, and Z. Shouze, "A Scanning Electron Microscopy Study of Carbides in High-Speed steels", *Materials Characterization*, 29 (1992), 15-24.

10. H. F. Fischmeister, R. Riedl, and S. Karagöz, "Solidification of High-Speed Tool Steels", *Metallurgical Transactions A*, 20A (1989), 2133-2148.
11. M. Boccalini, H. Goldenstein, "Solidification of high speed steels", *International Materials Review*, 46/2 (2001) 92-115.
12. Luan Y, Song N, Bai Y, Kang X, Li D, "Effect of solidification rate on the morphology and distribution of eutectic carbides in centrifugal casting high-speed steel rolls", *Journal of Materials Processing Technology* 210 (2010), 536-541.
13. Peidao Ding, Gongqi Shi, Shouze Zhou, "As-Cast Carbides in High-Speed Steels", *Metallurgical Transactions A*, 24A (1993), 1265-1272.
14. Hongshuag Di, Xiaoming Zhang, Guodong Wang, Xianghua Liu, "Spheroidizing kinetics of eutectic carbide in the twin roll-casting of M2 high speed steel", *Journal of Materials Processing Technology*, 166 (2005), 359-363.

3rd International Symposium on High-Temperature Metallurgical Processing
Edited by: Tao Jiang, Jiann-Yang Hwang, Patrick Masset, Onuralp Yucel, Rafael Padilla, and Guifeng Zhou
TMS (The Minerals, Metals & Materials Society), 2012

Influence of Elements Segregation on Creep Properties of A Single Crystal Nickel-Based Superalloy

ZHANG chao, TIAN Su-gui, YU Xing-fu, ZENG Zheng, LIU Chen

(School of Materials Science and Engineering, Shenyang University of Technology, Shenyang 110870)

Abstract: Single crystal nickel-base superalloy is prepared by using the various withdrawing rates. By measuring creep properties and microstructure observation, the influence of the element segregation on creep properties of the superalloys is investigated. Results show that the dendrite spacing and the segregation extent of the elements decrease with the enhancing withdrawing rate. The superalloy with smaller dendrite spacing has lower segregation of the elements and better creep resistance. The dislocations climbing over the rafted γ′ phase is thought to be the deformation mechanism of the alloy during steady state creep. In the later stage of creep, the fact that some dislocations shear into the rafted γ′ phase may twist the rafted γ′ phase. As the creep goes on, the initiation and propagation of the cracks occur up to occurring creep fracture, which is thought to be the fracture mechanism of the superalloy during creep.

Keywords: Single crystal nickel-based superalloy, withdrawing rates, dendrite spacing, creep properties, microstructure, deformation mechanism

1. Introduction

Single crystal nickel-based superalloys consist of high volume fraction of γ′ strengthening phase and γ matrix, and possess the excellent high-temperature mechanical and creep properties, therefore, they have become the main material to make the blades of the advanced aeroengines[1-3]. Some literatures report that the temperature-bearing and creep-resistance properties of the single crystal nickel-based superalloys can be remarkably improved as the increases content of the refractory elements, such as W and Re[4-6].

During single crystal preparing, the solidification temperature and withdrawing rates have the important effect on the mechanical and creep properties of single crystal superalloys[7,8]. Although single crystal superalloys are produced in a vacuum directional solidification furnace under the condition of a high temperature gradient, the composition segregation occurs still in the regions between the dendrite and interdendrite, but the influence of withdrawing rates on the dendrite spacing, elements segregation and creep properties is not still clear.

In the paper, by means of different withdrawing rates, the bars of the single crystal nickel-based superalloy with different dendrite spaces were prepared for investigating the effect of the withdrawing rates on dendrite spacing, element segregation and creep properties with the aid of creep property measurements and microstructure observation.

2. Experimental procedure

The single crystal nickel-based superalloys with [001] orientation have been prepared by means of selecting crystal method in a vacuum directional solidification furnace under the condition of a high temperature gradient. All samples were within 7° deviating from the [001] orientation. The nominal chemical composition of the superalloy is Ni-5Cr-6Co-4Mo-5Al-8Ta-

9W (wt. %). The heat treatment regimes of the single crystal nickel-based superalloys are given as follows: 1280 ℃ × 2 h + 1310 ℃ × 4 h, A.C + 1080 ℃ × 4 h, A.C + 870 ℃ × 24 h, A.C。

After fully heat treated and the crystal orientation determined, the bars of the single crystal superalloys were machined into the plate-like tensile creep specimen along the direction parallel to the [001] orientation, the sizes of the cross-section in the sample are 4.5 mm×2.5 mm and the gauge length being 15 mm. The wide surface of the specimens are (100) plane. After the specimens surface being mechanically grinded and polished, uni-axial constant load tensile tests were performed in a creep testing machine (GWT504 model) under the conditions of different temperatures and stresses, for measuring the creep curves. The microstructures of the superalloys after heat treated and crept for different time were observed under the scanning electron microscope (SEM) and transmission electron microscopy (TEM). In addition, the apparent creep active energies and stress exponents of the superalloys were calculated according to the creep curves and the strain rates during steady creep stages of the alloys under different conditions.

3. Experimental results and analysis

3.1 Dendrite spacing and compostion segregation

The bars of the single crystal superalloys with different dendrite spacing were prepared using different withdrawing rates of 0.07 and 0.08 mm/s, which were denoted as alloys 1 and 2, respectively. The dendrite morphologies on the (001) crystal planes of the as-cast superalloys are shown in Fig1. The dendrites on the single crystal superalloys prepared at different withdrawing rates are regularly arranged along the [100] and [010] directions, and exhibit the feature of the "+" shape on (001) crystal planes. And the alloy 1 prepared at the low withdrawing rate has relatively larger dendrite spacing, as shown in Fig1(a). Compared to alloy 1, the alloy 2 prepared at the higher withdrawing rate has smaller dendrite spacing, as shown in Fig1(b). It can be measured according to Fig1(a) and (b) that the primary dendrite spacing of the alloys 1 and 2 are 166-186 and 144-164 μm, and the secondary dendrite spacing being 100-120 and 89-109 μm, respectively.

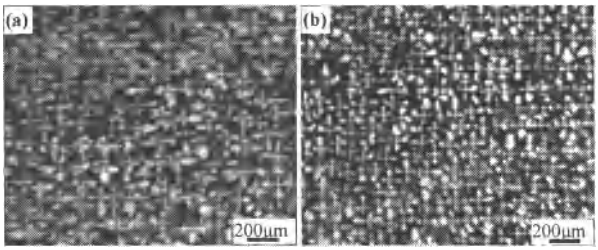

Fig1. Dendrite morphologies of as-cast alloys 1 and 2. (a) Alloy 1; (b) alloy 2.

Although the the dendrite of as-cast superalloys prepared at different withdrawing rates may be regularly grown, the composition segregation in the dendrite and interdendrite regions occurs obviously due to the refractory elements with high-content, such as Ta, Mo and W. The element distributions in the dendrite and interdendrite regions of the alloys 1 and 2 are shown in Table 1.

The formula of the calculated segregation coefficients is given as following :

$$K = \frac{C_{inter} - C_{den}}{C_{den}} \times 100\% \quad (1)$$

where K is the segregation coefficient, C_{inter} is the content of the element in the interdendrite region, and C_{den} is the content of the elements in the dendrite region.

Table 1.Distribution and segregation coefficients of the elements in the interdendrite / dendrite regions of the as-cast alloys

Alloy	Regions	Al	Ta	Cr	W	Co	Mo
I	Dendrite	3.56	8.74	5.58	9.73	4.46	5.98
	Interdendrite	4.4	13.03	4.62	6.92	5.29	4.18
	K	23.6	49.08	-17.2	-28.88	18.61	-30.1
II	Dendrite	4.19	9.07	5.57	9.42	4.42	5.75
	Interdendrite	4.68	12.36	5.06	7.03	4.83	4.21
	K	11.69	36.27	-9.16	-25.39	9.28	-26.78

It can be concluded according to Table 1 that two superalloys prepared at different withdrawing rates have the bigger composition segregation. This indicates that the elements Cr, W and Mo are richly distributed in the dendrite region, while the elements Al, Co and Ta are richly distributed in the interdendrite region. Thereinto, the element Ta is the strongest normal segregation one, and the segregation coefficients in the alloys 1 and 2 are calculated to be 49.08% and 36.27%, respectively. The element Mo is the strongest negative segregation one, and the segregation coefficients in the alloys 1 and 2 are calculated to be -30.1% and -26.78%, respectively. The segregation coefficient of the element W in ther alloy 1 and 2 are calculatede to be -28.88% and -25.39%, respectively. And the segregation coefficients of the elements in alloy 1 are bigger than the ones of the elements in the alloy 2. When the more refractory elements are un-homogeneously distributed in the alloys, it is easy for the refractory elements to accumulate in local regions, which may accelerate the formation of the TCP phase. And the creep resistance of superalloys shall be decreased to the great extent once the TCP phase is formed to deplete the refractory elements in the neighboring regions[9,10].

Table 2.Distribution and segregation coefficients of the elements in the interdendrite / dendrite regions of the alloys after fully heat treated

Alloy	Regions	Al	Ta	Cr	W	Co	Mo
I	Dendrite	4.01	9.38	5.87	9.03	4.89	5.64
	Interdendrite	4.52	11.12	5.31	7.52	5.3	4.62
	K	12.72	18.55	-9.54	-16.72	8.38	-18.08
II	Dendrite	4.29	9.88	5.73	8.86	4.97	5.63
	Interdendrite	4.56	10.91	5.46	7.72	5.23	4.87
	K	6.29	10.43	-4.71	-12.87	5.23	-13.5

After fully heat treated, the distribution and segregation coefficients of the elements in between the interdendrite / dendrite regions of the alloys 1 and 2 are shown in Table 2. It can be seen the uniformity extent of the elements between the interdendrite / dendrite regions is obviously improved for both alloys. Thereinto, the segregation coefficient of the element Ta in the alloy 1 has decreased from 49.08% to 18.55%, the ones of the element Mo decrease from -30.1% to -18.08%. And the segregation coefficient of the element Ta in the alloy 2 has decreased from 36.27% to 10.43%, the ones of the element Mo decrease from -26.78% to -13.50%. This suggests that solution treatment at high-temperature may decrease the segregation extent of elements in the interdendrite / dendrite regions of the superalloys, but the varous decreasing extents are displayed in the alloys with different dendrite spacings.

3.2 Creep properties of the superalloys

After the alloy 1 which has the bigger dendrite spacing is fully heat treated, the creep curves of the alloy at different conditions are measured as shown in Fig2. The creep curves of the alloy under the applied different stresses at 1040 °C are shown in Fig2(a), this indicates that the creep feature of the alloy 1 under the applied stress of 137 MPa at 1040 °C displays a shorter initial creep stage and longer steady creep stage, the strain rate of the alloy during steady state creep is measured to be 0.07266%/h, the creep lifetime is measured to be 65 h. As the applied stress increases to 150 MPa, the strain rate during steady state creep is measured to be 0.04589 %/h, the creep life of the alloy decreases from 65 h to 46 h. The creep curves of the alloy 1 under the applied stress of 137 MPa at 1030 °C and 1040 °C are shown in Fig2(b), it can be calculated according to the curves that the strain rates of the alloy during steady state creep are measured to be 0.0359%/h and 0.04589%/h, and the creep lifetimes of the alloy are measured to be 97 h and 65 h, respectively.

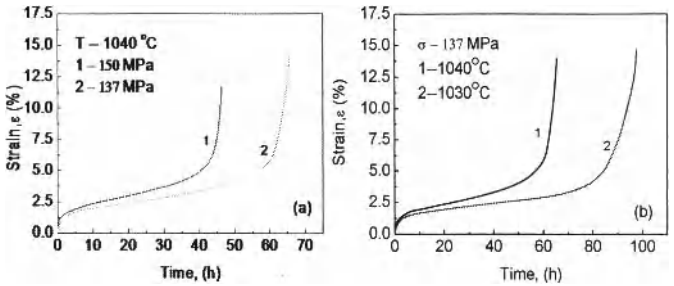

Fig2. Creep curves of the alloy 1 under different conditions
(a) Applied different stresses at 1040 °C, (b) applied stress of 137 MPa at different temperatures

After fully heat treated, the creep curves of the alloy 2 with smaller dendrite spacing are measured as shown in Fig3. Figure 3(a) shows the creep curves of the alloy 2 under the applied different stresses at 1040 °C, which is similar to the creep features of the alloy 1. Thereinto, under the applied stress of 137 MPa at 1040 °C, the strain rate of the alloy during steady state creep is measured to be 0.0331%/h, and the creep lifetime is measured to be 106

h. When the applied stress increases to 150 MPa, the strain rate of the alloy during steady state creep increases to be 0.05182%/h, and creep life decreases to 81 h. But the strain rate of the alloy during steady state creep increases to 0.07041%/h when the applied stress increases to 160 MPa, and creep life decreases to 58 h.

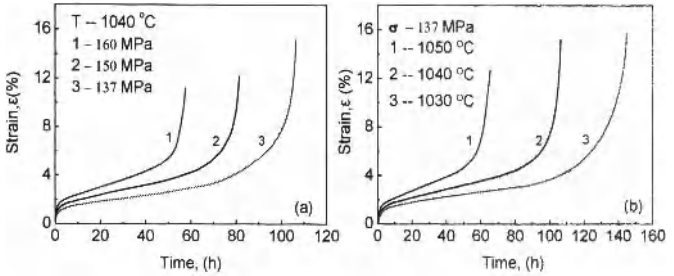

Fig3. Creep curves of the alloy 2 at different conditions. (a) Applied different stress at 1040 °C, (b) applied stress of 137 MPa at different temperatures.

Under the applied stress of 137 MPa at different temperatures, the creep curves of the alloy 2 are measured as shown in Fig3(b). The strain rates of the alloy during steady state creep at 1030℃, 1040℃ and 1050℃ are measured to be 0.02564%/h, 0.0331%/h and 0.04152%/h, respectively, and the creep lifetimes of the alloy 2 are measured, in turn, to be 145 h, 106 h and 65 h. This indicates that, in the ranges of the applied temperatures and stresses, the strain rate of the alloy 2 during steady state creep increases with the applied temperatures and stresses, and the creep lifetimes of the alloy 2 display an obvious sensitivity to the applied temperatures and stresses.

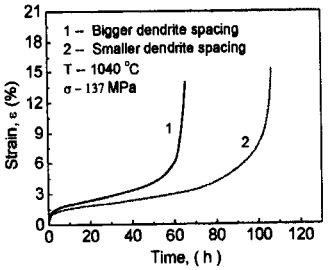

Fig4. Creep curves of the alloys with different dendrite spacing at 137MPa/1040 °C

Under the conditions of the applied stress of 137MPa at 1040 °C, the creep curves of the alloys 1 and 2 with different dendrite spacing are measured as shown in Fig. 4. It may be understood from Fig. 4 that, compared to the alloy 1, the alloy 2 displays a lower strain rate during steady state creep and longer creep lifetime. The creep lifetimes of the alloys 1 and 2 are measured to be 65 and 106 h, respectively, compared to the alloy 1, the creep lifetime of the alloy

2 under the applied stress of 137MPa at 1040 °C increases about 63%, and the alloy 2 with smaller dendrite spacing possesses a better creep resistance and longer creep lifetime.

3.3 Constitutive equation and creep parameters

The transient strain of the single crystal nickel-based superalloy occurs at the moment of the applying stress at high temperatures. As the creep goes on, the density of dislocations increases, which results in the strain hardening of the alloy, and increases the resistance of the dislocation movement to decrease the strain rate of the alloy. At the same time, the slipping and climbing of dislocations in the alloy are accelerated by means of the thermal activation, which results in the recovery softening of the alloy to relax the stress concentration. When the equilibrium of the strain hardening and the recovery softening is obtained, the strain rate of the alloy keeps constant for entering the steady state stage of creep. Therefore, the strain rate of the alloy can be expressed by the Dorn law:

$$\dot{\varepsilon}_{SS} = A\sigma_A^n \exp(\frac{-Q}{RT}) \tag{2}$$

In the equation, $\dot{\varepsilon}_{ss}$ is the strain rate during steady state creep, A is the constant related to material structure, σ_A is the applied stress, n is the apparent stress exponent, R is the gas constant, T is thermodynamics temperature, and Q is the apparent creep activation energy.

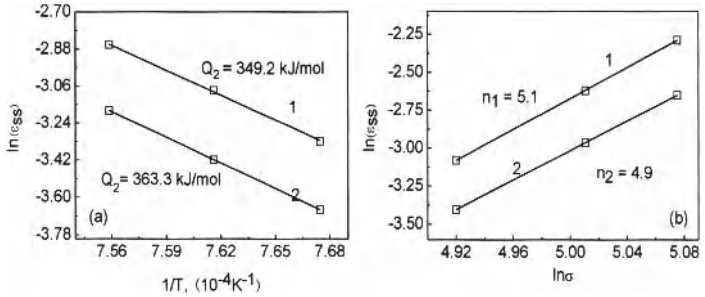

Fig5 .Relationships between the strain rates and applied temperatures, stresses during the steady state creep. (a) Strain rate vs. temperatures, (b) strain rate vs. applied stresses

According to the strain rates of the alloy during steady state creep in Fig. 2 and Fig. 3, the dependence of the strain rates on the applied temperatures and stresses are shown in Fig. 5(a) and (b), respectively. It can be calculated according to Fig. 5 that, in the ranges of the applied temperatures and stresses, the apparent creep activation energies and stress exponents of the alloys 1 and 2 are calculated to be $Q_1 = 349.2$ kJ/mol and $Q_2 = 363.3$ kJ/mol, respectively. And the stress exponents of the alloys 1 and 2 are calculated to be $n_1 = 5.1$ and $n_2 = 4.9$, respectively. This indicates that, compared to the alloy 1, the alloy 2 has a better creep resistance. And it can be deduced by analysis according to the stress exponents that, in the ranges of the experimental temperatures and stresses, the deformed mechanism of the alloys during steady state creep is the dislocation climbing over the γ′ phase.

3.4 Microstructure evolution and deformation features

Microstructure of the alloy 2 after fully heat treated is shown in Fig. 6, which is similar to the one of the alloy 1. This indicates that that the microstructure of the alloy consists of the cubical γ′ phase embedded coherently in the γ matrix. The volume fraction of the γ′ phase is 65%, and the edge size of the cubical γ′ phase is about 0.4 μm, the size of the γ matrix channel is about 50 nm in width, and the cubical γ′ phase is regularly aligned along <100> orientations.

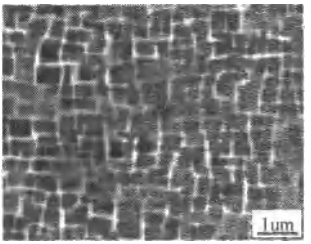

Fig6. Morphology of the alloy after fully heat treated

After crept for 106 h up to fracture under the applied stress of 137MPa at 1040°C, the microstructure in the different regions of the alloy 2 is shown in Fig. 7. The morphology in the region far from the fracture is shown in Fig7(a) in which the direction of the applied stress is marked by arrow, which indicates that the cubical γ′ phase in the alloy had been transformed into the rafted structure along the direction vertical to the stress axis. The rafted γ′ phase in the alloy had been twisted, the size of the rafted γ′ phase in thickness is about 0.6 μm, and there are some dislocations shearing into the rafted γ′ phase as marked by arrow. The morphology in the region near the fracture is shown in Fig7 (b), the bigger strain in the alloy occurs in the region due to the constriction of the sample neck, which results in the twisted and broken of the rafted γ′ phase as marked by letter A. The fact that significant amount of dislocations shear into the rafted γ′ phase indicates that the alloy has lost the creep resistance.

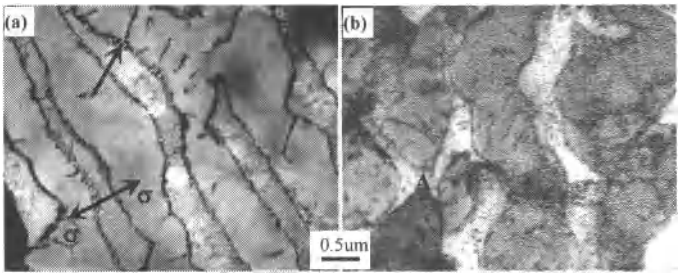

Fig. 7 Morphology after alloy 2 crept for 106 h up to fracture
(a) Twisted of the rafted γ′ phase, (b) dislocation shearing into the rafted γ′ phase

The alternative slipping of dislocations during later stage of creep occurs, which twists the rafted γ′ phase in the alloy, as shown in Fig7(b), and the cavities and micro-cracks are easily formed in the interfaces of the rafted γ′/γ phases due to the twisted of the rafted γ′ phase. As the creep goes on, the quantities of the dislocations shearing into the γ′ phase increase to bring the stress concentration, which promotes the propagation of the microcracks up to occuring fracture[11]. This is thought to be the fracture mechanism of the alloy during creep.

4. Conclusions

(1) The different dendrite spacing in the single crystal nickel based superalloy may be prepared, by using the various withdrawing rates, to obtain the various segregation degree of the elements in the dendrite / interdendrite regions, and the segregation degree of the elements in alloy diminishes with the dendrite spacing.

(2) The alloy with small dendrite spacing displays a better creep resistance. In the experimental temperature and stress ranges, the creep active energies of the alloy during steady state creep is measured to be Q = 363.3 kJ/mol.

(3) The alternative slipping of dislocations during later stage of creep may twist the rafted γ' phase to result in the initiation of the micro-cracks, and the quantities of the dislocations shearing into the γ' phase increase, as the creep goes on, to promote the propagation of the microcracks up to occuring fracture. This is thought to be the fracture mechanism of the alloy during creep.

Acknowledgements

Sponsorship of this research by National Natural Science Foundation of China under Grant No.50571070 is gratefully acknowledged.

References

[1] Ma W Y, Li S S, Qiao L, et al. Effect of heat treatment on microstructure and stress rupture life of Ni- base single crystal superalloy[J]. Chinese Journal of Nonferrous Metals, 2006,16: 937 - 944.

[2] Luo Z P, Wu Z T, Miller D J. The dislocation microstructure of A nickel- base single-crystal superalloy after tensile fracture[J]. Mater Sci Eng, A. 2003, A354: 358 - 368.

[3] Nystrom J D, Pollck T M, Murphy W H, et al. Discontinuous cellular precipitation in a high-refractory nickel-base supcralloy[J]. Metall. Mater. Trans. (A), 1997, 28: 2443–2450.

[4] Monajati H, Jahazi M, Bahrami R. The influence of heat treatment conditions on γ' characteristics in Udimet 720. Mater. Sci. Eng. A, 2004, 373: 286-293.

[5] Rae C M F, Reed R C. Precipitation of topologically close-packed phases in rhenium-containing superalloys[J]. Acta Mater., 2001, 49: 4113–4120.

[6] Yeh A C, Tin S. Effects of Ru and Re additions on high temperature flow stresses of nickel-base single crystal supcralloys[J]. Scripta Material, 2005, 52: 519–526.

[7] Chen Rongzhang. Development status of single crystal superalloys[J]. Journal of Materials Engineering.1995, (8): 3-12.

[8] LI Jinguo, WANG Zhen, JIN Tao, et al. Effects of withdrawal rate on microstructure of a nickel-base single crystal superalloy [J]. Materials For Mechanical Engineering, 2002, 26(4): 17-19.

[9] Li Jiarong, Tang Dingzhong, Liu Shizhong, et al. Effects of rhenium on creep rupture life of a single crystal superalloy. Journal of Materials Engineering, 1999, (3): 3-7.

[10] Giamei A F, Anton D L. Rhenium additions to a nickel-based superalloy: effect on microstructure. Metall. Trans. A, 1985, 16: 1997-2004.

[11] Tian Sugui, Zhou Huihua, Zhang Jinghua, et al. Creep-damage behaviour of a single crystal nickel-base superalloy. Acta Metallrugica sinica, 1998, 34(1): 57-62.

3rd International Symposium on High-Temperature Metallurgical Processing
Edited by: Tao Jiang, Jiann-Yang Hwang, Patrick Masset, Onuralp Yucel, Rafael Padilla, and Guifeng Zhou
TMS (The Minerals, Metals & Materials Society), 2012

PREPARATION OF TITANIUM BASED FERROUS ALLOYS WITH LOW OXYGEN CONTENT BY REDUCTION-SHS

Zhang Ting-an[1], Dou Zhihe[1], Zhang Hanbo[1], Zhang Zhiqi[1], Niu Liping[1], He Jicheng[1]
([1]Key Laboratory for Ecological Utilization of Multimetallic Mineral (Ministry of Education), NEU, Shenyang 110004)

Key words: SHS; high titanium ferrous with low oxygen; slag; complex reducer

Abstract: Rutile, ilmenite and Al-Ca complex reducer were used to prepare high titanium ferrous alloy by enhanced reduction-SHS method. The effects of the complex reducer compositions and slag types on the enhanced reduction-SHS process were investigated. The high titanium ferrous alloys were characterized by XRD and SEM. The results indicate that the high titanium ferrous alloys consist mainly of $TiFe_2$, $AlTi_3$ and Al_2O_3. The oxide inclusions exist resulting in directly the high oxygen content and micro-structural defects in the alloys. The titanium and oxygen contents decrease, but the aluminum content in the alloy increases while the mass ratio of calcium in the Al-Ca complex reducers increases. When the mass ratio of Al/Ca in the Al-Ca complex reducer is 6:1, titanium, oxygen and aluminum contents are 63.75%, 3.01% and 10.72% respectively. When the mass ratio of Al/Ca is 5:1 titanium content is 55.00% nearly and aluminum content is higher than 14.00%, but oxygen content is lower than 2.0%.

1. Introduction

The high titanium ferroalloys with 65%~75% titanium have the advantages of low melting point and high titanium content. They are widely used in special steel refining, while they are also a kind of very important quality orientation alloys in the rage of aviation and aerospace. At present, the methods of preparing high titanium ferroalloy include vacuum remelting and thermit reduction. The alloys prepared by the vacuum remelting method have good qualities and low oxygen content, so it is widely used in Russia, Western Europe and other developed countries. In China, there are abundant rutile resources, but waste titanium is lack, therefore, the preparation method is the thermit reduction. But there are many quality defects in the high ferrotitanium alloy, including high oxygen content, unstable quality and so on. In order to improve the qualities of the high titanium ferroalloy, especially to reduce oxygen content, the domestic and overseas have done a lot of further researches. For example, Sichuan E-mei ferroalloy plant and Beijing Nonferrous Metal Research Institute have prepared high titanium ferrous with 73.77% titanium with natural rutile, but the oxygen content is high. Through controlling the quality of raw material, they obtained the better qualities, but the oxygen content is still very high. South Africa Mintek company have prepared high titanium ferrous alloy with low nitrate by plasma heating under the isolation air conditions, but they couldn't also remove effectively oxygen in the alloy. The oxygen exists in the form of Al_2O_3 and titanium protoxide. So it can be speculated that except TiO_2 not being fully reduced, the no-sufficient alloy-slag separation is the direct reason resulting in high oxygen and poor microstructure. In view of present technical difficulties during preparing high titanium ferroalloy by thermit reduction, this paper proposed a new method of preparing high titanium ferrous with low oxygen by enhanced reduction-SHS with Al-Ca complex reducer. Ca in Al-Ca complex reducer has stronger reductive ability, it can effectively strengthen the reductive degree of TiO_2. The slagging agent CaO CaF_2 and MgO can effectively reduce the viscosity of Al_2O_3 slag to improve its liquidities to strengthen alloy-slag separation effects so that to remove inclusions and oxygen. In this

paper, effects of slagging agent type on the reduction and the qualities of high-titanium ferroalloy were studied.

2 Experiments

2.1 Experimental materials

The reactants include rutile (chemical compositions of TiO_2 89.2%, SiO_2 is 5.4%, Al_2O_3 is 2.4%), ilmenite (chemical compositions of TiO_2 is 50.6%, TFe is 32.3%, SiO_2 is 4.1%), CaO (>98%), $KClO_3$ (>98%),reducer Al (>99%) and Ca (>99%).

2.2Experimental Process

Tab1 Analysis results of micro-region in alloy samples/mass%

No	Al/Ca	slag compositions
(a)	12:1	10%CaO-90%Al_2O_3
(b)	6:1	20%CaO-80%Al_2O_3
(c)	5:1	25%CaO-75%Al_2O_3
(d)	5:1	3.6%CaF_2-24.1%CaO-72.3%Al_2O_3
(e)	7:3	36.6%CaO-63.4%Al_2O_3
(f)	7:3	6.4%MgO-30.2%CaO-63.4%Al_2O_3

Rutile, ilmenite, CaO and $KClO_3$ were dried at 400℃ for 12h, and then weighed to be mixed with complex reducer. The reductant compositions and smelting slag compositions are shown in table1. For tests (a)~(f), mass ratio of rutile and ilmenite is 3:1, tmass fraction of $KClO_3$ is mass 30% of rutile. For tests (b)~(d), mass ratio of rutile and ilmenite is 2:1, mass fraction of $KClO_3$ is mass 20% of rutile.

The reactant mixtures are put into graphite reactor enclosed magnesia lining, and magnesium powders was put to the reactant surface, and then magnesium was ignited to induce the SHS reaction. The high temperature melt was gotten and then casted into the mold to be cooled to room temperature,. At last, we pull out the ingot and collect slag samples.

2.3 Analytical methods

The alloy microstructures were analyzed by scanning electron microscope(SEM,,S300, Cambridge UK). Preparing process of alloy samples follows as: firstly polishing→corroding for 10~20s→washing→ scrubbing by alcohol→drying.. The corrosive liquid is mix acid of HF:HNO_3:H_2O=1~3ml:2~6ml:91~ 97ml.. The phase compositions of alloys and slags were analyzed by X'Pert Pro MPD (type PW3040/60, scanning speed of 2^0/min).The oxygen content in alloy was measured by the oxygen and nitrogen analyzer(type G8.Germany Bruker Ltd).

3. Results and discussions

3.1 XRD analysis

Fig.1 is XRD patterns of the samples (a)~(f). It can be seen from Fig.1 that the alloys consist mainly of $TiFe_2$, $AlTi_3$, Al_2O_3 and so on. Al_2O_3 exists in all samples which illustrates that metal-slag separation effect is not thorough. When mass ratio Al/Ca in 12:1 in the complex reducer, there exists still TiO_2 phase in sample (a); but when mass ratio of Al/Ca is 6:1, TiO_2 phase diffraction peak weakens significantly in sample (b), and it will transform into TiO, Ti_6O and so on. While mass ratios of Al/Ca are 5:1 and 7:3, there don't exist TiO_2 phase in the sample(c)~(f). However the existence of basic oxides, especially CaO, is beneficial for the reduction of TiO_2. With mass fraction of basic oxide slag in samples (a) ~(f) (CaO, MgO and CaF_2) increasing gradually, the thermodynamics reduction reaction of TiO_2 becomes more enough. Seen from Fig.1(a), mass fraction of CaO in slag is 10%, there exists unreduced TiO_2 phase in alloy; when CaO mass fraction is 20%, titanium exists in the form of suboxide TiO, Ti_6O and so on. With the mass of CaO increasing, it can combine with Al_2O_3 to generate

calcium aluminate which reduces the chance of TiO_2 combining with Al_2O_3, and then it can reduce the viscosity of Al_2O_3 slag and improve its liquidities to strengthen the alloy-slag separation effects.

With the mass fraction of calcium in the complex reducer increasing, as soon the reductive degree of TiO_2 was significantly strengthened, as the elementary substance Fe appeared in samples (c) ~ (f). Because of the mass fraction of calcium in the complex reducer increasing, the reductive abilities were remarkably enhanced, and more reaction heats were released to make adiabatic temperature higher. Since adding $KClO_3$ made fatherly the SHS reaction temperature increase significantly resulting in the metal titanium evaporating dramatically, Fe content in the alloy increased significantly and elementary substance Fe appeared. When adding CaF_2 (in samples (c) ~(d)) or MgO (in samples (e)~(f)) to reactants, they improved slag liquidities which was benefit for removing inclusions in alloys and improving its microstructures.

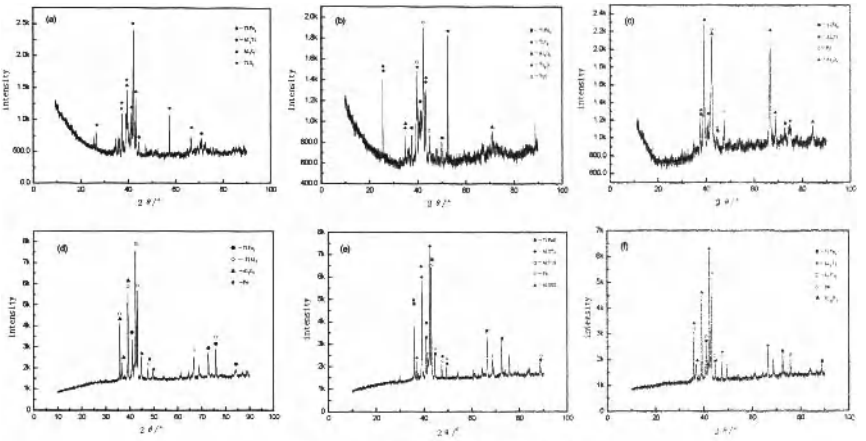

Fig. 1 XRD patterns of the alloy samples

3.2 SEM Analysis

Fig. 2 shows SEM photos of the samples (a) ~ (f). It can be seen from Fig.2 that there are three obvious different regions (region A, region B and region C) in all the alloys. Region A is high oxygen, high aluminum area. Region B, C are both the coexisting area of titanium, ferrum, aluminium, silicon and so on. Aluminum and ferrum contents in region B are higher than those in region C, but its titanium content is lower than one in region C. Table1 shows the relative micro-region analysis results of samples (a)~(f).

We can see from Fig.2 that region A with high oxygen, and high aluminum is the main existing area of inclusions, whose presence is the one of direct reasons to cause high oxygen content in alloys. When the reductive effect of TiO_2 is not complete, except Al_2O_3 inclusion exists, there will exist a litte ferrotitanium sosoloid with low oxygen(shown in Fig2(a) and Fig2(b)). As the mass fraction of calcium in the complex reducer increasing, reductive effect would be enhanced significantly, and the areas of region A would also shrink gradually (shown in the samples(c)~(f)). So the existence of Al_2O_3 is the main reason to cause high oxygen content in alloys. When the mass ratio of Al/Ca is 5:1, there has no oxygen existence in the regions B and C, which indicates that TiO_2 has been completely reduced. As shown in samples (a), (b), (c) and (e) in Fig.2, the inclusions were effectively removed, the defects, porosity and crack disappeared gradually (such as red arrow in sample a), and the alloy micro-structures became more uniform because the slag liquidities were improved significantly to strengthen he metal-slag separation effects with CaO mass fraction increasing. It could be seen Fig.2(f) that the metal-slag

separation effects are better and alloy micro-structures are denser when MgO was added to the reactants. Because the slag of 6.4%MgO-30.2%CaO-63.4%Al_2O_3 has lower melting point, lower viscosity and better liquidity, metal-slag separation effects were more sufficient and inclusions were removed more thoroughly. When adding CaF_2 to reactants, there are certain porosity in the alloys(shown in Fig2(d)). Because CaF_2 has strong volatility, and combines with other slag element to generate chloride and then volatilize violently at high temperature, which led to porosity existence in alloys.

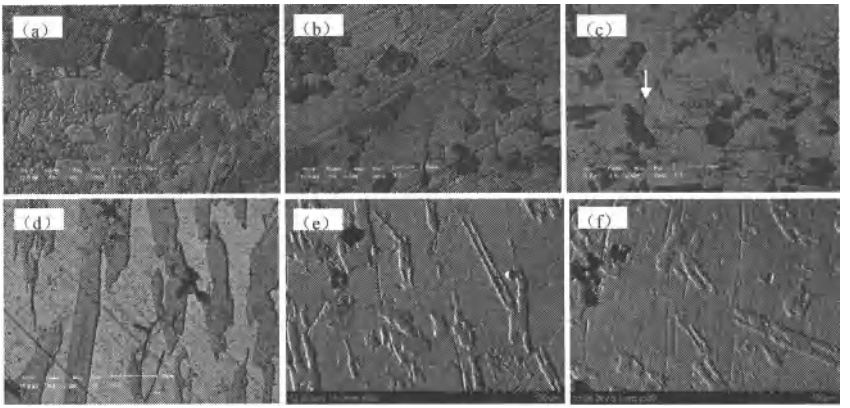

Fig. 2 SEM photos of the alloy samples

Tab2 Analysis results of micro-region in samples/%

No	Region	Ti	Fe	Al	Si	O
	a	69.87	7.90	7.83	4.93	9.43
(a)	b	45.04	26.91	24.65	1.46	1.95
	c	57.82	22.07	15.97	1.26	2.89
	a	71.06	7.43	7.28	3.94	10.28
(b)	b	52.52	20.75	21.13	2.60	3.01
	c	55.46	22.65	14.00	2.54	5.35
	a			44.54		55.46
(c)	b	31.69	36.41	28.61	2.14	1.15
	c	68.43	2.43	4.11	18.87	6.17
	a			46.08		53.92
(d)	b	46.25	28.68	22.60	0.88	1.58
	c	66.29	2.62	5.23	18.73	7.14
	a			46.11		53.89
(e)	b	46.54	34.72	18.72		
	c	75.68	3.15	3.67	17.50	
	a			49.46		50.54
(f)	b	47.11	34.85	17.01	1.03	
	c	76.67	3.65	5.62	14.06	

As Known from reference[1], with the mass fraction of calcium in the complex reducer increasing, the actual reaction heat effects per weight increased, and the actual reaction temperature increased too which would make more enough thermodynamics conditions for the reduction of TiO_2. With the reaction temperature increasing, slag liquidities were improved significantly, so metal-slag separation effects were enhanced and inclusions were removed significantly.

3.3 Chemical Composition Analysis

Table3 shows chemical compositions of all the high-titanium ferrous alloy samples.

Table 3 Chemical Compositions of alloy samples/mass%

NO	Ti	Fe	Al	Si	O
(a)	60.02	18.33	12.47	3.65	5.19
(b)	63.75	18.80	10.72	3.04	3.01
(c)	55.62	24.46	14.35	3.88	1.12
(d)	55.30	20.65	18.48	2.62	1.94
(e)	48.70	23.10	22.01	4.01	1.08
(f)	50.05	24.30	19.50	3.36	0.95

It can be found from table3 that with mass fraction of calcium in the complex reducer increasing, the oxygen content in alloys decreases rapidly. When mass ratio of Al/Ca is 12:1, the oxygen content is 5.19%, the mass ratio of Al/Ca is 6:1, the oxygen content is 3.01% and when mass ratio of Al/Ca is 5:1, the oxygen content reduces lower than 2.0% which is lower than the oxygen level in high titanium ferrous alloys prepared by the vacuum remelting. With mass fraction of calcium increasing, the titanium content decreases and aluminum content increases. When mass ratio of Al/Ca is 6:1, the titanium content is 63.75% and the aluminum content is 10.72%; When mass ratio of Al/Ca is 5:1, the titanium content is about 55.00% and the aluminum content is higher than 14.00%. Since Ca has stronger reductive abilities than Al, Ca would react firstly with TiO_2 to generate Ti and CaO. And then Al will react with unreduced TiO_2 to generate Ti and Al_2O_3. Because Al has strong combinability abilities with Ti, Al will react with Ti to generate Ti-Al compounds which causes aluminum residues increasing. The more Ca in the complex reducer is, the more Ti-Al compounds form, which results in the higher content of aluminum residues.

With the calcium mass fraction increasing, the reaction heat effects increase, the actual reaction temperature increases which leads to volatile loss of Ti increasing at high temperature. In order to prepare the excellent high titanium ferrous alloy, we must further optimize designs of reductant component, slag component and reaction conditions.

4. Conclusions

(1)The alloys consist mainly of $TiFe_2$, $AlTi_3$ and Al_2O_3. Al_2O_3 existence indicates that metal-slag separation effects is insufficient, and it directly results in the higher oxygen contents.

(2)There are three obviously different regions (region A, B and C) in the alloys. Region A consists of Al_2O_3inclusion; Regions B and C coexists of Ti, Fe, Al and Si. Region B has higher content of Al and Fe than region C, but has lower content of Ti.

(3)With the mass fraction of calcium in the complex reducer increasing, the content of O and Ti in alloys decreases rapidly and the content of Al increases.

ACKNOWLEDGEMENT:

This research was supported by National Natural Science Foundation(NSFC) (50974035,51074047, 51004033,

51002025,50644016,50704011), National Basic Research Program of China (973 plan) (2007CB613504) , the Fundamental Research Funds for the Central Universities (N090402015).

REFERENTS

1.Dou Zhi-he, Zhang Ting-an,Zhang Han-bo,etal. Basic Research on Preparation of High Titanium Ferrous with Low Oxygen Content by Thermit Reduction[J]. The Chinese Journal of Process Engineering, 2010,10(6): 1119~1123.

2.Mo Wei .Titanium[M]. Beijing:Metallurgy Industry Press,2008, 1-12.

3.Wang Fang, Gao Jing. Present Status and Development Trend of World Titanium Market in Non-Aviation Field [J].Titanium Industry Progress, 2009, 26 (6): 9-26.

4.Wang Hanchen. The Vacuum Melting of High Titanium Ferroalloy with Waste Titanium[J]. Ferroalloys, 1996, (1): 36-38.

5.Xia Dongdong,Wang Xiaodong. Melting High Titanium Ferroalloy by Thermite Method[J].Shanghai Metals, 2008, 30 (2): 28-31.

6.Deng Guozhu.Three High Quality Products in Titanium Metallurgy[J]. *Iron steel vanadium and titanium*, 2005, (12): 60-63.

7.Benjamin J S. Dispersion strengthened super-alloys by mechanical alloying [J],Metallurgical Transactions, 1970, 1(10): 2943-2951.

8.Xiao Xianghong, Liu Mingyang, Luo Faying. Technology of ferrotitanium by Aluminum thermal [J] .*Iron steel vanadium and titanium*, 2001, 22(4): 47-51.

9.Jones R T, Barcza N A, Curr T R. Plasma developments in Africa [J].Journal of Alloys and Compounds, 1993, 8(11): 2819.

10.Song Xuejing, Wei Li, Zhang Ting-an, etal. Analysis of forming mechanism of oxygen in high ferrotitanium and deoxidizing oxygen experiment [J], The Chinese Journal of Process Engineering, 2008, 8(S1): 176-179.

11.Xu Lei, Zhu Peixian, Yuan Yiyao. A new process of making high titanium ferroalloy [J], Southern Metals, 2008, (4): 4~7.

12.Xia Wentang, Zhang Qixiu. Research on Melting High Titanium Ferroalloy by Electroslags Crucible Remelting[J]. Ferroalloys, 2004, (4): 36-39.

13.Paton B E, Medovar B L, Benz M G. ESR for titanium: yesterday, today, tomorrow[A], In: Processing of The Ninth World Conference on Titanium.2000[C], Saint-Petersburg, Russia, 1999, 1385-1398.

14.Chen G Z, Fray D J, Farthing T W. Direct electrochemical reduction of titanium dioxide to titanium in molten calcium chloride [J].Nature, 2000, 407(9): 361.

15.Li Zongqian. Calcium Aluminate Premelted Slagand its Application on Converter Wash Heat[D]. Wuhan: Wuhan University of Technology, 2006.

3rd International Symposium on High-Temperature Metallurgical Processing
Edited by: Tao Jiang, Jiann-Yang Hwang, Patrick Masset, Onuralp Yucel, Rafael Padilla, and Guifeng Zhou
TMS (The Minerals, Metals & Materials Society), 2012

PREPARING ALUM INUM-SCANDIUM ALLOYS USING DIRECT HALL REDUCTION PROCESS

Chunyang Guan, Jilai Xue, Jun Zhu, Qiaochu Liu

School of Metallurgical and Ecological Engineering
University of Science and Technology Beijing
Xueyuan Road 30, 100083 Beijing, China

Keywords: Al-Sc alloy, Cryolite Melt, Electrolysis, Ultrasound.

Abstract

Al-Sc Alloys have showed many advanced properties for a wide range of industrial application, which is usually produced using thermal reduction process. This work is aimed to develop an electrochemical process to make Al-Sc alloy using industrial Hall aluminum reduction cells. The experiments have been carried out in a lab cell where NaF/AlF_3-Al_2O_3-LiF as electrolyte, Sc_2O_3 as raw material, and liquid aluminum as cathode were used at operating temperature of 950 °C. The resulting Al contained 0.2 - 0.5 wt.% Sc that is the common range in its content for advanced applications. However, a small fraction of Sc was found from thermal reduction at Al melts interface. SEM-EDS and ICP-AES analysis showed a uniformed distribution of Sc at varying locations of the Al-Sc alloy sample. In addition, a higher Sc content in Al-Sc alloy can be obtained with introducing ultrasound through the cathode than that without it.

Introduction

In recent years, scandium has been investigated as an alloying element for aluminum alloys. With addition of a small amount of Sc, Al alloys can improve the strength, weld ability, resistance to re-crystallization and corrosion resistance [1-3]. Due to their advanced properties and potential applications, the demand for Al-Sc alloys will increase in the future. However, the difficulties in reduction technologies and the high costs in production process may limit their expansion in application areas.

The current major method of producing Al-Sc alloys is to mix Sc into Al by melting Al-Sc master alloy. This alloying process has several technical problems, such as easy segregating and heavy burning loss, etc. The price of Sc metal or starting material is also high, so the mixing process is an expensive alloying method. Molten salt electrolysis is alternative method to prepare RE metal and RE alloys [4, 5]. It also can reduce the segregation of alloying elements. Sc_2O_3 is an ideal material as raw material with low price and decomposition voltage. Some work has proved that Al-Sc alloys can be obtained by electrolysis Sc_2O_3 directly in cryolite [6-8], or $CaCl_2$ molten salt [9].

Ultrasonic has been applied in many areas of metallurgical processes, in which one of important applications is for refinement of alloy microstructures [10]. And ultrasound has been also revealed to have effects on electrolysis process for making aluminum [11]. However, the ultrasonic effect on the cathode during electrolysis preparing Al-RE Alloys has not been reported.

In this work, preparing Al-Sc alloys in cryolite molten salt electrolysis has been investigated. A series of experiments on cathode current density have been carried out in laboratory cell, and the ultrasonic effects on aluminum electrolysis and Al-Sc alloying process have been also studies.

Experimental Procedures

Chemicals and Materials

Table I lists the chemicals used in this study. Cryolitic melt of 2.2NaF/AlF_3-5 wt.% LiF was used as electrolyte, 3 wt.% Al_2O_3 and Sc_2O_3 as raw materials, and liquid Al as a collecting metal.

Table I. Chemicals and Materials Used in Experiments

Materials	Purity (%)
Na_3AlF_6	> 99.0
AlF_3	> 98.0
LiF	> 98.5
Al_2O_3	> 99.0
Sc_2O_3	99.99
Al	99.999

Electrolysis Experiments

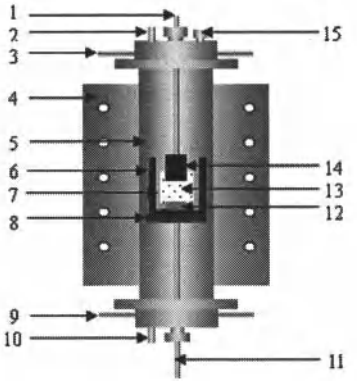

Figure 1. Experimental apparatus for molten salt electrolysis(1-Anode guide bar; 2-Gas outlet; 3-Cooling water tube; 4-Resistance furnace; 5-Furnace tube; 6-Graphite crucible; 7-Corundum tube; 8-Graphite stock; 9-Cooling water tube; 10-Gas inlet; 11-Cathode guide bar; 12-Liquid aluminum; 13-Electrolyte and Sc_2O_3; 14-Graphite anode; 15-Thermocouple).

In Figure 1, the schematic illustration of experimental apparatus for making Al-Sc alloy is presented. The electrolyte was contained in a graphite crucible with an alumina lining of Φ50 mm in inner diameter, and the aluminum metal was in a Φ25 mm hole at the bottom. The crucible was placed in a vertical tube furnace. The carbon anode was Φ25 mm in diameter and 50 mm in length.

The electrolyte was melted at 950 °C and the electrolysis was performed under an argon atmosphere. The cathode current density was varied from 0 to 1 A/cm^2. In addition, ultrasound was introduced through a stainless steel rod into the cathode – electrolysis interface. The total power of ultrasound was 360 W with a constant frequency of 20 kHz, and the ultrasound was loaded into the system every 2 s and stopped for 2 s, alternatively. The metal after experiment was cooled down to room temperature for measurement.

Analysis of Sc Content in Alloys

The metal sample after electrolysis was cut to two pieces in form of semi-spheres, as illustrated in Figure 2. The sections of both semi-spheres were divided into five areas for SEM-EDS (scanning electron microscopy-Energy dispersive X-ray spectroscopy) analysis. Drilled Al scraps from the five areas in another semi-sphere were also analyzed by ICP-AES (inductively coupled plasma-atomic emission spectrometry) technique.

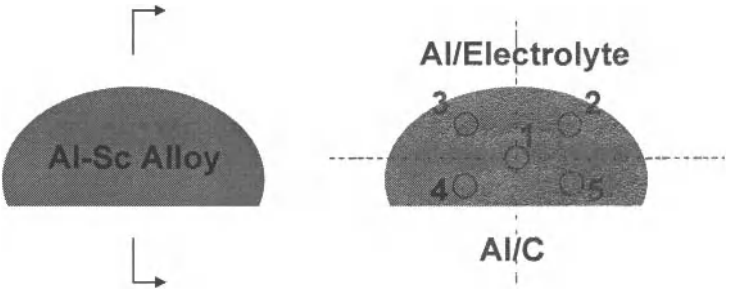

Figure 2. The illustration of sampling location on the metals (1 - Middle; 2 - Up-Right; 3 - Up-Left; 4 - Down-Left; 5 - Down-Right).

Results and Discussion

Change of Metals Mass

Figure 3 is a typical photograph showing Al-Sc alloy obtained after the electrolysis experiment in cryolitic melts. The electrolysis in 2.2NaF/AlF_3-LiF melt were carried out with A_2O_3 and Sc_2O_3 addition, where Al and Sc were reduced together electrochemically into liquid aluminum metal pad on the cathode.

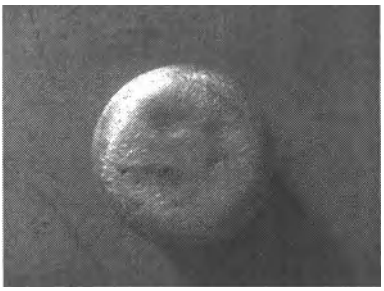

Figure 3. Photograph showing Al-Sc alloy obtained after the electrolysis in cryolitic melts with liquid aluminum cathode (T=950 °C, time = 2 h, current density=1 A/cm^2).

The electrochemical reactions with the metal production can be described as:
At the cathode:

$$Al^{3+} + 3e - Al\ (l) \quad (1)$$

$$Sc^{3+} + 3e - Sc\ (s) \quad (2)$$

At the anode:

$$C\ (s) + xO^{2-} - CO_x\ (g) + 2x^{e-} \quad (3)$$

Table II. Mass of Aluminum Metals before and after Electrolysis (ICP-AES Analysis)

Cathode Current Density (A/cm^2)	Mass before Electrolysis (g)	Mass after Electrolysis (g)	Average Sc Content *(wt.%)	Mass Increase (g)		
				Total	Sc	Al
0	16.03	15.35	0.14	-0.68	0.021	-0.701
0.5	16.06	17.60	0.25	1.54	0.044	1.496
1.0	15.93	17.91	0.41	1.98	0.073	1.907

* Average value from 5 locations at the metal sample

Table II lists the mass of metals before and after electrolysis. In general, the metal mass increased after electrolysis at the current density from 0.5 to 1.0 A/cm^2, and the increase in mass became larger with increased current. Although thermal reduction from thermodynamic calculation is difficult, the increase in metal mass as well as a 0.14 % Sc content in the alloy was appeared when the current was set to none. This result demonstrates that Sc can be produced by Al thermal reduction in cryolitic melt at the testing temperature. The thermal reduction can be expressed as below:

$$Sc_2O_3 + [\text{F containing salt}] - ScOF_x^{n-} \quad (4)$$

$$ScOF_x^{n-} + Al - Sc + AlOF_x^{n-} \quad (5)$$

$$Sc + Al - (Al\text{-}Sc) \quad (6)$$

Sc_2O_3 dissolved in cryolitic melt changes into the fluorine containing complex, thus reducing the difficulty of aluminum thermal reduction reaction.

Sc Content with Electrolysis Time

As shown in Figure 4, Sc content in aluminum metals increases with electrolysis time from 0.5 to 2.0 hours at cathode current density of 1 A/cm^2, and the curve trend become flattened as the electrolysis time is longer than 1.5 h. Further increasing time can make the electrolyte volatilized seriously.

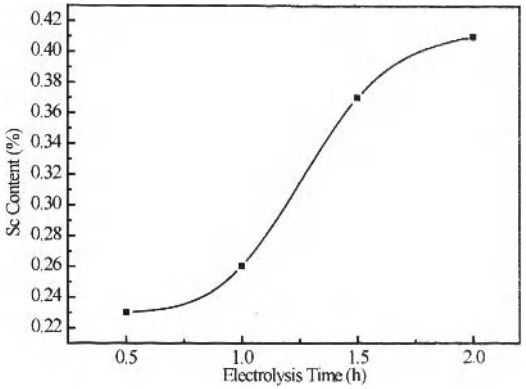

Figure 4. Curve of Sc content in aluminum metal vs. electrolysis time (T=950 °C, current density=1 A/cm^2).

Table III. Mass of Aluminum Metals before and after Electrolysis (ICP-AES Analysis, T=950 °C, current density=1 A/cm^2)

Electrolysis Time (h)	Mass before Electrolysis (g)	Mass after Electrolysis (g)	Average Sc *(wt.%)	Mass Increase (g)		
				Total	Sc	Al
0.5	15.88	16.47	0.23	0.59	0.038	0.552
1.0	16.06	17.60	0.26	1.54	0.042	1.498
1.5	15.92	17.53	0.37	1.61	0.065	1.545
2.0	15.93	17.91	0.41	1.98	0.073	1.907

* Average value from 5 locations at the metal sample

Distribution of Sc in Alloys

Table III shows the analysis result of SEM-EDS and ICP-AES techniques. The concentrations of Sc from different areas in the metal sample varied from 0.17 wt.% to 0.59 wt.% with SEM-EDS

analysis. Because of the concern on Sc distribution problem, ICP-AES method was applied to analyze the same 5 locations on the same samples, in which the data showed relative small variation in Sc concentration, from 0.19 wt.% to 0.27 wt.% with ICP-AES method.

Table IV. Sc Content in Aluminum Metals after Electrolysis at 0.5 A/cm^2

Sampling Area	Location	Sc Content in Metal (wt.%)	
		EDS	ICP-AES
1	At middle	0.17	0.19
2	At up-right	0.32	0.26
3	At up-left	0.27	0.27
4	At down-left	0.59	0.26
5	At down-right	0.47	0.23

Although part of the data is different between the two methods, the variation in Sc concentration from different areas may not as large as that in the metal produced from electrolysis in $CaCl_2$ molten salt [9]. Later experiment in this investigation also shows the Sc distribution in the alloy can be somewhat uniform. However, this may strongly depend on the experimental conditions and operating technique.

Effect of Current Density and Ultrasound

Table V. Sc Content in Aluminum Metals after Electrolysis (ICP-AES Analysis)

Analysis Area	Location	Sc (wt.%)		
		0.5 A/cm^2	1 A/cm^2	1 A/cm^2 (with Ultrasound)
1	At middle	0.19	-	0.45
2	At up-right	0.26	0.43	0.48
3	At up-left	0.27	-	0.51
4	At down-left	0.26	0.39	0.47
5	At down-right	0.23	-	0.48

Table V presents Sc concentrations in the metal samples from different experiment conditions analyzed by ICP-AES. The results demonstrate that the concentrations of Sc in the samples can increase with increased current density. This Sc level in the alloy can increase a little further with ultrasound, compared with those under the same current density and other conditions as well.

Use of ultrasound to the cathode in electrolysis may increase Sc content and improve its distribution in the metal. This phenomenon hasn't been reported in literature before. When applying ultrasound to cathode during electrolysis process, the ultrasound can cause a shaking action at the interface of liquid Al and electrolyte, improving the transporting conditions of reaction. The mechanism of ultrasonic needs further study in the future.

Conclusions

1. Al-Sc alloys with 0.2 - 0.5 wt.% Sc was obtained by cryolite melt electrolysis process, with Sc_2O_3 and Al_2O_3 as raw materials. The results demonstrate that Al and Sc in cryolite melt can be co-deposited. Preparing Al-Sc alloys in Hall aluminum reduction cells is possible, while thermal reduction process may also proceeded to make a small fraction of Sc into Al alloys.

2. SEM-EDS and ICP-AES analysis indicate that Sc in the resulting Al-Sc alloys is uniformly distributed, and this can be a contributing factor to enhance the properties of Al-Sc alloys.

3. The concentration of Sc in the samples is found being related to the cathode current density that can be optimized to improve Sc distribution in Al-Sc alloys.

4. Ultrasound on cathode process can be beneficial to increase the concentration of Sc in Al-Sc alloys. The ultrasound might cause shaking at the interface of liquid Al and electrolyte, thus promoting the reaction rate. The mechanism of ultrasonic effect needs further study.

Acknowledgement

Part of work has been supported by National Natural Science Foundation of China (NSFC No. 50874012).

References

1. J. Röyset, "Scandium in Aluminium Alloys Overview: Physical Metallurgy, Properties and Applications," *Metallurgical Science and Technology*, 25 (2) (2007), 11-21.

2. J. Röyset, N. Ryum, "Scandium in Aluminium Alloys," *International Materials Reviews*, 50 (1) (2005), 19-44.

3. G. Cacciamani et al., "Thermodynamic Measurements and Assessment of the Al-Sc System," *Intermetallics*, 7 (1999), 101-108.

4. T. Iida, T. Nohira, and Y. Ito, "Electrochemical Formation of Sm-Co Alloys by Co-deposition of Sm and Co in a Molten LiCl-KCl-$SmCl_3$-$CoCl_2$ System," *Electrochimica Acta*, 48 (2003), 2517-2521.

5. Q. Shi et al., "Electrolytic Co-deposition of Y (III) and Al (III) and Surface Metalliding in Molten Fluorides-Oxides Systems," *Rare Metals*, 18(1) (1999), 21-26.

6. M. Zhang, J. Li, and J. Liang, "Preparation of Al-Sc Alloys by Molten Salt Electrolysis," *Journal of Northeastern University (Natural Science)*, 24 (4) (2003), 358-360 (In Chinese).

7. R. Guo et al., "Preparation of Al-Sc Application Alloys by Molten Salt Electrolysis Method," *Chinese Journal of Rare Metals*, 32 (5) (2008), 645-648 (In Chinese).

8. S. Yang, Q. Li, and S. Gu, "The Thermodynamics of Electrolysis Al-Sc Alloys," *Nonferrous Metals (Extractive Metallurgy)*, 2 (2003), 26-29 (In Chinese).

9. M. Harata et al., "Electrochemical Production of Al-Sc Alloy in $CaCl_2$-Sc_2O_3 Molten Salt," *Journal of Alloys and Compounds*, 474 (2009), 124-130.

10. G.I. Eskin, Y.P. Pimenov and G.S. Makarov, "Effect of Cavitation Melt Treatment on the Structure Refinement and Property Improvement in Cast and Deformed Hypereutectic Al-Si Alloys," *Materials Science Forum*, 242 (1997), 65-70.

11. J. Xue et al., "Experimental and Numerical Studies on Bubble Removal under Anodes by Using Ultrasound in Water Solutions and Cryolitic Melts," *Light Metals 2005*, ed. H. Kvande (Warendale, PA: The Minerals, Metals & Materials Society, 2005), 553-558.

3rd International Symposium on High-Temperature Metallurgical Processing
Edited by: Tao Jiang, Jiann-Yang Hwang, Patrick Masset, Onuralp Yucel, Rafael Padilla, and Guifeng Zhou
TMS (The Minerals, Metals & Materials Society), 2012

PRODUCTION OF $NbAl_3$ POWDERS THROUGH SODIUM REDUCTION OF OXIDES IN MOLTEN SALTS

Chao Du, Na Wang, Yao Zhang Shuqiang Jiao, Hongmin Zhu

School of Metallurgical and Ecological Engineering, University of Science and Technology Beijing; 30 Xueyuan Rd, Beijing, China, 100083

Keywords: niobium aluminides, molten salts, sodium reduction, co-reduction.

Abstract

Na_2NbAlO_5 was synthesized using Nb_2O_5 and $NaAlO_2$ as raw materials in molten NaCl-$CaCl_2$ by a solid reaction. With an addition of sodium into the melts, Na_2NbAlO_5 was subsequently reduced to form $NbAl_3$ intermetallic compound with a particle size of 50-300nm.

Introduction

The intermetallic compounds of niobium aluminides have been a subject of research interests as high temperature materials because of their properties such as high melting temperature, large specific strength at elevated temperature, good resistance to high temperature oxidation, low density and large ductility [1,2]. They are applicable for turbine blades in aircraft engines and stationary gas turbines [3,4].

In recent years, the methods of powder synthesis have been widely discussed. There are many methods to synthesis intermetallic compounds such as conventional melting and solidification [5], powder metallurgy [6,7], reaction sintering [8] and reaction sintering with prior mechanical activation [9,10]. There is a prominent weakness in such methods that they use metal to produce intermetallic compounds by the means of diffusion reaction. Although the metal can diffusion sufficiently, it is still hard to avoid maldistribution of the constituents which impairs the properties of the materials.

Armstrong method is a representative technique of producing an alloy or ceramic by the exothermic subsurface reduction of a mixed halide vapor of the alloy or ceramic constituents with liquid alkali or alkaline earth reductant metal or mixtures. For example, Ti-Al-V was produced by Armstrong method using $TiCl_4$, $AlCl_3$ and VCl_3 through sodium reduction. The solids of $TiCl_4$, $AlCl_3$ and VCl_3 were mixed and boiled until an equilibrium with the vapor was attained, and thereafter introducing the equilibrium vapor into the liquid reductant Na to form

alloy powders of the equilibrium vapor constituents in the preselected atomic ratio. One critical advantage of Armstrong method is that starting materials were mixed in the form of gases forming a homogeneous system which could be reduced by sodium in situ [11].

In our previous work, fine intermetallic compounds powders have been synthesized from a homogeneous system in which raw materials of chlorides were mixed uniformly in the preselected atomic ratio. Nb-Sn and Nb-Ta intermetallic powders were prepared by hydrogen reduction of $NbCl_5$-$SnCl_2$ and $NbCl_5$-$TaCl_5$ vapors which were mixed easily [12] and Nb-Al powders were produced by sodium reduction of $NbCl_5$-$AlCl_3$ dissolved in the eutectic molten salts [13].

Armstrong method and our previous studies demonstrated that a homogeneous system would be favorable for fine intermetallic powders synthesis. However, the high vapour pressure of chlorides makes the difficulty in operation of controlling such reactions. It is important to find an approach using oxides as raw materials to directly prepare intermetallic compounds. Conventionally, molten salt has been used as medium to synthesize the single phase multinary through solid reaction. The purpose of this paper is going for synthesizing the multiplex oxide of Na_2NbAlO_5 in a NaCl-$CaCl_2$ melt using Nb_2O_5 and $NaAlO_2$. Subsequently, the sodium will be added into the melt to reduce the as-prepared multinary oxide for forming $NbAl_3$ intermetallic compound.

Experimental Procedures

In order to prepare the multinary oxides of Na-Nb-Al-O, Nb_2O_5 and $NaAlO_2$ were mixed using an agate mortar with a molar ratio of 1:6, and then put into a corundum crucible with NaCl-52mol%$CaCl_2$ salt. These raw materials were subsequently heated up to 700°C in the resistance furnace under an argon atmosphere. After keeping the temperature at 700°C for various times, the reactor was cooled down to ambient temperature and white powders were obtained after washing, filtering and drying.

To synthesize intermetallic powders, sodium was incised to pellets in the glove box and then carried into the reactor by the nitrogen gas at 700°C. After the sufficient time for reaction, the reactor was cooled down to ambient temperature. The products were obtained by washing, filtering and drying. X-ray diffraction (XRD) and scanning electron microscopy (SEM) were used to determine the product phase, shape and particle size.

Results and Discussion

Fig. 1 shows the dependency of reaction time for Na_2NbAlO_5 synthesis from Nb_2O_5 and $NaAlO_2$. Pattern (a) and (b) show the products heated at 700°C for 1h and 2h. The major phase is Na_2NbAlO_5 coexisted with a small amount of $Na_2Nb_4O_{11}$. It was thought that 1 h or 2 h was not the sufficient reaction time preparing pure Na_2NbAlO_5. In the reaction, majority of the oxides reacted and formed Na_2NbAlO_5, while a small quantity of Nb_2O_5 reacted with molten salt forming $Na_2Nb_4O_{11}$ and residual $NaAlO_2$ was washed off by distilled water after the reaction.

However, by lengthening the reaction to 4 h, the single phase of Na_2NbAlO_5 was obtained by complete reaction as shown in Fig.1 (c).

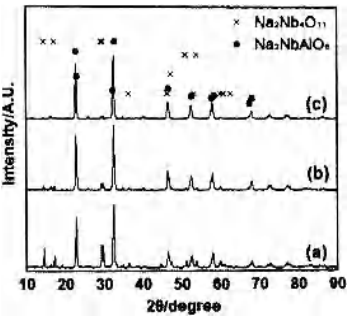

Fig. 1. XRD pattern of the products using the starting material of Nb_2O_5 - $NaAlO_2$ (1:6 molar ratio) in the molten salts for (a) 1 h, (b) 2 h, (c) 4 h.

Sodium was added into the melts to reduce the oxides, the interesting results show that the feasibility of synthesizing pure $NbAl_3$ comes from those melt with only Na_2NbAlO_5 phase prepared at 700°C for 4h (Fig. 2). In comparison, with the use of the melts prepared at 700°C for 1h, the products are $NbAl_3$ coexisted with Nb and Al metals (Fig. 3). The result is readily seen that, when a mixture of Nb_2O_5 and $NaAlO_2$ was heated at 700°C for a period of time, only a portion of oxides forming Na_2NbAlO_5 could be reduced to $NbAl_3$ and residual Nb_2O_5 and $NaAlO_2$ was reduced to Nb and Al respectively. Relatively, $NbAl_3$ powders could be produced from pure Na_2NbAlO_5 when oxides mixture was heated at 700°C for sufficient time.

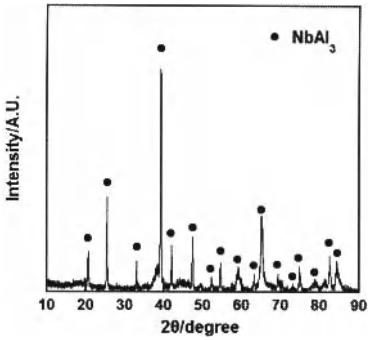

Fig. 2. XRD pattern of the products by sodium reduction using the starting material of Nb_2O_5 - $NaAlO_2$ (1:6 molar ratio) keeping in the molten salts for 4 h at 700°C.

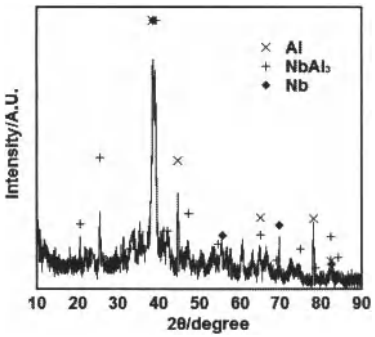

Fig. 3. XRD pattern of the products by sodium reduction using the starting material of Nb_2O_5 - $NaAlO_2$ (1:6 molar ratio) keeping in the molten salts for 1 h at 700°C.

The SEM in Fig. 4 reveals the morphology of the reduced $NbAl_3$ powders. Fine black powders remained after the removal of molten salts by leaching and the particle sizes of the powders were appropriately in the range of 50-300nm.

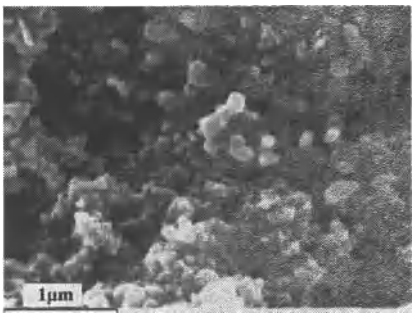

Fig. 4. SEM image of the $NbAl_3$ powders

Conclusions

$NbAl_3$ intermetallic powders could be produced from the starting materials of Nb_2O_5 and $NaAlO_2$ by sodium reduction in molten salts. The Na_2NbAlO_5 synthesized by solid reaction in molten salt was considered necessary for co-reduction to produce $NbAl_3$ powders. The particle size of $NbAl_3$ was appropriately in the range of 50-300nm.

References

1. V. Gauthier, C. Josse, F. Bernard, E. Gaffet, J.P. Larpin, "Synthesis of niobium aluminides using mechanically activated self-propagating high-temperature synthesis and mechanically activated annealing process," *Mater. Sci. Eng.* A 265 (1999) 117-121.

2. C. Milanese, F. Maglia, A. Tacca, U. Anselmi-Tamburnini, C. Zanotti, P. Giuliani, "Ignition and reaction mechanism of Co–Al and Nb–Al intermetallic compounds prepared by combustion synthesis," *J. Alloys Compd.* 412 (2006) 156-159.

3. B.A. Glowacki, X.Y. Yan, D.J. Fray, G. Chen, M. Majoros, Y. Shi, "Niobium based intermetallics as a source of high-current/high magnetic field superconductors," *Physica C* 372 (2002) 1315-1320.

4. D. Dew-Hughes, *Metallurgy of Superconducting Materials*, Academic Press, New York, 1979.

5. W. Loser, R. Hermann, M. Leonhardt, D. Dtephen, R. Bormann, "Metastable phase formation in undercooled near-eutectic Nb-Al alloys," *Mater. Sci. Eng. A* 224 (1997) 53-54.

6. E. Hellstern, L. Schultz, R. Bormann, D. Lee, "Phase formation in mechanically alloyed Nb-Al powders," *Appl. Phys. Lett.* 53 (1988) 1399-1401.

7. Z. Peng, C. Suryanarayana, F.H. Froes, "Mechanical alloying of Nb-Al powders," *Metall.*

Mater. Trans. A 27 (1996) 41-48.
8. C.R. Kachelmyer, A.S. Rogachev, A. Varma, "Mechanisms of structure formation during combustion synthesis of materials," *J. Mater. Res.* 10 (1995) 2260-2270.
9. E. Gaffet, F. Charlot, D. Klein, F. Bernard, J.C. Niepce, "In situ time-resolved diffraction coupled with a thermal i.r. camera to study mechanically activated SHS reaction: case of Fe–Al binary system," *Mater. Sci.* Forum 269–272 (1998) 379-380.
10. F. Charlot, E. Gaffet, B. Zeghmati, F. Bernard, J.C. Niepce, "Mechanically activated synthesis studied by X-ray diffraction in the Fe–Al system," *Mater. Sci. Eng.* 262 (1999) 279-288.
11. Armstrong et al, "Preparation of alloys by the Armstrong method," U.S. Patent US7041150 B2, 2006.
12. Jun Zhu, "Production of ultra-fine powder of Niobium, Tantalum and their alloys via hydrogen reduction" (P.G. thesis, USTB, 2005) 49-59.
13. Na Wang, "Direct synthesis of niobium aluminides powders by sodiothermic reduction in molten salts" (Paper presented at the EPD Congress 2011).

3rd International Symposium on High-Temperature Metallurgical Processing
Edited by: Tao Jiang, Jiann-Yang Hwang, Patrick Masset, Onuralp Yucel, Rafael Padilla, and Guifeng Zhou
TMS (The Minerals, Metals & Materials Society), 2012

Recrystallization of L-605 Cobalt Superalloy during Hot-Working Process

TMS[1], Julien Favre[2, 3], Yuichiro Koizumi[2], Akihiko Chiba[2], Damien Fabregue[3], Eric Maire[3]

[1]TMS (The Minerals, Metals & Materials Society);
184 Thorn Hill Rd.; Warrendale, PA 15086-7514, USA
[2]Institute for Materials Research, Tohoku University
2-1-1 Katahira, Aoba-ku, Sendai, 980-8577 Japan
[3]MATEIS Laboratory, INSA de Lyon
7, Avenue Jean Capelle, 69621 Villeurbanne cedex, France
Keywords: cobalt, superalloy, deformation behavior, recrystallization, EBSD

Abstract

The mechanical behavior of Co-20Cr-15W-10Ni alloy is studied by compression tests at high temperature. Microstructures after deformation are evaluated using SEM-EBSD. Significant grain refinement occurs by dynamic recrystallization for high temperature and low strain rate ($T>1100°C$, $\dot{\varepsilon}<0.1s^{-1}$), and at high strain rate ($\dot{\varepsilon}\sim10s^{-1}$). Dynamic recrystallization is discontinuous and occurs by grain boundaries nucleation, leading to a necklace structure. The nucleation mechanism is most likely to be bulging of grain boundaries. However, recrystallization occurs also by rotation of annealing twins which can bulge as well. The modeling of mechanical behavior gives a fair quantification of flow softening due to dynamic recrystallization, indicating the progress of dynamic recrystallization with deformation.

Introduction

Cobalt-chromium alloys are used in biomedical applications for the elaboration of implants due to their outstanding mechanical properties and their high resistance to corrosion. For stent application a large ductile behavior is required in addition to the high mechanical strength. Indeed stents have to undergo a deformation until ≈40% during their expansion [1]. Conventional Co-Cr-Mo (CCM) alloys exhibit limited ductility (maximal deformation about ε≈30%) [2]. Co-Cr-W-Ni (L-605) alloy is a better candidate for stent elaboration since its fracture strain can exceed 40% (comparable to nickel superalloys (Figure 1), while it keeps high mechanical strength. In spite of the presence of nickel element in this alloy, biocompatibility is sufficient for vascular implants, therefore L-605 alloy is extensively used for heart valves and stent elaboration [3].

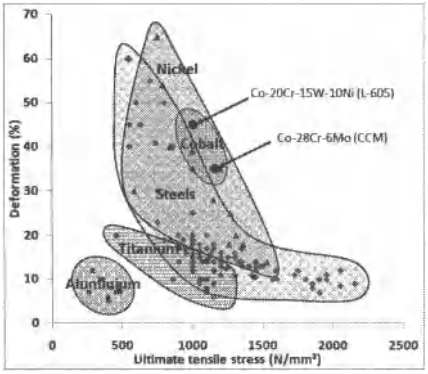

Figure 1. Ashby map of the ultimate tensile stress and ultimate deformation for steels and superalloys (data Aubert & Duval 2011)

In order to get optimal in life mechanical resistance, the evolution of microstructure during the elaboration process must be studied.

In the case of L-605 alloy, the main microstructural feature which will tailor the mechanical behavior is the grain size [4]. This grain size can be customized by choosing the right process parameters during the high temperature extrusion process of tubes to produce stents. Therefore the high-temperature deformation conditions must be smartly selected to obtain the best microstructure design leading to both significant ductility and maximal strength of the material. The aim of this study is thus to evaluate microstructure after high-temperature deformation for a large scale of temperature and strain rate conditions. The mechanical performances of the different microstructures obtained will be investigated in an upcoming publication.

Experimental procedure

High-temperature behavior is studied by high temperature deformation of 25 cylinder-shaped samples at different temperatures and strain rates. Samples have Rastegaev geometry (diameter 8mm x height 12mm), with 0,2mm depth grooves carved on the two edges to keep the lubricant. Compression tests are carried out under vacuum on a hot-deformation simulator (Thermec-master Z device, Fuji Electronic Industrial Co. Ltd., Japan). Quick heating rate of 5°C/s is reached thanks to high-frequency induction heating. A solution treatment of 10min at 1200°C is applied in-situ in the Thermec-master device in order to homogenize microstructure and to dissolve potential precipitates. Then compression tests are carried out at a temperature range of 1000°C to 1200°C with a strain varying from $0.001s^{-1}$ to $10s^{-1}$. Compression is uniaxial with a maximum engineering strain of 60%, corresponding to a maximal true strain of 0.92. Samples are finally gas-quenched by a mixture of He and N_2 just after compression in order to preserve high-temperature microstructure.

After hot compression, samples are sliced parallel to the compression axis and polished for metallographic observations. Microstructure is observed by optical microscopy and SEM-EBSD. As the effective strain is non-homogeneous in the sample, microstructure is always considered at the same position, at 1/3 of the width of the sample. At this location finite element simulations [5] have shown that the strain experienced is about 0.65 for a macroscopic strain of 0.92.

Experimental results

Compression curves

The Figure 2 shows compression curves after subtraction of the elastic regime. All the curves exhibit a peak stress followed by flow softening. Peak stress occurs later for higher strain rate and lower temperatures. For high temperatures and low strain rate flow softening occur relatively early in the deformation process, giving a very broad and smooth peak stress. Finally it can be seen that L-605 alloy exhibits a usual viscoplastic behavior, with a decrease of stress values when temperature increases. Moreover flow stress increases with the strain rate due to the positive strain rate sensitivity as usual on most metals [6].

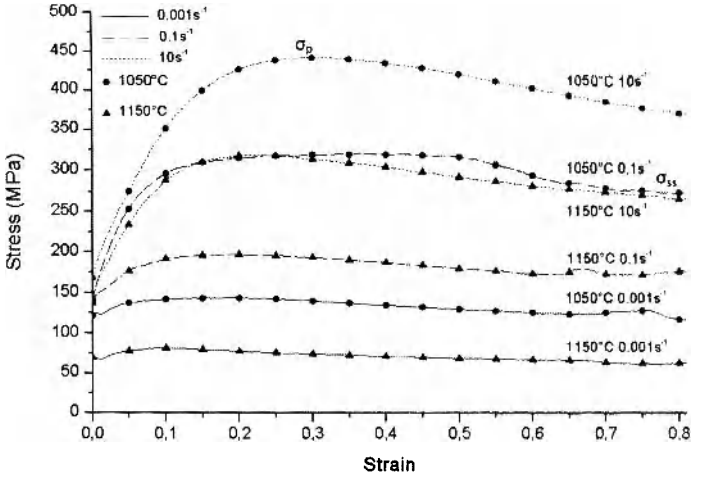

Figure 2. Compression curves of L-605 alloy at 1050°C (●) and 1150°C (▲) for strain rates of $0.001s^{-1}$ (full line), $0.1s^{-1}$ (dashed line) and $10s^{-1}$ (dotted line)

The flow softening occurring after the peak stress leads to a steady-state regime for strain $\varepsilon<1$, suggesting that the dynamic recrystallization operating is following a discontinuous mechanism [7, 8]. During the steady-state, hardening due to the creation of defects by plastic deformation is balanced by the elimination of defects due to dynamic recovery and to discontinuous dynamic recrystallization [9]. The peak stress can be finally interpreted physically as the transition from a mechanical behavior controlled mainly by hardening before the peak stress, to a behavior controlled also by dynamic recovery and discontinuous dynamic recrystallization operating jointly at steady-state. Further discussion on compression curves require to separate the contribution of the three effects of hardening, recovery and recrystallization to obtain a quantitative analysis of each metallurgical phenomenon taking place during high temperature deformation process.

Microstructure after deformation

High temperature deformation generate significant recrystallization for high temperature (T>1100°C, Figure 3b and 3c) and for low or high strain rate (SR=$0.001s^{-1}$ Figure 4a; and SR=$10s^{-1}$ Figure 4c). Recrystallization is nearly complete and leads to a homogeneous equiaxial microstructure with a single mode grain size. Grain refinement is noticeable, and the grain size drops from the initial grain size of 100μm to an average size about 10μm.

For intermediate strain rate (Figure 4b) and low temperature (Figure 3a), recrystallization is partial and leads to a very heterogeneous microstructure. Recrystallized grains are very small (lower than 1μm) and recrystallized fraction is low. Grain refinement is localized at the initial grain boundaries only, leading to a bimodal distribution of grain size.

It can be concluded from microstructure examination that maximal grain refinement is obtained for a minimal recrystallized fraction, and reciprocally. In other words, a compromise must be made to get the maximal grain refinement both in term of grain size and volume fraction.

Figure 3. Microstructure after compression at ε^*=0.65: grain boundary map from EBSD for the following deformation conditions: $0.1s^{-1}$ at (a) 1000°C, (b) 1100°C and (c) 1200°C

Figure 4. Microstructure after compression at ε^*=0.65: grain boundary map from EBSD for the following deformation conditions: 1100°C at (a) $0.001s^{-1}$, (b) $0.1s^{-1}$ and (c) $10s^{-1}$

Discussions

Dynamic recrystallization mechanisms

Observation of the microstructure at different strain levels gives further information on the mechanism of dynamic recrystallization. On the Figure 5, microstructure for engineering strain levels ε=10%, 30% and 50% (true strains ε=0.10, ε=0.36 and ε=0.69) are shown.

The condition T=1000°C and strain rate $1s^{-1}$ leads to the creation of many low angle boundaries with deformation (Figure 3a). The high concentration of defects in initial grains is due to the lack of dynamic recovery at low temperature. Recrystallization is visible at grain boundaries by the formation of very small grains (<1μm), corresponding to a final recrystallization fraction of 10% of the area. It can be concluded that for this deformation condition, the creation of defects is enough to generate nucleation of new grains by bulging of initial grain boundaries, but the low temperature is not favorable to the growth of new grains. Therefore the size of new grains is small, and recrystallized area is very low. The final microstructure is comparable to the ones obtained on Figures 3a (1000°C $0,1s^{-1}$) and 4b (1100°C $0,1s^{-1}$). These observations point up that for process conditions between $0,1s^{-1}$ and

$1s^{-1}$ and for temperatures lower than 1100°C the recrystallization is proceeding mainly by nucleation from grain boundaries, with a limited grain growth of new grains.

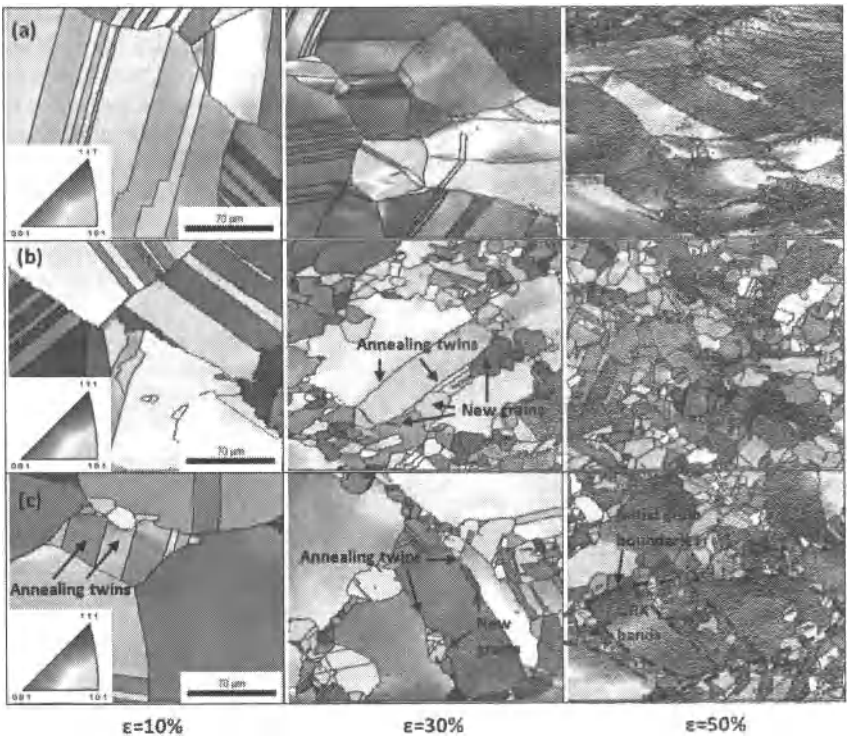

Figure 5: Observation of grain boundaries by EBSD after deformation at strain of ε=10%, 30% and 50% for the deformation conditions: (a) 1000°C $1s^{-1}$, (b) 1100°C $0.001s^{-1}$, (c) 1200°C $10s^{-1}$

The condition 1100°C $0.001s^{-1}$ leads to significant dynamic recrystallization, with a final recrystallization fraction of 90% of the area after compression at ε=50%. Recrystallization occurs at grain boundaries, and significant grain growth allow to the new grains to develop properly and to spread in the initial grains (Figure 5b). The final grain size is the size of recrystallized grains, and initial microstructure is totally erased. As both dynamic recovery and dynamic recrystallization are very active due to high temperature and low strain rate, few low angle grain boundaries are visible in the microstructure during compression. Therefore substructure is hardly visible for this condition as it is eliminated by recovery and recrystallization.

The condition 1200°C $10s^{-1}$ gives very similar results as for 1100°C $0.001s^{-1}$ (Figure 5c). Recrystallization proceeds from grain boundaries, and lead to a high recrystallization fraction of 70% of the area for ε=50%. Due to high temperature and in spite of the high strain rate, few

defects are visible due to the activity of recovery and recrystallization. For this condition annealing twins rotate from their initial angle of 60° to become high angle grain boundaries with an angle about 55°. After rotation, nucleus bulge from the annealing twins (Figure 5c). This mechanism leads to the formation of recrystallized bands on annealing twins. On the Figure 5c for a deformation level of ε=50%, the non-recrystallized grains observed have the same crystalline orientation, and thus belong to a same initial grain that was fragmented by recrystallization in bands. The disposition and spacing of these bands is similar to the one of annealing twins, and suggest that twins were initially present on this place. The evolution of annealing twins into grain boundaries and its bulging can be observed for the condition 1100°C $0.001s^{-1}$ as well (Figure 5b). However for 1100°C $0.001s^{-1}$ this mechanism is not frequent, while for 1200°C $10s^{-1}$ it seems very usual. The fraction of annealing twins (Σ3 grain boundaries) was evaluated from EBSD data after compression at ε^*=0.65 and is detailed in the Table I. The high twin fraction at 1200°C $10s^{-1}$ explain the high frequency of nucleation mechanism by bulging from twins, while this mechanism is rarer for 1100°C $0.001s^{-1}$ and not observed for 1000°C $1s^{-1}$ due to the lack of twins available for nucleation.

Table I: Flow stress and annealing twin fraction after compression at ε^*=0.65

Deformation condition	HAG fraction (15-180°)	Σ3 twin fraction (60°)
1000°C $1s^{-1}$	0.89	0.11
1100°C $0.001s^{-1}$	0.72	0.28
1200°C $10s^{-1}$	0.58	0.42

Grain refinement and elimination of crystalline misorientations

Microstructure is analyzed by EBSD after deformation at ε^*=0.65. The EBSD cartography is partitioned to separate recrystallized and non-recrystallized material. The average size of dynamic recrystallized grains is represented versus temperature and log (strain rate) on Figure 6a. The surface fraction of recrystallized material is represented on Figure 6b. For temperature higher than 1100°C and strain rate lower than $0.01s^{-1}$, recrystallized grain size can reach until 10μm, and the recrystallized fraction is about 100%. Similar behavior occurs for temperature higher than 1100°C and strain rate above $1s^{-1}$, with a recrystallized grain size attained around 5μm. The deformation regime at low temperature (<1100°C) and strain rate in the range $0.01s^{-1}$-$1s^{-1}$ exhibit limited recrystallization with a recrystallized fraction between 10 and 30%. Recrystallized microstructure is very fine for this conditions range, with an average grain size about 1μm.

The two maps on Figures 6a and 6b highlight a strong correlation between dynamically recrystallized grain size and recrystallized fraction: large grain size correspond to large fraction, and reciprocally. Grain size is larger for higher temperature and for lower strain rate because grain growth is very active in this case. The growth of recrystallized grains induces an increase of recrystallized fraction.

Average crystalline misorientation inside grains was evaluated by EBSD cartography after compression at $\varepsilon^*=0.65$. Crystalline misorientation can be quantified by the Kernel Average Misorientation parameter (KAM): for a given point on the EBSD map, this parameter corresponds to the average misorientation with neighbor points. The global average misorientation was then evaluated by taking the average over the whole scanned area (273x92µm). This mean KAM parameter is represented versus deformation parameters on Figure 6c. It can be seen on this map that misorientation parameter follows inverse evolution with grain size and recrystallized fraction: when misorientation parameter is high, recrystallized fraction is low and grain size is low. This correlation is due to the erasing of misorientations by the growth of new recrystallized grains [10] leading to the elimination of misorientation. During the development of a new grain, the moving grain boundaries sweep the material and erase the dislocations structure, leading to a decrease of KAM parameter. Therefore, KAM misorientation parameter is directly an indicator of the operation of recrystallization process, in the same way as recrystallized fraction.

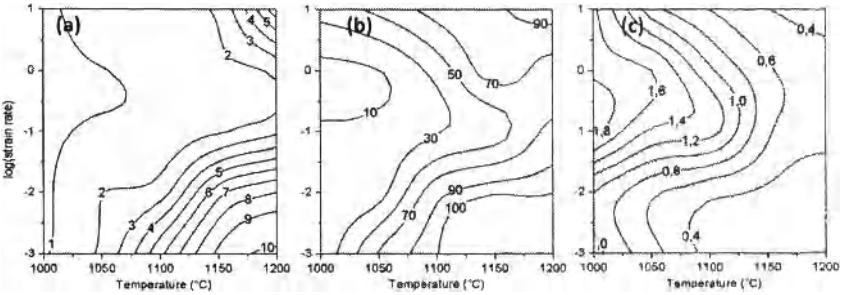

Figure 6. Maps versus temperature and log(strain rate) of: (a) Dynamic recrystallized grain size (µm), (b) Recrystallized fraction area (%), (c) Average KAM misorientation parameter

Conclusion

L-605 follows a usual viscoplastic deformation behavior at high temperature: stress increases with strain rate and decreases with temperature. Compression curves exhibit a peak stress followed by flow softening, and stabilizes to a steady-state stress value.

Microstructure observations revealed the operation of dynamic recrystallization for all deformation conditions. For temperature higher than 1100°C and strain rate lower than $0.1s^{-1}$ or higher than $1s^{-1}$, dynamic recrystallization leads to an homogeneous equiaxial microstructure with a grain size about 10 µm. Deformation at temperature lower than 1100°C and strain rate in the range $0.1\text{-}1s^{-1}$ result into an heterogeneous microstructure with grain size lower than 1µm. While recrystallization usually occur from grain boundaries, a second nucleation mechanism involving annealing twins was highlighted at temperature higher than 1100°C. In a first step, Σ3 annealing twins rotate from 60° to 55°, and then in a second step bulging can operate. The recrystallized fraction was shown to evolve inversely with dynamic recrystallized grain size and misorientation parameter.

References

[1] C. Dumoulin, B. Cochelin, "Mechanical behaviour modelling of balloon-expandable stents", *Journal of Biomechanics* 33 (2000), 1461-1470

[2] K. Yamanaka, M. Mori, A. Chiba, "Mechanical properties of as-forged Ni-free Co-29Cr-6Mo alloys with ultrafine-grained microstructure", *Materials Science and Engineering A* (2010), doi:10.1016/j.msea.2011.04.027

[3] R.V. Marrey, R. Burgermeister, R.B. Grishaber, R.O. Ritchie, Fatigue and life prediction for cobalt-chromium stents : A fracture mechanics analysis, Biomaterials, 2006, 27(9), 1988-2000

[4] R. K. Gupta, M. K. Karthikeyan, D. N. Bhalia, B. R. Ghosh, P. P. Sinha, "Effect of microstructure on mechanical properties of refractory Co-Cr-W-Ni alloy", *Metal Science and Heat Treatment*, 50 (2008), 175-179

[5] Y.P. Li, E. Onodera, A. Chiba, "Friction coefficient in hot compression of cylindrical sample", *Materials Transactions*, 51, No.7 (2010), 1210-1215

[6] U.F. Kocks, H. Mecking, "Physics and phenomenology of strain hardening: the FCC case", *Progress in Materials Science*, 48 (2003), 192-198

[7] Recrystallization and Related Annealing Phenomena, F. J. Humphreys, M. Hatherly, Oxford: Pergamon Press; 2004

[8] F. Montheillet, O. Lurdos, G. Damamme, "A grain scale approach for modeling steady-state discontinuous dynamic recrystallization", *Acta Materialia* , 57 (2009), p.1602-1612

[9] T. Sakai, J. J. Jonas, "Dynamic recrystallization: mechanical and microstructural considerations", *Acta Metallurgica*, 32 (1984), p189-209

[10] R. Sandström, R. Lagneborg, "A model for hot working occurring by recrystallization", *Acta Metallurgica*, 23(1975), p387-398

3rd International Symposium on High-Temperature Metallurgical Processing
Edited by: Tao Jiang, Jiann-Yang Hwang, Patrick Masset, Onuralp Yucel, Rafael Padilla, and Guifeng Zhou
TMS (The Minerals, Metals & Materials Society), 2012

RESEARCH ON INCLUSIONS IN CUCR ALLOY PREPARED BY THERMIT REDUCTION

DOU Zhihe[1], ZHANG Ting'an[1], ZHANG Zhiqi[1], NIU Liping[1], LV Guozhi[1], LIU Yan[1], HE Jicheng[1]
([1]Key Laboratory of Ecological Utilization of Multi-metal Intergrown Ores of Ministry of Education, School of Materials and Metallurgy, Northeastern University, Shenyang, Liaoning 110004 , China)

Key words: CuCr alloy, thermit reduction, inclusions

Abstract: CuCr alloy can be extensively used as contact materials in integrated circuit, electrodes, electric contact and high strength conductor. We proposed thermit reduction-electroslag remelting method of preparing the large scale CuCr alloy. But there are pores and oxide inclusions in CuCr alloy prepared by thermit reduction process. This paper studied mainly the effects of ratio of reactant and additive on the inclusion type and their occurrences in CuCr alloy. The slags and CuCr alloy were characterized respectively by XRD and SEM. The results show that when the additive is Na_3AlF_6, the slag consist of Al_2O_3 and Cr. When the additive is CaF_2, the slag consist of Al_2O_3, Cr, CaF_2 and $CaAl_4O_7$. The inclusions in CuCr alloy are mainly Al_2O_3 and pores which disperse in Cu-rich zone and Cu-Cr phase interface. When 5% CaF_2 and 5% $KClO_3$ are added, there are fewer pores and inclusions, and the more better microstructure.

1 Introduce

CuCr alloy is the contact terminal material with an eximious properties[1,2], which gradually replaces CuBi alloy becoming the first choice for contact terminal material in the medium and high power vacuum switch after the 1970s. The traditional preparation methods of CuCr alloy mainly contain powder metallurgy, infiltration process and vacuum electric arc melting methods. But the above methods exist some shortcomings, such as poor product quality, high cost of production, processes complex ect[3-9]. CuCr alloy is made by the thermit reduction self-propagating method, which uses CuO, Cr_2O_3 and Al as raw material to get the high-temperature melt, and then casts to manufacture CuCr alloy ingot, which response equation follows as:

$$CuO+Cr_2O_3+4Al=3Cu+2Cr+2Al_2O_3 \qquad (1)$$

Therefore, it must be existing oxide inclusions like Al_2O_3 in CuCr alloy. And then metal slag's separation degree has great influences on purity and microstructure of CuCr alloy. Improving the slag liquidity is the effective way of strengthening the metal slag's separation effect in order to remove the impurities and improve its microstructure. Combining with the phase diagrams of A_2O_3-Na_3AlF_6 and Al_2O_3-CaF_2, we can know that adding Na_3AlF_6 and CaF_2 to slag would reduce the melting point of Al_2O_3 slag effectively and improve its liquidity. So metal slag's separation degree was strengthened and the impurity content in alloy reduced and its microstructures were improved. This paper mainly researched the effects of the additive type and its adding amount on metal slag's separation effects.

2 Experiment

2.1 Experiment procedure

Ratio of reactants follows as:

the amount of CuO in actual ingredients are more excess of 5 %than the theoretical amount, Al powder are more excess of 10% than the theoretical amount, additive CaF_2 or Na_3AlF_6 ingredient quantity is accounted for 5% or 10% of the total mass of the reactants, and heating agent $KClO_3$ ingredient quantity is accounted for 5% of the total mass of the reactants. Specific ingredients are listed in table 1.

CuO,Cr_2O_3 and Al powder were mixed and put into the SHS reactor. A little magnesium powder was put to the reactants surface to ignite SHS reaction. Electromagnetic stirrer started working as soon as SHS reaction took place. The high-temperature molten formed while thermit eaction generating. The

molten metals separated from slag. The molten metals was cooled rapidly through water cooling and cast into the graphite mold while electromagnetic field stirred the molten metals for 7mins. The cooling water was stopped when temperature descended to room temperature. We took out the alloy ingot from the mold and collected the slag.

Table1 Reactant ratio for the different experiments /mass%

No	additive/%		$KClO_3$ /%
	Na_3AlF_6	CaF_2	
1#	5	/	/
2#	10	/	/
3#	5	/	5
4#	/	/	/
5#	/	5	/
6#	/	5	5
7#	/	10	/

2.2 Testing

Different CuCr specimens were made into different specifications sheets, and then the sheets were grinded and polished and corroded by corrosive liquid for 5-10s. The compositions of corrosive liquid were85%H_3PO_4:65% HNO_3:36%CH_3COOH:36%HCl (volume ratio) of 3:5:2:2. The corroded sample were characterized by microscope and scanning electron microscopy(SEM) to study the microscopic structure and inclusion distribution. The slag was grinded to 200 mesh for X-ray diffraction analysis to determine their phase composition(X ray diffraction analyzer for PW3040/60 X'Pert Pro MPD, 40KV, 40mV, copper target and the scanning speed 10° / min).

3 Results and Discussions

3.1 Analyses of Experiment phenomena

It was found that the thermit reaction completed quickly as soon as the reaction was ignited. Especially when there was heating agent $KClO_3$ in reactants, the thermit reaction was ignited more easily, it took place fiercely and seriously could explore. The reaction emitted the massive heat to make the reaction system high temperature, which ensured the metal separation from slag quickly. Figures1~2 are CuCr alloy macroscopic pictures when adding different amounts of Na_3AlF_6, CaF_2 and more excess of 5% of CuO respectively. It could be seen from the surface and the planning surface of CuCr alloy that there were the massive blowholes and the inclusions in CuCr alloys. Especially $4^{\#}$ and $5^{\#}$ samples, it's difficult to be cutted by line cutting. Because there were many non-metallic inclusions and the blowhole flaws in CuCr alloy, its electrical conductivity is very bad. It could be inferred that the metal-slag separation effect is very bad.

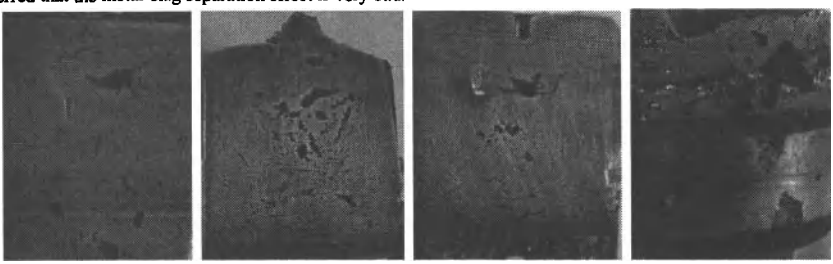

1-recruitment of Na_3AlF_6 is 5%; 2-recruitment of Na_3AlF_6 is 10%; 3-recruitment of Na_3AlF_6 is 5% and $KClO_3$ is 5%; 4-no additive

Fig.1 Macro-photograph of CuCr alloys when adding Na_3AlF_6 to reactants

In addition, there generated some flaws, shrink holes and the neck shrinks and so on in alloys during the casting process. While adding Na_3AlF_6 or CaF_2 to reactants, the microscopic structures of alloy were improved distinctly, its compact degree increased and the blowholes in alloys reduced(seen in sample $1^{\#}$). Compared the samples

1~2# with the samples 5~6#, it was found that additive Na_3AlF_6 there were more obvious influences than CaF_2 on the microstructures of the alloy. When add the amount of Na_3AlF_6 is 10% of the total reactants, the compact degree of CuCr alloy became bad, and the blowholes increased. While adding the 5% CaF_2 and 5% $KClO_3$, CuCr alloy was the most compact, and the blowhole flaws in alloys reduced significantly.

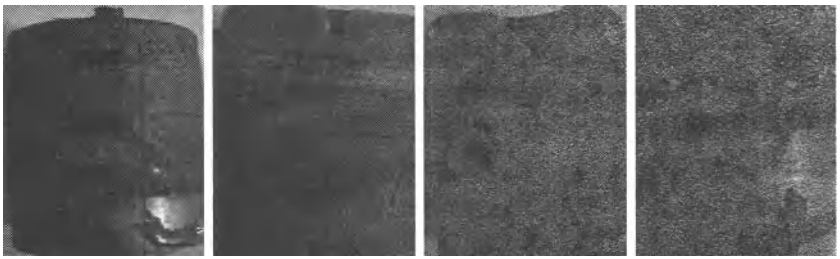

5-recruitment of CaF_2 is 5%; 6-recruitment of CaF_2 is 5% and $KClO_3$ is 5%; 7-recruitment of CaF_2 is 10%; 8-no additive

Fig.2 Macro-photograph of CuCr alloys when adding CaF_2 to reactants

We known from the above results that adding Na_3AlF_6 and CaF_2 could reduce the slag melting point and improve its fluidity to strengthen the metal-slag separation effect. And then the alloy microstructures were improved. We also known that the additive Na_3AlF_6 had more obvious effects than CaF_2. While adding 5% CaF_2 and 5% $KClO_3$ simultaneously, the comprehensive effects were best. Because the reaction temperature would increase significantly while adding heating agent to the reactants, the metal separated from slag more completely. But Na_3AlF_6 and CaF_2 have the very strong volatility, so the adding amount of Na_3AlF_6 and CaF_2 cannot be too much. There would have better reaction effects when the heating agent $KClO_3$ and the additive CaF_2 were used simultaneously.

3.2 XRD analysis of slags

Fig.3 is the XRD patterns of slag when CuO was more excesses 5% and different amounts of Na_3AlF_6, CaF_2 were added. It could be seen from Fig.1 that when adding Na_3AlF_6 to reactants, the slags consisted of Al_2O_3,Cr_2O_3 and a small amount of Cr. When adding CaF_2 to reactants, the slags consisted of Al_2O_3, CaF_2 and a little Cr, at the same time a little $CaAl_4O_7$ phase appeared. A little Cr phase in slags indicated that the metal-slag separation effect was not ideal, which was also the direct reason resulting in the existence of microscopic defects and inclusions in alloy. The Cr_2O_3 phase included the no-reduced Cr_2O_3 and the secondary oxidation of reduced Cr. In addition, there existed the weak diffraction peak of $CaAl_4O_7$ phase in slag, because CaF_2 reacted with Al_2O_3 to generate

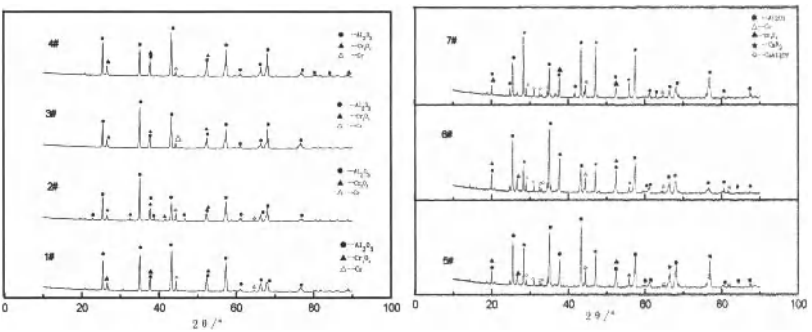

1-recruitment of Na_3AlF_6 is 5%; 2-recruitment of Na_3AlF_6 is 10%; 3-recruitment of Na_3AlF_6 is 5% and $KClO_3$ is 5%; 4- no additive; 5-recruitment of CaF_2 is 5%; 6- recruitment of CaF_2 is 5% and $KClO_3$ is 5%;7-recruitment of CaF_2 is 10%

Fig 3 XRD patterns of slag when adding Na_3AlF_6 and CaF_2 to reactants

AlF_3（gasification point is 1549K）and CaO, and then AlF_3 volatilized, but CaO reacted with Al_2O_3 to generate $CaAl_4O_7$ phase at the high temperature. We could find from half quantitative analysis results of the XRD patterns of 1-7# slag samples, the diffraction peaks of metal Cr phase in the samples of 1~3# were relatively weak. Because additive Na_3AlF_6 and heating agent $KClO_3$ were added in sample 3#, there was a higher reaction temperature, which improved the slag liquidities. So the metal-slag separation effect was better, and the microscopic defects and inclusions in alloys reduced. As for samples 1~2#, 5% and 10% Na_3AlF_6 were added to the reactants respectively, the slag liquidities was improved, but the adding Na_3AlF_6 would lead to reaction temperature reducing. At lower temperature, the metal-slag separation effect would became worse, which led to Cr content increasing. As for the samples 5-7#, the Cr content in samples 6~7# was higher than that in sample 5#. The relative intensity of Cr phase diffraction peak in the sample 4# was also weaker, but there were many microscopic structure flaws. Because slag Al_2O_3 fluidity was very bad, the metal-slag separation effect was also worse resulting in massive Al_2O_3 inclusions in alloys. The above results were consistent with the results in Fig.1and Fig.2.

3.3 SEM Analysis

Fig.4 and Fig.5 showed the SEM photos of CuCr alloys when CuO was more excesses 5% and different amounts of Na_3AlF_6 and CaF_2 were added. And the microanalysis results in the different CuCr alloys were listed in Tab.2 and Tab.2. It could be seen from Fig.4 and Fig.5 that there were Cr rich area(area a), Cu rich area(area b) and inclusion phase area(area c), and the phase of Cu and Cr distributed evenly, dendrite colud also be seen indistinctly, and most of the dendrites were globular crystal like.

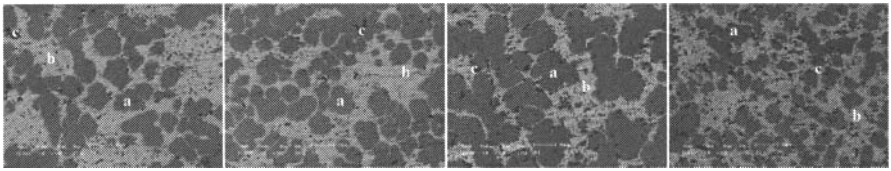

1-recruitment of Na_3AlF_6 is 5%; 2-recruitment of Na_3AlF_6 is 10%; 3-recruitment of Na_3AlF_6 is 5% and $KClO_3$ is 5%; 4- no additive

Fig 4 SEM Photos of CuCr Alloy when adding Na_3AlF_6 to reactants

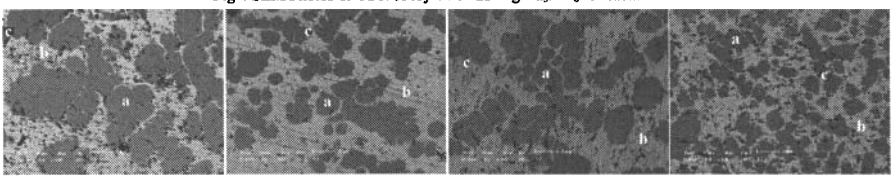

4- no additive; 5-recruitment of CaF_2 is 5%; 6- recruitment of CaF_2 is 5% and $KClO_3$ is 5%;7-recruitment of CaF_2 is 10%

Fig 5 SEM Photos of CuCr Alloy when adding CaF_2 to reactants

Tab.2 Energy spectrum analysis results for samples 1~4#/mass%

No		Cu	Cr	O	Al	Si	Fe
	a	4.26	93.26			0.37	2.11
1	b	96.61			3.386		
	c	22.44		30.05	47.52		
	a	2.57	95.16			0.30	1.97
2	b	97.30			2.697		
	c	9.221		37.36	53.28		0.14
	a	3.125	93.61				3.26
3	b	93.73	3.71		2.57		
	c	53.01		30.04	11.27	5.07	
	a	6.61	90.75				2.64
4	b	94.46	1.86	3.68			
	c	8.74	1.34	36.92	53.01		

Comparing the samples 1~7# in Fig.4 and Fig.5, we could find that the inclusions and pore flaws in the 1~3# samples and the 5~7# samples were significantly less than that of the 4# sample. The SEM photos of 1~3# samples indicated that there are dendrite in Cr rich area a; area b is Cu rich phase; and area c consists of inclusions and pores, which distributes in the whole alloy band most of which distribute in Cu rich area b.

Tab.3 Energy spectrum analysis results for samples 5~7# for samples 5~7#

No		Cu	Cr	O	Al	Si	Fe
	a		89.99	10.01			
5	b	98.69			1.31		
	c	9.71	14.97	33.06	42.27		
	a	3.23	87.31	9.47			
6	b	100.00					
	c	9.627		33.91	56.47		
	a	3.53	90.41	6.07			
7	b	96.25	1.81		1.95		
	c	25.64	6.68	28.90	0.99	26.00	

The microstructures of samples 5~7# are similar with samples 1~3#. The grain sizes and phase distribution uniformities in samples 6# and 7# are better, but the microstructure defects of inclusions and pores in sample 5# is very obvious and the segregation is very severe. Because the freezing point of Cr is much higher than that of Cu, Cr precipitates before Cu during the solidification process. As the casting temperature goes down, Cu with a low melting temperature begins to precipitate. At the same time, the slag fluidities will become worse, so the slag precipitates with Cu forming the microstructures and distribution state in Fig.4 and Fig.5. In other words, most of the inclusions distribute in Cu rich area.

From Tab2 and Tab.3, we know that the Cr contents in Cr rich area in the samples 1~4# are higher than 90%, the others include a little Cu and iron(the impurity Fe from the raw materials); the Cu contents in Cu rich area are higher than 93%, and there are a little Cr and Al residues. Expect for the pores in the inclusion area c, the main phases include Al_2O_3 and Cu. Especially in the sample 4#, there exists a little Cr_2O_3 which indicates that the metal-slag separation effects are not ideal. The results are consistent with the XRD results of the slags. The Cr contents in Cr rich area in the samples 5#~7# are lower, and there is lots of oxygen residue, which indicates that the Cr_2O_3 were not reduced completely. Cu contents in Cu rich area are higher than 96%, but there are a little Cr and Al residues. Expect for the pores in the inclusion area c, the main phases include Al_2O_3 and Cu and Cr.

The above results indicate that Na_3AlF_6 has more effects of strengthening the metal-slag separation than CaF_2. Adding heating agent $KClO_3$ to the reactants will increase the reaction temperature significantly which provide favorable conditions for the metal-slag separation to remove the inclusions in the alloy and to improve its microstructures.

4 Conclusions

(1).When adding Na_3AlF_6 and CaF_2 to reactants, the metal-slag separation effects were strengthened and the alloy microstructures were improved.

(2).When adding Na_3AlF_6 to reactants, the slags consisted of Al_2O_3,Cr_2O_3 and a small amount of Cr. When adding CaF_2 to reactants, the slags consisted of Al_2O_3, CaF_2 and a little Cr, at the same time a little $CaAl_4O_7$ phase appeared.

(3).There were Cr rich area(area a), Cu rich area(area b) and inclusion phase area(area c), and the phase of Cu and Cr distributed evenly, dendrite colud also be seen indistinctly, and most of the dendrites were globular crystal like.

ACKNOWLEDGEMENT:

This research was supported by National Natural Science Foundation(NSFC) (50974035,51074044, 50704011).

Referents

1. Yang H, Zhang T A, Niu L P, et al. Elementary research on CuCr alloy prepared by SHS-melting technology[J].The Chinese journal of nonferrous metals.2001,11(3):390~393.
2. Yang H，Zhang T A，He J C. Research of CuCr alloy[J].The Chinese journal of nonferrous metals,1998, 8（S2）:347.
3. Slade P G. Advances in material development for high powder, vacuum interrupter contacts[J]. IEEE trans comp pack manu technol, 1994,17(1):96.
4. Slade P G. Contact materials for vacuum interrupters[J].IEEE trans comp hybrids packaging PHP, 1972,10(1):43.
5. Rieder W F, Schussek M, Giatzle W, et al. The influence of composition and Cr particle site of Cu-Cr contacts on chopping current, contact resistance and breakdown voltage in vacuum interrupters[J].IEEE comp hybrids manu. technol,1989,12(2): 273.
6. Kippenberg H. Cr-Cu as a contact material for vacuum interrupters[A].Pro 13th Int. Conf on electric contacts[C].Zurich: Schweiz Elektrotachnischer Verein, 1986.140.
7. Frey P, Jager K, Klink N, et al. Investigation on the release of gas from contact materials for vacuum switching devices during operation[A].Proc 11th Int. Conf on electric contacts[C].Berlin,1982.317.
8. Ding B J, Li H, Wang X, et al. Residual carbon in Cu-Cr contact materials[J].IEEE tans Comp Hybrids Manu Technol, 1991,14(2): 386.
9. Ding B J, Yang Z M, Wang X T. Influence of microstructure on dielectric strength of CuCr contact materials in vacuum[J]. IEEE trans on Tans Comp Pack Manu Technol, 1996,19A(1):76.
10. Wang J X, Huang J R, Lin J S. The solidification and its control on metal[M].Beijing: Mechanical industrial press,1983.6
11. Spizer K H, Georg Reiter, Klaus Schwerdtfeger. Multi-frequency electromagnetic stirring of liquid metals[J]. ISIJ international,1996, 36(5):487~492.

3rd International Symposium on High-Temperature Metallurgical Processing
Edited by: Tao Jiang, Jiann-Yang Hwang, Patrick Masset, Onuralp Yucel, Rafael Padilla, and Guifeng Zhou
TMS (The Minerals, Metals & Materials Society), 2012

SETTLING OF INCLUSIONS IN TOP-CUT SOLAR GRADE SILICON (SOG-SI) UNDER ELECTROMAGNETIC FIELD

Lucas Nana Wiredu Damoah[1], Lifeng Zhang[1,2]

[1]Department of Materials Science & Engineering
Missouri University of Science and Technology (Missouri S&T)
223 McNutt Hall, Rolla, MO 65409-0340, USA
Email: zhanglife@mst.edu

[2]School of Metallurgical and Ecological Engineering
University of Science & Technology Beijing
Beijing 100083, China
Email: zhanglifeng@ustb.edu.cn

Keywords: Settling, Inclusions, Electromagnetic, Silicon

Abstract

Increasing demand for Solar Grade Silicon (SoG-Si) due to rising interest in renewable energy has lead to increased SoG-Si Top – cut scraps generated from the multi-crystalline silicon making process. Due to the high cost of SoG-Si and the potential to use the top-cut scraps as feedstock material, there has been increased effort to develop cost effective and efficient technologies. As a result, several methods to recycle the top-cut scraps are currently been applied, and researched. These include settling under gravitation field, which is a slow process to be industrially applicable. Natural settling of inclusions by gravitational force is a slow process and not attractive to the industry. Recent experiments on Top-cut SoG-Si scrap under high frequency, high voltage, electromagnetic field showed that SiC inclusions settled within a short time to the bottom of the crucible and the characteristic rod-like morphologies of Si_3N_4 inclusions in SoG-Si were not detected. This study investigates the enhanced settling of SiC inclusions and the behavior of Si_3N_4 particles under the influence of high frequency, high voltage, electromagnetic field in Top-cut SoG-Si.

Introduction

The photovoltaic industry depends on silicon based PV materials either as single-crystalline silicon, or multi-crystalline Si (MC-Si), or amorphous Si [1] for over 90 % of its market share. [2] MC-Si produced by directional solidification of solar grade silicon melt dominates the silicon PV market. During the directional solidification process, SiC and Si_3N_4 particles within the melt are pushed by the solidification front to the top of the ingot which is the last to solidify. Therefore the top of the ingot is cut generating what is known as top-cut solar silicon scraps. The Si_3N_4 particles are mainly from the coating material at the inside surface of the silica crucible and from air absorption during the solidification process. The SiC particles mainly stem from the carbon reduction process of the primary production of silicon [3]. Due to the growth of the PV industry as a result of global demand for clean, reliable, and affordable energy [4], there is the need to develop new methods to compliment exiting ones to recycle SoG-Si waste (e.g. top-cut) for sustainability.

Settling of inclusions in silicon has been investigated as one of the methods to purify silicon.[5] However, settling of particles based on natural densities could take too long to accomplish and therefore not industrially attractive. It is well known that particles settle in highly convective fluids though there are limits to the level of convection [6] due to the likelihood of turbulent diffusion of particles which may hamper effective settling of particles. The application of an AC electromagnetic field to the molten metal system may induce fluid flow, enhancing the convection with the ability to improve the settling rates of particles. Hori [7] concluded in his study that by the application of electromagnetic field to a mixed phase fluid even particles of density less than the fluid can be settled and particles of density greater than the fluid could float or rise to the top. Tanimoto and Kakuda have utilized the magnetization force resulting from electromagnetic field gradient and based on the magnetic susceptibility difference between suspended particles and the fluid to settle red blood cells in a solution [8]. These indicate the potential existing for the use of electromagnetic field to settle inclusions in molten metal.
In this study the feasibility of using high frequency AC electromagnetic field to settle suspended inclusions in top-cut silicon is investigated.

Experimental Procedure

Top-cut solar grade silicon materials containing mainly SiC and Si_3N_4 inclusions were used in this study. Figure 1 shows a schematic of the experimental set-up employed in this study. The EM apparatus was composed of a high frequency power supply (50-200 kHz, and 100 kW), an induction coil, and a graphite crucible system. The graphite crucible acted as a shield to the EM Archimedes force on the suspended particles, whiles also acting as a susceptor for heating and melting of the silicon scraps. The melted silicon was allowed to stay under the EM field for 2 minutes after melting at a temperature of 1500 °C. Then the sample was allowed to cool down to room temperature. Table I gives information about the experimental schemes utilized for the EM settling process. Samples were prepared and studied with the optical and scanning electron microscopes.

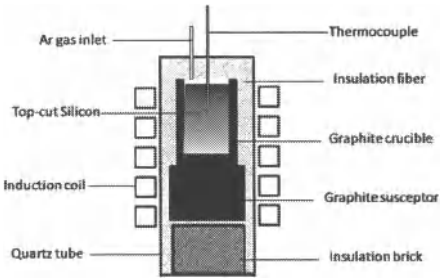

Figure 1. Schematic of the experimental set-up used for the electromagnetic settling experiments

Results and Discussion

Inclusions in Top-cut SoG Si

Top–cut solar grade silicon contains mainly SiC and Si_3N_4 inclusions with respective characteristic lumpy and rod-like morphologies as shown in Figure 2. The Si_3N_4 inclusions on

the topmost surface appeared with hexagonal cross-sections and are needlelike, several mm long and approximately 20 μm in diameter. The SiC particles were lumpy and as big as several hundred micrometers. These particles were pushed upward to the top surface by the solidification front during the directional solidification process. Inside the silicon, Si_3N_4 inclusions were usually shorter than 500μm and with average diameter of ~20μm, and SiC inclusions were smaller than 200μm. The quantity, size and morphology of inclusions changed with depth beneath the top surface. Inclusion clusters with complex morphologies were observed, and these clusters contained both SiC and Si_3N_4 particles deeper beneath the top-surface.

Table I Experimental scheme used for the EM sedimentation experiments

Exp. #	Coil Current, I_{rms} (A)	Frequency (kHz)	Temperature (°C)
Si-SD–1	180	76	1500
Si-SD–2	180	64	1500

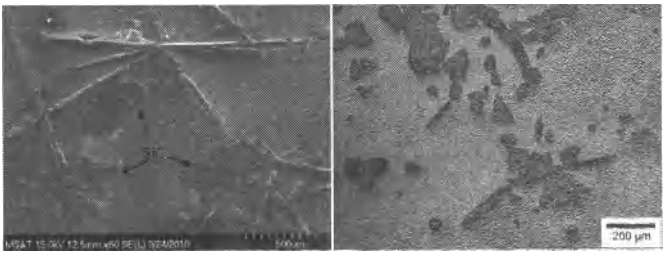

Figure 2. Optical micrographs of inclusions in a top-cut SoG-Si scrap on the surface (left) and at a depth of 1mm beneath the top surface showing lumpy SiC and rod-like Si_3N_4 particles.

Settling of Particles in Top-cut SoG Silicon

To investigate the distribution of particles in the top-cut silicon scraps under natural settling, 50 g of top-cut scrap was prepared and heated in an Al_2O_3 in a high temperature furnace without electromagnetic field. The sample was heated at a rate of 4 °C/min to 1600 °C and held for two hours at this temperature and then cool at 4 °C/min to room temperature. The samples from this experiment were sectioned through the center vertically and the surface prepared and observed under the optical microscope. Figure 3 shows the distribution of inclusions after the experiment. It can be clearly seen that after the over 3 hr settling time almost all the inclusions stayed close to the top of the sample, an indication of how slow the settling process could be. This makes settling under gravity an industrially unattractive process.

When an electromagnetic field was imposed the distribution of inclusions had a different pattern. Figure 4 shows the distribution of inclusions close to the bottom of the sample from experiment Si-SD–1. As can been seen the particles in this case went to the bottom of the sample. Similar result was obtained in the case of experiment Si-SD–2, indicating reproducibility. The mechanism for settling is still under study. The distributions of particles along the direction of gravity from the top of the particles to the bottom are showed for the two experiments in Figure 5. As clearly demonstrated, the particles moved to the bottom of the sample under the electromagnetic field. A continuous phase of SiC particles were also observed at the walls of the

crucible and at the bottom as a result of interaction between the graphite crucible material and the molten silicon as showed in Figure 6. On the top of the samples, a continuous phase of SiO_2 was observed indicating silicon oxygen interaction leading to slag formation.

Figure 6 shows a very serious interaction between the graphite crucible and the molten silicon to generate SiC particles. In Figure 7 further details about inclusions distribution in the samples from experiment Si-SD–2 showing part of the top surface and the bottom are provided. As can be observed in all the inclusions distribution micrographs of the samples, the characteristic Si_3N_4 rod-like morphologies were not observe. This will be briefly discussed in a later section.

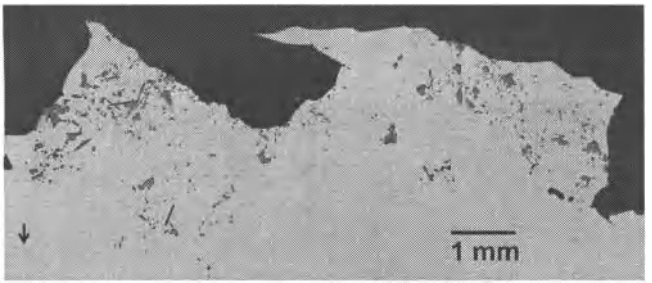

Figure 3. Collection of optical micrographs showing the distribution of inclusions in a top-cut SoG-Si scrap melted at 1600 °C at a heating rate of 4 °C/min. and held for two hours before cooling at 4 °C/min to room temperature in a high temperature furnace without EM field. Almost all the particles stayed at the top part of the sample. The arrow shows the direction of gravity

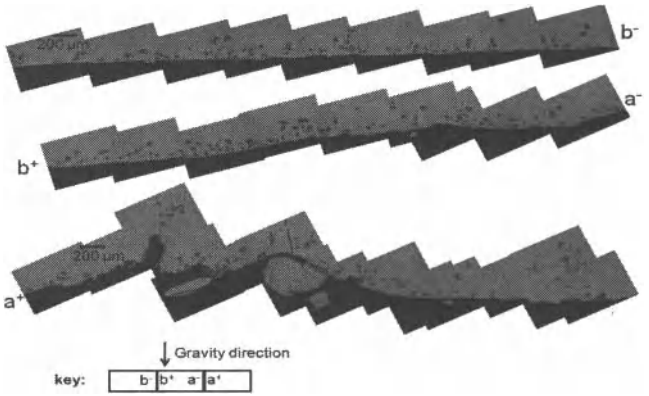

Figure 4. Optical micrographs of the bottom of the sample after the EM settling experiment Si-SD–1 showing that inclusions settled to the bottom of the crucible and were well distributed along the diameter. The characteristic rod-like Si_3N_4 morphologies were not observed after the experiment.

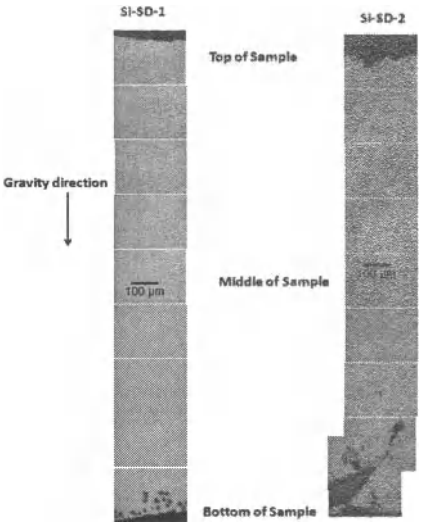

Figure 5. Optical micrographs from top to bottom of the samples after the EM settling experiments Si-SD–1 and Si-SD–2 showing a cleaner inner silicon matrix and settled particles to the bottom of the samples. A study of the apparent particle at the top of the sample in Si-SD–2 shows a continuous layer SiO_2 layer indicating top slag layer.

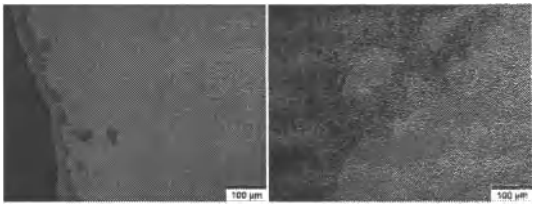

Figure 6. Optical micrographs showing a continuous SiC phases generated as a result of the interaction between graphite crucible and the molten silicon at the walls of the crucible. This photos show serious interactions between Si and carbon to generate inclusions.

Settling Mechanism

The mechanism responsible for the settling of inclusions to the bottom of the sample is still not clearly understood. However, two possible mechanisms could contribute individually or together for the settling process.

Electromagnetic stirring: under the electromagnetic field the molten metal experiences an induced fluid flow which stirs it up, increasing the Reynolds number thereby increasing the settling rate. The settling velocity of particles could be described by Eq.(1).

$$v_p = \sqrt{\frac{4d_p g}{3C_D}\left(\frac{\rho_p - \rho_m}{\rho_m}\right)}; \quad C_D \approx \frac{24}{\mathrm{Re}} \text{ (for stokes regime)} \qquad (1)$$

Magnetization force due to magnetic field gradients: the magnetization force [9] could be used to separate phases based on magnetic susceptibility difference under a gradient magnetic field.[8] Due to the presence of different materials within the experimental domain, this could have resulted in different EM field intensities leading to a gradient magnetic field that could enhance the settling rates of particles. The steady-state settling velocity of particles under the electromagnetic field may be derived as:

$$v_p = \sqrt{\frac{4d_p}{3C_D\rho_m}\left[\left(\rho_p - \rho_m\right)g + \left(\chi_m - \chi_p\right)\frac{1}{\mu_o}B\frac{\partial B}{\partial z}\right]} \qquad (2)$$

Equation (2) provides a lot of possibilities to electromagnetic particle removal. Currently, due to the availability of superconductive magnetic materials high magnetic field gradients could be used to float or settle the particles as desired. Since the drag coefficient C_D is inversely proportional to the Reynolds number Re higher EM field leading to high EM stirring implies smaller C_D and hence high particle settling velocity. However, there is a limit to how much stirring is necessary for effective settling due because of the effect of turbulent diffusion, which may cause the settle particles to re-entrain into the molten metal stream at higher fluid convention rates.

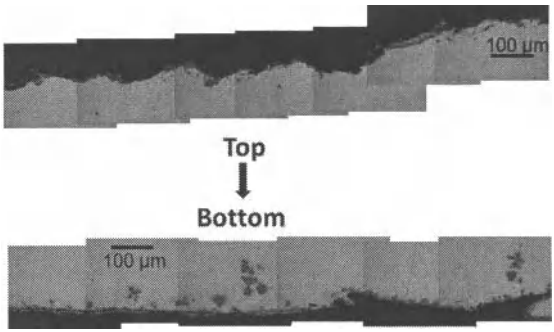

Figure 7. Part of the top and bottom views of the sample from experiment Si-SD–2 showing settled particles to the bottom, a continuous slag layer on top and a continuous SiC layer at the bottom as a result of graphite – molten silicon interaction.

Further confirmatory experiment using a silicon – ~8 wt% aluminum containing dispersed inclusions of 10 µm average size (see microstructure in Figure 8) melted in SiO_2 and EM field applied at a frequency of 64 kHz and coil current of 350 A for 10 s was carried out. The result of this experiment is shown in Figure 9. Figure 9 shows the accumulated of the small particles at the bottom of the crucible and also at the wall. Since SiO_2 crucible was used, the electromagnetic Archimedes force was effective close to, and acts toward the wall of the crucible. Therefore as the induced fluid flow by the EM field carried particles close to the vicinity of the crucible wall where this force was effective the particles were trapped to the wall. The high fluid flow also

acted to bring the small particles together thereby improving their settling rate to the bottom of the crucible. This resulted in the accumulation of more particles at the bottom of the crucible as showed in Figure 9. This result holds significant potential to the future design of industrial electromagnetic inclusions separation process.

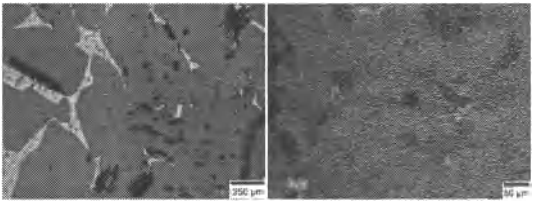

Figure 8. Microstructure of Si – 8 wt% Al alloy showing white Al phase and dispersed particles in silicon matrix.

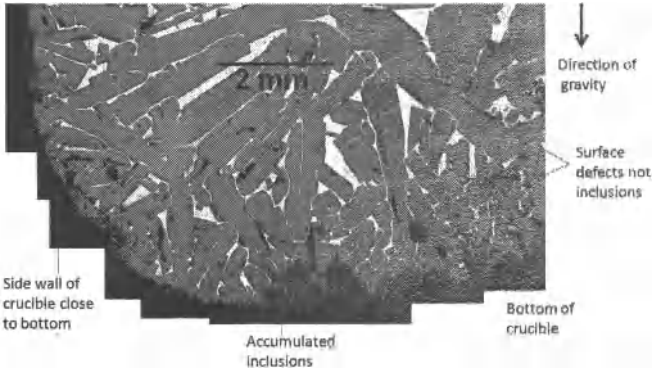

Figure 9. Microstructure of part of the vertical cross-section of EM separated sample of Si – 8 wt% Al alloy showing the accumulation of the originally dispersed particles after 10 seconds of the application of EM field at I_{rms} = 350 A and f = 64 kHz to the bottom and to the wall of the SiO_2 crucible used. The matrix of the material away from the wall and bottom were generally free of the dispersed particles after the EM application.

Status of Si_3N_4 Particles in top-cut scraps after EM experiments

The characteristic rod-like morphologies of Si_3N_4 particles as seen in Figs. 2 and 3 were not detectable in the sample after the EM settling experiments as shown in Figs. 4 - 7. Optical micrographs and SEM/EDX analysis on the samples have both proven unsuccessful in detecting the Si_3N_4 particles in the samples. Several possibilities could explain this observation:

- Decomposition of Si_3N_4 due to contact with air or water molecules to gaseous Si-O-H species and N_2 or NO_x gas species.
- Thermal decomposition of Si_3N_4 resulting from local heating under such a high voltage field (the coil voltage was 300 – 500 V).

- Reaction of Si_3N_4 oxygen to form silicon oxynitride glassy phases in a top slag layer. No TEM or SEM study has been conducted on the top layer yet. Considering this possibility, why would SiC prefer to go to the bottom while Si_3N_4 particles go to the top?
- Recrystallization of Si_3N_4 in the melt. The solubility of nitrogen in the melt is appreciably low to allow for Si_3N_4 to recrystallize.

These likelihoods require further investigation to establish the actual reason responsible to the non-detection of Si_3N_4 particles in the samples after the EM settling experiments.

Summary

The feasibility of using high frequency AC electromagnetic field to settle suspended inclusions in the top-cut silicon was investigated. It was found in all the experiments that, SiC particles settled to the bottom of the sample within a short experimental time of 2 minutes under the electromagnetic field. This is contrary to the result of settling by gravity in a high temperature furnace without electromagnetic field for over three hours in which almost all the particles stayed in the top-half of the sample. The possible mechanisms responsible for the improved settling under electromagnetic field are electromagnetic stirring and the effect of the magnetization forces due to the difference in magnetic susceptibility for Silicon and SiC under a gradient electromagnetic field. Si_3N_4 inclusions were not detected after the experiments and this is attributed to a number of factors which includes thermal decomposition due to local heating.

References

1. A. Lotnyk, O. Breitenstein, and H. Blumtritt, A TEM study of SiC particles and filaments precipitated in multicrystalline Si for solar cells. *Solar Energy Materials & Solar Cells*, 92 (2008), p. 1236-1240.
2. N.B. Mason. *Industry Developments that Sustain the Growth of Crystalline Silicon PV Output.* in *Proceedings of the Photovoltaic Science, Applications & Technology Conference.* 2007. Durham UK.
3. L. Zhang, E. Øvrelid, S. Senanu, B. Agyei-Tuffour, and A.N. Femi. *Nonmetallic Inclusions in Solar Cell Silicon: Focusing on Recycling of Scraps.* in *Rewas2008: 2008 Global Symposium on Recycling, Waste Treatment and Clean Technology.* p.1011-1026
4. D. Sarti and R. Einhaus, Silicon feedstock for the multi-crystalline photovoltaic industry. *Solar Energy Materials and Solar Cells*, 72(1-4) (2002), p. 27-40.
5. A. Ciftja, E. Ovrelid, M. Tangstad, and T. Engh. *Settling of Particles in Molten Silicon Before Directional Casting of a Solar Grade Silicon Ingot.* in *The TMS 2009 Annual Meeting Supplemental Proc, Vol2: Materials Characterization, Computation and Modeling.*
6. G. Lavorel and M. LeBars, Sedimentation of particles in a vigorously convecting fluid. *PHYSICAL REVIEW E*, 80 (2009), p. 046324-1-046324-8.
7. M. Hori, *Application of Electromagnetic Force in Mixed-phase Fluid.* (Japan Atomic Energy Research Institute, JAERI 1055, 1964).
8. Y. Tanimoto and Y. Kakuda, Influence of strong magnetic field on the sedimentation of red blood cells *Journal of Physics: Conference Series*, 156 (012030) (2009).
9. S. Asai, Recent Development and Prospect of Electromagnetic Processing of Materials. *Science and Technology of Advanced Materials*, 1 (2000), p. 191-200.

3rd International Symposium on High-Temperature Metallurgical Processing
Edited by: Tao Jiang, Jiann-Yang Hwang, Patrick Masset, Onuralp Yucel, Rafael Padilla, and Guifeng Zhou
TMS (The Minerals, Metals & Materials Society), 2012

STUDY AND APPLICATION OF THE TAPHOLE CLAY WITH HIGH STRENGTH AND ENVIRONMENT-FRIENDLY IN A NEW BLAST FURNACE WITH 3800M^3 VOLUME

Guotao Xu [1], Huaiyuan Li [2], Yafei Xiong [2], Yue Wang [1], Shuzhong Li [2]

[1] R&D Center, Wuhan Iron & Steel (Group) Co., Wuhan 430080
[2] Iron-making Total Plant of Wuhan Iron and Steel Company Ltd. Co., Wuhan 430083

Abstract

The composition, properties and structure of taphole clay with high strength and friendly surrounding used in a new blast furnace with 3800 M^3 volume was studied. The developed taphole clay had been applied in the blast furnace for four months, pouring times were 11-13 every day, flowing rate of hot iron was 7.5 t/min and the consumption of taphole clay was 0.49Kg per ton iron, which can make the new blast furnace attach the designed production quickly and decrease the cost of hot iron. The taphole clay is easy to be opened in the channel of hot iron which can be remained in stable shape under the corrosion of slag or hot iron, and it dose not produce poisonous smoke in yellow or dark color in the use process. The development of new taphole clay is useful to improve the work surrounding of the blast furnace.

Keywords: Blast furnace, taphole clay, surrounding-friendly, high strength

Introduction

In the iron-making process, the taphole clay's function is filling up the taphole and protecting the formation as well as the growth of the clay in the blast furnace, maintaining the enough taphole depth; simultaneously it is easily to open a hole and knock out the clay. The taphole clay has a good performance of molten slag and hot iron resistance. The traditional taphole clay uses coal tar or carbolineum as a binder, and the performance of taphole clay is good, but it has the black and yellow poisonous smoke, which is harmful for work condition. Through the investigation on the binder's composition and poisonous performance of taphole clay, the environmental taphole clay is developed by some foreign companies, which is named the third generation product with benzene is less than 300ppm, and it has been used in European steel companies. This application of the taphole clay with high strength and environment-friendly using in 3800m^3 blast furnace is introduced and the performance is discussed and analyzed in this paper.

Taphole Clay Experiments

The research of the taphole clay with high strength and environment-friendly was mainly related with the formula and the operation performance adjustment. Through the optimized formula composition, the suitable performance was obtained. The clay's primary materials were corundum aggregate and its fine powders, other raw materials such as coke, silicon carbide, bonding clay and nitride were used selectively. To reduce the cost, some factories use the bauxite as main material. Finally using the environment-friendly binder and the resolver to mix and roll for the product.

Take the taphole clay H-D formula as the foundation. H-D is a kind of taphole clay containing environment-friendly liquid binder. Replace bauxite with coke powder and the content was 10wt%, 13wt%, 16wt%, 19wt% and 22wt%. The binder was adjusted according to the kind and weight. The clay is fired up to 1400℃. The compressive strength and apparent porosity of the fired clay sample at 1400℃ were examined and the results were shown in Figure 1 to 2.

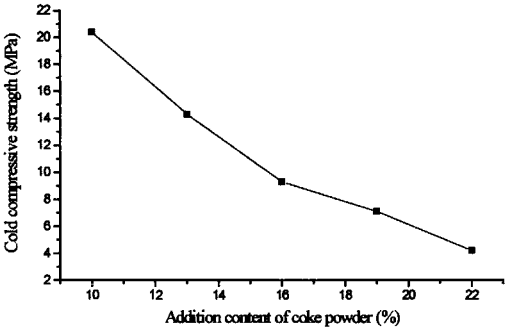

Figure 1 The relationship between strength and different addition content of coke powder containing clay

The strength change of clay was shown in Figure 1. It can be seen that more coke addition leads to lower strength. The influence factor and the trend were similar to the traditional clay. For the clay, coke was the main factor affecting the break and the addition amount must be controlled in a proper range. For the clay with new structure does not need to consider that but needs to consider the porosity and the size quantity of the clay to control the break performance.

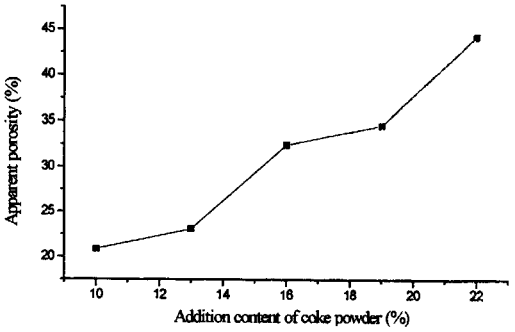

Figure 2 The relationship between apparent porosity and different addition content of coke powder containing clay

Figures 2 shows the relationship between apparent porosity and different addition content of coke powder containing clay. It is found that the apparent porosity of the traditional clay or the clay with coke as the main material can be controlled by the addition of coke, and the break performance can also be controlled. More addition of coke was harmful for the strength of the clay, so the clay with high coke composition has low burned strength, low molten iron and slag corrosion resistance, resulting in un-stability and high consumption of the taphole clay.

The plasticity regarding to the operation of blast furnace taphole clay is very important. The clay gun's pressure is insufficient and the break of hole is quite difficult. The large-scale blast furnaces use the anthracite oil combined taphoe clay, and an important reason is that taphole clay is quite soft and easy to break. However, its fatal weakness is the high-temperature strength is low and poor anti-corrosion performance and polluting environment. The anthracite oil, the asphalt includes the massive carcinogen--benzene, therefore it is harmful for the blast furnace staff's health and polluting environment.

Generally, room temperature plasticity of the anhydrous taphole clay is 0.65 MPa. The excessively high plasticity can cause the break clay difficult or the clay cannot sneak in the tap hole, but the softened performance of environment-friendly taphole clay is best at 150°C, the plastic value is lowest at about 0.8 MPa. For clay gun under normal operation, the barrel temperature is enough to guarantee the temperature. For the cold barrel of first use, it may use the external heating method to control the barrel temperature. Meanwhile the clay gun's system parameters of breaking the clay should make the adjustment, the fluctuation of pressure is 2MPa, and the pressure is steady, the clay quantity is stable, which may guarantee the stability of the

depth of the taphole.

For example, the environment-friendly taphole clay without traditional asphalt binder, the composition of taphole clay is according to H-D series, the binder addition by the matched type and quantity.The plastic value of taphole clay in the time which the clay had been produced was examined. The data are shown in Figure 3.

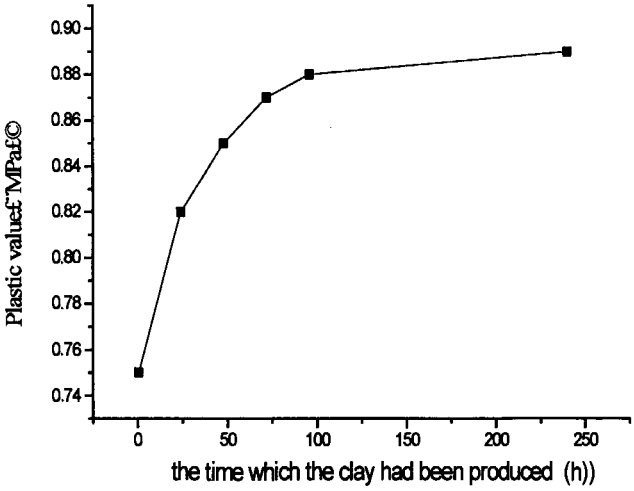

Figure 3 The relationship between the plastic value and time which the clay had been produced

For the traditional taphole clay, the adjustment of anthracite oil or the coal-tar oil can change compressive strength at room temperature considerably. The main reason is the carbon content of the tar or the anthracite oil is low and the strength of taphole clay is also low. Increasing the oil amount, the taphole clay can change soften, but plastic strength reduces. For the environment-friendly taphole clay, the quantity of binder influences plastic strength greatly. The binder quantity increases, taphole clay's Maxia value reduces. Therefore, it needs to control taphole clay Maxia value in proper scope.

The environment-friendly taphole clay using the improved binder has little benzene and the surplus benzene is mainly produced by the solid binder. When the taphole clay is extruded into blast furnace, it will be burnt down at high temperatures. Therefore the application of environment-friendly binder is useful for the work surrounding and worker's health. The

structure and the composition analysis of the burned clay are shown in Figure 4 to 5.

Figure 4 shows that the structure of burned clay is porous and has some ashes. The EDS result of one ash in Figure 5(b) is (wt%): Na_2O 1.16, Al_2O_3 43.04, SiO_2 53.27, K_2O 2.26, CaO 0.27.

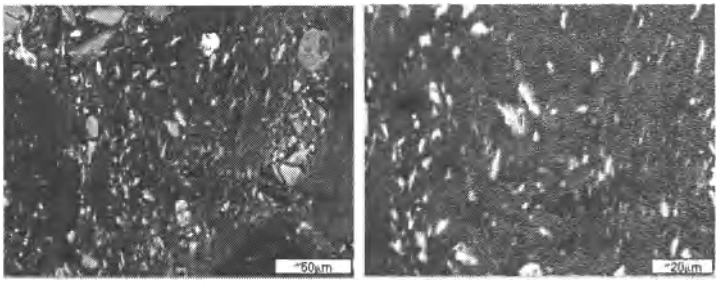

(a) (b)

Figure 4 The secondary electron images of high strength taphole clay with enviromental-friendly fired at 1400℃ ×3h black is carbon-bond phase

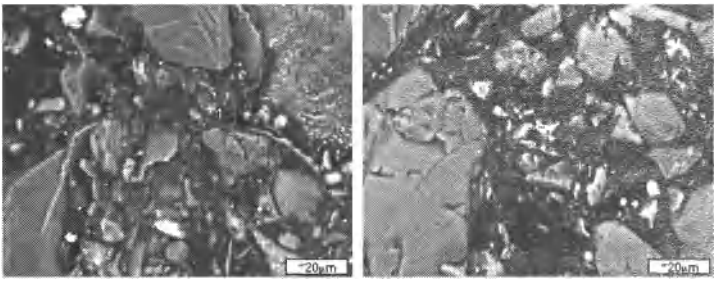

(a) (b)

Figure 5 The secondary electron images of basis for high strength taphole clay with enviromental-friendly fired at 1400℃×3h

The morphologies of the combination between aggregate and fine powders are indicated in Figure 5. The fixed carbon is as the main bonding phase in the fired clay. The EDS analysis of the marked point in matrix is (wt%): Na_2O 0.93, Al_2O_3 39.36, SiO_2 56.91, K_2O 1.74, CaO 1.07 (Figure 5a). The EDS analysis of the marked point in another matrix is (wt%): Na_2O 0.92, Al_2O_3 47.28, SiO_2 48.83, K_2O 0.99, CaO 1.98 (Figure 5b). Viewing on the two point compositions, the indigents change less and they mainly form the dense silicate phases.

Application of Taphole Clay

The composition of high strength environment-friendly taphole clay is shown in table I. Its Environment-friendly performance is good, and benzene(w,%) in the taphole clay is less than 0.005wt%, and it is high intensity, good slag resistance, without the yellow or black poisonous smog, which is used to have a trial in the 3200m^3 blast furnace, and the performance is good. The environment-friendly clay squeezes out the length more than 1 meter unceasingly, but the anthracite oil union taphole clay is broken at merely 0.2-0.5 meter. Firstly, five raids were tested, which chose one taphole , the depth of tap hole is maintained at three meters, the taphole clay consumption achieves 0.5Kg/t iron while that of anthracite oil is about 0.89Kg/t iron. In order to reduce the disperse spurts of the newly open blast furnace, the iron-plant decided to use the high strength environment-friendly taphole clay. Among four months long-term usage, the taphole clay consumption has achieved 0.49Kg/t iron, the molten iron speed 7.5 tons/minutes, the tapping number may achieve 7-8 times at least. Because the difficulty of the molten iron supply, we control the tapping 11~13 times. The 3800M^3 blast furnace reached production in four days, and the utilization sufficient achieves 2.3, the wind temperature achieves 1097°C, the molten iron temperature achieves 1488 °C and the top pressure achieves 0.199MPa. The disperse spurts problem was solved. However, the dispersed spurts time of former newly built blast furnace often achieves above three months.

Table 1 Composition and properties of taphole clay with environment-friendly

Chemical composition /wt%			Properties, 1400°C for 3h				
Al_2O_3	SiC+C	Si_3N_4	Apparent porosity /vol.%	Bulk density /g.cm^{-3}	High-temperature Compressive strength (1400°C)/MPa	low-temperature Compressive strength (250°C)/MPa	Lineal change /vol.%
≥22	≥25	≥2.0	≥36	≥2.0	≥8.0	≥4.0	±1.0

Figure 6 The trial photo of the developed high strength taphole clay with environment-friendly

Looked from the iron plant experience in the past, tap hole of newly open blast furnace in WISCO disperses spurts seriously, the new clay balls forms difficult, and the tap hole is unstable, which leads to maintain difficult, great work capacity, and it is unfavorable for the safety in production. Generally speaking, the tap hole of the blast furnace should undergo several grouting processing, after 6-12 months, the disperse spurt will be controlled permanently, but some blast furnaces running for years still have the tap hole disperse spurts. The developed taphole clay mainly aims at the characteristics such as iron-smelting furnace fast strengthening, disperses spurts, and high slag ratio. The taphole clay should have good aperture performance, the performance of anti-disperse spurts, slag resistance and the good environment-friendly performance. The chosen of taphole clay is depending on the ramming material and the performance of the bricking-up material of the tap hole. The good bonding quality and the replacement performance are emphasized. Using the improved environment-friendly taphole clay binder, the replacement between taphole clay and the taphole balling is easily to carry out. Each target of the taphole clay meets the blast furnace production need.

Discussion

When a blast furnace volume is small, the internal pressure is not high, and the molten iron flow speed and capacity are small, so the requirement and technique of the taphole clay is low. By the end of 20 century, the amount of large-scale blast furnaces has increased and the volume is becoming larger and larger. Taking WISCO for example, the blast furnaces below $2000M^3$ eliminated completely, and four blast furnaces are all above $3200M^3$, requiring high temperature

of blowing wind, high top pressure, high oxygen enrichment and smelting intensity, the environmental condition of the tap hole replaces the radical change, causing the role of blast furnace taphole clay changes from "the filling material" to the closely related stabilization function. The taphole clay is not only has an effect in filling the tap hole of the large-scale blast furnace, but also in controlling the flow speed and capacity of molten iron , the tap hole depth and the balling shape. The taphole clay's work process can decide a blast furnace's steady operation and influence tap hole and hearth service life.

The study of environment-friendly taphole clay is closely related to that of European country on poisonous materials. In Europe's product marking, the harmful product for human health including the carcinogen, the material of induced mutation that change inherit structural of humanity, the reproduction toxicity material, which possibly has the heredity consequence for the descendant. These study results caused ones should pay attention to the poisonous materials used in refractory field. In the refractory products, the widely used poisonous material is tar, which is the by-product of coke and it often used as the binder of taphole clay. The main constituent of tar is multi-hydrocarbons, and some of those are the poly-nuclear aromatic hydrocarbons (PAH). Some poly-nuclear aromatic hydrocarbons, such as the well-known benzene is the carcinogen. What needs to explain: In the several hundred kinds of PAH, there are only very few of them are poisonous products.

People pay more and more attention on the toxicity of tar, and thus some people propose a solution that using resin substitutes tar. At first, this plan was considered as an environmental choice. However, the late study found that the hot- solid resin ingredient including the phenol-formaldehyde polymer, whose characteristic of expediting setting has entrusted the taphole clay a new characteristic, but the two chemistry monomers have been classified to toxic products (CMR) since 2005. In addition, the formaldehyde may be classified as top-kind carcinogen. Viewing on the reports from the correlation data: in the binders of clay, benzene > 0.01wt%, cause carcinogen, induce mutation and reproduction toxicity; phenol > 1wt%, cause induced mutation; Formaldehyde > 0.2wt%, cause carcinogen. The all products above not only have the toxicity, usually has corrosiveness and the risk to the environment. Served as the phenolic resolver, the diglycol is also the hazardous material. Therefore the thought of using the traditional tar, anthracite oil, phenolic resin as the taphole clay binder has already confirmed to be the health harmful technology. To develop safe binder containing taphole clay is the work that the refractory researchers must carry out.

Less study on the aspect can be found in home. Some reports of environment-friendly taphole clay are the binder of phenolic resins. In study of the environment-friendly taphole clay, the use of pitch as a binder is avoided due to the fact that the benzene is also existed in pitch. Thus, the

environment-friendly taphole clay in the true sense is the improvement of low poisonous ones, either is new structure taphole clay which makes the improvement after the structural design. From the research process of high strength environment-friendly taphole clay we find that using the structural design method to achieve coordinate between the taphole clay environmental friendliness and the operational performance in the true sense.

Conclusions

1) The developed high strength environment-friendly taphole clay's burned strength is higher than 8 MPa, the content of benzene (wt,%) is less than 0.005wt%, and it is continuously applied on the new 3800M^3 blast furnace for four months. The taphole clay consumption achieves the 0.49Kg/t iron, the flow speed of molten iron achieves 7.5 ton/minute, the tapping time is generally controlled 11-13 times, and the effect is remarkable.

2) The high strength environment-friendly clay-strip is squeezes out longer, break effect is good, and has patching function for the slit of tap hole channel. The new blast furnace using environment-friendly taphole clay produces in 4 days. The normal work rate of tap hole achieves 100 percent, and numbers of changes presses of putty is zero, also the numbers of dropping pressure to clogging is zero. This taphole clay is made the adjustment in the production in view of the different situation. The plastic value at 50°C may adjust to 1.1-1.2MPa, and the disperses spurts of tap hole is contained. The disperse spurts question of molten iron of new blast furnace is solved.

References

1. Xiong Yafei. The operation and production of sixth blast furnace of WISCO. Ironmaking, 2005, 24(6): 4-7

2. Zhang Shijue. The development and innovation of technology of blast furnace of WISCO. Ironmaking, 2001, 24 (Added): 57-60

3. Liang Yibing. Study and application of taphole clay used in blast furnace with large scale of volume.Science and Technology in Tayuan Steel Company.2008,(3):1-6.

3rd International Symposium on High-Temperature Metallurgical Processing
Edited by: Tao Jiang, Jiann-Yang Hwang, Patrick Masset, Onuralp Yucel, Rafael Padilla, and Guifeng Zhou
TMS (The Minerals, Metals & Materials Society), 2012

3rd International Symposium on High-Temperature Metallurgical Processing

Sintering and Synthesis

Session Chairs:
Mark Philip Schwarz
Xiaohui Fan

3rd International Symposium on High-Temperature Metallurgical Processing
Edited by: Tao Jiang, Jiann-Yang Hwang, Patrick Masset, Onuralp Yucel, Rafael Padilla, and Guifeng Zhou
TMS (The Minerals, Metals & Materials Society), 2012

STRENGTHENING THE SINTERING OF IRON CONCENTRATE FINES BY HIGH PRESSURE ROLLER GRINDING PRETREATMENT

Yufeng Guo[1], Kelang Mu[1], Tao Jiang[1], Dao Su[1], Jinghua Zeng[1]

[1]School of Minerals Processing & Bioengineering, Central South University, Changsha, Hunan 410083, P.R.China

Keywords: High Pressure Roller Grinding, Iron Concentrate Fine, Sinter

Abstract

The influence of high pressure roller grinding (HPRG) on sintering of iron concentrate fines was investigated. Results of mini-sintering tests showed that assimilation temperature of iron concentrate fines decreased from 1230 ℃ to 1220 ℃ and assimilation time was shortened from 10 min to 5 min when the iron concentrate fines was pretreated by HPRG. Sinter pot tests showed that the yield of sinter increased from 60.33% to 72.92% , tumble index increased from 44.35% to 46.66%. The investigation indicated that, after being pretreated by HPRG, iron concentrate fines are improved in ballability and the fraction of fine particles increased, resulting in the improvement of granulation property and reactiveness in solid state reaction. As a result, sintering of iron concentrate fines were strengthened.

Introduction

With the rapid development of iron and steel industry and the decrease of high-grade ores, the imports of iron ore are increasing continually. It is of immensely strategic importance for development of iron and steel industry and energy security in our country to make good use of iron concentrate fine which is low price, high grade and has a refractory sintering property. When iron concentrate fine is used in sintering, granulation property of sinter mixture and permeability of sinter bed get poor. As a result, yield and quality of sinter fall down. Many researches show that, when HPRG is used in pelletization, quality of pellets is improved dramatically. Meanwhile, HPRG has a low energy consume, a large handing capacity and it is benefit for environment protect. At this theme, strengthening of sintering of iron concentrate fine pretreated by HPRG was investigated in this paper.

Experimental

Materials

Iron concentrate fine sample used in this investigation is hematite and obtained from Yuanjiacun Iron Mine of Mining Branch Company of Taiyuan Iron and Steel Group Corporation, Limited. Chemical composition and size distribution of iron concentrate fine are showed in Table I and Table II, respectively.

Table I. Chemical Composition of Iron Concentrate Fine /wt%

TFe	FeO	SiO_2	Al_2O_3	CaO	MgO	K_2O	Na_2O	P	S	LOI
67.44	9.01	2.54	0.56	0.21	0.23	0.023	0.026	0.019	0.023	0.62

Table II. Size Distribution and Specific Surface Area of Iron Concentrate Fine

Size Distribution /wt%			Specific Surface Area /$cm^2.g^{-1}$
>0.074	0.074~0.044	<0.045	
1.17	3.11	95.72	1647.00

Methods

Pretreatment by HPRG. The specification of HPRG machine is Φ250×120mm.The pressure value of double rolls is adjustable in range from 0 to 50 kN . Iron ore concentrate is mixed well before being pretreated by HPRG and fed steadily when pretreated. Pressure value was set at 30kN. The corresponding intensity of pressure was 1Mpa. Moisture ratio of iron ore concentrate for pretreatment was 8%.

Assimilability Test. When iron ore fine reacts with lime, a liquid phase of low melting point is formed. This behavior of iron ore fine is defined as assimilation. Assimilability, the reactivity of iron ore fine with lime, is regarded as a important evaluating indicator of basic sintering characteristic of iron ore fine. According to the classical theory of physical chemistry, the difficulty of a reaction is evaluated by time and temperature. In general, the lower the assimilation temperature is, and the shorter the assimilation time is, the easier the formation of liquid phase becomes[1]. The formation of liquid phase is beneficial to sintering.

The assimilability was tested as the following method: Iron ore fine, as well as the lime (analytic reagent) ,was milled to be powder with the fraction passing the 100 mesh sieve reaches 100%. Then, iron ore fine was pressed to be column under a certain pressure. The diameter and height of column were 8mm and 10mm, respectively. Lime was pressed to be column, too. The diameter and height of column were 25mm and 10mm, respectively. Next, the iron ore fine column was laid on the lime column. The two columns were put in mini-sinter machine together, and roasted in an analogous condition as sintering. Assimilation temperature and assimilation time were tested.

Sintering Pot Test. All the materials, including iron ore concentrate fine, return fines,

fluxes, fuels, were firstly proportioned by weight, and mixed for three times. After water added in, the mixture was mixed for three times. The moist mixture went on being granulated by a 600 mm×1400 mm drum into granular material and then charged into the sintering pot. Moisture ratio, size distribution and permeability index of granular material were tested immediately after granulation.

Small sinter pot experiments were conducted in a 100 mm diameter laboratory sinter pot. Sintering bed height was fixed at 650 mm. The weight of hearth layer was 0.5kg.Big sinter pot experiments were conducted in a 150 mm diameter laboratory sinter pot. Sintering bed height was fixed at 650 mm. The weight of hearth layer was 1.0kg. The ignition fuel was liquefied natural gas. Ignition time was 90s, and ignition temperature 1100±50℃, ignition negative pressure 5kPa, sintering negative pressure 10kPa. At the sinter terminal point, negative pressure was adjusted to be 5kPa. After cooled for 5min, sinter cake was discharged from the pot. The finished sinter was obtained after crushed and screened. Main performances such as yield, size distribution and tumble index were measured according to the relative criterions finally.

Results and Discussion

Properties of Iron Concentrate Fines by HPRG

Properties of iron concentrate fine before and after being pretreated by HPRG are showed in Table III and Table IV.

Table III. Specific Surface Areas and Maximum Capillary Water of Iron Concentrate Fine

Iron Concentrate Fine	Specific Surface Area /$cm^2.g^{-1}$	Maximum Capillary Water/%
No Pretreatment	1647.0	15.09
Pretreated by HPRG	2201.1	16.81

Table IV. Weight Percentage of Fine Particle in Iron Concentrate Fine /(wt%)

Iron Concentrate Fine	Size/mm					
	<0.028	<0.015	<0.010	<0.005	<0.002	<0.001
No Pretreatment	69.68	41.30	27.51	13.31	3.83	0.83
Pretreated by HPRG	78.46	53.74	39.99	22.20	7.41	2.04

As shown in Table III and Table IV , it is very effective for superfine of hematite fine by HPRG. After being pretreated by HPRG, the specific surface area of hematite fine increased from 1647.0 $cm^2.g^{-1}$ to 2201.1 $cm^2.g^{-1}$. The weight percentage of fine particles grows dramatically, the fraction of -0.010mm specially. The growth of fine

particles results in improvement in compactness of grains when granulating. Because fine particles have high inner energy and high surface activity, the granulation property and reactiveness in solid state reaction of iron ore concentrate pretreated by HPRG are improved.

Assimilability

Assimilability of iron concentrate fine before and after being pretreated by HPRG is showed in Table V. Assimilation time was tested at a fixed temperature. If assimilation time was too long, a higher roasting temperature was required. It is found that when roasting temperature is 1220℃, roasting time is 5min, iron concentrate fine before being pretreated does not react with CaO, however, iron concentrate fine after being pretreated does. When roasting temperature is raised up to 1230℃, assimilation time is 10min. Microscopy photos of liquid phase of iron ore fine columns formed in the roasting process are showed in Fig1. After iron concentrate fine is pretreated, quantity of calcium ferrite in liquid phase increased, otherwise, the penetration depth of CaO into iron ore is more deeper. In conclusion, assimilability of iron concentrate fine after being pretreated by HPRG is better than that of iron concentrate fine not pretreated.

Table V. Assimilability of Iron Concentrate Fine

Iron Concentrate Fine	Assimilability	
	Temperature /℃	Time /min
No Pretreatment	1230	10
Pretreated by HPRG	1220	5

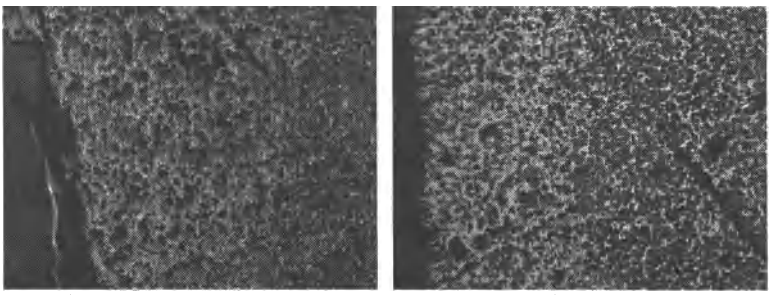

(Pretreated by HPRG) (No Pretreatment)

Fig I. Microscopy Photoes of Liquid Phase of Iron Ore Fine Columns roasting temperature is 1220℃, roasting time is 5min

The better assimilability of iron ore fine pretreated by HPRG attributes to improvement in specific surface area and ballability of iron ore fines, the looser

structure, and the higher content of crystallization water.

Sinter

The results of mini-sintering tests indicate that, assimilability of iron ore fine is improved by HPRG, which is benefit for formation of calcium ferrite even strength of sinter with iron ore fine. Based on the conclusion, sinter pot was carried out in order to study the influence of HPRG on sinter of hematite concentrate fine.

Basic Sinter Tests. In basic sinter tests, hematite concentrate fine used is not pretreated. Proper parameters such as moisture ratio of mixture and coke ratio are obtained. The results are showed in Table VI.

TableVI. Results of Sinter Pot Tests with Hematite Concentrate Fine not Pretreated

Moisture Ratio/%	Coke Ratio/%	Permeability Index/J.P.U	Yield /%	Tumble Index/%	Productivity /t·(m^2·h)$^{-1}$
8.8	5.3	0.57	55.21	38.6	1.471
7.8	5.3	0.64	52.03	37.47	1.468
	5.3	0.63	52.96	40.69	1.476
8.3	5.6	0.60	54.73	42.6	1.481
	5.9	0.70	60.33	44.35	1.556
	6.2	0.75	58.95	43.32	1.542

It can be seen from Table .VI that, the proper moisture ratio of mixture and coke ratio is 8.3% and 5.9%, respectively. Under the condition, the yield is 60.33%,the tumble index is 44.35%, the productivity is 1.556 t·(m^2·h)$^{-1}$.

Sinter Tests with Hematite Concentrate Fine Pretreated by HPRG. In sinter tests, hematite concentrate fine used is pretreated by HPRG. Proper parameters such as moisture ratio of mixture and coke ratio are obtained. The results are showed in Table VII.

TableVII. The Results of Sinter Tests with Hematite Concentrate Fine Pretreated by HPRG

Moisture Ratio/%	Coke Ratio/%	Permeability Index/J.P.U	Yield /%	Tumble Index/%	Productivity /t·(m^2·h)$^{-1}$
8.3	5.9	1.27	53.28	40.23	1.521
7.8	5.9	1.22	58.82	44.48	1.562
	5.9	0.80	72.92	46.66	1.689
7.3	5.6	0.77	59.46	46.32	1.663
	6.2	0.72	63.64	46.59	1.674
7.0	5.9	0.67	58.93	44.87	1.581

As shown in Table VII, the quality and yield of sinter are increased. The proper

moisture ratio decreases from 8.3% to 7.3%. The proper coke ratio is 5.9%. Under the condition, the yield is 72.92%, the tumble index is 46.66%, the productivity is 1.689t·$(m^2 \cdot h)^{-1}$.Compared to the indexes of sinter in Table .VI, The yield, tumble index and productivity are increased by 12.59%, 2.31% and 0.133 t·$(m^2 \cdot h)^{-1}$, respectively. By HPRG, sinter characteristic of hematite concentrate fine is improved dramatically. Therefore, better sintering indexes are obtained. The growth of content of fine particles and specific surface area of iron ore fines, results in improvement of surface activation energy, hydrophilicity and ballability of iron ore fines. As a result, the granulation property of iron ore fines is improved and permeability of sinter bed gets better. The higher productivity of sinter is directly due to the better permeability of sinter bed[2]. Otherwise, HPRG contributes to the better assimilability of iron ore fine which is benefit for formation of calcium ferrite and liquid phase in the process of sinter. The quality of sinter is improved, consequently.

Analysis and Discussion

Sinter-forming mechanism, including solid-state reaction sintering process, liquid phase formation and crystallization process, affects the sinter mineral composition and microstructure, has a very close relationship with the quality of sintering. Among them, the solid-state reaction which occur in the interface of the two solids before they are melt, due to the diffusion of solid particles and the reaction product is solid as well[3]. Rather than the final sinter mineral composition does the solid-phase reaction production decide to form new substances of low fusing point which are excluded in the raw material, and it can be known from the mechanism of sintering. With the continually rising of temperature, those new substances are the precursors to form liquid phase, decreasing the temperature of liquid formed. Consequently, the solid-state reaction plays a vital role in sintering process. The influence of particle size on the solid-state reaction is significant and the reaction rate constant is inversely proportional to the square of the particle radius when the temperature and time are in a certain circumstance:

$$k=C/r^2$$

k is the reaction rate constant, C is the scale factor, r is particle radius. In this study, the particle size of slaked lime shrank obviously when the quick lime as a binder fully slaked[4]. Table 4 shows that, after high pressure roll grinding, the hematite particle size decreased, the specific surface area increased and the content of fine particles increased from 69.68% to 78.46%, especially the number of particle size under 0.010mm was significantly increased. From the inverse relationship between the solid-phase reaction rate constant and particle radius we can know that, as hematite and lime particle size decreases after high pressure roll grinding, the solid-state reaction process will accelerate, enhancing the assimilation performance, promoting the formation of calcium ferrite in the solid phase, improving the strength of sinter at a certain temperature and time.

The factors that affect the mixing process are the wettability of minerals, grain size

and grain size composition. Studies have shown that the pelletization of fine particles begun in the wetting of particles and forming sufficient capillary force[5]. The capillary force between particles of easy wetting is stronger, resulting in the stronger pelletized ability of bulk particles, and the better granulation in the mixed process. In addition, studies in the structure of the ball in the sintering mixture granulation have shown that, the ball is made up by the nuclear particles and the adhesive fine-grained particle, called "quasi-particles", and its formation conditions are closely related to grain size. Less than 0.2mm particles are usually as adhesion particles in the studies, and the more adhesion particles, the better the pelletization in the fine concentrate. From Table III and Table IV we can see that, after being pretreated by high pressure roll grinding, hematite concentrate was improved in maximum capillary water that increased from15.09% to 16.81%, the adhesive particles that grew massively in the pelletization, which effectively enhanced the granulation of sintering mixture, the strength of pellets, the permeability of the mixture layer, and the yield of sintering further.

Conclusion

Ballability of iron concentrate fine was improved and the fraction of fine particles increased when the iron concentrate fines were pretreated by HPRG, resulting in improvement of granulation property and reactiveness in solid state reaction which is beneficial to formation of calcium ferrite and liquid phase in the process of sinter. As a result, sintering of iron concentrate fine is strengthened.

Assimilation temperature of iron concentrate fine is lowered from 1230℃to 1220℃, and assimilation time is shortened from 10min to 5min after the iron concentrate fines being pretreated by HPRG.

When the iron concentrate fines were dealt with HPRG, the yield, tumble index and the productivity of sinter are increased from 60.33%to72.92%, from 44.35% to 46.66%, and from 1.556 $t\cdot(m^2\cdot h)^{-1}$ to 1.689$t\cdot(m^2\cdot h)^{-1}$, respectively.

Reference

[1] Wu-Shengli et al, "Experiment Study of Assimilation Ability between Iron Ores and CaO" . *Journal of University of Science and Technology BeiJing*. 2002, 24(3). 58-261.

[2] Zhu-Deqing et al."Sintering Behaviors of Brazilian Hematite Concentrate and its Improvements," *J. CENT. SOUTH UNIV.* (Science and Technology), 2006, 37 (5) , 878-883.

[3] Fu Juying,Jiang Tao and Zhu Deqing. Sintering and pelletizing [M] . Changsha: *Press of Central South Universit y of Technology,* 1996.

[4]Hou-Huijun,Feng-Eelian."Produce Pratice of Dead Lime Slaking." *ShanXi Metallurgy*. 2007(5), 20-21.

[5] Zhou-Chuanqiang et al. "Discussion on models for the prediction of mixture effect for sinter feed". *Sciencepaper Online.*

3rd International Symposium on High-Temperature Metallurgical Processing
Edited by: Tao Jiang, Jiann-Yang Hwang, Patrick Masset, Onuralp Yucel, Rafael Padilla, and Guifeng Zhou
TMS (The Minerals, Metals & Materials Society), 2012

RESEARCH ON SINTERING PROPERTIES OF VANADIUM-TITANUM MAGNETITE CONCENTRATES

Xiaohui Fan, Qiang Wang, Xuling Chen, Min Gan, Lishun Yuan, Shan He
School of Minerals Processing & Bioengineering, Central South University, Changsha, Hunan,410083, P. R. China

Key words: Vanadium-titanium Magnetite, Sinter, Mineral Composition, Liquid Phase Formations, Metallogenic Performance

Abstract

The sintering properties of vanadium-titanium magnetite concentrate (VTC) was studied in this paper. Through the optimizing the sintering process of VTC, the suitable granulation moisture and coke proportion were determined. The sintering velocity decreased from 23.05 mm/min to 18.22 mm/min. With the increase of VTC proportion from 0 to 46%, the specific productivity and tumbler index were respectively decreased from 1.55 t/(m^2·h) to 1.21 t/(m^2·h), and 62.93% to 57.73%. The temperature of liquid phase formations of mixtures increased, the amount of liquid lowered, and the content and sharp of sintering mineral gradually changed with the increase of VTC ,these lead that sinter quality became worse.

Introduction

In recent years, the steel industry of China is developing rapidly. And the steel production was 627 million tons in 2010. At present, the resources of vanadium-titanium magnetite concentrate (VTC) was about 14.4% of the total national iron reserves of China[1]. VTC has been used as sintering material by Magang, Chenggang and Pangang. The amount of VTC in Pangang is maximum.

However, there exist many problems in VTC sintering, which involve in high specific productivity, bad sintering tumbler strength and high energy consumption[2~5]. That's why the proportion of VTC is limited in sintering.

The high quality of iron ore resources is worse in China. Therefore, it's necessary to study the properties of VTC sintering, and to find out the reason how the VTC ratio affect the sinter performance. Purpose and significance of the research is to get high-quality sinter with the proportion of VTC greatly raised.

Raw Materials and Test Methods

Raw Materials

The chemical composition of the materials was in Table I. For VTC, TiO_2, MgO and Al_2O_3 were relatively high, SiO_2 was low. For ore A, SiO_2 was 15.89%, and Al_2O_3 was 4.19% .SiO_2 of concentrate C was 8.13%, SiO_2 of concentrate F was 6.09%.

MgO of concentrate E was 4.13%.

Table I Chemical Compositions of Materials /%

Material	Fe	FeO	CaO	MgO	SiO_2	Al_2O_3	V_2O_5	TiO_2	LOI
VTC	53.69	31.78	0.45	**2.99**	3.09	**3.94**	0.53	**12.69**	2.85
Ore A	47.85	4.48	0.99	1.12	**15.89**	**4.19**	-	-	4.66
Concentrate C	58.19	19.82	1.60	0.94	**8.13**	1.72	-	-	2.73
Ore B	60.82	0.37	0.10	0.10	4.16	2.03	-	-	5.10
Concentrate D	**67.44**	9.01	0.21	0.23	2.54	0.56	-	-	0.62
Concentrate E	61.85	22.55	0.80	**4.13**	2.68	1.90	-	-	2.81
Concentrate F	61.80	24.61	1.42	0.83	**6.09**	1.73	-	-	2.40
Flue dust	37.23	6.70	6.30	1.81	6.45	3.06	-	-	16.67

Test Method of Liquid Phase Formations

Materials was grinded to less than 0.074 mm, then mixed with suitable water thoroughly. The mixture was made into prism of which the length of the triangle is 7mm and the height is 20 mm. Test equipment was the horizontal pipe furnace with the speed of temperature rise of 10℃/min. The changing of the shape and area of the prism was recorded by a camera, and automatically identified with the image processing software.

Test Method of Metallogenic Performance

Materials was grinded to less than 0.074 mm, then mixed with suitable water thoroughly. After that, the mixture was pressed under the pressure of 300 kg/cm^2 for 1min, and made into agglomerate which was 10 mm diameter and 10 mm high. The agglomerate was roasted in different temperature for 10 min and cooled to room temperature. At last, mineral composition of the agglomerate was tested with optical microscope.

Sintering Experiment

The sinter mixture granulated in the cylinder mechanism for 4min. After the sinter was produced with the sintering pot which was Φ180 mm, sintering indexes were tested according to national standards. The sinter mineral composition was tested with the optical microscope and XRD.

Results and Discussion

Experimental Scheme

Experimental scheme was shown in Table II. From scheme A to scheme E, proportion of concentrate C, ore B, ore A and flue dust kept the same, the proportion of concentrate D, concentrate E and concentrate F gradually decreased, and the proportion of VTC increased gradually.

Table II Experimental Scheme /%

Scheme	VTC	Concentrate D	Concentrate E	Concentrate F	Concentrate C	Ore B	Ore A	Flue dust
A	0	10	28	8	19	10	5	3
B	12	8	20	6	19	10	5	3
C	24	7	11	4	19	10	5	3
D	36	5	3	2	19	10	5	3
E	46	0	0	0	19	10	5	3

Chemical composition of sinter was in Table III. From scheme A to scheme E, SiO_2, CaO and MgO content were basically unchanged, but for scheme E, CaO content was 10.93%, MgO was 2.34%.TiO_2,V_2O_5 and Al_2O_3 increased gradually, Total Fe content decreased gradually.

Table III Chemical Composition of Sinter /%

Scheme	TFe	SiO_2	CaO	MgO	Al_2O_3	TiO_2	V_2O_5	R
A	54.37	5.36	10.73	2.16	1.89	0	0	2.00
B	53.36	5.37	10.73	2.18	2.19	1.66	0.06	2.00
C	52.42	5.37	10.73	2.15	2.49	3.34	0.13	2.00
D	51.40	5.37	10.74	2.17	2.80	5.03	0.19	2.00
E	50.30	5.36	10.93	2.34	3.11	6.44	0.27	2.04

Effect of VTC Proportion on Sinter Performance

The suitable granulation moisture and coke proportion were reduced from scheme A to scheme E seeing table IV. Each scheme of sintering indexes in suitable conditions was in Fig. 1. The sintering velocity reduced from 23.05 mm/min to 18.22 mm/min, specific productivity decreased from 1.55 t/(m^2·h) to 1.21 t/(m^2·h), tumbler index lessened from 62.93% to 57.73% with the increase of VTC from 0% to 46%. In a word, sintering indexes all decreased.

Table IV The Suitable Technological Parameters /%

Scheme	granulation moisture	coke proportion
A	8.50	5.00
B	8.50	4.50
C	8.25	4.50
D	8.25	4.00
E	8.00	4.00

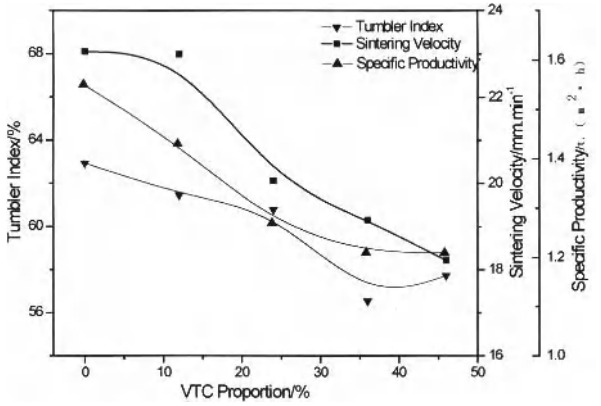

Fig. 1 Each Scheme of Sintering Indexes in Suitable Conditions

Mineral Composition of VTC Sinter

Sintering mineral composition was in Fig.2.with content of TiO_2 in the sinter increased, content of hematite and perovskite gradually increased, content of magnetite and calcium ferrite gradually decreased. The content of calcium ferrite reduced approximately from 30% to 10%,and content of metasilicate was about 10% , so the liquid amount of sinter gradually decreased.

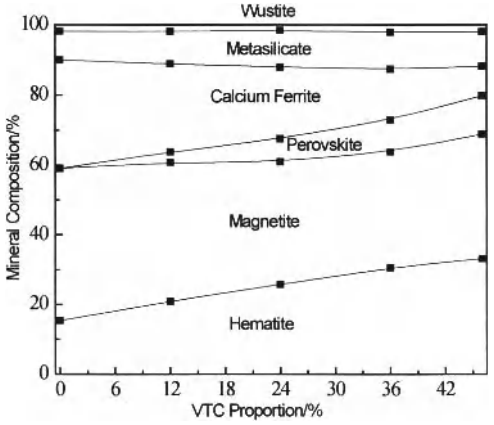

Fig. 2 Effect of VTC Proportion on Sintering Mineral Composition

The results of sintering mineral composition shown that, with TiO_2 content in sinter increased, the amount of dendrites and the scattered bone structure of hematite increased. The content of magnetite which had closely embedded relations with calcium ferrite decreased. The content of perovskite gradually increased, and the

shape of calcium ferrite from the needle gradually developed into the column.

Reasons of VTC Affected on Sinter Performance

The liquid phase formations of VTC was in Fig. 3.With the increase of VTC, the beginning temperature of forming liquid approximately increased from 1250℃to 1270℃the ending temperature of forming liquid approximately increased from 1330℃ to 1360℃ liquid amount in 1330℃approximately decreased from 85% to 60%. The results shown that the liquid phase of mixture formations was more and more difficult, and the amount was lower and lower. Those were basically consistent with the change law of that tumbler index gradually reduced.

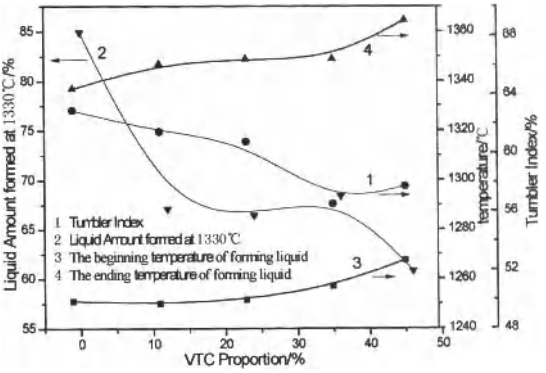

Fig. 3 The Liquid Phase Formations of VTC

Less than 0.5 mm iron ore and returning mines, all flux in the mixture were easily metallogenic. Iron ore and returning mines were weighed by the experiment scheme. After that, sieved out the part of less than 0.5 mm, and mixed the whole flux with suitable water thoroughly. The agglomerate which was made according to the method of metallogenic performance was separately roasted in 1200℃,1270℃,1300℃ and 1320℃ for 10 min.

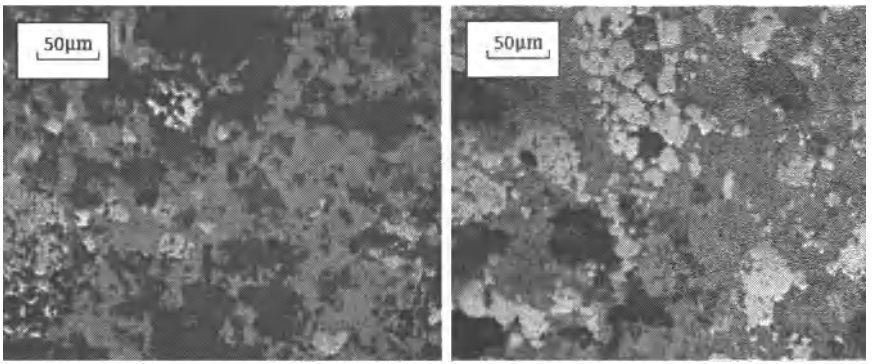

(a) 1200℃ (b) 1270℃

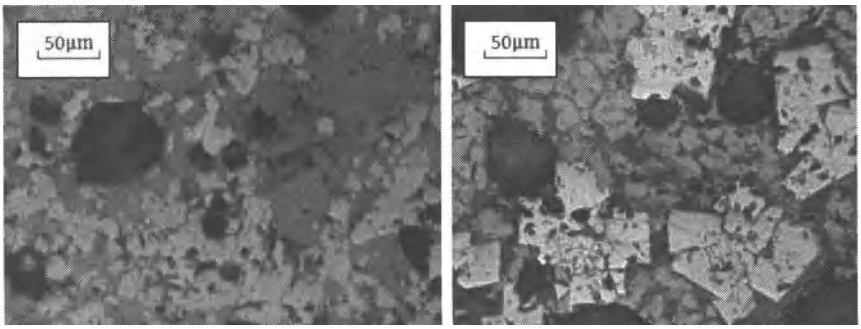

(c)1300℃ (d)1320℃

White—Hematite, Brown—Magnetite, French grey—Perovskite, Gray—Calcium Ferrite, Dark grey—Metasilicate, Black—Hole.

Fig. 4 The Microstructure of the Sinter in Different Temperature

The microstructure of the sinter shown in Fig. 4. With the increase of roasting temperature, VTC's oxidation reaction mainly got improved just in the low temperature, and calcium ferrite was generated a lot in a temperature range from 1200℃ to 1270℃.Liquid distributed uniformly and interweaved with magnetite, and it's amount achieved maximum. Perovskite continued to be generated in 1300℃.The amount of calcium ferrite in 1320℃ was less than in 1300℃.The amount of perovskite in 1320℃ was more than in 1300℃. Perovskite was easily generated, and calcium ferrite was hard to exist when temperature was over 1300℃.The VTC sinter below 1300℃ was good for calcium ferrite existing, hard for perovskite generating.

Conclusion

(1) With VTC increased from 0% to 46%, the suitable granulation moisture and coke proportion reduced, and the sintering velocity, specific productivity and tumbler index all decreased. The amount of hematite and perovskite increased, magnetite and calcium ferrite decreased, liquid amount lowered.

(2) With the increase of VTC, the temperature of liquid beginning and endding gradually increased, liquid amount in 1330℃ gradually decreased, the content of fragile perovskite whose melting temperature was high increased, and the content of calcium ferrite decreased. Those were part of the reasons why VTC sinter properties became bad.

References

1. Songquan Heng,Zhong Liu,Fuding Yang, "Introduction to the iron ore resources at home and abroad", *Jilin Geology*,27(3)(2008),5-12. (in Chinese)

2. Jiayuan Ma, Xiwen Sun,Risheng Diao, *The Theory and Practice of VTC BF Operation* (Metallurgical Industry Press .BeiJing,2000). (in Chinese)
3. Xiqing Wang,*BF operation of VTC*(Metallurgical Industry Press). (in Chinese)
4. WenhuaYu,QunHe,FanglinFan, "Sintering Properties of Baima Vanadium-Titanum Magnetite", *Iron Steel Vanadium Titanium*,21(21) (2000),24-28. (in Chinese)
5. Ruitu Xu,Shengli Wu,*China's Iron Ore Sintering Research—the Memoir of Quding Zhou*(Metallurgical Industry Press.1997),94-107. (in Chinese)

3rd International Symposium on High-Temperature Metallurgical Processing
Edited by: Tao Jiang, Jiann-Yang Hwang, Patrick Masset, Onuralp Yucel, Rafael Padilla, and Guifeng Zhou
TMS (The Minerals, Metals & Materials Society), 2012

INFLUENCE OF LIMONITE PROPORTION ON SINTER QUANTITY AND QUALITY

Xiaohui Fan[1], Dao Su[1], Ganghua Fu[1], Xuling Chen[1], Min Gan[1], Tao Jiang[1], Yufeng Guo[1]

[1]School of Minerals Processing & Bioengineering, Central South University, Changsha, Hunan 410083, China

Key words: Sintering, Limonite, Magnetite, Hematite,

Abstract

The sinter quantity and quality of limonite in the magnetite and hematite sintering models were studied and compared. For the sintering of magnetite, the results showed that the increase of limonite improved the permeability of sinter mixture, increased the sinter quantity and quality. The sinter strength and productivity were decreased when the proportion of limonite exceeded 50%. The appropriate proportion of limonite was 40%-50%. For the sintering of hematite, the sinter quantity and quality were first maintained at the same level thereafter declined, more obviously when the proportion of limonite exceeded 40%. The amount of calcium ferrite increased whose shape changed from acicular to leaflike and block gradually with the proportion of limonite increased from 0% to 80%.

Introduction

With the fierce competition of domestic and overseas iron markets in the twenty-first century, cheap ores such as limonite are used to be sintering raw materials to cut the costs of sinter and pig iron for steel making, and boosts the competitiveness of steel companies [1, 2]. In addition, as the reserve volume of hematite of high grade is reducing year by year, the usage amount of limonite in sintering are expanding in major domestic and international sintering plant [3, 4]. Sintering can be divided into two types, majoring in concentrates and fine ores, according to the different types of raw materials. The sintering characteristics of limonite in the two types above have been studied and compared in this paper, which makes a significant sense for the research of limonite sintering properties and guidance of ore proportioning in sintering plants.

Experiment

Materials

The chemical composition and size distribution of raw materials are shown in Table I and Table Ⅱ, respectively.

Table I. Chemical Composition of Raw Materials /%

Materials	TFe	FeO	SiO_2	CaO	MgO	Al_2O_3	LOI
L	58.94	0.70	4.84	0.09	0.10	1.82	8.46
H1	62.47	0.45	5.53	0.25	0.08	1.72	2.04
H2	60.81	0.51	8.42	0.12	0.07	1.82	2.08
M1	64.89	28.33	5.24	0.30	0.52	1.02	1.56
M2	64.56	25.96	6.71	0.35	0.50	1.03	0.77
Dolomite			0.89	32.37	19.26	0.24	45.15
Limestone			0.66	53.11	0.52	0.31	42.64
Quicklime			1.09	66.99	2.35	0.25	24.76
Coke			6.80	0.89	0.20	4.25	76.75

* LOI: loss on ignition

Table Ⅱ. Size Distribution of Raw Materials /%

Materials	+8mm	5~8mm	3~5mm	1~3mm	0.5~1mm	-0.5mm
L	11.49	18.19	20.72	15.40	13.99	20.21
H1	4.59	10.12	15.91	18.16	10.75	40.47
H2	5.00	10.02	14.51	15.59	9.49	45.38
M1	0.00	0.00	0.03	0.47	1.60	97.91
M2	0.00	0.70	1.95	4.26	7.16	85.93
Dolomite	0.00	0.00	24.27	24.97	16.45	34.30
Limestone	0.00	0.35	11.11	41.76	4.97	41.81
Quicklime	0.00	2.90	13.45	32.20	16.55	34.90
Coke	0.30	1.40	17.75	17.95	14.46	48.16

Table I and Table Ⅱ showed that limonite (L) had a low grade (58.94%), high LOI (8.46%), big size which percentage of -0.5mm was only 20.21%. Two kinds of magnetite (M1 and M2) had a high grade (both exceeded 64%) and small size which percentages of -0.5mm exceeded 85%. Two kinds of hematite (H1 and H2) had a middle grade, LOI and size between limonite and magnetite.

Methods

Mini-sintering Test Mixed the part whose size below 3mm of ore blender with fluxes and

suitable moisture. Mixture was pressed under the pressure of 300kg/cm^2 for 1min to make the agglomerate with specification of Φ10×10 mm. The agglomerate was roasted at 1300℃ for 15min (sintering atmosphere: $CO:O_2:N_2:CO_2$=1:1:2:5). The microstructure of roasted agglomerates was observed with optical microscope.

Sintering Pot Test The granulating time of mixture was 4min; the test utilized the sintering pot with specification of Φ150 mm. The thickness of mixture layer was 670mm, and the ignition temperature and time were 1050℃ and 1min.The sintering negative pressure was 12000 Pa. Tested yield and tumbler strength of sinter after cooling for 3min.

Results and Discussion

Sintering Proportioning Schemes

Fixing the sinter's chemical composition at the same level, which TFe 55%-57%, SiO_2=5.45%, MgO=2.3%, basicity (R) =1.9. Fixing the proportion of H2 or M2 at 10% respectively, M2 or H2 is replaced by L, thus 13 schemes are designed. Schemes and the properties of ore blender are shown in Table Ⅲ.

Table Ⅲ. Proportioning Schemes and Properties of Ore Blender

Scheme	Iron Ores Proportion/%					Properties of Ore Blender		
	L	M1	M2	H1	H2	Average Size/mm	FeO Content/%	LOI/%
S1	0	90			10	0.24	25.58	1.62
S2	20	70			10	1.07	20.04	3.00
S3	40	50			10	1.71	14.51	4.37
S4	50	40			10	2.04	11.74	5.06
S5	60	30			10	2.36	8.98	5.75
S6	70	20			10	2.68	6.21	6.44
S7	80	10			10	3.01	3.45	7.13
S8	0		10	90		2.53	3.00	1.91
S9	20		10	70		2.66	3.05	3.19
S10	40		10	50		2.78	3.10	4.48
S11	50		10	40		2.84	3.13	5.13
S12	60		10	30		2.91	3.15	5.76
S13	80		10	10		3.03	3.20	7.05

Influence of Limonite Proportion on Sinter Quantity and Quality

Coke and moisture optimization experiments have been conducted for S1-S13, and the appropriate coke proportion, moisture and corresponding mixture permeability indexes are shown in Figure 1. As shown in Figure 1 (a), with the increase of limonite the

appropriate proportions of coke were on a rise because of the increase of LOI and decrease of FeO (Table Ⅲ), the mixture permeability got better and then remained at the same level (about 1.07JPU). Moisture remained 8.0% when the limonite proportion changed from 0% to 60% and 8.5% when the limonite proportion exceeded 60%. As shown in Figure 1 (b), with the increase of limonite proportion, the appropriate coke proportion which were higher than that of S1-S8 generally and moisture increased obviously, the mixture permeability got slightly better.

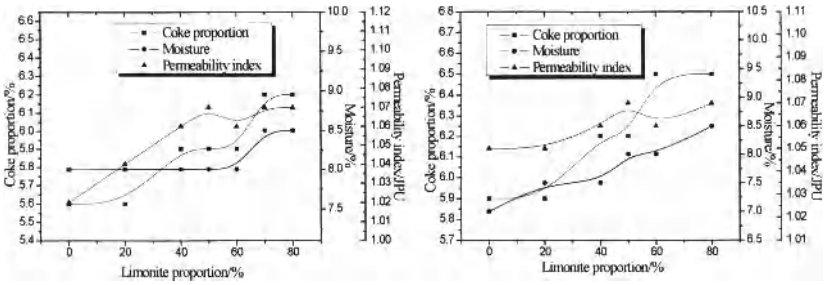

(a) L-M1(S1-S7) (b) L-H1(S8-S13)

Figure 1. Appropriate Coke Proportion, Moisture and Corresponding Permeability for S1-S13

Under the condition of appropriate coke proportion and moisture, the sinter quantity and quality are shown in Figure 2. As shown in Figure 2 (a), with the increase of limonite proportion the sintering velocity was on a rise obviously, and reached to be the highest (24.62 $mm \cdot min^{-1}$) when the limonite proportion was 80%; the sinter productivity and tumbler strength rised at the beginning and both got to the best (1.69 $t \cdot m^{-2} \cdot h^{-1}$ and 70.02%, respectively) when the limonite proportion was 40%, then declined obviously when the limonite proportion exceeded 50%. As shown in Figure 2(b), with the increase of limonite proportion the sintering velocity got slightly faster generally, and got to be fastest (24.00 $mm \cdot min^{-1}$) when the limonite proportion was 40%. The sinter productivity and tumbler strength were the best without limonite (1.65 $t \cdot m^{-2} \cdot h^{-1}$ and 68.43%, respectively), and remained at the same level when the limonite proportion was not more than 40%, then got worse obviously especially for the sinter productivity.

The experiments under the conditions of fixing mixture moisture (8.0%) and different coke proportions (5.6% and 5.9%) have been conducted for sintering of L-M1 (S1-S7), and corresponding sinter quantity and quality are shown in Figure 3. By comparing Figure 3(a) and (b), with the increase of limonite proportion the sinter quantity and quality changed with the same pattern for the sintering of two coke conditions, and were improved obviously when coke proportion was higher. And the sinter quantity and quality were the best when limonite proportion was 40%-50%.

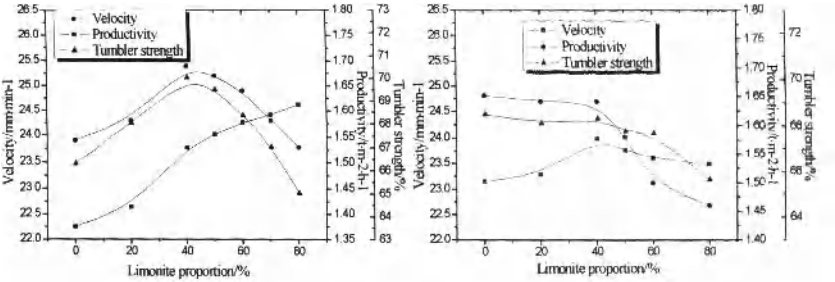

(a)L-M1(S1-S7) (b)L-H1(S8-S13)

Figure 2. The Sinter Quantity and Quality under the Condition of Appropriate Coke Proportion and Moisture for S1-S13

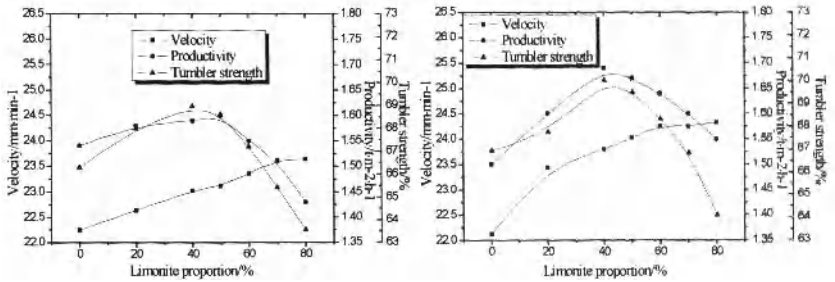

(a) Coke proportion=5.6% (b) Coke proportion=5.9%

Figure 3. Fixing Moisture 8.0%, The Sinter Quantity and Quality of Different Coke Condition for S1-S7

The experiments under the conditions of fixing the coke proportion (5.9%) and different mixture moistures (appropriate moisture and 8.0%) have been conducted for the sintering of L-H1 (S8-S13), and corresponding sinter quantity and quality are shown in Figure 4. By comparing Figure 4(a) and (b), with the increase of limonite proportion the sintering velocity declined rapidly if moisture was constant. And the sinter productivity and tumbler strength declined rapidly when the limonite proportion exceeded 40%.

By comparing Figure 3(b) and Figure 4(b), under the same condition (moisture is 8.0% and coke proportion was 5.9%), the sinter quantity and quality for the sintering of L-M1 were better than the sintering of L-H1 when the limonite proportion exceeded 20%.

In conclusion, for the sintering of magnetite (S1-S7), increased limonite could improve the mixture permeability and increase sinter quantity and quality which would decline rapidly if the limonite proportion was more than 50%. The appropriate proportion of

limonite was 40%-50%. For the sintering of hematite (S8-S13), the sintering indexes maintained at the same level at first with the increase of limonite proportion, and then declined, more obviously when the proportion of limonite was high which should not be more than 40%. For the sintering of limonite, it could be helpful to improve the sinter quantity and quality if coke increased suitably.

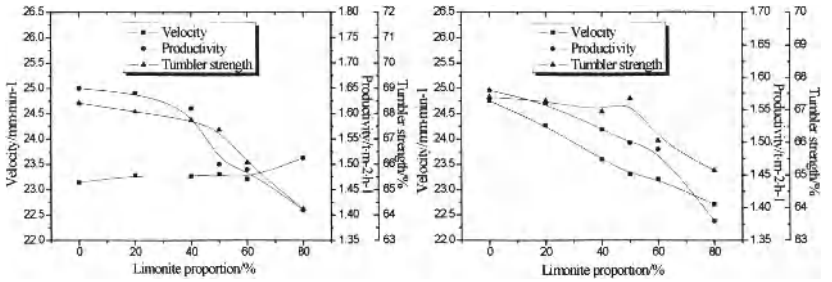

(a) Appropriate moisture (b) Moisture =8.0%

Figure 4. Fixing Coke Proportion 5.9%, The Sinter Quantity and Quality of Different Moisture Condition for S8-S13

Influence of Limonite Proportion on Sinter Microstructure

The quality of sinter especially for the strength are closely related with the mineral composition and microstructure of sinter. The microstructures of roasted agglomerates for S1, S2, S3, S5 and S7 are shown in Figure 5 and S8-S13 are shown in Figure 6.

As shown in Figure 5 (a), (b) and (c), calcium ferrite were mainly shaped as acicular along with the increase of limonite, and magnetite whose shape turned into grainy from block embeded tightly in the binding phase (calcium ferrite) and made a compactness of structure. When the limonite proportion reached to 60 %, large amount of calcium ferrite were shaped as leaf and bulk (Figure 5(d)). When the limonite proportion reached to 80%, massive calcium ferrite had been developed (Figure 5(e)), penetrated and assimilated the porous residual limonite. Therefore the increase of limonite was beneficial to form acicular calcium ferrite and improve the strength of sinter. But as the sharp increase of coarse limonite, resulted the reduction of small particles in the sintering mixture and the raise of the fluxes content in small particles relatively when the size of flues kept constant, which was harmful to the strength of sinter due to the easy generation of liquid phase and its degraded quality.

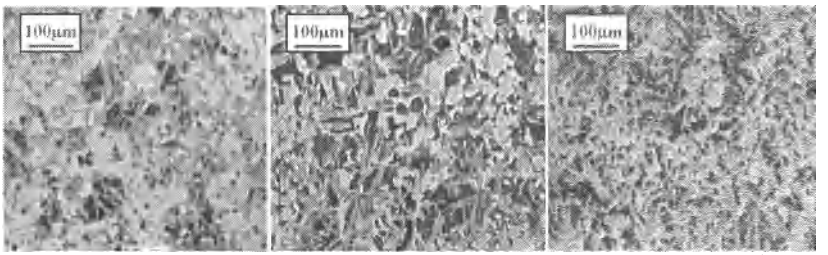

(a) S1 (b) S2 (c) S3

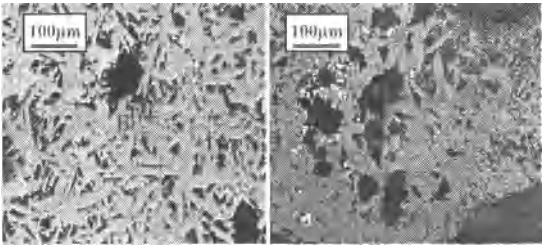

(d) S5 (e) S7

A: Magnetite B: Calcium Ferrite C: Hematite D: Hole

Figure 5. The Microstructures of Roasted Agglomerates for S1, S2, S3, S5 and S7 100×

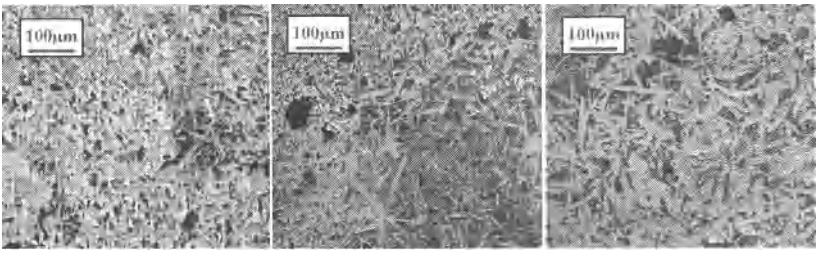

(a) S8 (b) S9 (c) S10

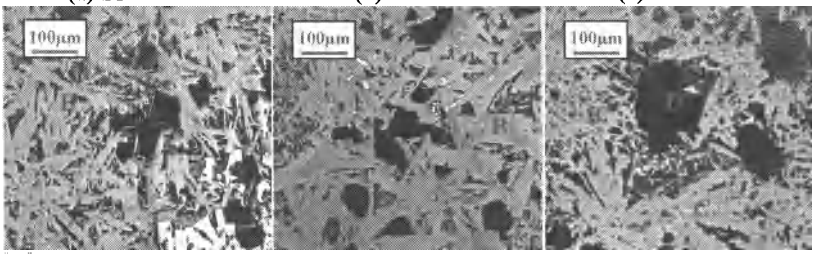

(d) S11 (e) S12 (f) S13

A: Magnetite B: Calcium Ferrite C: Hematite D: Hole E: Silicate

Figure 6. The Microstructures of Roasted Agglomerates for S8-S13 100×

As shown in Figure 6, the grainy magnetite embeded in the acicular calcium ferrite when the limonite proportion was 0%(Figure 6(a)), leaded to a compact structure; the shape of calcium ferrite changed from acicular to leaflike and block gradually as the increase of limonite, resulted the growth of calcium ferrite(Figure 6(b), (c) and (d)), massive calcium ferrite formed when the proportion of limonite was 60%-80%(Figure (e) and 6(f)), penetrated and assimilated the porous residual limonite, which reduced the strength of sinter.

Conclusions

1) For the sintering of magnetite, increased limonite could improve the mixture permeability and increase sinter quantity and quality. The appropriate proportion of limonite was 40%-50%. For the sintering of hematite, with the increase of limonite the sintering indexes were first maintained at the same level thereafter declined, more obviously when the proportion of limonite exceeded 40%.

2) For the microstructure of roasted agglomerates, the shape of calcium ferrite changed from acicular to leaflike and block gradually when the proportion of limonite increased from 0% to 80%.

3) The sintering properties of limonite-magnetite and limonite-hematite were different because of the differences of size and the other physical and chemical properties between magnetite and hematite. In comparison, sinter quantity and quality were better for the sintering of limonite- magnetite, and coke proportion was lower.

References

1. Wei Chen, Jianmin Xing and Zhaoyun Fu, "Influence and Measures on Sintering Production by the Change of Raw Material Structure,"*Henanmetallurgy*, 14(2006), 24-27.

2. Zhenlin Liu, Hongxia Wen,"Echnology Developments of Limonite Domestic and International," *Chinametallurgy*, 5(2003), 8-11.

3. Chin Eng Loo, "Properties and Sintering of Yandi Ore," *World Steel*, 1(1999), 12-16.

4. Chin Eng Loo, "A Perspective of Goethitic Ore Sintering Fundamentals," *ISIJ*, 45(2005), 436-448.

3rd International Symposium on High-Temperature Metallurgical Processing
Edited by: Tao Jiang, Jiann-Yang Hwang, Patrick Masset, Onuralp Yucel, Rafael Padilla, and Guifeng Zhou
TMS (The Minerals, Metals & Materials Society), 2012

In SITU Observation of High Temperature Properties of Iron Ore during Sintering Process

Minge Zhao, Yuandong Pei *, Zhixing Zhao, Lili Ban, Zejun Ma

Shougang Research Institute of Technology,

Beijing 100043,, China

Keywords: Confocal Scanning Laser Microscope, In Situ Observation,Sinter, Iron Ore, High Temperature Properties

Abstract

Confocal scanning laser microscope (CSLM) has been applied to carry out the in-situ observation of melting and solidifying characteristics during iron ore sintering process, accompanied with TG-DSC test. It can be found that apparent Liquid phase forming temperature(LFT) and ending solidifying temperature(EST) is about 1190℃ and 1160℃, respectively. Forming liquid phase during sintering process goes through four courses, these are shrinking, expanding, shrinking and expanding coexisting and expanding totally. For Yandi fine, the corresponding temperature of these four courses is about 1120-1160℃, 1190-1196℃, 1218-1220℃ and 1233-1270℃, respectively. Although CAJ fine has more difficulty in forming initial liquid phase, but when liquid phase expands, it may have better fluidity and easier for liquid phase formation. Adding enough CaO, CAJ fine takes on high fluidity like Yandi fine, because liquid phase during sintering process is formed mainly by reaction between CaO and Fe_2O_3.

Introduction

Confocal scanning laser microscope (CSLM for short) has been applied to carry out the in-situ observation of metallurgical phenomena, especially in steelmaking process. Recently, many researches on ironmaking process were conducted with CLSM. While for high temperature properties during sintering process, there are limited reports on in situ observation[1-2]. In this paper, melting and solidifying characteristics of iron ore were observed with CLSM under simulated sintering temperature, and high temperature properties of iron ore during sintering process was clarified based on the in situ observation results and TG-DSC research.

Experimental

Initial melting temperature (IMT for short) and ending solidifying temperature (EST for short) of liquid phase during sintering process was determined in authors' former paper[2], in which the mixture samples of iron ore and flux were made to powders. In this paper, disk-shaped sample was made and more detailed observation was carried out. Furthermore, determination method about

IMT was revised according to new explanation.
Iron ores used were typical pisolitic ore Yandi fines from Australia and hematite CAJ fines from Brazil, whose chemical compositions are listed in **Table I,** and chemically pure reagent of CaO was used as flux. Iron ore and CaO were crushed to be under 0.075mm respectively and then they were mixed by two methods, one is with the basicity of 4, and the other is with mol ratio between Fe_2O_3 and CaO of 1. The mixture was pressed into a disk-shaped sample(3×3mm) and then it was put onto platinum slice(8×8mm), then the platinum slice was set into bottom of an alumina crucible(10×8mm) before putting in CLSM. The sample was sintered in CSLM using a simulated sintering temperature profile[3], as shown in **Fig. 1**. The experimental atmosphere was air. TG-DSC research was carried out to validate the temperature at which endothermic and exothermic reaction occur, with heating rate of 10℃/min.

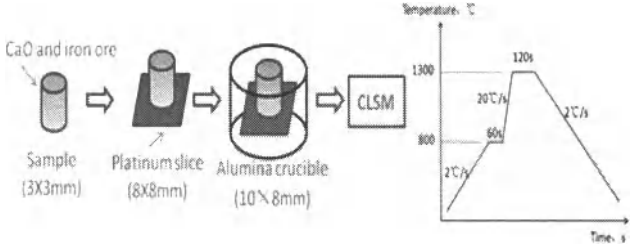

Results

Observation of CLSM For Iron Ore during Sintering Process

Schematic maps of in situ observation of melting and solidifying process for sample 1-4 were shown in **Fig 2** to **Fig 6** respectively as follows.

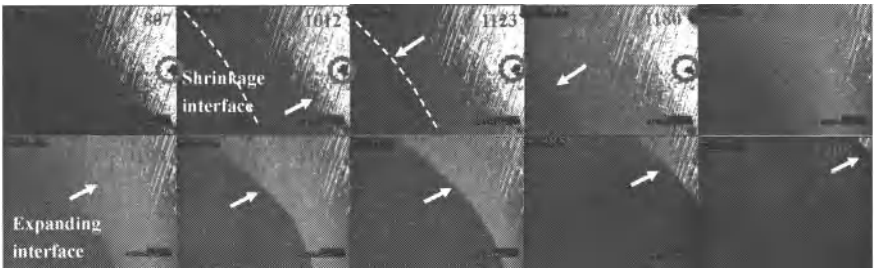

Note: Screen field move left at1186℃ for observation and transformation temperature from shrinkage to expanding is 1193℃

Fig. 2. Schematic Map of in Situ Observation of Melting Process for Sample 1

It can be seen from **Fig. 2.** that when temperature rises from 800 to about 1150℃, sample 1 shrinks slowly firstly and then fleetly. Sample 1 changes from shrinkage to expanding state at 1193℃, and then the speed of expanding is fast. As shown in **Fig. 3**, when temperature drops, liquid phase crystallizes instantly at 1200℃. When temperature drops to about 1120℃, basically all liquid phase solidifies completely.

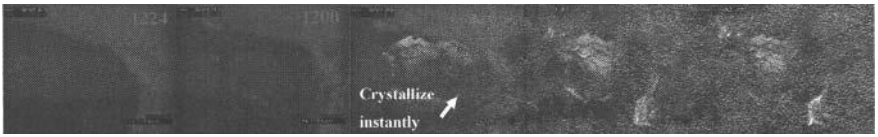

Fig. 3.Schematic Map of in Situ observation of solidifying process for sample 1

Fig 4 shows that sample 2 nearly don't move, which means that sample 2 don't go through melting phenomenon, and so dose solidifying phenomenon. The reason is that SiO_2 content of CAJ is low, so under the condition of basicity of 4, CaO addition is few and liquid phase formed is not sufficient for flowing.

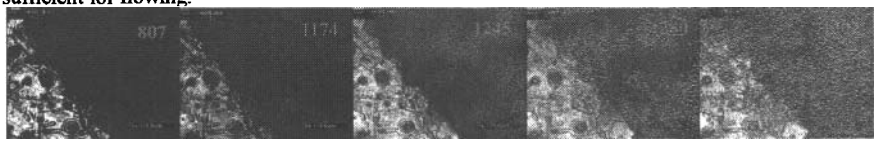

Fig. 4. Schematic map of in situ observation of melting process for sample 2

From **Fig. 5.**, it can be seen that during 800℃-1000℃, sample 3 shrinks slowly like sample1; from 1196℃, Sample 1 changes from shrinkage state to expanding state, which means liquid phase forms apparently. It is worth to mention that during 1220-1240℃, there are co-existence of shrinkage and expanding. Till 1241℃, expanding speeds up and most of the sample expand, indicating that liquid phase forms largely. The reason why existing second shrinkage can be explained by change of liquid phase composition (will be discussed in next section). From **Fig. 6.** it can be seen that when temperature drops to about 1180℃, there are crystallization phenomenon in different zone, and till about 1120℃, these different crystallization zone link all together basically, indicating the end of solidifying process.

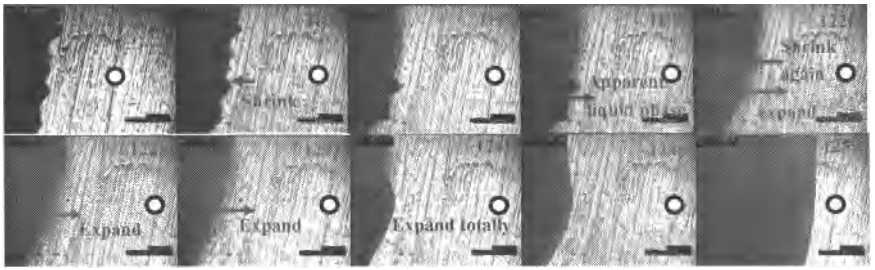

Note: a circle is fixed in Fig as a reference for observing due to adjustment of the screen field
Fig. 5.Schematic map of in situ observation of melting process for sample 3

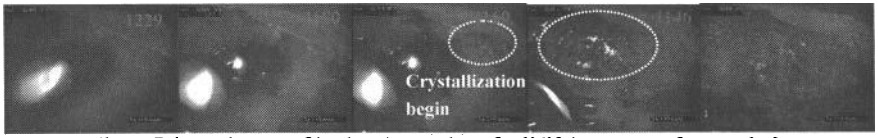

Fig. 6. Schematic map of in situ observation of solidifying process for sample 3

There are many similar characteristic between sample 3 and sample 4, so schematic maps for sample 4 are omitted limited to length of paper. The difference between sample 4 and sample 3 is that the second shrinkage period for the former is 1220-1270℃, that is to say, the former goes through longer period of shrinkage. There are two reason which can explain this phenomenon, one is that platinum slice for sample 4 is somewhat uneven, which makes the liquid phase flow towards inside, the other is that change condition of liquid phase of sample4 is larger than that of sample 3 due to difference of CaO addition during the second shrinkage period. When temperature drops to about 1174℃, there are crystallization phenomenon for sample 4, and till about 1150℃, crystallization finishes.

TG-DSC of Iron Ore during Sintering Process

Fig. 7. shows TG-DSC curves of CAJ and Yandi fines under different CaO addition condition. **Table Ⅱ.** shows endothermic temperature points between 800 and 1300℃. It can be found that for CAJ fines, there are five endothermic temperature points and four for Yandi fine.
It is apparent that later three points (Td, Te and Tf) are involved of liquid phase forming, and Td of CAJ is higher than that of Yandi, while Te and Tf of CAJ are lower than those of Yandi. This indicates that although CAJ has more difficulty in forming initial liquid phase, but when liquid phase expands, CAJ may has better fluidity and easier liquid phase formation.

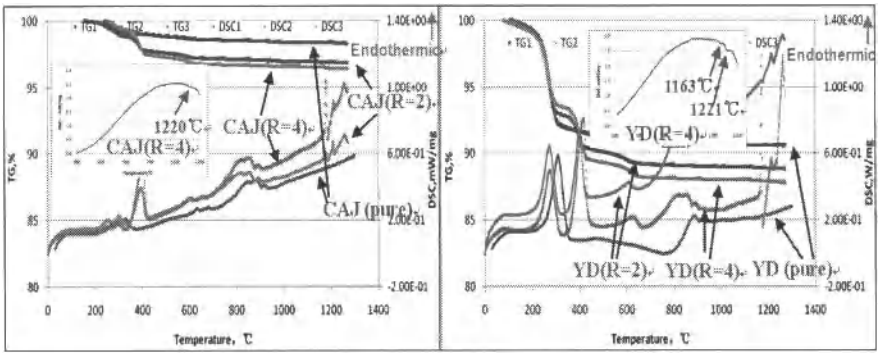

Fig. 7. TG-DSC Curve of CAJ and Yandi Ore Fines

During cooling process, there is one exothermic temperature point for CAJ at 1220℃and two for Yandi at 1221 and 1163℃, respectively. Although these endothermic and exothermic temperature

points are not strictly homologous to those observed by CLSM, it can be attributed to difference in CaO addition and experimental condition. To some extent, about 1200 and 1240℃ measured by TG-DSC are corresponding to IFT and MFT observed by CLSM as shown in later section.

Discussions

Determination of Melting And Solidifying Temperature of Iron Ore During Sintering Process

Table III shows comparison of melting and solidifying of samples. Four temperature points T1-T4 were defined as shrinking temperature (ST), initial forming liquid phase temperature (IFT), most liquid phase forming temperature (MFT), and ending solidifying temperature (EST), respectively. Physical meaning of these temperature points are explained as follows.

T1——shrinking temperature

Samples begin to move and shrink slowly from 800-900℃, and this phenomenon continue till about 1150℃, Furthermore, the sample shrinks with fast speed at latter stage. According to $CaO-Fe_2O_3$ and $CaO-Fe_2O_3-SiO_2$ phase diagram, shrink thing during in-situ observation need not be regarded as liquid phase, because the temperature at which the sample shrinks is far lower than temperature of lowest melting temperature in phase diagram, as shown in Fig 8.

The reason of shrinkage before forming liquid phase can be explained in following three aspects.

1)**Solid phase reaction**: Before forming liquid phase in sintering process, solid phase compounds with low melting temperature were formed among oxides with high melting temperature(Fe_2O_3,CaO,SiO_2 and Al_2O_3, etc). Accompanied with the formation of solid phase compounds with low melting temperature, there is exothermic phenomenon. However, TG-DSC curve of mixture between CAJ, Yandi fines and CaO show that there is not apparent exothermic point between 800 to 1100℃

2) **Crystal shape transformation**. Some oxides have crystal shape transformation, for example, the shape of SiO_2 changes at 870℃, and Fe_2O_3 changes from a-Fe_2O_3 to r-Fe_2O_3 type between 400 and 600℃. However, Accompanied with these crystal shape transformations, expanding phenomenon occurs.

3) **Shrinkage caused by solid phase sintering.** Iron ore sintering belongs to liquid phase sintering. However, before liquid phase forms, there are solid phase sintering phenomenon for powder sample. At high temperature(<1200℃), pore of iron ore closes and powder agglomerates as heating, and this will make sample shrink. Authors think the third reason may explain why sample shrinks before forming liquid phase.

T2 and T3—initial forming liquid phase temperature and most liquid phase forming temperature

From phase diagram of $CaO-Fe_2O_3$, $CaO-Fe_2O_3-SiO_2$ and $CaO-FeO_x-SiO_2$, the lowest melting temperature can be obtained, and they are 1200, 1192 and 1125℃, respectively. So from theory, considering not Al_2O_3, MgO and other minor content, sample can form liquid phase from any temperature points between 1125 and 1200℃ due to change of chemical composition of the mixture during sintering process.

Table II Endothermic Temperature Points between 800-1300℃

	Ta	Tb	Tc	Td	Te	Tf
CAJ(pure)	850	880	919	-	-	-
CAJ(R=2)	850	880	920	1207	1235	1288
CAJ(R=4)	849	882	920	1208	1239	1287

Yandi(pure)	-	888	918	-	-	-
Yandi (R=2)	-	882	920	1197	1243	1292
Yandi (R=4)	-	878	917	1200	1242	1292

Table III Melting and Solidifying Temperature of Samples, ℃

	T1	T2	T3	T4
S1	900	1163	1193	1120
S2	-	-	-	-
S3	860	1160	1196	1120
S4	870	1120	1170	1150

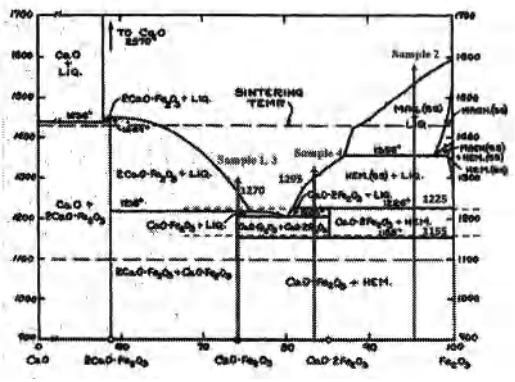

Fig. 8. Phase diagram of CaO-Fe_2O_3

In former paper, IMT is regarded as the temperature when mixture starts to move rapidly from still state with a speed of 0.1-0.3 mm/s under thermal treatment. Through our detailed observation, it can be found that samples go through slow shrinking before fast shrinking, the transformat

on temperature may be IMT. It is worth to mention that some powder close to sample takes on characteristics of liquid phase forming (expanding), as shown in dashed circle of Fig.2.

T3 is regarded as temperature at which main body of samples begins to expand, and in this temperature, sample change from shrinkage state to expanding state fast.

Apparently, liquid phase forming temperature for sample 2 is far higher than that of sample1, 3 and 4. This is because liquid phase during sintering process is formed mainly by reaction between CaO and Fe_2O_3. CAJ fine has lower SiO_2 content than Yandi fine, and under the same basicity condition, fluidity of CAJ fine is far lower than that of Yandi fine. However, if adding enough CaO, CAJ fine takes on high fluidity like Yandi fine.

T4——Ending solidifying temperature

EST is regard as the temperature when the surface of mixture is covered completely by solid phase. This definition is the same as the one in former study. During sintering process, from forming liquid phase to ending solidifying process, time is short, so EST is significant for consolidating sinter ore.

According to observation of CLSM, it can be found that forming liquid phase during sintering process go through four courses, that is shrinking, expanding, shrinking and

expanding coexisting and expanding totally. For Yandi fine, the corresponding temperature of this four courses is 1120-1160℃, 1190-1196℃, 1218-1220℃ and 1233-1270℃, respectively.

Conclusion

According to observation of CLSM, melting and solidifying process of CAJ and Yandi fine during sintering process were analyzed, and conclusions are obtained as follows:

(1) The slow shrinkage occurred before forming liquid phase may be caused by solid phase sintering. At 1120-1160℃, a little liquid phase forms corresponding to lowest temperature point of CaO-FeOn-SiO_2. At around 1190℃, much liquid phase forms corresponding to lowest temperature point of CaO-Fe_2O_3-SiO_2.

(2) Forming liquid phase during sintering process go through four courses, that is shrinking, expanding, shrinking and expanding coexisting and expanding totally. For Yandi fine, the corresponding temperature of this four courses is 1120-1160℃, 1190-1196℃, 1218-1220 ℃ and 1233-1270℃, respectively. Liquid phase forming temperature and ending solidifying temperature is about 1150 and 1120℃, respectively; as far as large extent is concerned, these two temperatures are 1190℃ and 1160℃, respectively.

(3) Although CAJ has more difficulty in forming initial liquid phase, but when liquid phase expands, CAJ may have better fluidity and easier liquid phase formation. Adding enough CaO, CAJ fine takes on high fluidity like Yandi fine, because liquid phase during sintering process is formed mainly by reaction between CaO and Fe_2O_3. But under the same basicity condition, fluidity of CAJ fine is far lower than that of Yandi fine.

Reference

1. Hiroyuki MATSUURA, et al. Melting and Solidifying Behaviors of the CaO–SiO_2–FeOx Slags at Various Oxygen Partial Pressures. *ISIJ International*, 49(2009), 1283.

[1] PEI Yuan-dong, ZHAO Zhi-xing, and BAN Li-li. Determination of Initial Melting Temperature and Ending Solidifying Temperature of Liquid Phase during Sintering Process.*CAMP-ISIJ*, 24 (2011), 226.

[2] C.E.LOO and W. LEUNG. Factors Influencing the Bonding Phase Structure of Iron Ore Sinters. *ISIJ International*, 43(2003),1393.

3rd International Symposium on High-Temperature Metallurgical Processing
Edited by: Tao Jiang, Jiann-Yang Hwang, Patrick Masset, Onuralp Yucel, Rafael Padilla, and Guifeng Zhou
TMS (The Minerals, Metals & Materials Society), 2012

AIR LEAKAAGE ONLINE MONITORING AND DIAGNOSIS MODEL FOR SINTERING

FAN Xiao-Hui[1], JIANG Li-Juan[1], CHEN Xu-Ling[1]

[1]School of Minerals Processing and Biological Engineering, Central South University, Changsha 410083, Hunan, China

Key Words: sintering, air leakage rate, model, expert system, fuzzy control

Abstract

In order to solve air leakage of sintering testing cumbersome, inaccurate results, and other issues, the sinter machine air leakage characteristics were studied, and combining the mathematical modeling and the field detection. The temperature before air leakage was calculated by mathematical model, energy balance equation was established according to sintering process, using Adams prediction correction method which has stronge stability and high precision, to solve hyperbolic partial differential equation with astringency problem. The temperature after air leakage is detected by instruments, according to energy conservation calculation the sintering air leakage rate. According to the sintering continuity and periodicity, sintering air leakage location diagnosis expert system was established to judge specific air leakage locations.

Introduction

Strengthening of modern blast furnace production depends on the quality of the raw material preparation to a large extent [1]. Technical and economic index of modern blast furnace production is advanced; the most important reason is the use of concentrated feed. Sintering plant is the "kitchen" of blast furnace's concentrate. As we all know, sintering plant is major energy consumption of steel plant, in sinter process energy consumption, the solid fuel consumption of total energy consumption is 75%~80%, power is 13%~20%, ignition and combustion is 5%~10%. To reduce the air leakage of sintering plant is an effective measurement to save energy consumption. At present, our air leakage of sintering compared to the other developed countries is still a

long way to go. Japan's air leakage rate is about 30%, and 35%~60% air leakage of sintering machine at home, a big gap exists between the plants. At present the determination of air leakage is all for manual operation, long measuring period, considerable manpower and resources, and the results are significantly affected by operation. For air leakage of sintering control lag issues, research and development of diagnosis expert system for on-line monitoring model for air leakage and, through this research can reduce the use of detection equipment, detect sintering air leakage, improve the yield and quality of sintering production, reduce energy consumption, and extend equipment life span.

System Design

The commonly used method is detected chemical composition and content of before and after air leakage points' gas. The air leakage rate is calculated by the mass balance principle [1-2]. But this cannot achieve online detection of air leakage. This study used a calorimetric method to realize online detect, which is by measuring the temperature before and after air leakage points. According to the study of Jin Yonglong[3-5], the air leakage rate and the air leakage point's temperature has the following relationship:

$$K = \frac{C_O[(1-\lambda)T_O - T_m]}{C_O[(1-\lambda)T_O - T_m] + C_A(T_m - T_A)} \tag{1}$$

Where K is the air leakage rate, λ is the heat loss rate, T_O is the temperature enter in air leakage points, T_A is the air temperature, T_m is the temperature out of the air leakage points, C_O is the specific heat capacity enter in the air leakage points, C_A is the specific heat capacity out of the air leakage points.

When sintering production is in a stable state, gas composition in bellows is relatively constant, but each bellow has different temperature and gas composition. Based on gas composition and components, we can calculate the specific heat capacity of each bellow. If we can get the temperature online before air leakage, which is the trolley grate temperature, combined with the sintering scene bellow temperature as the temperature after air leakage, on-line calculation of air leakage rate can realize. So the temperature field model of sintering waste gas is one of the content of this paper. According to the calculation air leakage rate, diagnose the air leakage situation by fuzzy control algorithm.

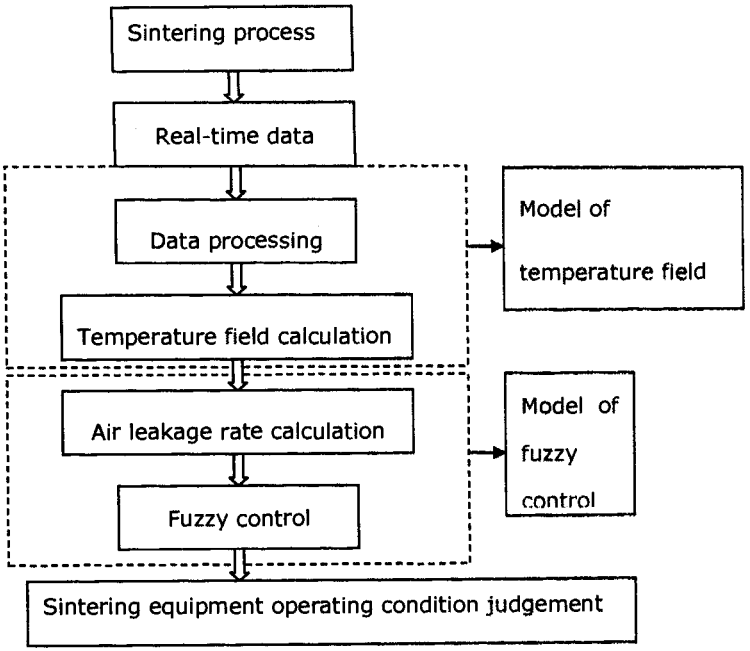

Fig.1 System construction

Model of Temperature Field

Derivation of Basic Equations Ventilation of sintering process diagram, material layer moves slow on the portrait (x direction), gas flow along the vertical (z direction) perpendicular to the bed surface, y direction is the horizontal. [6-7]
Gas-phase heat transfer equation:

$$f_g C_{pg}\left(\frac{\partial T_g}{\partial x}+\frac{\partial T_g}{\partial y}+\frac{\partial T_g}{\partial z}\right)+\rho_g \varepsilon C_{pg}\frac{\partial T_g}{\partial t}=-h_{gs}a_s(T_g-T_s)+Q_g \qquad (2)$$

Solid energy balance equation:

$$v_s f_s(1-\varepsilon)C_{ps}\left(\frac{\partial T_s}{\partial x}+\frac{\partial T_s}{\partial y}+\frac{\partial T_s}{\partial z}\right)+f_s C_{ps}\frac{\partial T_s}{\partial t}=-h_{gs}a_s(T_g-T_s)+Q_s \qquad (3)$$

Where f_g and f_s are the gas and solid mass flux separately, C_{gs} and C_{ps} are the gas and solid specific heat capacity separately, h_{gs} is the gas-solid phase convective heat transfer coefficient, T_g and T_s are the gas and solid temperature separately, Q_g and Q_s are the gas and solid phase reaction heat separately, a_s is the material layer specific surface area, v_s is the solid flow.

Solution of Model Based on heat and mass transfer theories, the energy balance equations for sintering process's five belt are build. The equations are simple hyperbolic partial differential equations, and its typical characteristics are the low convergence of numerical solution. The convergence problem can be solved by adopting stable and high accuracy Adams predictor-corrector method. In order to make equations discretization, a difference grid is established, that is, in the sinter layer thickness is divided the uniform grid into the direction of the network system (interlayer is $\Delta z = 2mm$, and time intervals is $\Delta t = 2s$).

Adams-Bashforth prediction equation:

$$y_{n+1}^{(0)} = y_n + \frac{h}{24}(55f_n - 59f_{n-1} + 37f_{n-2} - 9f_{n-3}) \tag{4}$$

Adams-Moulton modified equation:

$$y_{n+1}^{(1)} = y_n + \frac{h}{24}[(9f(x_{n+1}, y_{n+1}^{(0)}) + 19f(x_n, y_n) - 5f(x_{n-1}, y_{n-1}) + f(x_{n-2}, y_{n-2})] \tag{5}$$

$$y_{n+1}^{(2)} = y_n + \frac{h}{24}[(9f(x_{n+1}, y_{n+1}^{(1)}) + 19f(x_n, y_n) - 5f(x_{n-1}, y_{n-1}) + f(x_{n-2}, y_{n-2})] \tag{6}$$

$$y_{n+1}^{(3)} = y_n + \frac{h}{24}[(9f(x_{n+1}, y_{n+1}^{(2)}) + 19f(x_n, y_n) - 5f(x_{n-1}, y_{n-1}) + f(x_{n-2}, y_{n-2})] \tag{7}$$

Where $y_{n+1}^{(0)}$ is values which are forecasted by the Adams-Bashforth, and $y_n, y_{n-1}, y_{n-2}, y_{n-3}$ is the first fourth values of y_{n+1}, $y_{n+1}^{(num)}$ is the value of $y_{n+1}^{(num-1)}, y_n, y_{n-1}$ and y_{n-2} through the Adams-Moulton method with amendments; f_n is the differential equation。

Diagnosis System

Temperature fluctuations of sintering machine bellows are primarily affected by three

factors: (Ⅰ) change of sintering raw material and/or process parameters; (Ⅱ) instability of the sintering process; (Ⅲ) air leakage of sintering equipment. Factor Ⅰ affects gas temperature before air leakage, it is regular and long-term; Factor Ⅱ affects gas temperature after air leakage, it is disorder and temporary; FactorⅢaffects gas temperature after air leakage, it is regular and long-term. Temperature field model can exclude factor Ⅰ; expert diagnosis system according to the discipline and long-term of temperature fluctuations, can exclude factor Ⅱ and Ⅲ, finally implementation the real-time diagnostics of bellows air leakage.

There are 11 main air leakage points of sintering machine [8], which can be divided into moving points and fixed points. Fixed points of air leakage on the influence of air leakage into: bellows air leakage rate of turn increased, and the cycle;

Sintering is a time-varying process, when raw material is changed; the best range of status parameters are changed, at the same time the control objectives are changed. Therefore, the fuzzy control algorithm must have an adaptive capacity which can automatically track system's changes, and the appropriate changes are made. Adaptation control algorithm includes the following several points [9-10]:

User-Defined Centering Air leakage rate of the actual production process is analyzed, and air leakage rate data of normal yield and quality of sintering production is taken, of which average air leakage is for its central value. The basic domain of air leakage rate is based on a number of central, and the range of the center value is a symmetric distribution, difference is called deviation of the average and the target value. Change of the center value of the air leakage rate is equal to translate the basic domain. In order to better meet the change of production process, it allowed the user modify the center value of air leakage rate and its appropriate range through the interface.

Nonlinear Quantization Quantitative formula is:

$$y=\begin{cases} G(x/b)^z & (0\le x\le b) \\ -G(-x/b)^z & (a\le x<0) \end{cases} \tag{8}$$

Where x is precision value of variable, y is fuzzy value of variable, a and b are basic domain of variable, a is equals to -b, G is quantization level, and the value is 6, z is a quantitative factors, the initial value is 1/2, and can be changed according to the actual situation.

Self-Adjusting Control Rules Control rules can be expressed as:

$$U=-\sum_{i=1}^{p} w_i X_i / \sum_{i=1}^{p} w_i \tag{9}$$

Where X is fuzzy language values for input variables, the value is {-3, -2, ... , 2, 3}; w_i is the weight of input variables, according to the expert experience decide the value, [0,1]; it can also be modified through the interface; U is the Fuzzy language

value of the rule conclusion, by rounding method; p is the number of input variables.

Realization and Application of the System

Realization of System

A powerful object-oriented programming language Visual C++2003 was used as a development tool. SQL Server2003 database management system was used as back-end databases. When the system is running, a multi-period run mode is used. When the system is reading the air leakage rate data, it updates the model database according to the real-time collection data, and based on this data to verify whether the device correctly. When the system calculates a value, which is outside of the normal range of air leakage rate, the system will automatically alarm. The system can view air leakage condition of each bellows real time. Based on this running mode fully reflects the whole change of sintering air leakage and devices' abnormal operation warning can be achieved.

Application of System

The production data of a sintering factory was used for the software test. The software can correctly calculate the air leakage rate of each bellows, and those data can be recorded and viewed. The system can automatically diagnose equipment is running properly. If the system be used, it would provide air leakage data and diagnosis air leakage situation in real time. It turns that sintering production can smoothly running, and sintering power consumption effectively reduced, the production quality can be improved, and intelligent of sintering process can be realized.

Table Ⅰ. The Air Leakage Rate of Each Bellows

Bellow's number	2	3	5	7	9	11	13	14	15	16
Temperature before air leakage/℃	203	110	84	81	75	79	173	288	755	675
Temperature after air leakage /℃	100	78	72	68	66	67	151	228	412	298
Air leakage rate/%	58	38	21	24	19	22	15	23	47	58

Conclusions

By using a temperature field model, combined with calorimetry method, the air leakage online testing system was established, timely reaction the air leakage of sintering machine.

Use the fuzzy control theory, combined with real time calculation of air leakage rate, a diagnostic system was developed, which can set the normal operation scope of the air leakage rate and enables abnormal production alarm.

Through the sintering scene data detection, the system is stable and handy; realize online detection and diagnosis of the air leakage rate.

References

1. HUO Jiang-nan, "Air Leakage Rate and Determination of Sintering Machine," *Sintering and Pelletizing*, 6(1985), 64-72.

2. HUANG Tian-zheng, JIANG Tao, "Air Leakage Determination of Belt Sintering," *Sintering and Pelletizing*, 2 (1986) , 32-41.

3. JIN Yong-long, XU Nan-ping, WU Shi-ying et al., "Study and Application of a New Technology for Measuring the Leakage Ratio of Sintering Machine," *JOURNAL OF IRON AND STEEL RESEARCH*, 11(3)(1999),67-70.

4. WU Ying, Jing Yonglong, "Online Air Leakage Measurement Technique and Application of Sintering Machine," *Sintering and Pelletizing*, 33(4)(2008),9-11.

5. JIN Yonglong, XU Nanping and WU Shiying, "study and application of test technique for leakage determination on sintering machine," *IRON AND STEEL*, 38(3)(2003),1-3.

6. LONG Hongming, FAN Xiaohui, MAO Xiaoming, "Sintering bed temperature distribution model based on heat transfer," *J.Cent.South Univ.(Science and Technology)*, 39 (3) (2008), 436-441.

7. XIA Dehong, JIAO Honglei, ZHANG gang,et al., "Numerical Simulation of Combustion and Heat Transfer in Sintering Process," *Industrial Furnace*, 28 (3) (2006), 30-32.

8. SUN Shenchun, "The Measurement for Reducing Sintering Air Leakage rate of Nippon Steel, "*Sintering and Pelletizing*,3(1988),40-44.

9. FAN Xiaohui,WANG Haidong, *Mathematical Model and Artificial Intelligence of Sintering Process*, (CHINA, Changsha: Central South University Press, 2002),118-128.

3rd International Symposium on High-Temperature Metallurgical Processing
Edited by: Tao Jiang, Jiann-Yang Hwang, Patrick Masset, Onuralp Yucel, Rafael Padilla, and Guifeng Zhou
TMS (The Minerals, Metals & Materials Society), 2012

INVESTIGATION ON THE INTERFACES OF M42/45 STEEL BIMETAL COMPOSITES SINTERED BY SPARK PLASMA SINTERING

Jinfu Xu[1,2], Hang You[2], Peng Jiang[2], Yuting Lv[2], Youqing Cao[2]

[1]Institute of Materials Engineering, Ningbo University of Technology, Ningbo 315016, P.R. China;

[2]Institute of Materials Science and Engineering, East China University of Science and Technology, Shanghai 200237, P.R. China.

Keywords: M42 Powder High-speed Steel, 45 Steel, SPS, Interfaces

Abstract

In present work, we reported the fabrication of composites consisted of M42 powder metallurgy high speed steel and 45 steel at one step via spark plasma sintering (SPS) technology. The interface microstructure, compositions and microhardness with the interface forming mechanism were investigated. The results show that the morphology and microhardness within the M42/45 steel interfaces exhibit a gradient distribution. The interfaces possessed a transition layer up to 10.2 μm with few distortions and microcracks. The formation of M42/45 steel interfaces were driven by both fusion and diffusion processes. The former one was primary at the early sintering process, while the later one becomes dominant over the followed sintering process.

Introduction

Powder high-speed steels have been widely used in cutting tools, cold-hot tools and dies, as well as in cut materials and structure parts with wear resistance and high-temperature resistance, due to its high hardness, good wear resistance, desirable cutting toughness and favorable hot hardness [1-2]. For materials of some parts in practical production, not only the favorable toughness is required to resist the impact action, but also the high hardness and exceptional wear resistance are demanded. According to the functional requirements and working conditions, bimetal composite materials are prepared in a certain mode, proportion and distribution, by designing two metals with different chemical and physical properties [3-6]. Considering the composites exhibit different properties in different positions of the parts with a combination of the advantages of two metals, they can obtain enhanced properties that the single one can not achieve.

In current work, we reported the joining of M42/45 steel by SPS at on step. The microstructure, composition and microhardness of interfaces within the bimetal joints were investigated, which suggest that as-fabricated joints are of high quality.

Sample Preparation and Experimental Methods

Experimental Materials

M42 high speed steel (HSS) powder and 45 steel were used as the raw materials and commercially available from the company. The machine-finishing size of 45 steel was a block of $\phi 20\times 10mm^2$. The Chemical composition of commercial M42 HSS powder (grain size < 100 mesh, 99%) is shown in Table Ⅰ.

Table Ⅰ. Composition of M42 HSS Powder (wt%)

C	V	Mo	W	Co	Cr	Fe
1.15	3.15	4.96	6.22	8.37	4.23	Bal

Experimental Methods

M42 HSS powders were milled by the Planetary Ball Mill QM-SB with agate balls (balls to powder mass ratio: 7:1), a rotation speed of 280 r/min and milling time of 24 h, respectively. The obtained M42 HSS and machined 45 steel were put into a graphite die (Figure 1) with a pressure of 6 MPa, and sintered in SPS-1030 machine at 970℃×10 min×70 Mpa.

The combination of the interface of the polished sample, cutted from the sintered along the longitudinal section, was observed by a cold field emission scanning electron microscope (S4800) and a PME3-323UN metalloscope. The element distribution of the interlayer was studied using the S4800 SEM with elemental analysis facilities (EDS). After high temperature quenched (1180℃×5 min, oil) and high temperature tempered (550℃×1 h, 3 times), the microhardness of the sintered sample was obtained using a MH-5 microhardness tester.

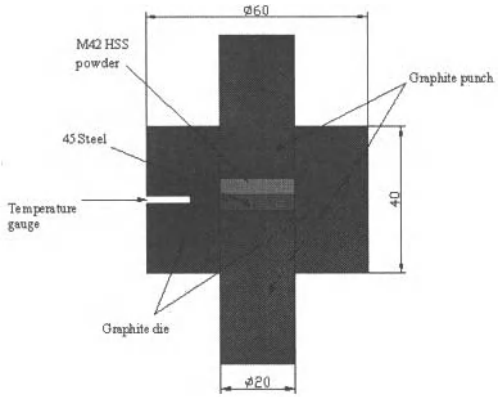

Figure 1. Spark Plasma Sintering Die

Results and Analysis

Microstructure of the Interfaces

Figure 2 (a) displays the metallographic photos of transition layer of the joint after corrosion, which reveals that the interlayer of the bimetal joint possesses a perfect microstructure with few micro cracks and defects. Figure 2 (b) shows some tiny pores within the joint, which can be attributed to following reasons: the adsorbed gas in as-received materials; the coefficients of heat expansion and sintering shrinkage of M42 HSS being less than those of 45 steel. The formed transition layer is obviously different from the connection of metal, suggesting the relevant elements have been

diffused into both sides of the joint.

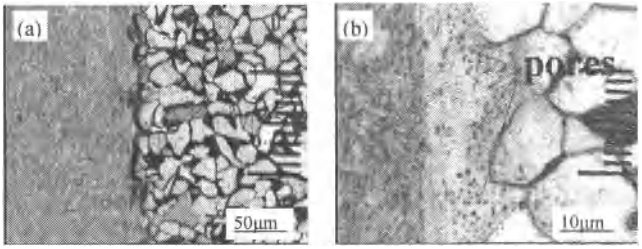

Figure 2. Metallographic Morphologies of Gradient Interlayer of the Joint under Different Magnification

Figure 3(a) shows the interface microstructures within the bimetal joint, implying that the interfacial bonding between M42 steel and 45 steel is well without cracks. The thickness of the as-fabricated thickness is typically sized in 10.2 μm (Figure 3b). In the transition layer, no obvious interface and diffusion transition zone can be observed, implying that the transition layers are metallurgically bonded. It is worthy noting that all interfaces are distinguished by various degrees bend straight lines, clearly indicating that the diffusion degree within the transition layer is different. The "jagged" interface can favor the bonding of the interlays with excellent properties.

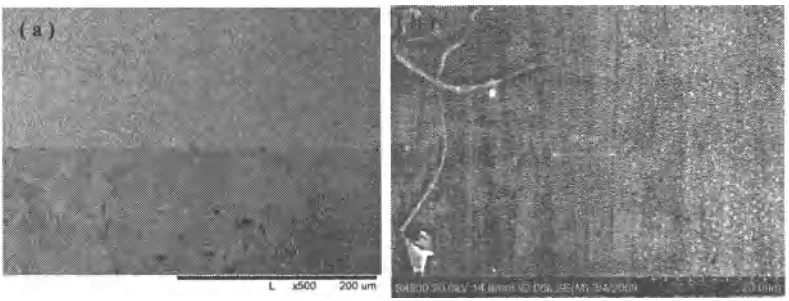

Figure 3. Typical SEM Images Showing the Interface Microstructures of M42/45 Steel Joints

Composition within the Interfaces

Figure 4 presents the composition distribution of the transition layer of M42/45 steel joint. The results suggust that Cr, W, Co and V from left to right increase gradually, while the Fe and C reduce gradually. Meanwhile, Mo element is not obvious changed, which owns to its low content. These show that the elements of Cr, W, Co and V in M42 powder high speed steel have been diffused to 45 steel, while those of Fe and C in 45 steel have been diffused to M42 powder high speed. The structure of the diffusion zone are uniform, showing the excellent metallurgical bonding of the joint.

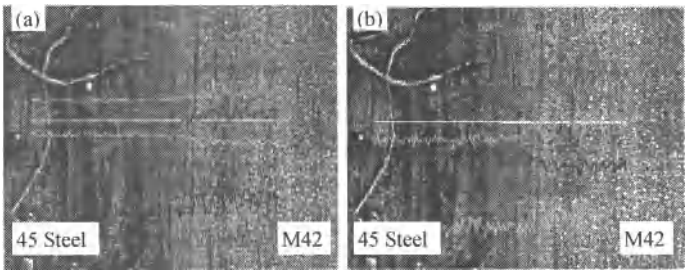

Figure 4. Composition Distribution of Different Elements within M42/45 Steel Joint

Microhardness of the Interface

The hardness is a index to show the resistance of deformation in a local area of materials, and has a direct correlation to the strength of metals. In addition, the hardness test can be a valuable manner to reveal the continuous changes of microstructure and properties of the gradient layer. The microhardnesses of the interface within the joint were investigated with the heat treatments after high temperature quenched (1180 °C×5 min in oil) and high temperature tempered (550 °C×1 h for 3 times), as shown in Figure 5. It seems that the microhardnesses differ greatly from one side of the interface to the other one, and change smoothly at the interface with a gradient change, suggesting the good combination of the two materials.

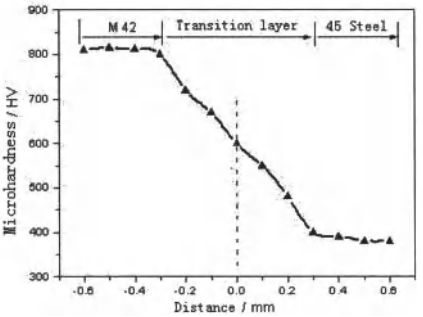

Figure 5. Microhardness Profile of the Transition Layer in M42/45 Steel Joint

Formation Mechanism of the Interface

With the rapid increasing of sintering temperature, as well as the existence of applied pressure and the restriction from the sintered die, M42 high speed steel powder becomes semi-melted followed by connected to the bulk 45 steel after interacting[7]. Figure 6 shows the schematical model of interface structure within the joint. It suggests that M42/45 steel joints are mainly composed of three parts: 45 steel area (region I), interfacial transition zone (region II) and high-speed steel solidification zone (region III). The formation of such interface structure can be attributed to

synthetic synergism of two jointing mechanisms, namely, the result of fusion and diffusion collaborative mechanism. On the one hand, attributed to discharge plasma, the gap temperature between M42 high speed steel powder particles raise instantaneously, resulting in a semi-molten state of M42 HSS powder due to the melting of the powder surface. Meanwhile, the top surface of 45 steel becomes melted slightly due to the energy transfer. Consequently, a fusion contact zone will be formed at the interface between M42 high speed steel powder and 45 steel, leading to the bonding of M42 high speed steel powder and 45 steel at the early SPS sintering process. On the other, in the condition of high temperature and pressure, as well as the effect of electric field from the impulse current, the elements in both M42 HSS powder and 45 steel diffuse into each other to botain a state of relative balance at the interface, finally forming a diffusion joint[8].

In a word, The interface bonding of M42/45 steel is a comprehensive synergy between fusion connection and diffusion connection. The former one takes priority at the early sintering process, while the later one becomes dominant over the following sintering process. It is believed that following processes would happen during the bonding of M42 powder high speed steel and 45 steel:

(1) M42 high speed steel powder adhered tightly to 45 steel caused by the axial pressure. (2) Induced by the discharge plasma during SPS process, the temperature of the powders rised instantly, making the powder surface melt and turning M42 high speed steel powder into a semi-melted state. (3) The temperature of 45 steel increased sharply due to the energy transfer, leading to the surface of contacted area being melted slightly. Subsequently, the fusion contact could be formed. (4) With the increase of the sintering temperature, the alloying elements in the M42 high speed steel powder and the 45 steel could be diffused into each other at the interface under liquid state. (5) The interface bonding process under undergo till to the end of sintering process, resulting the joint bonded.[9]

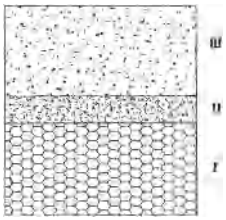

Figure 6. Schematical Model of Interface Structure in the M42/45 Steel Joint

Conclusions

(1) M42/45 steel joint were fabricated at one step by using SPS.

(2) The morphology and microhardness of M42/45 steel joint exhibit as a gradient distribution with few distortions and microcracks, suggesting the high quality of the interfaces.

(3) The formation of M42/45 steel interfaces were driven by both fusion and diffusion processes. The former one were primary at the early sintering process, while the later one becomes dominant over the followed sintering process.

Acknowledgement: This work is supported by the K.C.Wong Education, Hong Kong.

References

[1] B. Levenfeld, A. Várez and J.M. Torralba, "Effect of residual carbon on the sintering process of M2 high speed steel parts obtained by a modified metal injection molding process," Metallurgical and Materials Transactions , 33(6) (2002) , 1843-1851.

[2] E.M. Ruiz-Navas, R. García, E. Gordo and F.J. Velasco, "Development and characterisation of high speed steel matrix composites gradient materials," Journal of Materials Processing Technology, 143-144(20) (2003), 769-775.

[3] M. Şimşir, L.C. Kumruoğlua and A. Özera, "An investigation into stainless-steel / structural-alloy-steel bimetal produced by shell mould casting," Materials & Design, 30(2) (2009), 264-270.

[4] O. Yilmaz and H. Çelik, "Electrical and thermal properties of the interface at diffusion-bonded and soldered 304 stainless steel and copper bimetal," Journal of Materials Processing Technology, 141(1) (2003), 67-76.

[5] B.V. Krishna, P. Venugopal and K.P. Rao, "Co-extrusion of dissimilar sintered P/M performs – an explored route to produce bimetallic tubes," Materials Science and Engineering A, 407(25) (2005) , 77-83.

[6] D.C. Ko, S.K. Lee, B.M. Kim and H. Jod, "Evaluation of copper coating ratio in steel / copper clad wire drawing," Journal of Materials Processing Technology, 186(1-3) (2007) , 22-26.

[7] M. Omori, "Sintering, consolidation, reaction and crystal growth by the spark plasma system (SPS)," Materials Science and Engineering A, 287(2) (2000), 183-188.

[8] Z.A. Munir, U. Anselmi-Tamburini and M. Ohyanagi, "The effect of electric field and pressure on the synthesis and consolidation of materials," Journal of Materials Science, 41(3) (2006) , 763-777.

[9] Z. J. Shen and M. Nygren, "Microstructural prototyping of ceramics by kinetic engineering: application of spark plasma sintering," The Chemical Record, 5 (3) (2005) , 173-184.

3rd International Symposium on High-Temperature Metallurgical Processing
Edited by: Tao Jiang, Jiann-Yang Hwang, Patrick Masset, Onuralp Yucel, Rafael Padilla, and Guifeng Zhou
TMS (The Minerals, Metals & Materials Society), 2012

3rd International Symposium on High-Temperature Metallurgical Processing

Energy and Environment

Session Chairs:
Mansoor Barati
Hongmin Zhu

3rd International Symposium on High-Temperature Metallurgical Processing
Edited by: Tao Jiang, Jiann-Yang Hwang, Patrick Masset, Onuralp Yucel, Rafael Padilla, and Guifeng Zhou
TMS (The Minerals, Metals & Materials Society), 2012

CURRENT STATUS OF HEAT RECOVERY FROM GRANULATED SLAG

Shaghayegh Esfahani[1], Mansoor Barati[2]

[1,2]Materials Science and Engineering, University of Toronto
184 College Street
Toronto, Canada M5S 3E4

Keywords: Metallurgical Slags, Heat Recovery, Granulation, Blast Furnace

Abstract

The slag from extraction of ferrous and non-ferrous metals is a potential heat source which if treated properly can contribute to recovery of a significant amount of energy. The waste heat of slag may be used to generate steam, synthetic fuel gas, or electricity. Although several technologies have been investigated for this purpose, very little has been achieved in terms implementing the technology in industry. In this article, the development and application of various granulation techniques are reviewed and the methods to recover energy from granulated slag are discussed.

Introduction

Every year, more than 422 million tons of slag is being produced around the world as a by-product of the metal manufacturing at temperatures of up to 1300-1600°C [1, 2]. Currently slags are either disposed of or treated by processes such as granulation. Through the granulation process, most slags can be converted into a material which may be fully used as a cement feedstock. Conventional cement production is an energy intensive process with large emissions of CO_2; therefore, the replacement can both be energy saving and environmentally friendly. However, for this purpose, the slag should have what is known as a "glassy" content (i.e. it should be amorphous) which requires rapid cooling rates that are not easily achieved due to the very low thermal conductivity. The main challenge in all these processes is to granulate the slag at a high cooling rate while the heat is also being recovered.

Currently, in many granulation processes, the thermal energy of slag is released into the atmosphere with limited recovery attempt, due to the technical difficulties arising from its high temperature, high viscosity and adhesiveness. Most commercial methods of heat recovery such as heat exchangers and fluidized beds are not energy efficient. In addition, the produced energy is not easily transportable and can even be pollutant in some cases. However, a more sophisticated method have been developed recently by converting the sensible heat in slag to chemical energy by methane reforming reaction and producing fuel which can be transported in long distances which have shown to be very promising [3].

Metallurgical Slags and their Application

Slag is a by-product of smelting processes in which metal is extracted from its ore. It is a mixture of oxides, sulphides and sometimes fluorides and is generated from the ore gangue, reacted

components of the melt, and fluxes. Metallurgical slags are classified as ferrous and non–ferrous slags, according to the respective metal produced in each process.

Ferrous Slags

Ferrous Slags make up 90% of the by-products produced in the iron and steel production [1]. There are four major types of iron and steel making slags categorized by the furnace that they are produced in: 1) Blast Furnace (BF) Slag, 2) Basic Oxygen Furnace (BOF) Slag, 3) Electric Arc Furnace (EAF) Slag 4) Ladle Furnace (LF) Slag or Refining Slag. Each of these groups will be further explained in the following paragraphs.

The typical composition of different types of ferrous slags and their production rate are presented in Table 1. The slag production rate is given as the amount of slag (ton) that a typical steel making plant would produce per ton of crude steel. The total slag amount produced in the year 2009 is calculated based on the world's steel production in the year 2009 [1]. From these data the total amount of iron and steel slag production adds up to more than 422 Mt.

Table I -The average composition of different types of slags and their production rate.

	Typical Slag composition [3]						Typical slag temperature [4]	Slag (kg)/ t crude steel [4]	Annual slag rate (Mt/Y) [1, 4]
	CaO	SiO_2	Al_2O_3	MgO	MnO	FeO+ Fe_2O_3			
BF [3]	35-38	34-38	6-9	10-14	0.5-2	0.5-1	1400-1450°C	275	336
BOF	30-55	8-20	1-6	5-15	2-8	10-35	1300°C	126	154
EAF	35-60	9-20	2-9	5-15	3-8	15-30	1550°C	169	206
LF	30-60	2-35	5-35	1-10	0-5	0.1-15	1300°C	-	-

Benefits of Substitution of Portland Cement with BF Slag Cement

Substituting Portland cement with slag cement is one of the most common uses of slags (specifically BF/BOF slags). The history of replacing Portland cement with slag cement goes back to about a century in United States and even earlier in Europe.

Portland cement is an essential component of concrete which binds the concrete together and mostly contains lime and silica. However the production of cement has been recognized as a major CO_2 emitting source. It is estimated that about 5% of the global CO_2 generation is a result of cement production [6]. Generally, for the production of 1 ton of cement, 1 ton of CO_2 is released during the process of calcining limestone to produce lime. Using any CaO containing material with proper chemistry instead of calcined lime can reduce the overall CO_2 emission from cement production. Slag has similar properties to Portland cement when reacting with water which is forming a cementitious substance known as calcium-silicate hydrate. Except for the

smaller content of CaO, the composition of slag is strikingly similar to Portland cement. For example, it has latent hydraulic properties, which means that after grinding and activating e.g. with calcium oxide, it hardens just like cement. The similar chemical composition along with its glassy nature, make rapid-cooled slag a suitable material and appropriate substitute for Portland cement [7].

Other advantages include: higher strength and durability of concrete as a result of less permeability and higher resistance against alkali-silica and sulfate attack, less energy consumption and reduced material extraction. In fact, substituting Portland cement with 50% of slag cement can reduce the energy consumption up to 34% [8].

Ferrous Slag World Market and Capacity

The available data on slag prices are limited to the prices in the United States; however, it could give us an insight into the significant changes in the slag prices over the last 70 years. The price change from the year 1940 to 2009 according to the US Geological Survey is presented in Figure 1. The prices in the figure are the weighted average for a variety of ferrous slag types. Actual prices per ton ranged widely in 2008 from about $0.50 for steel slags in areas having abundant competing natural aggregates to almost $110 for some GBFS (Granulated Blast Furnace Slag) which is another name for the cement slag.

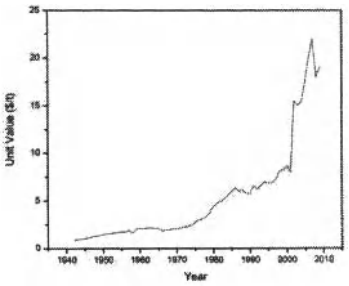

Figure 1-Average price for ferrous slag per ton in the US (US Geological Survey).

Steel and iron slag prices in the US are compared in Table II. Based on these values and the world's production, the total value in the world is estimated in Table III. According to Unites States Geological Survey (USGS) [9] steel slag was sold at 5.2 US$/t while BF slag was sold at a price six times greater.

Table II- Iron and steel production amount and price in USA [8].

Year	Blast furnace slag			Steel Slag		
	Mtons	Value (million US$)	US$ per ton	Mtons	Value (million US$)	US $ per ton
2008	10.1	288	28.5	8.7	43	4.9
2009	6.8	205	30.1	5.7	30	5.2

Table III- Value of produced ferrous slag in the world [8].

	Blast furnace slag	Steel Slag
Total world production 2009 (Mt)	336	360
Value (million $)	10,114	1,872

Based on world iron and steel production and US prices for the year 2009 if all of the world's slag was granulated and sold, it would be worth more up to12 billion dollars. It has also been predicted by Mineral Media International that the ferrous slag market will reach $28 billion dollars by the year 2020.

According to a new study released by IntertechPira, Leatherhead, UK, due to the new environmental policies related to lower CO_2 emissions, the demand for slag, especially in the cement industry, has become much higher than the supply.

Non-Ferrous Slags

The main non-ferrous slags that are produced are from copper, nickel, lead and zinc extraction. The annual metal production from non-ferrous ores is much less than iron and steel, however their slag production rate is much higher than iron and steel slags. Table IV shows an approximation of the world's annual non-ferrous slag production since there is no official information.

Table IV- World's non-ferrous granulated slag production.

Smelter Type	Slag production in 2009 (Mt/Y) [9]	% Granulated Slag (Estimated) [10]	Estimated world granulated production (Mt)
Copper	4.1	50	2.05
Nickel sulfide	7.6	50	3.8
Nickel laterite	22	50	11
Platinum Group Metals (PGM)	2.5	100	2.5
Zinc	1.6	50	0.9
Lead sulfide	1.8	50	0.9
Total	76.5	-	21.15

Fundamental Problems Associated with the Heat Recovery from Slags

In the past, over 90% of the produced slag was treated by slow cooling [11]. Molten slag was discarded onto slag heaps and used in road construction or land filling or as coarse aggregate for concrete. When slag undergoes slow cooling in air, it tends to combine and crystallize the CaO, SiO_2 and Al_2O_3 forming a hard, heavy solid.

Molten slag is a highly viscous material which makes it very difficult to handle. It has a very low thermal conductivity (1~2 W/mK) compared to other common materials such as steel with about 40-55 W/mK conductivity. Thermal conductivities in temperature ranges from 20-1550°C were measured by Goto *et al.* [12]. Based on their values, the thermal conductivity of slag increases by increase of temperature, however after the slag reaches 1200°C (the transition from glassy to liquid state), the conductivity starts to decrease and at about 1400°C to 1500°C the conductivity will be as low as 0.1-0.3 W/mK.

The large amount of slag produced, the growing energy costs and environmental concerns make it necessary to find the most suitable method for recovering this energy source and utilizing it in the most convenient form. In the following sections different methods that convert slag to such useful products will be discussed.

Granulation Techniques

A large number of metallurgical operations dump molten slag into a slag pit that is gradually cooled and solidified. Alternatively, the slag can be granulated to facilitate its subsequent use as road pavement material or cement feed. An appropriate slag granulation technique should have: 1) capacity for treating large volumes of slag 2) minimum negative environmental effects 3) ability to recover the sensible heat in slag at the same time the granulation is being undertaken. In order to have efficient heat recovery, the hot slag should acquire a large specific surface area to have the maximum amount of heat extracted and at the same time the cooling should result in high quality slag with suitable properties for the end use. In other words, the energy recovery process must not interfere with the properties of the slag that make it a valuable by-product. Ideally, the slag should be granulated while the heat is exchanged to another medium. Existing granulation technologies are described in the following paragraphs.

Water Granulation

Water granulation of blast furnace slag was introduced in 1977. In the treatment, slag is rapidly cooled to produce glassy slag granules with strong hydraulicity. For using slag as cement, some properties of the water-cooled slag should be controlled. These parameters include: the size range of the granules, the glassy content, the strength and the density [7]. However if the entire heat content is lost either to the atmosphere or water with little attempt made to recover to energy, the process will be less economically and environmentally efficient. The issues with water granulation include: excessive amounts of water consumption and water contamination by alkaline element, loss of thermal energy of high temperature, drying requirement after granulation [11].

Dry Granulation

Due to the problems with water granulation, it was not considered to be an efficient method of slag heat recovery and new methods were exploited. Thus, several dry granulation techniques were subsequently developed from about 1980's. In the following sections, previous attempts to improve the dry granulation process are discussed.

Granulation by Air Blasts

The air blast granulation technique was first established by Mitsubishi Heavy Industries [13] during 1970–80 (Figure 2). In this method, the slag is first pre-treated to optimize the flow and to adjust the viscosity. The slag is poured to a gutter under which the main air nozzle exists. Other nozzles are also used to avoid scattering upward and sideward. Through this process, molten slag is atomized and broken up to granules. The air flow rate, position of the gutter, and the nozzle size should be carefully controlled to meet the requirements and to achieve acceptable size distribution of slag granules. The flying granules are then collected and introduced into a heat exchanger.

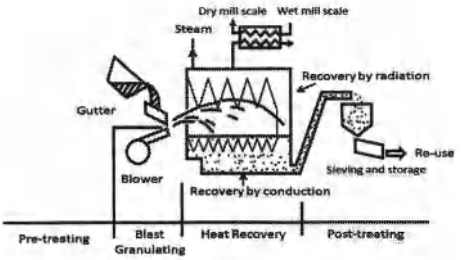

Figure 2- Schematic diagram of air blast granulation [13].

Granulation Using Rotating Drum-Disk

In a collaborative work by Mitsubishi Heavy Industries and Sumitomo Metal Industries in 1981-83, a new process was developed that was based on letting a flow of slag impinge on a hard surface that would not wet with the molten slag [11]. The molten slag is fragmented into droplets that solidified in air to produce granules. After the molten slag hits the surface, it is transformed into a disk. The disk then expands and forms a ring which is later fragmented and scatter to the air, where each droplet will become spherical by surface tension. The surface where the slag flow is impinged on can be the surface of a single drum or a spinning disk.

The operating conditions of a typical large scale application of this method of granulation have been analyzed by J. Ando *et al* [13]. It was shown that for a 5mm diameter granulated slag exiting the nozzle at be 5m/s when exiting the nozzle, to obtain an amorphous granulated slag when cooled from 1300°C to 850°C, the average cooling rate should be about 60°C/s at lower temperatures and about 100°C/s at higher temperatures. This would mean that it would take about 4-6 seconds for the slag to cool down. In this period of time the granules would have covered a distance of about 25 m, which would require large equipment with high energy extraction capacity. A solution to this problem is to suspend the granules in a fluidized bed in which the liquid droplets are mixed with dry-powder, water-quenched slag and a jet of air from a hot blast furnace. To have the least heat loss in the fluidized bed, it should be maintained at high temperatures; however, this might contribute to the agglomeration of the slag granules. Therefore, the temperature of the bed should be fully controlled [11].

Granulation by Impingement with Solid Slag

In 1981, a Swedish group developed a new method for slag heat recovery named MEROTEC [14]. The method involves mechanical disintegration of falling liquid slag film by impingement with solid slag particles that have previously been granulated with simultaneous heat recovery in fluidized bed which produces dry and dust-free granules. The size of the granules produced through this method when slags are at ordinary viscosity is normally 95%- 6mm. The mixture of these particles is then injected into a fluidized bed where the heat is absorbed by air. Depending on the type of slag etc. the typical granulated slag temperature in the fluid bed is between 500-800°C which is controlled mainly by the ratio of recycled to liquid slag. The hot air can then be used for generating steam of up to 300°C and can be also used for drying, preheating or combustion purposes by heat exchangers. Through this process, 65% of the slag energy input is recovered as high pressure steam and 10% from the granulator fluidizing air [15]. This method is currently used in Merox Company in Sweden.

Rotary Cup Atomizer (RCA)

The rotary cup atomizer was first designed in Britain by Pickering *et al.* [16]. It essentially atomizes the molten slag by a rotary-cup with an air-blast and cools it to produce a glassy product. The particles are cooled as they travel through air and are later introduced to a fluidized bed which prevents the slag particles from agglomeration and at the same time provides rapid cooling.

In a typical plant which uses RCA, 14% of the total slag flow would overflow the slag accumulator and thus be wasted because of the fluctuation of the flow. From the remaining 86%, 32% of the heat content cannot be recovered because 1) the total latent heat is not released when the glassy slag is formed 2) the solid slag is discharged from the heat recovery process at 250°C and 3) heat is lost in the slag accumulator. Therefore only 58.5% of the sensible heat content of the slag discharged from the furnace would be recovered. This amount is equivalent to 0.3GJ/t of iron produced or about 1% of the furnace energy requirement [16].

The main advantages of RCA are known to be high productivity and controllable granule diameter. It has also been proposed by Akiyama *et al.* [3, 17, 18] that by impinging reactive gas such as mixture of methane and steam, the sensible heat of the slag can be efficiently recovered.

Recovery of Thermal Energy from Slag

The techniques to recover sensible heat of slag may be categorized into (a) those that recover the energy as heat, *i.e.* transfer heat of the slag to another medium such as steam or hot air and (b) those that convert thermal energy to chemical energy through an endothermic reaction. These methods are explained in this section.

Recovery as Thermal Energy

Energy Recovery from Molten Ferrous Slag Using Molten Salt Medium In a study by Donald and Pickles [19] a method to recover the thermal energy of slags using molten salts was proposed

but has yet to be applied in industrial processes. A molten salt consisting of LiCl, KCl and NaCl was chosen as the absorbing medium because of its high heat capacity, low melting point, relatively high thermal conductivity, and low cost. Another advantage of this selection is the less reactivity of salts with slags and thus being less pollutant with no emission of harmful gases.

The results show the efficiency of heat transfer from the slag to the salt increases with stirring and with increasing the heat capacity of the salt. The X-ray diffraction pattern of the salt-quenched slag was similar to that for the water-quenched slag.

Heat recovery from Slag by Waste Heat Boiler In most heat recovery processes, air is used as a medium to recover the waste heat from dry granulation process. This thermal energy is later used to produce electricity or for preheating air. However, since the specific heat of air is low, the amount of air that is consumed in the process is high and therefore not very efficient in terms of energy recovery. To overcome this problem, utilization of heat boilers for producing high pressure steam for electrical power generation or other proposes such as preheating, was developed. Heat exchangers recover the sensible heat in solid slag granules dispersed in air by contact with the surface of tubes containing water flow.

Some key factors of heat transfer in this process were studied by Liu *et al* [20] and noted here. The results indicated that increasing the slag granule diameter decreases the heat transfer coefficient and the heat recovery of the heat exchanging system. Moreover the heat transfer coefficient increases linearly, and the cooling rate increases gradually as the slag granule descent velocity increases. Overall, the transfer coefficient can be up to 111 W/ m^2.K with the heat recovery of 90%. If the granule diameter is less than 2.5 mm and the descent velocity is greater than 1.0 mm/s, the cooling rate of slag granule is over 10K/s which are high enough to produce a glassy slag as a substitute for Portland cement.

Recovery as Chemical Energy

Energy Recovery by Methane Reforming

Most of the work on heat recovery from slag has been focused on heat transfer from molten slag to air and air to water for producing steam. However, the heat loss associated with these methods is considerably high specially at increased transport distance, therefore, other stream of research was focused on investigating possible processes to granulate slag, and at the same time, convert sensible heat of slag to chemical energy (i.e. fuel) through endothermic reactions. The produced fuel can later be easily transported and used for different purposes such as generating steam for producing electricity.

In 1977 Kasai *et al.* [18] proposed a new method that mainly focused on exchanging thermal energy of molten slag to chemical energy using CH_4/H_2O reaction and producing CO and H_2 gas mixture as denoted in (1). This reaction is well recognized as an efficient process for long distance transport of energy and has also been evaluated by Akiyama *et al.*[17]

$$CH_4(g) + H_2O(g) \rightarrow 3H_2(g) + CO(g) \qquad \Delta H = 206\ kJ/mol \tag{1}$$

In this process, both steam and the thermal energy needed for the endothermic reaction to take place are supplied by the slag granulation process and the recovered energy is later used for power generation.

Energy Recovery by Coal Gasification

The only work on recovering slag heat through coal gasification is the study of Peng *et al.* [21] in China. In the proposed coal gasification system, CO_2 is used as the gasification agent or the oxidizer (2) and is injected into molten slag through a nozzle, along with coal at a temperature range of 1073K to 1573K. The molten slag bath is both the heat source and main reaction district.

$$C + CO_2 \rightarrow 2CO \quad (2)$$

The initiation temperature of the coal gasification reaction is 900°C; therefore, with the slag temperature being 1450°C, the reaction will take place. The kinetics of the coal-CO_2 reaction was studied by thermogravimetry. The results [21] indicated that the coal conversion and reaction rate increase with gasification temperature increasing reach a maximum when the gasification temperature equals the ash fusion temperature.

According to mass and heat balance it was estimated that supposing a steelmaking industry produces 100 tonnes of molten BF slag, 5.6 million tonnes of carbon monoxide and 4.4 million tonnes of carbon dioxide would be produced and consumed respectively resulting in a profit of up to 18.75 million dollars per year according to the prices of gases.

Conclusion

The significance of heat recovery from slag was outlined and the main related difficulties were defined as low thermal conductivity and high viscosity. Various methods of slag granulation combined with thermal heat recovery such as heat exchangers and fluidized beds were analyzed. The main issue of these heat recovery techniques was found to be the low efficiency and difficult transportation of the recovered heat.

However, if the sensible heat in slag is converted to chemical energy such as syngas it will be a much more effective heat recovery process for long-distance transport of energy. The only extensive study so far that investigates this new approach is heat recovery of slag by methane reforming reaction. Due to its low exergy loss this process has been recognized as a promising efficient heat recovery system.

Acknowledgements

The authors would like to thank OGSST and NSERC for their financial support of this research.

References

1. http://www.worldsteel.org/Steel (Statistical Yearbook 2010) [cited Feb 2011].
2. W .Bengt, "Slag Heat Recovery," Int. Iron & Steel Inst, (1983), 245-256.

3. T. Akiyama et al., "Thermodynamic analysis of thermochemical recovery of high temperature wastes," *ISIJ International*, 40 (2000), 286-291.
4. J. Vlcek et al., "Alkali-activated composites based on slags from iron and steel metallurgy," *Metalurgija*, 48 (2009), 223-227.
5. Allibert, M., *Slag Atlas* , (Germany: Verlag Stahleisen, 1995).
6. E.Worrell et al., "Carbon dioxide emissions from the global cement industry," *Annual Review of Energy and the Environment*, 26 (2001) 303-329.
7. Jahanshahi, D.Xie, "Waste heat recovery from molten slags," Paper presented at the International Congress on Steel Gifu, Japan 2008)
8. www.us-concrete.com/news/features.asp [cited Nov 2010].
9. http://www.usgs.gov/ [cited Nov 2010].
10. M.P. Sudbury, and D.J. Kemp "The properties and uses of granulated non ferrous slags," (Paper presented at the TMS Annual Meeting, San Antonio, TX, United states, Minerals, Metals and Materials Society, March 2006)
11. Nakata Tetsuro, H.N., Kiochi Fujii and Tsukio Iwahashi ,"Heat Recovery in Dry Granulation of Molten Blast Furnace Slag," *Energy Development in Japan*, 55 (1983), 287-309.
12. K.S. Goto, H.W. Nagata, K.H. Linder, *Thermal Conductivities of Blast Furnace Slags and Continuous Casting Powders in the Temperature Range 100 to 1550 °C*, 105 , *Stahl und Eisen*, (1985) 63-70,
13. J. Anko et al., "Development of Slag Blast Granulating Plant Characterized by Innovation of the Slag Treatment Method", *Technical Review-Mitsubishi Heavy Industries*, 22 (1985) 136-142.
14. N. Tiberg, "Heat Recovery from Molten Slag, A New Swedish Granulation Technique," (Paper presented at the New Energy Conservation Technologies and Their Commercialization International Conference. Berlin, Ger: Springer Verlag 1981)
15. C.P. Broadbent, and N.A. Warner, *Reveiw of the Current Status on Energy Recovery from Slag* (Proceedingss of Energy and the Process Industries Conference, 1985)
16. S.J Pickering et al., "New Process for Dry Granulation and Heat Recovery From Molten Blast Furnace Slag," *Ironmaking and Steelmaking*, 12 (1985), 14-21.
17. T.Shimada et al., "Effects of Slag Compositions on the Rate of Methane-Steam Reaction," *ISIJ International*, 41 (2001), 111-115.
18. E. Kasai et al., "Rate of Methane-Steam Reforming Reaction on the Surface of Molten BF Slag - for Heat Recovery from Molten Slag by Using a Chemical Reaction," *ISIJ International*, 37 (1997), 1031-1036.
19. J.R.Donald, and C.A. Pickles, *Energy Recovery from Molten Ferrous Slags Using a Molten Salt Medium, (*Proceedings of the 77th Steelmaking Conference Chicago, IL, USA: Iron & Steel Soc of AIME 1994), 681-692
20. L.Junxiang et al, "Experimental study on heat transfer characteristics of apparatus for recovering the waste heat of blast furnace slag,"*Advanced Materials Research,* 97-101 (2010), 2343-6.
21. P.Li, et al. *Feasibility study for the system of coal gasification by molten blast furnace slag* (Proceedings of the International Conference on Manufacturing Science and Engineering, ICMSE, Zhuhai, China: Trans Tech Publications 2010), 2347-51

3rd International Symposium on High-Temperature Metallurgical Processing
Edited by: Tao Jiang, Jiann-Yang Hwang, Patrick Masset, Onuralp Yucel, Rafael Padilla, and Guifeng Zhou
TMS (The Minerals, Metals & Materials Society), 2012

CONTRIBUTION TO THE ENERGY OPTIMIZATION IN THE PYROMETALLURGICAL TREATMENT OF GREEK NICKELIFEROUS LATERITES

K. Karalis[1], C. Zografidis[2], A. Xenidis[1], S. Tabouris[2], E. Devlin[3]

[1]National Technical University of Athens, School of Mining and Metallurgical Eng.; Zografos Campus; Athens, 157 80, Greece
[2]General Mining and Metallurgical Company S.A. LARCO; Larymna Lokridos, 350 12, Greece
[3]NCSR Demokritos, Ag. Paraskevi; Athens, 153 10, Greece

Keywords: Laterite, Pyrometallurgy, Energy, Nickel, E/F

Abstract

The main parameters affecting energy and electrode consumption in smelting reduction of Greek nickeliferous laterites in submerged arc electric furnaces (E/F) were investigated. Within this framework, the operational data of E/Fs, such as energy consumption indicators, electrode consumption indicators and chemical characteristics of Fe-Ni and slag, were correlated with the physicochemical characteristics of the calcine, produced by roasting reduction of laterite in rotary kilns (R/Ks), such as reduction degree, temperature, chemical composition and granulometry. The results obtained provide a significant input for further research on the modelling of the roasting reduction – smelting reduction process, which is a critical tool for energy optimization.

Introduction

The two main steps of pyrometallurgical treatment of greek nickeliferous laterites for ferronickel production include: i) drying, pre-heating and controlled pre–reduction of laterite ores with solid fuel reducing agents and fuel oil in rotary kilns (R/Ks) for the production of a calcine, and ii) smelting reduction of the calcine in open-bath submerged-arc electric furnaces (E/Fs) for the production of Fe-Ni alloy with 12-16% Ni [1].

The energy absorbed from the endothermic reductive reactions of iron, nickel and cobalt oxides (Fe_2O_3, FeO, NiO and CoO) of the calcine with the remaining carbon in the E/Fs, corresponds to about 16% of the total energy output in the smelting reduction step [1]. This is indicative of the significance of the calcine's reduction degree for the electric energy requirements in the E/Fs. Moreover, the chemical characteristics and the granulometry of the calcine constitute critical parameters for the energy requirements as well as the smooth operation of the E/Fs.

The electric energy in the E/Fs of the Greek ferronickel industry is transferred into each furnace via 3 self-baking Söderberg electrodes immersed in the molten slag. The electric energy is converted into thermal and reduction energy using the electric resistance of the molten slag, reinforced by the electric resistance of an arc between the slag and the electrodes. The electrodes of the E/Fs in the Greek ferronickel industry can be classified as low loaded electrodes, i.e. electrodes with a low current density, but high furnace load. The metal tapping temperature is about 1450°C, higher than the liquidus temperature of the superheated slag.

The current work, based on both industrial and experimental data, mainly focuses on the correlation of the physical and chemical characteristics of the calcine produced by the R/Ks of the Greek ferronickel industry with the operational data of the E/Fs.

Experimental

The methodology of work in the current study included firstly sampling the calcine (2-3 kg) once a day over a time period of 20 days. The calcine samples were produced by a selected R/K and were taken from the charging pipes of the E/F which was fed exclusively by the aforementioned R/K. The calcine samples were immediately cooled to room temperature using nitrogen gas at a high flow rate to avoid re-oxidation phenomena. In addition, daily slag samples of approximately 0.5 kg were taken over the same time period from the same E/F. The temperatures of the slag and metal phase were measured with a laser pyrometer. Transmission Mössbauer spectroscopy was carried out on powder samples at room temperature in constant acceleration mode using a thin iron foil for calibration.

The experimental and operational data being studied in order to correlate the physicochemical characteristics of the calcine with the operation and the energy consumption of the E/F, are the following:

- Reduction Degree (RD) of the calcine, calculated based on iron speciation determined by Mössbauer spectroscopy [2].
- Chemical analysis of the calcine and slag samples by AAS spectrometry and LECO induction furnace for the determination of carbon and sulfur content.
- Temperature values of calcine and slag within the examined time period, measured with the optical pyrometer.
- Melting temperature of slag samples, determined by the triangular diagrams.
- Grain - size analysis of the calcine samples, determined experimentally by the use of standard test sieves.
- Fe (%) & SiO_2 (%) content of the laterite feed in the R/K within the examined time period, based on the R/K operational data.
- E/F energy consumption index (kWh / T of calcine & kWh / T of laterite feed in the R/K, including laterite ore, pellets and crusher product).
- Chemical analysis of nickel in the Fe-Ni alloy within the examined time period.
- E/F electrode consumption index (mm of slipping / MWh per 24h).

In Table I the chemical analysis of the calcine and slag samples is given, including the minimum and maximum values for each element or oxide. Further analysis of the calcine samples was conducted using Mössbauer spectroscopy for a quantitative and qualitative appraisal of the iron phases. Previous laboratory studies conducted on the roasting reduction of Greek laterite samples [3] have revealed that iron in the calcine is mainly found in the form of hematite (α-Fe_2O_3), non-stochiometric magnetite (Fe_3O_4), and complex iron-silica phases, such as fayalite ($2FeO.SiO_2$). Metallic iron was detected in none of the current samples while magnetic iron oxides in the form of hematite and non-stochiomteric magnetite, were detected. The Mössbauer spectroscopy yields an accurate quantitative analysis of the non-magnetic ferric and ferrous (%) content of the mineral phases present thus allowing the determination of the degree of reduction (RD = (Fe^{2+} / Fe^{tot}) %).

Table I. Chemical Analysis of the Calcine & Slag Samples (Min-Max Values)

Component (%)	Calcine	Slag
Fe^{tot}	25.73-32.55	24.6-30.7
NiO	1.16-1.39	0.09-0.51
SiO_2	30.32-40.22	37.7-43.8
CaO	1.88-5.89	3.3-5.7
MgO	4.91-8.60	6.6-7.9
Al_2O_3	4.55-9.94	5.8-7.2
Cr_2O_3	2.19-2,99	2.2-4.90
MnO	0.33-0.42	0.4-0.5
C	1.50-5.30	0.02-0.06

Results and Discussion

The results of reduction degree for the 20 samples tested are given in Figure 1. Furthermore, the Mössbauer spectra of two representative samples from days 4 and 14 (#2, #4), with different degrees of reduction are presented in Figure 2. Ferrous and ferric components are observed as well as intermediate states (Fe2.5+) which represent iron sites such as the B-site in magnetite which are mixtures of Fe2+ and Fe3+ iron states. Non-magnetic ferrous and ferric iron, and magnetic oxides (hematite, non-stochiometric magnetite) containing ferrous and ferric iron components are observed. These different subspectral components are graphically distinguished in Figure 2 on the basis of the iron oxidation state. The different fractions of the iron components present in these samples are accurately determined from their relative sub-spectral areas. The significantly higher non-magnetic ferrous content of sample 4 is clearly visible in Figure 2.

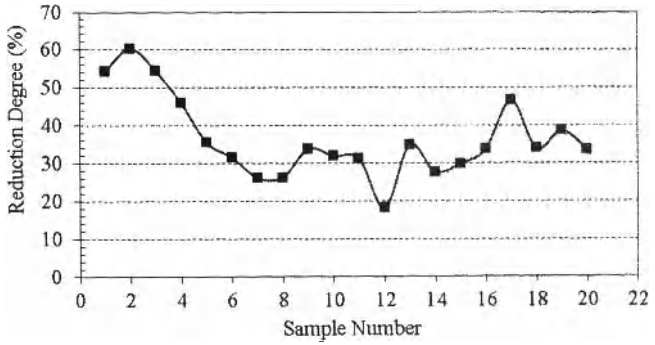

Figure 1. Reduction degree of the calcine samples

The effect of the calcine temperature, as determined by the use of an optical pyrometer, on the calcine reduction degree, can be seen in Figure 3. It should be noted that the temperature measurements of the calcine samples took place in the place of the E/F freeboard. More precisely, the temperature of the calcine used in the present study corresponds to the temperature of the calcine fed into the charging pipes of the E/F. Comparing these values with the calcine's temperature at the exit of the R/K, it is revealed that the temperature of the calcine fed into the E/F is about 100° C lower than that of the calcine exiting the R/K. It is clear that an increase of the calcine temperature favors the reduction.

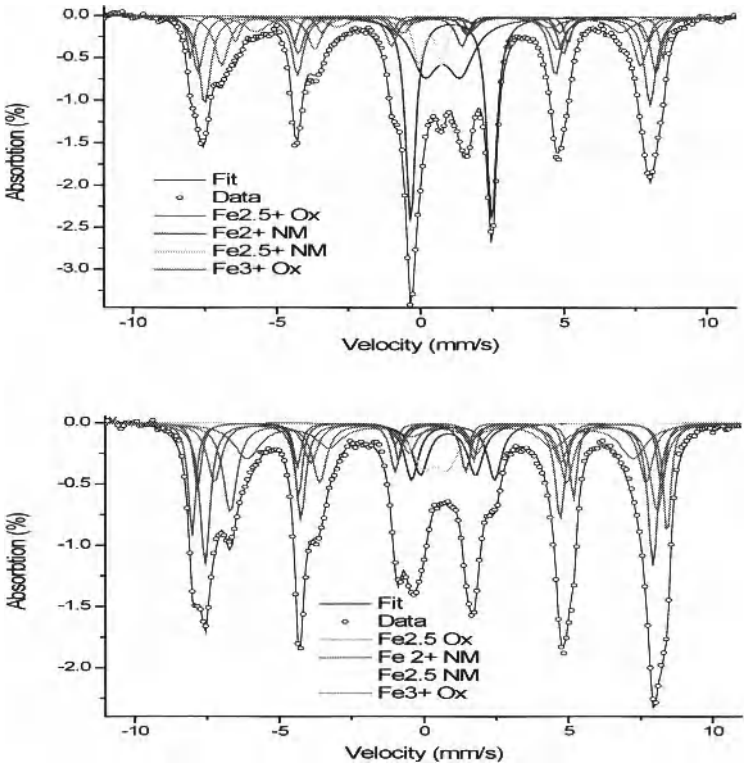

Figure 2. Room temperature Mössbauer spectra of samples 4 (upper) and 14 (lower). Ox: Magnetic iron oxides. NM: nonmagnetic iron containing phases.

Previously published work on reducibility of Greek nickeliferous laterites [4] concluded that temperature is one of the most important operational parameters in rotary kiln roasting reduction. According to the equilibrium diagram of the Fe-C-O system, hematite reduction can take place above 570°C. Increasing the temperature, which involves the maintenance of a stable temperature profile along all the zones of the R/K (drying, preheating and reduction zone), favours both the reduction degree and the reduction rate. In contrast, increase of the reduction degree of calcine results in a decrease of the calcine's carbon content, as seen in Figure 4. Both temperature and calcine carbon content are critical parameters for the smelting reduction procedure in the E/F. A higher calcine temperature corresponds to reduced electric energy requirements both for smelting and for the endothermic reductive reactions of iron and nickel oxides of the calcine in the E/F. Apart from that, limited calcine carbon contents result in fewer operational problems and a quieter smelting reduction process, as smaller volumes of reduction gases are generated through the slag in the E/F.

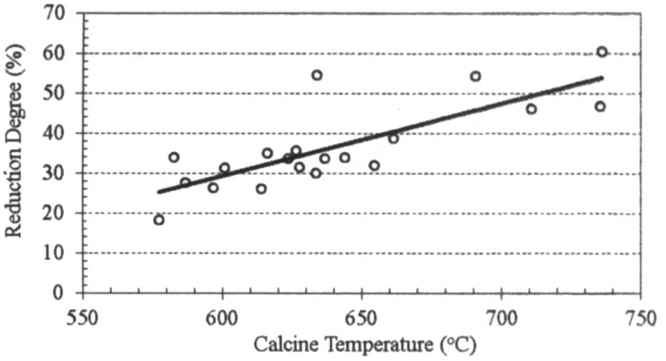

Figure 3. Reduction degree of calcine vs. temperature

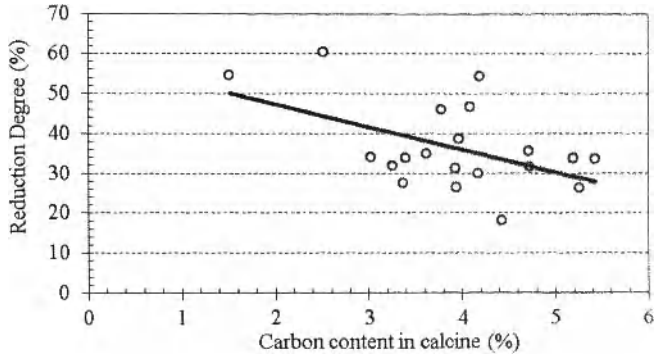

Figure 4. Reduction degree of calcine vs. residual carbon content

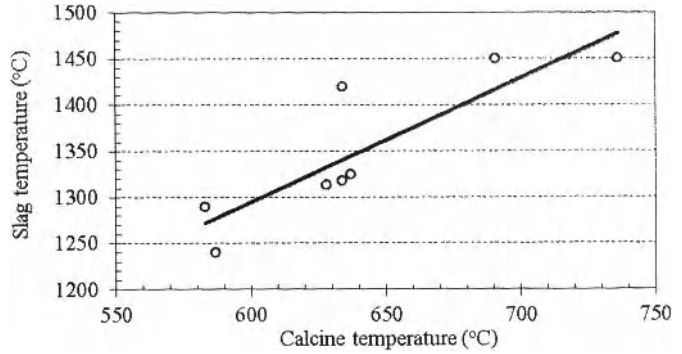

Figure 5. Variation of slag temperature vs. calcine temperature

Increasing the calcine temperature increases the temperature of the slag, as seen in Figure 5. The slag melting temperature, determined by the use of triangular diagram, ranges from 1100 to 1400.°C approximately. The superheated slag temperature, as determined by the use of the optical pyrometer, constitutes a critical parameter affecting the energy consumption in the E/F as is shown in Figure 6. This graph reveals a decreased energy consumption index, expressed as kWh / ton of calcine, with increasing slag temperature slag. Furthermore, the energy requirements in the E/F are considerably affected by the chemical and physical characteristics of the calcine. A decrease in the E/F energy consumption index is achieved by either an increased (%) content of the -1 mm fraction or an increased iron minus silica content of the calcine, as is deduced from Figures 7 and 8. However, it should be noted that an increased -1 mm fraction content combined with a low calcine temperature can cause power losses and serious operational problems due to the occurrence of intense flames. Additionally, an increased content of silica and a low iron content in the slag bath may also cause serious E/F operational problems, due to severe foaming of the slag.

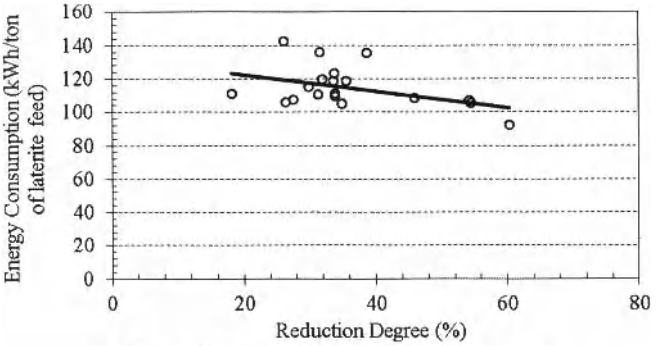

Figure 6. Energy consumption vs. slag temperature

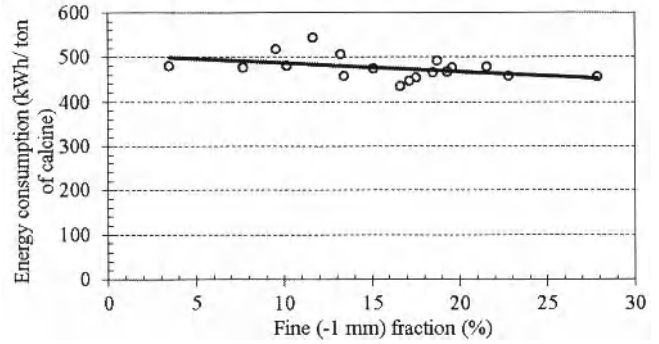

Figure 7. Energy consumption vs. fine fraction percentage

Another critical parameter for the economics of the smelting reduction process in the E/F is the electrode consumption which is strongly correlated with the nickel content of the ferronickel produced in the E/F. More precisely, the lower calcine carbon content due to the higher reduction

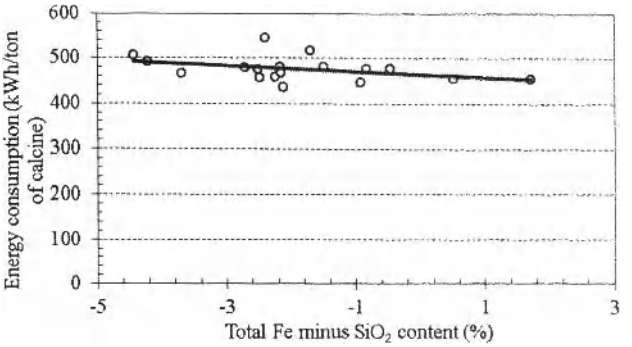

Figure 8. Energy consumption vs. total iron minus SiO_2 content

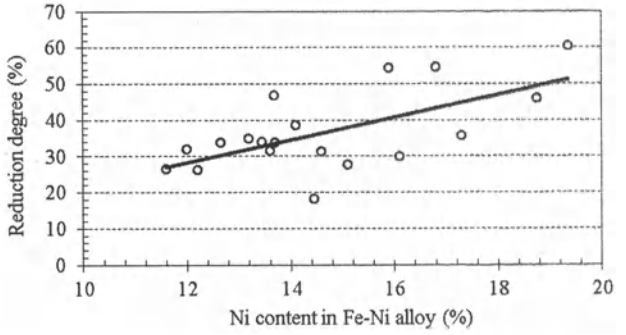

Figure 9. Calcine reduction degree vs. Ni content in Fe-Ni produced in E/F

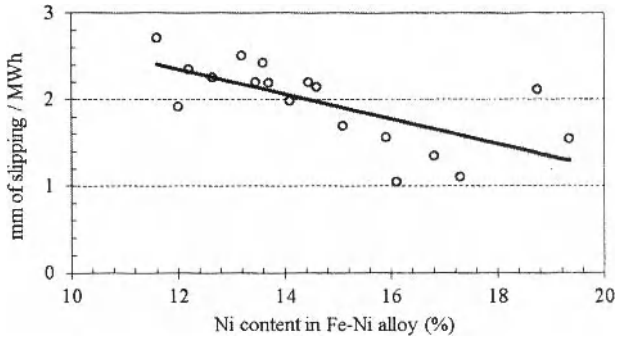

Figure 10. Electrodes slipping vs. Ni content in Fe-Ni produced in E/F

degree results in a lower reduction degree of the iron oxides inside the E/F, as seen in Figure 9. This corresponds to an increased nickel content in the Fe-Ni alloy and therefore increased iron content in the slag. Increased iron content in the slag in turn results in lower slag resistivity, which means that the electrodes are lifted more out of the slag and the electrode current increases. In turn, the decreased contact between electrode and the slag leads to a decreased electrode consumption. These effects are clearly revealed in Figures 10 and 11, where the electrode consumption, expressed in terms of the index mm of electrode slipping per MWh, is correlated with the iron and silica content of the laterite feed and the iron content of slag, respectively.

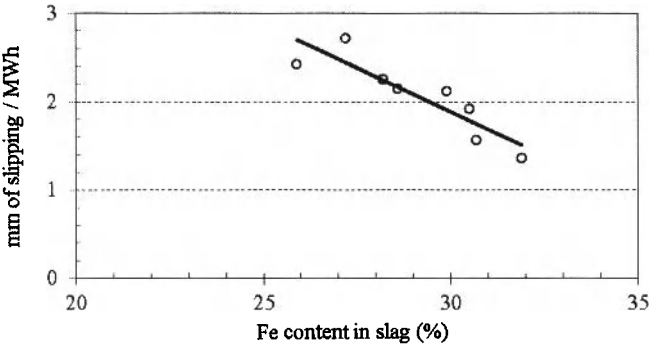

Figure 11. Electrodes slipping vs. iron content in slag

Conclusions

The optimization of open-bath submerged-arc E/F operation for laterite smelting reduction, in terms of energy consumption, electrode consumption and limitation of the operational problems, is a multi-parametric problem. The temperature and the reduction degree of the calcine feeding material, the iron and silica content of the calcine and slag, the ore grain size of the calcine and the temperature of slag all constitute critical parameters. Mathematical modelling of the roasting reduction-smelting reduction process using comprehensive sets of such raw data, should be the goal for optimization of the metallurgical method.

References

1. E.N. Zevgolis et al., "Energy Requirements in Nickeliferous Laterite Treatment" *EPD Congress 2006*, ed. S.M. Howard (Curran Associates, Inc., 2006), 487-496

2. ASTM Standard E277 *Test Method for Total Iron in Iron Ores by Stannous Chloride Reduction and Dichromate Titration* (1988)

3. Zevgolis, E.N. et al. (2009) Roasting reduction study of Greek nickeliferous laterites, *138th TMS Annual Meeting*, , San Francisco, California.

4. Zevgolis, E.N., Zografidis, C. and Halikia I. (2009). The Reducibility of the Greek Nickeliferous Laterites: A Review. *Mineral Processing and extractive metallurgy*, in press.

3rd International Symposium on High-Temperature Metallurgical Processing
Edited by: Tao Jiang, Jiann-Yang Hwang, Patrick Masset, Onuralp Yucel, Rafael Padilla, and Guifeng Zhou
TMS (The Minerals, Metals & Materials Society), 2012

STRENGTHENING REFRACTORY IRON ORE SINTERING WITH BIOMASS FUEL

Xiaohui Fan , Zhiyun Ji , Min Gan , Xuling Chen , Wenqi Li , Zhiyuan Yu

School of Minerals Processing & Bioengineering, Central South University, Changsha, Hunan, 410083, P.R.China

Key words: Specularite, Vanadium-titanomagnetite, Sinter, Biomass

Abstract

Specularite and vanadium-titanomagnetite are difficult to granulate, and with the increase of their proportions, the permeability of sintering bed is deteriorated together with the combustion velocity of fuel for the shortage of air through the sintering bed, which can lower sintering speed and specific production capacity significantly. The biomass fuel has a higher combustion velocity than coke breeze, therefore, the productivity of specularite and vanadium-titanomagnetite ore can be improved remarkably by replacing coke breeze partly with biomass fuel .The results showed that, when the proportion of biomass fuel replacing coke is 40%,the sintering speed and specific production capacity of 35% specularite were improved from 19.06mm/min, 1.33 t/ (m^2·h) to 21.45mm/min, 1.47 t/ (m^2·h) ,and that of 55% vanadium-titanomagnetite were improved from 17.23mm/min, 1.11 t/ (m^2·h) to 22.80mm/min, 1.44 t/ (m^2·h) . As a conclusion, biomass fuel is effective to strengthen sintering of refractory iron ore.

Introduction

The iron and steel industry of our country has achieved significant development in the recent years. In 2010, the output of steel has reached to 0.627 billion tons. The increasing scale of iron and steel has led to rigorous domestic iron ore environment, and the reserves of hematite and magnetite that have superior sintering characteristics are on the decline with continually exploiting and utilizing [1]. Therefore, the RIO (refractory iron ores) SP (specularite) and VT (vanadium-titanomagnetite) have to be applied vastly. However, the quality of sinters can be deteriorated when utilizing RIO in high proportion due to their poor granulation and metallogenic performances [2, 3]. Generally, the ratio of SP is 3～5%,which should not exceed 10% in our country currently [4]. Though high rate of VT is adopted in PZH steel for a long time, the productivity is obviously low compared with normal sintering [5].

Materials and Methods

Properties of Materials

The chemical compositions of materials are given in table I, where it can be seen that VT has a low iron grade of 53.69% and silica content of 3.09%, while it has a relatively high contents of TiO_2, which achieves12.69%. SP is a type of hematite with a high iron content of more than 66%. Concentrate-1 is a type of ordinary magnetite which has a total iron content of 61.80% and silica content of 6.09%. Table II illustrates the size distribution of materials. It is quite evident that they all have a remarkable portion of fine-grained particles of -0.25mm, which overs 90%.

Table I. Chemical Compositions of Materials wt/%

Raw materials	TFe	FeO	SiO_2	Al_2O_3	CaO	MgO	V_2O_5	TiO_2	S	LOI*
VT	53.69	31.78	3.09	3.94	0.45	2.99	0.53	12.69	0.600	2.85
SP	66.8	1.54	4.02	0.1	0.53	0.8	---	---	---	1.05
Concentrate-1	61.80	24.61	6.09	1.73	1.42	0.83	---	---	0.64	2.40

Table II. Size Distributions of Materials

Raw materials	Size distributions /%							Particle mean size/mm
	>1mm	0.5~1 mm	0.25~0.5 mm	0.074~0.25 mm	0.045~0.074 mm	<0.045 mm	<0.25 mm	
VT	0	0	9.60	35.20	17.10	38.10	90.40	0.15
SP	0	2.47	6.78	41.71	16.55	32.50	90.76	0.27
Concentrate-1	0	0	0	1.17	3.11	95.72	100	0.12

Two types of fuels are utilized in the experiment, one is coke breeze, and the other is carbonized biomass fuel. Their chemical and industrial analyses are given in table III, and their ash compositions are given in table IV.

Table III. Chemical and Industrial Analyses of Fuels

Fuels	Chemical compositions /%				Industrial analyses (dry basis) /%			GCV/ MJ/kg
	GC	H	S	Others	FC	Ash	VM	
Coke breeze	78.89	2.46	0.224	18.43	74.68	19.54	5.88	26.84
Biomass fuel	94.64	2.77	0.0372	2.55	87.34	5.10	7.55	30.77

*GC is gross carbon; FC is fixed carbon; VM is volatiles matter; GCV is gross calorific value

Table III and table IV showed that, biomass fuel was distinguished from coke breeze by lower ash yield, higher VM, higher FC and higher GCV. The biomass fuel ash was also of higher basicity and alkali metal content. The biomass fuel , above all, was of lower content of sulfur, which was detrimental to sintering process.

Table Ⅳ. Chemical Composition of Fuel Ash wt/%

Fuels	TFe	SiO_2	Al_2O_3	CaO	MgO	Na_2O	K_2O	P
Coke breeze	37.92	24.26	17.34	14.21	2.58	—	—	—
Biomass fuel	40.14	10.30	2.52	18.18	2.89	0.58	3.67	0.65

Experimental Methods

A sintering pot with a dimension of 680 mm×Φ 150 mm is utilized to simulate sintering process completely. The procedure involves: ore proportioning, blending, cylinder granulation, feeding, igniting and sintering. After accomplishing the whole sintering process, drop strength and tumble index are measured, besides, the sinter chemical composition is analyzed as well.

Results and Discussion

Sintering Properties Of Refractory Iron Ore

Effects Of Refractory Iron Ore Proportions On Sintering Properties The chemical composition of SP sinter is maintained at a homogeneous level of w(MgO)=2.0、w(SiO_2)=4.8%、R=2.0, and that of VT sinter is w(SiO_2)=5.36%, R=2.0.

The operation parameters include 4 min for cylinder granulation, 1 min for both ignition and heat preservation, 3 min for cooling, and the ignition temperature is 1150 ± 50℃. The negative pressure of ignition and cooling process is -5000 Pa, and that of sintering process is -10000Pa.

The effects of increasing the proportions of both SP and VT on the quality of sinter are given in Fig.1, Fig.2, respectively. Fig.1 showed that, the vertical sintering speed decreased from 23.30 $mm \cdot min^{-1}$ to 19.06 $mm \cdot min^{-1}$ together with specific production capacity declining from 1.52 $t \cdot m^{-2} \cdot h^{-1}$ to 1.33 $t \cdot m^{-2} \cdot h^{-1}$ when the proportion of SP ranged from 0 to 35%; Fig.2 showed that, all sintering indexes were deteriorated when VT ratio ranged from 0 to55% ,especially the vertical sintering speed and specific production capacity which reduced from 23.05 $mm \cdot min^{-1}$、1.55 $t \cdot m^{-2} \cdot h^{-1}$to 17.23 $mm \cdot min^{-1}$、1.11 $t \cdot m^{-2} \cdot h^{-1}$respectively.

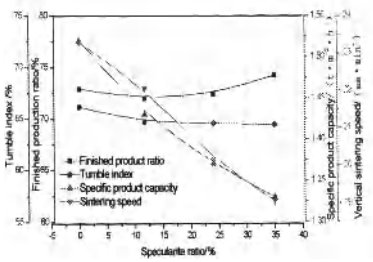

Fig.1 Effect of SP ratio on sinter indexes

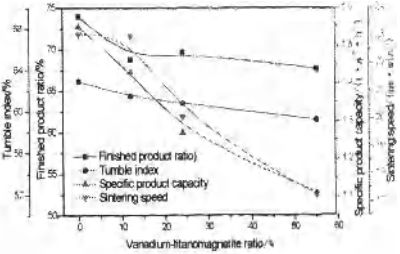

Fig.2 Effect of VT ratio on sinter indexes

Analyses Of Influence Of Refractory Iron Ore On Sintering Typical SEM images of iron ores were given in Fig.3 at a similar magnification. It illustrated that SP and VT tended to be smoother and more compacter than concentrate-1, which made them poor hydrophily and granulation property. Carves of relationships between refractory iron ore proportions and permeability were shown in Fig.4 where it could be seen that the permeability of both SP and VT were all deteriorated with proportions improving. Therefore, the airflow of sintering bed was insufficient as well as the combusting velocity was decreased that led to the dropping of vertical sintering speed and specific production capacity.

(a) SP (b) VT (c) Concentrate-1

Fig.3 Images (SEM) of iron ores

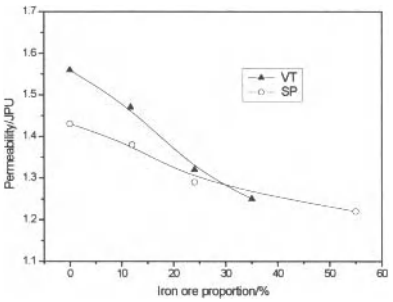

Fig.4 Effects of RIO proportion on permeability

Measure To Strengthen The Sintering Of Refractory Iron Ore

Results Of Biomass Fuel Strengthening The Sintering Refractory Iron ore The results of biomass fuel being applied to strengthen the sintering of 35% SP and that of 55% VT are given in table V and table VI, respectively.

Table V and table VI showed that, both the sintering speed and the specific production capacity of both SP and VT increased remarkably when coke breeze was partly alternated by biomass fuel. Apparently, when the proportion of biomass fuel replacing coke was 40% ,the sintering speed

and specific production capacity of 35% SP were improved from 19.06mm/min, 1.33 t/ (m^2·h) to 21.45mm/min, 1.47 t/ (m^2·h) ,and that of 55% VT were improved from 17.23mm/min, 1.11 t/ (m^2·h) to 22.80mm/min, 1.44 t/ (m^2·h) .Consequently , applying biomass is effective to strengthen the sintering of SP and VT.

Table V. Effect of Biomass Fuel on Strengthening SP Sintering

Ratio of biomass fuel replacing coke breeze /%	Moisture /%	Sintering speed / (mm·min^{-1})	Finished product ratio /%	Tumble index /%	Specific product capacity / (t·m^{-2}·h^{-1})
0	7.50	19.06	74.22	64.40	1.33
20	7.50	21.25	74.60	64.00	1.53
40	7.75	21.45	71.84	66.47	1.47

Table VI Effect of Biomass Fuel on Strengthening VT Sintering

Ratio of biomass fuel replacing coke breeze /%	Moisture /%	Sintering speed / (mm·min^{-1})	Finished product ratio /%	Tumble index /%	Specific product capacity / (t·m^{-2}·h^{-1})
0	8.25	17.23	67.65	59.24	1.11
20	8.50	20.30	71.26	60.93	1.39
30	8.50	20.40	72.06	59.45	1.33
40	8.75	22.80	69.94	60.27	1.44

Analyses Of Biomass Fuel Strengthening The Sintering Of Refractory Iron Ore The microstructure, TG-DSC and isothermal weight lose rate curves of the two kinds of fuels are demonstrated in Fig.5, Fig.6 and Fig.7, respectively.

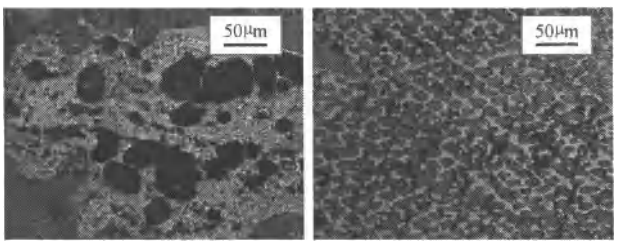

Coke breeze Biomass fuel

Fig.5 Fuel Microstructures

More micropores (Fig.5) were within biomass fuel than that were within coke breeze, which made biomass have greater reaction surface inside, contributing to a faster combustion velocity.
In Fig.6 where it could be seen that biomass fuel had higher maximum weight loss rate (Vmax) and maximum heat release value (Qmax), both Vmax and Qmax have a positive correlation with combustion velocity of fuels, than coke breeze under the same heating rate, whereas the ignition point of biomass is lower than that of coke breeze, which make biomass fuel combust more easily.
It's illustrated in Fig.7 evidently that biomass has a higher weight loss velocity than that of coke breeze under the identical circumstances, including reaction temperature , oxygen content, size distribution and weight. Therefore, when being utilized, biomass fuel can improve the fuel combustion status and increase the combustion front, which, in turn, enhance the sintering speed and specific production capacity.

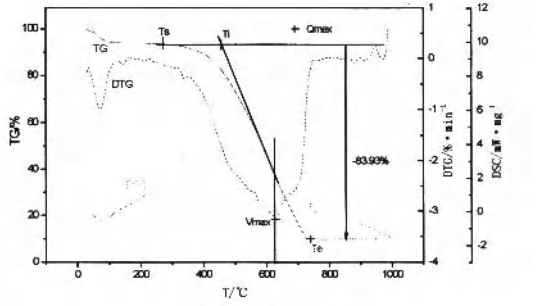

(a) Biomass fuel

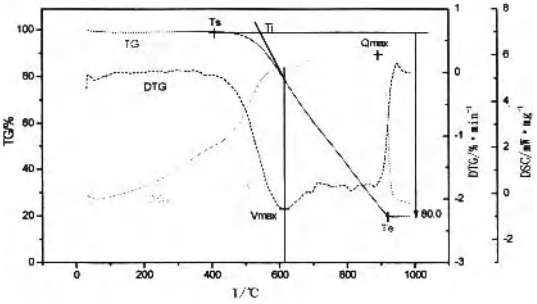

(b) Coke breeze

Fig. 6 TG-DSC carves of fuels

*Ti——ignition temperature ; Te——combustion suspended temperature; Vmax——maximum weight loss rate; Qmax——maximum value of heat release

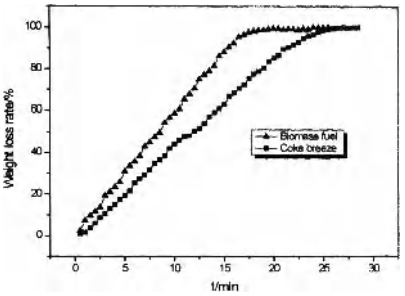

Fig.7 Weight lose rate curves of fuels at 1000 ℃

Conclusions

(1) Both specularite and vanadium-titanomagnetite have poor granulation property, therefore, permeability of sinter bed can be worsened as well as airflow can be decreased, which leads to the declining of sintering speed and specific production capacity.
(2) Being compared with coke breeze, biomass fuel has many different characteristics, including lower ash and sulfur contents, higher fixed carbon content, better combustion behaviors etc.
(3) Biomass fuel can be utilized to strengthen the sintering of RIO. The sintering speed and specific production capacity of both SP and VT can be improved remarkably when coke breeze is replaced partly by biomass fuel.

Acknowledgement

The authors want to express their thanks to Program for New Century Excellent Talents in University (NCET-05-0630), Program for Excellent Doctor's Degree Paper in Central South University, and Project(1343/74333001114) supported by the Postgraduate's Paper Innovation Fund of Hunan Province, China for financial support of this research.

References

1. J.H. Wei, "Study on the countermeasures of put domestic and overseas iron ore resources to rational utilization," *China Mining Magazine*, 20(5)(2011), 10-12,15.
2. D.Q. Zhu et al., "Improvement of Sintering Behaviors of Brazilian Specularite Concentrate by Damp Milling," *Iron & Steel*, 42(1)(2007),12-16.
3. M.G. He, and Y.X. Zhang, "Integration technique application of V-TI magnetite increase sintering intension," *Sichuan Metallurgy*, 32(3)(2010),7-11.
4. D.Q. Zhu et al., "Sintering behaviors of Brazilian hematite concentrate and its improvements," *Journal of Central South University, Natural Science*,37(5)(2006),878-883.

5. D.J. Jiang, et al., "Pangang intensifying sintering process with addition of burnt lime," *Sintering & Pelletizing*, 26(1)(2001),37-41.

3rd International Symposium on High-Temperature Metallurgical Processing
Edited by: Tao Jiang, Jiann-Yang Hwang, Patrick Masset, Onuralp Yucel, Rafael Padilla, and Guifeng Zhou
TMS (The Minerals, Metals & Materials Society), 2012

COMBUSTION BEHAVIOR OF PULVERIZED COAL INJECTION IN COREX MELTER GASIFIER

Shengfu Zhang *, Feng Zhu, Chenguang Bai, Liangying Wen, Guibao Qiu, Xuewei Lv, Meilong Hu, Yuelin Qin

College of Materials Science and Engineering, Chongqing University, Chongqing 400044, China
*Corresponding author. E-mail: zhangsf@cqu.edu.cn (Shengfu Zhang).

Keywords: COREX melter gasifier, Pulverized coal injection, Combustion rate, Coal blend

Abstract

The COREX process is the first reduction ironmaking technology with coal and pure oxygen to get high quality hot metal, which consumes a lot of high quality lump coal and some coke. In order to increase the utilization of fine coal, reduce coke consumption and enhance the competitiveness of the technology, the combustion behavior of pulverized coal injection in melter gasifier is studied experimentally. The results show that the combustion rate of PCI increases with the increase of temperature. And the combustion rate increases with decreasing coal particle size. Compared bituminous coal with anthracite, the former's burning ratio is higher than the latter in the same granularity. The combustion effect is remarkable when coal blend of bituminous coal and anthracite with the smaller particle size is pulverized in COREX process.

Introduction

The COREX process is the first reduction ironmaking technology with raw coal and pure oxygen to get high quality hot metal, which consumes a lot of high quality lump coal [1-3]. However, the proportion of lump coal in raw coal is very small, and it is avoidless to produce fine coal because of mechanical coal cutter and storage and transportation process, so it is important to resolve utilization of fine coal in COREX ironmaking process in order to energy conservation and reduce the cost of hot metal [4]. Currently, Coal briquetting technology is adopted to utilization of fine coal in COREX process [5], but coal briquetting system has high investment cost and requires feasible adhesive agent. The pulverized coal injection (PCI) into a blast furnace is being used on a global scale to improve the stability and reduce the cost of blast furnace operations [6]. The successful development of PCI in blast furnace is contributed to pulverized coal in COREX melter gasifier. However, it is different in PCI process between COREX melter gasifier and blast furnace, and the differences are as follows: firstly, The air is injected into blast furnace, which temperature is about 1200 ℃, but in COREX melter gasifier the normal temperature oxygen is blasted, so PCI in blast furnace begin burning in blowpipe, but

the combustion of PCI in COREX melter gasifier is only in raceway. Secondly, the racway of COREX is smaller than that of blast furnace of the same size. So, the combustion behavior of PCI is complex in COREX melter gasifier, which is not use for reference.

The research on PCI of COREX melter gasifier is currently in the initial stage. Jin et al. [7] analyzed the shortcomings of COREX process and discussed the possible effect of using PCI on COREX. In addition, some equipment of coal injection is recommended as an original design for COREX. Cao et al. [8] studied the combustion efficiency of pulverized coal in the raceway of COREX melter gasifier using a mathematical model, and their research results showed the combustion efficiency could keep at the level of 65 % when the mean particle size was 0.075 mm and the coal ratio was under 125 kg/t. The acceptable quantity of non-combustion coal for COREX melter gasifier was about 75 kg/t. When the coal ratio was 200 kg/t, the combustion efficiency of COREX process could be about 60 %. Li et al. [9] investigated the utilization rate of PCI with coaxial-jet sleeve lance and cross-jet slanted lance in the COREX coal injection process using combustion furnace. According to comparison of coal utilization rates under different parameter conditions, it indicated that the effect of sleeve-type lance is better than the one with slanted lance. Zhang et al. [10] had established a two-dimensional steady-state mathematical model and analyzed the combustion behaviors of PCI in different coal types, coal particle sizes and flow rates.

In raceway of COREX melter gasifier, if coal particles in combustion zone undergo incomplete combustion, the unburned or residual char will accumulate in the melter gasifier in which the char is depleted by means of reaction with slag and carbon dioxide [11]. If the accumulation rate of the char in the furnace is larger than the depletion rate, the movement of blast will be retarded, which results in a pressure fluctuation which further suppresses the operation of the furnace [12]. In consequence, enhancing the burning rate of PCI and reducing the accumulation ratio of unburned char is one of available methods to stabilize the performance of melter gasifier. Therefore, this research is to predict the combustion characteristics of PCI in COREX melter gasifier through experiment. By varying the temperature and coal particle size as well as coal blend, its impact on the burning behaviors of the PCI in COREX melter gasifier will be evaluated.

Experimental

Experimental Equipment

Thermal simulation is adopted to research combustion behavior of PCI in COREX melter gasifier. The schematic diagram of the thermal simulation assembly is showed in Figure 1, which is composed of melter gasifier, heating system, temperature controller, PCI unit, gathering unit for residual coal, air supply and dust removal device. For melter gasifier, the proportion of thermal simulation model and original apparatus of COREX C-3000 is 1:60, its furnace body is mould by alundum powder, which is heated by three sets of silicon carbides.

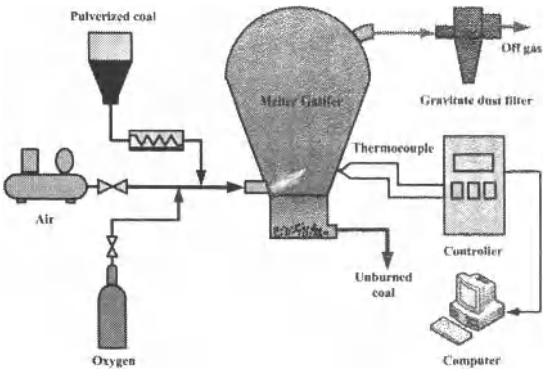

Figure 1. Schematic diagram of the thermal simulation assembly

Experimental Materials

Coal samples used in the experiment were coal pulverized into blast furnace of one iron and steel plant in China, and the proximate and ultimate analysis of coal samples are presented in Table Ⅰ. The coal samples were ground by vibration mill, and it was collected according to particle size (Ⅰ : <0.075mm, Ⅱ: 0.075-0.125mm, Ⅲ: 0.125-0.177mm, Ⅳ: 0.177-0.707mm). In experiment, PCI was pulverized into melter gasifier by compressed air. According to similarity principle and approximate modeling method, the flow rate of air and amount of PCI were calculated, and its values were 139.03 L/min and 15.6 L/min, respectively.

Table Ⅰ. Properties of the Coal Samples Used in the Experiment

Category	Proximate Analysis (wt %, ad)				Elemental Analysis (wt %, d)				
	Moisture	Volatile Matter	Ash	Fixed Carbon	C	H	O	N	S
Anthracite (A)	1.99	7.41	12.18	80.41	79.99	3.14	3.46	0.63	0.60
Bituminous Coal (B)	3.34	13.39	12.48	74.13	77.16	3.31	5.67	0.54	0.84

Calculation of Combustion Rate of PCI

Combustion rate (R) of PCI is a sign of good or bad for pulverized coal, it shows combustion status of PCI in raceway of COREX melter gasifier. In this experiment, assuming that components of coal is combustible except ash, combustion rate is calculated according the total mass of ash is same in the combustion as follows [13,14],

$$R = \frac{1 - A_O / A}{1 - A_O} \times 100\% \quad (1)$$

$$A_O = \frac{m_O}{m} \times 100\% \quad (2)$$

$$A = \frac{m_O^*}{m^*} \times 100\% \quad (3)$$

where, A_O is the ash content in coal sample; A is the ash content of residual coal after combustion; m is the mass of coal sample; m_O is the mass of ash in coal sample; m^* is the mass of residual coal after combustion, and m_O^* is the ash mass of residual coal after combustion.

When the two pulverized coals are blended, the total ash is as follows,

$$A_O = (a * A_{O1} + b * A_{O2}) \times 100\% \quad (4)$$

In above equation, A_O is the ash content of coal blend; A_{O1} and A_{O2} are the ash content of coal sample 1 and 2, respectively; a and b are mass fraction of coal sample 1 or 2 in coal blend, respectively.

Combustion rate of coal blend for different particle sizes is as follows,

$$R' = (a * R_i + b * R_j) \times 100\% \quad (5)$$

where, R' is weighted combustion rate of coal blend for different particle sizes; R_i and R_j are combustion rate of coal i and j with some particle size, respectively; and a and b are mass fraction of coal i and j in coal blend, respectively.

Results and Discussion

Effect of Temperature on Combustion Rate of PCI

Figure 2 shows combustion rate of anthracite and bituminous coal in different temperature. It can be seen that combustion rate of anthracite and bituminous coal is relevant to temperature, and the higher the temperature the higher the burning rate. It is more obvious that effect of temperature on the combustion rate of anthracite.

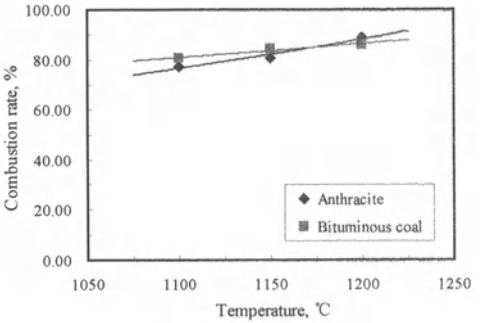

Figure 2. Combustion rate of anthracite and bituminous coal in different temperatures

Effect of Coal Particle Size on Combustion Rate of PCI

When the experimental temperature is 1150℃, combustion rate of anthracite and bituminous coal in different particle sizes is showed in Figure 3. From the figure we can see it is obvious effect that coal particle size on combustion rate of anthracite and bituminous coal, with increasing the coal particle size the combustion ratio decreases. For anthracite, when particle size is less than 0.075 mm its combustion rate is greater than 80%, but when particle size is 0.177-0.707 mm it is only 30%. For bituminous coal, when particle size is less than 0.075 mm its combustion rate is about 84%. Comparing anthracite and bituminous coal with the same particle size, combustion rate of bituminous coal is higher than that of anthracite except the particle size is 0.075-0.125 mm.

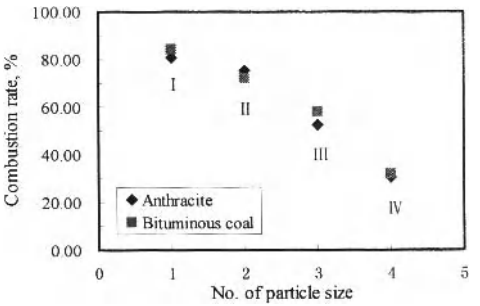

Figure 3. The relation between combustion rate and particle size of anthracite and bituminous coal

Combustion Rate of Different Coal Blend Injection

This section includes the following experiments: injection of two mixed anthracite with adjacent particle size, injection of two mixed bituminous coal with adjacent particle size, injection of mixture of anthracite and bituminous coal with the same particle size, and injection of mixture of anthracite and bituminous coal with the adjacent particle size.

Figure 4 shows combustion rate of two mixed anthracite and two mixed bituminous coal with adjacent particle size. From Fig. 4(1) and Fig. 3 we can observed that combustion rate of anthracite blend with 50% I (<0.075mm) and 50% II (0.075-0.125mm) equals to 82%, which exceeds combustion rate of particle size with I (<0.075mm). Combustion rate of anthracite blend with 50% II (0.075-0.125mm) and 50% III(0.125-0.177mm) is about 60%, which lies in between combustion rate (75.33%) of particle size with II and that (52.60%) of particle size with III. Combustion rate of anthracite blend with 50% III (0.125-0.177mm) and 50% IV (0.177-0.707mm) is 37.72%. It can be seen from the above analysis that anthracite blend with smaller particle size contributes to combustion of PCI, while anthracite blend with bigger particle size has negative effect on combustion of PCI.

It can be seen in Fig. 4(2) and Fig. 3 that combustion rate of bituminous coal blend with 50% I (<0.075mm) and 50% II (0.075-0.125mm) is less than 80%, and combustion rate of pulverized coal with 50% II and 50% III is about 60%, as well as it is only 22% with 50% III and 50%IV. It shows that bituminous coal blend with adjacent particle size has negative effect on combustion of PCI.

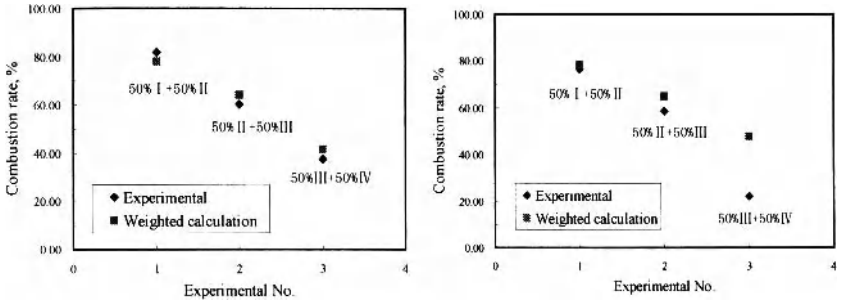

(1) Anthracite (2) Bituminous coal

Figure 4. Combustion rate of two mixing anthracite and two mixing bituminous coal with adjacent particle size

Figure 5 shows Combustion rate of anthracite and bituminous coal with same particle size and adjacent particle size, respectively. From Fig. 5(1) we can see that combustion rate of pulverized coal blend of anthracite and bituminous coal with the same particle size is appreciably

higher than that of their weighted calculation, and combustion effect of coal blend with smaller particle size is better than that of bigger particle size, all of which indicate mixture of anthracite and bituminous coal with the same particle size contributes to raise combustion rate.

In order to compare combustion effect of mixture of anthracite and bituminous coal with adjacent particle size, its combustion rates are showed in Fig. 5(2). In Fig. 5(2), for mixture of A and B, experimental is as follows: 50% I (anthracite) + 50% II (bituminous coal), 50% II (anthracite) + 50% III(bituminous coal) and 50%III(anthracite) + 50% IV(bituminous coal). Combustion rate of mixture of anthracite and bituminous coal with adjacent particle size is highest, which indicate mixture of anthracite and bituminous coal with the adjacent particle size can raise combustion rate. So, if mixture of anthracite and bituminous coal is pulverized in COREX melter gasifier, it may be considered to relax the particle size of bituminous coal in coal blend process.

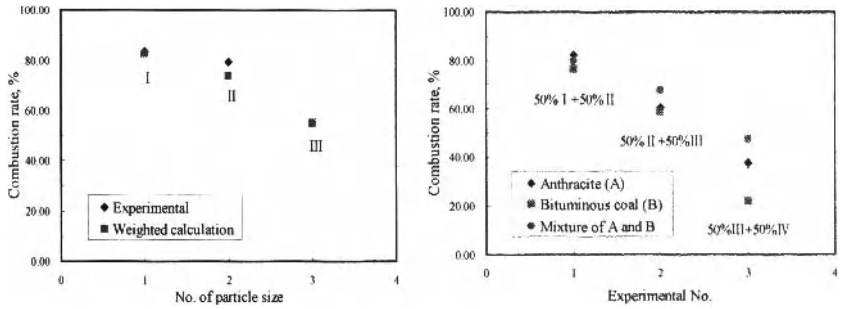

(1) Same particle size (2) Adjacent particle size

Figure 5. Combustion rates of anthracite and bituminous coal with same particle size and adjacent particle size, respectively

Conclusions

The combustion behavior of pulverized coal in COREX melter gasifier is experimentally examined, and the following conclusions are obtained.

(1) The combustion rate of anthracite and bituminous coal is relevant to temperature, and the higher the temperature the higher the burning rate.

(2) Compared bituminous coal with anthracite in the same temperature, the former's combustion ratio is higher than the latter in the same particle

(3) Combustion rate of mixture of anthracite and bituminous coal with adjacent particle size is highest, which indicate mixture of anthracite and bituminous coal with the adjacent particle size can raise combustion rate. In coal blend injection of anthracite and bituminous coal pulverized into CPREX melter gasifier; it may be considered to relax the particle size of

bituminous coal.

Acknowledgment

This research was supported by the National Natural Science Foundation of China (51104193) and Natural Science Foundation Project of CQ CSTC (2009BB4183).

References

1. J. K. Tandon et al., "Operational Success of COREX at Jindal Vijayanagar Steel Ltd." (Paper presented at the Asia Steel Int. Conf., Beijing, China, 26–29 September 2000), 140.
2. S. Pal and A. K. Lahiri, "Mathematical Model of COREX Melter Gasifier: Part I. Steady-state Model," *Metallurgical and Materials Transactions B*, 34B (2) (2003), 103-114.
3. P. Prachethan Kumar et al., "Factors Affecting Fuel Rate in Corex Process," *Ironmaking and Steelmaking*, 33 (4) (2006), 293-298.
4. H.F. Li et al., "Coal Injection Model for COREX and Its Application Analysis," *The Chinese Journal of Process Engineering*, 9 (Suppl. 1) (2009), 349-353.
5. China Metallurgical Group, "Coal Briquetting System Puts into Operation in Baosteel COREX Process," [2009-10-12], http://www.shgangyu.com/advanced/gangyu/sdynamicQueryContent.do?sdy_id=CF0F2FB9D74744929F140EFB1072F4AD.
6. Y. Ohno, T. Furukawa, and M. Matsu-ura, "Combustion Behavior of Pulverized Coal in a Raceway Cavity of Blast Furnace and Its Application to a Large Amount Injection," *ISIJ International*, 34 (8) (1994), 641-648.
7. Y. Jin and Z.L. Xue, "Discussion of Effect of Pulverized Coal Injection Technology on COREX," *Research on Iron and Steel*, 31 (2) (2003), 9-12.
8. X. R. Cao, B. H. Zhang, and H. B. Yang, "Research on the Combustion and Utilization of PCI for COREX," *Research on Iron & Steel*, 37 (2) (2009), 17-19.
9. K. Li et al., "Simulation Test Investigation with Different Lances in COREX Coal Injection Process," *Energy for Metallurgical Industry*, 29 (1) (2010), 22-24.
10. S.F. Zhang et al., "Numerical Simulation of Combustion Behavior of Pulverized Coal Injection in COREX Melter Gasifier," *Metalurgia International*, 16(2) (2011), 30-37.
11. Y. Iwanaga, "Gasification Rate Analysis of Unburnt Pulverized Coal in Blast Furnace," *ISIJ International*, 21 (5) (1991), 500-504.
12. S. W. Du and W. H. Chen, "Numerical Prediction and Practical Improvement of Pulverized Coal Combustion in Blast Furnace," *International Communications in Heat and Mass Transfer*, 33 (3) (2006), 327-334.
13. G.X. et al., "Study on Combustion of Mixed Coal Injection in Blast Furnace," *Ironmaking*, (5) (1992), 15-18.
14. X.R. Cao, "Research on Combustion Behavior of Pulverized Coal Injection into COREX Melter Gasifier," (Master degree thesis, Chongqing University, 2008), 1-67.

3rd International Symposium on High-Temperature Metallurgical Processing
Edited by: Tao Jiang, Jiann-Yang Hwang, Patrick Masset, Onuralp Yucel, Rafael Padilla, and Guifeng Zhou
TMS (The Minerals, Metals & Materials Society), 2012

IMPROVED SHORT COIL CORRECTION FACTOR FOR INDUCTION HEATING OF BILLETS

Mark William Kennedy[1], Shahid Akhtar[1], Jon Arne Bakken[1], Ragnhild E. Aune[1,2]

[1]Department of Materials Science and Engineering, Norwegian University of Science and Technology, N-7491 Trondheim,
NORWAY
[2]Department of Materials Science and Engineering, Royal Institute of Technology, 100 44 Stockholm,
SWEDEN
Communicating author: ragnhild.aune@ntnu.no

Keywords: Induction, heating, billet, short coil, magnetic field

Abstract

To determine the heating rate of billets using 'short coils', an appropriate correction factor must be applied to the theoretical relationship. In 1945, Vaughan and Williamson published a semi-empirically modified Nagaoka coefficient applicable for moderate frequency induction heating processes (10 kHz). Recently it was demonstrated that the method of Vaughan and Williamson gives <10% error in the estimated power when heating aluminum billets at 50 Hz.

In the present study, experiments have been conducted on aluminum billets in order to verify an empirical frequency corrected 'short coil' equation. Measurements of electrical conductivity (<± 0.5%), current (± 1%), heat (± 1-3%), and magnetic flux density (± 1-2%) have been performed. The results are compared with 1D analytical calculations, and 2D axial symmetric FEM modeling using COMSOL 4.2®. The frequency corrected equation has proven to provide accurate predictions of power (<4% error) within the frequency range 50 Hz to 500 kHz.

Introduction

Induction heating is commonly applied to the re-heating of billets before forging or extrusion processes. The resistive heating produced by eddy currents in the solid or semi-solid work piece during this procedure, is driven by the time varying magnetic flux density in the air-gap between the work piece and the coil. The flux in the air-gap is created by the current flowing in the induction coil, i.e. the magneto-motive force. In Figure 1 it can be seen that the currents present in the work piece are concentrated in the outer 'shell', or the first electromagnetic penetration depth (δ_w), and flow in a direction which opposes the magnetic field produced by the induction coil.

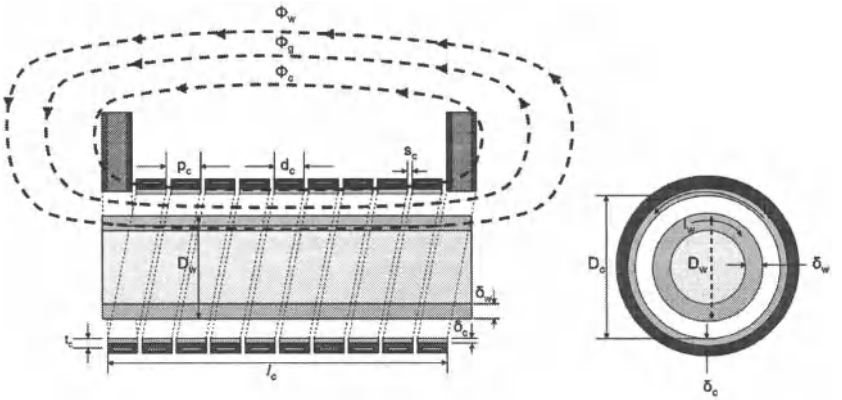

Figure 1. Schematic drawing of a 10 turn induction coil with a billet slightly longer than the coil [1]. (D_c = inner diameter of the coil [m]; D_w = outer diameter of the work piece [m]; l_c = length of the coil [m]; l_w = length of the work piece [m]; I_c = current in the coil [A, RMS]; I_w = current in the work piece [A, RMS]; δ_c = electromagnetic penetration depth in the coil [m]; δ_w = electromagnetic penetration depth in the work piece [m]; t_c = conducting thickness of the coil [m]; p_c = pitch of the coil [m]; d_c = width of the coil [m]; s_c = spacing of the coil [m]; Φ_c, Φ_g and Φ_w are the coil magnetic fluxes linking the coil, air gap and work piece respectively [Wb].)

Flux Densities of Long and Short Air-Core Coils

The magnetic flux density of a very 'long coil' can be predicted using the infinite coil formula:

$$\left|\overrightarrow{B_\infty}\right| = \frac{\mu_o \mu_r N_c I_c}{l_c} \tag{1}$$

where B_∞ is the axial flux density of an infinite coil [T], μ_o the magnetic permeability of the free space ($4\pi E^{-7}$ [H/m]), μ_r the relative magnetic permeability, N_c the number of coil turns, I_c the coil RMS current [A], and l_c the length of the coil [m]. However, coils used for induction heating are typically short and Equation (1) can not accurately estimate their magnetic flux density. When Equation (1) is multiplied by a 'short coil' correction factor, a more accurate estimate of the average z-component of the magnetic flux density is obtained for a typical induction coil.

It is important to point out that 'short coil' correction factors, such as the Nagaoka coefficient [2], have been found from the analytical solution of the inductance of a 'short coil', starting with a current sheet approximation. However, the Nagaoka coefficient can be estimated using numerical solvers to high accuracy, interpolated from the original 6 digit tabulated values, or estimated to approximately 3 significant digits, using the following relationships [3]:

$$k_N = \frac{1}{1 + 0.4502\left(\frac{D_c + \delta_c}{l_c}\right)} \tag{2}$$

$$\delta_c = \left(\frac{\rho_c}{\pi \mu_o \mu_r f} \right)^{0.5} \tag{3}$$

where k_N is the Nagaoka 'short coil' correction factor, D_c the diameter of the coil [m], δ_c the electromagnetic penetration depth into the coil [m], ρ_c the electrical resistivity of the coil [Ωm], and f the frequency [Hz].

Flux Densities of Short Coils Containing a Work Piece

If a high electrical conductivity work piece is inserted into an induction coil, the penetration of the magnetic flux from the air-gap into the work piece is greatly reduced. The flux in the air-gap is thereby increased significantly and becomes more uniform in both the axial and radial directions, as indicated in Figure 2 for a work piece of electrical grade aluminum billet.

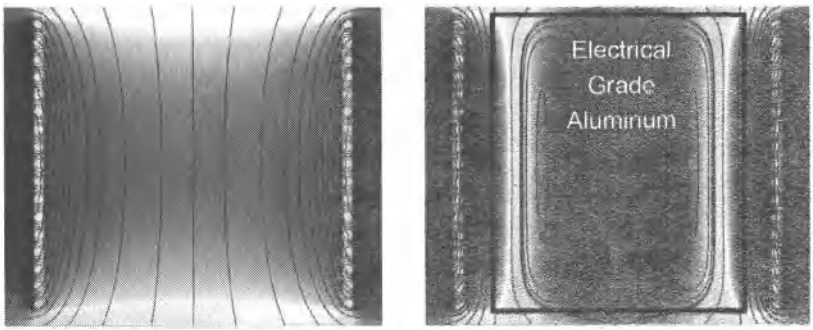

Figure 2. COMSOL 4.2® simulation showing the impact of the work piece on the magnetic flux density in the air-gap of a 'short coil' (17 turn), $D_c/l_c \approx 1.0$, 50 Hz.

As early as 1945, Vaughan and Williamson [4] proposed an empirical modification of the Nagaoka 'short coil' correction factor, based on the fraction of the volume of the air-gap occupied by the work piece. Experiments were conducted by Vaughan and Williamson at 10 kHz using non-magnetic cylindrical work pieces of brass, copper and 18-8 stainless steel to verify the general validity of their equation as given by the following relationship:

$$k_N^* = k_N \left(1 - \left(\frac{D_w}{D_c} \right)^2 \right) + \left(\frac{D_w}{D_c} \right)^2 \tag{4}$$

where k_N^* is the modified Nagaoka 'short coil' correction factor, and D_w the diameter of the work piece [m].

The present authors have recently proposed a modification to Equation (4) to account for variations in the electromagnetic penetration into both the coil and the work piece [5], i.e.:

$$k_N^* = k_N\left(1-\left(\frac{D_w-\delta_w}{D_c+\delta_c}\right)^2\right)+\left(\frac{D_w-\delta_w}{D_c+\delta_c}\right)^2 \tag{5}$$

$$\delta_w = \left(\frac{\rho_w}{\pi\mu_o\mu_r f}\right)^{0.5} \tag{6}$$

where δ_w is the electromagnetic penetration depth into the work piece, and ρ_w is the electrical resistivity of the work piece [Ωm].

The magnetic flux density present in the air-gap of a 'short coil' containing a work piece can then be calculated using Equations (1), (2), (3), (5) and (6). As Equation (5) is a one dimensional correction factor, it represents the integral average flux density over the full length and area of the coil air-gap. For round coils it has, however, been found adequate to equate ($D_c+\delta_c$) to the average coil diameter, over a wide range of frequencies from 50 Hz to 500 kHz [5].

Induction Heating Using Short Coils

The classical approach for the computation of heat generation in cylindrical work pieces [1] has been reviewed prior to the present study, and the required equations can be summarized as follows:

$$P_w = k_N^{*2}\sqrt{2}\pi(I_c N_c)^2 \rho_w \xi_w \varphi(\xi_w)/l_c \tag{7}$$

$$\xi_w = \frac{D_w}{\delta_w\sqrt{2}} \tag{8}$$

$$\varphi(\xi_w) = \frac{\sqrt{2}(ber\xi_w ber'\xi_w + bei\xi_w bei'\xi_w)}{ber^2(\xi_w)+bei^2(\xi_w)} \tag{9}$$

where P_w is the heat generated in the work piece [W], φ a correction factor accounting for the average phase shift between current and voltage in the work piece, and ξ_w a dimensionless penetration or reference depth, that is found in many of the equations in classical induction heating literature. *Ber*, *ber'*, *bei* and *bei'* are the real and imaginary parts of the zero order modified Kelvin Bessel functions and their derivatives, the solutions to which can be found using numerical solvers [6], look-up tables [7] or graphs [1].

Equation (7) can be used with the 'short coil' correction factor presented in Equation (5) to find the power induced by the 'short coil' in a work piece of length equal to or greater than that of the coil. If the work piece is shorter than the coil, Equation (7) can still be used, substituting the length of the work piece for the length of the coil.

Experimental Conditions and Procedures

In the present study, different sets of experiments have been performed to determine the actual heating rates and magnetic flux densities produced by different work piece and coil geometries, as a means of validating Equation (5). Some of the heating results will be presented in this publication, while more results including the magnetic field measurements will be presented elsewhere [8-9]. A schematic drawing of the main part of the experimental apparatus used is shown as Figure 3.

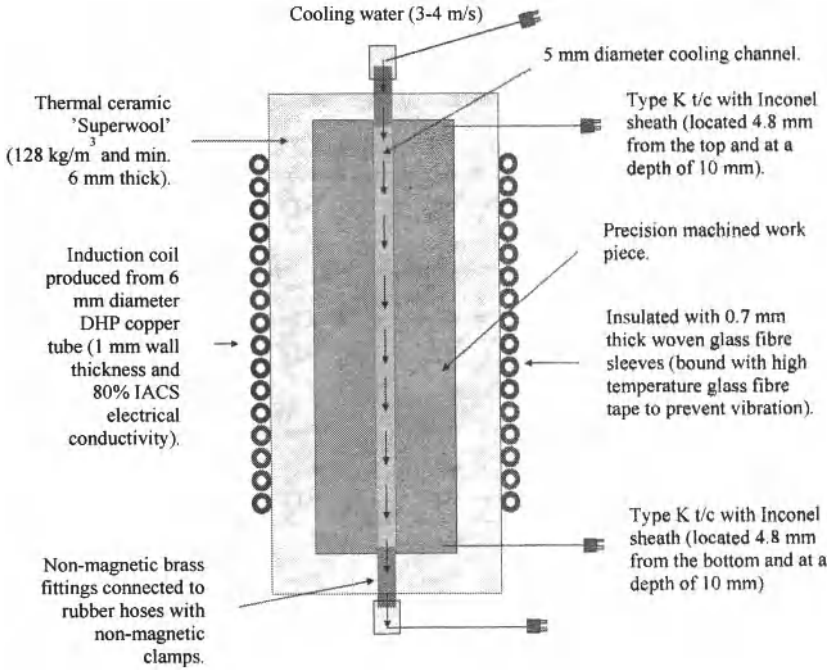

Figure 3. Schematic drawing of the water cooled induction heating experimental apparatus [8].

Thermal or 'calorific' heating measurements were performed, while applying a constant voltage to the coil. During the measurements, the temperatures of the thermocouples were carefully monitored, as well as the current flowing in the coil. When both electrical and thermal stability had been reached, a number of electrical readings were taken over a period of about 5 to 20 minutes, while the flow rate of the cooling water was logged simultaneously with the thermocouple data.

The electrical conductivity of the aluminum work pieces were measured using an AutoSigma 3000 conductivity analyzer (General Electric Inspection Technologies, UK) to an accuracy of

±0.5%. The instrument was calibrated prior to use against aluminum standards accurate to ±0.01% IACS [10]. Measurements were taken on both the machined ends of each work piece. An average of approximately 75 readings was used to estimate the room temperature conductivity of each work piece.

Power measurements were taken using a Fluke 43B power quality analyzer (Fluke, USA), with a resolution of ±100W. Coil current measurements were made with an i1000S inductive current probe (Fluke, USA) with an accuracy of ±1% and a resolution of 1A. The electrical data measured in the present study represents an average value based on 2 to 8 readings, while operating at steady state thermal conditions.

The water flow rate was determined using a scale which had a capacity of 100 kg and a resolution of 0.01 kg. The total weight difference over the hundreds of seconds used for each power estimation was then used to calculate the average water flow rate with <0.1% error.

Billets of two different alloys, i.e. billets (i) with different IACS electrical conductivities and (ii) with different dimensions, as well as a number of different coil geometries were operated in 10 separate experiments at 50 Hz. The main properties of the work pieces and coils are summarized in Tables I and II.

Table I. The Main Properties of the Work Pieces used in the Billet Heating Experiments [8]

Work Pieces	1	2	3
Alloy	A356	6060	6060
Diameter, mm	75.0	95.0	95.0
Length, mm	130.0	130.0	260.0
Measured IACS Electrical Conductivity, %	48.4	56.2	53.4
Penetration depth δw (mm) at 50 Hz and 293 K from Equation (6)	13.43	12.47	12.79
ξ_w from Equation (8)	3.948	5.388	5.252
$\varphi(\xi_w)$ from Equation (9)	0.823	0.862	0.859
Coil 1	1-1	1-2	
Coil 2		2-2	
Coil 3			3-3

Table II. The Main Properties of the Coils used in the Billet Heating Experiments [8]

Coils	Short Coil 1	Short Coil 2	Long Coil 3
Average Diameter, mm	132	155	132
Height, mm	106	108	218
Diameter to Height ratio	1.24	1.44	0.60
Number of Turns	16	16	32
Short Coil Correction Factor from Equation (2)	0.641	0.607	0.786
Electrically Determined IACS Conductivity, %	80	80	80
Penetration depth δc (mm) at 50 Hz and 293 K from Equation (3)	10.45	10.45	10.45
Modified Nagaoka Coefficient kN* for Work Piece 1 from Equation (5)	0.713		
Modified Nagaoka Coefficient kN* for Work Piece 2 from Equation (5)	0.770	0.710	
Modified Nagaoka Coefficient kN* for Work Piece 3 from Equation (5)			0.863

Results and Discussion

The validation of the proposed 1D correction factor presented in Equation (5) can best be accomplished by the comparison of the predicted analytical heating rate with the measured heating rate. This represents an 'integral' along both the length and phi directions of the work piece. As the heating rate obtained in a particular magnetic field is proportional to the square of the magnetic flux density, errors in Equation (5) are magnified in the error of the measured heating rates. This is indicated in Equation (7), making the suggested approach a particularly sensitive validation method.

The obtained data from the 10 heating experiments are summarized in Table III (5 conditions and 5 duplicates). As can be seen from the table, the average current and work piece electrical conductivity (evaluated at the average aluminum temperature) were used in evaluating Equation (7) and further used as input values in COMSOL 4.2® to derive estimates of the heating rate. Both the analytical approach and COMSOL 4.2® model excludes heat losses, i.e. the work piece is assumed to be perfectly insulated. The obtained values have also been added into Table III, together with the values calculated for the 'electrical' power, obtained as a result of the difference in the coil resistance with and without a work piece and the measured current.

Table III. Summary of the Experimental Data (with Duplicates) Obtained in the Present Study, and other Values of Importance used in the Analysis [8]

Coil (#)	Work Piece (#)	Average Aluminum Electrical Resistivity (Ω m) x10^{-8} *	Current (A)	Heating Energy Calorific (W)	Heating Energy Electrical (W)	Electrical Calorific Absolute Difference (%)	Heating Energy COMSOL (W)	COMSOL Calorific Absolute Difference (%)	Heating Energy Analytical Equation (7) (W)	Analytical Calorific Absolute Difference (%)
1	1	3.76	1001.3	636	631 ~	0.9	623	2.1	659	3.6
1	1	3.76	1001.0	634	611	3.6	623	1.7	659	3.9
1	2	3.44	1028.0	975	N/A	N/A	976	0.1	1035	6.1
1	2	3.42	1025.4	954	1019	6.8	970	1.6	1029	7.9
2	2	3.27	909.5	642	688	7.2	618	3.7	658	2.5
2	2	3.26	908.8	643	703	9.2	617	4.1	657	2.2
3	3	3.58	893.5	1884	2117	12.3	1888	0.2	1910.6	1.4
3	3	3.58	891.8	1894	2132	12.6	1881	0.7	1903.2	0.5
3	3	3.30	557.8	746	732	1.8	713	4.4	721.4	3.2
3	3	3.30	558.0	736	727	1.2	713	3.0	721.8	1.9
		* see [9]			Average:	6.2	Average:	2.2	Average:	3.3

The resulting uncertainty in the thermal heating estimate is believed to be primarily due to the obtained accuracy of ±0.05°C in the thermocouple delta-temperature. This temperature accuracy calculated as a fraction of the actual measured delta-temperature of the billet cooling water, represents an average uncertainty of less than 2%.

The heat losses (<0.6%, average of 0.4%) were estimated using a typical thermal conductivity value ($k_{insulation}$) for the Thermal Ceramics 'Superwool' used in the present experiments (~0.02 W/m/K) [11], and the actual thickness of the insulation used in each case. The insulation thickness varied depending upon the work piece, as well as the coil geometry.

Both estimates of heating presented in Table III, i.e. the analytical values and the COMSOL 4.2® values, have been plotted in Figure 4 along side the experimental data. As can be seen from Figure 4, there is good agreement between all the values. Only the electrical data for Coil #3 and

Work Piece #3 at high current have any significant errors. In these cases, the change in the coil operating temperature and resulting electrical conductivity, between the measurements made with an air-core and with the work piece, has been determined to be the main parameter causing the deviations.

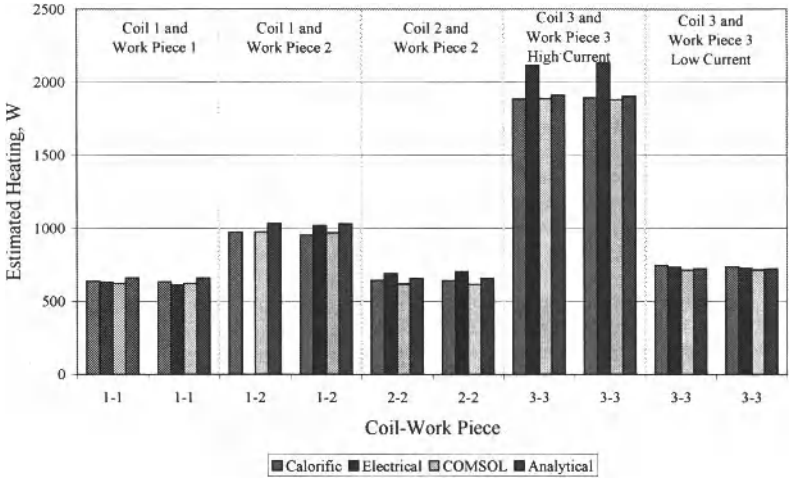

Figure 4. Experimental heating data resulting from calorific and electrical methods are compared with the estimates from the COMSOL 4.2® and the analytical modeling approach. Data are in the same order as listed in Table III, with 5 conditions and 5 duplicates [8].

From Table III it can be seen that the relative errors in the analytical heating estimates are lower for the 'long' Coil #3. This is believed to be the result of the initial 'air-core' Nagaoka coefficient being closer to unity and thus requiring less correction. Due to this, the data for Coil #1 and Work Piece #1, as well as for the larger diameter Coil #2 and Work Piece #2, should theoretically represent the most challenging cases for the proposed equations, i.e. Equations (5) and (7).

It can also be seen from Table III that the average difference in the estimated heat (power) resulting from both the COMSOL 4.2® and the analytical approach, is less than that of the electrical data when compared with the calorifically determined heating power. Given that the FEM model, as well as the analytical model is not considering the heat losses, it is believed that the heating estimates should be high by the average heat loss of 0.4%. In other words, the COMSOL 4.2® estimate has an error of < 2%, and analytical modeling estimates of <3% when compared with the experimental calorific data.

Comparison between Analytical Model and COMSOL FEM at Different Frequencies

A virtual experiment has also been performed comparing estimates of heating (power) as a function of frequency using the proposed analytical model against the COMSOL 4.2® model. Coil #1 and Work piece #1, which represent a challenging case due to the low length to diameter ratio, as well as the relatively large air-gap (low k_N^*), was used for the comparison. The following conditions were chosen, i.e. current of 1001 A, temperature of 37.1°C and $\rho_w = 3.76E^{-8}$ Ωm.

In Table IV the calculated estimates of heating (power) are presented. As can be seen, an offset of approximately 4% exists between the two models and this deviation appears to be consistent in the frequency range from 50 Hz to 500 kHz. The good agreement between the COMSOL 4.2® estimates and the experimental results at 50 Hz, appears to indicate that the obtained deviation in the analytical power estimate from Equation (7) is a result of the empirical nature of Equation (5). This 4% bias is particular to this geometry, a lower bias (0.8%) was found for the longer more 'ideal' Coil #3 [9].

Table IV. Comparison between the Estimates of Heating (Power) as a Function of Frequency for Coil #1 and Work piece #1. The Values are Based on the Analytical and COMSOL 4.2® Modeling Approaches

Frequency (Hz)	Experimental Power (W)	Analytical Power (W)	COMSOL Power (W)	Analytical-COMSOL Difference (%)
50	634	659	623	5.8
500	N/A	2567	2466	4.1
5000	N/A	8672	8370	3.6
50000	N/A	27957	26816	4.3
500000	N/A	88623	85247	4.0
			Average:	4.3

Conclusions

An improved 'short coil' correction factor has been developed and experimentally validated for use during induction heating of billets at frequencies from 50 Hz to 500 kHz. By adopting the improved correction factor, the errors obtained in the estimates of heating (power) have been reduced from <10% to <4%. The obtained results compare highly favorably with the factor of 2 error that would result from making a 'long coil' assumption, i.e. $k_N^* = 1.0$. The improved 'short coil' correction factor can be used to estimate the average flux density of a 'short coil' with an error of <2% based on the square root of the error in the heating estimation.

Acknowledgements

The present study was carried out as part of the RIRA (Remelting and Inclusion Refining of Aluminium) project funded by the Norwegian Research Council (NRC) - BIP Project No. 179947/I40. The industrial partners involved in the project are: Hydro Aluminium AS, SAPA Heat Transfer AB, Alcoa Norway ANS, Norwegian University of Science and Technology

(NTNU) and SINTEF Materials and Chemistry. The funding granted by the industrial partners and the NRC is gratefully acknowledged.

The authors wish to express their gratitude to Egil Torsetnes at NTNU for helping with the design and construction of the experimental apparatus. Sincere gratitude is also due to Kurt Sandaunet at SINTEF for his support and help, as well as for the use of the SINTEF laboratory.

References

1. M. W. Kennedy, S. Akhtar, J. A. Bakken, and R. E. Aune, "Review of Classical Design Methods as Applied to Aluminum Billet Heating with Induction Coils," EPD Congress, San Diego, California, February 27 - March 3, (2011), 707-722.
2. H. Nagaoka, "The Inductance Coefficients of Solenoids," *Journal of the College of Science*, 27, (1909), 18-33.
3. D. Knight, http://www.g3ynh.info/zdocs/magnetics/part_1.html, accessed September 22, (2011), [Online].
4. J. Vaughan and J. Williamson, "Design of Induction-Heating Coils for Cylindrical Nonmagnetic Loads," *Transactions of the American Institute of Electrical Engineers*, 64, (1945), 587-592.
5. M. W. Kennedy, S. Akhtar, J. A. Bakken, and R. E. Aune, "Analytical and Experimental Validation of Electromagnetic Simulations Using COMSOL®, re Inductance, Induction Heating and Magnetic Fields," submitted to the COMSOL Users Conference, Stuttgart Germany, October 26-28, (2011).
6. R. Weaver, http://electronbunker.sasktelwebsite.net/DL/NumericalExamples01.ods, accessed September 22, (2011), [Online].
7. N. McLachlan, *Bessel Functions for Engineers*, (Gloucestershire, Clarendon Press, 1955), 215 - 230.
8. M. Kennedy, S. Akhtar, J. A. Bakken, and R. E. Aune, "Theoretical and Experimental Validation of Magnetic Fields in Induction Heating Coils," submitted to *IEEE Transactions on Magnetics*, (2011).
9. M. W. Kennedy, S. Akhtar, J. A. Bakken, and R. E. Aune, "Analytical and FEM Modeling of Aluminum Billet Induction Heating with Experimental Verification," submitted to the TMS Light Metals, Orlando Florida, March 11-15, (2012).
10. *Copper Wire Tables Circular No. 31*: US Bureau of Standards, (1913).
11. "Superwool® Plus Blanket Datasheet Code EU: 11-5-01 US: 11-14-401," www.thermalceramics.com., accessed August 8, (2011), [Online].

3rd International Symposium on High-Temperature Metallurgical Processing
Edited by: Tao Jiang, Jiann-Yang Hwang, Patrick Masset, Onuralp Yucel, Rafael Padilla, and Guifeng Zhou
TMS (The Minerals, Metals & Materials Society), 2012

LIBERATION OF METALLIC-BEARING MINERALS FROM HOST ROCK USING MICROWAVE ENERGY

Matthew D. Andriese[1], Jiann-Yang Hwang[1], Zhiwei Peng[1]

[1]Department of Materials Science and Engineering, Michigan Technological University, Houghton, Michigan 49931, U.S.A

Keywords: comminution, sulfide ore, microwave energy, mineral liberation, grindability

Abstract

It has been demonstrated that metallic-bearing minerals are physically liberated from host rock when exposed to microwave (MW) energy. The metallic minerals are iron sulfides and spinel oxide minerals contained in peridotite rock. Experimental evidence has shown ore particles readily couple with MW energy at 2.45 GHz, 1000 W resulting in rapid heating. Thermal stresses are generated by highly absorbing metallic-bearing minerals resulting in cracking and embrittlement of ore particles that assists in crushing and grinding processes. The liberated metallic-bearing minerals are shown to report to coarser size fractions as a result of MW exposure.

Introduction

Comminution of ore material during beneficiation is a large energy expenditure for the mineral processing industry. Crushing and grinding operations alone consume 50-70% amount of energy used in mineral processing [1]. Size reduction becomes increasingly difficult with decreasing particle size making grinding the most energy-intensive step of comminution. The aim of comminution is to maximize liberation of economically valuable minerals from the host rock [2]. Overall, the less material that needs to be handled, then grinded, to create a useful product for hydro/pyro metallurgical processes will achieve the greatest reduction of energy.

Much of the scientific interest for use of microwave (MW) energy in mineral processing has been for improved hydro/pyro metallurgical techniques [3-6]. Early authors have employed MW energy for improved grinding of ore particles but most conclude the energy savings do not justify the energy input [7-9]. The effectiveness of MW assisted grinding is dependent on the ore mineralogy and the absorptive properties of minerals contained within it. Ore containing magnetic minerals should prove successful with MW assisted breakage from highly absorptive properties.

For heat and thermal stresses to be generated within an ore particle, it must contain minerals that readily absorb MW energy. The MW energy is converted into thermal vibrations of the lattice by polarization mechanisms such as electronic, atomic, ionic (conduction), orientational, (dipole) and Maxwell-Wagner polarization. The dielectric response is the amount of energy loss by transmission and absorption of energy in a material. Irradiation is the production of heat as a result of MW energy loss in a material.

The nature of bonding and atomic configuration of a structure determines the electronic and magnetic properties of a mineral. Most minerals are a combination of bonding types (ionic, covalent, and metallic) so the dielectric response is specific to the composition and structural properties. Iron sulfides are known semiconductors (n or p type dependent on composition) due to the high degree of covalent bonding exhibited by the sulfur structure in which charge carrying metal atoms are loosely bound. Conversely, oxide minerals have a high degree of ionic bonding in which conduction in the structure is very much dependent on oxygen fugacity. The mineral pyrrhotite (Po) has an iron deficient, vacancy laden structure in which its magnetic properties are dependent on composition. Ferro-spinel (Spl) oxide minerals form solid solutions having varying amounts of catonic substitution, are highly conductive and exhibit strong ferrimagnetic properties. Though, Po and Spl exhibit metallic bonding to some degree, and both strongly absorb MW energy, the polarization mechanisms of each structure that produce irradiation can be very different.

Experimental

Microwave Treatment of Particles

An ore body located in Michigan's Upper Peninsula contains metallic-bearing sulfide and spinel oxide minerals in peridotite rock. Particles were obtained by stage crushing core samples with jaw, gyratory, and roll crushers. All ore particles are from the same lot and are assumed to be homogenous with respect to metallic mineral content. The crushed material was then size classified then particles (-4+6 mesh) in size were sent through a splitter a dozen times. Material was exposed to microwave energy for 30 and 60 seconds with 100 gram samples contained in an alumina crucible placed in the center of the cavity. The microwave oven was a conventional type operating at 2.45 GHz, 1000 W power. Samples were removed from the crucible and allowed to cool on a ceramic plate.

Crushing and Grinding Experiments

For ball milling experiments, 1 kg of (-4+6 mesh) crushed material was ball milled dry for 100 revolutions, dumped, size classified, then put back into the ball mill for additional grinding totaling 500 revolutions (revs). This was repeated for another 500 revs totaling 1000 revs the material was ball milled. For roll crushed material, 1 kg of ore particles were passed through the roll crusher then size classified. The material retained on each Tyler mesh sieve was massed and recorded. All size classification experiments were performed with a Roe-Tap sieve shaker for 15 minutes.

Heavy Liquid Separation

Diiodomethane (CH_2I_2) of 99+% purity supplied by Acros Organics was used as heavy liquid for density separation having a specific gravity of 3.32. To start, 10 grams of material from crushing and grinding experiments was massed and put into a 50 ml centrifuge tube. The solution of heavy liquid and solid material is centrifuged for 30 min.

at 600rpm. Pieces of #1 filter paper in glass funnels were used to collect the float and sink material. The filter paper was washed with acetone to remove excess heavy liquid and filtered samples are allowed to dry overnight in an oven at 100°C.

X-ray Diffraction of Sink Material

The material obtained by heavy liquid separation was examined by x-ray diffraction. XRD work was performed using a *Scintag XDS 2000* powder diffractometer using CuK_{α} radiation λ=1.5418 Å. The ball milled material passing 100 mesh (147 μm) sink was scanned by XRD. The sink material of roll crushed mesh size fractions (-65+100), (-100+200) and (-200+325) were mounted in an aluminum holder and continuously scanned in the range of 10-75° to obtain diffraction patterns for qualitative phase identification in samples. *JCPDF Win* computer software was used for phase identification of the peaks obtained in diffraction patterns [JCPDS-International Centre for Diffraction Data v. 2.2; 2001].

Results and Discussion

Crushing and Grinding

The ball milled cumulative percent passing material for microwave (MW) treated and as-received (As-Rec'vd) ore particles are shown in Figure 1. Increasing the ball mill revolutions produced more fine material for MW treated ore particles shown by an increase in cumulative percent passing material then for As-Rec'vd material. Increasing the MW exposure time also increased the amount of passing material being a good implication for increased grindability of MW treated material. According to F. Bonds procedure [10], particles greater than 6 mesh (≈3.3mm) in size are forbidden for ball milling experiments which was the reason for not performing quantitative measurement of grindability. Work index experiments performed on the same ore material showed an increase in the grindability resulting in a decreased work index for MW treated material [11].

The increased grindability of ore particles after MW treatment is an interesting result but the macroscopic cracking produced in ore particles by MW exposure is not fully utilized by ball milling. Size reduction during grinding experiments is accomplished mainly by abrasion resulting in fine size material produced during ball milling. Particle size reduction by abrasion is highly inefficient so it was of interest to make use of the cracks produced in ore particles.

The roll crushed cumulative percent passing material for MW treated and As-Rec'vd ore particles are shown in Figure 2. The plots show the exact opposite trend then ball milled particles in that MW material produced *less* cumulative percent passing material. This result shows that MW treated ore particles passed through the roll crusher with less abrasion due to cracks that weakened ore particles. Increasing MW treatment time did not have a significant effect on the cumulative percent passing material showing increasing MW time may only assist with the grindability and does not have a significant effect on the overall breakage of particles.

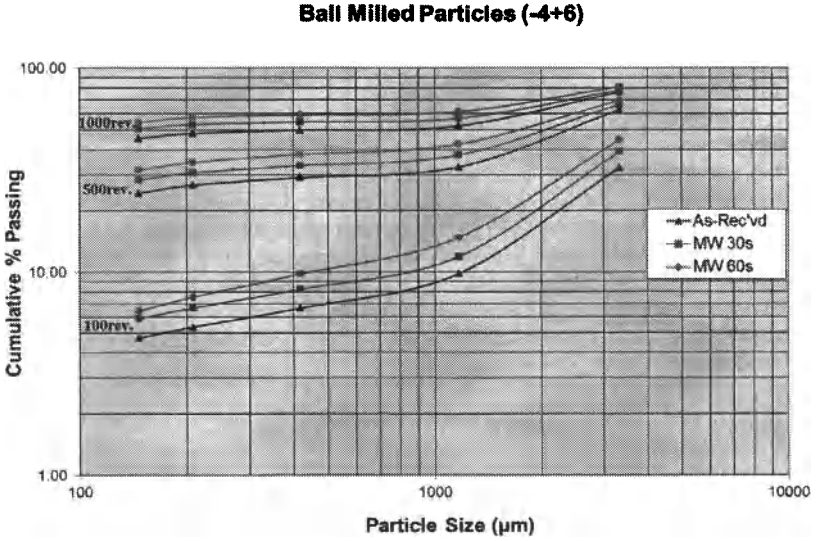

Figure 1. Particle size distribution of as-received and microwave treated particles (-4+6) ball milled for 100, 500, 1000 revolutions

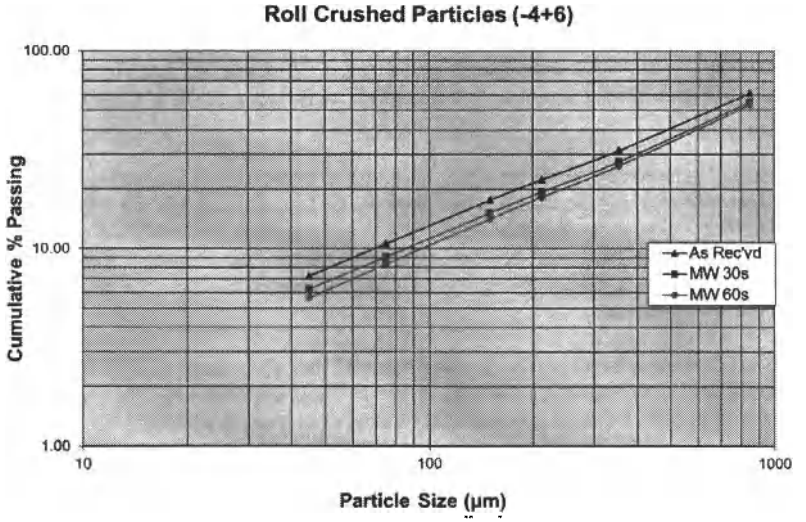

Figure 2. Particle size distribution for as-received and microwave treated ore particles (-4+6) passed through the roll crusher.

X-Ray Diffraction of Sink Material

The increased grindability of MW treated ore particles does not show any sizeable increase in the liberation of metallic-bearing minerals from host rock. The XRD pattern of sink material (Figure 3) shows signals from metallic-bearing minerals but all patterns in the spectrum have a similar intensity of signals. Peaks are convoluted do to masking of metallic peak signals from heavy silicates reporting to sink material, mainly that of Ca-rich pyroxene (Px). The much lower volume of metallic minerals with respect to silicates in ore particles is the main reason for such low intensity signals. The absence of various peak signals from MW 60s material but occurring in As-Rec'vd and MW 30s material is not completely known but could very likely be the result of phase change in mineral phases as a result of MW exposure. These signals are not the result of oxidation products produced by surface alteration during heating because the volume of oxidation product would be much less compared to the bulk material produced during ball milling thus oxidation products would fall under the limits of XRD detection.

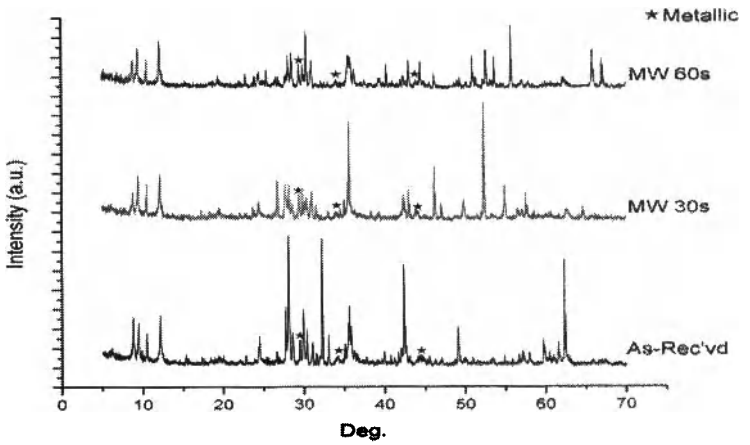

Figure 3. XRD pattern plotted as intensity (a.u.) vs. 2θ of ball milled sink material passing 100 mesh (147μm). Intense peaks of metallic sulfide phases are indicated by a star.

The XRD patterns in Figures 4-6 of sink material from various size fractions of the roll crushed particles (Figure 2). The material scanned by XRD in this range of size fractions was not reduced in size for powder diffraction experiments and remained the retained size to preserve disseminated mineral grains. Since the iron sulfide minerals form intergrowths, intense pyrrhotite (Po) peak signals were used as the main indicator of sulfide minerals present in scans to support peak identification. An intense Po peak occuring at ~44° corresponding to the (102) plane indicates the presence of iron sulfides.

As shown by ball milled material, many peaks are produced during XRD from the asymmetry of silicate structures that consequently mask metallic peak signals. Therefore, material passing (-325 mesh) that reported to the pan was not investigated because it likely contained a high amount of silicate minerals. Silicate minerals report to sink material by still being attached to metallic minerals, having density greater than diidomethane, or both.

Both sulfide and silicate minerals report to the (-65+100 mesh) size fraction (Figure 4). The intensity of metallic peak signals in the As-Rec'vd pattern are weaker then the MW 60s material. The clustering of silicate peak signals, along with other intense silicate peak signals in the pattern indicate a high amount of silicate minerals present in As-Rec'vd material. The most intense peak in MW treated material belongs to Ca-rich Px but other silicate peak signals are not as prevalent.

The (-100+200 mesh) size fraction shows metallic peak signals occurring in both sink materials (Figure 5). The presence of silicates creates background noise in patterns and introduces peak broadening to metallic signals but both these effects are reduced in MW 60s material. Metallic peak signals are apparent in MW treated material shown by numerous Po signals, an intense chalcopyrite (Ccp) peak and spinel (Spl) minerals now reporting to the (-100+200 mesh) size fraction.

Many types of silicate minerals report to the (-200+325 mesh) size fraction (Figure 6). The various silicate peaks that cluster around metallic peaks may be an indication of interlocked silicate and metallic minerals in As-Rec'vd material. The low intensity metallic peak signals in MW material are thought to be the result of metallic minerals reporting to larger size fractions.

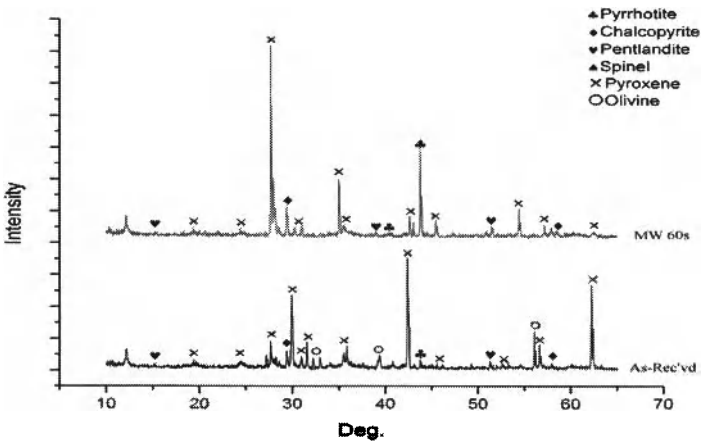

Figure 4. XRD pattern of as-received and microwave 60s material roll crushed (-65+100 mesh) sink material corresponding to (208-147μm) size fraction

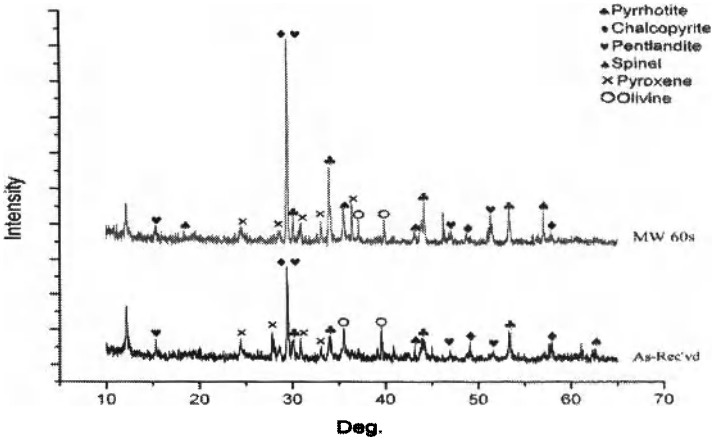

Figure 5. XRD pattern of as-received and microwave 60s material roll crushed (-100+200 mesh) sink material corresponding to (147-74μm) size fraction

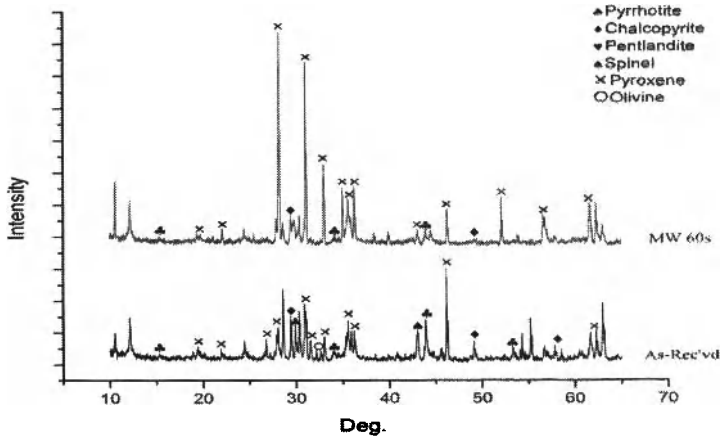

Figure 6. XRD pattern of as-received and microwave 60s material roll crushed (-200+325 mesh) sink material corresponding to (74-43μm) size fraction

Conclusion

Ore particles readily heat during MW exposure by highly absorbing magnetic mineral phases that generate thermal stresses and cracking in particles. The cracking can be used

as an aid in crushing and grinding processes of ore particles. MW treated ore particles are shown to produce more cumulative percent passing material when ball milled. MW is shown to aid in the breakage of particles shown by less abrasion of particles passed through the roll crusher. Heavy liquid separation along with XRD analysis shows that metallic bearing minerals reported to coarser size fractions by metallic-host rock liberation from MW exposure. Optimally, large size ore particles, containing sufficient amounts of highly absorbing minerals, would be MW treated to liberate metallic minerals prior to grinding in order to reduce the amount of material handling during beneficiation.

References

[1] B. A. Wills, T. J. Napier-Munn, *Mineral Processing Technology*, Elsevier, 1992

[2] A. Gupta and D.S. Yan, *Mineral Processing Design and Operations*, Elsevier, 2006

[3] Y. Hua, C. Liu, Y. Xu, "Application of Microwave Energy to Extractive Metallurgy," *Chinese Journal of Metal Science & Technology*, Vol. 6, 1990

[4] C. A. Pickles, "Microwaves in Extractive Metallurgy: Part 1- Review of Fundamentals," *Minerals Engineering*, Vol 22, pp.1102-1111, Elsevier, 2009

[5] C. A. Pickles, "Microwaves in Extractive Metallurgy: Part 2- A Review of Applications," *Minerals Engineering*, Vol 22, pp.1112-1118, Elsevier, 2009

[6] M. Al-Harahsheh, S .W. Kingman, "Microwave Assisted Leaching-a Review," *Hydrometallurgy*, Vol. 73, pp.189-203, Elsevier, 2004

[7] J.W. Walkiewicz, A.E. Raddatz, and S. L. McGill, "Microwave-Assisted Grinding," Reno Research Center, U.S. Bureau of Mines, 1989

[8] S.W. Kingman, W. Vorster, and N. A. Rowson, "The Influence of Mineralogy on Microwave Assisted Grinding," *Minerals Engineering*, Vol. 13, pp.313-327, 2000

[9] S.W. Kingman, K. Jackson, A. Cumbane, S. M. Bradshaw, N. A. Rowson, R. Greenwood, "Recent Developments in Microwave Assisted Comminution," *International Journal of Mineral Processing*, Vol. 74, pp. 71-83, Elsevier, 2004

[10] Fred C. Bond, "Crushing and Grinding Calculations Part 1," *Canadian Mining and Metallurgical Bulletin*, 1954, Vol. 47, No. 507, 466-472

[11] M. Andriese, J.Y. Hwang, W. Bell, Z. Peng, A. Upadhyaya, and S. A. Borker, "Microwave Assisted Breakage of Metallic Sulfide Bearing Ore," *2nd Annual International Symposium on High Temperature Metallurgical Processing*, TMS, Wiley, 2011

3rd International Symposium on High-Temperature Metallurgical Processing
Edited by: Tao Jiang, Jiann-Yang Hwang, Patrick Masset, Onuralp Yucel, Rafael Padilla, and Guifeng Zhou
TMS (The Minerals, Metals & Materials Society), 2012

EFFECTS OF BINDERS ADDITIVES ON COMPRESSIVE STRENGTH OF HEMATITE PELLETS IN FIRING PROCESS

Yanfang Huang, Guihong Han[1], Tao Jiang, Guanghui Li, Yuanbo Zhang, Dan Wang

School of Minerals Processing & Bioengineering, Central South University, Changsha, Hunan 410083, China

Keywords: Hematite, Oxidized pellets, Binder, Firing, Compressive strength

Abstract

Hematite concentrates are characterized by bad high-temperature reactivity and poor balling index, which restrict their large-scale application in the production of oxidized pellets. An organic additive, namely MHA, was authorized and used as binder recently in China. Compared with bentonite, the effects of MHA on compressive strength of hematite pellets at various firing conditions were investigated in this study. Experimental results showed the compressive strengths of preheated pellets with different binders were increased with increasing the preheating temperature and time. The compressive strength of preheated pellets with MHA binder was lower than that of pellets with bentonite, which can be ascribed to the high porosity of pellets with MHA binder. However, the compressive strength of roasted pellets with MHA binder was higher than that of pellets with bentonite. The compressive strength of finished pellets balled with MHA binder 1.0 wt% could meet the operation requirements of grate-kiln process.

Introduction

Hematite concentrates are characterized by bad high-temperature reactivity and poor balling index, which can lead to the appearance of those problems with increasing the energy consumption, shortening the useful life of equipment, and finally increasing the operation cost of oxidized pellets plants [1-2]. Some investigations have been conducted based on improving the pelletizing technique of hematite concentrates, such as pretreatment of raw materials [3-7], optimization of ore proportioning [8], addition of solid fuels [9-16], and so on. Employing high pressure grinding roller for the treatment of hematite concentrates revealed that the mechanical strength of wet green pellets could be improved. However, the mechanical strength of fired pellets was not improved obviously [7]. Huang, et al., pointed out that the preheating and roasting temperature may be decreased and the compressive strength of fired pellets could be increased by blending a certain proportion of magnetite concentrates with hematite [8]. Nevertheless, there are a variety of magnetite ores different in physical and chemical properties in China, resulting in the instability operation [17].
In foreign countries, travelling grate machine is widely adapted for the production of hematite oxidized pellets by mixing with solid fuels. However, the shortcoming of the technology

[1] Corresponding author: Guihong Han, Ph.D, Email address: guihong-han@hotmail.com.

above results in fuel consumption increasing [18]. Currently, grate-kiln process is the most popular process for the production of oxidized pellets in China. And there is a critical demand on the mechanical strength of fired pellets. The addition of solid fuels may decrease the strength of pellets and finally increase the preheating and roasting temperature in the grate-kiln process. Therefore, the addition of solid fuels is not suitable in China.

MHA binders, as a kind of complex additives composed of organic matters and inorganic matters, are extracted from brown coals. It is with quality of low residues (SiO_2 and Al_2O_3) and strong binding property. Generally speaking, it can serve the double purpose of binders and fixed carbon. What important is that MHA binders can perform reduction effect in weak oxidizing atmospheres [19]. In this paper, the effects of MHA binder on the preheating and roasting process of hematite pellets were investigated in this study.

Experimental

Raw Materials

The chemical composition of hematite concentrates sample is shown in Table I. According to Table I, the iron grade of sample was as high as 67.22% and the FeO content was only 0.55%. The chemical composition of bentonite is listed in Table II. The content of SiO_2 and Al_2O_3 were respectively 59.09% and 16.38%, which would decrease the TFe grade of pellets.

Table I. Chemical Composition of Hematite Concentrates (wt %)

TFe	FeO	SiO_2	CaO	MgO	Al_2O_3	LOI*
67.22	0.55	2.17	0.01	0.05	0.55	0.59

* LOI means loss of ignition.

Table II. Chemical Bomposition of Bentonite (wt %)

Fe_2O_3	SiO_2	Al_2O_3	CaO	MgO	K_2O	Na_2O	LOI
7.92	59.09	16.38	1.08	2.42	0.13	3.16	8.75

The MHA binder used in this paper was comprised of organic humic substances, as well as inorganic minerals [20-22]. The main elements of organic substances and the main chemical composition of inorganic minerals could be seen from Table III. From Table III, it could be obviously known that the content of organic substances was about 74.34%, while the main elements of organic substances were C, H and O. In addition, the main inorganic minerals were alumino-silicate. However, the content of SiO_2 and Al_2O_3 were much lower than those of bentonite.

Table III. Main Chemical Composition of MHA Binder (wt %)

Organic substances			Inorganic minerals							
C	H	O	Fe	SiO_2	Al_2O_3	CaO	MgO	P	S	Na_2O
36.93	2.87	34.54	3.37	11.41	6.63	0.27	0.18	0.05	0.58	2.12

Methods

The hematite concentrates were balled to green balls in a disc pelletizer, which was with a diameter of 1000 mm and a length of 500 mm. A certain proportion of MHA binder or bentonite was used as binder additives. In this paper, the dosage of MHA binder was fixed as 1.0 wt% while that of bentonite was 2.0 wt%. The diameter of wet green pellets was controlled in the range from 12 to15 mm. The wet pellets were dried in an oven at 110 °C for 4 h and used in the next experiments.

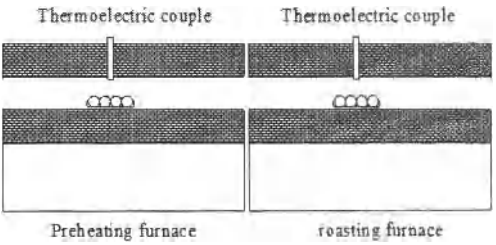

Figure1. Experimental apparatus for preheating and roasting experiments in Lab

The preheating and roasting tests were conducted in an electrically heated horizontal tube furnace shown in Figure1, which was with 50 mm internal and 70 mm external diameters. Temperature was measured with a Pt-Pt/Rh thermocouple, which was placed inside the furnace. Experiments were started when temperature profile had reached the desired value. Dried pellets were put into a corundum crucible, which was pushed into the preheating zone of the furnace. Preheated for a certain time at the preheating area, the pellets were removed to the roasting region and then roasted. At last, the roasted pellets were pulled out of the furnace and cooled in air atmosphere.

Results and Discussion

Effects of Preheating Temperature

The effects of preheating temperature on the compressive strength of preheated pellets were firstly investigated when preheating time was fixed as 10min.

Figure 2 showed that the compressive strength was increased obviously with the increase of preheating temperature. When temperature was increased to 950 °C, the compressive strength could reach to 624 N/pellet. During the preheating process, the compressive strength of pellets mainly depends on the connection between each Fe_2O_3 grain. The diffusion of Fe^{3+} enhances with increasing the preheating temperature. And the connections become stronger and stronger, resulting in the increasing of compressive strength. Compared those pellets with bentonite, the compressive strength of pellets balled with MHA binder was lower. When preheating temperature was 1000 °C, the compressive strength of preheated pellets with MHA binder was 749N/pellet. While the compressive strength of pellets with bentonite can

was above 1028 N/pellet.

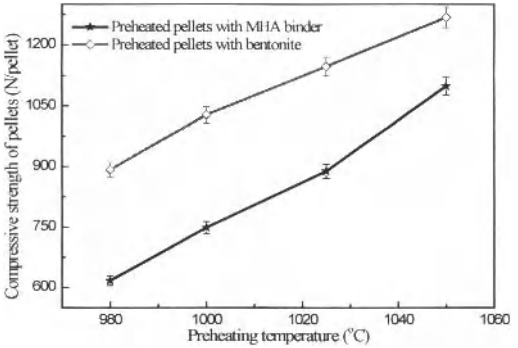

Figure 2. Effect of preheating temperature on the compressive strength of preheated pellets

The lower compressive strengths of preheated pellets with MHA binder can be caused by their higher porosity resulted by the disappearance of organic substances in MHA binder, which can be seen from Table IV. Table IV illustrated the porosity of preheated pellets with different binders under different preheating temperatures. Generally speaking, the porosity of preheated pellets with MHA binder was higher than that of pellets with benonite. When preheating temperature was 980 °C, the porosity of preheated pellets with MHA binder was 23.25%. While the porosity of preheated pellets with bentonite was only 19.28%, which was much lower than the former one. With the increase of preheating temperature, the porosities of pellets with both binders were decreasing. However, the porosity of preheated pellets with MHA binder was always higher than that of pellets with bentonite.

Table IV. Porosity of Preheated Pellets with Different Binders under Different Temperatures

Binder	Preheating temperature (°C)	Porosity (%)	Binder	Preheating temperature (°C)	Porosity (%)
MHA	980	23.25	Bentonite	980	19.28
	1000	22.48		1000	18.80
	1020	21.97		1020	18.36
	1050	21.42		1050	18.08

Effects of Preheating Time

Experimental conditions are described as follows: preheating temperature 1050 °C, preheating time changing from 6 to 15 min. The results of preheated pellets with varying preheating time are shown in Figure 3. Seen from Figure 3, it can be obviously seen that the preheating time makes an obvious effect on the compressive strength of preheated pellets. The compressive strength was also increased obviously with the increase of preheating time.

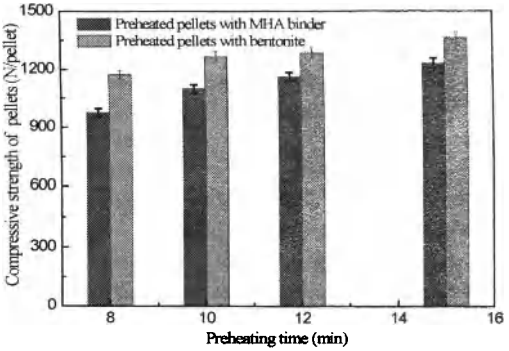

Figure 3. Effect of preheating time on the compressive strength of preheated pellets

Effects of Roasting Temperature

When preheating temperature and preheating time were kept constants as 1000 °C and 10 min, the effects of roasting temperature on the compressive strength of roasted pellets were investigated. And experimental results are listed in Figure 4. Figure 4 illustrated that the compressive strength of roasted pellets was increased obviously by increasing the roasting temperature. As the roasted temperature was 1250 °C, for instance, the compressive strength of pellets with benonite was only 2064 N/pellet. While roasted temperature was increased to 1300 °C, the mechanical strength of pellets could grow up to 2793 N/pellet. During the roasting process, the compressive strength of pellets was mainly depended on the connections between each Fe_2O_3 grains. The diffusion of Fe^{3+} can be enhanced with the increasing of preheating temperature and the connections became stronger and stronger, resulting into the increasing of compression strength.

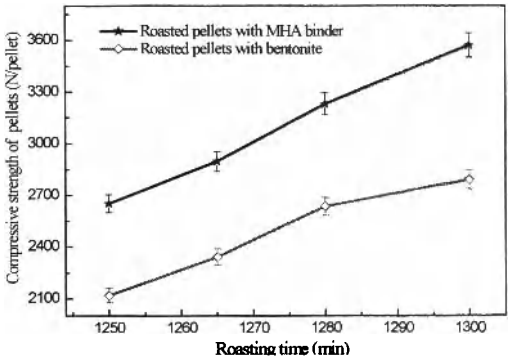

Figure 4. Effect of roasting temperature on the compressive strength of roasted pellets

However, what was worth noting was that the compressive strength of roasted pellets with MHA binder is higher than that of pellets with bentonite. In Figure 4, it could be obviously

known that the compressive strength of pellets with MHA binder was much higher than that of pellets with bentonite under the same roasting conditions. For example, the compressive strength of pellets with MHA binder can reach 2652 N/pellet at 1250 °C, which was much higher than that of pellets with bentonite. The main reason can come down to the reduction effect of MHA binder in preheating process. During preheating process, some Fe_2O_3 grains were reduced into Fe_3O_4. And the regenerated Fe_3O_4 would be reoxidized into secondary hematite in oxidizing atmosphere. The activity of secondary hematite is higher than that of original hematite. Therefore, recrystallization bonds between Fe_2O_3 particles can be enhanced by the secondary hematite grains at lower roasting temperature, which can improve the roasting properties of hematite and decrease the roasting temperature.

Effects of Roasting Time

Besides roasting temperature, roasting time is another important parameter in roasting process and it matters the production efficiency of pellets. When the roasting temperature was 1280 °C, the effects of roasting time on the firing process of pellets with different binders were investigated. And the results are shown in Figure 5.

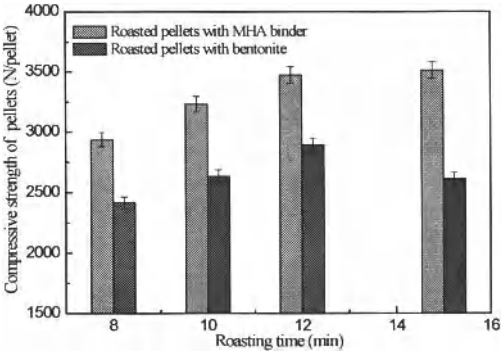

Figure 5. Effect of roasting time on the compressive strength of roasted pellets

Figure 5 indicated that the compressive strength of pellets with MHA binder was increased with the increase of roasting time in the range of 8 to 15 min. Different from MHA binder, the compressive strength of pellets with bentonite was firstly increased and then decreased. The compressive strength arrived to the maximum value when roasting time was 12 min.

Comparison of Properties of Fired Pellets Balled with Different Binders

Based on the former research, optimal preheating and roasting conditions for pellets with different binder were obtained and are shown in Table V. Under the optimized conditions, meantime, the chemical composition and compressive strength of pellets are listed in Table VI. Table V revealed that the porosity of preheated pellets with MHA binder was high to 22.48% whereas that of pellets with bentonite was only 18.80%. It can be confirmed that the

compressive strength of pellets balled with MHA binder was decreased by the higher porosity of pellets.

Table V. Optimal Conditions for Pellets with Different Binders

Binder	Preheating pellets				Roasting pellets			
	Temperature (°C)	Time (min)	Compressive strength (N/pellet)	Porosity (%)	Temperature (°C)	Time (min)	Compressive strength (N/pellet)	Porosity (%)
Bentonite	1000	10	1028	18.80	1280	10	2634	11.59
MHA	1000	10	749	22.48	1250	10	2652	12.61

Table VI. Composition of Roasted Pellets with Different Binders

Binder	TFe	FeO	SiO_2	Al_2O_3	CaO
Bentonite	65.90	0.21	3.28	0.86	0.03
MHA	67.02	0.30	2.28	0.61	0.01

When roasting temperature and time were respectively 1250 °C and 10 min, the compressive strength of pellets with MHA binder could arrive to 2652 N/pellet. For those pellets balled with benonite, however, the roasting temperature must be increased to 1280 °C that those pellets with compressive strength of 2634 N/pellet can be obtained. Table VI displayed that, the total Fe content of pellets with bentonite was only 65.90% and SiO_2 content was high to 3.28%. As it is comes to pellets with MHA binder, the TFe content was 67.02 % and SiO_2 content was decreased to 2.28%. Relatively speaking, the addition of MHA binder can decrease the roasting temperature and increase the total Fe content in roasting pellets.

Conclusions

1) With the increase of preheating temperature and preheating time, the compressive strengths of pellets with different binders were increased obviously. In addition, the strength of pellets with MHA binder was lower than that of pellets with bentonite under the same preheating parameters, which can be ascribed to the high porosity of preheated pellets with MHA binder.

2) The compressive strength of pellets was increased accompany with the increase of roasting temperature. And the compressive strength of roasted pellets with MHA binder was higher than that of pellets with bentonite. The interpretation lies in that a part of original hematite is able to be reduced to magnetite firstly, and be reoxidized to secondary hematite in oxidizing atmosphere because of the existence of MHA binder.

3) With the increase of roasting time, the compressive strength of pellets with MHA binder was increased, whereas the compressive strength of pellets with bentonite was increased firstly, and then decreased.

4) Compared with those pellets with benonite, the using of MHA binder could improve the roasting property of hematite. By replacement bentonite with MHA binder, the roasting temperature can be decreased. In addition, the addition of MHA binder also increases the TFe grade of pellets.

Acknowledgements

The authors want to express their thanks to National Science Fund for Distinguished Young Scholars (No.50725416) and Graduate Degree Thesis Innovation Foundation of Hunan Province (No.CX2010B063) for financial supporting of this investigation.

References

1. Liu Dong, "Status Quo and Analysis of China's Iron Ore Import in Recent Years Market investigation division of Iron & Steel Association," *Metal Mine*, 351(1) (2009): 12-17.
2. Chen Yao-ming, and Zhang Yuan-bo, "Study on Crystallization Rule of Oxidized Pellet," *Research on Iron and Steel*, 33(3) (2005): 10-12.
3. G. G. Hanish, "Comparison of Crushing Results Obtained by Compressive Stresses Acting upon Particle Layers," *Aufbereitungs-Tcchnik*, 10(1987): 582-590.
4. Qin Ying-wei, et al., "Improvement of Pellet Quality by Damp Milling," *Annual meeting of China's Iron & Steel*, 11(2007): 8-9.
5. Zhu De-qing, Pan Jian, and Qiu Guan-zhou, "Mechano-chemical Activation of Magnetite Concentrate for Improving its Pelletability by High Pressure Roll Grinding," *ISIJ International*, 44(2) (2004): 310-315.
6. Wang Chang-an, et al., "Effect of High Pressure Roller Mill Pre-treating Concentrates on Green Ball Propertys," *Sintering and Pelletizing*, 27(6)(2002):12-15.
7. Tang Yan-yun, A Study of the Process and Mechanism of Pelletizing PFC Specularite by Using High Pressure Roller Grinding" (Master, thesis, Central South University, 2008), 8-11.
8. Huang Zhu-cheng, et al., "Study on Mainly Made from Hematite Based Oxidized Pellets with Addition of Some Magnetite," *Iron & Steel*, 4(39) (2004): 9-14.
9. H. Wuestner, "Compressive Size Reduction: New Methods of Energy Saying in Cement Clinker and Slag Grinding," *Zement-Kalt-Oips*, 12(1985): 725-727.
10. S. C. Panigrahy, B. C. Jena, and M. Rigaud, "Characterization of Bonding and Brystalline Phases in Fluxed Pellets Using Peat Moss and Bentonite as Binders," *Metallurgical Transactions B*, 21(1990): 463-474.
13. M. Onoda, et al., "Quality improvements of lime fluxed pellets" (Paper presented at Proc of ISS-AIME 40th Iron making conference, Toronto, 1980), 286–298.
14. S. P. E. Forsmo, and A. Ha¨gglund, "Influence of the Olivine Additive Fineness on the Oxidation of Magnetite Pellets," *Int. J. Miner. Process*, 70(2003): 109-122.
15. A. A. Fabbeni, et al., "Blast Furnace Trial with Dolomite Fluxed Pellets at Whyalla Works" (Paper presented at 41th Ironmaking Proceeding, 1982), 34-36.
16. B. Bollman, "Olivine Fluxed Pellet Usage at Lone Star Steel's Blast Furnace" (Paper presented at Proc Ironmake Conf, 1985), 127-139.
17. Zhu De-qing, et al., "Pretreatment of Brazilian Specularite before Pelletization by High Pressure Roller Grinding," *Metal Mine*, 4(2008): 67-70.
18. Jiang Tao, et al., "Effects of atmosphere on roasting behaviors of carbon-burdened hematite pellets," *Journal of Central South University*, 40(4) (2009): 851-858.
19. Jiang Tao, et al., "Effects of Composite Binder (CB) on Oxidation Behavior of Iron Ore Pellets" (Paper presented at 1st International Symposium on High Temperature Metallurgical

Processing, TMS, 2010), 373-381.
20. Huang Yan-fang, et al., "Oxidation and Sintering Characteristics of Magnetite Iron Ore Pellets Balled with a Novel Complex Binder," *Mineral Processing and Extractive Metallurgy Review*. (In press)
21. Jiang Tao, et al., "Structure Characteristics and Adhesive Property of Humic Substances (HS) Extracted with Different Methods," *Journal of Central South University of Technology*, 18(4) (2011): 1041-1046.
22. Jiang Tao, et al., "Improving the Extraction Yield of Humic Substances (HS) from Lignite with Anthraquinone (AQ) in Alkaline Solution," *Journal of Central South University of Technology*, 18(1) (2011): 68-72.

3rd International Symposium on High-Temperature Metallurgical Processing
Edited by: Tao Jiang, Jiann-Yang Hwang, Patrick Masset, Onuralp Yucel, Rafael Padilla, and Guifeng Zhou
TMS (The Minerals, Metals & Materials Society), 2012

MECHANISMS OF NO FORMATION DURING SiO COMBUSTION

Nils Eivind Kamfjord[1], Halvard Tveit[1], Mari K Næss[1], Edin H. Myrhaug[2]

[1] Norwegian University of Science and Technology,
Department of Materials Technology, N0-7491 Trondheim, Norway
[2] Elkem Silicon, Alfred Getz vei 2, N0-7465 Trondheim, Norway

Keywords: Silicon process, SiO combustion, NO_x formation

Abstract

As a part of the FUME research programme being done by the Norwegian Ferroalloy Research Association (FFF), the SINTEF Group and NTNU, several measurements towards quantifying the gaseous and solid emissions from the draining of the silicon furnaces for metal have been carried out.
Based on the measured size distribution of the formed fume particles and known particle growth theory, an estimate of the growth time for the given particles has been calculated.
The formation time for the measured NO amount has also been calculated based on the fume measurements and a thermodynamic model of the furnace gases combusting with air.
The two "formation" times are in the same order of magnitude and they are therefore used as parameters in a CFD model, modelling that the formed fume particles are heating up the surrounding air and thereby forming NO according to the Zeldovich mechanism.
The measurements show an approximately equal constant NO formation per fume particle. The CFD model shows results in the same order of magnitude, supporting that the particle growth and NO formation happen under near stoichiometric conditions and are controlled by the formation of SiO_2 fume.

Introduction

NO_x is the common notion for the two gases nitric oxide (NO) and nitrogen dioxide (NO_2) formed during combustion of fuels. The main sources for human made NO_x emissions is on-/offshore transportation industry, power generations based on fossil fuels, agriculture and other industries [1].
NO_x is considered an environmental harmful gas because of its impact on air pollution [2] and has both environmental concerns [3] and health risks from exposures [4].

These consequences of NO_x emissions have led to the need for international attention and cooperation in reducing emission levels. The United Nations Economic Commission for Europe has through its "*Convention on Long-range Transboundary Air Pollution*" focused on emissions reduction and through its latest protocol "*The 1999 Gothenburg Protocol to Abate Acidification, Eutrophication and Ground-level Ozone*" set emission ceilings for 2010 for four pollutants: sulphur, NO_x, VOCs and ammonia [5].

NOx Formation Mechanisms in Combustion

In general there are three main mechanisms for NO_x formation in combustion processes: thermal NO_x, fuel NO_x and prompt NO_x [6]. Fuel NO_x is formed from nitrogen contained in the fuel itself and prompt NO_x is oxides formed quickly through the interaction between oxygen and nitrogen with active hydrocarbon species present.

The mechanism for formation of thermal NO_x was first described by Zeldovich [7] stating that at high temperatures the oxygen and nitrogen in the air would react with reactive radicals, such as O and N, to form NO, referred to as the Zeldovich mechanism. Zeldovich also stated that the mechanisms forming NO are highly dependent on the temperature reached in the O_2/N_2 mixture. A plot of the temperature dependency of the three mechanisms can be found in *Air Pollution Control Engineering* by De Nevers, page 449 [6].

Equations Describing the Formation of NO

The formation of NO is well described in literature and for our purpose we choose to use the equations and assumptions given by Turns [8]. Based on the reactions in the Zeldovich reaction scheme Turns gives the following equation for the NO formation:

$$\frac{dNO}{dt} = 2k_{1f}\left(\frac{K_{eq}P}{RT}\right)^{1/2}[N_2][O_2]^{1/2} \qquad (1)$$

Where $k_{1f} = 1.82\cdot10^{11}\exp(-38370/T)$ in $[m^3/mol*s]$, K_{eq} is the equilibrium constant for the equilibrium $O_2 \leftrightarrow 2O$ at the given temperature, T given in Kelvin, P is pressure and R is the ideal gas constant.
With the concentration of O radicals given by the equilibrium, assuming that $[N_2]$ and $[O_2]$ does not change over time and that the reverse reactions could be neglected over the time span of interest, integrating Eq. (1) from $NO_{(t=0)} = 0$ to $NO_{(t)} = NO(t)$ gives the following expression for the NO formation as a function of time, given in $[kmol/m^3]$:

$$NO(t) = 2k_{1f}\left(\frac{K_{eq}P}{RT}\right)^{1/2}[N_2][O_2]^{1/2}t \qquad (2)$$

The Silicon Process and Fume/NO Formation

Silicon is mainly produced in submerged arc furnaces through high energy consuming chemical reactions. A high temperature zone underneath the electrodes, called a crater, produces silicon and a gaseous mixture of SiO and CO. The gases from the crater zone flow upwards in the furnace and participate in reactions in the outer reaction zone (charge). The two reaction systems are strongly dependent of each other and to maintain a process with a high yield, the balance between the crater reactions and the charge reactions are vital. Above the furnace surface excess gas from the furnace combusts with air and an amorphous SiO_2 (silica fume) is formed together with CO_2.

Both of these reactions are exothermic, forcing the silicon producers to let in cold air at the furnace top to cool down the off gas before it is sent to a bag house filter.

The metal is drained from the furnace through tap holes located at the lower part of the furnace and tapping is done through one hole at a time.

The gases from the crater would mainly rise up through the furnace, but sometimes there is a connection between the crater and the taphole, giving combustion of crater gases right outside the tapping channel

NO and Silica Fume Measurements During Tapping

Several continuous measurements of the fume concentration and NO content in the off gas from the tapping of silicon have been done. The typical behaviour is shown in Figure 2, a low base level curve but with peaks in both fumes and NO.

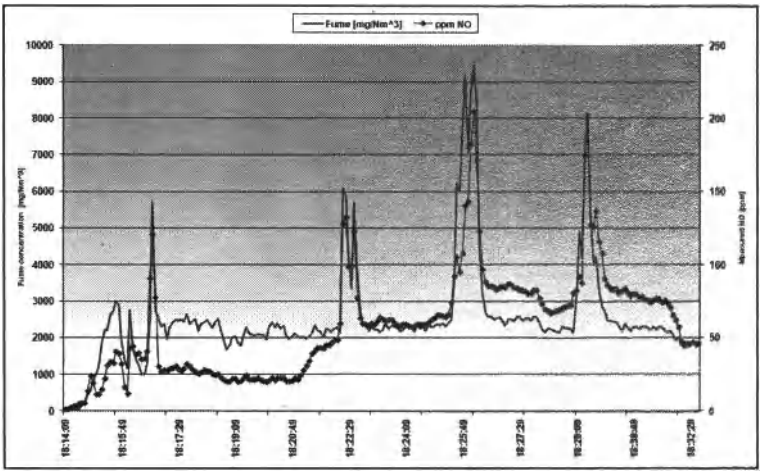

Figure 1: Fume and NOx measurements from tapping of silicon

The peaks are connected to the use of an oxygen lance to enhance the metal flow from the furnace. Both oxygen lancing (opening the tapping channel) and combustion of crater gases outside the furnace produces SiO_2 fumes, releasing high amounts of energy to the surroundings.

Chemical Analysis and Size Distribution of Fume

Silica fume samples were collected for subsequent analysis in order to ensure that the measured fume contains mainly SiO_2 and not other elements from the carbon materials in the runner or tap hole. The fume was analysed by atomic absorption spectroscopy (AAS) and combustion analysis (LECO TCH600). The content of SiO_2 in the fume was measured to 97.16 wt%.

The fumes were also examined using a scanning electron microscope (SEM). The SEM used was a Zeiss Ultra 55 Limited Edition field emission microscope. The images were recorded at an acceleration voltage of 2 - 5 kV, with magnifications 2 k - 50 k. From the SEM images, the particle size distribution and mean particle diameter where estimated by measuring and counting ~1000 particles in several images. The silica particles where perfect spheres with a size distribution of 0.001-3 μm, with 70-90% of the particles being < 0.05 μm. Based on this we also assume that the formed particles are vitreous.

Stoichiometric Combustion of the SiO/CO Gas – the NO Formation Hypothesis

A possible explanation for the observed correlation between formation of fume and NO is to assume that the energy released from the combustion heats up the air surrounding the particles, which then forms NO through the Zeldovich mechanism.

We imagine a three step reaction chain in forming both fume and NO as shown in Figure 2. Combining Ulrich's particle growth theory [9] with an additional chemical reaction forming NO we assume that SiO_2 is initially formed as a gas which in turn condenses to small droplets. These droplets collide and as time progresses, form a solid particle.

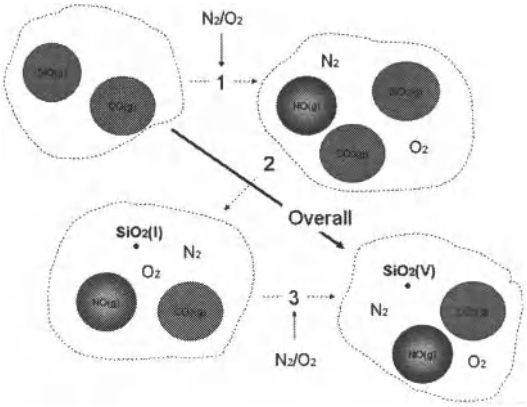

Figure 2: Reaction model for fume and NO

Step one: SiO and CO gas from the furnace (or SiO from the oxidation of metal) reacting with O_2 to form SiO_2 and CO_2 gas. Already at this stage we assume that the energy released is sufficient for NO formation.
Step two: The SiO_2 gas condenses to liquid droplets which collide into bigger and bigger droplets as described by Ulrich. The condensation into droplets is a highly exothermic reaction.
Step three: As the temperature drops the collisions between droplets will no longer result in new particles and the growth suspends. We now have an off gas of fume particles and a gas mixture consisting of NO, CO_2 and excess N_2/O_2.

NO Formation Time Based on Stoichiometric Combustion of the Furnace Gases

Based on the reaction chain in Figure 2 we set up a combustion model in HSC Sim [10] assuming that the gas mixture inside the silicon furnace consists of equal amounts of SiO and CO [11]. The model is set up to feed the reactions with just sufficient amounts of air to have a stoichiometric combustion and NO formation as measured. The furnace gas enters at 1600 °C and in the end the hot gas mixture is diluted with cold air.

Looking at Figure 3 we imagine that the second step produces a "cloud" of SiO_2 fume, and $CO_2/NO/N_2$ and that the NO content in this "cloud" is calculated to 12946 ppm.
To calculate the formation time of the NO we rearrange Eq. (2) to ppm basis and solve for the time, using the achieved temperature from the model and a pressure of one atmosphere[1].

$$t = \frac{\chi_{NO}[ppm] * P}{NO(t) * R * T} \tag{3}$$

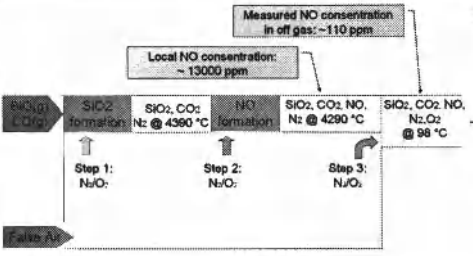

Calculated level of NO in "cloud"	Temperature in "cloud"	Formation time for NO
12946 ppm	4563 Kelvin	0.0429 Seconds

Figure 3: Combustion model and calculated results

Growth Time for Particles as Measured

The measured off gas particle concentration together with the growth theory for SiO_2 particles described by Ulrich enables us to calculate the growth time for the given mean particle size.
Ulrich gave the following equation for particle growth in a cloud of uniform particles, given that the Knudsen number[2] is greater than 10 and that the initial nuclei are already formed:

$$N = (6.8 \times 10^{-12} * c * T^{\frac{1}{2}} * C_0^{\frac{1}{6}} * t)^{-\frac{6}{5}} \left[\#/cm^3 \right] \tag{4}$$

N is the particle concentration, c is the number of successful collisions given by a sticking coefficient and C_0 defines the number of silica molecules/cm^3.

[1] T given in Kelvin, R given in [atm*m^3/kmol*K] and assuming O_2 and N_2 concentrations are constant equal to that in air

[2] The **Knudsen number** (***Kn***) being a dimensionless number defined as the ratio between the mean free path (distance travelled between collisions) and the particle diameter.

Using the equation for the specific surface area, SA = 3/(ρR), where ρ is the particle density and R is the particle radius, Ulrich also deduced an equation for the SA as a function of the above parameters, given as

$$SA = 1.81x10^{8}(T^{\frac{1}{2}} * c * C_0 * t)^{-\frac{2}{3}} \left[m^2/g \right] \quad (5)$$

Solving both equations for C_0 and combining them gives us an expression for the particle growth time:

$$t = \frac{SA^{1/2}}{\left(1.81 \cdot 10^{8} * T\right)^{1/2} * B^{6/5} * c * N} \quad (6)$$

B is the first part of Eq. (4), equal to $6.8x10^{-12}$ $[m^3/s*T^{1/2}]$ as given by Ulrich, and N is the particle concentration in the end gas mixture.

Choosing peak values in fume concentration we now calculate the growth time for the SiO_2 particles, assuming a diameter of 55 nm, density equal to 2200 kg/m^3 and at the temperature equal to the "cloud" temperature, we get the results shown in Table I.

Table I: Growth times of particles and calculated NO formation per particle. Sticking coefficient = 0.3

Fume concentrations [mg/Nm^3]	Calculated growth time of particles [sec]	Measured NO [ppm]	Moles of NO formed per fume particle
4400	0.028	110	2.14E-019
6000	0.021	133	1.90E-019
8700	0.014	210	2.07E-019

Comparing the formation time of NO from Eq. 3 to the growth time of the SiO_2 fume particles we see that they are in the same order of magnitude.

Descriptive Modeling of NO Formation from a Particle

A CFD model calculating the NO formation was set up using the COMSOL Mulitphysics software [12] together with the equation for the NO formation given by Eq. (1).

The model simulates a particle experiencing the calculated "cloud" temperature over the time span for the fume particle growth, assuming that the particle is surrounded by air and with no velocity field present. Instead of a heat source term the particle itself is given a temperature profile.

As a suited temperature profile for the particle we used the suggested combustion temperature profile given in *Air Pollution Control Engineering* by De Nevers, figure c) page 454 in [6] assuming that the particle is rapidly heated by the chemical reactions forming it and then looses heat to the surroundings over time.

Table II shows the CFD model results for each of the calculated growth times connected to the different fume concentration. The last row of Table II shows the CFD model result for the growth time of the NO formed in Step 2 in Figure 3.

If we compare the calculated amount of NO per fume particle given in Table I with the modeled NO formed in Table II we see that the results are within the same order of magnitude.

Table II: Results of the CFD simulations

Fume concentration [mg/Nm^3]	Calculated growth time [sec]	mol NO formed
4400	0.028	6.07E-19
6000	0.021	4.62E-19
8700	0.014	3.18E-19
Growth time of NO "cloud"	0.0429	9.38E-19

Discussion of Results

NO Forming Expressions

In the rate expression for NO formation (Eq. (2)) we have assumed that the content of O_2 and N_2 is at a constant level equal to that in air. If however the content of O_2 is lower the rate of NO formed would decrease. This would affect the total amount of NO formed as well as increasing the time of the NO formation in the combustion model (Eq. 3).
At a constant temperature of 4563 K, both the CFD model and Eq. (2) give a rate reduction of ~ 6 % when reducing the O_2 content with 2.5 %.
However, taking into consideration the low amount of furnace gases compared to the inlet of air in the tapping area, it is reasonable to believe that the content of O_2 in the heated air is close to 21 % and constant.

Combustion at Stoichiometric Conditions

The assumption that the combustion of the furnace gases happens at stoichiometric conditions defines the temperature at which the particle grows (Eq. (6)), the NO formation rate (Eq. (2)) and the growth time for the NO in the "cloud" (Eq. (3)).
An alternative situation would be to dilute the combustion with more air. The consequence of dilution is an end gas mixture with higher content of O_2/N_2 and a reduced "cloud" temperature. Calculations show that reduced temperature only has a minor consequence for the fume particle growth time, but the formation time for the NO "cloud" is highly affected.

As we see from Table I the measured amount of NO formed per fume particle is fairly equal and independent of the amount of fume formed. This suggests that each particle "experiences" somewhat equal conditions during growth. The similar results from the CFD model, based on parameters assuming stoichiometric combustion, and the measured NO formation per particle given in Table 1, indicate a situation where each particle experiences conditions close to a stoichiometric combustion.

Conclusions

The SiO_2 fume and NO formation during tapping of silicon have been measured. Using particle growth theory and fume properties, the growth time for the particles has been calculated.

Measured results for fume and NO have been theoretically calculated in a stoichiometric combustion model. The achieved model temperature is used in NO formation theory to calculate the formation time of the measured NO.

The calculated formation times and combustion temperature were used in a CFD modelling. The model simulates a fume particle experiencing a combustion temperature profile, which in turn was used to model the NO formation. The modelled results show NO formation in the same order of magnitude as the measurements.

Based on the correlation seen in Figure 1 between the amount of SiO_2 fume and NO formed it is therefore plausible that the combustion of SiO-gas to form SiO_2 particles controls the formation of NO. This is also supported by the calculations showing that the amount of moles NO formed per fume particle are reasonably equal, independent of the amount of fume formed.

Given the known consequences of NO_x, an increased effort to understand and explain the emissions is needed. In this respect this study has been able to describe NO formation in the silicon process in a new matter.

References

1. EEA (2009). "NEC Directive status report 2009", European Environment Agency. http://www.eea.europa.eu/publications/nec-directive-status-report-2009

2. WHO (2003). "Health Aspects of Air Pollution with Particulate Matter, Ozone and Nitrogen Dioxide". http://www.euro.who.int/__data/assets/pdf_file/0005/112199/E79097.pdf

3. Bireswar, P. and D. Amitava (2008). "Burner Development for the Reduction of NOx Emissions from Coal Fired Electric Utilitie", *Recent Patents on Mechanical Engineering*, **1**, pp:175-189.

4. WHO (2005). "Air quality guidelines for particulate matter, ozone, nitrogen dioxide and sulfur dioxide. Global update 2005 Summary of risk assessment. http://whqlibdoc.who.int/hq/2006/WHO_SDE_PHE_OEH_06.02_eng.pdf

5. UNECE (1999). "The 1999 Gothenburg Protocol to Abate Acidification, Eutrophication and Ground-level Ozone." http://live.unece.org/env/lrtap/multi_h1.html

6. De Nevers, N. (2000). *Air pollution control engineering*. Boston, McGraw-Hill.

7. Zeldovich, J. B. (1946). "Oxydation of Nitrogen in Combustion and Explotion", *Comptes Rendus (Doklady) de L'Acadèmie des Sciences de l'URSS* **LI**(3): 217-220

8. Turns, S. R. (2000). *An Introduction to Combustion: Concepts and Applications* - 2nd ed., McGraw-Hill Science Engineering.

9. Ulrich, G. D. (1971). "Theory of Particle Formation and Growth in Oxide Synthesis Flames". *Combustion Science and Technology* 4(1): 47 — 57.

10. Roine, A., P. Lamberg, et al. (2010). HSC Sim, Outotech Research Oy

11. Schei, A., J. K. Tuset, et al. (1998). *Production of High Silicon Alloys*, Tapir forlag, Trondheim

12. Comsol (2010). Comsol Multiphysics, Comsol, Inc.

3rd International Symposium on High-Temperature Metallurgical Processing
Edited by: Tao Jiang, Jiann-Yang Hwang, Patrick Masset, Onuralp Yucel, Rafael Padilla, and Guifeng Zhou
TMS (The Minerals, Metals & Materials Society), 2012

PILOT SCALE MEASUREMENTS OF NO EMISSIONS FROM THE SILICON PROCESS

Nils Eivind Kamfjord[1], Halvard Tveit[1], Ingeborg Solheim[2],

[1] Norwegian University of Science and Technology,
Department of Materials Technology, N0-7491 Trondheim, Norway
[2] SINTEF Materials and Chemistry, Sem Sælandsveg 2A, N0-7465 Trondheim, Norway

Keywords: Pilot Scale Silicon Process, Combustion, NO emissions

Abstract

Because of its negative environmental effect the attention towards NO emissions increases. This again leads to new demands from the authorities for better surveillance and control of emissions. Earlier and recent industrial measurements towards FeSi- and Si-metal furnaces reveal quite high NO-emission. The NO is believed to be produced in the combustion zone above the furnace surface, mainly as thermal NO.
In order to expand the knowledge on NO-formation in silicon metal production, a pilot scale experiment in a 440 kVA silicon furnace has been carried out. The experimental set-up was designed with a view to be able to copy and manipulate the formation mechanisms for NO by controlling the flow of false air into the off-gas system.
The resulting NO-values corresponding to the different air inlet to the furnace top, show significantly differences between the different air inlet geometries.

Introduction

NO_x is the common notion for the two gases nitric oxide (NO) and nitrogen dioxide (NO_2). Since combustion of fuels, such as gasoline, diesel, bio diesel, propane, coal, and ethanol, forms NO_x the dominating contributors to NO_x emissions are the on-/offshore transportation industry and power generation based on fossil fuels [1].

NO_x is considered an environmental harmful gas because of its impact on air pollution. NO would easily oxidize to NO_2 in the presence of ozone and NO_2 would further, in the presence of hydrocarbons and ultraviolet light, react to tropospheric ozone and nitriate aerosols. The latter being a source for ambient air particulate matter, $PM_{2.5}$ [2].
Other known environmental concerns regarding NOx are formation of acid rain when combined with oxides of sulphur (SO_x), deterioration of water quality through eutrophication (which leads to oxygen depletion) and global warming through formation and accumulation of N_2O in the atmosphere [3].
Exposure to NO_x has also a known effect on the respitory system, both with respect to long term and short term exposures [4].

These consequences of NO_x emissions have therefore led to the need for international attention and cooperation in reducing emission levels. The United Nations Economic Commission for

Europe has through its *"Convention on Long-range Transboundary Air Pollution"* focused on emissions reduction and through its latest protocol *"The 1999 Gothenburg Protocol to Abate Acidification, Eutrophication and Ground-level Ozone"* set emission ceilings for 2010 for four pollutants: sulphur, NO_x, VOCs and ammonia [5].

NO_x Formation Mechanisms in Combustion Processes

NO_x formation in combustion processes are described by three major formation processes: thermal NO_x, fuel NO_x and prompt NO_x [6]. Fuel NO_x is formed from nitrogen contained in the fuel itself and prompt NO_x is oxides formed quickly through the interaction between oxygen and nitrogen with active hydrocarbon species present.
The mechanism for formation of thermal NO_x was first described by Zeldovich [7] stating that at high temperatures the oxygen and nitrogen in the air would react to form NO via reactive radicals, such as O and N. Zeldovich also stated that the mechanisms forming NO is highly dependent on the temperature reached in the O_2/N_2 mixture. The temperature dependency for all three mechanisms can be seen in Figure 1 below.

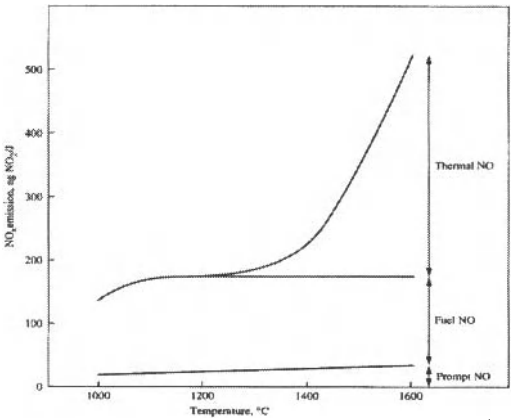

Figure 1: Temperature dependency in NOx formation mechanisms. From [7]

The Silicon Process and NO_x Formation

Silicon is mainly produced in submerged arc furnaces. A simple principle sketch of the silicon process with energy recovery utilization is given in Figure 2. The silicon process is a high energy intensity process and therefore demands production equipment that can withstand high temperatures.

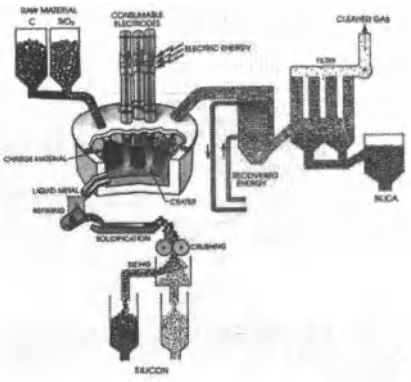

Figure 2: The silicon process. From [8]

The chemical reactions inside the furnace could be divided into an inner and outer reaction zone. The inner reaction zone, called the crater, produces silicon and a gaseous mixture of CO and SiO from the chemical reaction between quarts and SiC. The gaseous mixture will then rise up through the charge materials. The charge is considered the outer reaction zone, with chemical reactions like SiC production and SiO condensation, both vital to maintain a process with a high silicon yield. Figure 3 shows a cross section of the furnace with 2 of the 3 electrodes together with the material/gas flow patterns.

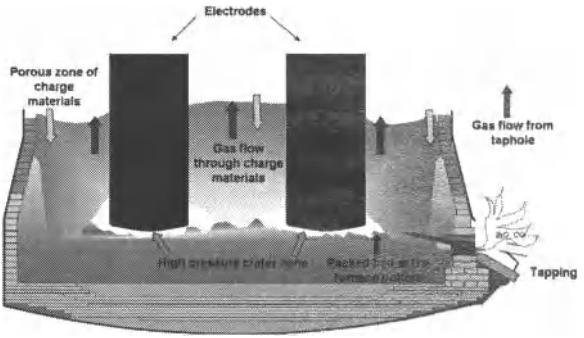

Figure 3: Cross section of a silicon furnace. From [9]

A reaction scheme of the two reaction zones are showed in Figure 4, this scheme giving 100% silicon yield from the process.

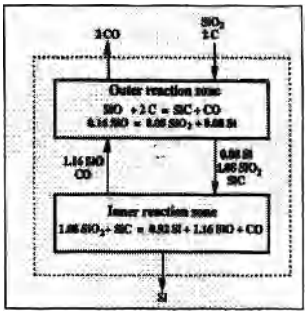

Figure 4: Reaction scheme with 100% silicon recovery. From [8]

In addition to the CO gas a real furnace always have some SiO gas escaping through the furnace top. These two gases combust with O_2 and produces CO_2 and amorphous SiO_2 (also called silica fume).
Setting y equal to the silicon recovery of the process, in other words the number of moles silicon produced per mole SiO_2 added, $0 \leq y \leq 1$, the overall process reaction becomes:

$$SiO_2(s) + (1+y)C(s) = ySi(l) + (1-y)SiO(g) + (1+y)CO(g) \quad (1)$$

The SiO combustion is a highly exothermic reaction forcing the producers of silicon to let in cold air to the furnace surface to cool down the off gases before sending them to the off gas system. This combination of hot combustion products and the inlet of air are believed to be one of the main sources for NO_x generation in silicon production. The correlation between the silica fume generation from the process and NO_x generation is showed in Figure 5 where measurements of the two was conducted towards the off gas of a 93 MVA silicon furnace in Norway.

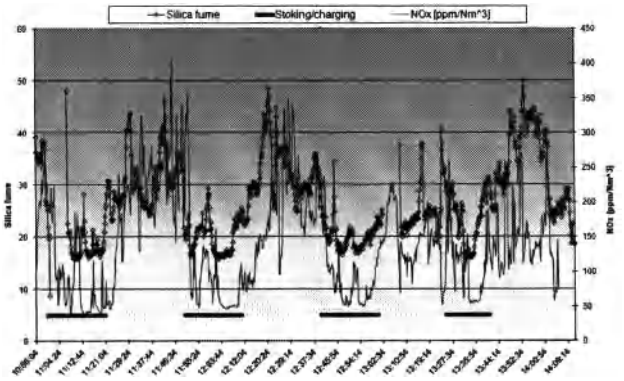

Figure 5: Silica fume and NOx measurements at a 93 MVA silicon furnace

The Pilot Scale Experiment

Based on the observations from the industrial measurements and the hypothesis that the NO_x generation is influenced by where the combusting furnace gases meet cold air, a new off gas hood was build to fit the pilot scale silicon furnace. The hood was made with two adjustable rings with holes, giving the possibility to control the height of the air inlet above the charge surface.
The pilot scale furnace with the installed hood is showed in Figure 6.

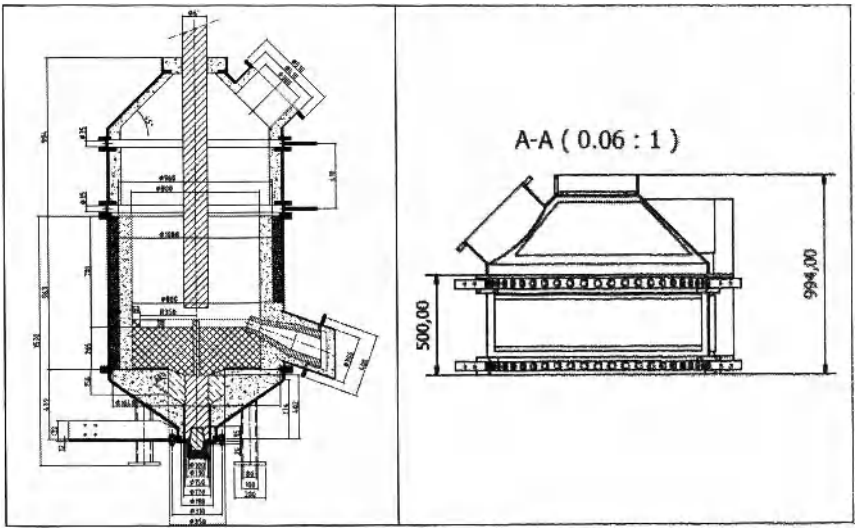

Figure 6: The pilot scale silicon furnace with hood and air inlet rings.

Each ring contains 50 holes with a diameter of 3.5 cm and is adjustable sideways, enabling the amount of inlet air to be reduced to a minimum if wanted. Design wise the rings where made in such that it was not possible to completely close the inlet of air, but when closing a ring the air inlet from that region was reduced to a minimum.

The main target for the experiment was to measure the difference between having one ring open and one ring closed. To gain a dataset which could cover any periodic behavior each ring constellation (one closed/one open) was kept for an entire charge cycle/run. At the end of the experiment other ring constellations where tested, like both closed and one closed/one ½ way open. In total there are 6 different ring configurations with data available, both rings open, both rings closed, top ring open/bottom ring closed, top ring closed/bottom ring open, top ring closed/ bottom ring ½ way open, top ring ½ way open/bottom ring closed.

The silicon pilot furnace was operating with charge materials for 44 hours, producing with a silicon yield of 62 %. It was tapped 13 times, giving a total of 87 kg's of silicon.

Measurements and Results

The chemical analysis, temperature and amount of off gas where measured right after the furnace. To analyze the off gas a Testo 350XL [10] was used and the measurements where done continuously throughout the experiment. The TESTO 350XL measures NO and measurements are done with an electrochemical measuring cell with an accuracy of 2 ppm from zero to 40 ppm and 5% of measured value for measurements above 40 ppm.

Figure 7 show the NO measurements for the entire experiment.

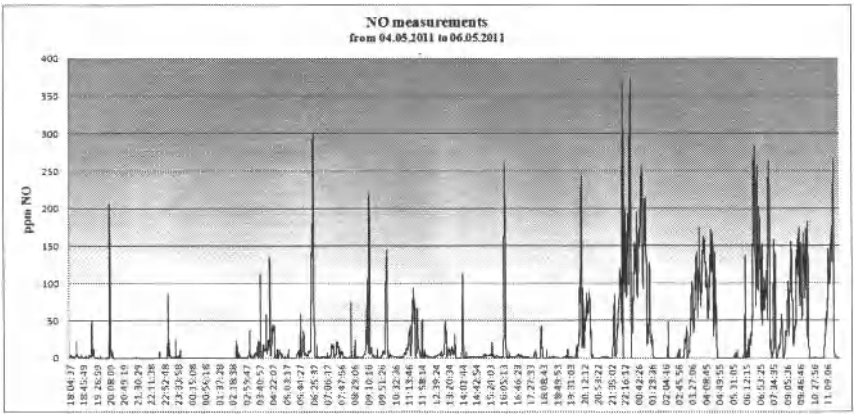

Figure 7: NOx measurements for the entire experiment.

As we see from the time chart the beginning of the experiment has a low NO formation, but with a lot of peaks in NO. Most of these peak measurements are connected to gas channels forming in the charge material, causing SiO gas to flow to the surface and combust. When a situation like this occurred the channel was covered with a small amount of fresh charge material. The general low NO formation could be explained by the fact that the chemical reactions within the furnace still is at an initial stage.
One time period is unique in that way that during this run there was no new raw materials added to the furnace. In this time period, 5 of May from 21:44 to 01:01, the NO formation is very high. As the furnace process tends to stabilize the level of NO increases and the behavior of the NO emission becomes more like the industrial behavior we see in figure 5.

Summarized results

In analyzing the results for the different ring constellations two limitations have been done. First of all the data for the run on the evening 5 of May has been removed since this run was not normal compared to the rest of the runs. Second of all, the electric power was shut off during tapping, so any data registered at electroc load below 130 kW are also removed from the resulting dataset.

Using the measured off gas amount the Testo results has been recalculated to grams/hour. Table I below shows the results for all 6 ring configurations and Figure 8 shows the same data.

Table I: Measured emissions in grams per hour. Temperature in Celsius.

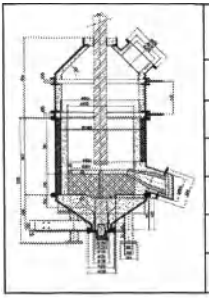

Ring position	NO	CO	Off gas temperature
Both rings open	65	98	83
Top ring open/bottom ring closed	244	164	91
Top ring ½ way open/bottom ring closed	451	119	97
Top ring closed/bottom ring open	267	251	93
Top ring closed/ bottom ring ½ way open	628	86	107
Both rings closed	656	101	107

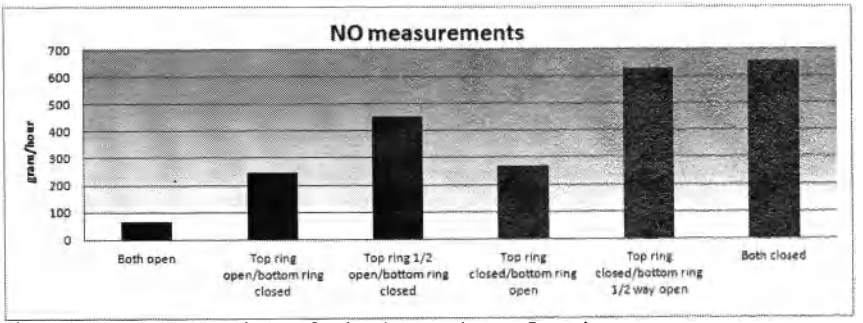

Figure 8: Measured NO emissions for the different ring configurations

Discussion

Measured Results Compared to Ring Configuration

Both the level and the difference of the different ring constellations are surprisingly high. Particularly interesting are the results showing that the NO level rise with a decreasing amount of air let into the furnace. This shows the ability to form NO even at a low supply of N_2 and O_2. One explanation might be that at a low inflow of air the overall velocity field through the hood is reduced, forming "hot spots" of air heated by the SiO combustion and still containing enough N_2 and O_2 to form NO. In that respect the velocity fields inside the hood will have a substantial effect on the NO formation.

Conclusions

Based on the data acquired from our experiment we can conclude the following for the pilot scale silicon furnace:

- Having the inlet of cold air close to the charge surface produces more NO than moving it higher towards the off gas channel.
- Decreasing the inlet of air to the combustion chamber increases the amount of NO produced substantially.
- Based on the NO results there is reason to believe that the velocity fields inside the hood influences the NO formation significantly.

Understanding the mechanisms in NO formation connected to the silicon process is of vital importance for working towards reduced emissions. In that respect this study shows that the NO emissions could be influenced by the air inlet design in the off gas system. A better understanding of the connection between the velocity fields above the furnace surface and the NO formation is needed.

References

1. EEA (2009). "NEC Directive status report 2009", European Environment Agency. http://www.eea.europa.eu/publications/nec-directive-status-report-2009

2. WHO (2003). "Health Aspects of Air Pollution with Particulate Matter, Ozone and Nitrogen Dioxide". http://www.euro.who.int/__data/assets/pdf_file/0005/112199/E79097.pdf

3. Bireswar, P. and D. Amitava (2008). "Burner Development for the Reduction of NOx Emissions from Coal Fired Electric Utilitie", *Recent Patents on Mechanical Engineering*, **1**, pp:175-189.

4. WHO (2005). "Air quality guidelines for particulate matter, ozone, nitrogen dioxide and sulfur dioxide. Global update 2005 Summary of risk assessment". http://whqlibdoc.who.int/hq/2006/WHO_SDE_PHE_OEH_06.02_eng.pdf

5. UNECE (1999). *The 1999 Gothenburg Protocol to Abate Acidification, Eutrophication and Ground-level Ozone*. http://live.unece.org/env/lrtap/multi_h1.html

6. De Nevers, N. (2000). *Air pollution control engineering*. Boston, McGraw-Hill.

7. Zeldovich, J. B. (1946). "Oxydation of Nitrogen in Combustion and Explotion", *Comptes Rendus (Doklady) de L'Acadèmie des Sciences de l'URSS* **LI**(3): 217-220

8. Schei, A., J. K. Tuset, et al. (1998). *Production of High Silicon Alloys*, Tapir forlag, Trondheim

9. Kadkhodabeigi, M., H. Tveit, et al. (2010). "CFD Modeling of the Effect of Furnace Crater Pressure on the Melt and Gas Flows in the Submerged Arc Furnaces". *Journal of Progress in Computational Fluid Dynamics* **Vol. 10**(No. 5/6): pp. 374-383.

10. TESTO. "Testo 350XL Portable Combustion Analyzer Specifications."

3rd International Symposium on High-Temperature Metallurgical Processing
Edited by: Tao Jiang, Jiann-Yang Hwang, Patrick Masset, Onuralp Yucel, Rafael Padilla, and Guifeng Zhou
TMS (The Minerals, Metals & Materials Society), 2012

3rd International Symposium on High-Temperature Metallurgical Processing

Treatment and Recycling of Solid Slag/Wastes

Session Chairs:
Xiangxin Xue
Zhiwei Peng

3rd International Symposium on High-Temperature Metallurgical Processing
Edited by: Tao Jiang, Jiann-Yang Hwang, Patrick Masset, Onuralp Yucel, Rafael Padilla, and Guifeng Zhou
TMS (The Minerals, Metals & Materials Society), 2012

AN INTEGRATED STRATEGY FOR WHOLE ECOLOGICAL UTILIZATION OF TYPICAL INDUSTRIAL SOLID WASTES IN CHINA

He Yang, Xiangxin Xue, Tao Jiang, Yong Li

School of Materials and Metallurgy, Northeastern University, Shenyang, 110819, PR China

Keywords: Industrial Solid Wastes, Titanium-bearing Blast Furnace Slag, High Silicon Iron Tailing, Boron-rich Slag, Oil Shale, Whole Ecological Utilization.

Abstract

In this paper, we describe the current status and research progress on the utilization of typical industrial solid wastes in China. We propose a creative method called "eco-utilizing wastes" with an aim of both integration and increment but without second-time waste and pollution, in terms of the characteristics of typical industrial solid wastes, such as titanium-bearing blast furnace slag, high-silicon iron tailing and boron-enriched slag as well as oil shale.

Situation of Typical Industrial Solid Wastes in China

Though mineral resources in China are abundant, most of these are low grade ores. Moreover, the distribution of mineral resources is asymmetric, which causes the increase of cost and decrease of the economic benefit. Over-exploitation of mineral resources results in a large number of solid wastes. The accumulation of solid wastes not only means the waste of valuable resources, but also causes environment deterioration. There exist some problems in the current practice of the disposal of industrial solid waste, such as only emphasizing the final results and causing new pollution and waste [1]. So the research and development of a high value-added method has a high practical relevance to our nation. Based on the present status and research progress of industrial solid wastes in China, a creative new idea and method for eco-utilization of solid wastes is proposed in this paper.

Titanium-Bearing Blast Furnace Slag

The reserve of vanadium titano-magnetite deposit is rich in China, accounting for over 36% in the world. There are more than four million tons of titanium-bearing blast furnace slag (nearly 0.8 million tons TiO_2) produced by iron and steel industries every year. Non-treated titanium-bearing blast furnace pulled into the Yangtze River not only results in the loss of precious vanadium titano-magnetite resources, but also causes environmental pollution and potential catastrophes.

Currently, the utilization of titanium-bearing blast furnace slag is classified into two parts: partial and overall utilizations. The former uses titanium-bearing blast furnace as raw material to refine titanium resources. Although the technique is valid with a clean, low cost and high productivity, the difficulty in purifying products and the low economic value of acquired perovskite material should not be ignored. The latter overall one is indeed to consider titanium-bearing blast furnace slag as the whole not only used for constructional materials but also for ecological utilization. Note that, for titanium-bearing blast furnace slag, traditional re-utilization processes aiming at preparation of dam concrete, ceramic wall brick and floor tile as well as glazed brick [2] is resource-consuming heavily. In order to efficiently utilize titanium resources and diminish influence of those solid wastes on environment deterioration, ecological utilization methods have

been proposed in this respect. As illustrated by our recent works, our groups have reported some ecological methods to utilize precious titanium resources from titanium-bearing blast furnace slag, such as photocatalysis material, antibacterial material, and plant nutritional material etc. The chemical composition of titania-bearing BF slags is shown in Table I.

Table I Chemical Composition of titania-bearing BF slags (wt %)

Chemical composition	TiO_2	SiO_2	Al_2O_3	Fe_2O_3	CaO	MgO
A slag	21.51	15.55	14.11	0.43	24.60	7.65
B slag	16.03	24.94	14.89	0.57	32.12	7.47
C slag	1.84	32.61	8.82	0.61	42.50	6.67

Notes: A slag is from Panzhihua Iron and Steel Corporation of China; B slag is from Chengde Iron and Steel Corporation of China; C slag is from Maanshan Iron and Steel Corporation of China

Photocatalysis Material

Our groups have achieved some progresses in the photocatalytic activity of titanium-bearing blast furnace slag. They are (1) photocatalytic degradation of dye Reactive Brilliant Red X-3B, Methylene Blue and Nitrobenzene and O-Nitrophenol, (2) photocatalytic reduction of Cr(VI), (3) relationship between photocatalytic activity and concentrations and particle sizes of TiO_2 in slag considered here, (3) effects of doping ions and intense magnetic field, (4) photocatalytic activity of perovskite, diopside and spinel, and (5) comparison photocatalytic activity with nanoscaled titania powders. For instance, Fig. 1 shows time-dependent photocatalytic degradation of Methylene Blue on titanium-bearing blast furnace slag under UV light irradiation.

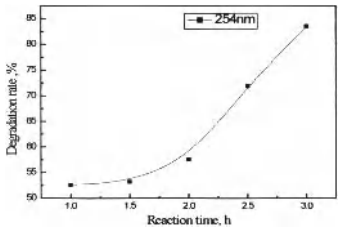

Fig. 1 Photocatalytic Degradation Rate of Methylene Blue with Titanium-bearing Blast Furnace Slag

Antibacterial Material

Escherichia coli (ATCC8099) were used to check the antibacterial activities of titanium-bearing blast furnace slag. We selected the coli bacteria (10^6CFU/ml) as the object to investigate. In order to form well-proportioned liquid film, the bacteria liquid was uniformly coated on nutrient agar in sterile Petri dish. Subsequently, the samples were put in sterile Petri dish and then the whole was placed in incubator for 18 h at 37 ℃ to observe bacterial growth. The results confirm antibacterial properties of titanium-bearing blast furnace slag from Panzhihua Iron and Steel Corporation. Furthermore, the comparison of antibacterial property of titanium-bearing blast furnace slag under different lights is presented in Table 2.

Table II Antibacterial Property of Titanium-bearing Blast Furnace Slag under Different Light

Lighting conditions	Thickness of antibacterial ring(mm)			Average
	Sample 1	Sample 2	Blank sample	
Natural-light	3.1	3.2	0	3.15
Sun-light	4.4	3.9	0	4.15
UV-light	4.1	4.3	0	4.2

Sialon

It is very expensive to synthesize TiN/Sialon multiphase electroconductive ceramics by pure nitride and oxide. From the perspective of utilizing resource and effectively reducing manufacturing cost, TiN/Sialon was fabricated by sintering with titanium-bearing blast furnace slag at ambient pressure. We already investigated their microstructures, mechanical properties, electrical conductivity, oxidation resistance and electro-discharge machining performance, as illustrated in Table III.

Table III Comparisons of combination properties among TiN/β'-Sialon, $MoSi_2$ and SiC

Properties	$MoSi_2$	Pressureless sintering SiC	TiN/β'-Sialo'
Bulk density /g·cm^{-3}	6.24	3.14~3.18	3.01
Flexure strength /MPa	150	470	120
Hardness /GPa	11.8	28.0	9.62
Linear expansion coefficient /℃^{1}	8.1×10^{-6}	4.0×10^{-6}	6.0×10^{-6}
Room temperature resistivity /Ω·cm	3×10^{-5}	0.2~300	5.0×10^{-3}
Oxidation resistance /mg·cm^{-2}	0.3（1200℃ ×200h）	0.1（1350℃ ×50h）	13.2（1200℃ ×2h）

Foam Glass-ceramics

Titanium-bearing blast furnace slag has been used to synthesize foam glass and foam glass-ceramics. Importantly, this kind of materials is found to exhibit a desired heat-insulating property and the utilization ratio of blast furnace slag is over 30 percent among raw materials. Without the affixion of nucleation agent, the synthesized sample shows best property but with a less cost. The main, minor and less crystalline phases of the glass-ceramic are P-type quartz, diopside-hedenbergite and magnesium titanate, respectively. The physical and chemical properties of the prepared sample and ordinary foam glass-ceramics are presented in Table 4.

Table IV Physical and chemical properties of the prepared sample and ordinary foam glass-ceramics

Material	Volume density	Aperture	Compression strength	Water absorption	Thermal conductivity
	/kg·m^{-3}	/mm	/MPa	/%	/W·(m·k)$^{-1}$
sample 1	255.3	4.81	19.1	10	0.12
sample 2	257.6	4.79	17.5	10	0.13
ordinary foam glass-	767-	-	9-18	5-20	0.29

ceramics	1076				

Compound Fertilizer for Plant Nutrition

With titanium-bearing blast furnace slag as a major raw material, a solid compound fertilizer was synthesized by melt method. This method enhances its dissolution, transforming nutritional elements into a form preferably absorbed by plants. The results show that the dissolution rate of titanium is over 88%.

The effects of solid compound fertilizer on growth condition, character, yield and nutritional components of soybean were investigated by agricultural cultivation experiment. The results show that compound fertilizer has two advantages to increase the plant height, pitch number, main root length, the chlorophyll content and leaf dry weight of soya and to increase the pod number per plant, pod weight per plant, grain number of single plant and grain weight per plant. In the meanwhile, compound fertilizer has little effect on the weight, content of protein and amylum per 100 grains. These results found that compound fertilizer based on titanium-bearing blast furnace slag can promote growth of soybean plant and root system and enhance the yield of soybean by increasing the pod weight per plant, grain number of single plant and grain weight per plant.

High-silicon Iron Tailings

China's iron ore tailings mainly consist of high-silicon iron tailings and its weight reaches about 80-83%. In general, high-silicon iron tailings don't contain associated elements and its average particle size is in the range from 0.04 mm to 0.2 mm. Most of high-silicon iron tailings in China located in Benxi, Anshan and Capital Iron and Steel Corporations. Chemical composition of iron ore tailings from Anshan is shown in Table 5. The mass accumulations of high-silicon iron tailings cause serious pollution and hazards to human's living environment. At the same time, high-silicon iron tailings as secondary resources have been attached importance by all the countries in the world. In recent years, the concept of converting iron ore tailings into value-added products has been scrutinized closely [3].

Table V Chemical composition of iron ore tailings (wt %)

SiO_2	CaO	Al_2O_3	MgO	Na_2O	K_2O	Fe_2O_3	TiO_2	SO_2	P_2O_5	MnO	Loss
73.27	3.04	4.07	4.22	0.41	0.95	11.60	0.146	0.25	0.19	0.315	2.18

Notes: Iron Ore Tailings from Anshan Iron and Steel Corporation of China

Porous Glass

The porous glass composite material is fabricated using a two-step method with iron ore tailings as raw material. In the first, the basic glass with uniform compositions is made via the iron ore tailings as the chief material. In the second, those obtained basic glasses are used to synthesize the high-performance porous glass composite material with appropriate additions of high aluminum bauxite, sodium carbonate, $NaPO_3$ and borax.

SiC Ceramics

SiC powder is synthesized by the carbonthermal reduction method, with iron ore tailings as the main material and carbon as the reduction agent. The main crystalline phase of the prepared sample is β-SiC and impurities crystalline phases are Fe_xSi_y (FeSi or Fe_5Si_3) and SiO_2. And then, SiC ceramics are prepared by SiC powder with the additions of Y_2O_3 and Al_2O_3 through high temperature (1800-1850 ℃) sintering under high-purity argon atmosphere. Apparent porosity, bulk density, linear shrinkage, bulk shrinkage, hardness and compressive strength of SiC ceramic at 1850℃ are found to be 25.19%, 2.49 g/cm^3, 7.56%, 13.69%, 10.8 GPa, 190.42 MPa, respectively.

TiN/Si_3N_4 Multiphase Electroconductive Ceramic

Si_3N_4 powder is synthesized by the carbonthermal reduction and nitridation method, with iron ore tailings as main material and carbon as the reduction agent. The main crystalline phase of the sample is β-SiC and impurities crystalline phases are Fe_xSi_y (FeSi or Fe_5Si_3) and SiO_2. TiN/Si_3N_4 multiphase electroconductive ceramic is fabricated by pressureless sintering under flowing nitrogen atmosphere and a powder bed from the Si_3N_4 powder and high titania slag, with Y_2O_3 and Al_2O_3 as the additives. TiN/Si_3N_4 multiphase electroconductive ceramic sintered at different temperature all contains Si_3N_4, TiN, O'-Sialon and Fe_xSi_y. For TiN/Si_3N_4 multiphase electroconductive ceramic sintered at 1550℃ using raw materials containing 25wt% TiO_2, apparent porosity, bulk density, linear shrinkage rate, bulk shrinkage, hardness and flexure strength are 10.15%, 3.32 g/cm3, 8.62%, 20.63%, 8.97 GPa and 79 MPa, respectively.

Precipitated Silica ($SiO_2 \cdot nH_2O$)

Silica ($SiO_2 \cdot nH_2O$) is a kind of ultra micro powder and widely used in the field of rubber, oil, coating, printing and medicine. Via chemical precipitation utilizing iron ore tailings and sodium hydroxide as starting materials, precipitated silica was successfully demonstrated. The SiO_2 purity in the precipitated silica was 92.3% by X-ray fluorescence analysis. It chemical formula is hydrated silicon oxide through FT-IR analysis. The structure of precipitated silica was amorphous by XRD analysis. The SEM and TEM micrograph showed that their shapes were nearly spherical and the average grain diameter was less than 150 nm. Here we further summarize some properties: the specific surface area of 108 m^2/g, pH of 5.5-6.0 in the suspending liquid, and 6.16% loss on ignition at 1000℃.

MCM-41

Owing to the high content of useful SiO_2 and Fe_2O_3 in iron ore tailings, it makes perfect economical sense to recover these minerals for industrial applications.To synthesize mesoporous materials through the natural iron ore tailings not only reduces the cost but also improves the potential pollution that is caused by the stacking problem of massive ore tailings of iron. The mesoporous material is synthesized by hydrothermal synthesis method, which has the advantage of easier process and controllability.

Experiments demonstrated that for synthesized mesoporous materials the surface area, BJH pore volume and pore wall thickness of sample was 527 m^2/g, 1.339 cc/g and 0.93 nm, respectively. The pore structure of MCM-41 was well-ordered in a tetrahedral silicon-oxygen network and symmetrical hexagonal structure with a pore diameter range between 2 and 3 nm.

Boron-rich Slag

After pyrometallurgical treatment, paigeite was turned into two products: pig iron containing boron and boron-rich slag. B_2O_3 grade of boron-rich slag was higher than that of paigeite .The highest content of B_2O_3 was up to 17%, which was much higher than the standard content of first-class boron rock which has a grade of 12% [4].

Borax

To prepare for borax, we adopted the technology route of molten sodium treatment-heating crystallization-water leaching treatment on basis of boron-rich slags as raw materials reacted with sodium carbonate at high temperature. During reaction, the molten slag was turned into sodium-modified slag after heat treatment. And then, it was leached by water at atmospheric pressure or at high pressure. Comparing with previous carbon-alkali process, this current process without kiln gas of CO_2 eliminates the need for boron roasting process and saves energy. It provides a theoretical basis for extracting boron from ludwigite with a high leaching rate of boron up to 85%.

α-Sialon-AlN-BN Composite Ceramic Material

By investigating the main chemical composition and content of boron-rich slag, we proposed a method of comprehensive utilization of boron-rich slag with an integrated, ecological and value-added aim. Based on its composition, the slag can be easily used to synthesize (Ca, Mg)-α-sialon by carbothermal reduction-nitridation (CRN) through hot-press sintering. During this process, B_2O_3 is converted into h-BN phase that possesses lubricity, high corrosion resistance, high thermal conductivity and high electrical resistivity. Measurement demonstrates that the hardness, toughness and bend strength of hot-pressed slag α-sialon ceramic reach 17 GPa, 3.74 $MPam^{1/2}$ and 333.5 MPa, respectively. These properties are very close to those of chemical α-sialon ceramics prepared by expensive chemical agents as starting materials. This method has been proven to be effective for the overall utilization of boron-rich slag.

Oil Shale Residue

The rich reserves of the oil shale resource in China rank fourth in the world. Along with the growing shortage of oil and gas resources, the oil shale has been widely recognized as an important alternative energy resource. This stresses the enormous reserves and abundant comprehensive utilization level. Oil shale residue belonging to kaolinite series is a subsidiary of waste, which is produced during the process of the dry distillation of oil shale. Aluminosilicates is the major mineral phase in oil shale residue (see Table 6). The other main components of oil shale residue are SiO_2, Al_2O_3, Fe_2O_3, which are contained in quartz and kaolinite ($Al_2Si_2O_5(OH)_5$) and nepheline ($NaAlSiO_4$), and Fe-based materials, respectively [5].

Table VI Chemistry composition of oil shale (wt %)

SiO_2	Al_2O_3	Fe_2O_3	K_2O	MgO	TiO_2	Na_2O	CaO	SO_3	P_2O_5	MnO
64.8	20.6	8.20	1.26	1.09	0.962	0.934	0.777	0.775	0.292	0.124

Glass-ceramics

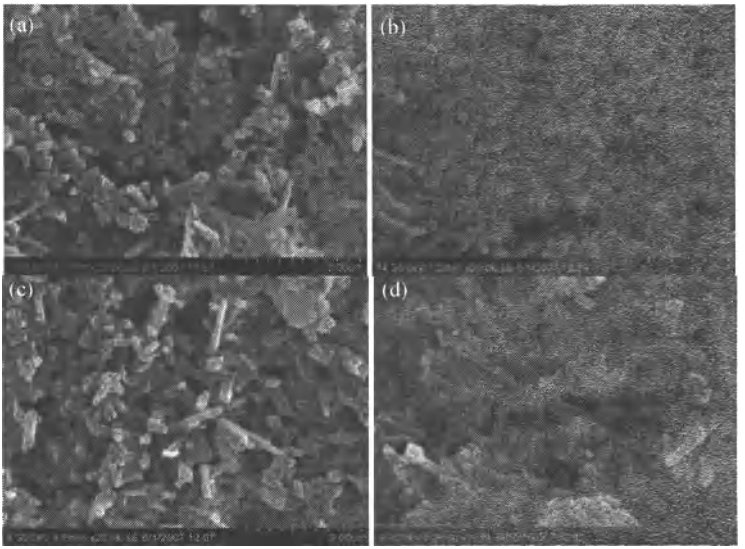

Fig. 2 SEM micrograph of glass-ceramics at various crystallization temperatures

One of the applications for oil shale residue is to synthesize the glass. As illustrated in Fig. 2, the main crystalline phase of the glass-ceramics is hedenbergite and the minor crystalline phase is anorthite consistent with the final phase of the fitted formula. The crystal of glass-ceramics forms fibrous fine crystal structure and the distribution of which is interlaced. Under the optimal condition of heat treatment, the produced glass-ceramics has the bulk density of 2.52 $g \cdot cm^{-3}$, the compressive strength of 506 MPa, the microhardness of 1020, the water absorption of 0.01, and the acid resistance of 0.02 as well as the alkali resistance of 0.01, respectively. Therefore, the performance of the glass-ceramics is better than that of ceramic tile, marble and granite, and decorative materials.

Alumina

With high activity and without roasting activation, oil shale residue can be used for preparing alumina directly by acid leaching. After extracting alumina from residue, the remaining waste with high-silicon can be used for extracting silica.The alumina produced by acid leaching main consists of prismatic-type γ-Al_2O_3, for which the extraction rate is 90.6%, the purity of the product is 91.7%, and the average particle size is 2μm. After acid leaching process, the content of SiO_2 in the slag is 92.2%, which is excellent material for preparing for silica in order to further improve the utilization value of oil shale residue.

Problems and Prospects

1) Prospect of ecological utilization technology of solid wastes is bright, but the task is arduous;
2) The composition of mineral resources in China is highly complex. With exploitation of low

grade ores, the components of tailings and slag are more complicated. Therefore, we should take an integrated strategy to solve related problems in terms of practical conditions;

3) Based on our results, effectively utilizing the valuable elements in solid wastes can be expected to promote development of the ecological utilization method for industrial solid wastes in China.

References

1. R. Y. Yin, "Steel Plant Modes vs. Industrial Ecological China-on Future Development Mode of Steel Industry," *China Metallurgy*, 38(S), (2003),1-7.
2. R. K. Wang, J. X.Zu, B. L.Gao, *et al.*, "On the Rational Ways for Comprehensive Utilization of Panzhihua Titanium Resources," *Sichuan Nonferrous Metals*, 3, (2001), 63-66.
3. J. R. Zhang and Q. M. Jia, "Research on Producing Tailing Bricks Using Ore Tailing with Abundant Silicon," *China Resources Comprehensive Utilization*, 1, (2005), 10-12.
4. X. J. Zheng, *Production and Application of Boron Hydrates*, (Beijing: Chemical Industry Press, 2007), 349-380.
5. X. M. Jiang, X. X. Han and Z. G. Cui, "New technology for the comprehensive utilization of Chinese oil shale resources," *Energy*, 32, (2007), 772-777.

3rd International Symposium on High-Temperature Metallurgical Processing
Edited by: Tao Jiang, Jiann-Yang Hwang, Patrick Masset, Onuralp Yucel, Rafael Padilla, and Guifeng Zhou
TMS (The Minerals, Metals & Materials Society), 2012

CHLORINATION BEHAVIORS OF COPPER PHASES BY CALCIUM CHLORIDE IN HIGH TEMPERATURE OXIDIZING-CHLORIDIZING ROASTING

Deqing Zhu, Dong Chen, Jian Pan, Tiejun Chun, Guolin Zheng, Xianlin Zhou

Department of Ferrous Metallurgy, School of Minerals Processing and Bioengineering, Central South University, Changsha 410083, China

Keywords: Chlorination Behaviors, Copper Oxide, Cuprous Oxide, Copper Sulphide, Calcium Chloride

Abstract

The high temperature oxidizing-chloridizing roasting is one of useful methods to separate nonferrous metals from pyrite cinder and metallurgy slag. However, as one kind of main nonferrous metals in pyrite cinder and metallurgy slag, copper's chlorination behavior is not demonstrated. In the present study, chlorination behaviors of CuO, Cu_2O and CuS at the temperature range of 1025-1175 °C in air by simulating the chloridizing roasting process of pyrite cinder and metallurgy slag have been investigated. It is shown that Cu_2O and CuS is much easier to remove, CuO is refractory to remove. In addition, the presence of SiO_2 and CaO increases the Cu removal rate from CuO while the presence of SiO_2, Al_2O_3, CaO and MgO decreases the Cu removal rate from Cu_2O. Fe_3O_4 influences the Cu removal rate from CuO and Cu_2O positively.

Introduction

As two kinds of significant secondary resources, pyrite cinder and metallurgy slag contain not only abundant iron but also considerable copper, lead, zinc etc. Millions of tons of pyrite cinder and metallurgy slag were discharged from nonferrous metal and chemical industries annually [1, 2] in China. The pyrite cinder and metallurgy slag are formed by roasting of minerals at a high temperature, so the properties of them are distinctly different from the natural iron ores, and the iron in them is closely associated with copper, lead, zinc and other nonferrous metals. High-quality pyrite cinder and metallurgy slag containing high iron and low impurities can hardly be obtained, leading to their low utilization degree [3]. Chlorination is characterized by the high reactivity of chloridion, the high volatility and low melting point of metal chlorides, and the big differences in the formation of metal chloride. Therefore, chlorination is widely applied in extraction metallurgy.

The authors have already developed the high temperature oxidizing-chloridizing reduction

roasting technology in grate-kiln to efficiently recover the valuable metals of iron, copper, zinc and lead [4]. However, the occurrences of nonferrous metals are complicated because of abundant iron oxides, silica and alumina in pyrite cinder and metallurgy slag, mainly existing in the form of oxides, sulfides, ferrites and silicates[5]. As one kind of main nonferrous metals in pyrite cinder and metallurgy slag, copper mainly exists in the form of CuS, CuO and Cu_2O.

In the 1970s, Titi-Manyaka and Iwasaki[6] formulated the chlorination and chloridization behaviors of copper oxides by thermogravimetric analyses in Cl_2 and HCl atmosphere below 1000℃, which clarified chlorination reaction steps and possible mechanisms. Masaki Kobayashi et al[7] have studied the chlorination of CuO with HCl-Ar mixture gas in the temperature range of 600 to 900℃ and found that chloridizing velocity of CuO increases with increasing the temperature, HCl partial pressure and the gas velocity.

Few researches have been done on the chloridization behaviors of copper phases with $CaCl_2$ additive while with the existing Al_2O_3, SiO_2, CaO, MgO and Fe_3O_4 by simulating system of chlorination of pyrite cinder and metallurgy slag in the temperature range of 1025-1175 ℃ in air. Thus, this work focuses on studying the chlorination behaviors of CuS, CuO and Cu_2O with the aim to understand their differences and the effects of Al_2O_3, SiO_2, CaO, MgO and Fe_3O_4 on the chlorination and to improve the high temperature oxidizing-chloridizing roasting technology.

Experimental

The chloridizing roasting tests were performed in a tube furnace (an open system in air) (see Figure 1) to simulate the chloridizing roasting in grate. Mixture of reagent grade powders were used to prepare briquettes (Φ10 mm×12 mm) and the compositions of briquettes (0.22 mass% Cu) which used to investigate the effects of chlorination temperature, time and molar ratio of Cl to Cu (n_{Cl}/n_{Cu} ratio) on Cu removal rate are shown in Table I. These compositions were determined to simulate the contents of pellet feed [4], which was composed of metallurgy slag and pyrite cinder. Table II, Table III and Table IV present the compositions of briquettes which were used to investigate the effects of Al_2O_3, SiO_2, CaO, MgO and Fe_3O_4 dosages on the chlorination.

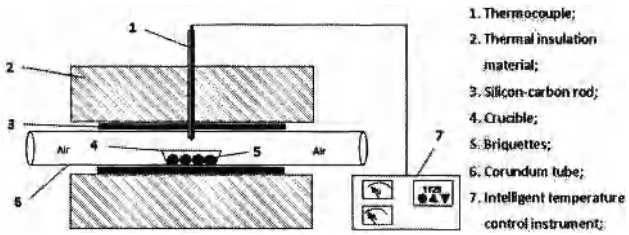

Figure 1. Schematic Diagram of Tube Furnace

Table I Chemical Compositions of Briquettes (mass %)

Sample No.	Fe_2O_3	Fe_3O_4	SiO_2	Al_2O_3	CaO	MgO	$CaCl_2$	CuS	CuO	Cu_2O	Total
No.1	25.09	65.57	6.43	1.21	0.51	0.41	0.45	0.33	0	0	100
No.2	25.15	65.57	6.43	1.21	0.51	0.41	0.45	0	0.27	0	100
No.3	25.17	65.57	6.43	1.21	0.51	0.41	0.45	0	0	0.25	100

Table II Chemical Compositions of Various Briquettes (mass %)

	Fe_2O_3	Al_2O_3	$CaCl_2$	CuO	Cu_2O		Fe_2O_3	SiO_2	$CaCl_2$	CuO	Cu_2O
	99.28	0	0.45	0.27	0		99.28	0	0.45	0.27	0
	98.03	1.25	0.45	0.27	0		96.78	2.5	0.45	0.27	0
	96.78	2.50	0.45	0.27	0		94.28	5.0	0.45	0.27	0
Effect of	95.53	3.75	0.45	0.27	0	Effect of	91.78	7.5	0.45	0.27	0
Al_2O_3	99.30	0	0.45	0	0.25	SiO_2	99.30	0	0.45	0	0.25
	98.05	1.25	0.45	0	0.25		96.80	2.5	0.45	0	0.25
	96.80	2.50	0.45	0	0.25		94.30	5.0	0.45	0	0.25
	95.55	3.75	0.45	0	0.25		91.80	7.5	0.45	0	0.25

Table III Chemical Compositions of Various Briquettes (mass %)

	Fe_2O_3	CaO	$CaCl_2$	CuO	Cu_2O		Fe_2O_3	MgO	$CaCl_2$	CuO	Cu_2O
	99.28	0	0.45	0.27	0		99.28	0	0.45	0.27	0
	98.03	1.25	0.45	0.27	0		98.03	1.25	0.45	0.27	0
	96.78	2.50	0.45	0.27	0		96.78	2.50	0.45	0.27	0
Effect of	95.53	3.75	0.45	0.27	0	Effect of	95.53	3.75	0.45	0.27	0
CaO	99.30	0	0.45	0	0.25	MgO	99.30	0	0.45	0	0.25
	98.05	1.25	0.45	0	0.25		98.05	1.25	0.45	0	0.25
	96.80	2.50	0.45	0	0.25		96.80	2.50	0.45	0	0.25
	95.55	3.75	0.45	0	0.25		95.55	3.75	0.45	0	0.25

Table IV Chemical Compositions of Various Briquettes (mass %)

	Fe_2O_3	Fe_3O_4	$CaCl_2$	CuO	Cu_2O
	99.28	0	0.45	0.27	0
	66.19	33.09	0.45	0.27	0
	33.09	66.19	0.45	0.27	0
	0	99.28	0.45	0.27	0
Effect of Fe_3O_4	99.30	0	0.45	0	0.25
	66.30	33.10	0.45	0	0.25
	33.10	66.20	0.45	0	0.25
	0	99.30	0.45	0	0.25

When the experimental temperature of the tube furnace centre reached to the target value, ten dry

briquettes loaded in a corundum crucible were pushed into the corundum tube (Φ50 mm×600 mm). In order to simulate the rotary grate technology, five minutes were required for moving the corundum crucible into the centre of tube furnace. After staying in the centre for the setting time, the corundum crucible loaded with briquettes was drawn out immediately and cooled by nitrogen gas. The removal rate of nonferrous metals was worked out by Eq. (1) based on the chemistry of fired briquettes and dry briquettes.

$$R_m = (M_0 \times m_0 - M_t \times m_t)/(M_0 \times m_0) \times 100 \quad (1)$$

Where R_m is removal rate (%), M_0 is the content of nonferrous metals in dry green briquettes (%), m_0 is mass of dry green briquettes (g), M_t is the content of nonferrous metals in fired briquettes (%) and m_t is mass of fired briquettes (g).

Results and Discussion

Chlorination Behavior of Cu Phases

Figure 2 illustrates the effect of chlorination temperature on Cu removal rates from copper phases including Cu_2O, CuO and CuS. It can be seen that the Cu removal rates from Cu_2O, CuO and CuS increase with increasing the roasting temperature, especially CuO. The higher temperature favors the formation of HCl (see Figure 4), which promotes the chlorination of Cu_2O, CuO and CuS. CuO is an unstable compound and begins to decompose to Cu_2O at about 1075°C in air [8, 9]. The higher the temperature is, the more CuO decomposes to form Cu_2O which is easier to remove by chlorination. So the effect of temperature is more important for chlorination of CuO. When the temperature reached 1175°C, the Cu removal rate from CuO decreased. The reasons may be that the volatilizations of $CaCl_2$ and HCl dramatically increase with an increase in roasting temperature. The experimental results show that the Cu removal rate from CuS is the highest and the Cu removal rate from CuO is the lowest. But the thermodynamic calculation (see Figure 3.) shows CuS is the most difficult to remove. According to the literature [10], CuS is oxidized to Cu_2O at 422-585°C or above 1000°C. SO_2, which is obtained from oxidation of CuS, can promote the formation of Cl_2 [11] which is more effective agent than HCl [6]. So the Cu removal rate from CuS is the highest.

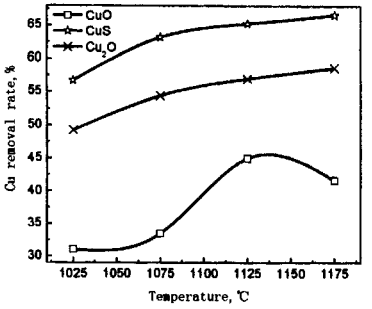

Figure 2. Effect of Chlorination Temperature on Cu Removal Rates from Copper Phases (chlorinating for 10min, $n_{Cl}/n_{Cu} = 2.4:1$)

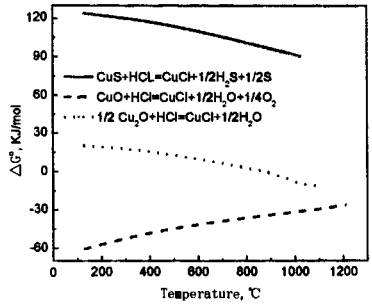

Figure 3. Relationships between Gibbs Free Energy of Copper Phases Chlorination and Temperature

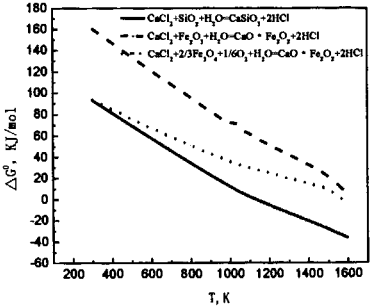

Figure 4. Gibbs Free Energy of The Formation of HCl by The Reaction of $CaCl_2$ with SiO_2,

Fe_2O_3 and Fe_3O_4

With extending the time, the Cu removal rates from Cu_2O and CuS slightly increase, while the Cu removal rate from CuO increases from 41.91% to 50.34% (see Figure 5). With an extension of the roasting time, part of CuO decomposes to form Cu_2O which is easy to chloridize. So the effect of time is more important for CuO. It gets obvious that the chlorination of CuO and Cu_2O happen simultaneously within 20min because of the low decomposition rate of CuO to Cu_2O, and the chlorination of CuO needs longer time than that of CuS and Cu_2O. Compared to CuO, the Cu removal rate from CuS is almost constant when the time exceeds 5min, which indicates the oxidation rate of CuS is much faster than the decomposition rate of CuO.

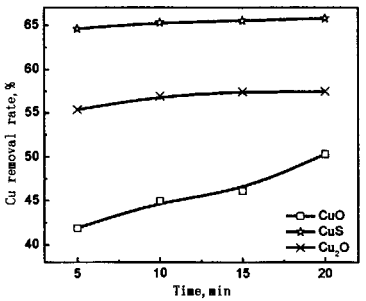

Figure 5 Effect of Time on Cu Removal Rate from Copper Phases (chlorinating at 1125℃ and $n_{Cl}/n_{Cu} = 2.4:1$)

By fixing the temperature at 1125℃, a roasting time of 10min, the effect of Cl dosage was investigated. With increasing ratio of n_{Cl}/n_{Cu}, the Cu removal rates from Cu_2O, CuO and CuS dramatically increase (see Figure 6). It is probably the reason that the higher the n_{Cl}/n_{Cu} ratio, the higher HCl concentration for chlorination, which promotes the Cu removal from copper phases. When the n_{Cl}/n_{Cu} ratio increases from 1.2 to 6.0, the Cu removal rates from CuO, Cu_2O and CuS increase from 20.76%, 28.97% and 51.94% to 74.71%, 84.47% and 81.85%, respectively. Therefore, the Cu removal strongly depends on the amount of Cl addition, especially CuO and Cu_2O.

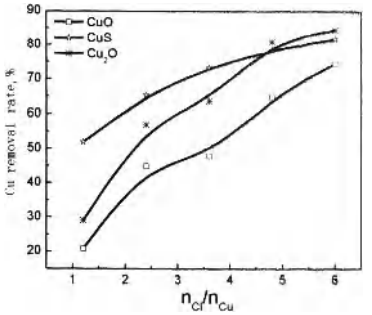

Figure 6. Effect of Cl Dosage on Cu Removal Rate from Copper Phases (chlorinating at 1125℃ for 10min)

Effect of Al_2O_3, SiO_2, CaO, MgO and Fe_3O_4 on Chlorination of Cu Phases

As shown in Figure 7, Al_2O_3, SiO_2, CaO and MgO decrease the Cu removal from Cu_2O while SiO_2 and CaO increase the Cu removal from CuO, and Al_2O_3 does not have effect on the removal of CuO. The presence of SiO_2 and Al_2O_3 contributes to the formation of more stable aluminate $Cu_2O{\cdot}Al_2O_3$ and silicate $2Cu_2O{\cdot}SiO_2$ by reacting with Cu_2O. The presence of SiO_2 increases Cu removal from CuO as SiO_2 promotes the formation of HCl (see Figure 4). CaO, which captures the released Cl and reduces the HCl volatilization into air, results in the increase of Cu removal rate from CuO. However, $CaCu_2O_3$, which is produced by the reaction of CaO with Cu_2O [12], may reduces the removal of Cu_2O. In addition, the reaction of MgO with Fe_2O_3 can reduce the reaction of $CaCl_2$ with Fe_2O_3 and H_2O from which HCl is produced, so the production of HCl decreases and the volatilization of $CaCl_2$ into air increases. That is why Cu removal rate from CuO and Cu_2O decreases.

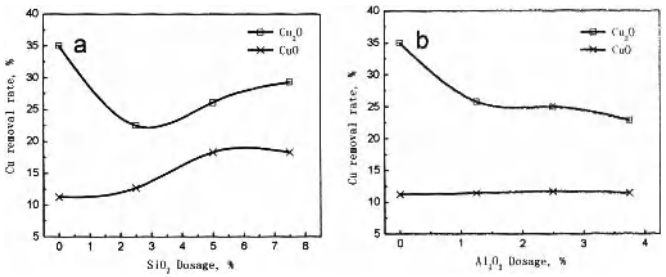

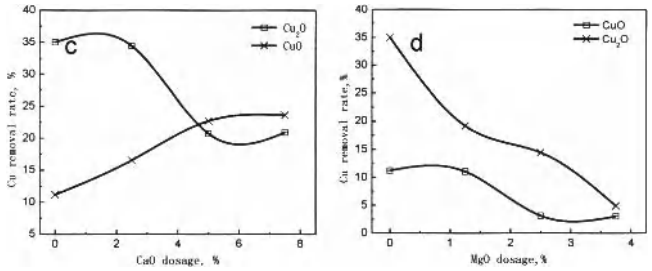

Figure 7. Effect of Al_2O_3, SiO_2, CaO and MgO Dosage on Cu Removal (chloridizing at 1125℃ for 10min, and n_{Cl}/n_{Zn} = 2.4:1; a-effect of SiO_2 on Zn removal, b- effect of Al_2O_3 on Zn removal, c- effect of CaO on Zn removal, d- effect of MgO on Zn removal)

As shown in Figure 8, the presence of Fe_3O_4 increases the Cu removal rate from CuO and Cu_2O. Fe_2O_3 oxidized from Fe_3O_4 is easier to promote the formation of HCl (see Figure 4), so Fe_3O_4 activates Cu removal from CuO and Cu_2O. Furthermore, oxidation of Fe_3O_4 provides more energy for chlorination reactions and decreases the oxygen concentration in the briquettes. The less oxygen concentration favors the CuO decomposes to Cu_2O [9].

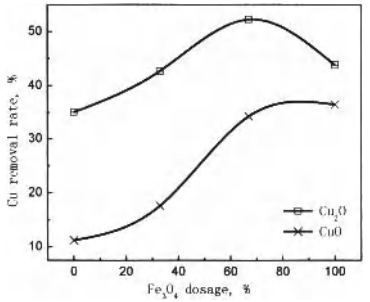

Figure 8. Effect of Fe_3O_4 Dosage on Cu Removal (chloridizing at 1125℃ for 10min, n_{Cl}/n_{Zn} = 2.4:1)

Conclusions

1. The thermodynamic equilibrium calculations and experiment results show that Cu_2O is the easiest to remove, CuS is the most difficult to remove and CuO is in the middle in the high temperature oxidation-chlorination technology. Most of CuS are oxidized to oxides and then chloridized. In addition, the Cu removal strongly depends on the amount of Cl addition, especially CuO and Cu_2O.
2. The experiment results indicate that the gangues (Al_2O_3, SiO_2, CaO and MgO) and Fe_3O_4

clearly influence Cu removal. The presence of Al_2O_3, SiO_2, CaO and MgO decreases Cu removal from Cu_2O. SiO_2 and CaO influence the Cu removal positively from CuO while MgO influences the Cu removal negatively from CuO. In addition, Al_2O_3 does not have a relevant effect on the removal of CuO. The existence of Fe_3O_4 increases the Cu removal from CuO and Cu_2O.

References

1. Z. H. Guo, et al., "Mineralogical characteristics and environmental availability of non-ferrous slag," *Journal of Central South University (Science and Technology)*, 38(2007), 1100-1105.
2. X. Liu, et al., "Comprehensive utilization of burned slags of sulphuric acid making," *Metal Mine*, 315(2002), 51-54.
3. P. Chen, X. J. Lv, and X. Q. Cui, "A Study and Application of Pyrite Cinder Beneficiation," *EXPRESS INFORMATION OF MINING INDUSTRY*, 5(2008), 71-74.
4. D. Q. Zhu et al., "'One Step' Technology to Separate Copper, Zinc, Lead Form Iron in Metallurgical Slag And Pyrite Cinder: Part 2 - Pilot Test," 2nd International Symposium on High-Temperature Metallurgical Processing,The Minerals, Metals and Materials Society., ed. J. Y. Hwang, et al. 2011, United States of America.: WILEY.
5. Metallurgical Laboratory of Central South College of Mining and Metallurgy, *Chlorination Metallurgy* (Beijing: Metallurgical Industry Press, 1978).
6. Titi-Manyaka and Iwasaki, "Thermogravimetric Investigation of the Chlorination Behaviors of Some Common Metals and Their Oxides," *Society of Mining Engineers, AIME*, (252)1972, 307-313.
7. M. Kobayashi, Y. Ueda, and F. Noguchi, "On the Mass Transfer in the Chloride Volatilization of CuO by HCl Gas," *Journal of the Japan Institute of Metals*, 39(1975), 240-245.
8. R. J. Dong, *Metallurgy Principle*(Beijing: China Machine Press, 1980).
9. Z. Z. Zhu and J. Q. He, *Modern Metallurgy of Copper*(Beijing: Science Press, 2003).
10. J. G. Dunn and C. Muzenda, "Thermal oxidation of covellite (CuS)," *Thermochimica Acta*, 369(2001), 117-123.
11. R. Z. Vracar and K. P. Cerovic, "The study of chlorination kinetics of copper(I)sulfide by calcium chloride in the presence of oxygen," *Metallurgical and Materials Transactions B-Process Metallurgy and Materials Processing Science*, 31(2000), 723-731.
12. G. H. Hou, X. Sheng and Z. Z. Xu, "Effect of Copper Oxide on Decomposition Kinetics for Calcium Carbonate," Journal of the Chinese Ceramic Society, 33(2005), 109-114.

3rd International Symposium on High-Temperature Metallurgical Processing
Edited by: Tao Jiang, Jiann-Yang Hwang, Patrick Masset, Onuralp Yucel, Rafael Padilla, and Guifeng Zhou
TMS (The Minerals, Metals & Materials Society), 2012

Effect of Iron containing Metallurgical Byproducts on Pulverized Coal Combustion Efficiency

ZOU Chong, WEN Liangying, ZHANG Shengfu, BAI Chenguang, TAN Xiuqin

College of Materials Science & Engineering, Chongqing University, Chongqing 400044, China

Key words: pulverized coal injection, combustion efficiency, metallurgical byproducts containing iron, TG-DSC method

Abstract

Eight typical metallurgical byproducts containing iron were selected based on the effect of the chemical composition, particle size, additives on the burnout degree of pulverized coal. Effect of three typical byproducts including fine iron ore, BOF dust and BOF sludge on combustion reactivity and combustion efficiency were investigated using TG-DSC method. The results indicated that the three additives have obvious catalytic effects on pulverized coal. By comparison, the relative active sequence of byproducts to the catalytic combustion can be described as follows: BOF dust>BOF sludge>fine iron ore. Moreover, adding BOF dust as component of additives also shows significant catalytic effects on combustion efficiency during rapid heating process.

Introduction

China is the largest producer in the world with an annual output reaching over 6 billion tons. Solid wastes arising from iron and steel making increases the environment pressure in recently years. For instance, annual output of dust during the production of iron and steel making in China reach up to 5 million tons, which is close to 8%~15% of the amount of steel [1]. Another characteristic of these byproducts is they are finer particle which are just harder to deal with. Since some of solid wastes, including dusts, scales, and sludge, usually contain high iron content, sintering plants have traditionally been used to recycle byproducts in integrated steel plants in China. However these byproducts also have noticeable effects on sinter quality, sinter strength and productivity and, therefore, waste recycling is limited depending on the analysis of the waste materials [2]. Another method which is pre-treatment of byproducts in pelletizing process, increases of energy consumption and production cost. In addition, metallurgical byproducts often contain heavy metals and alkalis. For these reasons, recycling rate of the byproducts in China is very low. Therefore, how to recycle the byproducts in iron and steel making process is an important subject.

Pulverized coal injection (PCI) is an effective technology to reduce blast furnace coke consumption and, therefore, cokemaking-related environmental problems [3]. Investigations have recently been made on the combustion properties of pulverized coal with admixtures, such as Shredded light fraction [4], plastic wastes [5], tyre powder [6], biomass [7], etc. The purpose of mixed injection is to enhance the combustion efficiency and deal with wastes. Besides, many studies have carried out to investigate the catalytic combustion behavior of coal [8~10]. However, most of catalysts of coal combustion are chemical compounds, resulting in high cost of investment.

Recent studies have suggested that Fe_2O_3 has excellent catalytic effect in coal combustion process [10]. Other studies have shown that metallurgical dust can increase of the combustion degree of some coals by the "solid oxygen" supply from iron oxides and catalytic effects, respectively [11]. Owing to the high iron oxides in

metallurgical byproducts, this research is to examine the possibility of injection metallurgical byproducts as catalysts together with coal into the blast furnace, which is a closed loop recycling processes. The main objective is to provide the preliminary information on the combustion behavior of coal with metallurgical byproducts addition.

Experimental

Samples

The fuel selected is a typical PCI coal, ground and sieved to -0.074mm. Table 1 presents the ultimate and proximate analysis of the pulverized coal, and Table 2 presents their ash composition. Anthracite is dried at 110℃ in oven for 3 h.

Table1 Proximate and ultimate analysis of the coal (mass%)

Proximate analysis result				Ultimate analysis result				
M_{ad}	A_{ad}	V_{ad}	FC_{ad}	C_{ad}	H_{ad}	O_{ad}	S_{ad}	N_{ad}
0.46	12.54	10.80	76.71	78.22	2.49	4.86	0.52	0.91

Table 2 Ash compositions analysis of coal (mass%)

SiO_2	CaO	Al_2O_3	MgO	Fe_2O_3	TiO_2
58.22	6.10	27.65	0.55	4.12	2.84

Eight typical metallurgical byproducts containing iron are selected. These include iron ore, sintering dust, bag dust, gravitational dust, BOF dust, EAF dust, BOF sludge and mill scale. The compositions of metallurgical byproducts are given in table 3.

Table 3 Compositions of metallurgical byproducts (mass %)

	Iron ore	Sintering dust	Bag dust	Gravitational dust	BOF dust	EAF dust	BOF sludge	Mill scale
TFe	64.4	39.9	34.9	39.6	39.6	32.25	48.38	73.87
Fe_2O_3	69.07	56.48	49.76	56.34	56.2	49.82	61.38	93.90
CaO	0.5	14.6	3.8	3.5	8.9	27.20	11.25	0.05
SiO_2	5.36	6.62	7.05	6.60	13.91	9.64	3.61	0.32
MgO	0.43	3.83	3.32	2.99	4.74	0.88	5.49	0.18
Al_2O_3	1.81	3.04	4.18	4.27	2.75	0.15	1.02	0.15
Zn	0.053	0.047	2.92	0.53	0.41	21.86	0.25	0.046
C	—	4.28	10.31	12.51	5.82	1.43	0.32	—
S	0.208	0.485	0.511	0.281	0.095	1.08	0.220	0.45
P	0.086	0.073	0.084	0.081	0.104	0.289	0.130	0.086

2.2 Experimental method

In order to screen metallurgical byproducts, additives are added to the dry pulverize coal (mass 2%, 4% and 6%) respectively and ground physically for 30 min in a quartz crucible. Coal samples combustion in muffle furnace in the preparation experiment. The heating temperature is 850℃, the holding time is 30min.

A thermogravimetric-analyzer couple d with Differential Scanning Calorimetry (NETZSCH, STA449C) are used to determine the combustion process of anthracite. The reference samples are 10±0.2mg at a heating rate of 15℃/min. The heating temperature range is from room temperature to 1000 ℃. The atmosphere is air at a

flow rate of 50 L/min.

The expand experiment is performed in by injecting pulverized coal into a specially designed heating furnace, as shown in Fig.1. This system is comprised of heating furnace, coal injection apparatus, air supply apparatus, solid residue collecting apparatus. The furnace temperature is 1100℃ and its heating rate is 3.6℃/min

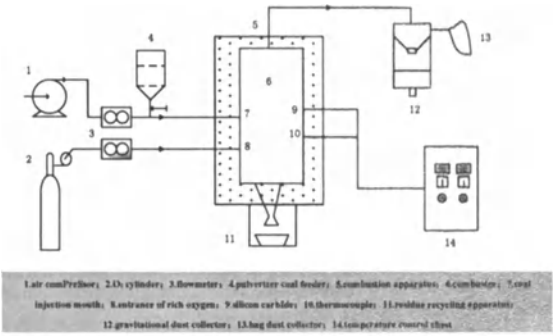

Fig.1 pulverized coal injection apparatus

Results and discussion

Selection of metallurgical byproducts

Effect of metallurgical byproducts on burnout rate of pulverized coal is shown in Fig.2. It can be seen from Fig.2(a) that fine iron ore and bag dust can increase burnout rate of pulverized coal obviously, and sintering dust can increase burnout rate when the addition amount is blew 4%. However, there is no obvious improvement in burnout rate of pulverized coal with gravitational dust addition. It can be seen from Fig. 2(b) that BOF dust and BOF sludge can increase the burnout rate. BOF dust has best catalytic effect when the addition amount is 4%, while the effect of BOF sludge is enhanced by increasing the addition amount. By contrast, there is negative effect on burnout rate with mill scale addition. However, EAF dust has no obvious effect on burnout rate of pulverized coal.

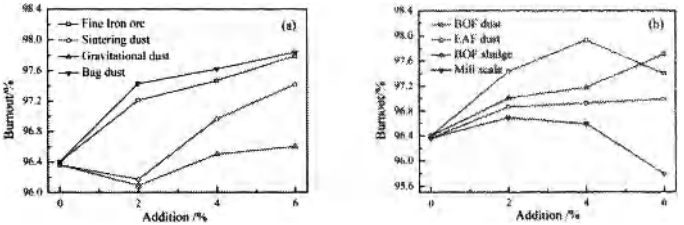

Fig.2 Effect of metallurgical byproducts on burnout rate of pulverized coal

In addition, for a stable operation of a blast furnace an increased input of zinc should be avoided [2], thus the amount of zinc of additives should very few. It can be seen from table 3 that the amount of zinc of bag dust and EAF dust are 2.92% and 21.86%, respectively. Such these dust should not use as additives of pulverized coal to avoid the negative effect of zinc on blast furnace.

What's more, another significant indicator to the catalysts is particle size. The size distribution of metallurgical byproducts is given in table 4. It can be seen that the mean particle size is blew 100μm. The

relative particle size sequence of metallurgical byproducts can be described as follows: sludge < dust < iron ore < mill scale. Base on distribution in pulverize coal and catalytic effect, mill scale should been use as additives of pulverized coal combustion.

Table 4 The size distribution of metallurgical byproducts (mass %)

	Iron ore	Sintering dust	Bag dust	Gravitational dust	BOF dust	EAF dust	Steel plants sludge	Mill scale
0~10	0.30	53.80	54.74	35.98	61.75	59.59	99.94	1.36
10~50	24.13	45.77	45.24	33.42	38.12	20.52	0.06	12.37
50~100	39.44	0.42	0.00	18.74	0.14	9.42	0.00	38.10
100~200	29.81	0.00	0.00	10.21	0.00	8.12	0.00	41.26
above 200	6.32	0.00	0.00	1.65	0.00	2.40	0.00	6.92
Mean particle size /μm	72.89	12.93	12.01	45.58	10.79	5.58	1.64	97.73

In conclusion, considering from chemical compositions, particle size, and additives on the burnout degree of pulverized coal, we choose iron ore, BOF dust, and steel plants sludge as additives. The zinc amount of these additives are blew 0.5%, particle size is blew 74μm, and they have obvious positive effect on burnout rate.

Effects of metallurgical byproducts on coal combustion reactivity

TG-DTG curves of combustion process of coal with iron ore, BOF dust, and steel plants sludge are shown in Fig. 3. It can be seen from the Fig. 3 that additives can improve the combustion process of coal above 500℃. Three characteristic parameters of combustion, the ignition temperature, combustion rate and the burnout temperature, are disscussed on the following.

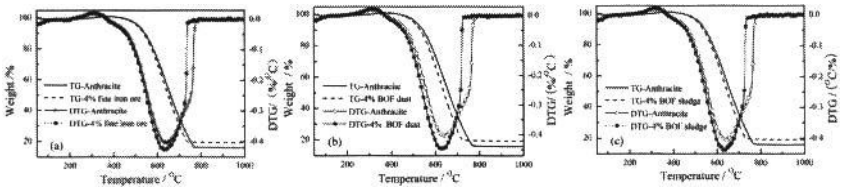

Fig.3 TG and DTG curves of coal samples during combustion process (a: iron ore, b: BOF dust, c: steel plants sludge)

The ignition temperature is an important parameter describing the combustion reactivity. In this work, the ignition temperature is determined by TG-DTG methods [10]. The ignition temperature of coal is 543℃. By contrast, the ignition temperature of coal with iron ore, BOF dust, and steel plants sludge are 533℃, 534℃and 534℃, respectively. That is, the reduction in the ignition temperature of coal with additives are about 10℃, which show that additives had a positive effect on decreasing the ignition temperature. Chemically, metallurgical byproducts contain 50%~70% Fe_2O_3 compound from compositions analysis. Studies conducted by many researchers [9, 10] have shown that Fe_2O_3 compound has catalytic effects on coal pyrolysis. It is found that catalytic pyrolysis resulted in the volatile matter released and pore structure developed. Moreover, Fe_2O_3 compound can increase free radicals and functional group on the char surface, and therefore reduce the ignition temperature.

The combustion rate reflects violence of the reaction between carbon and oxygen. It can be seen from Fig. 3 that combustion rate of coal increase significantly above the ignition temperature when adding additives. Furthermore, the maximum combustion rate increase and its corresponding time shift to earlier. Fe_2O_3 compound of metallurgical byproducts can accelerate the oxygen transfer between carbon and O_2, therefore

improve the oxidation and combustion processes. In this work, the flammability index C [12] is used to evaluate the combustion characteristic, which can be described as follows:

$$C = \frac{(dw/dt)_{max}}{T_i^2} \quad (1)$$

The larger value of index C, the better flammability. The characteristic parameters of blends with additives and coal-raw are obtained from combustion curves are listed in table 5. The flammability index C of coal-raw is 6.38. By contrast, the flammability index C of coal with iron ore, BOF dust, and steel plants sludge are 7.02, 7.05 and 7.01, respectively. The result also further shows that additives improve reaction rate between the corresponding time of the ignition temperature and the maximum combustion rate.

Burnout behavior is the other important parameter describing the combustion reactivity. The shorter the burnout time, the better combustion reactivity. From table 5, it can be seen that the burnout temperature of coal-raw is 775℃. However the burnout temperature of coal with iron ore, BOF dust, and steel plants sludge are 739℃, 723℃and 732℃, which decrease by 36℃, 52℃and 43℃, respectively. Besides, the burnout index D_f is used to evaluate the burnout characteristic, which can be described as follows [9]:

$$D_f = \frac{(dw/dt)_{max}}{\Delta t_{1/2} t_m t_f} \quad (2)$$

The larger the D_f, the better the burnout behavior. As shown in table 5, the burnout index D_f of coal-raw is 14.68. However the burnout index of coal with iron ore, BOF dust, and steel plants sludge increase to 19.01、20.39 and 19.72, respectively. The results indicate that the burnout temperature and burnout time reduce, and combustion become concentrated and shorten with additives addition.

Table.5 Effects of metallurgical byproducts on the combustion reactivity of coal

Samples	T_m/℃	T_f/℃	T_i/℃	$\Delta t_{1/2}$/min	t_m/min	$(dw/dt)_{max}$ (%/min)	C (10^6%·min^{-1}·K^{-2})	D_f ($\times 10^{-5}$)
Anthracite-raw	635	775	543	14.67	40.00	4.25	6.38	14.68
Iron ore fines	634	739	533	12.80	39.93	4.56	7.02	19.01
BOF dust	631	723	534	12.35	39.73	4.59	7.05	20.39
BOF sludge	632	732	534	12.53	39.80	4.57	7.01	19.72

Effects of metallurgical byproducts on coal combustion efficiency

As we all know, the main function of coal injection in blast furnace is providing heat for raceway, which result in saving coke. Thus, in addition to investigate the metallurgical byproducts on combustion reactivity, but also need to study the effects of additives on heat release and its rate of coal combustion. In this study, DSC measurements are carried out to estimate the heat release rate. DSC results of coal samples during combustion process are shown in Fig. 4. It can be observed that additives have no obvious effect under 400 ℃ However, the shape of curves changed, indicate that heat release rate speed up after adding additives above 400 ℃ The closed area of DSC curves and baseline peak area are obtained, and the total values of enthalpy can be calculated using Eq. (3) as follows:

$$\Delta Q = \frac{k\int h(t)dt}{m_0} = \frac{kS}{m_0} \quad (3)$$

Where $h(t)$ is the ordinate value of DSC (mW), k is a constant, m_0 is an initial mass of samples (mg), and S is the peak area between the DSC profile and baseline. Using the above data and Eq. (3), a comparison of the heat release ΔH is shown in Fig. 5(a). The heat release ΔH of coal is 12.16K KJ/g. By contrast, the heat release of coal with iron ore, BOF dust, and steel plants sludge are 11.91KJ/g, 12.22 KJ/g, 11.98KJ/g. It shows that BOF dust has positive effect on heat release, but the other additives have negative effect on heat

release. It can be speculated that fine iron ore and BOF dust absorb heat, result in the total heat release amount decrease. However the BOF sludge has more than 5% carbon which can release heat during combustion, result in making up the loss of heat release.

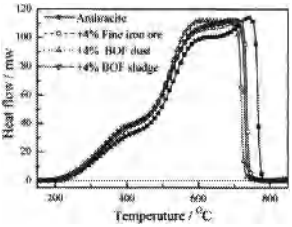

Fig. 4 DSC curves of coal samples during combustion process

In order to remove the interference of absorbing heat of the metallurgical byproducts on the combustion efficiency, combustion efficiency can be modified as follows:

$$\Delta Q' = \frac{\Delta Q}{(1-x)} \tag{4}$$

Where x is the content of additives (%), Using the above data and Eq. (4), a comparison of the combustion efficiency is shown in Fig. 5(b). It can be seen from Fig. 5(b) that combustion efficiency of per unit of fuel increase by 2%~5% with these three metallurgical byproducts addition. By comparison of Fig. 5(b), it indicates that the release heat of pulverized coal increase with byproducts addition. However, the most compounds of additives can absorb heat, resulting in restraining the improvement. When the additives contain some of carbon, it can make up the loss of heat release during combustion.

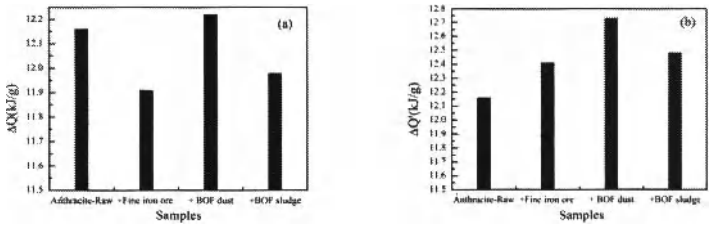

Fig.5 Combustion efficiency of different coal samples

From the results and analysis mentioned above, it can be seen that fine iron ore, BOF dust and BOF sludge can decrease the ignition of pulverized coal, increase combustion rate and burnout behavior. Adding BOF dust can increase combustion efficiency obviously. By comparison, the relative active sequence of byproducts to the catalytic combustion can be described as follows: BOF dust>BOF sludge>fine iron ore.

Effects of metallurgical byproducts on combustion behavior of pulverized coal during rapid heating process

From above results, it can be seen that BOF dust has best catalytic effect on combustion process, thus the effect of BOF dust on combustion behavior of pulverized coal during rapid heating process is investigated. Effect of different amount of BOF dust on burnout rate of pulverized coal during rapid heating process is shown in Fig. 6. It can be seen that from Fig. 6 that the burnout rate increase with BOF dust addition. What' s more, with the increase the amount of additive, the burnout rate of pulverized is increased obviously. The burnout rate increase by 8% when the adding amount of BOF dust is 1%. The above results indicate that BOF dust can improve pulverized coal combustion behavior also during rapid heating process.

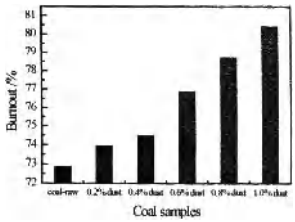

Fig.6 Effect of BOF dust on burnout rate of pulverized coal during rapid heating process

In order to obtain more effective and low-cost catalyts of pulverized coal combustion, the BOF dust is added with different proportinoal chemical compounds as the composite catalysts (total mass 0.6 %). The catalyst numbuer is shown in table 6. The A, B, and C are transition-metal and alkaline-earth compounds which have high catalytic activity. The burnout of pulverized coal with different composite catalysts addition is shown in Fig. 7. From Fig. 7, it can be seen that the burnout rate increase by 3.0%~8.5% with these catalysts addition. What's more, the maximum burnout rate increases by 8.56% with 3# catalyst addition. By comparison of Fig.6, the effect of composite catalyst which has 20% BOF dust is better than the chemical compounds. It is clear that exploiting composite catalysts with metallurgical byproducts containing iron is reasonable and feasible in mechanism and effect.

Table 6 Compositions of composite catalysts

Catalyst number	Compound A	Compound B	Compound C	BOF dust
0#	—	—	—	—
1#	50%	30%	20%	—
2#	40%	30%	20%	10%
3#	30%	30%	20%	20%
4#	20%	30%	20%	30%
5#	10%	30%	20%	40%
6#	—	30%	20%	50%

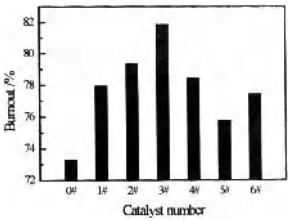

Fig.7 The effect of composite catalysts on pulverized coal combustion

Conclusions

Eight typical metallurgical byproducts containing iron were selected based on the effect of the chemical composition, particle size, additives on the burnout degree of pulverized coal. The three typical byproducts including fine iron ore on combustion behavior the pulverized coal have been investigated using the thermogravimetry-differential thermogravimetry (TG-DTG) and differential scanning calorimeter (DSC).The results are show: 1) The three additives, including iron ore, BOF dust, and steel plants sludge, have improved

combustion reactivity of coal. The reduction in the ignition temperature of coal with additives are about 10℃. 2) The release heat of pulverized coal increase with byproducts addition. However, the most compounds of additives can absorb heat, resulting in restraining the improvement. When the additives contain some of carbon, it can make up the loss of heat release during combustion. 3) By comparison, the relative active sequence of byproducts to the catalytic combustion can be described as follows: BOF dust>BOF sludge>fine iron ore. 4) Moreover, adding BOF dust as component of additives also shows significant catalytic effects on combustion efficiency during rapid heating process. Exploiting composite catalysts with metallurgical byproducts containing iron is reasonable and feasible in mechanism and effect.

Acknowledgements

The work is supported by the Natural Science Foundation Project of CQ CSTC (CSTC，2008BB6170) and Key Scientific and Technological Project of China Chongqing (CSTC，2009AB4042).

References

[1] Sheng Xuefeng, Xue Qingguo, Dong Jieji, et al. Study on Basic Properties of Typical Industrial Dust from Iron and Steel Plant and Analysis of Its Utilization. The Chinese Journal of Process Engineering, 2009, 9(z1): p. 7-12.

[2] Hannu Tapani Makkonen, Jyrki Heino, Leena Laitila, et al. Optimisation of steel plant recycling in Finland: dusts, scales and sludge. Resources, Conservation and Recycling, 2002, 35(1-2): p. 77-84

[3] L. Lu, V. Sahajwalla, D. Harris. Coal char reactivity and structural evolution during combustion-Factors influencing blast furnace pulverized coal injection operation. Metallurgical and Materials Transactions B: Process Metallurgy and Materials Processing Science, 2001, 32 (5): p. 811-820.

[4] Despina Vamvuka, Guido Schwanekamp, Heinrich W. Gudenau. Combustion of pulverized coal with additives under conditions simulating blast furnace injection. Fuel, 1996, 75(9): p. 1145-1150.

[5] A. Ziębik, W. Stanek.Forecasting of the energy effects of injecting plastic wastesinto the blast furnace in comparison with other auxiliary fuels. Energy, 2001, 26(12): p.1159-1173.

[6] Ajay Atal, Yiannis A. Levendis. Comparison of the combustion behavior of pulverized waste tyres and coal. Fuel, 1995, 74(11): p. 1570-1581.

[7] Wei-Hsin Chen, Jheng-Syun Wu. An evaluation on rice husks and pulverized coal blends using a drop tube furnace and a thermogravimetric analyzer for application to a blast furnace [J]. Energy, 2009, 34(1): p. 1458-1466.

[8] L. Fangxian, L. Shizong, C. Youzhi. Thermal analysis study of the effect of coal-burning additives on the combustion of coals. Journal of Thermal Analysis and Calorimetry, 2009, 95(2): p. 633-638.

[9] X. G. Li, B. G. Ma, L. Xu et al. Catalytic effect of metallic oxides on combustion behavior of high ash coal. Energy and fuels, 2007, 21(5): 2669-2672.

[10] Xuzhong Gong, Zhancheng Guo, Zhi Wang. Reactivity of pulverized coals during combustion catalyzed by CeO_2 and Fe_2O_3. Combustion and Fule, 2010, 157(2): p. 351-356.

[11] Dieter SENK, Heinrich Wilhelm GUDENAU , Stephan GEIMER, et al. Dust Injection in Iron and Steel Metallurgy. ISIJ International, 2006, 42(16): p. 1745-1751.

[12] Yu Taoran, Li Chengyun. Thermal analysis method to study the combustion characteristic of coal. Metallurgical Energy Engineering, 1989, 8(5): p.41-44.

3rd International Symposium on High-Temperature Metallurgical Processing
Edited by: Tao Jiang, Jiann-Yang Hwang, Patrick Masset, Onuralp Yucel, Rafael Padilla, and Guifeng Zhou
TMS (The Minerals, Metals & Materials Society), 2012

EFFECT OF SiO_2 ADDITION ON REDUCTION OF Fe-Si-Mn ALLOY FROM ADJUSTED CONVERTER SLAG

Min Chen, Jian-hong Dong, Zhen Tian, Cui-huan Huang

School of Materials and Metallurgy, Northeastern University
3-11, Wen-hua road, Heping district, Shenyang 110819, China

Keywords: Converter Slag, Melting Modification, Selective Reduction, Fe-Si-Mn Alloy

Abstract

The present work studied the production of Fe-Si-Mn alloy from adjusted converter slag by thermodynamic analysis. The results showed that solubility of SiO_2 in the molten slag increased with increment of temperature, and it is about 80% at 1800 ℃. With increment of SiO_2 content, $a_{(MnO)}$ and $a_{(CaO)}$ decreased, and $a_{(FeO)}$ increased to the maximum when $w(SiO_2)$ is about 30%. As a result, the reduction of the slag was in the order of Fe→Mn→P before SiO_2 reduction, the reduction order was Fe→P→Mn→Si when SiO_2 content in the slag was from 46.4% to 54.2%, and changed to Fe→Si→P→Mn when SiO_2 content exceeded 54.2%. The mass fraction of Si in the alloy phase increases with increasing of $w(SiO_2)$ in the slag, and the mass fraction of Si in the alloy reached to 62.2% at 1800 ℃.

Introduction

Ferroalloy production is a high energy consumption and high pollution industry[1-2]. If ferroalloy production could be produced from molten slag by addition of carbon-reducing agent, the valuable metal and oxide in the slag can be recycled, most importantly, if the high-temperature resource carried by molten slag can be made full use in the field of ferroalloy production, the power consumption of ferroalloy production could be cut down greatly.

Converter steel slag is a kind of byproduct in steelmaking processing increasing rapidly with the increment of crude steel, but the utilization ratio is low. Most heat recovery research is still in the experimental stage except the heat recovery of blast furnace slag by water quenching method, at present[3-4]. It is of great significance for enterprises to energy saving and emission reduction if the molten steel slag could be utilized directly. Not only the reuse methods of liquid steel slag material can be promoted, but also the use of heat carried in the slag could be achieved.

The basicity of converter slag is high and the activity of SiO_2 is low so the reduction of SiO_2 in the slag is little. The compositions of slag and metal phases were calculated by Factsage program on different conditions to explore the reduction of converter slag for recovery of valuable metals and an efficient new way to use the high-temperature heat combining with the current reuse and research status of converter slag. Further, the improvement of components activity in slag and the increase of Si concentration in the metal were also dicussed.

Thermodynamic Calculation

Most of the thermodynamic calculation is under the Equilib module, one part of the international software Factsage and the pressure is set P=1atm, the amount of carbon is set as variable mass% of the raw slag and modifier. Different modifier content of SiO_2 (30%, 40%, 50%) in slag, reducing temperature and the addition of carbon were investigated by taking a factory converter slag (composition shown in Table.I) as raw slag.

Table I Composition of Converter Slag (mass%)

CaO	SiO_2	FeO	MgO	Al_2O_3	P_2O_5	MnO
45	16	15	15	3	1	5

Results and Discussion

Solution Behavior of SiO_2

Fig.1 shows the solution of modifier SiO_2 in CaO-MgO-SiO_2-FeO system at different temperature. As shown in Fig.1 in the slag system the solubility of SiO_2 rapidly increased but began to be flatten since 1750 ℃ with increasing temperature. That is because the melting point of silicon dioxide is about 1750 ℃ and the content of SiO_2 eutectic compounds decreased. There are a variety forms of the silicon in the steelmaking slag and the simplest structure of silicate is the silicon-oxygen tetrahedron SiO_4^{4-}, around which the bonds are unsaturated and SiO_2 will further polymerize to produce more complex silicon-oxygen tetrahedron by adding more. The addition amount of modifier SiO_2 must be less than its solubility in the slag system, or the extra SiO_2 will be suspended in the liquid slag as free solid form instead of eutectic solid solution increasing slag viscosity.

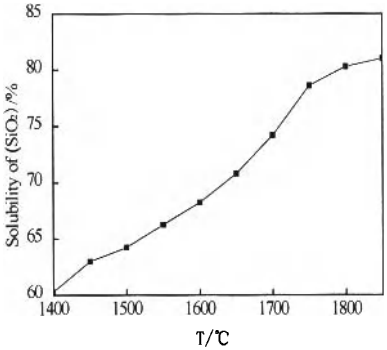

Fig. 1 Solubility of (SiO_2) at Different Temperature

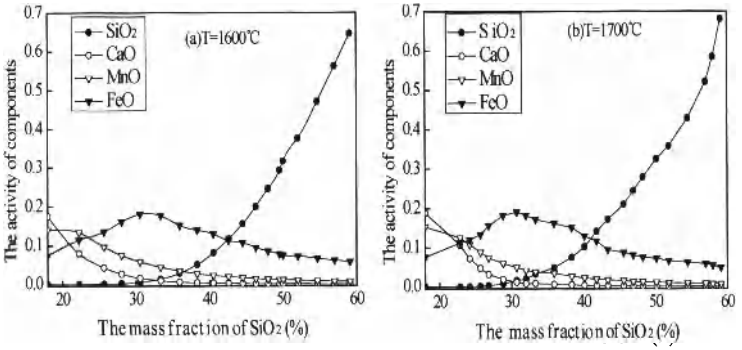

Fig. 2 Activity of Components at Different Temperature

Activity of Components in Slag

The basicity of converter slag is high and the activity of SiO_2 is low. Fig.2 shows the activity of components at different temperature 1600℃ and 1700℃ respectively. The activity of SiO_2 and CaO were indicated by circles, MnO and FeO were indicated by triangles. Initially, the concentration of SiO_2 in the slag was 16 mass% at various teperature and the activity of it was very small. The activity of SiO_2 increased slowly in the mass fraction interval from 16 to 30 mass%. It was clear that the activity increased heavily as the mass fraction of SiO_2 was beyond 30 mass%. The value of SiO_2 was almost the same to the activity diagram of SiO_2 in the SiO_2-MnO-Al_2O_3-CaO system[6,7]. In order to increase the reactivity of SiO_2, the more modifier must be added to the initial slag. The activity of FeO at first increased as the increase of SiO_2 but then decreased. The alkalinity of slag was high at first, part of FeO existing in the slag system as calcium ferrite. Due to the affinity between SiO_2 and CaO is much stronger than CaO and FeO, most of FeO in the calcium ferrite was replaced by SiO_2, so the activity of FeO increase; however, fayalite phase dominated the slag phase as the concentration of SiO_2 continued to rise, it was thus clear that the activity of FeO droped. The activity of MnO and CaO in the slag kept decreasing as the increase of SiO_2 till to the end of the calculation, the addition of SiO_2 result in a decrease in the activity of CaO and MnO. Yuanxi Zou published an idea which was similar to us[8,9]. Thus, it can be concluded that the activity of other components is affected by the addition of SiO_2. On comparing (a) and (b) the activity of SiO_2 in the slag phase increase as the temperature gets higher.

Effect of Temperature on Selective Reduction

The variations in the composition of metal phase are shown in Fig.3; here [mass% M] denotes the concentration of M in the metal phase. Different components keep the same reduction order when (SiO_2) is 50 mass% after modified in the slag. It is clear that all the FeO was reduced to metallic Fe. Subsequently, P_2O_5 were reduced preferentially followed by MnO and SiO_2 leading to a decrease in the concentration of Fe. This result indicated that SiO_2 is thermodynamically more stable than MnO in this slag system. The concentration of Mn in the metal phase increased in the carbon content interval from 0 to 2, however after 2, the SiO_2 phase dominated the slag phase and only the concentration of Si increased. It is well known that SiO_2 addition to MnO result in a significant increase of $MnSiO_3$, and the formation of $MnSiO_3$ has two aspects impact on the slag. On one hand $MnSiO_3$ has low melting point (1243℃), leading to a increase reactivity which promote the reduction of SiO_2, on the other hand the formation of $MnSiO_3$ result in significant decrease in activity of MnO. The concentration of P_2O_5 was diluted in the slag by modifying to decrease the concentration of P in the metal phase, which will be good for the refine of alloy. On comparing (a) and (b) the concentration of Si in the metal phase increase as the temperature gets higher.

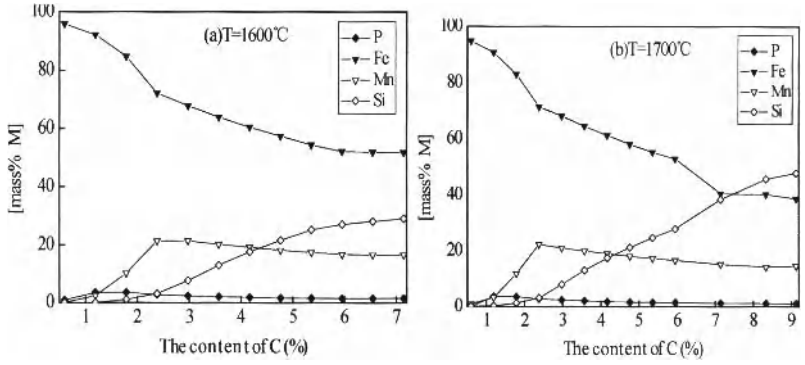

Fig. 3 Compositions of Metals in Ferro-alloy for Different Carbon Content

Affect of Temperature on Reduction Rate of Si

The variations in the recovery rate of Si are shown in Fig.4; here the SiO_2 30 mass% in the slag was indicated by diamonds, circles represent the data points resulting from the reduction of 40 mass% SiO_2 and the triangles denotes the 50 mass% SiO_2 in the slag. It was clear that the recovery rate of Si increased heavily as the mass fraction of SiO_2 rose, according to Fig.2 that the activity of SiO_2 increase as its mass fraction got up. The addition of SiO_2 result in an increase in the activity of SiO_2 and the volume fraction of liquid phase in the slag. Consequently, the reduction rate of SiO_2 in the CaO-SiO_2-FeO-MgO slag increase with increasing SiO_2 content. When the weight of modifier SiO_2 was set as 50 mass%, the recovery of Si could be as high as 51% at 1800℃. The results indicate that increasing activity of SiO_2 and that of temperature improved seletive reduction of SiO_2 from CaO- SiO_2-FeO-MgO oxide system.

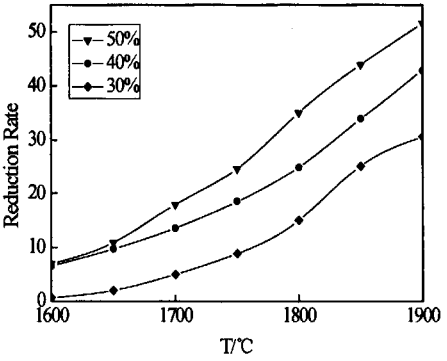

Fig. 4 The Relationship between Reduction Rate of Si and Temperature

Conclusions

The favorable conditions for the production of Fe-Si-Mn alloy from converter slag were conculated.The following conclusions were obtained.

(1) Thermodynamic behavior of slag is closely related with the temperature and slag composition. The addition of SiO_2 to the slag system led an increase in the activity of SiO_2 and a decrease of CaO and MnO, but the activity of FeO in slag increased at first then decreased.
(2) The reactivity between carbon and silica was improved by increasing the temperature and the concentration of Si increased to about 50 mass% in the metal phase.
(3) When the weight of modifier SiO_2 was set as 50 mass%, the recovery of Si could be as high as 51% at 1800℃.

Acknowledgements

This research work was funded by the National Natural Science Foundation of China (Grant No. 51074093).

References

1. J.S. Leng, F.L. Sun and J. Zhou, "Analysis on Energy Loss and Test of Heat Balance in Sunberged Arc Furnace". *Ferro Alloy*, 203(6)(2008), 10-13.
2. T.Takagawa et al., "Production of Mn-Fe Alloy from Slag Generated in Mn-Removal Treatment of Molten Cast Iron", *ISIJ International*, 49 (11)(2009), 1673-1677.
3. C. S. Jiang et al., "Physical and Chemical Properties of Steel Slag and Developing Tend of Comprehensive Utilization Technology", *Science and Technology of Overseas Building Materials*, 23(3) (2002), 3-5.
4. R. Sripriya, Ch. V.G.K. Murty, "Recovery of Metal from Slag/mixed Metal Generated in Ferroalloy Plants - A Case Study", *International Journal of Mineral Processing*, 75 (1-2)(2005), 123-134.
5. G. Z. Ye et al., "Reduction of Steel-making Slags for Recovery of Valuable Metals and Oxide Materials", *Scandinavian Journal of Metallurgy*, 32 (1)(2003), 7-14.
6. J. S. Wu, L. Li, "Thermodynamics Behavior of Silicon Dioxide in Smelting the Alloy of Silicon and Manganese", *Journal of East China University of Metallurgy*, 2003, 17 (4): 300-304.
7. J. Zhang, *Calculating Thermodynamics of Metallurgical Melts*(Beijing: Metallurgical Industry Press, 1998), 81-96.
8. Z. Q. Zhang et al., "Activity of CaO in liquid $CaO-SiO_2-Al_2O_3$ system", *Acta Matellurgica Sinaca*, 22(5)(1986), 256-264.
9. Y. X. Zou, "Thermodynamics of Liquid Blast Furnace Slag", *Acta Matellurgica Sinaca*, 1(2) (1956), 127-140.

3rd International Symposium on High-Temperature Metallurgical Processing
Edited by: Tao Jiang, Jiann-Yang Hwang, Patrick Masset, Onuralp Yucel, Rafael Padilla, and Guifeng Zhou
TMS (The Minerals, Metals & Materials Society), 2012

SOLIDIFICATION OF EAF STAINLESS STEEL DUST

Bing. Peng [a, *], Ji Peng [a], Liyuan Chai [a], Di Yu [b]

[a] School of Metallurgical Science and Engineering, Central South University, Changsha 410083, China
[b] School of Information Science and Engineering, Central South University, Changsha 410083, China

Abstract

Electric arc furnace (EAF) stainless steel dust has been classified as a hazardous waste by various government regulatory agencies as it releases heavy metals to environment. The solidification of EAF dust is to stabilize the hazardous components to the amorphous silica-alumina-based clays. The process of solidification is investigated and the softening temperatures of dust and additive clay mixtures are measured for economical thermal treatment. The results indicate that the mixture of dust and local clay with the ratio of 1:1 has the lowest softening temperature 1100 °C and it could pass the toxicity characteristics leaching procedure (TCLP) test for the environmental regulatory limits after thermally treated at softening temperature for 15 min. Major phases of thermal solidification product clinker are $CaAl_2Si_2O_8$, $(Fe, Cr)_2O_3$, $(Fe, Mg)(Cr, Al)_2O_4$ and $Al_6Si_2O_{13}$.

Key words: Stainless steel dust; Thermal solidification; Softening temperature; Heavy metals

Introduction

The yield of stainless steels in China arrived to 10 million tons in 2006 and more than 0.2 million tons of stainless steel dust are produced annually. Approximately 1-2 wt.% of scrap charged to an electric arc furnace (EAF) enters the off-gases and then is converted into the dust and reported to the bag-house. The disposal or landfill of the dust becomes a serious environmental problem in China due to the increased production of stainless steels in recent years. The dust contains elements such as chromium (Cr), nickel (Ni), lead (Pb), zinc (Zn), cadmium (Cd) and their solubility in leaching media exceeds the environmental regulatory limits [1]. Even though easily feasible for low-grade MgO, it is not appropriate to stabilize the heavy metals from the heavily contaminated soils after the dust landfill [2]. Several dust treatment technologies have been developed and they can be divided into two types. One is to recover the metals from the dust [3, 4] and another is to stabilize hazardous components present in the dust [5, 6]. Recycling of the dust generated in EAF is a remediation option for cleaner production. Direct recycling of EAF stainless steel dust was developed to recover the metal value from the dust and protect the environment [7], but it was only suitable for the dust with high contents of Ni, Cr and Fe. As for the dust with low valuable metal content, thermal solidification is an appropriate choice for the dust treatment.

Solidification technology has been widely used for the treatment of inorganic wastes and contaminated soils before final disposal. Conner [8] summarized the solidification

*Corresponding author. Tel: +86-731-8830875; Fax: +86-731-8710171; *E-mail address*: pb@csu.edu.cn

technologies and indicated that fly ash was one of the most common binders in waste stabilization. Rodriguez-Pinero [9] described the chromium behave in the solidification of a steel industry waste using a common fly ash from a pulverized coal power station as the binder and indicated that the stabilization of Cr(VI) present in the waste required a reducing pretreatment with ferrous sulfate to attain the toxicity characteristics leaching procedure (TCLP) leachates within the limits. The TCLP tests had a low metal content and alkalinity, wchich could be used to estimate the metal concentration leached by typical acid rain and ground water. Pisciella [5] stabilized the hazardous materials by vitrification of EAF dust and other industrial wastes. Hassett [10] made use of coal combustion by-products for the solidification of hazardous wastes. Pelino [1] developed a vitrification process to immobilize the hazardous elements in EAF dust by mixing the dust with cullet and sand. He pointed out that the stability of the product was influenced by the glass structure which depended on the Si/O ratio. It seemed that the trivalent chromium in the thermally treated dusts could be gradually oxidized to hexavalent chromium when exposed to atmospheric oxygen. But the chromium was bound in the matrix in various silicate or spinel phases and the oxidation reaction ceased within 12 months [11]. The thermal behavior of the EAF dust from stainless steel and carbon steel operations was determined and a thermal process for the stabilization of the dust by vitrifying with clay was developed [12]. Furthermore, recycled sewage sludge solidified using converter slag solidification technology was used as an effective landfill cover [13]. The key point for the thermal solidification of EAF stainless steel dust is the processing temperature, which deals with the consumption of power. The temperature of dust vitrification by swirling-flow furnace was very high [14], which is inappropriate for economical treatments of the dust. But it was found that EAF stainless steel dust softened above 1600 °C. This temperature is too high to process the solidification of the dust economically. Therefore, it is necessary to reduce the melting temperature of the dust by adding certain modifying ingredients. Silica and alumina are additives that readily modify the melting temperatures of ceramic ware. They are also effective glass forming substances which help immobilize the heavy metals present in the EAF stainless steel dust.

The objectives of this study are to find a low cost additive for the solidification of EAF stainless steel dust, to optimize the compositions of the dust/additive mixture and process conditions and to ensure that the clinkers of solidification accord with environmental regulation for TCLP test. The mixture of the dust and additive was investigated and the softening temperature was measured. The thermal processes of solidification were detected using Thermo-Gravimetric Analyzer (TGA), Differential Thermal Analysis (DTA) and Fourier Transform Infrared Spectroscopy (FTIR). The products of solidification clicks were characterized by TCLP for the leachability of hazardous materials, X-ray Diffraction (XRD) for crystal phases and Scanning Electron Microscope (SEM) for morphology.

Experimental

Two types of EAF stainless steel dust samples used in this study were obtained from a stainless steel plant, a dry fine powder newly acquired from the bag-house and a wet stockpile agglomerate located in the open air. The stockpile dust was so wet and inapposite to be processed in the experiments that was dried for 24 h at 100 °C and crushed down in a

rod-roller. Since the dusts were formed in air at high temperature, all the metal elements within them were oxidized. Elemental analysis of the dust samples was performed using X-ray Fluorescence (XRF) and Inductively Coupled Plasma (ICP). The compositions of the samples are given in Table I. Low cost local clay was used as the additive for the solidification of EAF stainless steel dust. The main chemical compositions of the clay are given in Table II. The clay was spread on the floor, dried for a few days, and then split using a sample splitter before processing. In order to determine the effect of chemical composition on softening temperature, pure alumina and silica were used in the study.

Table I Chemical Composition of Dust / mass%

Chemical composition	SiO_2	Al_2O_3	CaO	Cr_2O_3	Fe_2O_3	MnO_2	NiO	PbO	ZnO	MgO	TiO_2	P_2O_5	Na_2O	C	CdO	K_2O
Bag-house dust	5.14	0.64	9.02	16.3	51.3	4.41	6.25	0.29	0.96	3.63	0.08	0.30	0.60	0.70	0.01	0.72
Stockpile dust	5.45	0.66	9.14	15.1	48.0	4.67	6.70	0.16	0.93	3.48	0.12	0.62	0.53	0.60	0.01	1.47

Table II Chemical Composition of Clay

Chemical composition	SiO_2	Al_2O_3	Fe_2O_3	CaO	MgO
(%)	54.13	14.37	6.82	3.63	2.74

The EAF stainless steel dust and the additives such as alumina, silica or clay were mixed in different dust/additive ratio, and then molded into the brick and dried at room temperature for three days. A muffle furnace was used to heat the bricks in the rate of 4 $^{\circ}C \cdot min^{-1}$ to a given temperature and then kept for 15 min. A K-type thermocouple was used to detect the temperature of the bricks and to control the process. The softening temperatures of bricks were measured by checking the volume changes of the clinkers in the thermal processing. The ratio of EAF stainless steel dust to clay in the mixture was ascertained according to the lowest softening temperature [15] in the consideration of economical solidification. The leachability and thermal characteristics of the clinkers were inspected after thermal treatment.

It was found in our previous investigations [16, 17] that the EAF stainless steel dust sinters without melting at high temperature over 1300 $^{\circ}C$ and softens above 1600 $^{\circ}C$. The melting temperatures of the dust have to be lowered down for economical solidification by addition of additives. The processing temperatures of solidification depend on the softening temperature of dust and additive mixture. The densities of clinker change in the thermal process. They are small at low temperature in the beginning of solidification and will increase with the increase of temperature. The volume of thermally treated clinkers increases under softening temperature and decreases sharply at softening temperature. In this consideration, the softening temperatures can be determined by measuring the sharp volume changes after the clinkers cooled down.

TGA was used to monitor the weight change of the mixtures as a function of temperature and time in thermal processes of the solidification and the thermal behavior of clinker. DTA was used to detect the temperature changes caused by chemical or physical reactions as a function of temperatures and time in the sample thermal treatment. FTIR was used to identify gaseous

species evolution during the thermal processes of the mixtures and clinkers. The clinkers produced through thermal solidification were subjected to leaching tests as specified in the US Environmental Protection Agency (EPA) regulations for solid waste. The tests involved breaking down the clinkers and selected some small particles less than 10 mm in diameter as samples, and then followed by leaching at room temperature for 24 h (longer than 18h, so stricter than TCLP) in a buffered solution of acetic acid and acetate (pH value 5.0). ICP was used for the elemental analysis of the leachate to compare the results with EPA regulations.

Results and Discussion

Figure 1 shows the results of volume changes of dust/clay mixtures with the temperature. It can be seen by comparing Figure 1a with Figure 1b that the bag-house dust/clay and stockpile dust/clay mixture samples had the same thermal characteristics. The softening temperatures of the mixtures with 40%, 45%, 50% and 55% dust were 1280 °C, 1200 °C, 1100 °C and 1180 °C respectively. The main concern for thermal solidification of EAF stainless steel dust is the energy consumption. The processing temperature of thermal solidification is dependent on the softening temperature because only thermally treated over this temperature can the hazardous materials present in the dust be immobilized. The mixture of dust and clay with the ratio of 1:1 had the lowest softening temperature for the thermal solidification in the present study. Therefore, the composition of the mixture could be determined in this way and 1100 °C was confirmed as the thermal processing temperature. The main chemical composition of clay is silica and alumina. The softening temperatures were measured in dust/silica/alumina ternary system for extending the thermal solidification technology to general additives. Figure 2 shows the computer analysis of the softening temperature profile. The isotherms in the figure indicated that the softening temperatures were lower in the compositional region of 35-37% silica, 18-20% alumina and 45-50% EAF dust.

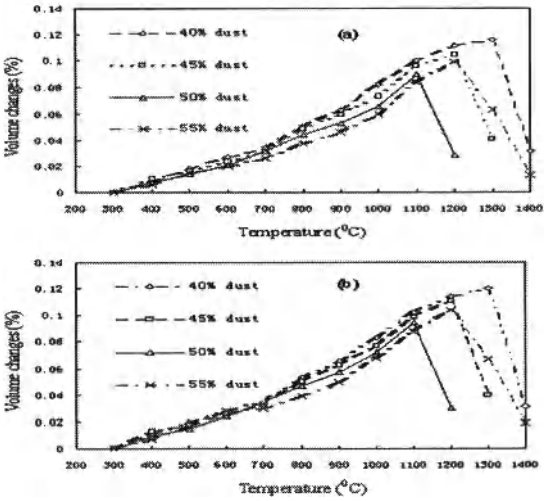

Figure 1 Volume of Dust/Clay Mixture at Different Temperature

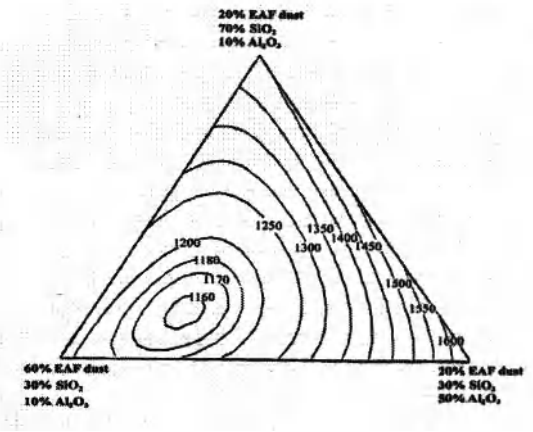

Figure 2 Profile of Softening Temperature

The thermal process of solidification was analyzed with TGA, DTA and FTIR after dry mixtures were prepared by weighing and combining equal amounts of EAF stainless steel dust and local clay. Figure 3 shows the diagram of TGA/DTA/FTIR of the mixture in the thermal process. TGA/DTA highlighted that the weight loss of the mixture was 6.5 wt.% after the temperature reached up to 1200 °C. 2% weight loss in the temperature range of 580-800 °C was caused by the decomposition of $CaCO_3$. Above this temperature range, the weight losses were also observed due to the volatilization of zinc and lead, accompanied by an endothermic effect in the DTA trace. FTIR analysis showed that the water evaporated at about 120 °C and small amounts of HCl, SO_2 and HF were detected at high temperature over 950 °C. SiF was also detected and it resulted from the reaction of HF and SiO_2 at high temperature.

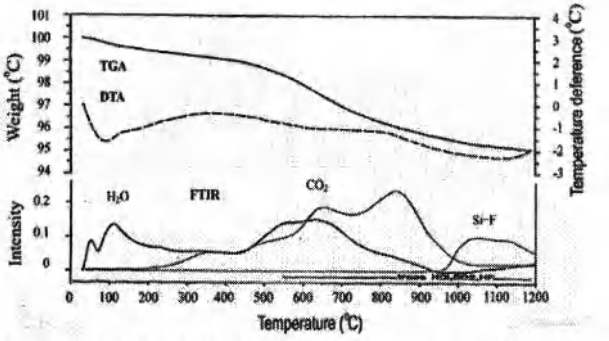

Figure 3 TGA/DTA/FTIR Profile of Mixture in Thermal Process

The major crystal phases of thermal solidification products clinkers identified by XRD were $(Fe, Cr)_3O_4$, $(Fe, Cr)_2O_3$, Fe_2O_3 with minor amounts of anorthite and quartz (see Figure 4).

Most (Fe, $Cr)_3O_4$ present in the dust was oxidized into (Fe, $Cr)_2O_3$ and Fe_2O_3. The clinker appeared visually porous and had a sinter-like texture. SEM examinations for the clinkers of bag-house dust (Figure 5a) and stockpile dust (Figure 5b) indicated that extensive liquefaction and evolution of gaseous phases had occurred during thermal process. The formation of large vesicles within the clinker was resulted from gases evolution from the liquefied regions of sample. Although the quartz particles retained in original angular morphology, the liquefaction and vitrification occurred and calcite completely disappeared. The heavy metals within the dust were packed in this way and distributed in the (Fe, $Cr)_3O_4$ and (Fe, $Cr)_2O_3$ phases, while some Mn, Zn, Al, Mg and Ti were distributed in silicate phase. Clinkers were also subjected to thermal analysis as shown in Figure 6. It can be seen from the TGA/DTA/FTIR results that the clinker was very thermally stable (Figure 6). The weight loss of the clinker was less than 0.5% when the temperature reached up to 1200 °C. There were no significant reaction appeared on the DTA curves and only traces of moisture and carbon dioxide were detected by FTIR.

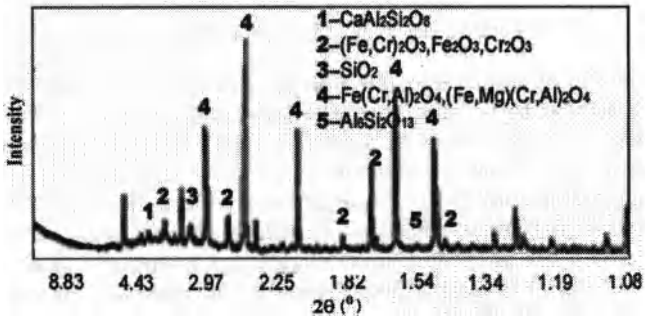

Figure 4 XRD of Thermal Solidification Product

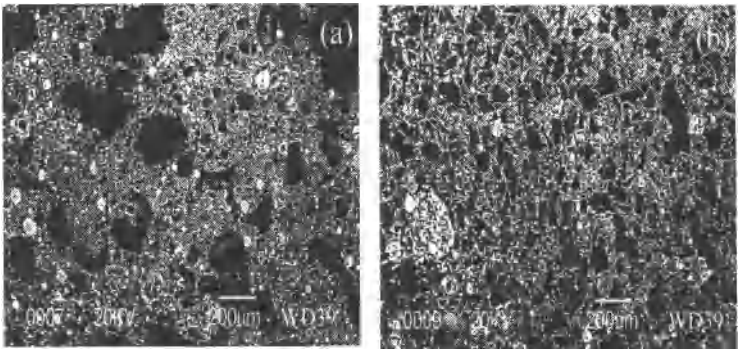

Figure 5 SEM of Thermal Solidification Products

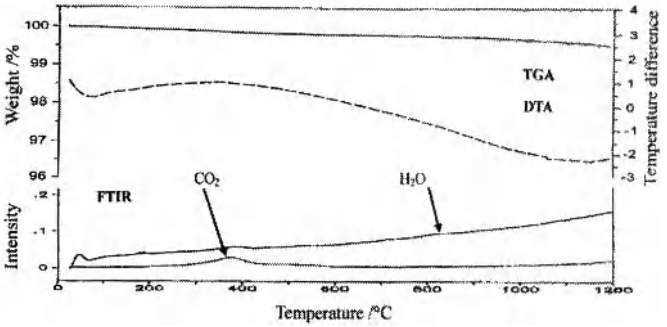

Figure 6 TGA/DTA/FTIR Profile of Solidification_Product

In order to assess the stabilization of the hazardous elements present in the EAF stainless steel dust after thermal solidification, clinkers of bag-house dust and stockpile dust were subjected to US EPA TCLP test. Table III shows the leaching results of the tests for the clinkers, which were thermally solidified at 1100 °C for 15min. It was observed that the heavy metals released to the solution were in the concentration limits of the regulatory for the solid waste disposal. But it would be noted that the amounts of Hg and Se in the solutions were below the detection limit of the instrumentation (0.0024 $\mu g \cdot L^{-1}$).

Table III_Content of TCLP Leachate /$\mu g \cdot L^{-1}$

Element	As	Cd	Cr	Cu	F	Ni	Pb	Zn	Se	Hg
EPA regulation	5.0	0.5	5.0	10	150	10	5.0	10	1.0	0.2
Bag-house clinker	0.002	0.002	0.31	0.3	0.15	0.31	0.05	0.4	<0.0024	<0.0024
Stockpile clinker	0.04	0.02	0.54	0.3	0.40	0.40	0.03	0.2	<0.0024	<0.0024

Conclusions

This study was conducted to develop a novel thermal solidification process of EAF stainless steel dust. A local clay, low cost and easily available, was mixed with the dust as the additive in the ratio of 1:1. The clinkers were obtained after the mixture was treated at 1100 °C for 15 min and exceeded the US EPA leaching quality. Lower softening temperatures, crucial parameter that affected the quality and the leaching results of clinkers, could be achieved in the compositional region of 35-37% silica, 18-20% alumina and 45-50% EAF dust based on the profile of softening temperature on alumina-silica-EAF dust mixtures. The final products of solidification were porous sinter-like textures and the major phases were (Fe, $Cr)_3O_4$, (Fe, $Cr)_2O_3$ that packed the heavy metals. The characteristic of final products clinkers was thermally stable and no significant reaction occurred in the further thermal processes when temperature reached up to 1200 °C.

Acknowledgement

This project was supported by the National Natural Science Foundation of China (50274073) and the authors of this paper would like to give the thanks for the financial support.

References

[1] M. Pelino et al., "Vitrification of electric arc furnace dusts", *Waste Manage*, 22(2002), 945-94

[2] M.A. Garcia et al., "Low-grade MgO used to stabilize heavy metals in highly contaminated soils",. *Chemosphere*, 56(2004), 481-491

[3] J. Lobel et al., "Pilot-scale direct recycling of flue dust generated in electric stainless steelmaking", *Iron & Steelmaker*, 27(2000), 41-45

[4] K.W. Grieshaber, C.T. Philipp, and G.F. Bennett, "Process for recycling spent potliner and electric arc furnace dust into commercial products using oxygen enrichment", *Waste Manage*, 14(1994), 267-276

[5] P. Pisciella et al., "Chemical durability of glasses obtained by virtification of industrial wastes", *Waste Manage*, 21(2001), 1-9

[6] A.I. Fernandez et al., "Stabilization of electrical arc furnace dust with low-grade MgO prior to landfill", *Jenviron Eng-ASCE*, 129(2003), 275-279

[7] B. Peng et al., "Non-isothermal reduction kinetics of EAF dust-based pellets", *CIM BULL*, 94(2001), 64-70

[8] J.R. Conner and S.L. Hoeffner, "Critical review of stabilization/solidification technology", *CRIT REV ENV SCI TEC*, 28(1998), 397-462

[9] M. Rodriguez-Piñero et al., "Stabilization of a chromium- containing solid waste: immobilization of hexavalent chromium", *Waste Manage*, 48(1998), 1093-1099

[10] D.J. Assett and D.F. Pflughoeft-Hassett, "Use of coal combustion by-products for solidification/ stabilization of hazardous wastes", (Paper presented at The Annual meeting of the North Dakota Academy of Science, Washington, DC, 1997), 24-25

[11] K. Pillary, H. Von Blottnitz, and J. Petersen,. "Ageing of chromium(III)-bearing slag and its relation to the atmospheric oxidation of solid chromium(III)-oxide in the presence of calcium oxide", *Chemosphere*, 52(2003), 1771-1779

[12] S.A Mikhail, A.M. Turcotte, and J. Aota, "Thermoanalytical study of EAF dust and its vitrification product",. *Thermochim ACTA*, 287(1996), 71-79

[13] E.H. Kim, J.K. Cho, and S. Yim, "Digested sewage sludge solidification by converter slag for landfill cover", *Chemosphere*, 59(2005), 387-395

[14] I. Tadashi, "Vitrification of fly ash by swirling-flow furnace", *Waste Manage*, 16(1996), 453-460

[15] A. Siegmann, M. Narkis, and N. Rosenzweig, "Softening temperature of glassy polymers as affected by residual stresses", *Polym ENG SCI*, 19(1979), 223-225

[16] J. Peng et al., "Thermo-analytical study on stainless steelmaking dust", *J CENT SOUTH UNIV T*, 10(2003), 20-26

[17] B. Peng et al., "Study on the zinc reduction of stainless steelmaking dust", (Paper presented at Sohn International Symposium, Iron and Steel and Recycling and Waste Treatment, Edited by F. Kongali and R.G. Reddy, TMS, 2006), .497-505

3rd International Symposium on High-Temperature Metallurgical Processing
Edited by: Tao Jiang, Jiann-Yang Hwang, Patrick Masset, Onuralp Yucel, Rafael Padilla, and Guifeng Zhou
TMS (The Minerals, Metals & Materials Society), 2012

STUDY ON CEMENTING MATERIAL MAKING WITH ELECTROLYTIC MANGANESE RESIDUE

Jia Wang, Bing Peng[1], Liyuan Chai, Qiang Zhang, Qin Liu

School of Metallurgical Science and Engineering, Central South University, Changsha 410083, China

Key words: electrolytic manganese residue, activation, cementing material activator

Abstract

Electrolytic Manganese Residue (EMR) was used as the main material to prepare cementing material activator for the utilization of the residue from electrolytic manganese dioxide (EMD) or electrolytic metallic manganese (EMM) production. The effects of chemical activation, thermal activation and mechanical activation on retarding activity and excitation activity of EMR were investigated according to the setting time and activity index of EMR-slag cementing material. The results showed that the EMR exhibited good activating performance after being ball-milled for 18 min and then treated for 1-2 hours at temperature range of 350-450 ℃. The optimal properties of cementing material activator were achieved at the weight percent ratio 30 : 3 : 5 of EMR/$Ca(OH)_2$/cement clinker.

Introduction

Many hazardous industrial solid wastes such as blast furnace slag, fly ash, steelmaking slag, chromic slag and electrolytic manganese residue [1] are generated in China and their amounts increases every year. The accumulation of the solid wastes during past years is very huge and they could be hardly recycled effectively as a sustainable resource. 2.35 billion tons of industrial solid wastes have been produced up to now [2]. It is estimated that they would exceed 3.3 billion tons by the end of 2015 [3]. On the other hand, the quick development of Chinese infrastructural construction needs more cementing materials. The production of traditional building materials consumes lots of natural resource such as clay and limestone and discharges at least 1 ton CO_2 and other pollutants per ton clinker [4]. Therefore, it is necessary to develop new types of cementing materials instead of clinker [5,6].

Electrolytic manganese residue(EMR) is a kind of solid waste from filtering procedure after sulfuric acid leaching of manganese carbonate ore, MnO_2 oxidative deferrization and lime neutralization. By the end of 2009, 130 kt of Electrolytic manganese was produced and about 480-560 kt of residue was discharged to the environment. The deposited EMR occupied fertile land, threatened crop, polluted

[1] Bing Peng, professor of Central South University, Phone: +86-073188830577, E-mail: pb@csu.edu.cn,

environment, limited the development of corporation and became one of the serious local water pollution sources [7,8]. Recycle and complex reutilization of EMR were fundamental solutions to its environmental contamination.

Preparation of chemical products and building material are two ways for EMR recycle and complex reutilization. DE Jianqi [9] used EMR to make fertilizer based on abundant $MnSO_4$, iron compounds, Cu and other trace elements. Chen Bo and PAN Qijing [10] used EMR to make manganese dioxide by precipitation, pyrogenation and electroanalysis, the recovery of Mn reached 85.4%. Ke Guojun [11] substituted the EMR calcinated at 750 °C and 850 °C for part of cement clinker to make cementing material. Feng Yun and Liu Fei [12] studied the feasibility of substituting dried EMR for gypsum and found that EMR could be used to completely replace gypsum as retarder in Portland cement.

EMR has the properties of both gypsum and hydraulic industrial solid wastes [13-15] due to its main chemical components that contains $CaSO_4 \cdot 2H_2O$, SiO_2 and a small amount of Al_2O_3, Fe_2O_3, MnO_2, and etc [11, 16]. High moisture of 20% to 30% water in EMR makes it hard for cementing material making. Meanwhile calcium sulfate in EMR which appeared in the form $CaSO_4 \cdot 2H_2O$ has low activity. Besides of that, other contents such as SiO_2 and Al_2O_3 have low hydration rate. Therefore EMR could not be used to prepare chemical activator for cementing materials applied in construction field until it is modified to promote its contents activity and mixed with other appropriate auxiliary-activators [17,18].

In this research, the effects of treating temperature and time, ball milling time, types of auxiliary-activators and mixture ratio on EMR's retarding activity and excitation activity were investigated according to setting time and activity index of blast furnace slag cementing material modified by EMR. The preparation of cementing material activator making with EMR was studied and EMR admixture was obtained.

Materials and Methods

Raw Materials

EMR and fly ash was taken from Xiangtan EMD Group CO. LTD. S75 (A7≥55, A8≥75) Blast Furnace Slag was taken from Hunan Valin Xiangtan Steel CO. LTD. Cement clinker was taken from Hunan Pingtang Cement Plant. The chemical composition of used raw materials in the experiment was given in Table I. The milling was carried out by a planetary ball mill(Model: QM-3SP2, Nanjing NanDa Instrument Plant, China).

Table I. Chemical Composition of Raw Materials /%

Material	SiO_2	Al_2O_3	Fe_2O_3	CaO	MgO	SO_3	MnO	Loss
EMR	30.60	6.83	7.19	17.10	0.94	24.50	5.45	5.45
Blast furnace slag	32.15	16.82	0.97	37.94	8.76	2.56	0.34	0.09
Cement clinker	22.13	5.41	3.62	66.33	0.68	0.5	—	0.38

Wet EMR was dried to consistent weight at 80 ℃ in a vacuum drying oven and artificially broken to pass through a 16 square mesh sieve. Milling of broken EMR was undertaken for 6 min at 580 rmp using 2 mm diameter steel balls with the weight percent ratio of ball to EMR fixed at 3.8. The pretreated EMR was characterized by a median size (X_{50}) of 0.568 μm and BET surface area 13.14 m^2/g. Finally, The pretreated EMR was treated at 350 ℃ in the muffle furnace for 1 h and cooled down naturally to prepare modified EMR.

The blast furnace slag was artificially broken to pass through a 16 square mesh sieve. Then milling of broken slag was undertaken for 30 min at 580 rmp using 2 mm diameter steel balls with the weight percent ratio of balls to EMR fixed at 3.8. The slag was characterized by a median size (X_{50}) of 5.67 μm and BET surface area 4.6677 m^2/g.

The clink was artificially broken to pass through a 16 square mesh sieve. Then milling of clinker was undertaken for 30 min at 580 rmp using 2 mm diameter steel balls with the weight percent ratio of balls to EMR fixed at 3.4. The clinker was characterized by a median size (X_{50}) of 16.42 μm and BET surface area 2.2699 m^2/g.

Chemical, Thermal and Mechanical Activation on EMR

The modified EMR, CP $Ca(OH)_2$, CP CaO, clinker were mixed to prepare EMR mixture and the mixture was added into the slag and fly ash according to the composition and ratio as Table II left part to obtain slag or fly ash-slag cementing material modified by different compositions of EMR mixture. The modified EMR, CP $Ca(OH)_2$ and clinker were mixed according to L9(3 4) orthogonal table (Table III) to prepare EMR mixture. The EMR mixture was added into slag with the weight percent ratio of EMR to slag fixed at 3 : 7 to obtain slag modified by different ratios of EMR mixture. The two kinds of modified slag's 7 days activity index (A7) and 28 days activity index (A28) were determined. They were used to evaluate EMR's excitation effect on the slag and choose the optimal composition and ratio for EMR mixture.

Some of pretreated EMR was treated at 120 ℃, 250 ℃, 350 ℃, 450 ℃, 550 ℃ and 750 ℃ for 1 h respectively and cooled down naturally in the muffle furnace to obtain the thermally activated EMR. Another pretreated EMR was treated at 350 ℃ for 0 h, 0.5 h, 1 h, 2 h, 4 h, 6 h, 8 h respectively and cooled naturally in muffle furnace. The EMR thermally activated in different time was obtained in this way. Finally, EMR's retarding activity and excitation activity were evaluated to choose the optimal treating temperature and time.

The broken EMR was milled for 6 min, 12 min, 18 min, 24 min and 30min respectively at 580 rmp using 2 mm diameter steel balls under weight percent ratio of balls to EMR fixed at 3.8 to obtain a mechanically activated EMR. Finally, the EMR's retarding activity and excitation activity were evaluated to determine the optimal milling time.

Characterization and Evaluation of EMR Activities

ASAP 2010 volumetric adsorption analyzer produced by Micromeritics Instrument Corp. was used to determine BET surface area. LS601 laser diffraction size analyzer produced by Zhuhai Omec Instruments Corp. was used to measure particle size. ISO Vicat apparatus was used to determine the water requirement of normal consistency for cementing materials.

Retarding time and strength were EMR's main activation factors of cementing materials. They were defined as EMR's retarding activity and excitation activity and evaluated indirectly in following method.

Thermally or mechanically activated EMR, CP $Ca(OH)_2$ and cement clinker were mixed to prepare EMR mixture. Some of the mixture was added into blast furnace slag as an activator to obtain a modified slag. The weight percent ratio of EMR/$Ca(OH)_2$/cement clinker/slag was fixed at 20 : 3 : 7 : 70. 7 days activity index (A7) and 28 days activity index (A28) of modified slag were measured according to GB/T18046-2000 [19] to evaluate EMR's excitation function on the slag. Another mixture as a retarder agent was added into cement clinker and blast furnace slag to make EMR-slag cement. The weight percent ratio of EMR/$Ca(OH)_2$/cement clinker/slag was fixed at 10 : 3 : 40 : 47. This cementing material's setting time was measured according to GB/T1346-2001 [20] to evaluate EMR's retarding function on slag cement.

Results and Discussion

Chemical Additives on EMR Excitation

Alkaline medium is required for the $CaSO_4$ in EMR to activate cementing material. Hydrating rate of the hydraulic components in EMR such as activated SiO_2 and Al_2O_3 could be accelerated by the Alkaline medium. Lime, white lime and clinker were chosen as auxiliary-activators for EMR to make cementing material admixture for they were cheap and had been widely applied in industry.

The effect of different chemical additives on EMR's excitation activity A7 and A28 was presented in Table II. S75 slag's activity indexes in sample 3-6# were obviously promoted with alkali added as compared to that of sample 1-2#. The sample 5# and 6# with $Ca(OH)_2$ added had higher A7 while the sample 2# and 6# with $Ca(OH)_2$ added had higher A28. It indicated that $Ca(OH)_2$ and clinker had more effective auxiliary-activation effect on EMR than CaO, $Ca(OH)_2$ was better for EMR to increase the slag cementing material's early strength and clinker was better for EMR to increase its later strength, the excitation effect of EMR on slag was guaranteed with $Ca(OH)_2$ and clinker added at the same time as sample 6#. Sample 2# with fly ash partly substituted for slag had lower activity indexes than Sample 1#. It illustrated that it was better for EMR to activate slag than to activate fly ash.

Ratio of Materials on EMR Activation

The EMR mixture was composed of EMR, $Ca(OH)_2$ and clinker according to above

experiment. Its ratio of them on activation performs was studied using orthogonal experiment.

The values of four levels for every factor were based on our early exploratory single factor experiments and literature [21]. The samples' A7 and A28 were presented in Table III. The optimal levels group for A7 was A1B2C4, its weight percent ratio of $Ca(OH)_2$/cement/clinker EMR was 3 : 4 : 30. The optimal levels group for A7 was A1B3C4, its weight percent ratio of $Ca(OH)_2$/ cement/clinker EMR was 3 : 6 : 30. The final optimal weight percent ratio of $Ca(OH)_2$/cement/ clinker EMR was fixed at 3 : 5 : 30 to guarantee the best early and later excitation of EMR on slag. The importance order of three factors was studied by rang analysis in the orthogonal table and_based on A7 was EMR, $Ca(OH)_2$ and clinker. The importance order of three factors based on A28 was EMR, clinker and $Ca(OH)_2$. It indicated that EMR was the most important activator, $Ca(OH)_2$ had more effective activation effect on slag's early activity than clinker while clinker had more effective activation effect on slag's later activity than $Ca(OH)_2$. It certified the result in former experiment.

Table II. Effect of Chemical Additives on EMR Excitation Activity /%

No.	EMR	Clinker	CaO	$Ca(OH)_2$	Fly ash	Slag	A7	A28
1#	20%	—	—	—	—	80%	73	89
2#	20%	—	—	—	20%	60%	67	86
3#	20%	10%	—	—	—	70%	86	92
4#	20%	—	5%	—	—	75%	80	87
5#	20%	—	—	5%	—	75%	106	85
6#	20%	5%	—	5%	—	70g	94	92

Treating Temperature on EMR Activities

The gypsum was found to have five crystal phases [22-24] $CaSO_4 \cdot 2H_2O$, $CaSO_4 \cdot 0.5H_2O$, $CaSO_4$(III), $CaSO_4$(II) and $CaSO_4$(I), which had different microstructures and macroscopic properties. The crystal pattern of gypsum would transform in heat treatment processes. However, EMR had not only gypsum but also other compounds such as SiO_2, Al_2O_3, Fe_2O_3, MgO, and MnO. Effect of temperature on gypsum's crystal pattern was significant for us to study the thermal activation of EMR. It was found that the gypsum in EMR did not have the same transformation rules as pure gypsum.

Setting time of EMR-slag cement was provided in Table IV. It was found that the setting time shortened with the increase of treating temperature. The slag cementing material added with raw EMR had the longest initial setting time 6 h while other slag cementing material added with thermally activated EMR had shorter ones. The initial setting time was almost steady when the treating temperature was over 350 °C, but the final setting time still shortened to some extent. Although all of the samples' setting time accorded with Chinese national standard well, 3 h initial setting time would be more suitable for application.

Table III. Orthogonal Experiment for the Ratio of EMR Admixture

No.	Factors						Activity index	
	A	$Ca(OH)_2$	B	Clinker	C	EMR	A7	A28
1	1	3g	1	2g	1	15g	83	64
2	1	3g	2	4g	2	20g	98	89
3	1	3g	3	6g	3	25g	89	82
4	1	3g	4	8g	4	30g	96	81
5	2	4g	1	2g	2	20g	68	74
6	2	4g	2	4g	1	15g	74	73
7	2	4g	3	6g	4	30g	91	97
8	2	4g	4	8g	3	25g	71	65
9	3	5g	1	2g	3	25g	71	76
10	3	5g	2	4g	4	30g	91	85
11	3	5g	3	6g	1	15g	72	72
12	3	5g	4	8g	2	20g	80	83
13	4	6g	1	2g	4	30g	103	75
14	4	6g	2	4g	3	25g	79	70
15	4	6g	3	6g	2	20g	76	77
16	4	6g	4	8g	1	15g	77	78
	A7	A28	A7	A28	A7	A28		
∑ (1)	366	326	325	289	306	287		
∑ (2)	304	309	342	317	322	323		
∑ (3)	314	316	328	328	310	293		
∑ (4)	335	300	324	307	381	338		
∑ (1) / 4	91.5	81.5	81.25	72.25	76.5	71.75		
∑ (2) / 4	76	77.25	85.5	79.25	80.5	80.75		
∑ (3) / 4	78.5	79	82	82	77.5	73.25		
∑ (4) / 4	83.75	75	81	76.75	95.25	84.5		
R	15.5	6.5	4.5	9.75	18.75	12.75		
	A7			A28				
Optimal level	A1	B2	C4	A1	B3	C4		
Importance order	C>A>B			C>B>A				

EMR had low effective sulfate solubility and gypsum hydration rate when it was untreated or just treated under 300 °C. The sulfate could make such thin AFt layer by reacting with C_4AH_{13} slowly that the EMR-slag cementing material had long setting time. The sulfate and gypsum had higher solubility and hydration rate after EMR treated at 300 °C to 600 °C. Plenty of AFt formed quickly and grew up as acicular crystals, which overlapped among cement particles in reticular structure and made slurry set normally and the setting time of EMR-slag cementing material short. The sulfate's solubility was still higher than that of EMR treated under 400 °C although the gypsum had the lowest hydration rate after treated above 600 °C. AFt enwrapping

layer formed so quickly that the setting time of EMR-slag cementing material was much shorter.

Table IV. Effect of treating temperature on EMR retarding activity

NO.	T/℃	Water requirement of normal consistency	Initial setting time(min)	Final setting time(min)
1	None	0.292	360	430
2	120	0.304	250	290
3	250	0.314	240	290
4	350	0.312	165	300
5	450	0.320	170	280
6	550	0.328	170	270
7	750	0.364	160	225

Activity indexes of modified slag were presented in Figure 1. As viewed from the A7 dates, the activity of slag modified by raw EMR or by the one dried at 120 ℃ was higher than that of the slag modified by the one treated at higher temperature. This means that the latter had lower early strength than the former. As viewed from the A28 dates, the activity of slag modified by thermally activated EMR was higher than that of the slag modified by raw EMR, particularly the EMR treated at 350 ℃ and 450 ℃ illustrated stronger effective excitation effect on slag.

It was found that sustaining existence and high concentration of Ca^{2+} and SO_4^{2-} not only kept the fast formation of AFt phase steady, but also provided Ca^{2+} saturation for $Ca(OH)_2$ nucleation in cement hydrating process [25]. The nucleation of $Ca(OH)_2$ could accelerate the hydration of C_3S and C_2S. EMR had higher sulfate solubility and gypsum hydration rate after treated at 300 ℃ to 600 ℃, which could provide plenty of Ca^{2+} and SO_4^{2-} for the production and agglomeration of AFt and C-S-H. A compact hydration product was obtained for the cement particles were packed tightly. This made A28 of slag modified by these EMR higher. On the other hand, sulfate solubility and gypsum hydration rate in raw EMR were lower so that its sulfate excitation effect on slag was not obvious and A28 of slag modified by these EMR was very low.

The thermally treated EMR had not only good retarding activity but also obvious excitation effect on the slag. It could promote the strength of slag cement and be used to make retarding and excitation addict for cementing material.

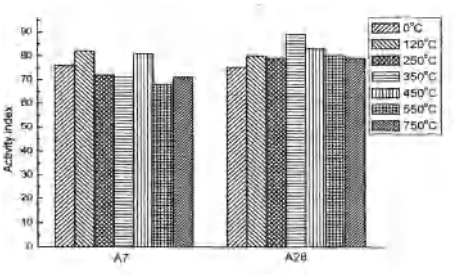

Figure 1. Effect of Treating Temperature on EMR Excitation Activity

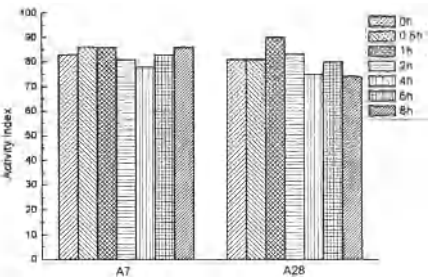

Figure 2. Effect of Treating Time on EMD Residue Excitation

Treating Time on EMR Activities

Treating time is one of primary influence facts during EMR thermal modification and should be taken into account except for the treating temperature.

Table V. Effect of treating time on EMR retarding activity

No.	Thermal time(h)	Water requirement of normal consistency	Initial setting time (min)	Final setting time (min)
1	0	0.316	220	295
2	0.5	0.316	225	315
3	1	0.316	165	265
4	2	0.316	190	305
5	4	0.320	185	285
6	6	0.320	245	315
7	8	0.324	220	305

The experimental data for setting time of EMR-slag cement was provided in Table V. It was seen that the setting time shortened first and then prolonged with the extension of treating time. The initial setting time of slag cementing material added with EMR treated for 1 h to 4 h accorded with the application preference in China. Activity indexes of modified slag were presented in Figure 2. The slag modified by EMR treated for 1h to 2 h illustrated highest activity up to 90 for A28.

The effect of treating time on EMR activity, as well as the effect of treating temperature discussed before, could be understood by analyzing the formation of different gypsum crystal. $CaSO_4 \cdot 0.5H_2O$ was dehydrated to form $CaSO_4$(III) step by step with the extension of treating time, meanwhile $CaSO_4$(III) crystal particles grew up and integrated. This made its activity higher. But excessively prolonging treating time not only caused the crystal particles agglomerating but also led alkali or other sulfate decomposed. Thus, EMR activity was weakened and A28 of slag modified by this EMR declined.

Milling Time on EMR Activities

The particle size of EMR was very small and easy to agglomerate for dehydration after thermal treatment. Therefore, mechanical activation would not only increase its surface area by reducing its particle size but also promote its activity by increasing its crystal defects.

The effect of milling time on EMR retarding and excitation activities was presented in Table VI and Figure 3. The median size (D_{50}) of EMR particles decreased first and increased afterwards with milling time prolonged. Its decrease illustrated that the agglomerated EMR particles were separated by ball milling. But the separated particles were agglomerated again by mechanical power under excessively extending the milling time this resulted in the D_{50} increasing again and made.EMR particles' surface area increases by mechanical activation. On one hand, the surface area

increased with particle size decrease as sample 1# to 3#. The surface area got larger with surface roughness and cracks of EMR particles by the milling. It was the reason for that sample 4# and 5# had the bigger D_{50} than sample 1# on the same surface area. It was found that the initial setting time of EMR-slag cementing material decreased firstly and later increased, A28 of the slag modified by EMR increased firstly and decreased later, both of them reached the peak with the EMR milled for 18min. The activity of gypsum in EMR was promoted with particle size decrease and surface area increase. The gypsum's solubility and hydration rate were also improved. It increased A28 and shortened the setting time. Besides of that, it was mentioned in Ke Guojun's research [26] that the dispersed small quartz particles could make the AFt form on its surface. These prevented it from deposited on the cement particles and greatly accelerated the C_3A's hydration rate. In this experiment, the SiO_2 in milled EMR had small particle size, large surface area and high activity. The AFt was absorbed on its surface and the hydration rate of C_3A in EMR-slag cementing material was improved indirectly. It shortened the setting time and promoted the sample's strength.

Table VI. Effect of Ball Milling Time on EMR Retarding Activity

No.	Ball milling time(min)	D_{50} (nm)	BET surface area (m^2/g)	Water requirement of normal consistency	Initial setting time (min)	Final setting time (min)
1#	6	568	13.14	0.312	270	360
2#	12	476	15.94	0.311	230	320
3#	18	372	16.66	0.306	150	310
4#	24	647	15.90	0.296	290	360
5#	30	641	15.98	0.294	240	315

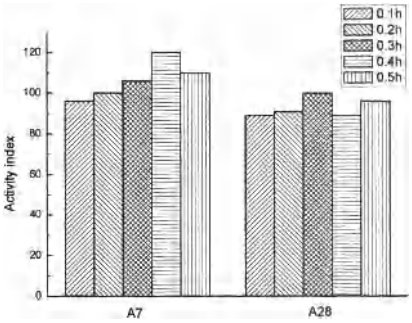

Figure 3. Effect of Ball Milling Time on EMR Excitation

Conclusions

EMR has good retarding and excitation functions after chemical, thermal and mechanical activation. The modified EMR contributes to both increasing slag cementing material's strength and adjusting its setting time. The following conclusions are drawn from this study.

(1) The activity indexes of the slag are promoted with EMR added. EMR could be

used to prepare activator for slag cementing materials after chemical activation. The excitation of EMR improves with clinker and $Ca(OH)_2$ mixed. The optimal weight percent ratio of EMR/$Ca(OH)_2$/ cement clinker for making cementing material activator is 30 : 3 : 5.

(2) The setting time of EMR-slag cementing material prolongs with residue content. It is better to use as much residue as possible in cementing material admixture on the promise of accordance with the Chinese GB and treated at low temperature. Therefore, 350 ℃ and 1h are the best parameters for EMR thermal modification based on high residue content utilization, energy-saving and habit of using 3h initial setting time cementing material in China.

(3) The retarding and excitation activities of EMR are influenced by its particle size and surface area determined by mechanical activation. Small particle size and lager surface area result in high hydration rate for EMR components and contribute to better excitation performance on slag. Eighteen min is the optimal milling time for EMR mechanical activation.

Acknowledgements

The authors acknowledge the financial support of the National 863 Key Project (SQ2010AA06XK1489330).

References

1. Chaoming Pang, Hong-gen Qin and Chunmei Zhang, "Influence of Activators on Properties of Binding Materials with Industrial wastes," *China Concrete and Cement Products*, 3 (2005), 11-13

2. Weiguo Shen, Zhi Cai and Wei Ma, "Investigation on the Thermodynamic of the Industrial Solid Waste Cementitious Materials," *Journal of Wuhan University of Technology*, 30(5) (2008), 19-23

3. Yiyun Lin, Jiangshan Zhang and Changqing Liu, "Generation Prediction and Countermeasure of Industrial Solid Waste in China," *Environmental Science and Management*, 33(7) (2008), 47-50

4. Hong Huang, Mingliang Tang and Xiaodong Shen, "The Resourcing of Industrial Waste and Its Sustainable Development-Combine Tightly with Cement and Concrete Industrial for Sustainable Development," *Materials Review*, 2(5)(2006) , 455-458

5. Huifen Yang, *Solid Waste Treatment Technology and Application* (Bei Jin, BJ: Machine Press, 2003), 55-62

6. Qing Shi, *Building Materials of Industrial Waste* (Bei Jin, BJ: China Environmental Industry Press, 1992), 47-59

7. Bilinshki H, Kwokal Z and Branica M, "Formation of some manganese minerals from ferromanganese factory waste disposed in the Krka River Estuary," *Water Research*, 30(30)(1996), 495-500

8. Jun Yao, Wenxue Wu and Xiaoduan Yang, "The Pollution From the Electro-manganese Plant in Wan Rong Jiang River," *Journal of Jishou University (Natural Science Edition)*, 20(3)(1999), 30-33

9. Jianqi De, "Preparation of Mn fertilizer with waste manganese residue," *Phosphate and Compound Fertilizer*. 3(1997), 14-16.
10. Bo Chen, Qijing Pan and Benguo Zhong, "Chemical Manganese Dioxide Made from Slag Containing Manganese," China's Manganese Industry, 14(1)(1996), 32-36
11. Guojun Ke and Zhuanbo Liu, "Binding Material Made of Waste Electrolyzed Manganese Slag," *Construction Conserves Energy*, 3 (1995):19-20
12. Yun Feng, Yanxin Chen and Fei Liu, "Studies on replacement of gypsum by manganese slag as retarder in cement manufacture," *Modern Chemical industry*, 26(2)(2006), 57-60
13. Songlin Gao, Yun Feng and Lifeng Song, "Set Controlling Admixture Test Using Electrolytic Manganese Slag Instead on Gypsum," *Cement Technology*, 6 (2001), 75-76
14. Zhongwei Wu, "High Performance Concrete-Green Concrete," *China Concrete and Cement Products*, 1 (2000), 3-6
15. Weizu Tan. "Review and Looking Forward to High Performance Concrete," *Architecture Technology*, 1 (2004), 12-16
16. Tanping Li, Hualin Xie and Xiaomei He, "Experimental Study of Calcinated Electrolysis Manganese Residue and Fly Ash Complex admixture," *Bulletin of the Chinese Ceramic Society*, 26(3)(2007), 567-592
17. Jun Xie and Huiming Bao, "study on service test of cement mortar and concrete mixed with manganic sintering temperature," *Subgrade Engineering*, 5(2007), 156-158
18. Zhenying Guan. "Study on Using Residue From Electrolysing Manganese as Cement Retarding Agent," *China's Manganese Industry*, 18(2)(2000), 36-37
19. National Cement Standardization Technical Committee, *GB/T18046-2000 Ground Granulated Blast Furnace Slag Used for Cement and Concrete* (Bei Jin, BJ: China Standards Press, 2000), 1-15
20. National Cement Standardization Technical Committee, *GB/T1346-2001 Test Methods for Water Requirement of Normal Consistency, Setting Time and Soundness of the Portland Cements* (Bei Jin, BJ: China Standards Press, 2001), 1-10
21. Runzhang Yuan. *Cementing Material* (Wu Han, WH: Wu Han Industry University Press,1996), 78-89
22. POWELL D A. "Transformation of the α- and β- forms of calcium sulphate hemihydrates to in soluble anhydrite," *Nature*, 182(1958), 792-796
23. France National Society of Plaster Industries, *Plaster: Physic-Chemistry and Fabrication-Application*, ed. Yang Deshan(Bei Jin, BJ: China Building Industrial Press, 1987), 67-70
24. ASKLAND D R, *The Science and Engineering of Materials* (London, L: Van Nostrand Reihold Co Ltd, 1988), 124
25. Barnes P, *Cement Construct and Property* (Bei Jin, BJ: China Building Industrial Press,1987), 182-210
26. Guojun Ke, "Hydration Mechanism of Binding Material Made of Burnt Manganese-Cement," *Journal of Central-South Institute of Technology*, 11(2)(1997), 8-13

3rd International Symposium on High-Temperature Metallurgical Processing
Edited by: Tao Jiang, Jiann-Yang Hwang, Patrick Masset, Onuralp Yucel, Rafael Padilla, and Guifeng Zhou
TMS (The Minerals, Metals & Materials Society), 2012

STUDY ON THE DESULFURATION OF PYRITE CINDER PELLETS

Zhiyong RUAN[1, 2], Deqing ZHU[1], Tiejun CHUN[1], Jian PAN[1]
[1] School of minerals processing and bioengineering, Central South University, Changsha, 410083, P.R.China
[2] Liuzhou iron and steel group, Liuzhou, 545002, P.R.China

Keywords: Pyrite Cinder; Pelletizing, Sulfur Content; Desulfuration

Abstract

In this paper, the desulfuration of pyrite cinder pellets was carried out. Phase analysis shows that most sulfur of pyrite cinder exists in the form of elementary sulfur. Most sulfur was removed in preheating stage. 81.25% sulfur was removed and the average SO_2 concentration of exhaust gas was 1365ppm when the pellets were preheated at 950°C for 9 min. The final product, assaying 62.42wt%Fe and 0.02wt%S content at 96.88% desulfuration was achieved under the conditions of preheating at 950℃ for 9 min and roasting at 1200℃ for 15 min, which can be used as the burden for blast furnace.

Introduction

Pyrite cinder, as a subsidiary product of sulfuric acid production by roasting of pyrite ores, was solid waste in sulfuric acid enterprises. According to the statistics, the annual production of pyrite cinder is about 15 million tons in China. Besides, there is lots of pyrite cinder deposited for many years [1-3]. The pyrite cinder consumed in the cement and other industries as auxiliary additives only accounts for less 30% of its total discharge and the left is stored in waste pond, occupying much land and polluting environment in China [4-5]. Moreover, pyrite cinder contains iron between 30-63% which can be utilized as a cheap raw material for ironmaking by sintering or pelletizing processes, which can not only prevent pollution but also provide cheap raw materials for ironmaking [6-7]. However, compared to traditional iron ore concentrate, pyrite cinder possesses higher sulfur content.

There are extensive researches carried out on the utilization of pyrite cinder [8-11], such as high grade pyrite cinder containing over 60wt%Fe can be directly used to produce oxidized pellets, and lower grade pyrite cinder can only be used directly to produce sinter or to prepare oxidized pellets only after being upgraded. However, the researches about the desulfuration of pyrite cinder pellets are very few. Therefore, the desulfuration of pyrite cinder pellets was studied in this paper.

Experimental

Raw Materials

The raw materials include the pyrite cinder and bentonite. Their chemical compositions of materials are documented in Table 1. The iron grade of the pyrite cinder is 63.34%Fe, which is suitable for pelletizing feed. However, the sulfur content is 0.64%, which is much higher than traditional iron concentrate. The particle size of pyrite cinder 89.54% passes 0.074mm. The sulfur content distributions in pyrite cinder are given in Table 2. The sulfur of pyrite cinder exists in the form of elementary sulfur. The particles morphology of pyrite cinder under SEM is depicted in Figure 1. It can be seen that pyrite cinder particles possesses high porous rough surface.

Table I. Chemical Compositions of Raw Materials

Types	Fe_{total}	FeO	Al_2O_3	CaO	MgO
Pyrite cinder/%	63.34	15.9	1.60	0.85	0.23
Bentonite/%	3.88	—	16.34	1.98	2.02

Na_2O	K_2O	SiO_2	P	S	LOI
0.024	0.19	6.58	0.017	0.64	0.75
2.40	2.00	54.85	0.028	0.029	12.08

Table II. Sulfur Content Distributions in Pyrite Cinder

Types	Sulfate	Elementary sulfur	Sulfide	Total
Content/%	0.07	0.56	0.01	0.64
Distribution/%	10.94	87.50	1.56	100

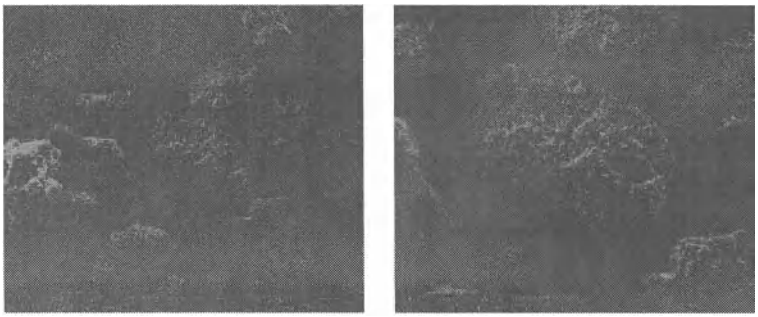

(a) Pyrite cinder 1000X (b) Pyrite cinder 2000X

Figure 1. Morphological Photographs of Pyrite Cinder under Scanning Electron Microscope (SEM)

The quality of bentonite is excellent due to higher content of montmorillonite of 90.5%, higher swelling volume of 15.8mL/g and water adsorption of 416% and fine size of 86.72% passing 0.074 mm.

Experimental Procedure

The experiment flow sheet includes main procedures, such as mixing pyrite cinder with bentonite at a given ratio, pelletizing in a disc pelletizer, drying in the oven, preheating and roasting in a tube furnace to make roasted pellets.

Green pellets were made from the mix of pyrite cinder and bentonite in a disc pelletizer of 0.8m in diameter and 0.2 m rim depth, rotational speed at 38 rpm and inclined at 47° to the horizontal. The green pellets were then sized between 12 and 16mm. Dried pellets were obtained under the condition of drying the green pellets in the oven at 105°C for 2h. Eight dried pellets were preheated and roasted in a tube furnace of 50mm in diameter and 600mm width. The sulfur content of preheated pellets and roasted pellets was tested. The flow rate of air was 1L/min, and the SO_2 concentration in exhaust gas was calculated by the sulfur content in pellets at different time in preheating and roasting stages.

Green pellets were made under the following conditions: mixing pyrite cinder with 1.5wt% dosage bentonite and pelletizing for 13min at 13% moisture in disc pelletizer. The green pellets were dried in the oven at 105°C for 2 h. The sulfur content of green pellets and dried pellets are 0.64wt%, and the sulfur cannot be removed by drying in the oven.

Results and discussions

Preheating and Roasting

Preheating Temperature. Figure 3 illustrates the effects of preheating temperature on the S content of preheated pellets and desulfuration. S content of preheated pellets reduces from 0.15% to 0.058%, and the desulfuration increases from 76.56% to 90.94% when the temperature is elevated from 850°C to 1000°C. The higher the preheating temperature was elevated, the lower S content of preheated pellets was obtained. The reason is that sulfur of pyrite cinder exists in the form of elementary sulfur, which was oxidized into SO_2 to exhaust when pellets were preheating in the air.

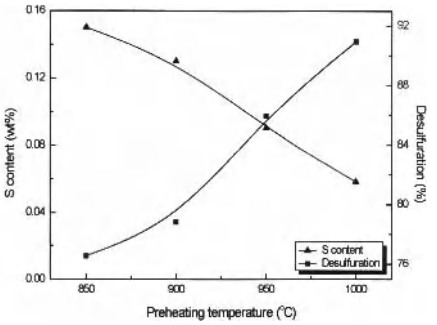

Figure 3. Effects of Preheating Temperature on S Content of Preheated Pellets and Desulfuration (Preheating for 15 min)

Preheating Time. The effects of preheating time on S content of preheated pellets and desulfuration are presented in Figure.4. As the preheating time exceeds from 9 min to 18 min, the S content of preheated pellets decreases from 0.12% to 0.085%, and the desulfuration climbs from 81.25% to 86.72%. Compared to preheating temperature, preheating time possesses less influence on S content of preheated pellets and desulfuration.

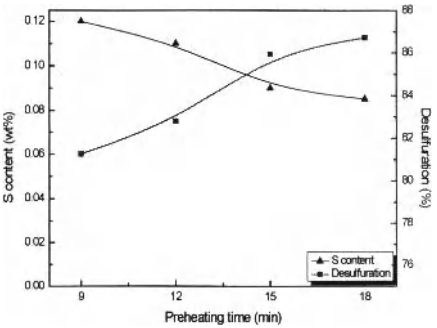

Figure 4. Effects of Preheating Time on S Content of Preheated Pellets and Desulfuration (Preheating at 950℃)

Roasting Temperature. It can be seen from Figure 5 that with an increase in roasting temperature, S content of roasted pellets drops significantly from 0.036% to 0.018%, and the desulfuration (including preheating process) increases from 94.38% to 97.19%. In summary, increasing temperature can improve the desulfuration significantly in preheating and roasting process.

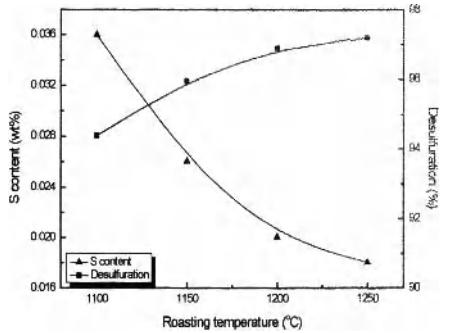

Figure 5. Effects of Roasting Temperature on S Content of Roasted Pellets and Desulfuration (Preheating at 950°C for 9 min and roasting for 15min)

Roasting Time. Figure 6 demonstrates the effects of roasting time on S content of roasted pellets and desulfuration. The S content of roasted pellets reduces from 0.022% to 0.020%, and the desulfuration (including preheating process) increases slightly from 96.56% to 96.88% when roasting time extends from 9 min to 15 min. However, the S content of roasted pellets remains unaffected when roasting time prolongs to 18 min. It can be concluded that roasting time brings about slight impact on reducing S content of roasted pellets in roasting process.

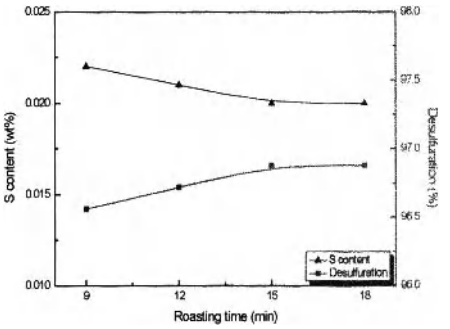

Figure 6. Effects of Roasting Time on S Content of Roasted Pellets and Desulfuration (Preheating at 950℃ for 9 min and roasting at 1200℃)

The roasted pellets, assaying 62.42wt% iron grade and 0.02wt% S content at 96.88% desulfuration was achieved under the conditions of preheating at 950°C for 9 min and roasting at 1200°C for 15 min , which meets the requirement of the burden for blast furnace.

SO_2 Concentration of Exhaust Gas

Figure 7 shows SO_2 concentration of exhaust gas in preheating and roasting process. The SO_2 concentration of exhaust gas drops noticeably when time increases from 0 to 12 min. The SO_2 concentration of exhaust gas reduces slightly from 105ppm to 42ppm when time is exceeded from 12 to 24 min. Moreover, the SO_2 concentration of exhaust gas in preheating stage is much higher than that in roasting stage. In preheating stage, the average SO_2 concentration of exhaust gas is 1365ppm, much higher than that of 132ppm in roasting stage. It can be conclude most sulfur of pyrite cinder was removed in preheating stage, which agrees with the results of Fig.4 that 81.25% sulfur was removed when dried pellets preheating at 950°C for 9 min.

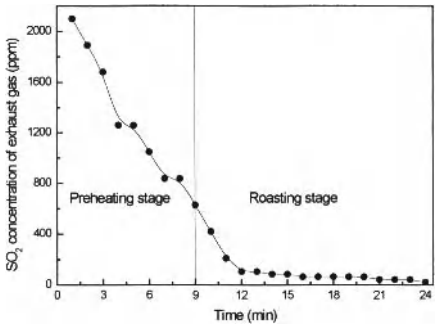

Figure 7. SO_2 Concentration of Exhaust Gas in Preheating and Roasting Process (Preheating at 950℃ for 9 min and roasting at 1200℃ for 15 min)

Conclusions

(1) Most sulfur of pyrite cinder exists in the form of elementary sulfur, and the sulfur cannot be removed when the green pellets dry in the oven at 105 ℃. The sulfur can be removed in preheating and roasting stage. Desulfuration effects of preheating stage are superior to those of roasting stage. Compared to the average SO_2 concentration of 132ppm in roasting stage, the average SO_2 concentration of exhaust gas is higher of 1365ppm in preheating stage.

(2) The final product, assaying 62.42wt%Fe and 0.02wt% S content at 96.88% desulfuration, was obtained under the conditions of preheating at 950°C for 9 min and roasting at 1200℃ for 15 min, which met the requirement of blast furnace burden.

References

1. Tang, G D, "Research on Pyrite Cinder Used in Pellet Production," *China Resources Comprehensive Utilisation*, 7(2006), 5-7.

2. Dong, F Z, Yao, D and Sun, Y F, "Investigation and Application of Magnetisation-Roasting Process for Iron Separation from Pyrite Cinder," *Pollution and Control*, 26(5)(2004), 387-389.

3. Zhu, D Q and Li J, "Preparation of high quality magnetite concentrate from pyrite cinder by composite pellet reduction-roasting and magnetic-separation," *The Chinese Journal of Nonferrous Metals*, 17(4) (2007), 649-656.

4. Liu, Q J and Zhou, X L, "Current Situation and Progress of Research on Comprehensive Utilisation of Roasted Pyrite," *Yunnan Metallurgy*, 32(2)(2003), 27-30.

5. Chen, T J and Zhang, Y M, "Experiments of Acid Pellet Using Treated Pyrite Slag and Its Commercial Application," *Research on Iron&Steel*, 142(1)(2005),1-4.

6. Zhang, Y M and Yang, S Y, "Experimental Study of Pyritic Slag Concentrate Pelletising," *Sintering and Pelletising*, 27(2)(2002), 11-14.

7. Peng, Z J and Li, Q X, "Researches on the Balling and Roasting Properties of the Slphuric Acid Dregs," *Sintering and Pelletising*, 28(6)(2003), 21-24.

8. Sun, X Q and Yao, Z S, "Experimental feasibility study on production of oxidised agglomerate by utilisation of SA cinder". *Phosphate &Compound Fertilize*, 20(6)(2005),13-15.

9. Zhu, D Q and Li, J, "Study on Pelletising of Magnetite Concentrate from Pyrite Cinder," Mining and Metallurgical Engineering, 26(6)(2006), 49-52.

10. Zhu, D Q and Chen, D, "Pretreatment of Pyrite Cinder Before Pelletisation by High Pressure Roller Grinding," In Proceedings of the 5th *Congress on the Science and Technology of Ironmaking*, (Shanghai), 2(2009), 348-351.

11. Yu W, Zhu,D Q, and Li,Q H, "Improving pelletisation of pyrite cinder by high pressure roller grinding," *XXV International Mineral Processing Congress*, (Brisbane Australia), 2010, 213-221.

3rd International Symposium on High-Temperature Metallurgical Processing
Edited by: Tao Jiang, Jiann-Yang Hwang, Patrick Masset, Onuralp Yucel, Rafael Padilla, and Guifeng Zhou
TMS (The Minerals, Metals & Materials Society), 2012

3rd International Symposium on High-Temperature Metallurgical Processing

Pelletizing and Raw Materials Processing

Session Chairs:
Ender Keskinkilic
Guanghui Li

3rd International Symposium on High-Temperature Metallurgical Processing
Edited by: Tao Jiang, Jiann-Yang Hwang, Patrick Masset, Onuralp Yucel, Rafael Padilla, and Guifeng Zhou
TMS (The Minerals, Metals & Materials Society), 2012

EFFECTS OF SODIUM SALTS-MODIFIED PAIGEITE ON DEPHOSPHORIZATION OF HIGH-PHOSPHORUS OOLITIC HEMATITE DURING REDUCTION

Guanghui Li, Ting Lei, Mingjun Rao, Tao Jiang*

(School of Minerals Processing & Bioengineering, Central South University, Changsha, Hunan 410083, China)

Key Words: Oolitic hematite, Sodium salts, Paigeite, Dephosphorization, Direct reduction

Abstract

With the rapid development of iron and steel industry, the supply of iron ores can not meet the present demand for iron and steel industry in China. Large reserves of oolitic hematite have been discovered with low iron grade (30% ~ 45%) and high phosphorus content (0.4% ~ 1.8%). Traditional processes for utilization of this ore are characterized as either high cost or low dephosphorization. In this study, sodium salts-modified paigeite (SSMP) was added to enhance on the dephosphorization of high-phosphorus oolitic hematite by using reduction roasting followed by magnetic separation. Various parameters, including the amount of SSMP, reduction time, reduction temperature, grinding fineness and the magnetic field intensity were investigated. As a consequence, a magnetic concentrate of metallic iron powder with total iron grade of 93.2% and phosphorus content of 0.08% was obtained under the optimal conditions. The results also provide a potential avenue for the comprehensive utilization of paigeite ore.

Introduction

Oolitic hematite is currently recognized as one of the most refractory iron ore resources in the world. Over 4.0 billion tons of reserves of such resources have been found in China, and more than 10 billion tons in the long-term. This kind of ore is characterized as low iron grade (30%~45% TFe) and high phosphorus content (0.4%~1.8% P), as well as fine particle size distribution of ferrous minerals (the size distribution varies from 5~30 μm, even less than 2 μm) and the complex association between iron and other gangue elements [1~5]. The unique structural characteristics of the high phosphorus oolitic hematite make it difficult to obtain high iron recovery and good dephosphorization efficiency by using the conventional processes [1,2]. Traditional processes are characterized as high cost and low dephosphorization for oolitic hematite beneficiation [9~15].

The methods reported for dephosphorization of oolitic hematite mainly include physical

* Corresponding Author: Dr. Tao Jiang, jiangtao@csu.edu.cn

separation, flotation, magnetic roasting-magnetic separation and reduction roasting-magnetic separation, etc. [8~12]. Chemical leaching and bio-leaching are also used to treat high phosphorus content iron ore [6, 7]. Currently, dephosphorization from oolitic hematite ore was widely studied by reduction roasting in the presence of additives followed magnetic separation and the dephosphorization was improved. For an example, a magnetic concentrate with 85% total iron grade and 0.2%~0.5% phosphorus content was obtained when reduced at 1150~1300℃ with addition of burnt lime [13], and also a metallic iron powder with 93.84% total iron grade and 0.083% phosphorus content was obtained when reduced in the presence of sodium salts, however, a smelting problem of the materials during reduction roasting causes difficulties in practice [13, 14].

Aiming to eliminate the fusion problem resulted from the addition of sodium salts, a new additive of sodium salts-modified paigeite (SSMP) was developed to enhance the dephosphorization of oolitic hematite. The effects of SSMP dosage, as well as reducing temperature and time, magnetic separation, on the ephosphorization were investigated.

Experimental

Materials

The oolitic hematite ore used in this study was taken from Hubei province of China. The chemical compositions were given in Table I. The XRD pattern presented in Figure 1 shows that the ore mainly contains hematite (Fe_2O_3), quartz (SiO_2), talc ($Mg_3(Si_4O_{10})(OH)_2$), chlorite and calcite, etc.. The chemical phase and distribution of elements presented in Tables II, III indicate that hematite (limonite) is the main iron-bearing mineral, accounting for 97.7%, and apatite is the main phosphorus-bearing mineral which takes the percentage of 95.5%.

Table I. Main Chemical Composition of the Oolitic Hematite Ore (mass fraction, %)

Total iron grade	P	SiO_2	Al_2O_3	MgO	CaO	Na_2O	S	LOI*
43.20	0.90	19.47	7.27	0.75	3.90	0.11	0.02	4.03

LOI*-Loss On Ignition

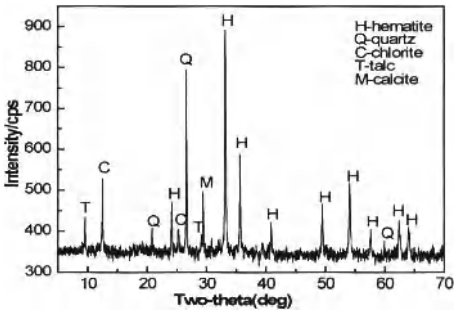

Figure 1. XRD Pattern of the Oolitic Hematite Sample

Table II. Chemical Phase and Distribution of Iron in Oolitic Hematite Ore

Occurrence phase	hematite(limonite)	ferrosilite	siderite	sulfide	Total iron
Fe content /%	42.04	0.79	0.16	0.02	43.01
Fraction/%	97.74	1.84	0.37	0.05	100.00

Table III. Chemical Phase and Distribution of Phosphorus in Oolitic Hematite Ore

Occurrence phase	apatite	iron-containing minerals	others	Total P
P content /%	0.85	0.019	0.021	0.89
Fraction/%	95.51	2.13	2.36	100.00

Methods

The Experimental flowsheet is shown in Figure 2. The ground oolitic hematite was agglomerated after thoroughly mixed with a certain amount of SSMP. The reduction roasting tests of dry agglomerate were carried out in a vertical furnace at the given temperature for a given period. Lignite was used as the reductant. Reduced agglomerate was subjected to low intensity magnetic separation after crushed and ground, and the magnetic product was metallic iron powder. Subsequently, the recovery of iron and the dephosphorization ratio can be calculated as follows:

$$\gamma=\frac{m_0\beta}{m_1\alpha}\times 100\% \quad ; \qquad \eta=\frac{m_0 P_0}{m_1 P_1}\times 100\% \qquad (1)$$

Where: γ is the magnetic recovery of Fe, %; η is the dephosphorization ratio, %; m_1 is the weight of reduced agglomerate, g; m_0 is the weight of magnetic product, g; α is the iron grade of reduced agglomerate, %;β is the iron grade of magnetic product, %; P_0 is the phosphorus grade of magnetic product, %; P_1 is the phosphorus grade of reduced agglomerate, %.

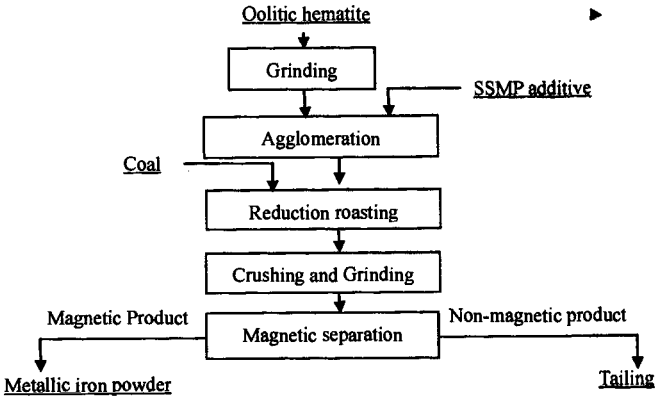

Figure 2. Experimental Flowsheet

Results and Discussion

Effects of SSMP Dosage on the Magnetic Separation and Dephosphorization Ratio

The results shown in Figure 3 evaluate the effect of SSMP on the magnetic separation and dephosphorization ratio. Experiments were performed under the condition of reduction roasting at 1050°C for 60min, grinding fineness of 93.5% undersize 74 μm and magnetic field intensity 1000Gs.

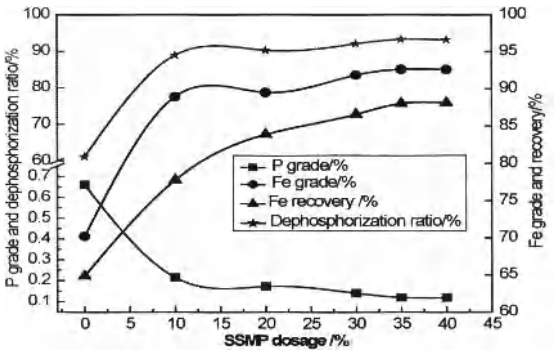

Figure 3. Effects of SSMP Dosage on Magnetic Separation

It can be observed that the presence of SSMP improved the quality of the magnetic product effectively. The total iron grade of magnetic product without SSMP is only 70.2% and phosphorus grade is 0.67% , and the iron recovery is 64.8% and dephosphorization ratio is 61.1%. With increasing of the dosage of SSMP from 10% to 40%, the quality of magnetic product is gradually improved. Adding 35% SSMP, the iron grade of metallic iron powder reaches 92.6%, and the phosphorus grade goes down to 0.12%, 93.3% dephosphorization ratio is obtained correspondingly.

Effects of Reduction Temperature on Reduction and Magnetic Separation

Effects of reduction temperature on quality of magnetic product and the recoveries of iron and dephosphorization ratio are shown in Figure 4. SSMP dosage is 35%, and reduction time is fixed at 60min. Grinding fineness is 93.5% undersize 74 μm and magnetic field intensity is 1000Gs.

The roasting temperature had significant effects on phosphorus grade of the magnetic product and dephosphorization ratio. It can be seen that the grade of iron and iron recovery increase obviously with reduction temperature increasing from 900°C to 1050°C, and P grade decreases to 0.10%, however, these indexes turn into the opposite direction when reduced at 1100°C~1150°C and P grade increases accordingly. It can be concluded that the appropriate roasting temperature range is 1050°C to1100°C.

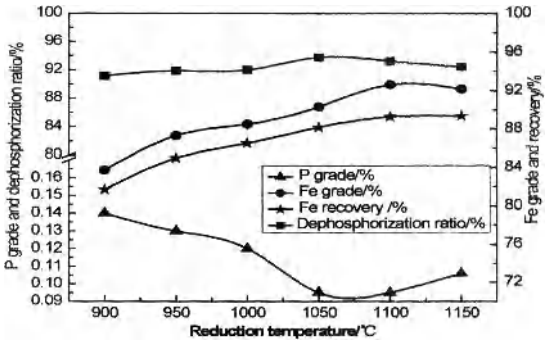

Figure 4. Effects of Reduction Temperature on Magnetic Separation

Effects of Reduction Time on Reduction and Magnetic Separation

The phosphrous content and total iron grade of magnetic product are given in Figure 5 as a function of reduction time under the conditions of 35% SSMP dosage, reduction temperature 1050°C, grinding fineness of 93.5% undersize 74 μm and magnetic field intensity 1000Gs.

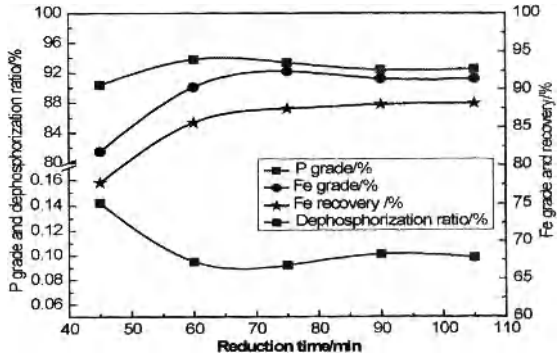

Figure 5. Effects of Reduction Time on Magnetic Separation

The results indicate that the grade of iron , iron recovery and dephosphorization ratio increase significantly with increasing of reduction time from 45 min to 60 min. At the same time, the phosphorus grade of the magnetic product decreases to 0.10%. With the reduction time increases from 60min to 75min, the grade of iron and iron recovery increase from 90.3% to 92.5% and from 85.6% to 88.2% respectively, and the phosphorus grade is as low as 0.09%. The proper reduction time of 75min is recommended at 1050°C.

Effects of Grinding Fineness on Magnetic Separation

The effect of grinding fineness on the quality of magnetic product and the recovery of iron and dephosphorization ratio are shown in Figure 6. Reduction tests were performed with 35% SSMP under the condition of reduction temperature 1050°C for 75min, and magnetic field intensity 1000Gs.

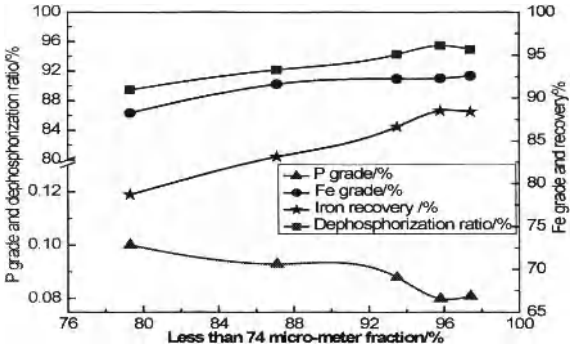

Figure 6. Effects of Grinding Fineness on Magnetic Separation

The results in Figure 6 show that the grade and recovery of iron are influenced obviously by the grinding fineness. When grinding fineness of undersize 74 μm increases from 79.3% to 95.8%, iron grade and recovery of magnetic product increases from 90.2% and 75.7% to 92.6% and 88.5% respectively, meanwhile, phosphorus grade decreases from 0.10% to 0.08%, and dephosphorization ratio goes up to 95.5% correspondingly. There is no significant improvement in the results with smaller particle size. Therefore, 95.8% undersize 74 μm is the proper grinding fineness.

Effects of Magnetic Field Intensity on Magnetic Separation

Figure 7 shows the effect of magnetic field intensity on the quality of magnetic product and the recovery of iron and dephosphorization ratio when oolitic hematite was reduced at 1050°C for 75min in the present of 35% SSMP and grinding fineness of 95.8% undersize 74 μm.

The result shows that the recovery of iron and dephosphorization ratio increase with the rising of magnetic field intensity, and the iron grade is not significantly changed. 93.2% of total iron grade of metallic iron powder, 88.5% and 94.5% of the iron recovery and dephosphorization ratio is achieved respectively. The phosphorus grade of the magnetic product is only 0.08% under 1000Gs magnetic field intensity. The appropriate magnetic field intensity is about 1000Gs.

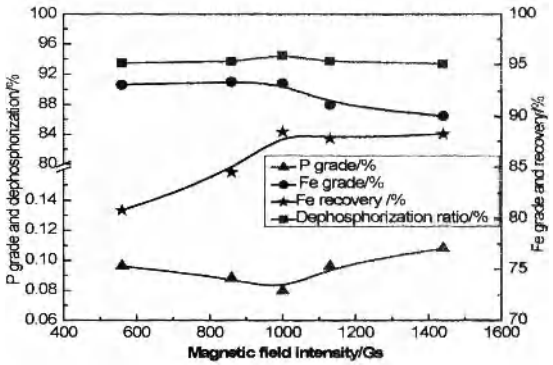

Figure 7. Effects of Magnetic Field Intensity on Magnetic Separation

Metallic Iron Product Propertites

The main chemical composition of the metallic iron product presented in Table IV was obtained under the following optimal conditions: 35% dosage SSMP, reducting temperature 1050℃, reducting time 75min, grinding fineness of 95.8% undersize 74 μm, magnetic field intensity: 1000Gs.

Table IV. Main Chemical Compositions of the Metallic Iron Product (mass fraction, %)

Total iron grade	P	SiO_2	Al_2O_3	Na_2O	CaO	MgO
93.24	0.08	2.33	0.45	0.31	0.21	0.61

Conclusions

(1) The new SSMP additive has an obvious effect on the recovery of iron and dephosphorization of oolitic hematite.
(2) The optimum conditions of direct reduction process to treat the high phosphorus oolitic hematite are as follows: the ground oolitic hematite was agglomerated after thoroughly mixed with 35% SSMP under the condition of reduction temperature 1050°C for 75min, grinding fineness of 95.8% undersize 74 μm and magnetic field intensity 1000Gs.
(3) A metallic iron product with iron grade of 93.2% and phosphorus content of 0.08% was obtained under the optimal conditions, at the same time, the recovery of iron was 88.5%, and the corresponding dephosphorization ratio was up to 94.5%.

Acknowledgement

The authors want to express their thanks to National Science Fund for Distinguished Young Scholars (50725416) and National Natural Science Foundation of China (51174230) for financial support of this research.

References

1. H. Zhong, Z.F. Chao, and J.G. Fu, "Measure method of phosphorus of Ningxiang type iron ore containing high phosphorus," *Express Information of Mine Industry*, 21 (2)(2005) , 28.
2. W.Z. Yin, Y.Z. Ding, "The utilization of the hard-to-beneficiate iron ore resources in our country," *Non-ferrous Mining and Metallurgy*, 8(2006), 163-168.
3. Y.L. Wang, Z.Y. Liu, Y.Q. Cheng, "The geology of Hunan Ningxiang iron ore," *Geological Report*, 2(1961), 112-128.
4. J.M. Fu, "The phase and causes of Ningxiang iron ore in western Hubei Province," *The Geology Journal*, 2(1961), 112-128.
5. Y.S. Zhang, Y.Z. Ding, and W.Q. Gong, "The beneficiation research progress of Ningxiang type oolitic hematite," *Metal Mining*, 8(2010), 92-96.
6. R. Forssberg, G. Asolfsson, "Dephosphorization of high-phosphorus iron ores by means of acid leaching," *Hydrometallurgy*, 34(1981), 316-322.
7. C.Y. Cheng, V.N. Misra, and J. Clough, "Dephosphorization of western Australian iron ore by hydrometallurgical process," *Minerals Engineering*, 9(1999), 1083-1092.
8. C.Y. Qi, Y.F. Yu, and Y.H. Zhang, "Analysis of the reduction roasting mechanism and an effective way of benefication of oolitic hematite," *Metal Mining*, 10(2010), 57-60.
9. C.X. Wang, X. Tong, and J.P. Sun, "Investigation oolitic hematite by magnetic roasting - magnetic separation process," *Metal Mining*, 5(2009), 57-59.
10. J.C. Zhou, Z.L. Xue, and Z.Q. Li, "Investigation of the characteristics of iron grain grown of high-phosphorus oolitic hematite by means of direct reduction process," *Wuhan University of Science Technology Journal (Natural Science)*, 5(2007), 458-460.
11. D.W. Yang et al., "The dephosphorization of high-phosphorus oolitic hematite by reduction roasting process," *Mining and Metallurgical Engineering*, 1(2010), 29-31.
12. Q.L. Wang et al., "Investigation of high-phosphorus oolitic hematite by roasting magnetic antiflotation process," *Hunan Nonferrous Metals*, 4(2009), 12-15.
13. G.H. Li et al., "Infulence of additive on dephosphorization of oolitic hematite by direct reduction process," (Paper presented at TMS2010, 2nd International Symposium on High Temperature Metallurgical Processing", Seattle, 14 February 2011), 505.
14. G.H. Li et al., "Method for preparing steel smelting furnace materials from phosphorus-containing oolitic hematite", Chinese patent 101693948 (2009).
15. S.W. Chen, Q.P. Chen, "Investigation of Guizhou oolitic hematite by means of direct reduction-magnetic separation proces," *Metal Mining*, 11(1997), 13-16.

3rd International Symposium on High-Temperature Metallurgical Processing
Edited by: Tao Jiang, Jiann-Yang Hwang, Patrick Masset, Onuralp Yucel, Rafael Padilla, and Guifeng Zhou
TMS (The Minerals, Metals & Materials Society), 2012

STUDY OF CERTAIN PARAMETERS IN LABORATORY-SCALE SMELTING OF SIVRIHISAR LATERITE ORES OF TURKEY

Ender Keskinkilic[1], Saeid Pournaderi[2], Ahmet Geveci[2], Yavuz A. Topkaya[2]

[1]Atılım University; Department of Metallurgical and Materials Engineering; Incek, Ankara 06836, Turkey
[2]Middle East Technical University; Department of Metallurgical and Materials Engineering; Ankara 06531, Turkey

Keywords: Smelting, Laterite, Ferronickel

Abstract

Conventional ferronickel smelting has five main steps: Drying, calcination, prereduction, smelting and refining. In the scope of the current work, smelting experiments were conducted using Sivrihisar laterite ores (1.26% Ni) of Turkey. The ore samples previously subjected to drying, calcination and prereduction stages were smelted in alumina crucibles in a laboratory-scale horizontal tube furnace under argon atmosphere. Smelting experiments were performed at 1500, 1550 and 1600 °C. The amount of excess coal used in prereduction step was another variable. Sivrihisar laterite ore is a limonitic one with low MgO composition. Therefore, MgO was added to the smelting charge as a flux. The effects of experimental variables on metal Ni content and slag composition were investigated.

Introduction

There are three main laterite ore bodies in Turkey. Two of them are located in western region of the country, named as Gordes and Caldag reserves. The third one, recently found in Sivrihisar region at the beginning of the millennium, is in central Anatolia. Certain hydrometallurgical and pyrometallurgical studies have been conducted by using Gordes and Caldag laterites [1-7]. Currently, Caldag reserves are operated by European Nickel, while hydrometallurgical treatment of Gordes laterites are performed by META Nickel & Cobalt Co. Mining facilities have been continued especially in Yunusemre location of Sivrihisar by the same company. This ore body has an average Ni content of 1.26% and it is a limonite type laterite containing relatively low MgO content and high iron content. Industrial scale pyrometallurgical treatment of Sivrihisar laterites will hopefully be performed in a short while. In this respect, a ferronickel plant will probably be established in Yunusemre region by META Nickel & Cobalt Co. in couple of years.

Last year, a project dealing with laboratory-scale ferronickel production from Sivrihisar laterites was supported by The Scientific and Technological Research Council of Turkey (TUBITAK). This project involves drying, calcination, prereduction and smelting stages of ferronickel production. Up to now, the first three stages of ferronickel production were studied. The readers are addressed to the related work for drying, calcination [8] and prereduction [9].

In the current study, smelting of Sivrihisar laterites was investigated. The ore samples previously subjected to drying, calcination and prereduction stages were smelted in alumina crucibles in a laboratory-scale horizontal tube furnace under argon atmosphere. Smelting experiments were performed at 1500, 1550 and 1600 °C. The amount of excess coal used in prereduction step was

another variable. Due to the nature of the ore, MgO was added to the smelting charge as a flux. The effects of experimental variables on metal Ni content and slag composition were studied.

Experimental

As explained in the previous stages [8] of the current project, representative samples prepared from run of mine ore (ROM) were first subjected to drying and calcination. The ore samples calcined at the optimum conditions were then prereduced using reductant coal. The degree of reduction of nickel, iron and cobalt to their metallic form were examined as well as the extent of conversion of Fe^{3+} into Fe^{2+}. The results were discussed in the related work, in detail [9]. The prereduced calcines produced at the optimum conditions were used as the main charge materials in smelting experiments.

A laboratory-scale horizontal tube furnace was used in the smelting experiments. In each run, charge materials were mixed and charged into alumina crucibles with dimensions of 60 mm length, 32 mm height and 25 mm width. In each experiment, charge mixture was heated to predetermined temperature and it was held at that temperature for predetermined time. At the end of this period, the furnace was cooled down to room temperature using its cooling program. From the start of the experiment till the shutdown of the furnace, argon gas was sent into the system with an average rate of 10 cc/min. A schematical picture of the experimental setup is given in Figure 1.

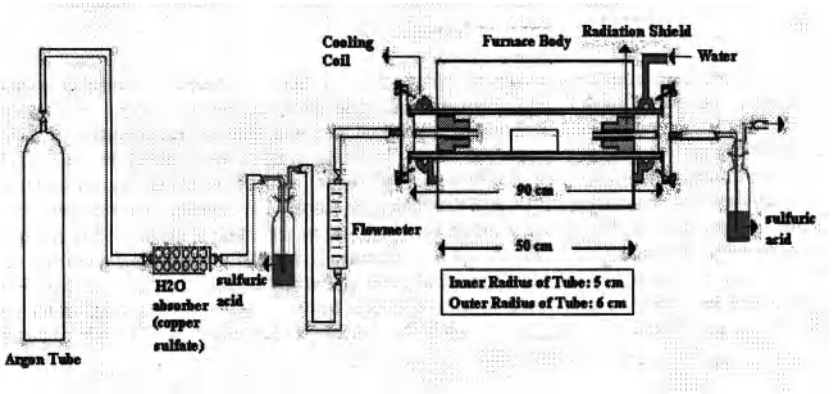

Figure 1. Schematical View of the Experimental Setup

Sivrihisar laterite ore is a limonitic one indicating that its MgO composition is very low. MgO content of the calcined ore was reported as 1.44% [9]. Therefore, MgO was added to the smelting charge to obtain a suitable slag composition satisfying desired SiO_2/MgO ratio, which is very important in ferronickel smelting. In each run, at the end of pyrometallurgical treatment as described above, alumina crucible was taken out of the furnace and crushed carefully. Solidified metal and slag particles were collected and subjected to chemical analysis. Metal and slag particles were first examined using SEM-EDS. For more accurate chemical analysis of metal and slag particles, ICP and XRF were applied, respectively.

Results and Discussion

Smelting experiments were performed at 1500, 1550 and 1600 °C. In the runs conducted in the scope of this work, no coal addition was made. Although not included in this paper, the experiment conducted with the addition of coal produced a metal bullion, which was very poor as well as the nickel content was concerned. In the prereduction stage, use of around 50% excess coal was decided as the optimum coal content considering the degree of reduction of nickel and iron as well as the extent of conversion of Fe^{3+} into Fe^{2+} [9]. Therefore, this preliminary smelting experiment clearly showed that use of coal in smelting stage is not advised under optimum prereduction conditions. As indicated previously, Sivrihisar laterites are almost devoid of MgO so it was added to the smelting charge such that MgO wt./Total charge wt. ratio was adjusted as 0.20. In all runs, charges were waited at the predetermined temperature for 40 minutes. The effect of temperature on metal nickel content is illustrated in Figure 2.

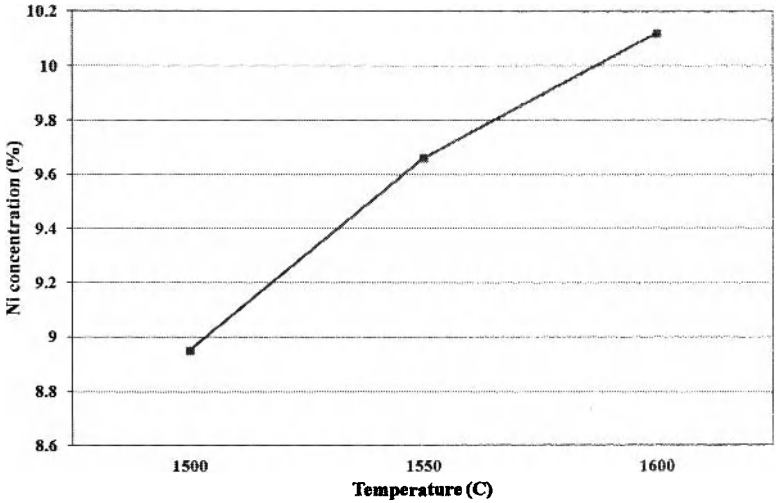

Figure 2. Variation of Metal Ni Concentration (%) with Temperature

The results showed that an increase in experiment temperature led to an increase in nickel content of iron-nickel alloy. Ni content was reported to increase from 8.95% to 9.66% when the temperature was increased from 1500 to 1550 °C. A further increase in temperature to 1600 °C produced an iron-nickel alloy having a nickel content of 10.12%. Apart from this slight increase in metal nickel concentration, the highest distribution term, defined as [Ni wt in metal / (Ni wt in metal + Ni wt in slag)]*100, was obtained at 1550 °C. At this temperature, this distribution term was calculated as 97%. Corresponding values at 1500 and 1600 °C were reported as 89% and 95%, respectively. Normally, the use of recovery concept is more appropriate to evaluate the extent of nickel presence in metal. On the other hand, mass balances regarding to nickel input to the smelting system and nickel output from the system gave slightly different values for each

run. These variations were mostly attributed to certain variations created in preceeding calcination and prereduction stages as well as the mass losses while collecting the metal and slag particles from the crushed crucible. The extent of error created due to mass losses is more pronounced since the total charge weight was 15.40 grams in each run and therefore the weights of metal and slag particles is only a few grams. Due to these difficulties encountered, both the nickel weight in metal and the distribution term defined above were evaluated instead of recovery.

The variation of slag NiO composition with temperature is shown in Figure 3. Although not given here, the slag weights were not very much different from one another. Therefore, NiO content of the slag is a valuable tool to analyze nickel losses. The highest nickel loss was reported at the run conducted at 1500 °C. NiO content of the slag was reported as 0.162% at this temperature. NiO composition was found to be less than 0.100% at higher temperatures. NiO values were obtained as 0.048% and 0.085% for 1550 and 1600 °C, respectively. The lowest nickel loss was reported at the experiment conducted at 1550 °C. As indicated in the previous paragraph, the run performed at this temperature produced the highest distribution term. Correspondingly, the highest %Ni/%NiO partition and metal/slag wt. ratio values were obtained. Therefore, for the experimental system under consideration, 1550 °C was determined as the optimum temperature for smelting. It was also inferred that 50% excess coal use at the prereduction stage led to formation of iron-nickel alloy having nickel content of around 10%, which is less than the minimum amount to be present in raw ferronickel.

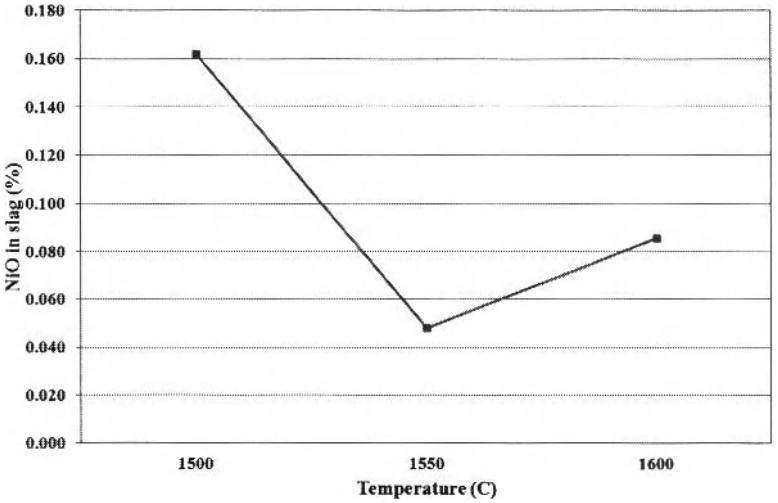

Figure 3. Variation of Slag NiO Concentration (%) with Temperature

Regarding to slags obtained at the end of these experiments, one of the most important points to be mentioned is the variation of Al_2O_3 content with temperature. The extent of interaction of alumina crucible with metal-slag system was reported to be directly proportional with temperature. This behavior was clearly observed especially at the end of the run conducted at 1600 °C. Some parts of the bottom and side walls of alumina crucible turned down to brown like color, indicating the chemical reaction(s) between the crucible and the system. The chemical analysis of the slags produced clearly showed a great increase in Al_2O_3 composition when the experiment temperature was raised. As graphically shown in Figure 4, the slag obtained from the run conducted at 1500 °C was reported to contain 14.07% Al_2O_3. Alumina compositions of the slags produced at 1550 and 1600 °C were found as 22.45% and 38.33%, respectively. Although the numerical values are not included in the scope of the current work, this increase in Al_2O_3 content took place with a decrease in FeO and SiO_2 compositions yielding lower SiO_2/MgO values. Therefore, for the system under consideration, it was inferred that excessively high temperatures like 1600 °C must be avoided not to increase the extent of interaction between the crucible and the system.

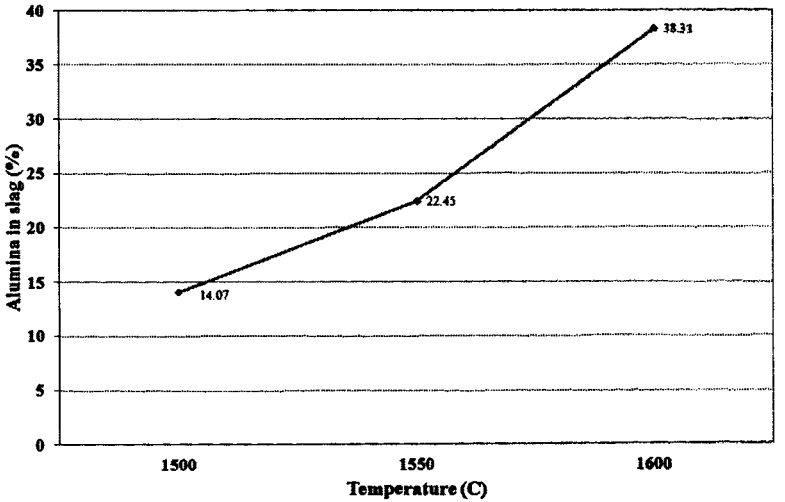

Figure 4. Variation of Slag Al_2O_3 Concentration (%) with Temperature

As indicated previously, nickel content of the iron-nickel alloy was reported as ~10% even at 1600 °C when 50% excess coal was used at the prereduction stage. In an effort to upgrade nickel content and to evaluate the degree of change in nickel composition, prereduced calcines were first produced with different excess coal additions and then subsequently smelted at 1550 °C for 40 minutes. Prereduced calcines were produced using 37.5%, 25%, 12.5% and 0% excess coal. Prereduction experiments were conducted at 1000 °C for 40 minutes, as described in related work, in detail [9]. As the excess coal amount was reduced from 50% to 0%, nickel content of the iron-nickel alloy was reported to increase from ~10% to ~34%. The variation of nickel

composition with excess coal used at prereduction stage is shown in Figure 5. The distribution term values were found to be comparable in [12.5%,50%] interval. As the excess coal content was decreased from 50% to 12.5%, a slight decrease in distribution term from 97.3% to 93.5% was noted. On the other hand, nickel recovery was very poor when no excess coal was used at the prereduction stage. The distribution term was reported as 51.6% for this experiment. Very small amount of metal beads were formed, although their nickel composition was around ~34%. Therefore, it was concluded that excess coal practice at prereduction stage is a must to obtain the desired degree of recovery of nickel at smelting for the experimental system used in the present study. It was also inferred that production of raw ferronickel having nickel content higher than 20% is possible using Sivrihisar laterites.

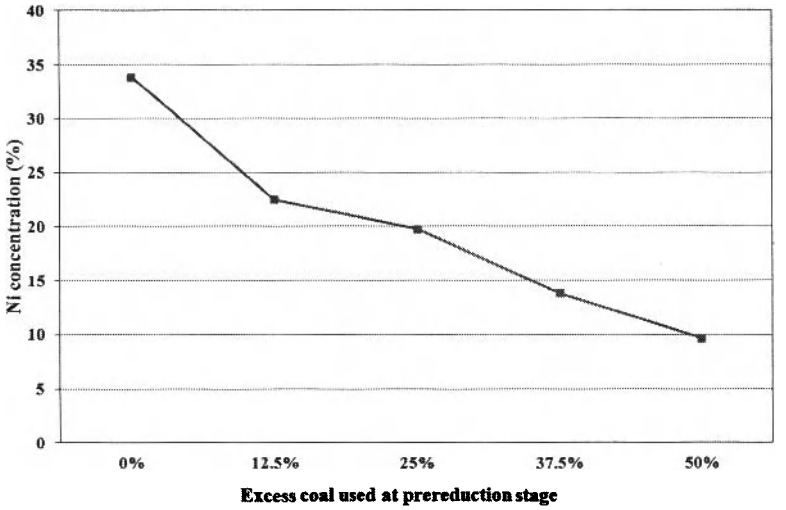

Figure 5. Variation of Ni Concentration (%) with Excess Coal Used at Prereduction Stage

The similar behavior was observed in the variation of slag NiO content (Figure 6). In [12.5%,50%] interval, NiO composition were reported to stay below 0.100%. The lowest NiO content was obtained as 0.048% when 50% excess coal was used at the prereduction stage. There was a slight increase in slag NiO composition while excess coal was decreased from 50% to 12.5%. The maximum value of NiO was reported when no excess coal was used at the prereduction stage. For this run, NiO composition of the slag was reported as 0.464% indicating that considerable amount of nickel oxide was remained in the system as unreduced. These results were in agreement with the findings related to metal Ni content, as described in the previous paragraph.

As indicated previously, Sivrihisar laterites are limonite type containing very little amount of MgO. Therefore, addition of fluxes like magnesia or dolomite is necessary in smelting stage of ferronickel production to obtain desired slag properties. In the laboratory-scale present study, smelting charges were prepared such that MgO wt./Total charge wt. ratio was fixed as 0.20. The

experiments conducted with this ratio gave satisfactory results indicating that smelting of ferronickel from Sivrihisar laterites is possible.

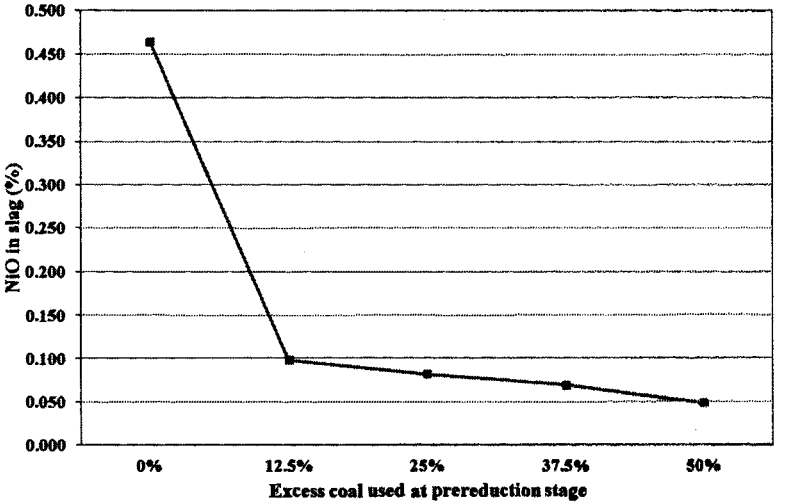

Figure 6. Variation of Slag NiO Concentration (%) with Excess Coal Used at Prereduction Stage

One of the most important parameters in ferronickel smelting like the other pyrometallurgical systems is the amount of fluxes to be charged to the system. The metallurgical purpose of the system must be satisfied with a high production rate. In order to increase the production rate, the amount of slag should be decreased as much as possible. In most of the pyrometallurgical systems, a great portion of the slags are coming from the fluxes added to the furnace at various stages of the process. Therefore, the weight of the slag produced in the process can be decreased by decreasing the amount of fluxes. This is especially important in ferronickel smelting, in which substantial amount of slag is produced. Therefore, experiments were conducted to analyze whether the amount of magnesia to be added can be decreased or not. For this purpose, charges were prepared and smelted such that MgO wt./Total charge wt. ratio was adjusted to 0.10, 0.15 and 0.20, respectively. These runs were performed with prereduced calcines having reduced with 25% excess coal at the prereduction stage. Charges were smelted at 1550 °C for 40 minutes. Although the detailed results are not included in the scope of this work, it was found that metal and slag weights were comparable when the ratio was reduced from 0.20 to 0.10. Metal nickel concentration was reported as 19.77% when the ratio was fixed to 0.20. There was an increase in nickel content when the ratio was reduced. Metal nickel content values were noted as 25.51% and 23.82% for the ratios 0.15 and 0.10, respectively. These results showed that higher nickel concentration values can be obtained with lower MgO wt./Total charge wt. ratio values for the metal-slag system under consideration. This result was very important especially to determine the necessary amount of magnesia to be added during smelting of Sivrihisar laterites. A charge having lower MgO wt./Total charge wt. ratio value and a batch with no MgO addition were also smelted. On the other hand, the chemical analysis of the metal and slag samples has not been determined yet. The detailed results will be included in a future work. However, it is important to

mention that very aggressive slags were created in these runs such that other than the brown like appearance on the crucible walls described before, the alumina crucible was found to stick to the bed material in the furnace. Therefore, lower MgO additions and/or zero MgO addition should not be preferred. Studies on flux addition are currently continued.

Conclusions

Smelting behavior of Sivrihisar laterite ores of Turkey was investigated. Experiments conducted to study the effect of temperature showed that 1550 °C was the optimum temperature for smelting. 50% excess coal used at the prereduction stage yielded ~10% Ni in the metal produced. Nickel content of the metal was successfully upgraded when excess coal amount was lowered to around ~25%. On the other hand, excess carbon practice should be applied at prereduction stage to obtain desired nickel recoveries at the end of smelting. It was therefore concluded that production of raw ferronickel from Sivrihisar laterites is possible with acceptable recoveries. A decrease in MgO wt./Total charge wt. ratio from 0.20 to 0.10 was reported to be beneficial to increase the nickel composition of the raw ferronickel produced. However, lower MgO additions and/or zero MgO addition caused formation of aggressive slags. Studies on flux addition are currently continued and will hopefully be discussed in a future work, in detail.

Acknowledgements

The authors would like to thank The Scientific and Technological Research Council of Turkey (TUBITAK) for the financial support given under the Project No: 109M068 and META Nickel & Cobalt Co. for supplying the lateritic ore samples of Sivrihisar.

References

1. Yuksel, Melih, "Recovery of Nickel from Lateritic Caldag Deposit" (MS Thesis, Middle East Technical University, 1985).
2. Y.A. Topkaya, "Nickel Extraction from Lateritic Nickel Ores" (TUBITAK Project, Project No: 106M079, 2009).
3. E. Buyukakinci, "Extraction of Nickel from Lateritic Ores" (MS Thesis, Middle East Technical University, 2008).
4. E. Buyukakinci and Y.A. Topkaya, "Extraction of Nickel from Gordes Lateritic Ore with Atmospheric Leaching" (Paper presented at the ALTA 2008 Nickel/Cobalt Conference, Perth, Western Australia, June 2008).
5. E. Buyukakinci and Y.A. Topkaya, "Extraction of Nickel from Lateritic Ores at Atmospheric Pressure with Agitation Leaching", Hydrometallurgy, 97 (2009), 33-38.
6. V. Ozdemir, "Ferronickel Production from Manisa Caldag Lateritic Ore" (Report, General Directorate of Mineral Research and Exploration, 2008).
7. C. Colakoglu, "Production of Ferronickel from Domestic Lateritic Ores" (MS Thesis, Istanbul Technical University, 2008).
8. E. Keskinkilic, S. Pournaderi, A. Geveci, Y.A. Topkaya, "Calcination Behavior of Sivrihisar Laterite Ores of Turkey", 2011 TMS Annual Meeting, 2nd International Symposium on High Temperature Metallurgical Processing, San Diego, California, USA.
9. E. Keskinkilic, S. Pournaderi, A. Geveci, Y.A. Topkaya, "Study of Certain Parameters in Laboratory-Scale Prereduction of Sivrihisar Laterite Ores of Turkey" (Paper presented at the ALTA 2011 Nickel-Cobalt-Copper Conference, Perth, Western Australia, May 2011).

3rd International Symposium on High-Temperature Metallurgical Processing
Edited by: Tao Jiang, Jiann-Yang Hwang, Patrick Masset, Onuralp Yucel, Rafael Padilla, and Guifeng Zhou
TMS (The Minerals, Metals & Materials Society), 2012

EFFECT OF BASICITY AND MgO ON THE PELLETZING OF SPECULARITE CONCENTRATE

Deqing Zhu, Jinliang Zhang, Jian Pan

School of Minerals Processing & Bioengineering, Central South University, Changsha, Hunan, 410083, P.R. China

Keywords: Specularite Pellets, Basicity, Burnt Magnesite, MgO Content, Pellet Strength.

Abstract

Limestone and burnt magnesite were added to vary MgO content and basicity (CaO/SiO_2 ratio) of pellets for investigating their influences on the properties of specularite pellets. At fixed MgO content, the addition of limestone does not affect on the properties of green balls significantly. The addition of burnt magnesite has obvious influence on the quality of green balls, especially on the thermal shock temperature. Without burnt magnesite, the thermal shock temperatures are about 400°C, and, the thermal shock temperature increases to 600~630°C by adding burnt magnesite. For preheated pellets, when the burnt magnesite is added, the compressive strength will be decreased. For roasted pellets without burnt magnesite, the calcium additives can form binding phase of calcium-ferrite, and suitable liquid phase will improve recrystallization of hematite, but excessive liquid will destroy the structure of pellets, so the compressive strength of pellet increases firstly and then decreases. When adding burnt magnesite, the compressive strength will increase as the basicity increases. When the basicity is more than 0.2, the compressive strength of the pellets various MgO content and basicity is above 2500N/pellet and then MgO-bearing fluxes can be added to prepare pellets with good high temperature properties.

Introduction

With the rapid development of the steel industry in China, oxidized pellets, possessing good mechanical and metallurgical properties, are becoming indispensable burdens for blast furnace ironmaking [1-3]. However, this has resulted in the shortage of domestic iron concentrates, so many Chinese steel plants begin to use imported hematite concentrate to prepare pellets. Compared with magnetite pellets, the hematite pellets require high roasting temperature and narrow roasting temperature range (1300–1350°C) and possess low compressive strength [4,5].[1]

Many researches have been conducted on how to acquire high mechanical strength pellets from hematite concentrates. Some effective solutions have been developed. It has been shown that blending magnetite into hematite pellets feed is not only able to reduce the preheating and roasting temperatures but also to improve the compressive strength of preheated and roasted pellets[3,6]. Adding additives to generate fluxed pellets is another choice[6,7]. Generally pellets plants in China produce high strength pellets by blending magnetite with hematite, but as the hematite/magnetite ratio increases the influence of magnetite will be weakened tremendously. The fluxed pellets by adding CaO flux require lower roasting temperature than acid pellets and

Corresponding author: Jinliang Zhang Postgraduate student; E-mail: zhangjinliang_csu@126.com

possess good reducibility, but the pellets are known for their poor high temperature properties like softening-melting characteristics and high reduction swelling[8-10]. Earlier studies made it clear that the addition of MgO improved the high temperature properties and descreased reduction swelling[11,12]. So the aim of this research is to find the suitable basicity and MgO to produce qualitified pellets.

In this paper, efforts have been made to understand the effects of MgO and CaO additives on the quality of specularite concentrate pellets. The properties of green balls were examined. The cold compressive strength and porosity of roasted pellets were tested.

Experimental

Raw Materials

One kind of specularite (PFFT from Vale, Brazil), bentonite, limestone and burnt magnesite (BM) were used for preparing balls with various MgO content and basicity. PFFT, limestone and burnt magnesite were ground separately in laboratory ball mill to get the required specific surface areas or fineness for pelletizing. The chemistry and physical properties of all the raw materials used are shown in Tables I and II respectively.

Table I Chemical Compositions of Raw Materials (mass %)

Contents	TFe	SiO_2	Al_2O_3	CaO	MgO	K_2O	Na_2O	P	S	LOI
PFFT	66.90	1.93	1.02	0.28	0.028	0.012	0.032	0.016	0.010	0.58
Bentonite	2.34	53.75	14.59	2.68	3.84	0.96	3.01	0.029	--	12.60
Limestone	0.14	1.28	0.18	54.53	0.20	0.0052	0.0094	0.0036	0.025	40.59
BM	0.39	4.96	0.14	3.25	85.57	0.040	0.030	0.064	0.060	4.80

Table II Size Distributions and Specific Surface Areas of Finely Ground Feeds Used for Balling

Materials	Size Distribution/mass %				SSA
	+0.074mm	-0.074+0.045mm	-0.045+0.038mm	-0.038mm	cm^2/g
PFFT	3.10	12.73	10.46	73.71	1460
Limestone	11.69	8.89	5.72	73.70	3982
BM	11.36	7.06	3.40	78.18	3852

Experimental Procedures

Balling was conducted in a laboratory balling disc pelletizer with a diameter of 1000 mm, a rim height of 200 mm and a tilting angle of 45°. Green balls were made in the disc at 24 rpm each batch from 4kg feed. Bentonite dosage was fixed at 1.2% (mass fraction). The mass of fluxes were determined by the requirements of basicity and MgO content. During balling, green pellets were screened at 10 mm and 12.5 mm to get qualified green balls. Before roasting, pellets were dried in the hot air oven at 110 °C for 5–6 h to ensure that all balls are completely dried. Roasting of dry pellets was carried out using electrically horizontal tube furnace in two stages: first a preheat cycle and then a roasting cycle.

Method for determination of porosity was using Beckman air pycnometer and wax coating of sample. Volume measurements were made using the Beckman air pycnometer on uncoated sample, after wax coating and on ground sample to -200 meshes. From the weight of the sample the corresponding densities ρ_a(uncoated sample), ρ_t(coated sample), ρ_m(-200 mesh) are calculated and the three porosities are determined from the following: total porosity=$(1-\rho_t/\rho_m)\times 100\%$; open porosity=$(1-\rho_t/\rho_a)\times 100\%$; closed porosity=$(\rho_t/\rho_a-\rho_t/\rho_m)\times 100\%$.

Results and Discussion

Effect of Basicity and MgO on Green Balls

The effect of basicity on the properties of green balls is shown in Figure 1. All the properties of green balls can meet the required standard. The wet drop strength and crushing strength do not change obviously as the basicity increases. However, when adding burnt magnesite, the wet drop number increases and the crushing strength decreases. The thermal shock temperatures of green balls are about 400°C, while adding burnt magnesite in the pellet feed thermal shock temperatures of green pellets augments dramatically up to 600~630°C. The MgO in the burnt magnesite was hydrated into colloid $Mg(OH)_2$, which can be used as a binder due to its huge specific surface areas and strong hydrophilicity, so the wet drop strength and the thermal shock temperatures increases with higher dosage of burnt magnesite.

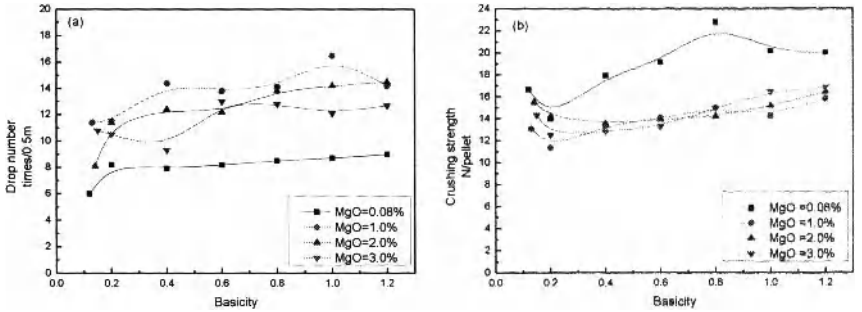

Figure 1 Effects of Basicity on the Wet Drop Number and Crushing Strength of Green Balls (Balling at 8.5% moisture for 12min)

Effect of Basicity and MgO on Preheated Pellets

Preheating time was fixed as 10min and preheating temperature was respectively 1100°C and 1150°C. Effects of basicity and MgO content on preheated pellets were illustrated in Figure 2. When burnt magnesite was added, the basicity has no efficient effect on the compressive strength of preheated pellets, no matter at 1100°C or 1150°C. This state is paradoxical with the former state, the curve of compressive strength of pellets preheated at 1100°C is almost flat, but the compressive strength of preheated pellets at 1150°C increases first then drops, the trend is much like the roasted pellets' curve as shown in Figure 3(a).

However, the compressive strength of the preheated pellets adding burnt magnesite is much lower than those at natural MgO of 0.08%. This is due to the endothermic decomposition of $Mg(OH)_2$,which was formed during balling. At 1100°C and 1150°C, MgO can not react with Fe_2O_3, there are unmineralized fluxes hinder the micro crystallization of hematite, which decrease the compressive strength of preheated pellets.

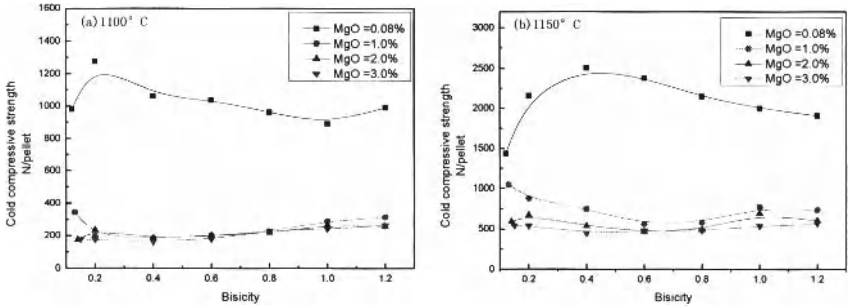

Figure 2 Effects of Basicity and MgO on Compressive Strength of Preheated Pellets (Preheating for 10min, at 1100°C (a) and 1150°C (b))

Effect of Basicity and MgO on Roasted Pellets

The temperature and time of preheating was set at 1100℃, for 10 min. The temperature of roasting was 1250℃, and the time was 10 min. Figure 3(a) shows that without burnt magnesite addition, the compressive strength of the roasted pellets increases to the peak 5290N/pellet and then drops a little, when adding burnt magnesite the compressive strength increases as the basicity increases. The compressive strength decreases with the increase of MgO content.

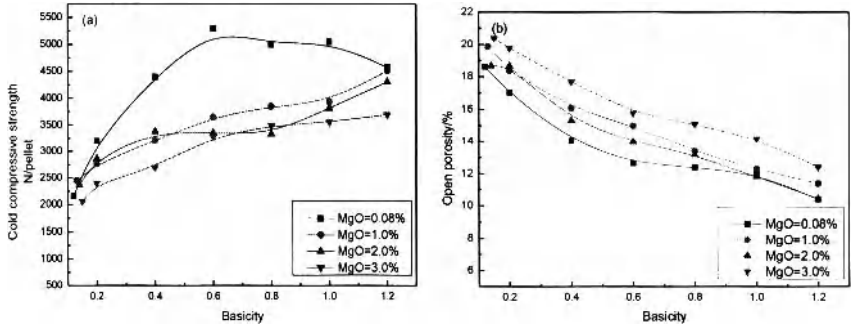

Figure 3 Effects of Basicity and MgO on Compressive Strength and Open Porosity of Roasted Pellets

The microstructures of roasted pellets are shown in Figure 4. Figure 4(a) indicates that with no additives the main mineral of pellets is hematite, so the compressive strength is determined by the

recrystallization of hematite. Figure 4(b) shows that with adding limestone, CaO reacts with Fe_2O_3 and SiO_2, respectively, and calcium-ferrite and intergranular liquid slag phase are formed, at this roasting temperature. A proper amount of liquid phase can improve the solid diffusion and enhance the recrystallization of hematite, but too much liquid phase will destroy the structure of pellets [3]. That is the reason that the strength of roasted pellets increases firstly and then decreases a little with the increase of basicity. Figure 4(c) indicates that when adding burnt magnesite, MgO react with Fe_2O_3 and form magnesium ferrite, which cannot become liquid phase at the roasting temperature. Besides, MgO can also holdback the recrystallization of hematite and cause the strength of roasted pellets to be decreased when increasing the content of MgO.

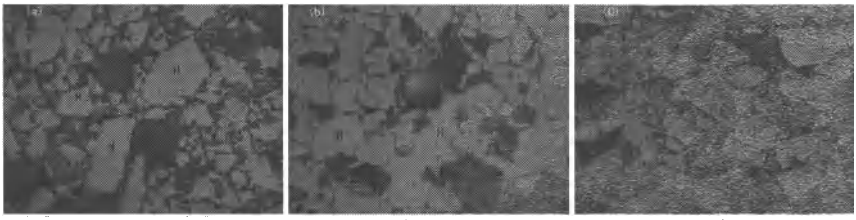

(a) (b) (c)

Figure 4 Microstructures of Roasted Pellets (H—Hematite; CF—Calcium ferrite; MF—Magnesium ferrite; S—Liquid slag phase; Si—Free SiO_2 crystalline):
((a) No additives; (b) Basicity1.2 with adding limestone; (c) Basicity 1.2 and MgO 3.0%)

The total porosity of the pellets varying basicity and MgO content arranges 25~27%, the open porosity of the pellets drops (see Figure 3(b)), and the close porosity increases with the increase of basicity. Figure 5 indicates that with the additives adding, the outer layer of the pellet is denser than the middle layer and central field. The strength development is a linear function of the degree of densification; the porosity which can be used to indicate the degree of densification increases with the MgO/CaO increases [13, 14]. The degree of densification and thickness of outer layer which can determine the strength of the pellets are dependent upon the open porosity of pellets. When the basicity increases, the more liquid phase formed causes the open porosity decreases, the compressive strength increases. That is why there is a linear relationship between pellet compressive strength and open porosity in the strength versus basicity curve (Figure 6).

(a) (b) (c)

Figure 5 Microstructures of Roasted Pellet with MgO 2.0% and Basicity 1.2
((a) Outer layer; (b) Middle layer; (c) Inner layer)

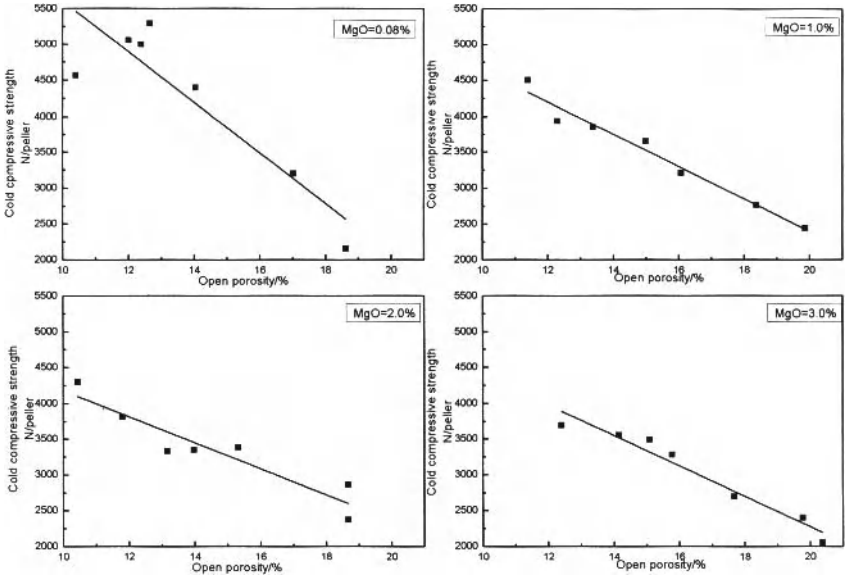

Figure 6 The Relationship between Cold Compressive Strength and Open Porosity of Roasted Pellets

Conclusions

(1) The basicity which is varied by adding limestone makes no obvious effects on the quality of green pellets. While adding burned-burnt magnesite, the drop number and thermal shock temperatures of green pellets increase and the crushing strength decreases, because the MgO in burned-burnt magnesite will hydrated into $Mg(OH)_2$ which is also a binder during balling.

(2) The compressive strength of preheated pellets has no significant change with the increase of basicity. When adding burnt magnesite, the compressive strength of preheated pellets decreases sharply, because unmineralized MgO hinders the micro-crystallization of hematite and the formation of solid calcium ferrite. For the roasted pellets without adding burnt magnesite, the compressive strength increases firstly and then drops with the increase of basicity. The reaction of CaO with Fe_2O_3 and SiO_2 will form binding phase of calcium-ferrite and liquid slag phase, and the suitable liquid phase will improve the recrystallization of hematite, but the excessive liquid phase will destroy the structure of pellets.

(3) When adding burnt magnesite, the compressive strength of roasted pellets increases with the increase of basicity, because of the existence of MgO there is no excessive liquid phase formed, as the basicity increases, that is helpful to improve the compressive strength of roasted pellets.

(4) When burnt magnesite was added the compressive strength of roasted pellets decreases, because the magnesium-ferrite formed by MgO and Fe_2O_3 can not become liquid phase at roasting temperature.

(5)There is a linear relationship between pellet compressive strength and open porosity in the strength versus basicity curve, because the degree of densification and the thickness of the outer layer which determine the strength of roasted pellets are dependent upon the open porosity of roasted pellets.

References

1. Z. Zhao, "Review of Pellet Production for Last 30 Years at Jinan Iron and Steel Group Corporation," *Iron Steel*, 34 (5) (1999), 1-4.
2. K. W. Ye, "Review of Three Kinds of Pelletizing Process," *Sintering and Pelletizing*, 27 (1) (2002), 1-7.
3. G.H. Li et al., "Reduction Swelling Behavior of Hematite/Magnetite Agglomerates with Addition of MgO and CaO," *Ironmaking Steelmaking*, 37(6) (2010), 393-397.
4. T. Jiang et al., "Preheating and Roasting Characteristics of Hematite-Magnetite (H-M) Concentrate Pellets," *Ironmaking Steelmaking* 35 (1) (2008), 21-26.
5. G. H. Li et al., "Induration Mechanisms of Oxidized Pellets Prepared from Mixed Magnetite-Hematite Concentrates," *Ironmaking Steelmaking* 36(5) (2009), 393-396.
6. D. Q. Zhu et al., "Research on Influence of the Alkalinity and Fuel Flux to the Intensity of Hematite Pellets," Metal Mine, 420 (6) (2011), 104-108.
7. G. S. Wu, M. Z. Bian, F. M. Shen, "Use of Magnesium-Bearing Basic Pellet and Reasonable Burden Design," *Iron &Steel*, 41(12) (2006), 19-22.
8. M. Onoda et al., "Quality improvements of lime fluxed pellets," (Paper presented at ISS-AIME 40th Iron making conference, Toronto, Ontario CANADA), (1980) 286–298.
9. Mustafa Kelami Sesen, "The Influence of CaO on the Precipitation Behavior of Iron in the Reduction of Iron Oxide," *Scandinavian Journal of Metallurgy*, 30(2001), 1-7.
10. S. C. Panigrahy, B. C. Jena, and M. Rigaud, "Characterization of Bonding and Crystalline Phases in Fluxed Pellets Using Peat Moss and Bentonite as Binders" *Metallurgical Transactions B*, 21(1990),463-474.
11. Srinivas Dwarapudi et al., "Effect of pyroxenite flux on the quality and microstructure of hematite pellets," *International Journal of Mineral Processing*, 96 (2010), 45–53
12. J. J. Frill, Jr. E.S Erickson, "Chemistry, microstructure, and reduction characteristics of dolomite-fluxed magnetite pellets," *Metallurgical Transactions B* 11(1980), 233-243.
13. S. C. Panigrahy, M. Jallouli, M. Rigaud, "Porosity of Sinters and Pellets and Its Relationship with some of Their Properties, " *Ironmaking Proceedings*, 43(1984), 233-238.
14. J. R. Wynnyckyj, T. Z. Fahidy, "Solid State Sintering in the Induration of Iron Ore Pellets," *Metallurgical Transactions* (5) (1974), 991-1000.

3rd International Symposium on High-Temperature Metallurgical Processing
Edited by: Tao Jiang, Jiann-Yang Hwang, Patrick Masset, Onuralp Yucel, Rafael Padilla, and Guifeng Zhou
TMS (The Minerals, Metals & Materials Society), 2012

EFFECTS OF MHA BINDER ON ROASTING BEHAVIORS OF OXIDIZED PELLETS FROM SPECULARITE CONCENTRATE

Youlian Zhou, Yuanbo Zhang , Tao Jiang, Guanghui Li, Daoyuan Zhang

(School of Minerals Processing & Bioengineering, Central South University, Changsha, Hunan 410083, China)

Key Words: organic binder, specularite, iron ore, pellet

Abstract

Modified humic acid (MHA) has been developed by Central South University (CSU) and authorized in China. It has been reported that MHA is an effective binder for oxidized pellets prepared from specularite concentrates. In this research, effects of MHA binder on roasting behaviors of the specularite pellets are studied. MHA is an organic binder, containing much carbon, hydrogen, oxygen, etc. During the roasting, MHA can provide some heat because of combustion of hydrocarbon, which is beneficial for the recrystallization of Fe_2O_3 in the specularite pellets at high temperature. Simultaneously, part of hematite particles within the pellets are firstly reduced to magnetite, then, magnetite is oxidized into secondary hematite, which obviously improves the roasting performance of specularite pellets.

Introduction

Oxidized pellets have been widely used in steel production as a kind of high quality burden for blast furnace ironmaking [1]. In recent years, production of oxidized pellets is developing very fast. Therefore, the supply of high quality magnetite concentrates, which is the most suitable for pellet production, becomes scarce. It is imperative to pursue new alternative materials for oxidized pellet production [2]. Specularite concentrates have attracted widespread attention due to the advantages of high total Fe grade and low impurity content. However, due to the poor ballability and firing performance, specularite has not yet been widely applied into pellet production [3, 4].

Many researches have been done to solve the above difficulties in balling and roasting when specularite is used in pellet production. But, the mass percentage of specularite in the mixture, as reported, is not in excessive of 20% yet [4]. Otherwise, the quality of finished pellets becomes inferior. To solve the above problems, effective measures already in use include: a) adopting appropriate pretreatment to improve the ballability of them [5-8]; b) adding some carbon-containing materials into the mixtures [4, 9]; c) using superior bentonite or new binders instead of traditional bentonite [10-13].

MHA binder, invented by CSU and authorized in China [14], has been proven to be an effective binder for preparing iron ore pellets. The authors have studied and reported the process parameters for preparing oxidized pellets from 100% Brazilian specularite concentrates, using MHA binder

* Corresponding author: Yuanbo Zhang, email: zybcsu@126.com

instead of bentonite [15]. The quality of green balls, preheated and roasted pellets meet the requirements for the blast furnace ironmaking. Based on the previous research, this study further focuses on effects of MHA binder on the roasting behavior of specularite pellets and provides theoretical basis for putting the novel MHA binder into the specularite oxidized pellets.

Experimental

Materials

Specularite and bentonite Characteristics of Brazilian specularite concentrates and bentonite used in this study are reported in Reference [15].

MHA binder MHA binder, extracted from Liling lignite of Hunan, China, is a kind of organic macromolecule compounds. The chemical compositions, LOI, main function groups and infrared spectrum of MHA binder are also reported in Reference [15], of which the TG-DSC curve is presented in Figure 1.

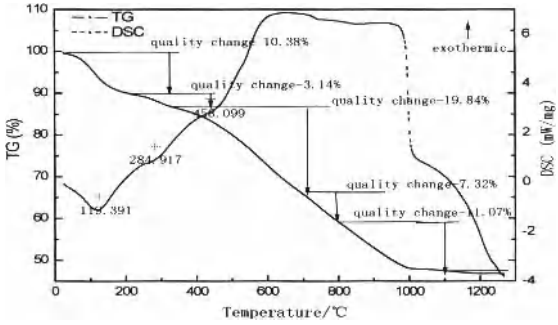

Figure 1. TG-DSC curve of MHA binder

It can be seen from Figure 1 that, combustion and degradation reactions of organic matters occur during the heating of MHA binder. Because crystal water in MHA binder is decomposed, the endothermic peak appears at 119℃. From 458℃, strong exothermic peak began to emerge until the temperature was close to 1000℃, which is the result of thermal decomposition or combustion of organic compounds in MHA binder. It can be observed from TG curve, the weight change is large at this stage. The results show that the thermal stability of MHA binder is good and its decomposition temperature range is relatively wide.

Anthracite In this study, the proximate analysis of anthracite is listed in Table I.

Table I. Proximate analysis of anthracite /%

Fixed carbon	Volatile	Ash	Moisture
82.56	8.00	7.74	1.70

It can be seen from Table I that the fixed carbon, volatile, ash content of anthracite is separately 82.56%, 8.00%, and 7.74%, so that the anthracite can give out much heat and the amount of residual is low after burning.

Method

Specularite green balls with certain proportion of binder are prepared in a disc pelletizing machine with the diameter of 1000mm. Green balls of 10-12.5mm in diameter are selected to dry at 105℃ for 4 hours and used for the subsequent experiments. Roasting tests are carried out in a vertical tube furnace, of which the inner diameter is 88mm. Temperature is controlled by an intelligent temperature controller. The mixture of N_2 and O_2 gas is led into from the bottom, and the mixed gas flow rate remains a constant. The oxygen content can be adjusted by changing the N_2 and O_2 flow, and the roasting equipment is shown in Figure 2. In each test, ten dried pellets are selected and tiled in the hanging basket, and then roasted according to the set temperature and time. After roasted, the pellets are cooled to room temperature in N_2 flow. Finally, FeO content, compression strength and microstructure of the roasted pellets are measured.

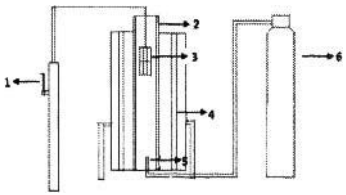

1. hand cranking device; 2. furnace wall; 3.hanging basket; 4. silicon molybdenum rods; 5. air inlet; 6.air bottle.

Figure 2. Schematic diagram of high temperature shaft-kiln for roasting

Results and Discussion

For identifying the different behaviors of MHA binder in specularite oxidized pellets, the change of pellet compressive strength, FeO content and microstructure are investigated.

Effects of oxygen content on the roasting of MHA binder pellets

During the roasting process, oxygen content has great influence on the roasting behaviors of specularite pellets with reductive materials.

FeO content in the specularite pellets with reductive materials not only derives from reduction of

Fe_2O_3 by reductive materials, but also results from the decomposition of Fe_2O_3 at higher temperature. Whether Fe_2O_3 is decomposed or not is apparently affected by oxygen content and roasting temperature, according to the following equation of Fe_2O_3 decomposition:

$$6Fe_2O_3=4Fe_3O_4+O_2\ (\Delta G=140380-81.38T) \quad (1)$$

The equation of oxygen content and Fe_2O_3 decomposition temperature can be expressed as:

$$\ln p_{O_2}=-70649.22/T+40.96 \quad (2)$$

The decomposition temperature at different oxygen content is calculated and the results are given in Table Ⅱ.

Table Ⅱ. Relationship between oxygen content and decomposition temperature of Fe_2O_3

Oxygen content/%	0	1	5	10	15	20
Decomposition temperature/℃	1203	1278	1334	1360	1375	1389

Fe_2O_3 can be decomposed at 1203℃ in inert atmosphere. The decomposition temperature gradually goes up with the increase of oxygen content and the conversion from Fe_2O_3 to Fe_3O_4 is more difficult. At this point, FeO in the pellets mainly derives from the reduction of Fe_2O_3 by reductive materials [9, 16].

As for specularite pellets with bentonite, internal FeO only derives from Fe_2O_3 decomposition. Taking the three kinds of specularite pellets with 1.0% MHA binder, 1.0% anthracite and 2.0% bentonite as research objects, effects of oxygen content on roasting consolidation of MHA binder pellets are studied by investigating the changes of compressive strength and FeO content of them under conditions that the gas flow is 10L/min, roasting temperature is 1280℃ and the roasting time is 12min. The results are plotted in Figure 3.

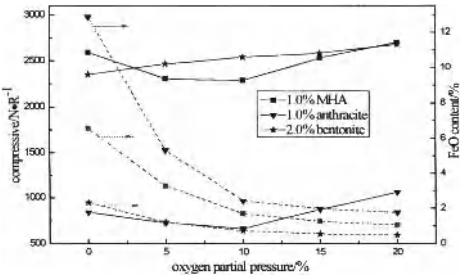

Figure 3. Effects of oxygen content on compressive strength and FeO content of different pellets

It can be seen from Figure 3 that, effects of oxygen content on the compressive strength and FeO content of the MHA pellets are as like as the anthracite pellets, that is, the compressive strength both firstly drops down then goes up while the FeO content decreases with the oxygen content increasing. Compared with anthracite pellets, the compressive strength of MHA binder pellet is greater while FeO content is relatively less. Combining the TG-DSC curve of MHA, it can be seen that the organic components in MHA binder can be thermally decomposed and burn in the roasting process of specularite pellets. However, the anthracite can release more heat because of its higher fixed carbon content, which results in the melt phenomenon inside the pellets. The pellet porosity obviously increases due to the combustion of carbon, which decreases the compressive strength of roasted pellets [17]. When oxygen content reaches 10%, the compressive strength of the two pellets both reaches the minimum. As for the bentonite pellets, the consolidation of Fe_2O_3 recrystallization is little affected by oxygen content.

Because MHA binder and anthracite both contain fixed carbon and volatile substance, FeO can be produced because of reduction of Fe_2O_3 in the roasting process of specularite pellets. At the same time, when the oxygen content is low, the decomposition temperature of Fe_2O_3 is low, also producing partial FeO. Comparatively speaking, the reduction atmosphere in the anthracite pellets is relatively stronger and FeO content is greater. As for bentonite pellets, in inert atmosphere, FeO only derives from the decomposition of Fe_2O_3. When the oxygen content increases, the decomposition temperature of Fe_2O_3 goes up, so that decomposition amount of Fe_2O_3 becomes less.

The microstructures of the roasted pellets with 1.0% MHA at different oxygen content are given in Figure 4.

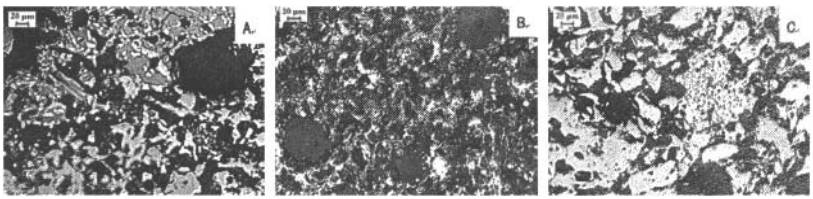

Figure 4. Microstructures of MHA pellets at different oxygen content
A-N_2, B-10%O_2, C-20%O_2
1-primary hematite; 2-secondary hematite; 3-magnetite.

From Figure 4, many magnetite particles are clearly observed in the pellets roasted in N_2 atmosphere, and most particles have been recrystallized and interconnected with each other. At the same time, separate primary hematite particles are also observed. Its consolidation strength mainly depends on the recrystallization connection of magnetite and primary hematite particles.

When the oxygen content increases to 10%, magnetite is nearly not observed in the pellets. During the roasting, magnetite is oxidized into secondary hematite particles. The pores between particles are enlarged, the crystal connection is relatively loose, and the recrystallization of hematite becomes poor.

When the oxygen content rises up to 20%, most secondary hematite particles are observed and connected with one another. Most of magnetite particles are entirely oxidized into secondary

hematite particles, so FeO content decreases rapidly. The recrystallization of secondary hematite particles significantly improves the pellet compressive strength.

Findings mentioned above show that the reduction of Fe_2O_3 by MHA binder occurs in the roasted pellets, producing a lot of magnetite, and when the oxygen content increases, magnetite is oxidized to secondary hematite. What's more, combustion reaction of MHA binder occur during the roasting, improving the inside temperature of the pellets and promoting the crystal particle growth and interconnection, so that the pellet compressive strength is enhanced.

Effects of MHA binder dosage on the roasting behavior of pellets

Under the conditions of oxygen content 20%, gas flow 10L/min, roasting temperature 1280℃ and roasting time 12min, the effects of MHA binder dosage on the pellet compressive strength and FeO content are investigated and presented in Figure 5.

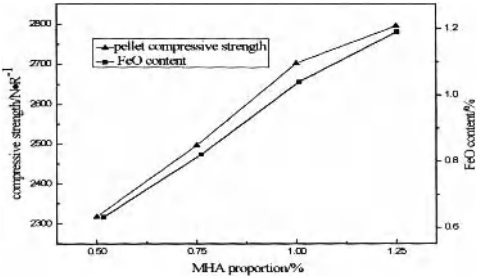

Figure 5. Effects of MHA binder dosage on compression strength and FeO content of pellets

Figure 5 shows that pellet compressive strength and FeO content both increase with the increase of MHA binder dosage. On the one hand, organic matters in MHA binder burn and give out heat when roasted, so that the increase of MHA dosage results in the increase of inside temperature of pellets, which is good for improving the pellet compressive strength; on the other hand, when the additive amount of MHA binder rises, the reductive materials in pellets increase. So many hematite particles are reduced to magnetite, and the FeO content also increases.

The microstructures of the specularite pellets with 0.5% and 1.0% MHA are shown in Figure 6.

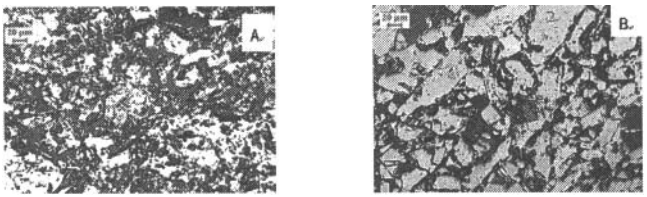

Figure 6. Microstructure of pellets at different MHA dosage

A-0.5% B-1.0%

1-primary hematite; 2-secondary hematite; 3-magnetite.

From Figure 6, it can be known that when MHA binder dosage is 0.5%, the crystal connection is relatively loose. When the dosage of MHA increases to 1.0%, much magnetite is produced at the initial stage of roasting, and then magnetite is oxidized to secondary hematite. The activity of secondary hematite is good, which is beneficial to the crystallization of crystal grains. Moreover, the combustion of MHA binder in pellets releases more heat, which also improves the pellet internal temperature, so that the consolidation of pellet is intensified.

Conclusions

Researches on the behaviors of MHA binder in the roasting process of specularite pellets shows that specularite pellets are obviously affected by oxygen content and MHA binder dosage. MHA binder can not only combust and give out heat, but also reduce Fe_2O_3 to Fe_3O_4. During the roasting, partial primary hematite is firstly reduced to magnetite, and further oxidized to secondary hematite with high activity, improving the roasting performance of specularite.

Acknowledgements

The authors want to express their thanks to National Natural Science Foundation of China (No. 50804059) and National Science Fund for Distinguished Young Scholars (No.50725416) for financial support of this research.

References

1. X. Zhou and X. Hao, "China Pellet Industry Development Status and Trends Analysis", *Industry Analysis*, 6(2010), 16-18.
2. L.T. Kong, "Discussion on China's Development of Pellets" (Paper presented at the National Iron Production technology Conference, Beijing, 2008), 28-32.
3. G.S. Feng, "Add Imported Ore Reasonably and Improve the Quality of Pellets"(Paper presented at the National Sintering and Pelletizing Technology Annual Communicating Conference, 2009), 190～191.
4. A.P. He, "Study on Brazil Specularite Pellets Process and Mechanism" (Master Degree thesis, Central South University, 2005), 7～11.
5. C.A. Wang, "Study on the Technology of Strengthening the Process of Preparing Pellets and on the Mechanical Chemical Mechanism" (Master Degree thesis, Central South University, 2002), 9～14.
6. H.M. Li, "Study on Compound Additive Containing Boron Strengthening Preparation of Brazil hematite Pellets and the Mechanism" (Master Degree thesis, Central South University, 2009), 15～18.
7. L.M. Tavares, "Particle weakening in high-pressure roll grinding", *Minerals Engineering*, 65(18)(2005), 651～657.
8. H. Zhao and C.M. Wang, "Study on the Application of High Pressure Roller Mill in Iron Ore Pellets Production", *Mining machinery*, 10(3) (2004), 9～10.
9. X.Q. Li, "Study on the behaviors of carbon burdened in the preparation of hematite oxidation pellets" (Master Degree thesis, Central South University, 2009), 1～4.

10. Y.Z. Zhang et al, "Study on the Effects of Bentonite Physical and Chemical Properties on the Pellets Performance", *Sintering and Pelletizing*, 31(2) (2006), 21～24.
11. Z.C. Huang et al, "Study on the Mechanism of Action of Bentonite in Ore Pellets", *Chemical Mineral and Processing*, 8(2005), 13～15.
12. J.X. Yin, "Analysis on the Effects of Binder on Pellets Performance", *Journal of Tianyuan University of Technology*, 31(5)(2000), 556～558.
13. X.B. Zhang and M.W. Zhu, "Effects of Bentonite on Pellets Production in Our Country", *Sintering and Pelletizing*, 28(6)2003, 3～6.
14. T. Jiang et al, "A Compound Type Organic Binder of Iron Ore Pellets and Its Usage"(Patent, China, CN 101693950 A, 2010.04.14).
15. G.H. Bai et al, "Oxidized Pellet Preparation from Refractory Specularite Concentrates Using Modifiifed Huminc Acid (MHA) Binders" (Paper presented at the 2rd International Symposium on High Temperature Metallurgical Processing 2010),1~7.
16. T. Jiang et al, "Effects of Atmosphere on Roasting Behaviors of Carbon-Burdened Hematite Pellets". *Journal of Central South University(Natural Science Edition)*, 40(4) (2009), 851～855.
17. Q. Wang, Technology of Iron Ore Pellets within Carbon (Beijing: Metallurgical Industry Press, 2006), 29～31.

3rd International Symposium on High-Temperature Metallurgical Processing
Edited by: Tao Jiang, Jiann-Yang Hwang, Patrick Masset, Onuralp Yucel, Rafael Padilla, and Guifeng Zhou
TMS (The Minerals, Metals & Materials Society), 2012

A STUDY OF CARBON-BURDENED AND COLD-BONDED PELLETIZING-ELECTROSMELTING PROCESS DISPOSING LOW-GRADE MANGANESE ORE

Zhao Qiang Ning Shun-ming Chen Wen Tang Sanchuan Li Zhao-jia Wang Hong-qiang
Changsha Research Institute of Mining and Metallurgy, Changsha 410012,China

ABSTRACT The carbon-burdened and cold-bonded pelletizing-electrosmelting process is used to dispose low-grade manganese, and the qualified rich-manganese slag is obtained. On the condition that reduction roasting temperature was 1000℃, reduction time was 45min, particle-size was -1mm, reductant dosage was 1.6%, basicity was 0.3, smelting temperature was 1410℃, smelting time was 60min, it had a good effect on the melting between slag and metallographic phase, the manganese content was 32.58%, manganese recovery was 92.16% in the slag; while the iron content was 94.40%, iron recovery was 95.32% in the metallographic phase. It was proved by the demonstration tests.

KEY WORDS carbon-burdened; cold-bonded pellets; low-grade manganese; electrosmelting

Introduction

Manganese is an important raw material for steelmaking, which is extensively utilized in modern industry, the consumption of manganese for iron and steel industry accounts for 90% to 95%. After mining over 30 years, the high-grade manganese resources drop markedly, especially with the hypergrowth of steel industry, the domestic manganese is far from the requirement , as a result, we have to buy significant quantities of manganese overseas. Besides, the property of imported manganese is more and more complex, and the high-grade and lump manganese decrease year by year, while the fines and high-crystal water manganese are on the increase. Therefore, how to make effective use of domestic low-grade manganese and intensify the manganese's smelting is an effective approach to reduce the cost of manganese series ferroalloy and improves market competitiveness[1-4]. It has important practical meaning.

After years of research on low-grade manganese, a lot of developments have been achieved in the field of ferromanganese smelting, rich-manganese slag, Si-Mn alloy, electrolytic manganese dioxide and manganous-manganic oxide. According to the component content and mineral properties of manganese ores, the right smelting process must be choosed. Carbon-burdened and cold-bonded pellets–electrosmelting process, namely rich-manganese slag process, is an effective way to dispose low-grade manganese, which is only for low-grade manganese.The product rich-manganese slag is mainly used for ferromanganese smelting. Rich-manganese slag process is an enriching manganese ore method which accords with Chinese actual conditions, because China has very little rich-manganese, and high iron-high phosphorus-refractory manganese accounts for 40% of manganese ore reserves[5]. For these reasons, we use carbon-burdened and cold-bonded

pellets–electrosmelting process to deal with low-grade manganese from Hunan Province, and we can obtain qualified rich-manganese slag.

1. Raw Material Characteristics and Experimentation Methods

1.1 Characteristics of Raw Material

1.1.1 Low-grade manganese

The chemical composition of the Hunan's low-grade manganese is shown in Table1. It indicates that this manganese is a low-grade manganese , according to the manganese grade. The distribution size of the low-grade manganese is shown in Table2, it can be seen that the size is quite coarse, so the blend have to be crushed before briquetting experiments.

Table1 Chemical Compositions of Low-grade Manganese Ore /%

Element	Fe	Mn	S	P	As	Ca	Mg	Al	Si
Content	41.51	11.89	0.014	0.016	0.011	2.54	0.28	1.11	3.36

Table2 Disrtibution Size of Low-grade Manganese Ore /%

Size Fraction /mm	+10	7~10	5~7	3~5	1~3	-1
Proportion /%	16.57	7.37	9.19	12.63	8.69	45.56

Table3 Mineral Phase Analysis of Iron and Manganese in The Low-grade Manganese Ore /%

Iron Phase	Siderite	Pyrite	Magnetite	Limonite	Ferrosilite	TFe
	0.27	0.02	0.10	40.47	0.38	41.51
Manganese Phase	Manganese Oxide	Manganous Silicate	TMn			
	10.98	0.71	11.89			

The results of iron and manganese phase analysis of low-grade manganese are shown in Table3, according to the results, we can see that the main existence form of iron is limonite and the proportion is 97.5%; while the main existence form of manganese is manganese oxide and the proportion is 92.3%.

1.1.2 Reductant

Coke breeze is used as reductant for the experiment. It is broken to -2mm, the industrial analysis of coke breeze is shown in Table4. It is observed that this coke breeze is a good reductant, because its Fcad is high and its Vdaf is low.

Table4 Industril Analysis of Coke Breeze /%

Fcad	Ad	Vdaf
73.37	17.88	0.97

1.2 Experimentation Method

The 300g low-grade manganese is mixed with proportional coke breeze and silica, and then we crush them to different size fraction; the equipment used for granulation is 10B Type Hydraulic Universal Tester, and the pressure is fixed at 350kg/cm^2, after granulation, the compressive strength of green pellets is 10kg, while the standard is Φ25 mm×20 mm ; then we put the

agglomerate into the Type FN202-1 Electrically Heated Drying Cabinet for drying and concreting (200℃)for two hours, the compressive strength of dried agglomerate is 50kg; the next, we place the dried agglomerate into SX2-12-16 Box Type Resistance Furnace, the reduction roasting conditions are as follows: the temperature increase from room temperature to 1000℃, stay for 45min,being reduced. After reduction roasting, under scheduled temperature, the hot agglomerate keep on smelting for a certain time in the Resistance Furnace, and the smelting temperature condition is that the temperature increases to melting temperature from 1000℃ within 120min, holding for 60min at the melting temperature, after discharge, we must observe the melting result of the smelting product, one is slag phase rich-manganese slag, the other is metallic phase pig iron. The flowsheet is shown in Fig1.

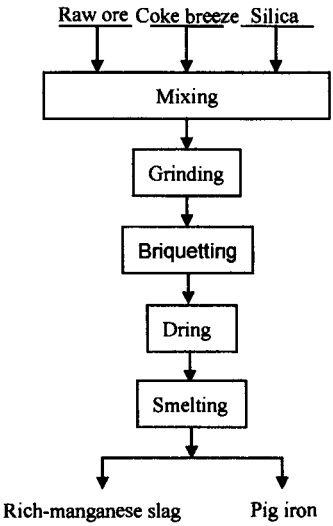

Fig1.The flowsheet of carbon-burdened and cold-bonded pelletizing-electrosmelting process

2. Experiment Principle

The process for smelting rich-manganese slag is the beneficiation of manganese in the slag phase. It contains crystal water's decomposition at high temperature, the decomposition of carbonate, the lost of oxygen in high valence manganese and the selective reduction of iron and phosphorus in reduction condition, etc. The most essential is the selective reduction of iron and phosphorus among them.

The smelting principle is that iron, phosphorus and high valence manganese can be reduced adequately and the low valent manganese (MnO) is hard to be reduced under strong reducing condition. Because of the different reducing condition, the reduced iron, phosphorus and a small amout of manganese enter into secondary product manganese, while most manganese exist in slag in the form of MnO, we can separate iron and manganese, improve rich-manganese slag's Mn/Fe and bring down the P/Mn, finally, achieve the purposes of beneficiation. The reaction equations of smelting principle are shown as follows:

$$MnO+C=Mn+CO\ -279470KJ(1370℃)$$

$$FeO+C=Fe+CO\ -158800KJ(685℃)$$

$$2P_2O_5+10\ C=4\ P+10\ CO\ -1767250\ KJ(763℃)$$

The reduction temperature of iron and phosphorus is lower, when the reduction temperature is below 1350℃. And iron and phosphorus will be reduced and enter molten iron phase, while manganese will enter slag in the form of MnO and react with SiO_2. Under such reduction conditions, rich-manganese slag can be obtained. It is specified that the content of manganese is generally 35%～45%, the iron content is 1.5%～4.5% and ≤0.03% in the qualified rich-manganese slag.

3. Experimental Results and Discussion

3.1 Orthogonal test

The tests mainly examine the effect of smelting temperature, reductant dosage, basicity of slag phase and size of raw ore on smelting, and the orthogonal tests are taken. We design experiment according to orthogonal table $L_9(3^4)$, the test program is showm in Table5 and Table6.

Table 5 Factorlevel Encode Table

Factor		Temperature (A) /℃	Basicity (B)	Reductant Dosage (C) /%	Size (D) /mm
Level	1	1390	Nature (0.76)	1.4	-10
	2	1410	0.5	1.6	-3
	3	1430	0.3	1.8	-1

Table6 The Testing Schedule

No.	Temperature (A) /℃		Basicity (B)		Reductant Dosage (C) /%		Size (D) /mm	
1	1	1390	1	Nature	1	1.4	1	-10
2	1	1390	2	0.5	2	1.6	2	-3
3	1	1390	3	0.3	3	1.8	3	-1
4	2	1410	1	Nature	2	1.6	3	-1
5	2	1410	2	0.5	3	1.8	1	-10
6	2	1410	3	0.3	1	1.4	2	-3
7	3	1430	1	Nature	3	1.8	2	-3
8	3	1430	2	0.5	1	1.4	3	-1
9	3	1430	3	0.3	2	1.6	1	-10

Table7 Orthogonal Test Results

No.	Chemical Analysis Results of Metallographic Phase			Chemical Analysis Results of Slag Phase		
	Weight/g	Fe/%	Mn/%	Weight /g	Fe/%	Mn/%
1	Can't be melted			Can't be melted		
2	130.02	93.57	2.53	86.93	3.05	34.87
3	128.64	95.68	1.32	107.57	1.18	31.61
4	136.28	91.96	5.45	78.27	6.98	34.61
5	126.23	94.20	2.61	88.89	3.83	34.66
6	128.11	98.22	0.43	111.19	1.38	30.59
7	135.74	88.86	6.25	75.58	2.24	33.78
8	133.39	94.58	2.11	91.61	2.05	34.04
9	122.69	96.11	0.52	110.97	2.63	31.41

As shown in Table7, the smelting product is very different under different conditions. Especially when the test condition is level 1, the slag phase and metallographic phase can't be melted. This suggests that if we want to get better result, the right condition must be choosed. The results of recovery analysis range of iron in metallographic phase and manganese in slag phase is shown in Table8. We consider the iron recovery in metallographic phase and Mn recovery in slag phase first when we analyse range. According to Table8, in metallographic phase , the influencing factors could be arranged as follows: D>A>B>C, that is the order is size, temperature, basicity and reductant dosage. The most suitable factor combination in metallographic phase is $A_2B_3C_2D_3$. While in slag phase, the influencing factors could be arranged as follows: B>A>C>D, that is to say the order is basicity, temperature, reductant dosage and size. The most suitable factor combination in slag phase is $A_2B_3C_2D_3$. It is obvious that the most suitable factor combination is completely the same,that is temperature is 1410℃, basicity is 0.3, reductant dosage is 1.6% and size is -1mm.

Table8 Analysis of Orthogonal Test Datas

Factor	Iron Analysis in Metallographic Phase /%							
	K1	K2	K3	$\overline{K_1}$	$\overline{K_2}$	$\overline{K_3}$	Optimal Level	Range
A Temperature	189.90	287.17	282.97	63.30	95.72	94.32	2	32.42
B Basicity	190.83	284.59	284.62	63.61	94.86	94.87	3	31.26
CReductant Dosage	195.52	283.13	281.39	65.17	94.38	93.80	2	29.21

D Size	183.79	285.62	290.63	61.26	95.21	96.88	3	35.62

Factor	Manganese Analysis in Slag Phase /%							
	K1	K2	K3	$\overline{K_1}$	$\overline{K_2}$	$\overline{K_3}$	Optimal Level	Range
A Temperature	189.72	271.12	270.12	63.24	90.37	90.04	2	27.13
B Basicity	155.22	272.29	303.45	51.47	90.76	101.15	3	49.41
CReductant Dosage	192.32	272.15	266.49	64.11	90.72	88.83	2	26.61
D Size	193.70	265.05	272.22	64.57	88.35	90.73	3	26.16

3.2 Demonstration Test

In order to prove the accuracy of orthogonal test and analysis results, we take composite tests according to the most suitable factor combination of orthogonal test. The composite tests include two parallel tests, the test condition of demonstration1 and demonstration 2 is that temperature is 1410℃,basicity is 0.3, reductant dosage is 1.6% and size is -1mm.

Table9 The Results of Demonstration Tests

No.	Chemical Analysis Results of Metallographic Phase			Chemical Analysis Results of Slag Phase			Iron Recovery of Metallographic Phase /%	Manganese Recovery of Slag Phase /%
	Weight/g	Fe/%	Mn/%	Weight/g	Fe/%	Mn/%		
Demonstration1	129.19	95.60	1.46	109.8	0.35	30.44	95.83	98.60
Demonstration2	129.69	95.40	1.73	110.46	1.80	30.25	96.00	98.57

As shown in Table9, the demonstration tests achieve good result, besides, the results of two demonstration tests are almost the same. For this reason, we can ensure the results are accurate and reliable.

3.3 Optimized Condition Test

The optimum process conditions of using rich-manganese slag method to deal with low-grade manganese is as follows: reduction roasting temperature is 1000℃, reduction time is 45min; particle-size is -1mm, reductant dosage is 1.6%, basicity is 0.3, smelting temperature is 1410℃, smelting time is 60min. It had a good effect on the melting between slag and metallographic phase, the manganese content is 32.58%, manganese recovery is 92.16% in the slag; while the iron content is 94.40%,iron recovery is 95.32% in the metallographic phase.

Table10 The Results of Synthetical Condition Test

Chemical Analysis Results of Metallographic Phase			Chemical Analysis Results of Slag Phase			Iron Recovery of Metallographic Phase /%	Manganese Recovery of Slag Phase /%
Weight /g	Fe/%	Mn/%	Weight/g	Fe/%	Mn/%		
130.14	94.40	2.70	95.89	6.74	32.58	95.32	92.16

4. Conclusion

(1) The manganese content of the low-grade manganese in Hunan Province is only 11.89%, the iron content is 41.51%, Mn/ Fe is 0.29. It is difficult for beneficiation. The carbon-burdened and cold-bonded pelletizing-electrosmelting process is used to dispose low-grade manganese,and the qualified rich-manganese slag is obtained.

(2) The optimum process conditions to deal with low-grade manganese is as follows: reduction roasting temperature is 1000℃, reduction time is 45min; particle-size is -1mm, reductant dosage is 1.6%,basicity is 0.3, smelting temperature is 1410℃, smelting time is 60min, it had a good effect on the melting between slag and metallographic phase, the manganese content is 32.58% and manganese recovery is 92.16% in the slag; while the iron content is 94.40% and iron recovery is 95.32% in the metallographic phase.

(3) Using rich-manganese slag method can make effective use of domestic low-grade manganese and intensify the manganese's smelting, it is an effective approach to reduce the cost of manganese series ferroalloy and improves market competitiveness, it has important realism meaning.

References

[1]Wen Y C, Zhao H L, Gong M X. Kinetics on Direct Alloying in Steelmaking by Using Manganese Pellets.Journal of University of Science and Technology Beijing, 1999, 21(5): 428~431

[2]Zou W L. On a Talk of Internationalized Enterprise of Mn-industry in China. China's Manganese Industry,2007, 25(1): 48~50

[3]Zhang Z S,Wang G W,Gao Q J. Research of manganese pellets in EAF steelmaking.Metallurgical Standardization & Quality, 2005, 5: 29~31

[4]Tong J. Analysis and Suggesttions on Imported Manganese Ore.Ferro-alloys ,2004, (1): 31~33

[5]Tan Z Z,Mei G G,Li W J.Manganese Metallurgy.Hunan:Central South University Press,2004:199

AUTHOR INDEX
3rd International Symposium on High Temperature Metallurgical Processing

L

M

N

P

Q

R

S

T

W

X

Y

Z

SUBJECT INDEX
3rd International Symposium on High Temperature Metallurgical Processing

S

T

U

V

W

X